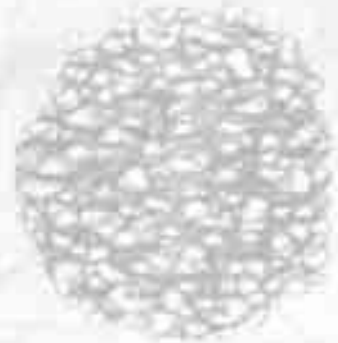
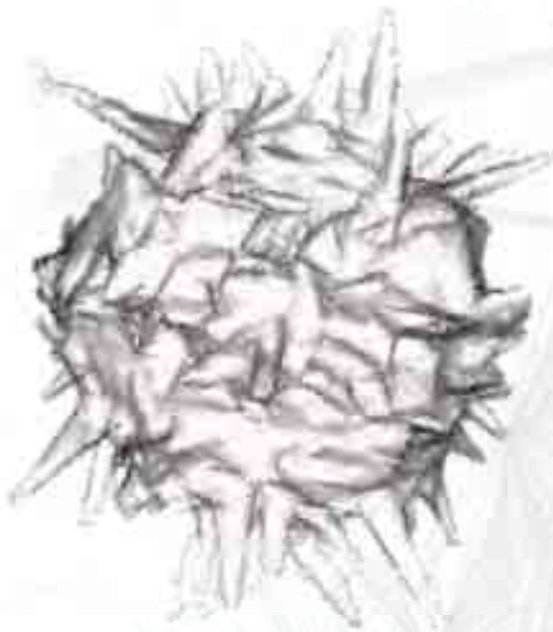


Magnetic-plasmonic nanoparticles for multimodal bioimaging and hyperthermia

Ph.D. Thesis

Cristina de la Encarnación Bermúdez



Supervised by:

Prof. Luis M. Liz-Marzán

Dr. Dorleta Jimenez de Aberasturi

Donostia-San Sebastián 2022



Universidad
del País Vasco

Euskal Herriko
Unibertsitatea

Magnetic-plasmonic nanoparticles for multimodal bioimaging and hyperthermia

PhD thesis

Cristina de la Encarnación Bermúdez

Supervised by:

Professor Luis Manuel Liz Marzán and

Dr. Dorleta Jimenez de Aberasturi Arranz

Donostia – San Sebastián 2022



Magnetic-plasmonic nanoparticles for multimodal bioimaging and hyperthermia

A manuscript submitted to the University of the Basque Country

For the degree of doctor in sciences

Presented by Cristina de la Encarnación Bermúdez

Under the supervision of:

Luis Manuel Liz Marzán (CIC BiomaGUNE)

Dorleta Jimenez de Aberasturi Arranz (CIC BiomaGUNE)

Donostia - San Sebastián 2022



**TESI ZUZENDARIAREN BAIMENA TESIA
AURKEZTEKO**

**AUTORIZACIÓN DEL/LA DIRECTORA/A DE TESIS
PARA SU PRESENTACIÓN**

Zuzendariaren izen-abizenak / Nombre y apellidos del/la director/a: Luis Manuel Liz Marzán

IFZ /NIF: 33304170D

Tesiaren izenburua / Título de la tesis: Magnetic-plasmonic nanoparticles for multimodal bioimaging and hyperthermia

Doktorego programa / Programa de doctorado: Química Aplicada y Materiales Poliméricos

Doktoregaiaren izen-abizenak / Nombre y apellidos del/la doctorando/a: Cristina de la Encarnación Bermúdez

Unibertsitateak horretarako jartzen duen tresnak emandako ANTZEKOTASUN TXOSTENA ikusita, baimena ematen dut goian aipatzen den tesia aurkez dadin, horretarako baldintza guztiak betetzen baititu.

Visto el INFORME DE SIMILITUD obtenido de la herramienta que a tal efecto pone a disposición la universidad, autorizo la presentación de la tesis doctoral arriba indicada, dado que reúne las condiciones necesarias para su defensa.

Tokia eta data / Lugar y fecha: San Sebastián, 14 de diciembre de 2022

**Luis Liz
Marzán**

Firmado
digitalmente por
Luis Liz Marzán
Fecha: 2022.12.14
22:12:41 +01'00'

Sin. / Fdo.: Tesiaren zuzendaria / El/La director/a de la tesis



**TESI ZUZENDARIAREN BAIMENA TESIA
AURKEZTEKO**

**AUTORIZACIÓN DEL/LA DIRECTORA/A DE TESIS
PARA SU PRESENTACIÓN**

Zuzendariaren izen-abizenak / Nombre y apellidos del/la director/a: Dorleta Jimenez de Aberasturi Arranz

IFZ /NIF: 44674648T

Tesiaren izenburua / Título de la tesis: Magnetic-plasmonic nanoparticles for multimodal bioimaging and hyperthermia

Doktorego programa / Programa de doctorado: Química Aplicada y Materiales Poliméricos

Doktoregaiaren izen-abizenak / Nombre y apellidos del/la doctorando/a: Cristina de la Encarnación Bermúdez

Unibertsitateak horretarako jartzen duen tresnak emandako ANTZEKOTASUN TXOSTENA ikusita, baimena ematen dut goian aipatzen den tesia aurkez dadin, horretarako baldintza guztiak betetzen baititu.

Visto el INFORME DE SIMILITUD obtenido de la herramienta que a tal efecto pone a disposición la universidad, autorizo la presentación de la tesis doctoral arriba indicada, dado que reúne las condiciones necesarias para su defensa.

Tokia eta data / Lugar y fecha: San Sebastián, 15 de Diciembre 2022

**JIMENEZ DE
ABERASTURI
ARRANZ DORLETA
- 44674648T**

Firmado digitalmente por
JIMENEZ DE ABERASTURI
ARRANZ DORLETA -
44674648T
Fecha: 2022.12.15 09:18:45
+01'00'

Sin. / Fdo.: Tesiaren zuzendaria / El/La director/a de la tesis

**AUTORIZACION DEL TUTOR/A DE TESIS
PARA SU PRESENTACION**

Dra. Miren Ostra Beldarrain, como Tutora de la Tesis Doctoral: Magnetic-plasmonic nanoparticles for multimodal bioimaging and hyperthermia, realizada en el Programa de Doctorado Química Aplicada y Materiales Poliméricos por el Doctorando Doña Cristina de la Encarnación Bermúdez, y dirigida por el Dr. Luis Manuel Liz Marzán y la Dra. Dorleta Jimenez de Aberasturi autorizo la presentación de la citada Tesis Doctoral, dado que reúne las condiciones necesarias para su defensa.

En San Sebastián a 14 de diciembre de 2022

EL/LA TUTOR/A DE LA TESIS

**MIREN OSTRA
BELDARRAIN
- 72449374H**

Firmado digitalmente
por MIREN OSTRA
BELDARRAIN -
72449374H
Fecha: 2022.12.15
10:04:48 +01'00'

Fdo.: MIREN OSTRA BELDARRAIN

AUTORIZACIÓN DE LA COMISIÓN ACADÉMICA DEL PROGRAMA DE DOCTORADO

La Comisión Académica del Programa de Doctorado en reunión celebrada el día 15 de diciembre de 2022, ha acordado dar la conformidad a la presentación de la Tesis Doctoral titulada: Magnetic-plasmonic nanoparticles for multimodal bioimaging and hyperthermia dirigida por el/la Dr. Luis Manuel Liz Marzán y Dr. Dorleta Jimenez de Aberasturi Arranz y presentada por Dña. Cristina de la Encarnación Bermúdez

adsrita al Departamento de Química aplicada

En San Sebastián a 15 de diciembre de 2022

EL/LA RESPONSABLE DEL PROGRAMA DE DOCTORADO

MIREN OSTR
BELDARRAIN
- 72449374H

Firmado digitalmente
por MIREN OSTR
BELDARRAIN -
72449374H
Fecha: 2022.12.15
10:02:12 +01'00'

Fdo.: MIREN OSTR BELDARRAIN

AUTORIZACIÓN DEL DEPARTAMENTO

El Consejo del Departamento de Química aplicada en reunión celebrada el día 20 de diciembre de 2022, ha acordado dar la conformidad a la admisión a trámite de presentación de la Tesis Doctoral titulada: *"Magnetic-plasmonic nanoparticles for multimodal bioimaging and hyperthermia"*, dirigida por el Dr. Luis Manuel Liz Marzán y la Dra. Dorleta Jimenez de Aberasturi Arranz y presentada por Dña. **Cristina de la Encarnación Bermúdez** ante este Departamento

En Donostia a 20 de diciembre de 2022

Vº Bº DIRECTOR DEL DEPARTAMENTO

SECRETARIA DEL DEPARTAMENTO

JOSE
MANUEL
SECO
BOTANA -
15990909K

Firmado
digitalmente por
JOSE MANUEL
SECO BOTANA -
15990909K
Fecha:
2022.12.20 ®
13:21:49 +01'00'



ROSA
MARIA
GARCIA
ARRONA -
72435622C

Firmado
digitalmente por
ROSA MARIA
GARCIA ARRONA
- 72435622C
Fecha:
2022.12.20 ®
14:55:45 +01'00'

Fdo.: JOSE MANUEL SECO BOTANA

Fdo.: ROSA GARCIA ARRONA

ACTA DE GRADO DE DOCTOR O DOCTORA ACTA DE DEFENSA DE TESIS DOCTORAL

DOCTORANDO/A DON/DÑA: Cristina de la Encarnación Bermúdez

TITULO DE LA TESIS: Magnetic-plasmonic nanoparticles for multimodal bioimaging and hyperthermia

El Tribunal designado por la Comisión de Postgrado de la UPV/EHU para calificar la Tesis Doctoral arriba indicada y reunido en el día de la fecha, una vez efectuada la defensa por el/la doctorando/a y contestadas las objeciones y/o sugerencias que se le han formulado, ha otorgado por _____ la calificación de:
unanimidad ó mayoría

SOBRESALIENTE / NOTABLE / APROBADO / NO APTO

Idioma/s de defensa (en caso de más de un idioma, especificar porcentaje defendido en cada idioma):

Castellano _____

Euskera _____

Otros Idiomas (especificar cuál/cuales y porcentaje) _____

En _____ a _____ de _____ de _____

EL/LA PRESIDENTE/A,

EL/LA SECRETARIO/A,

Fdo.:

Fdo.:

Dr/a: _____

Dr/a: _____

VOCAL 1º,

VOCAL 2º,

VOCAL 3º,

Fdo.:

Fdo.:

Fdo.:

Dr/a: _____ Dr/a: _____ Dr/a: _____

EL/LA DOCTORANDO/A,

Fdo.: _____

Aknowledgments

A **Luis**, por creer en mí y darme la oportunidad que me ha traído hasta aquí a escribir estas palabras, por tu gran capacidad de hacer siempre las preguntas correctas, por saber cómo y cuándo enderezar el camino cuando se tuerce.

Gracias por estos 3 años y medio de aprendizaje y cariño. Gracias por la capacidad de crear y mantener a un grupo totalmente unido que trabaja desde la amistad y el compañerismo. Siento una enorme gratitud y admiración hacia ti y me siento muy afortunada de haber formado parte de este increíble grupo.

A **Dorleta**, por apoyarme en todo momento y guiarme también en la distancia, por enseñarme el lado positivo de aprender a ser independiente a base de fallos, por escuchar mis ideas y celebrar mis éxitos como si fueran tuyos, gracias por esa locura tan especial y por acompañarme hasta aquí. Ha sido un placer ser la Dorletina II y si me dieran a elegir volvería a hacer esta tesis una y otra vez.

A **mis padres**, que siempre confiaron en mí y que me apoyaron hasta el final, mamá, papá gracias por financiar todos mis sueños y dejarme hacerlos realidad.

A mi **hermana Sara**, por contagiarme su ambición y su afán de superación, por acompañarme en la distancia y porque hemos pasado las mejores navidades de nuestras vidas, gracias por ser el mejor ejemplo a seguir.

A mi compi **Arrate**, porque siempre supo cuando estar, por todas las cosas que descubrimos tener en común, gracias por tu altruismo, tu tiempo, tus consejos, las vainitas que ricas, los piercings improvisados, todas las clases de euskera, las mañanas de gymsito y, sobre todo, gracias por escucharme siempre en los días buenos y en los malos.

A mi compi **Iñigo**, por tu sencillez y tu generosidad, por estar siempre dispuesto a ayudar a los demás, por la babadora y porque estoy harta de tus viajecitos Gru! Siempre Carcedo pringao, gracias por elegirme en el casting de Got Talent de los pisos de Donosti y, sobre todo, gracias por tu bondad.

Arrate, Iñi, habéis sido mi familia aquí, compartir piso con vosotros ha sido un regalo, gracias por haber hecho todo más fácil.

A **Ada**, ay Adaren, si a alguien tengo que AGRADECER, en mayúsculas, es a ti. Gracias por tu paciencia, por toda tu ayuda, por todo el tiempo que has invertido en enseñarme una y otra vez las mismas cosas, por tus clases de euskera y por tu eterna disponibilidad. Ojalá hubiera una Ada en cada laboratorio del mundo y ojalá allá donde vaya encuentre a alguien que sea la mitad de todo lo que eres tú. Mil gracias por estar siempre ahí, Adacadabra.

A **Elisa**, Elaisiiiiiii, che ti devo dire, grazie per esserci sempre. Grazie ad ogni consiglio, ad ogni caffè, ad ogni secondo che mi hai regalato, ad ogni NON MI DIRE DAIIIIIIII. Grazie per i bei momenti che abbiamo condiviso, sei stata un pilastro essenziale in questo viaggio. Dal inicio alla fine, abbiamo sofferto, abbiamo saltato il coprofuoco facendo misure di Raman... ma soprattutto abbiamo riso e abbiamo compartido i momenti più importantes dei nostri dottorati. Da la piattaforma di persone colpite dalle tesi tesi di Dorleta alla coperta di Hussein. Grazie di cuore. Non c'era una persona migliore per essere la mia Dorletina 1.

A **Malou**, por tu disponibilidad y ayuda constante, por todas las células que has alimentado con mis partículas, por tu organización y la claridad de tus ideas, gracias por aportar siempre de una manera tan constructiva y por todo lo que me has ayudado en esta caótica racha final.

Vished, oh Vished van Gogh! Selfie ma'am! Thank you for all the good moments in the lab, for being the Dj of Lab2 and for our paper-bin-ball championship. If I've been able to scale up my nanostars is because you help me that Friday afternoon! Thank you for being always there, playing Alan Walker with your smile.

A **Javi Lobatón**, por todas esas estrellas que hemos hecho juntos, por compartir el almacén de balones conmigo y porque al final sí pude ser un poco independiente! Gracias por las risas y por acompañarme en los primeros y desastrosos pasos del doctorado.

A **Pauliña**, por todos esos planes de los que no te has escurrido, por tu espíritu aventurero, por el título de supervivencia cuando sacamos tu coche del barro, por todos los momentos que hemos compartido y porque Vigo es feísimo! Espero que aún nos queden muchas partidas de "Adiviña a palabriña". Gracias por tus ganas constantes de hacer cualquier plan, aunque siempre gane el de escalar!

A **Paula V**. porque nunca olvidaré esa conversación sobre la silk-epig, por abastecernos de sangría desde la txalupa y por estar ahí para resolver esas dudas biológicas! Gracias por los buenos momentos.

A **Uxu**, por todas esas mañanas haciendo rodes y esas tardes en la txalupa bañándonos en alta mar, gracias Uxu por transmitir siempre tanta paz y por tu apoyo en los días malos. Te dejo al timón del barco de las dorletinas, aunque estoy segura que llegará a un buen puerto.

A **Laura A**. por ser mi compañera de fiestas, por ir mano a mano a llenarnos de purpurina en Bilbao, a dar puñetazos a la clase de boxing o a vender farolillos en Bayona. Gracias por tu simpatía y tus ganas de hacer planes!

A **Mathias**, porque la primera frase que me dijiste me ha perseguido todo este tiempo: "verás que en el doctorado a veces estás arriba y a veces abajo", gracias por todos tus consejos, los cafés, y

todos los planes fuera del lab. Ha sido un placer meterme siempre con tu acento francés! Gracias por ser buen compañero y mejor amigo.

A **Plou** por esas tardes jugando a volley, los pintxopotes, y esas noches haciéndonos selfies con Miguelito. Dudo que encuentre un rival a tu altura para jugar a "Adivina de qué año es esta canción". Gracias por ver todo siempre con optimismo y por ser el alma de la fiesta, aunque sólo sea de cuando en cuando.

A **Clara**, (distinta Clara), por compartir absolutamente todos los cafés desde el día que llegué, siempre serás la que me recogió en la puerta el primer día! Gracias por todos tus consejos, tu ayuda y por poner siempre un poco de calma a la locura del lab2!

A **Charlie**, por los viajes a mercadona, por las excursiones y por todas las veces que has hecho de mi chofer, Ambrosio, gracias por todas las comidas en tu casa y por acompañarme a casi cualquier sitio! Por todas las veces que me has llevado a casa y por todos los audios explicándome conceptos de física! Gracias por tu ingenuidad, por tu bondad y por estar siempre disponible.

A **Judith**, gracias por tus lecciones de Raman y por las cervecitas después del trabajo. No echaré de menos las medidas eternas en el WITec... pero a ti si!

A **Marita**, por las spiky antennas! Por la punta de diamante que nos cargamos, por ese oro que no agitamos y por todas las promos de bulldog que hemos hecho juntas. Ha sido un placer trabajar contigo, en todos los ambientes, gracias por tu alegría!

A **Pablo**, porque llegaste y cambió todo, por todas las excursiones y los barquitos de Uxu, por esas mañanas con los viejos del gym y esas cenas con Arrate en tu casa o en la mía, gracias por ser tan del sur, con todo lo bueno que eso conlleva.

A **David**, por todas las canciones que hemos versionado en el lab, por las meriendas y por haber visto la creación y destrucción de la pizza vegana. Por esas tardes corrigiendo presentaciones slide by slide. Gracias por tu apoyo y por hacer la request del bidón azul!
Zorte on! (Que significa buena suerte en euskera)

Xiaolu, thank you for all the moments shared doing PMA or in the TEM expert. It's been a real pleasure learning from you.

A **Lariña**, por el increíble verano que hemos pasado, por el equipo bulldog y ese atardecer en San Juan de Luz. Por seguir comentando los cotilleos gallegos! Gracias por tu dulzura y por tu cariño.

Veronica, per la migliore estate della tesi, per tutti i viaggi e le risate. Grazie per essere sempre pronta per una birra, una passeggiata o qualsiasi cosa. Grazie per tutte le cattiverie condivise!

A **Patri**, porque tu historia está mal contada y nadie te la cree! Es una pena que no hayamos podido compartir más ratos de fiesta. Gracias por tu locura y por tu apoyo al final de la tesis.

A **Bea** porque todavía no tengo una copia completa del notebook y aun así sigues hablándome. Por ser compañera de trabajo y amiga, gracias por tu paciencia y tu simpatía.

A **Andrés**, oh señorita Patricia, lo digo y lo repito: eres mi novio favorito! Gracias por tu locura, por tus constantes ganas de ir de fiesta y por todas las risas que nos hemos echado.

A veces Cris la mala no es tan mala: sois lo mejor.

Heloise, Jhoan, Cristian, Oscar, Kyle, Anish, Lorena, Yizhi... thank you for your support and your help!

A **Álex**, por todos los buenos momentos que hemos compartido, por estar siempre a pesar de la distancia y porque tu apoyo incondicional ha sido imprescindible para llegar hasta aquí, gracias por todo el tiempo que me has dedicado.

A **Damián**, porque fuiste mi primer amigo aquí, por todas las risas que hemos compartido, por esas noches en el Victoria y todas las sesiones de fotos que hemos hecho, gracias por ser amigo por encima de todo.

Ceci grazie per tutti i momenti insieme, per i viaggi è per essere lì dall'inizio. Per quelli allenamenti alla Perla e per tutte le foto di unghie che ci abbiamo girato!

A **Anna**, por todos los viajecitos que hemos compartido, porque PINTA MAL, y porque no me intentes convencer de que eres genial y te echaré de menos.

A **Donato**, por estar desde el principio hasta el final, por decir siempre que si a cualquier plan. Porque, aunque a veces haya querido matarte, en el fondo siempre te he tenido un cariño especial. Gracias por todos los buenos recuerdos que hemos creado.

A **Antonio**, por que por fin vas a dejar de preguntarme que cuando acabo! Gracias por integrarme cuando llegué allá por mayo de 2019. Gracias por todos los planes que has organizado y me has invitado. Ancoñito, vales oro!

A **Félix**, gracias por los buenos momentos, por ofrecerme siempre un sofá donde dormir cuando había toque de queda y por compartir esos desayunos al día siguiente.

A **Joaco**, Joaquinitooooo, gracias por todos los planes, los viajecitos y las cervezas en el murito. Ya sabes que si la ciencia no nos va muy bien tenemos un negocio pendiente.


A **Pauli**, porque me has visitado en todos los sitios en los que he vivido, y este no iba a ser menos. Siempre lo diré, viniste el mejor día. Muchas gracias por tu amistad y por estar siempre ahí, en lo bueno y en lo malo.

A **Cinti**, por estar siempre, a pesar de la distancia. Gracias por mostrar siempre interés por todo lo que hago, por tu admiración y tu apoyo incondicional. Por celebrar mis éxitos como si fueran tuyos. GRACIAS, porque eres el ejemplo más real de lo que es la amistad.

A **Andrew**, porque, aunque nuestros caminos tomaron direcciones diferentes sé que siempre estarás ahí para echarnos unas risas, gracias por tu amistad porque cada vez que pienso en ti solo tengo recuerdos felices.

Claire, thank you for the opportunity to learn from you, it was a quick and hard journey but... what a journey! **Charles, Elliot, Shubam, Efra**... thank you for all your help, I don't know what I would have done without you... thank you for opening me the doors at IPGG, for saving me when I got stuck, thank you for showing me the city and going out to eat cheeses with me. Thank you because from the first until the last day, you made me feel at home.





*A mi familia
por su amor incondicional*

“Las pequeñas mejoras diarias producen con el tiempo increíbles resultados. Yo lo llamo ‘efecto multiplicador’. Los pequeños actos que se realizan todos los días se multiplican hasta alcanzar un éxito inimaginable”

————— *Robin S. Sharma*



General contents

| | |
|--|-----|
| Resumen | 1 |
| Abbreviations | 7 |
| Aims and scope | 11 |
| 1. Introduction | 17 |
| 1.1 The importance of cancer theranostics | 18 |
| 1.2 Nanoparticles: <i>a multifunctional alternative</i> | 23 |
| 1.3 Nanoparticles for bioimaging | 31 |
| 1.4 Nanoparticles for hyperthermia | 36 |
| Thesis contents | 40 |
| References | 42 |
| 2. Synthesis of hybrid nanostars for multimodal bioimaging | 69 |
| 2.1 Introduction | 70 |
| 2.2 Synthesis of magnetic nanoparticles | 71 |
| 2.3 Synthesis of plasmonic nanoparticles | 72 |
| 2.4 Synthesis of hybrid iron oxide-gold nanoparticles | 73 |
| 2.5 Functionalization | 78 |
| 2.6 Application of nanoparticles for imaging | 87 |
| 2.7 Conclusions | 100 |
| 2.8 Experimental Section | 101 |
| References | 113 |
| 3. Synthesis of hybrid nanostars for hyperthermia | 119 |
| 3.1 Introduction | 120 |
| 3.2 Optimization of hybrid nanoparticles for hyperthermia | 121 |
| 3.3 Photothermal characterization | 126 |
| 3.4 Hyperthermia in 2D cell cultures | 134 |
| 3.5 Hyperthermia in 3D cell spheroids | 135 |
| 3.6 Conclusions | 136 |
| 3.7 Experimental Section | 137 |

| | |
|---|-----|
| Rereferences | 142 |
| 4. Synthesis of hybrid core-shell nanoparticles for hyperthermia | 147 |
| 4.1 Introduction | 148 |
| 4.2 Synthesis of hybrid nanoparticles: a new approach | 149 |
| 4.3 Photothermal characterization of hybrid nanoparticles | 157 |
| 4.4 Hyperthermia in 2D cell cultures | 160 |
| 4.5 Hyperthermia in 3D cell cultures | 162 |
| 4.6 Selective hyperthermia through cell targeting | 163 |
| 4.7 Conclusions | 164 |
| 4.8 Experimental Section | 165 |
| References | 173 |
| 5. Guidelines on reporting the photothermal effect of plasmonic nanoheaters | 181 |
| 5.1 Introduction | 182 |
| 5.2 Synthesis and characterization of gold nanostars | 184 |
| 5.3 Photothermal measurements | 185 |
| 5.4 Results | 190 |
| 5.5 Conclusions | 191 |
| 5.6 Experimental Section | 193 |
| References | 194 |
| 6. Conclusions | 199 |
| Publications list | 203 |
| Appendix A | 205 |

Esta tesis se ha centrado en la síntesis y optimización de nanopartículas (NPs) híbridas compuestas de oro y óxido de hierro, para su uso como agentes de contraste para bioimagen multimodal y como fotosensibilizadores para terapia fototérmica. La bioimagen multimodal consiste en la combinación de diferentes técnicas de imagen con el fin de obtener información complementaria de cada una de ellas y así compensar las limitaciones propias de cada técnica individual. Las técnicas que se han seleccionado durante esta tesis son la imagen por resonancia magnética (MRI), imagen por dispersión Raman mejorada en superficie (SERS) y la microscopía de fluorescencia. Cada una de dichas técnicas posee ciertas ventajas y limitaciones, que pueden ser contrarrestadas mediante su combinación. En particular, MRI es una técnica cuyo uso está muy extendido en clínica para obtener imágenes de alta calidad de una manera no invasiva y evitando el uso de radiación ionizante (rayos X). Además, no tiene límites en cuanto a su penetración a través de tejidos biológicos, lo cual le permite atravesar las estructuras del cuerpo humano para su estudio. Sin embargo, su baja resolución espacial no permite el estudio en detalle de dichas estructuras.

Por otro lado, el uso de la técnica de microscopía de fluorescencia está ampliamente extendido ya que permite la visualización de procesos biológicos a nivel molecular, mediante procedimientos no invasivos y sin radiaciones ionizantes. De manera similar, SERS es una técnica emergente de bioimagen cuyas principales ventajas sobre la microscopía de fluorescencia incluyen la posibilidad de multiplexado y la estabilidad de la señal a largo plazo. De esta forma, se pueden obtener imágenes más detalladas dentro de sistemas biológicos y durante periodos más largos de tiempo.

Para aumentar la calidad de las imágenes y, mejorar así su valor diagnóstico, generalmente se utilizan agentes de contraste. Dichos agentes de contraste mejoran la visualización de estructuras normales o lesiones en las imágenes producidas y ayudan a distinguir las áreas del cuerpo seleccionadas de los tejidos circundantes. Las NPs híbridas de oro y óxido de hierro ofrecen la posibilidad de combinar sus propiedades plasmónicas y magnéticas, respectivamente, para su uso como agentes de contraste. Las propiedades intrínsecas de estos materiales permiten su aplicación directa en algunas de las técnicas, por ejemplo, NPs magnéticas para MRI, sin embargo, suele ser necesario funcionalizar las NPs con diferentes moléculas para dotarlas de propiedades específicas para su uso en SERS, fluorescencia y otras aplicaciones adicionales como el etiquetado específico de células.

Además, estas NPs se pueden utilizar también como agentes fotosensibilizadores para terapia por hipertermia. La palabra hipertermia se refiere a una condición en la que la temperatura aumenta anormalmente en el cuerpo por encima de 42 °C, causando daño celular. Por encima de esta temperatura, se desencadenan en las células diversos procesos, como la desnaturalización de proteínas, la alteración del citoesqueleto o cambios en la transducción de señales, que dan lugar a la activación de mecanismos de muerte celular. A lo largo de esta tesis se ha realizado un estudio detallado del uso de NPs plasmónicas como fotosensibilizadores que actúan absorbiendo luz y

convirtiéndola en calor. Por lo tanto, se ha evaluado su aplicación como agentes para calentamiento fototérmico.

Esta tesis se ha estructurado por consiguiente en torno a tres objetivos principales: (1) la síntesis, optimización y caracterización de NPs híbridas con diferente conformación a través de la combinación de NPs de oro y de óxido de hierro con diferentes morfologías; (2) el estudio de las propiedades de las NPs híbridas para su uso como agentes de contraste para bioimagen multimodal y (3) el estudio del uso de NPs híbridas como fotosensibilizadores para su aplicación en calentamiento fototérmico.

A continuación, se presenta un breve resumen de cada uno de los capítulos en los que se estructura la tesis.

En el **Capítulo 1** se presenta una introducción general de los principales aspectos relacionados con la síntesis y caracterización de NPs, así como aspectos técnicos y analíticos sobre técnicas de bioimagen e hipertermia que se consideran necesarios para comprender la descripción del trabajo. En particular, se explican los métodos de obtención más utilizados para la síntesis de NPs de óxido de hierro y de oro, así como la morfología de las estructuras más usadas para ambos materiales. Asimismo, en este capítulo se describen las diferentes combinaciones de ambos materiales para la obtención de NPs híbridas, junto con las técnicas de funcionalización más utilizadas para su aplicación en diferentes campos. Se ha incluido una explicación de las principales técnicas de caracterización para partículas híbridas, destacando la importancia de una correcta caracterización de dichas nanoestructuras complejas, a fin de analizar la potencial influencia de cada componente sobre las propiedades inherentes del otro. Además, dado que tanto las NPs de oro como las de óxido de hierro se pueden utilizar como agentes de contraste, su combinación en estructuras híbridas resulta de gran interés para disponer de las características de ambos componentes en una única NP. Esto permite su uso como agentes de contraste multimodales para la obtención de imágenes correlativas. Por ello, se analizan los principios básicos de las principales técnicas de imagen y la forma en la que actúan las NPs para generar contraste en dichas técnicas.

Asimismo, a lo largo de este capítulo se explica el uso de NPs para como agentes terapéuticos. Las técnicas de hipertermia localizada, incluyendo la terapia fototérmica (PTT) y la hipertermia magnética (MHT), han surgido como tratamientos innovadores y selectivos, para los cuales se pueden usar NPs magnéticas y plasmónicas como fotosensibilizadores. En particular, las NPs plasmónicas actúan como fotosensibilizadores muy eficientes en PTT, mientras que las NPs magnéticas pueden utilizar la energía absorbida de campos magnéticos externos para generar calor en MHT. En este capítulo se describe el uso de partículas de oro y óxido de hierro de manera individual para PTT y MHT y, además, se discuten las ventajas y desventajas de la combinación de ambas para potenciar un incremento de temperatura usando NPs híbridas.

En el **Capítulo 2** se presenta en detalle una nueva estrategia para la síntesis y optimización de NPs híbridas (magnéticas-plasmónicas) multifuncionales, haciendo hincapié en su aplicación como

agentes de contraste en bioimagen multimodal. En particular, se ha estudiado su uso para la combinación de MRI, SERS y microscopía de fluorescencia.

El método consiste en la síntesis de NPs multinúcleo de hierro y la posterior adsorción de pequeñas NPs de oro en su superficie. A continuación, se realiza el crecimiento controlado de un revestimiento de oro en forma de estrella. Además, se ha determinado que el grosor de la capa de oro y la morfología y longitud de las puntas pueden controlarse mediante modificaciones, tanto de la densidad de NPs de oro depositadas sobre los núcleos de óxido de hierro, como de las condiciones del posterior crecimiento de las nanoestrellas híbridas. Esta síntesis se optimizó en cada paso para maximizar el potencial de las NPs para las aplicaciones deseadas. Las NPs híbridas se funcionalizaron con diferentes moléculas, en este caso se usaron moléculas activas en Raman y moléculas fluorescentes. En este capítulo se reporta además una caracterización completa de las NPs híbridas, incluyendo técnicas de tomografía electrónica, reconstrucciones 3D y análisis elemental, que se llevaron a cabo en colaboración con el grupo de Microscopía Electrónica para Ciencia de Materiales dirigido por la Prof. Sara Bals en la Universidad de Amberes. Además, se muestra el estudio del rendimiento de las NPs híbridas como agentes de contraste multimodales para la obtención de imágenes correlativas usando las técnicas de imágenes mencionadas sobre modelos celulares *in vitro*. El estudio se realizó primero usando modelos celulares (en 2D y 3D) y posteriormente en muestras de tejido *ex vivo*.

En el **Capítulo 3** se ha seguido el mismo protocolo para la síntesis de NPs híbridas que en el capítulo anterior, pero se ha realizado una optimización adicional prestando especial atención a su uso potencial como fotosensibilizadores para calentamiento fototérmico (PTH). En especial, las NPs de metales nobles pueden utilizarse como fotosensibilizadores ya que son altamente eficientes en la conversión de la luz absorbida en forma de calor. Al irradiar las NPs de oro con un láser que emite un haz coherente y focalizado de fotones a una longitud de onda específica, se produce un rápido proceso de calentamiento que comienza con una excitación de electrones libres en las NPs metálicas. Los electrones saltan a un estado de energía excitado, seguido de un proceso de relajación que comprende la dispersión electrón-electrón y que, en última instancia, conduce a un aumento de la temperatura en la superficie. Uno de los procesos por los que la temperatura se estabiliza y regresa a un estado de equilibrio, consiste en interacciones fonón-fonón con el medio circundante. Dichas interacciones fonón-fonón disipan el calor a través de la interfaz partícula-medio, hasta que las NPs vuelven a su temperatura superficial inicial. La eficiencia fototérmica de las NPs como fotosensibilizadores depende en gran medida de la morfología y el tamaño de las NPs. En términos de eficiencia, es preferible que las NPs presenten una eficiencia baja en la dispersión de luz y una absorción elevada en la longitud de onda de emisión del láser que se va a utilizar para la irradiación. Así, el ajuste del máximo de absorbancia para las NPs, el cual depende de su tamaño y forma, permite seleccionar la morfología más adecuada para la longitud de onda del láser que se va a utilizar. Para el uso de las NPs híbridas como fotosensibilizadores para PTH se ha considerado necesario disminuir el tamaño total de las NPs. Para ello, se ha investigado el papel de la presencia de agua durante la síntesis de los núcleos de óxido de hierro. De esta forma, se pudieron obtener NPs con diámetros inferiores y, junto a la estrategia descrita en el capítulo

anterior para modificar el recubrimiento con oro, fue posible obtener NPs híbridas de menor tamaño y estudiar sus propiedades como fotosensibilizadores. Los experimentos de PTH que se describen en este capítulo fueron realizados principalmente durante una breve estancia de investigación (5 semanas) en el grupo de Macromoléculas y Microsistemas en Biología y Medicina (MMBM), en el Instituto Pierre Gilles de Gennes (IPGG, París), bajo la supervisión de la Dra. Claire Wilhelm. Este estudio de la capacidad de NPs de diferentes tamaños y morfologías se realizó inicialmente en disolución, a fin de comparar NPs de diferentes tamaños y también de determinar la concentración necesaria para alcanzar un calentamiento significativo, para su posterior aplicación en sistemas biológicos. Además, se sintetizó una serie de muestras de control con capacidad de calentamiento, determinando así la implicación de cada uno de los componentes de las NPs híbridas en dicho proceso de calentamiento. A continuación, se estudió el efecto fototérmico de las NPs híbridas usando cultivos celulares, primero en 2D y luego en estructuras celulares más complejas en 3D.

Mientras que el sistema de NPs descrito en los primeros capítulos consiste en un núcleo magnético con una cobertura de oro en forma de estrella, en el **Capítulo 4** se presenta la síntesis, optimización y caracterización de un modelo alternativo de NPs híbridas, para su uso como agentes fotosensibilizadores.

En este caso, el componente plasmónico, que consiste en nanobastones de oro (en inglés nanorods, AuNRs), se localiza como núcleo central de la NP híbrida. Los núcleos de AuNRs se recubrieron posteriormente con una capa de sílice y, finalmente, se crecieron NPs de óxido de hierro sobre la superficie de la capa de sílice mediante ciclos de descomposición térmica de un precursor organometálico. Las variaciones con respecto a las NPs híbridas de los capítulos 2 y 3 aportan una mayor eficiencia de los AuNRs para la generación de calor, ya que su absorbancia máxima (790 nm) es muy cercana a la longitud de onda del láser que se usó para irradiarlas (808 nm). Además, en este caso, las NPs magnéticas se sintetizaron en la parte exterior de la NP híbrida, lo cual permite mejorar la respuesta magnética, con posibles aplicaciones en separación magnética. La separación magnética es una técnica que consiste en unir específicamente una molécula (o una célula) a una partícula magnética y así separarla de su entorno a través del uso de imanes o campos magnéticos externos.

El uso de estas nuevas NPs como fotosensibilizadores se estudió en disolución, atendiendo al incremento de temperatura que producían, estableciendo así la concentración mínima necesaria para conseguir un calentamiento por encima de 42 °C (condiciones de hipertemia). Posteriormente, se realizaron estudios en 2D con cultivos celulares y en 3D con modelos similares a los del capítulo 3, pudiendo así comparar la eficiencia de ambas NPs híbridas.

A continuación, se procedió a funcionalizar las NPs híbridas con anticuerpos. En este caso, se seleccionó como anticuerpo de interés aquel que reconoce al antígeno CD44, debido a que se observa su expresión en células cancerígenas con potencial implicación en procesos de metástasis y migración celular. Los anticuerpos se unieron a la superficie de las NPs híbridas y posteriormente se utilizaron dos controles, uno positivo con células que expresan el anticuerpo CD44, para

confirmar la correcta funcionalización de las NPs, y uno negativo, que consistía en un cultivo celular en el que no todas las células expresan este anticuerpo en su superficie. De este modo, se evaluó la capacidad de las NPs para unirse de manera específica a un tipo de células determinado, con la idea de poder separarlas magnéticamente haciendo uso de imanes externos y de irradiarlas para conseguir el calentamiento específico de dichas células.

En el **Capítulo 5** se abordó la importancia de proporcionar un informe completo de las condiciones utilizadas para las medidas de calentamiento fototérmico, así como las posibles consecuencias derivadas de no especificar las condiciones de irradiación, sobre la reproducibilidad y comparabilidad de los diferentes sistemas y sus medidas.

Una parte de esta tesis se ha centrado en la aplicación de NPs híbridas para calentamiento fototérmico. Dentro de los objetivos de aprendizaje acerca del efecto fototérmico y las técnicas utilizadas para medir y evaluar el rendimiento de NPs como fotosensibilizadores, se llevó a cabo una estancia breve en el grupo de la Dra. Claire Wilhelm. Tras dicha estancia, se intentó implementar los protocolos aprendidos en nuestro laboratorio, pero se observó que las medidas, al igual que ocurre en literatura, no eran fácilmente reproducibles. En consecuencia, se procedió a analizar los parámetros que podrían afectar a las medidas, con el fin de comprender la procedencia de las diferencias observadas. Tras un estudio exhaustivo, se descubrió que algunos parámetros, de los que rara vez se informa al reportar mediciones fototérmicas son, sin embargo, clave para la reproducibilidad de las medidas. Por lo tanto, en este capítulo se describe el efecto de algunos componentes del sistema de calentamiento por irradiación con láser sobre los resultados obtenidos. Como resultado, se presentan algunas directrices que se consideran cruciales para reportar estudios del efecto fototérmico de fotosensibilizadores basados en NPs.

En este estudio, se destacaron parámetros importantes que influyen en el aumento de temperatura producido por NPs bajo irradiación láser. Además, se identificaron aspectos que rara vez son discutidos, como el uso de un colimador del haz láser, la posición del láser durante la calibración, o el uso de láseres multimodo o monomodo, como parámetros cruciales para la reproducibilidad de los resultados experimentales. Este estudio se llevó a cabo utilizando nanoestrellas de oro y se fijaron 8 condiciones diferentes, variando los parámetros mencionados. Así, se evaluó la importancia de dichos parámetros y cómo se ven afectados los valores de calentamiento obtenidos al medir la misma muestra en condiciones diferentes. Este estudio permitió concluir que es imprescindible proporcionar información precisa sobre la configuración del equipo de calentamiento, para asegurar una mínima reproducibilidad de dichas medidas.

Finalmente, aunque será necesario realizar más investigaciones, los resultados obtenidos en esta tesis han revelado el gran potencial de las NPs híbridas multifuncionales para su aplicación como agentes de contraste para bioimagen multimodal y su potencial aplicación como agentes fotosensibilizadores para terapia fototérmica. Tanto la metodología desarrollada para la obtención de NPs híbridas como los resultados obtenidos, resultarán de utilidad para la síntesis de NPs optimizadas para otras aplicaciones y podrían suponer un paso más hacia el desarrollo de plataformas teranósticas basadas en NPs.

Abbreviations

| | |
|---------|---|
| 2D | Two-dimensional |
| 2-NAT | Napthalene-2-thiol |
| 3D | Three-dimensional |
| 4-BPT | Biphenyl-4-thiol |
| Ab | Antibody |
| ADF | Annular dark field |
| Au | Gold |
| AuNCs | Gold nanocages |
| AuNPs | Gold nanoparticles |
| AuNRs | Gold nanorods |
| AuNSHs | Gold nanoshells |
| AuNTs | Gold nanotriangles |
| BF | Bright field |
| BW-I | First biological window |
| C | Carbon |
| CBED | Convergent beam electron diffraction |
| cDMEM | Complete DMEM |
| CT | Computed tomography |
| CTAB | Hexadecyltrimethylammonium bromide |
| DLS | Dynamic light scattering |
| DY-633 | 2-(3-{2-tert-butyl-7-[ethyl(3-sulfonatopropyl)amino]chromenium-4-yl}prop-2-en-1-ylidene)-1-(5-carboxypentyl)-3,3-dimethylindoline-5-sulfonate |
| ECM | Extracellular matrix |
| EDC | N-ethyl-N'-(3-(dimethylamino)propyl)carbodiimide |
| EDX | Energy Dispersive X-Ray Analysis |
| EELS | Electron energy loss spectroscopy |
| EELS | Electron energy loss spectroscopy |
| EM | Expectation Maximization |
| Fab | Fragment antigen-binding |
| FBS | Fetal bovine serum |
| FC | Field cooled |
| Fc | Fragment crystallizable |
| Fe | Iron |
| Gd | Gadolinium |
| HAADF | High angular annular dark field |
| HDF | Human dermal fibroblast |
| HRSTEM | High resolution scanning transmission electron microscopy |
| ICP-MS | Inductively coupled plasma mass spectroscopy |
| IO | Iron oxide |
| IOAuNPs | Iron oxide-gold nanoparticles |
| IOAuNSs | Iron oxide-gold nanostars |
| IONCs | Iron oxide nanocubes |
| IONFs | Iron oxide nanoflowers |
| IONPs | Iron oxide nanoparticles |
| LDH | Lactate dehydrogenase |
| LSPR | Localized surface plasmon resonance |

| | |
|------------------|--|
| MCF7 | Breast cancer cell line |
| MDA.MB.231 cells | Epithelial, human breast cancer cell line |
| MES | 2-(N-morpholino)ethanesulfonic acid |
| MHT | Magnetic hyperthermia |
| MIP | Maximum intensity projection |
| MLRA | Multiple linear regression analysis |
| MP | Multiphoton |
| MPI | Magnetic particle imaging |
| MRI | Magnetic resonance imaging |
| NaAc | Sodium acetate |
| NHS | N-Hydroxysulfosuccinimide |
| NIR | Near infrared region |
| NP | Nanoparticle |
| PAA | Polyallylamine hydrochloride |
| PAI | Photoacoustic imaging |
| PB | Phosphate buffer |
| PBS | Phosphate buffered saline |
| PC3 | Human prostate adenocarcinoma cells |
| PDDA | Poly(diallyl dimethyl ammonium chloride) |
| PdI | Polydispersity index |
| PE | Polyelectrolite |
| PEG | O-[2-(3-mercaptopropionylamino)ethyl]-O'-methylpolyethylene glycol |
| PEI | Polyethyleneimine |
| PLA | Polylactic acid |
| PLGA | Poly(lactic-co-glycolic acid) |
| PMA | Dodecylamine/polyisobutylene-alt-maleic anhydride |
| PS | Penicillin-streptomycin |
| PSS | Poly (Sodium-4-styrenesulfonate) |
| PTH | Photothermal heating |
| PTT | Photothermal therapy |
| PVA | Polyvinyl alcohol |
| PVP | Poly(vinylpyrrolidone) |
| r | Magnetic relaxivity |
| RaR | Raman-active Reporter molecules |
| ROI | Region of interest |
| SAED | Selected area electron diffraction |
| SAR | Specific absorption rate |
| SEM | Scanning electron microscopy |
| SERS | Surface-enhanced Raman scattering |
| SQUID | Superconducting quantum interference device |
| STEM | Scanning transmission electron microscopy |

| | |
|-----------|----------------------------------|
| TAMRA | 5-Carboxytetramethylrhodamine |
| TEM | Transmission electron microscopy |
| TEOS | Tetraethyl orthosilicate |
| U87 | Human glioblastoma cell line |
| UV-Vis | Ultraviolet/Visible |
| VSM | Vibrating sample magnetometer |
| XDR | X-ray diffraction |
| XPS | X-ray photoelectron spectroscopy |
| Z_{avg} | Average diameter |
| ZFC | Zero field cooled |

This thesis has been carried out in the framework of an ERC Advanced Grant entitled "Four-Dimensional Monitoring of Tumour Growth by Surface Enhanced Raman Scattering (ERC AdG 787510, 4DBIOSERS)". Within the overall objectives of this project, the use of surface-enhanced Raman scattering (SERS) for bioimaging and the photothermal treatment of cancer are major topics. In this context, the thesis has focused on the synthesis and optimization of hybrid nanoparticles (NPs) composed of gold and iron oxide, for their use as multifunctional contrast agents for multimodal bioimaging and as photosensitizers for photothermal therapy. Multimodal bioimaging is the combination of different imaging techniques to obtain complementary information and thus, overcome the limitations of each individual technique. In general, contrast agents are used in these techniques to increase the quality of the images and thereby improve their diagnostic value. Hybrid NPs made of gold and iron oxide offer the possibility of combining their plasmonic and magnetic properties, respectively, for their use as contrast agents in various imaging modalities. Functionalization of the hybrid NPs with molecular ligands, such as Raman-active molecules and fluorescent dyes, together with the intrinsic properties of the NPs, facilitate their application as contrast agents for magnetic resonance imaging (MRI), surface-enhanced Raman scattering (SERS) and fluorescence imaging.

In addition, hybrid NPs can also be used as photosensitizers for hyperthermia treatment of diseases. The word hyperthermia refers to a condition in which the body temperature rises abnormally above 42 °C, causing cell damage. Thus, the plasmonic component of hybrid NPs can act as photosensitizer for photothermal heating by absorbing light and converting it into heat.

This thesis has therefore been structured around three main objectives: **(1)** the synthesis, optimization, and characterization of hybrid NPs with different conformations through the combination of gold and iron oxide NPs with different morphologies; **(2)** the study of the properties of hybrid NPs for their use as contrast agents for multimodal bioimaging; and **(3)** the use of hybrid NPs as photosensitizers for their application in photothermal heating.

The structure of the thesis is as follows: After a general introduction (**Chapter I**), where the main aspects related to the synthesis and characterization of NPs, as well as technical and analytical aspects of bioimaging and hyperthermia techniques, are introduced. The synthesis and optimization of multifunctional hybrid (magnetic-plasmonic) NPs are subsequently introduced, with an emphasis on their application as contrast agents for multimodal bioimaging (**Chapter II**). Then, the optimization of the same hybrid NPs is reported toward their potential use as photosensitizers for photothermal heating (**Chapter III**).

A second method is proposed and demonstrated in **Chapter IV**, with an alternative distribution of components within the hybrid NPs, and improved properties for their use as nanoheaters and in magnetic separation. Finally, in **Chapter V** we discuss the importance of providing a complete description of the conditions used for photothermal heating measurements, as well as the risks related to the reproducibility and comparability of different systems and their measurements,

should the irradiation conditions not be sufficiently described. The main conclusions of the thesis are then summarized.

Chapter I



1. Introduction

Contents

| | | |
|-------|---|----|
| 1.1 | The importance of cancer theranostics | 18 |
| 1.2 | Nanoparticles: <i>a multifunctional alternative</i> | 23 |
| 1.2.1 | Magnetic nanoparticles..... | 24 |
| 1.2.2 | Plasmonic nanoparticles | 25 |
| 1.2.3 | Hybrid nanoparticles..... | 26 |
| 1.2.4 | Surface functionalization of iron oxide nanoparticles..... | 27 |
| 1.2.5 | Surface functionalization of gold nanoparticles | 28 |
| 1.2.6 | Characterization of hybrid systems | 29 |
| 1.3 | Nanoparticles for bioimaging..... | 31 |
| 1.3.1 | Magnetic nanoparticles for bioimaging..... | 31 |
| 1.3.2 | Plasmonic nanoparticles for bioimaging | 32 |
| 1.3.3 | Hybrid nanoparticles for multimodal bioimaging | 33 |
| 1.4 | Nanoparticles for hyperthermia | 36 |
| 1.4.1 | Magnetic hyperthermia..... | 36 |
| 1.4.2 | Photothermal therapy | 37 |
| 1.4.3 | Towards multitherapy: <i>photothermal therapy + magnetic hyperthermia</i> | 38 |
| | Thesis contents..... | 40 |
| | References | 42 |

1.1 The importance of cancer theranostics

Cancer is a term given to a heterogeneous group of diseases that involve the uncontrolled growth of cells, which have the ability to invade surrounding tissues and spread to other parts of the body¹. Cancer remains one of the biggest causes of morbidity and mortality worldwide, with an estimated 19.3 million new cases and nearly 10 million deaths in 2020². Although primary tumours represent an important clinical burden, the presence of cancer metastasis often suggests low survival rates with poor prognoses. The metastatic process involves the migration of cancer cells from their initial site of formation (primary cancer) to another site of the body via the blood or the lymphatic system. Interestingly, some primary cancers have special niche tissues for metastatic formation, for example, metastatic breast cancer has a tendency to spread to the lung, thus forming a breast-derived lung cancer³. Secondary metastases are the main cause of cancer morbidity and mortality, causing approximately 90% of all cancer deaths⁴. The primary method to improve survival rates and lower morbidity is to improve early cancer detection, thus significantly enhancing the lives of cancer patients⁵. An early diagnosis implies that the detection is made when the patient is asymptomatic or exhibits no symptoms of the disease. For instance, it has been found that detection at early stages plays a key role in the management of specific cancers such as cervical and breast cancer and is likely to play an important role in the treatment of lung, prostate, and colorectal cancer⁶.

According to the World Health Organization, early diagnosis consists of three components⁷:

1. Understanding the signs of various cancers and the need of seeking medical help.
2. Accessibility to clinical assessment and diagnostic services.
3. Timely referral to treatment services

Before the appearance of symptoms, screening aims to identify people with evidence suggestive of a particular malignancy or pre-cancer. If abnormalities are found during screening, additional tests to confirm the diagnosis are performed. Whilst screening programs can be complicated and costly, they are generally very useful for correctly diagnosing some types of cancer, for example, colon and breast cancers, in populations at risk⁸. Research to improve early diagnosis is motivated by the fact that cancer treatment costs directly depend on the disease stage^{9,10} and that, as such, cancer has become one of the most serious issues to directly affect public health¹¹.

Modern medicine is placing more emphasis on precision and personalized medicine as a method to increase diagnosis accuracy and improve treatment. One such method involves pre-clinical imaging to better evaluate biological processes at the cellular and molecular level, allowing the early or presymptomatic detection of diseases¹².

Imaging techniques with quick acquisition times, high sensitivity, and manageable costs, enable the viewing of physiological and pathological processes with high specificity and in real time¹³. Imaging is essential for the treatment of cancer patients. It is necessary and often used for diagnosis, for the identification of abnormalities, and for guiding biopsies. Besides, it is also important for estimating the stage of the disease and, consequently, to choose an appropriate

treatment¹⁴. One of the most widely used imaging techniques for clinical applications is magnetic resonance imaging (MRI). MRI is a non-invasive and non-ionizing imaging technique with a spatial resolution of 100 μm ^{15,16}. In MRI, an external magnetic field is used to align atomic nuclei, i.e. water protons (^1H), which are the most abundant magnetic nuclei in our body. Such an alignment creates a magnetization vector that is parallel to the applied magnetic field. To generate images, radiofrequency energy pulses at the resonance frequency are applied and energy is absorbed by the protons, which then change their orientation by rotating toward the transverse plane. When the pulse ends, the protons return to their equilibrium state and the accumulated energy is delivered as an alternating current that is different depending on the molecular environment of the protons. This current is measured in a receiver coil and used for image construction. The time that the proton needs to return to its initial state is called relaxation time and can be divided into T1, which depends on the interaction between atoms and their environment, and T2, related to the interaction of atoms with each other. MRI relies on the differences in tissue proton density and relaxation times to generate contrast. T1 is given by the time required for the excited ^1H to return to their original position, causing some energy loss into surrounding nuclei (spin-lattice relaxation). On the other hand, T2, also known as spin-spin relaxation, is the exchange of energy between high and low energy nuclei, without loss of energy to surrounding nuclei.¹⁷ That said, discrimination of certain tissues gets complicated when the relaxation differences do not generate enough contrast. To improve that, gadolinium-contrast agents have been most commonly used to enhance the contrast in the regions of interest¹⁸. By enhancing local magnetic fields, contrast agents produce changes in the magnetic susceptibility. These effects result from interactions between the nuclear and magnetic moments of the contrast agent, which intensify transitions between spin states and shorten the T1 and T2 times. In particular, gadolinium-based contrast agents cause a decrease in the T1 relaxation time turning the images brighter. Also computed tomography (CT) is frequently used to visualize nearly all parts of the body. CT is a non-invasive technique that features high spatial resolution and tissue penetration depth. In this technique, an ionizing radiation, specifically X-ray radiation, is used to obtain cross-sectional images of internal organs, bones, soft tissues, vessels, etc., by differences in the absorption and attenuation of the radiation when passing through the different tissues. X-ray images are recorded while the detector moves around and a reconstruction of the individual images into cross-sectional images or “slices” is performed. A drawback of the technique is the high radiation dose required to reconstruct the images from those individual X-ray projections. In order to enhance the quality of the image, iodinated contrast media are commonly used in CT due to their high X-ray absorption coefficient¹⁹.

Additional optical imaging techniques are gaining importance for their use in pre-clinical imaging. Besides, new techniques have been developed and are under continuous growth due to their potential properties. In this regard, fluorescence imaging is a useful and widely used technique for bioimaging that enables the visualization of biological processes at the molecular level using non-invasive procedures without ionizing radiations²⁰. The acquisition modes in fluorescence imaging are based on the capacity of a certain fluorescent substance to emit light of a specific wavelength when excited by a light source of another appropriate wavelength. Many efforts have been made

in the development of desirable fluorophores with high brightness and biocompatibility for imaging of biological samples and tissues²¹, especially with regards to those with absorbance or excitation/emission in the near infrared region (NIR) (650 -1450 nm). This wavelength range is known as the biological transparency window due to its minimal tissue absorbance, thus making it suitable for bioapplications^{22,23}.

Photoacoustic imaging (PAI) is a hybrid imaging technique that combines optical excitation and ultrasound detection with a relatively deep tissue imaging capability²⁴. In PAI, tissues are irradiated with non-ionizing laser pulses, light is absorbed by chromophores and converted into heat, producing a time variant thermoelastic expansion. This expansion process generates pressure changes in the tissues that result in the emission of acoustic waves. By using laser pulses for irradiation, this process is repeated with each pulse, thereby generating multiple waves that constitute the PA signals that are recorded by an ultrasound transducer. The signal is then measured and amplified to reconstruct a sonogram image²⁵. It has been demonstrated that PAI is an effective method for visualizing blood vessels²⁶.

The development of new emerging imaging techniques has also gained interest. For instance, magnetic particle imaging (MPI) is an emerging pre-clinical imaging system that was developed in the early 2000s²⁷. MPI is a quantitative 3D imaging technique that enables real-time imaging with high sensitivity and spatial resolution. Static and oscillating magnetic fields combined with magnetic particles (typically iron oxide nanoparticles, or IONPs), as the name indicates, are applied in this technique. Thus, MPI measures changes produced due to the magnetization of IONPs, resulting in an image that can be reconstructed considering the spatial distribution of the IONPs. Hence, there is no background, and IONPs are the only source of signal, resulting in a signal that is proportional to NP concentration²⁸.

Raman scattering, which was first introduced by Raman and Krishnan²⁹, is the term for inelastic photon scattering given by a molecule. Due to the energy transfer between light and a molecular vibration when a molecule is illuminated, the scattered light has a different frequency than the incident light. The vibrational frequency of a chemical bond in a molecule is revealed by the frequency difference, or Raman shift. As a result, the analyte's spectral fingerprints can be seen in a Raman scattering spectrum (intensity against Raman shift, in cm^{-1}). In this regard, Raman scattering has given place to an imaging modality called Raman imaging that allows for high-resolution, real-time, non-invasive imaging of tissues³⁰. However, the low efficiency of Raman scattering and therefore the sensitivity of the technique is its major limitation. Thus, strategies to overcome this limitation have been investigated. Fleischmann and colleagues noticed that when pyridine was in close proximity to a rough silver electrode, a significant enhancement of the inelastic scattering from the molecule occurred, which led to the discovery of the surface-enhanced Raman scattering (SERS) effect in 1974³¹. Thus, SERS arose as a method to enhance the efficiency of Raman scattering as an analytical technique. In fact, it has been reported that the SERS signal can be enhanced up to 10^{10} - 10^{11} times compared to normal Raman scattering³². SERS is a versatile technique that allows the precise identification of molecules that are attached or closely located to the surface of plasmonic NPs³². Additionally, each molecule's distinct

vibrational fingerprint provides unmistakable identification and detection limits up to femtomolar concentrations can be readily achieved³⁴. The SERS mechanism relies on localized surface plasmon resonances (LSPR), i.e., collective oscillations of conduction electrons in nanoparticles (NPs), in resonance with an external electromagnetic radiation, resulting in intense absorption and scattering within the ultraviolet/visible range under this optical excitation³⁵. Additionally, an amplified localized electromagnetic field is generated at the NPs surface, which is ultimately responsible for the enhancement of the Raman signal of adsorbed molecules. NPs covered by a monolayer of so-called Raman Reporter molecules (RaR) are known as SERS tags. Through the enhancement of the signal of RaR molecules in contact with the NPs surface, a specific SERS code is generated (see **Figure 1.1**). Consequently, SERS is gaining interest for its application in bioimaging³³ and SERS tags are used as contrast agents for this technique. Interestingly, the size and shape of such NPs can be changed to modify their optical properties and make them maximally absorb at a desired wavelength. A clear example of this effect is seen in gold nanorods (AuNRs) which plasmon band maxima can be tuned by modifying their aspect ratio³⁶. Apart from the high sensitivity provided by the plasmonic enhancement, down to single molecule detection, the narrow bandwidth of the detected spectral peaks (vibrational molecular fingerprint) largely facilitates multiplexing, which is highly attractive for bioimaging³⁷.

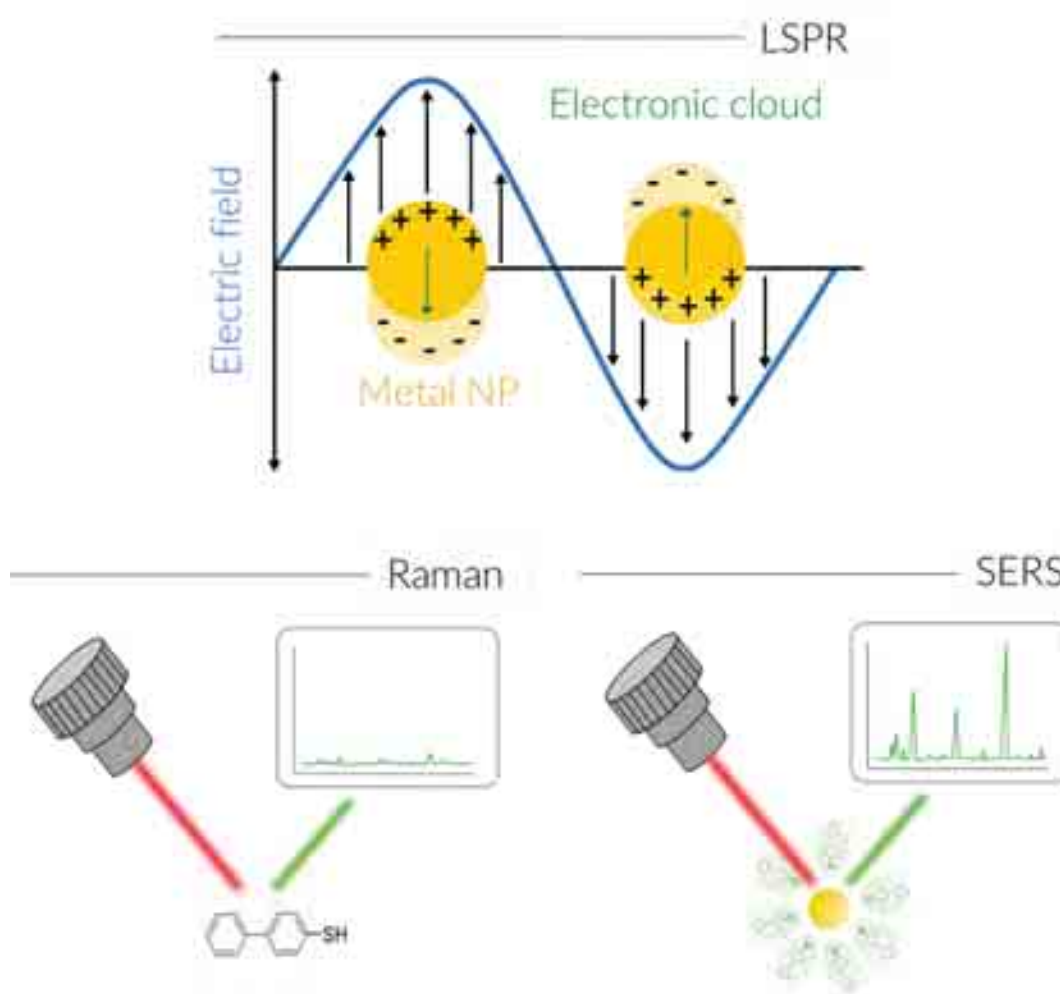


Figure 1.1. Upper part: Localized surface plasmon resonance generated when incident light interacts with a metal nanostructure smaller than the wavelength of light. Lower part: Comparison

between Raman and SERS. The enhancement of the signal is produced by the enhanced local electrical fields at metal NPs when their LSPR is excited.

Even if remarkable information can be achieved using these different imaging techniques, they present limitations. In **Table 1.1** a comparison of the presented imaging techniques is shown, pointing at their respective advantages and weaknesses^{38,39}.

Table 1.1. Comparison of the characteristics of the most used imaging techniques.

| Imaging technique | Acquisition time | Sensitivity | Advantages | Weaknesses |
|-------------------|------------------|-------------|---|--|
| Fluorescence | Rapid | Very high | High spatial resolution (200nm) Wide range of dyes available | Poor penetration (mm) Medium cost |
| SERS | Medium | Very high | High spatial resolution (1 μ m) | Poor penetration (mm) Mapping of small areas |
| MRI | Low | Low | No depth limit High soft tissue contrast | Low spatial resolution (100 μ m) Expensive |
| CT | Rapid | Low | No depth limit | Low spatial resolution (500 μ m) Ionizing radiation |
| PAI | Low | High | Low cost | Poor penetration (cm) Complex image reconstruction |
| MPI | Rapid | High | No ionizing radiation | Low spatial resolution (1mm) |

Considering the data shown in **Table 1.1**, there is not one ideal imaging technique that meets all the favourable conditions for bioimaging. Thus, multimodal imaging consisting of the combination of different imaging techniques to obtain complementary information while overcoming the limitations of each single technique has emerged as an interesting approach⁴⁰.

In this regard, fluorescence imaging is a technique that has been extensively used in bioimaging. Even so, it presents limitations such as significant tissue autofluorescence and strong light attenuation, which results in poor tissue penetration depth (less than 1 cm) and low sensitivity with high background signal⁴¹. Thus, the use of SERS imaging, which provides reduced background autofluorescence noise, in combination with fluorescence imaging, becomes an interesting approach to avoid the intrinsic limitations of fluorescence imaging alone. Even if promising performance and applications can be achieved from the combination of fluorescence imaging and SERS, issues such as suboptimal light penetration through tissue remain. Thus, their application with conventional imaging techniques used in clinical diagnostic applications, such as MRI, can be an interesting approach toward obtaining valuable information⁴². Although MRI yields excellent penetration through tissue, the low resolution of the technique gives poor information on small or single biological structures. In contrast, both SERS and fluorescence can offer excellent resolution and multiplexing, but they suffer from poor tissue penetration and a limited ability to image large areas. By combining these complementary techniques, the advantages of each one can be taken advantage of to better study biological samples or tissues.

1.2 Nanoparticles: *a multifunctional alternative*

During the last 50 years, materials at the nanometre scale (1-100 nm) have emerged as an interesting tool with different novel uses in imaging, diagnosis, and therapy. Since then, the application of nanomaterials in nanomedicine has advanced significantly, with an increase in their use to address unresolved medical issues⁴³. One of the most important developments in materials science is the use of metal NPs⁴⁴. The tuneable nature of their remarkable physicochemical properties has allowed their use in different biomedical fields, including medicine, biology, physics, chemistry, and sensing⁴⁵⁻⁴⁸. Due to their size-dependent optical, magnetic, and/or electronic properties, the application of metal NPs in the field of biomedicine can offer many advantages. In particular, plasmonic and magnetic NPs have been found to have suitable properties for their application in bioimaging techniques which typically require the use of contrast agents to enhance the signal from selected structures or fluids within the body to improve image contrast⁴⁹. For instance, MRI typically operates using contrast agents that are used to change the relaxivity of water molecules to create soft tissue contrast. Magnetic NPs are able to generate a local magnetic field resulting in a change in the nuclear relaxation of magnetic nuclei in the surroundings. These NPs can accelerate the relaxation process and shorten the relaxation time of protons nearby, enhancing the signal contrast between the surroundings and distal background in MR images. In particular, iron oxide nanoparticles (IONPs) have been studied in detail and slowly incorporated into clinical use⁵⁰. IONPs are commonly used as T2 contrast agents. However, in T2-weighted images the signal can be confused with signals from haemorrhage, calcification, or metal deposits. Therefore, the main interest is now focused on the development of T1 contrast agents⁵¹.

With regards to plasmonic NPs, such as gold or silver NPs, they present suitable properties for biomedical applications due to their respective chemical stability and antibacterial activity⁵². Their optical characteristics can be precisely adjusted by modifying NP shape and dimensions, from the visible range of the electromagnetic spectrum to the NIR, expanding their range of biological applications⁵³. Consequently, the physicochemical properties of plasmonic NPs with different morphologies and structures have been thoroughly studied, also demonstrating their potential for use in sensing, imaging, diagnostic, and therapeutic applications⁵⁴.

One interesting approach is the combination of NPs properties within the same nanostructure. This is how hybrid NPs were born, whereby two or more components with multifunctional capabilities are combined into hybrid nanostructures⁵⁵. The interest of combining magnetic and plasmonic NPs relies on the use of non-invasive imaging techniques for fast disease diagnosis.

The synthesis of magnetic and plasmonic NPs and their assembly into hybrid nanostructures will be discussed in the following section.

1.2.1 Magnetic nanoparticles

Regarding magnetic NPs, the colloidal synthesis of IONPs in particular, has been studied extensively⁵⁶. Methods for IONP fabrication can be selected to ensure control over size, shape, and composition⁵⁷. Co-precipitation, thermal decomposition, and hydrothermal processes are the most common synthesis methods⁵⁸. Co-precipitation comprises the simultaneous precipitation of Fe^{2+} and Fe^{3+} ions in a highly basic solution, usually under an inert atmosphere (N_2 or Ar), either at room temperature or at higher temperatures (above 70 °C); particles with sizes ranging from 5 to 20 nm are usually obtained via this method⁵⁹. In the hydrothermal procedure, IONPs are obtained by treating iron salt precursors at high temperatures (130–250 °C) in an autoclave, at pressures ranging from 0.3 to 4 MPa^{60–62}. By contrast, using the thermal decomposition method, IONPs are obtained through the decomposition of organometallic iron precursors, followed by oxidation in a high boiling point organic solvent containing surfactants. Monodisperse particles can be obtained with high reproducibility by using this method, but its main drawback is that biological applications require a post-synthesis phase transfer into a polar solvent⁶³. Dadfar *et al.*⁵⁰ have classified the synthetic methods for IONPs and coatings needed for different applications in diagnosis and therapy based on of their stability and non-toxic nature. Magnetite (Fe_3O_4) and its oxidized form maghemite ($\gamma\text{-Fe}_2\text{O}_3$) are the most widely used IONPs for biomedical applications⁶⁴. Both iron oxides present structural similarity comprising a cubic inverse spinel, the main difference being that magnetite is made of both Fe(II) and Fe(III) whereas maghemite contains ferric Fe(III) ions only, and shows higher thermal and chemical stability. Both materials are metastable oxides, show size-dependent magnetic properties⁶⁵, and are easily magnetized, i.e. show a magnetic response in the presence of an external magnetic field.

The magnetic properties of IONPs are directly related to their size and morphology. Particle size determines the paramagnetic or superparamagnetic response of the nanostructures, in connection to the size-dependent spin exchange effect. On the other hand, the morphology of the particles is involved through shape-induced magnetic anisotropy⁶⁶. Thus, the development of anisotropic

and faceted IONPs, such as iron oxide nanocubes (IONCs) or nanoflowers (IONFs), have been studied in connection with their use for both MRI and magnetic hyperthermia (MHT)⁶⁷.

The effect of particle size and shape on the relaxivity has also been extensively reported. Several studies have demonstrated that faceted NPs provide improved magnetism and relaxivity, as compared to spherical NPs of similar size, with an increase in the relaxation rates with increasing particle size⁶⁸. Additionally, multicore systems show an improved magnetic response in comparison to single-core NPs of similar size. While dipole-dipole interactions arise in single-core particles, exchange coupling occurs among individual crystallites in multi-core systems due to the short distance between them, thus leading to strong magnetic interactions⁶⁹. These assemblies represent a situation where aggregation of IONPs is controlled, so that no changes occur in the number of cores per particle. This system is advantageous for biomedical applications such as MRI and MHT, because of the obtained high saturation magnetization values⁷⁰. **Figure 1.2** shows the most common IONP morphologies synthesized for biomedical applications.

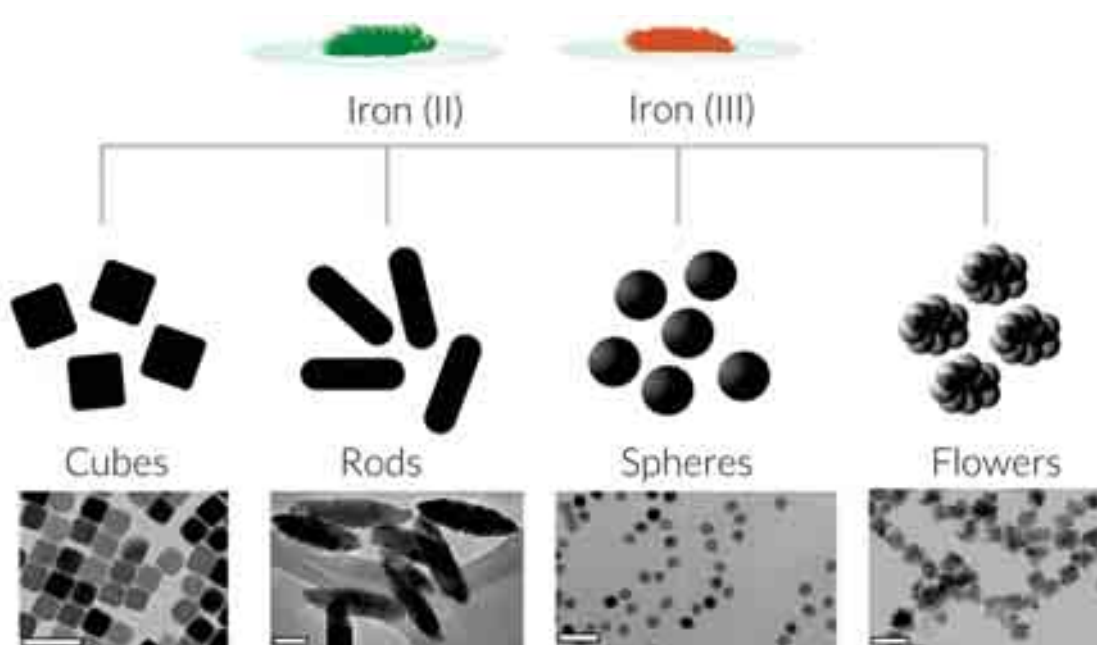


Figure 1.2. Most common morphologies of IONPs made of magnetite or maghemite, for biological applications. Scale bars correspond to 50 nm. Modified and reproduced from⁷¹⁻⁷⁴. Copyright (2012) (2018) (2021) American Chemical Society, (2008) John Wiley and Sons.

1.2.2 Plasmonic nanoparticles

Plasmonic NP synthesis can be achieved by means of a wide variety of chemical⁷⁵, physical⁷⁶ and biological⁷⁷ methods. After several decades of research on spherical gold nanoparticles (AuNPs)⁷⁸, the colloidal synthesis of anisotropic NPs has gained huge interest, mainly driven by their tuneable optical properties. Anisotropic NPs can accommodate multiple plasmon modes, related to their morphology and orientation with respect to the polarization of incident light. Additionally, elongated NPs can display LSPRs at lower energies, further in the NIR. Such an optical tunability is particularly relevant for biological applications^{44,79} because, as explained before, maximum light transmission through tissue and minimized autofluorescence are obtained in the NIR⁸⁰. AuNRs,

nanostars (AuNSs), or nanotriangles (AuNTs) are some examples of AuNPs that are anisotropic and display tuneable LSPR properties⁸¹. The most widely applied approach for the fabrication of anisotropic NPs is based on seed-mediated growth, comprising an initial step in which metal ions are reduced to form small metal nuclei, which are subsequently used as seeds for the growth of larger NPs with morphologies determined by the seed structure, surfactant (and other additives), and reaction kinetics. The most used AuNP morphologies for biological application are summarized in **Figure 1.3**.

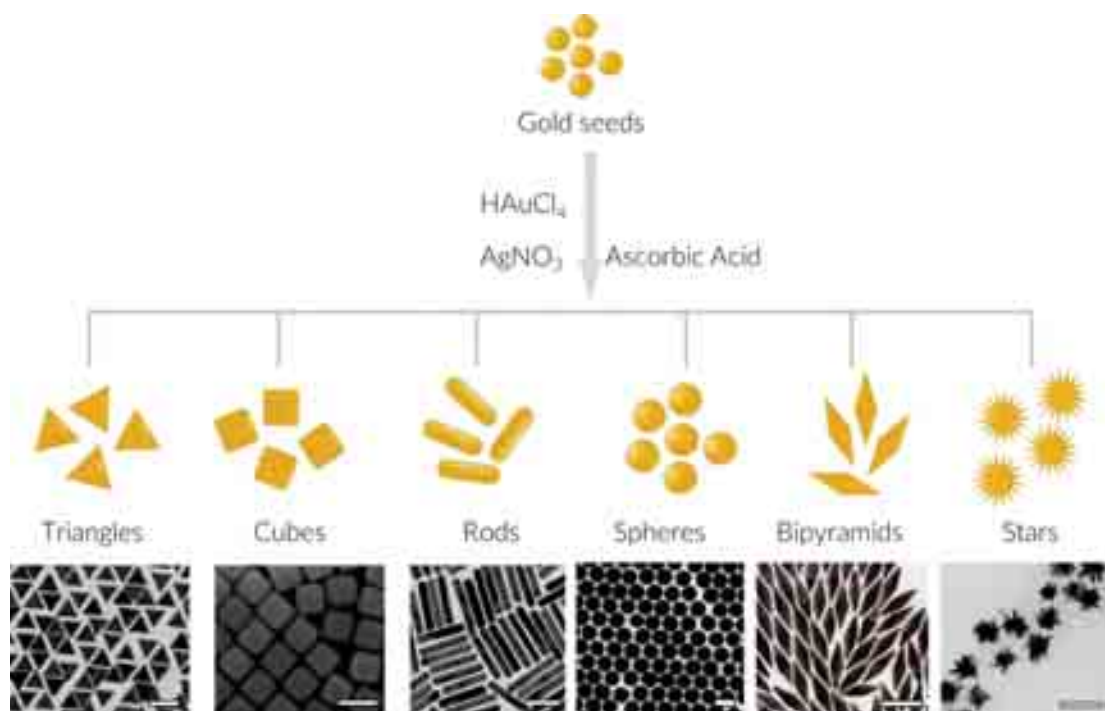


Figure 1.3. Most common morphologies obtained by seed-mediated growth of gold NPs. Scale bars correspond to 100 nm. Modified and reproduced from^{37,82-86}. Copyright (2010) (2014) (2016) (2017) (2019) American Chemical Society.

1.2.3 Hybrid nanoparticles

Considering the relative compatibility between IONPs and AuNPs in terms of size and surface functionalization methods, novel approaches for the fabrication of hybrid NPs (IOAuNPs) that combine both magnetic and plasmonic nanostructures have been reported (**Figure 1.4**). Most of these approaches require in situ synthesis of both components, as opposed to pre-synthesis steps and assembly. With regards to nanomaterials designed for biological applications, aqueous synthesis methods are the most explored ones, thanks to the lack of cytotoxic solvents and limited synthesis and functionalization steps, which reduce the possibility of contamination. Although various approaches exist, most of the plasmonic-magnetic NPs reported in literature are made of an iron oxide core surrounded by an outer plasmonic gold layer. The coating shell of such core-shell NPs is designed to enhance the stability of the IONPs and allow further diverse functionalization⁸⁷. The synthetic process comprises the reduction of Au precursors in the presence of IONPs, which act as seeds and become inner cores upon gold shell formation. For this purpose, two principal strategies have been used. On one hand, the direct synthesis of the

gold layer can be performed by adding gold precursors and a reducing agent to the dispersion of IONPs^{88,89}. This process is however hindered by a complicated control over the thickness and geometry of the gold shell. On the other hand, hybrid particles can also be achieved by first depositing an intermediate layer, which provides a suitable surface charge, facilitating the decoration with gold seeds. The density of seeds can subsequently determine the thickness and geometry of the gold shell, obtained upon reduction of gold ions⁹⁰. The intermediate layer usually comprises either silica⁹¹ or polymers such as polyvinylpyrrolidone (PVP)⁹² or polyethyleneimine (PEI)⁹³.

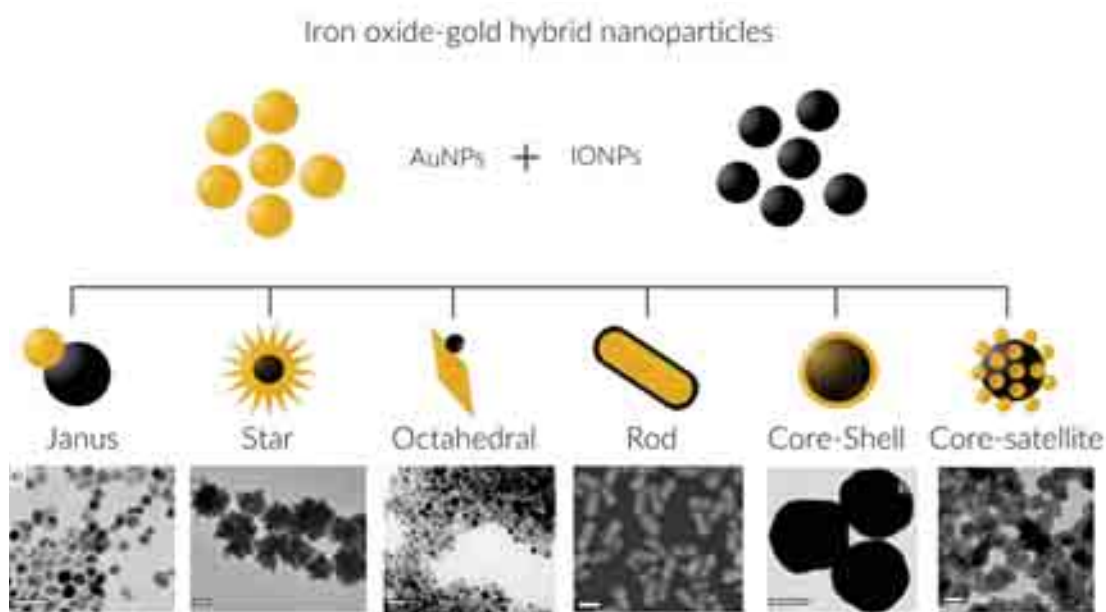


Figure 1.4. Schematic illustration and TEM images of common combinations of iron oxide and gold into hybrid NPs. Scale bars correspond to 50 nm. Adapted from ref.^{42,122,237-241}. Copyright (2009) (2016) (2017) American Chemical Society, (2017) Royal Society of Chemistry, (2013) John Wiley and Sons, (2018) Springer Nature.

1.2.4 Surface functionalization of iron oxide nanoparticles

Surface functionalization provides the IONPs with additional colloidal stability, biocompatibility and prevents the NPs from aggregation. Inorganic molecules, metals, polymers, proteins, silica, or organic compounds could be used to modify the surface of IONPs. In the following section we will briefly report the most commonly used molecules for the functionalization of IONPs.

Polymers. The most prevalent surface coating utilized in IONP functionalization is polymeric, thus providing stability and aiding to prevent oxidation⁹⁴. In this regard, polyethylene glycol (PEG)⁹⁵, poly(vinylpyrrolidone) (PVP)⁹⁶, polyvinyl alcohol (PVA)⁹⁷, poly(lactic-co-glycolic acid) (PLGA)⁹⁸, and chitosan⁹⁹ are the most commonly used polymers for surface functionalization of IONPs due to their biocompatibility.

Surfactants- IONPs tend to agglomerate due to magnetic attraction among NPs, van der Waals forces, and high energy surface¹⁰⁰. In order to achieve enough repulsive interactions to prevent agglomeration of the IONPs, coating with surfactants is frequently used. Surfactants, which can

change the surface charge and determine the biocompatibility, surround the magnetic NPs in layers and they are often added during the synthesis of IONPs¹⁰¹. Oleic acid and oleylamine are normally used as surfactants for the obtention of highly uniform IONPs magnetic NPs. However, a subsequent ligand exchange is needed for transforming hydrophobic to water-soluble IONPs for bioapplications¹⁰².

Biomolecules. Enzymes, antibodies, proteins, bovine/human serum albumin (BSA/HSA), biotin, avidin, and polypeptides have all been attached to the surface of IONPs¹⁰³. Due to their biocompatibility, biomolecule functionalized magnetic IONPs have recently emerged as a popular and successful techniques in biological separation, detection, sensing, and other bioapplications¹⁰⁴⁻¹⁰⁶.

Inorganic compounds. For IONPs, SiO₂ is the most common inorganic coating. The silanol groups provide ligands with the ideal anchoring, supplying the nanosystem with a variety of functional groups. SiO₂ coatings have been shown to provide stability, hydrophilicity, and high biocompatibility⁹⁷. Also carbon based materials are being used as IONP coatings¹⁰⁷. These materials are water soluble, have strong electrical conductivity, are chemically and thermally stable, and act as a barrier against IONP oxidation, thus making these coatings ideal for IONP applications.

1.2.5 Surface functionalization of gold nanoparticles

In similarity to IONPs, AuNP surface functionalization is also especially important for their functionality, stability, and biological compatibility¹⁰⁸. The main strategy for the functionalization or surface modification of AuNPs is through thiol groups that allow a strong interaction with the gold surface. Thus, the AuNPs are functionalized via direct conjugation with thiol containing molecules.

Raman active molecules. Thiolated aromatic molecules easily adsorb onto gold surfaces and are therefore employed in the development of SERS tags that offer distinctive Raman spectra. Examples using different thiolated molecules can be found in the literature¹⁰⁹. However, most of the Raman active molecules used for AuNPs functionalization are soluble in organic solvents, thus, phase transfer or an additional coating are needed to provide the NPs with hydrophilicity for their use in bioapplications³³.

Polymers. In order to increase the stability of AuNPs, polymers have also been used as coating molecules. Longer stability, high surface density, and the capacity to modify the solubility are some of the benefits of polymer-stabilized AuNPs. PEG is one of the most often utilized molecules for functionalizing AuNPs¹¹⁰. Apart from the polymers used for IONPs, which have also been used for AuNPs, polyethyleneimine (PEI), poly(diallyl dimethyl ammonium chloride) (PDDA), and polystyrene, among others, are all also used for surface functionalization of AuNPs¹¹¹. Additional molecules, such as fluorescent dyes, can be chemically coupled to specific functional end groups of the polymers to provide the NPs with additional functionalities. It has been proven that the fluorescence is not quenched by the presence of AuNPs allowing the application of multicolour

fluorescent NPs in biological applications such as bioimaging^{112,113} or visualization of biological processes¹¹⁴. In the same way, bifunctional ligands are used to modify biomolecules; one moiety is employed to anchor the biomolecule to the surface, and the other is directed to interact specifically with the system. Antibodies (Ab), DNA oligonucleotides, enzymes, and drugs are used for specific targeting of cells, immunoassays, specific bindings and drug delivery applications¹¹⁵.

Inorganic compounds. As shown in the functionalization section of IONPs, SiO₂ is also extensively used for the surface modification of AuNPs and different strategies have been developed and previously reported¹¹⁶. Silica shells provide rich surface chemistry that allows for further conjugation with biomolecules or drugs, great biocompatibility, tuneable porosity and outstanding transparency¹¹⁷. Hence, AuNPs coated with SiO₂ have found their application in biomedicine including bioimaging¹¹⁸, photothermal therapy^{119,120}, and SERS detection¹²¹.

1.2.6 Characterization of hybrid systems

One important concern during the synthesis of hybrid plasmonic-magnetic particles is the potential influence of each metallic component on the other's inherent properties (magnetic and plasmonic), and thus, a meticulous characterization of their properties is crucial. Whilst various works have shown that magnetic properties remain unchanged after growing Au around IONPs,^{42,122,123} subsequent functionalization in the form of coatings or shells may affect their performance for bioapplications. Coatings may reduce, for example, the accessibility of water protons to IONPs cores, which can be detrimental to their relaxation times and thus compromise the application of hybrid NPs for MRI¹²⁴. Although various synthetic protocols for the fabrication of plasmonic-magnetic NPs and functionalization strategies have been reported in detail,¹²⁵⁻¹²⁸ as well as the biomedical application of these hybrid nanostructures^{129,130}, limited description of the relevant characterization techniques is reported. Therefore, we describe below the characterization methods that should be considered when working with IOAuNPs for their correct and full characterization.

From both the synthetic and applied points of view, appropriate analysis of the prepared nanostructures is essential. Characterization of plasmonic NPs requires UV-visible-NIR spectroscopy, which provides information about the plasmon modes excited upon irradiation of the NPs, such that the extinction bands can usually be correlated to their size, shape, or aspect ratio¹³¹. Transmission electron microscopy (TEM) and scanning electron microscopy (SEM) are widely used to retrieve NP morphological and structural characterization, with precise information regarding size distribution, morphology, crystalline phase, elemental composition, etc. Dynamic light scattering (DLS) is typically used to measure the hydrodynamic diameter and polydispersity of NPs in a colloidal dispersion. Whereas characterization of anisotropic NPs provides inaccurate results by DLS⁶², reliable results are often obtained when working with spherical NPs^{132,133}.

Regarding the characterization of magnetic NPs, apart from the above-mentioned techniques for morphological characterization, spectroscopic methods are used to collect information on their chemical composition for a correct identification of metal oxide phases. For this purpose, X-ray diffraction (XRD), Mössbauer spectroscopy¹³⁴, or X-ray photoelectron spectroscopy (XPS) can be

used to identify crystalline structures and composition. To understand the magnetic response of IONPs, superconducting quantum interference device (SQUID) is generally used as a magnetometer, to measure the response of IONPs under external magnetic fields. The so-called zero field cooled—ZFC, field cooled—FC measurement provides information regarding the iron phase. For instance, a metal-insulator transition known as Verwey transition can be detected around 110 K and is associated with the magnetite phase¹³⁵. Additionally, the blocking temperature T_B – below T_B magnetic ordering occurs whilst above T_B the thermal energy dominates the NPs response to the applied magnetic field – can be also obtained from the ZFC/FC curves. Magnetic hysteresis loops at room temperature can be obtained by vibrating sample magnetometry (VSM), from which the saturation magnetization, M_s , can be determined. For IONPs, M_s values typically range from 45 to 80 emu/g-Fe and give information about their magnetic response^{136,137}. Additionally, magnetic relaxivity (r) and relaxation time shortening values (T_1 and T_2) can be determined using a contrast agent analyser or an MRI scanner⁴².

In general, IOAuNPs can be characterized using the same methods as for their individual components. However, it may be complicated to distinguish both metals within the same nanostructure. Thus, more sophisticated methods should be applied for a complete characterization of hybrid NPs. For example, in core-shell type IOAuNPs it is usually difficult to distinguish the core from the shell using TEM. In this respect, identification of the presence of both domains in single NPs can be made by using energy dispersive X-ray spectroscopy (EDXS). When the electron beam hits the sample, it produces electron transitions from a high-energy (outer) shell to a lower-energy (inner) shell of the atom, the energy difference produced by the electron displacement is released as X-rays and is characteristic for each element¹³⁸, so different metals within the same nanostructure can be distinguished¹³⁹. Another useful tool is electron energy loss spectroscopy (EELS) coupled to TEM. In EELS, one measures the distribution of electron energies that have been inelastically scattered while passing through the sample, due to interactions of primary beam electrons with the electrons in the sample. Thus, information about electronic structures, bonding states or coordination number can be acquired by looking at the characteristic energy loss spectra¹⁴⁰. Differentiation of metals can also be achieved by high-angle annular dark field (HAADF) scanning transmission electron microscopy (STEM), as the contrast of the images depends on the atomic mass of the elements¹⁴¹. Electron diffraction techniques are also readily available on any TEM, by which the interaction between electrons and crystalline materials produces patterns that allow characterization of the crystalline structure. For example, specific information related to structural determination or the growth direction can be acquired by using selected area electron diffraction (SAED), while symmetry, thickness and unit-cell parameters can be studied using convergent beam electron diffraction (CBED)¹⁴². High-resolution TEM (HRTEM) can also provide precise information, even about the atomic distribution in complex systems. Electron tomography can also be used to achieve quantitative three-dimensional (3D) information of nanostructures¹⁴³. In electron tomography, multiple images are acquired at different angles and, by applying mathematical algorithms, 3D volumetric reconstructions of the sample can be retrieved. This versatile tool, with resolution from the nanometre to the atomic level, provides a better understanding of the structure and composition of NPs, even allowing the

distinction between different elements at different depths when combined with EDXS or EELS analysis¹⁴⁴.

1.3 Nanoparticles for bioimaging

Both AuNPs and IONPs have been used as contrast agents for different imaging techniques, hence the interest of their combination into hybrid NP structures. Having the characteristics of both components in a single NP allows their use as multimodal contrast agents for correlative imaging. In the following section, the aspects regarding magnetic and plasmonic NPs that can act as contrast agents for each imaging technique are presented.

1.3.1 Magnetic nanoparticles for bioimaging

IONPs for Magnetic Resonance imaging. Normally, MRI operates using contrast agents to enhance the quality of the acquired images. The majority of clinically available T1 contrast agents are paramagnetic metallo-chelates comprising gadolinium, which acts by shortening the relaxation time of protons, producing a bright contrast that improves the quality of the images. Unfortunately, it has been demonstrated that Gd³⁺ complexes may cause renal toxicity¹⁴⁵, hence the development of efficient and safer contrast agents for MRI is essential. Magnetic NPs are great candidates as contrast agents for MRI, as they produce a magnetic field that alters the relaxation time of water protons resulting in an enhancement in the contrast between tissues with and without NPs^{146,147}. In particular, IONPs have been widely used as negative (T2) contrast agents in MRI. IONPs reduce magnetic relaxation times, thereby inducing a hyperintense change of the resonance signal in MRI and providing a so-called negative contrast. Magnetic mono-domains at the nanometre scale in the appropriate iron oxide phase, together with appropriate saturation magnetization values, provide IONPs with excellent T2 contrast. Additionally, superparamagnetic IONPs present strong and controllable magnetic responses under external magnetic fields. IONPs can thus act as “magnets” and yield signal suppression during MRI, appearing as dark spots (negative contrast)¹⁴⁸. Notwithstanding, due to the limitations in the signal intensity of T2-driven diagnosis, research nowadays focuses mainly on the development of T1 contrast agents based on small IONPs (<5nm) with medium size coatings (hydrodynamic sizes of 10–20nm), which display high water exchange rate, so they may eventually replace the current Gd-based contrast agents and provide positive contrast (brighter images) while avoiding kidney toxicity¹⁴⁹. Coatings on NPs play an important role as bulkier coatings (i.e., hydrodynamic diameter >30–40nm), thereby restricting water access to the nanoparticle core, increasing the outer-sphere contribution to the relaxation mechanism, and hindering the T1 effect. Coatings leading to small hydrodynamic diameters (<7nm) do not provide enough stability to the particles, resulting in aggregates that may enhance the T2 effect¹⁵⁰.

IONPs for magnetic particle imaging. Although magnetic contrast agents are also used in MRI, the signal is produced by the relaxation of hydrogen protons from water molecules that are around the tracers. Because of this indirect approach, it is challenging to precisely measure tracer amounts *in vivo*¹⁵¹. By contrast, the magnetic response of the magnetic tracers directly produces contrast in MPI and the intensity is proportional to the mass of the tracer¹⁵². Thus, MPI has

provided promising results for vascular imaging, oncology, inflammation and cell tracking *in vitro* and *in vivo*¹⁵³⁻¹⁵⁵. However, most of the current MPI systems are designed only to handle small animals with chamber diameters between 3 and 12 cm. Therefore, human-scale scanners are starting to be manufactured for its clinical translation¹⁵⁶. Additionally, research is being done to improve MPI's performance in terms of sensitivity and spatial resolution by adjusting the size, shape, composition, surface, crystallinity, and aggregation state of the IONPs¹⁵⁷ so that it can compete with current modalities and lead to clinic application¹⁵⁸.

1.3.2 Plasmonic nanoparticles for bioimaging

AuNPs for computed tomography. AuNPs express a high X-ray absorption and, in combination with their ability to accumulate in tissues via targeted or non-targeted methods, they have been proposed as contrast agents for CT. Consequently, imaging time is reduced resulting in a reduction in overall radiation exposure and the risk of acute kidney injury¹⁵⁹. Several examples have been reported on the use of AuNPs as contrast agents for CT¹⁶⁰. Although theoretically the contrast properties are expected to vary depending on the NP properties, a study by Dong et al. on the CT contrast capacity of AuNPs with different sizes, ranging from 4 to 152 nm, did not show meaningful differences in terms of signal contrast¹⁶¹.

AuNPs for photoacoustic imaging. When using plasmonic AuNPs, which can efficiently absorb and scatter light, a difference in the PA signal is registered, allowing the acquisition of images with improved contrast. Thus, anisotropic AuNPs are excellent contrast agents for PAI, which allows obtaining information in real time, with high spatial resolution and deep penetration when using NIR wavelengths. For an optimal amplification of the photoacoustic signal, it is important to control the morphological and optical properties of the NPs¹⁶². Another important feature of AuNPs is the absence of photobleaching, which may readily occur when using other molecules as contrast agents, e.g. fluorescent dyes¹⁶³. AuNPs with different geometries, including nanoprisms¹⁶⁴, nanocages¹⁶⁵, nanospheres¹⁶⁶, nanovesicles¹⁶⁷ and nanostars¹⁶⁸ have been studied, but AuNRs are still the preferred geometry for use as contrast agents in PAI¹⁶⁹. A theoretical study on the optimal geometry and size for AuNRs and AuNSs proposed AuNSs with small cores (30 nm) and relatively long tips (17 nm) as the optimum NP geometry toward the development of biocompatible PAI contrast agents, which was validated by experimental PAI measurements¹⁷⁰.

AuNPs for surface-enhanced Raman scattering imaging. The contrast agents in SERS bioimaging are SERS tags¹⁷¹⁻¹⁷³, as defined above. Different designs have demonstrated the possibility of creating large libraries of SERS barcodes¹⁷⁴. Another key advantage of SERS tags is their stability against photobleaching^{175,176}, which renders them excellent candidates for long-term bioimaging experiments. SERS imaging has been used for live imaging of *in vitro* complex cell systems³³, as well as *in vivo* imaging, e.g. for visualization of the boundaries between tumour and normal tissues in mice¹⁷⁷, or the detection of gastrointestinal tumours in rats¹⁷⁸. In a further development, the use of SERS tags for image-guided surgery is gaining interest, for example

toward improving intraoperative tumour-resection procedures, in which SERS tags have been used to detect residual tumours at the margins of freshly resected tissue¹⁷⁹.

1.3.3 Hybrid nanoparticles for multimodal bioimaging

The development of NPs that can provide contrast simultaneously for different techniques has largely progressed with the general advances in colloidal synthesis methods. The potential of such plasmonic-magnetic NPs as multimodal imaging probes has now been sufficiently demonstrated^{180,181}, as well as the resulting imaging combinations. **Figure 1.5** shows a collection of selected images that illustrate the use of plasmonic-magnetic NPs in different imaging modalities for *in vitro* and *in vivo* models. PAI, SERS and CT imaging modalities can all be applied thanks to the gold component, whereas MPI and MRI rely on the iron oxide part.

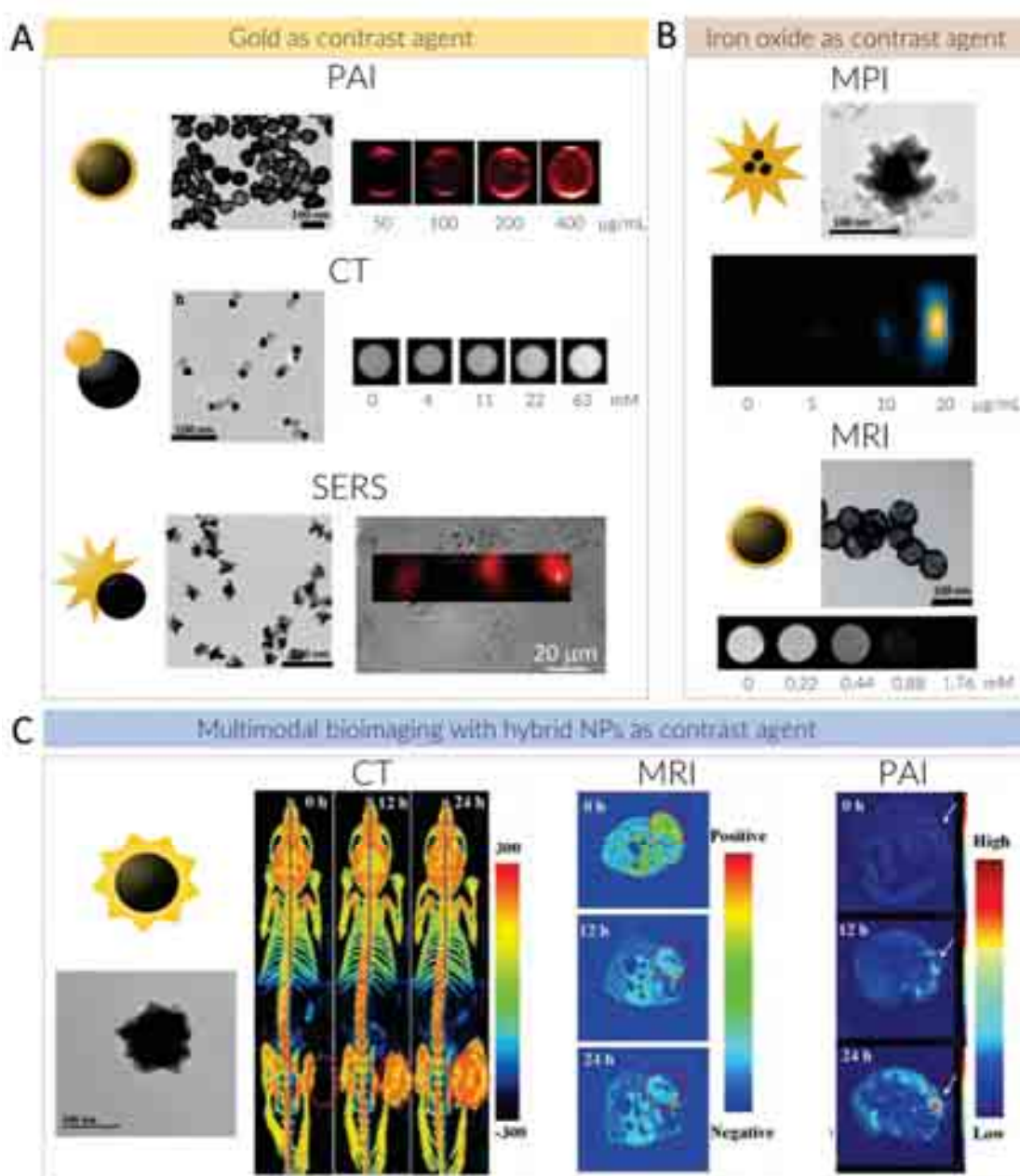


Figure 1.5. (A) Hybrid NPs as contrast agents for PAI, CT and SERS. Core-shell, spherical Janus NPs and star-like Janus NPs are used respectively for each technique. The gold component is

involved in the capacity of the hybrid NPs to act as contrast agents for these techniques. **(B)** Core-shell NPs containing either smaller iron oxide cores or a unique big core, have been used as contrast agents for MPI and MRI due to the magnetic component. **(C)** CT, MRI and PAI of a HeLa tumour in a mouse model, at different points after injection of 200 μ L, 40 nM of star-like hybrid NPs. Both components are exploited for multimodal imaging. Graphical representations and representative TEM images are shown for the various NPs, next to corresponding images generated from the different techniques. Increasing contrast can be observed when increasing the dose concentration of gold or iron oxide in each case. Adapted from ref.^{42,182-186} Copyright (2019) (2020) American Chemical Society, (2017) Royal Society of Chemistry, (2018) John Wiley and Sons, (2020) Springer Nature.

In addition to these examples, an extensive literature search of the most relevant plasmonic-magnetic NPs for multimodal imaging is summarized in **Table 1.2**, highlighting the morphology, the imaging modalities, the target disease, and the harmless maximum concentration that was used for each system. Examples include hydrophilic and biocompatible Au-Fe₂O₃ heterodimers for MRI, CT and PAI¹⁸³, plasmonic-magnetic NPs obtained by laser ablation of a bulk Au-Fe alloy for MRI, CT, and SERS¹⁸⁷, Au-IO Janus NPs for MRI, CT, SERS, and PAI⁴², IONPs and AuNRs as contrast agents for dual MRI/CT¹⁸⁸, and hybrid star-shape NPs for MPI, MRI and PAI¹⁸⁶.

Table 1.2. Summary of plasmonic-magnetic NPs for multimodal bioimaging.

| Nanostructure | Type | Synthesis of the magnetic NP | Imaging modalities | Target disease | Model | Harmless (up to) | Ref |
|--|--------------|------------------------------|--------------------|--|-----------------------------------|---|------------|
| M-Fe ₃ O ₄ (M = Au, Ag, and Pd) | Heterodimers | Laser-pyrolysis | MRI, CT, PAI | Lung cancer | <i>in vivo</i> | 0.5 μ g/mL | 183 |
| Au-Fe NPs | Alloy | Laser ablation | MRI, CT, SERS | Breast, prostate cancer and histiocytic lymphoma | <i>in vivo</i> | [Au] 290 μ g/mL [Fe] 10 μ g/mL | 187 |
| Fe ₃ O ₄ @Au | Core-shell | Co-precipitation | MRI, CT | Brain diseases Lung cancer | <i>in vitro</i> <i>in vivo</i> | 100 μ g/mL | 189 190 |
| Fe ₃ O ₄ @AuNPs | Janus | Co-precipitation | MRI, CT, PAI, SERS | Adenocarcinoma | <i>in vitro</i> | [Au] 50 μ M | 42 |
| Fe ₃ O ₄ @Au | Core-shell | Co-precipitation | MPI | Glioblastoma | <i>in vitro</i> | 50 μ g/mL | 191 |
| Fe ₃ O ₄ -AuNSs | Core-shell | Co precipitation | MRI, MPI, PAI | HIV | <i>in vitro</i> | 50 μ g/mL | 186 |

| | | | | | | | |
|---|----------------|-----------------------|----------------|-------------------------------------|-----------------|--|-----|
| Fe ₃ O ₄ @SiO ₂ @Au | Core-shell | Thermal decomposition | MRI, CT | Liver cancer | <i>in vitro</i> | 200 µg/mL | 185 |
| spiky Fe ₃ O ₄ @Au | Core-shell | Co-precipitation | MRI, PAI, CT | Cervical carcinoma | <i>in vivo</i> | 200 µg/mL | 184 |
| Fe ₃ O ₄ @ SiO ₂ @Au | Core-shell | Thermal decomposition | MRI, CT, FI | Cervical carcinoma | <i>in vitro</i> | 350 µg/mL | 112 |
| Fe ₃ O ₄ @AuNPs | Janus | Thermal decomposition | MRI, CT | Liver cancer | <i>in vivo</i> | [Fe] 3.2 mM | 192 |
| Fe ₃ O ₄ @AuNPs | Core-satellite | Co-precipitation | MRI, CT | Liver cancer | <i>in vivo</i> | 1 mg/mL | 193 |
| Fe ₃ O ₄ @AuNPs | Core-satellite | Hydrothermal | MRI, CT | Epithelial carcinoma | <i>in vivo</i> | 100 µg/mL | 194 |
| Fe ₃ O ₄ @Au | Core-shell | Co-precipitation | MRI, PAI | Glioblastoma and breast cancer | <i>in vitro</i> | [Fe] 2.5-20 mM | 195 |
| Fe ₃ O ₄ @AuNPs | Dumbbell | Thermal decomposition | MRI, CT | Liver cancer | <i>in vivo</i> | [Au] 48 mg kg ⁻¹ [Fe] 36 mg kg ⁻¹ | 159 |
| Fe ₃ O ₄ @BCP@AuNPs | Janus Vesicles | Thermal decomposition | MRI, PAI | Glioblastoma | <i>in vivo</i> | [Fe] 0.125 mM | 196 |
| Fe ₃ O ₄ @AuNPs | Core-shell | Co-precipitation | MRI, CT, SPECT | - | NPs in solution | - | 197 |
| Fe ₃ O ₄ @AuNSs | Core-shell | Hydrothermal | MRI, CT | Cervical carcinoma and glioblastoma | <i>in vitro</i> | [Au] 2 mM | 198 |

It can be noticed that almost all of the NPs found in the literature correspond to core-shell NPs made of an iron core covered by a gold shell. Additionally, the most extended use is the combination of MRI and CT. These techniques have been widely studied and are also used in pre-clinical imaging. From this bibliographic research we can confirm that new multifunctional probes with novel morphologies and optical properties for multimodal imaging are still needed. Novel arrangements of the magnetic and plasmonic domains should be explored in order to vary the optical and magnetic properties of the NPs and combine conventional techniques with new emerging techniques such as SERS and MPI. Thus, new hybrid NPs beyond core-shells could be used for multimodal bioimaging providing valuable information from different techniques.

1.4 Nanoparticles for hyperthermia

The main therapeutic techniques used today to remove tumors include radiotherapy and chemotherapy¹⁹⁹. However, using these techniques it is difficult to avoid harming both healthy and cancerous cells²⁰⁰.

In addition to bioimaging applications, plasmonic-magnetic NPs can also be used as therapeutic agents. For example, hyperthermia refers to a condition in which the temperature is abnormally increased, causing cell damage. In biological environments the hyperthermia temperature threshold is at ca. 42 °C. Above this temperature, various processes including protein denaturation, cytoskeleton disruption, or changes in signal transduction, are triggered in cells resulting in the activation of cell death mechanisms or uncontrolled cell ablation²⁰¹. Indeed, a recent study showed that cell death mechanisms depend on the specific temperature reached, so that apoptosis prevails at temperatures between 43 - 49 °C, whereas necrosis dominates above 49 °C²⁰². However, application of hyperthermia as a therapeutic technique has the drawback that it can affect both diseased and healthy cells, thereby resulting in unwanted side-effects. Therefore, localized hyperthermia techniques including photothermal therapy (PTT) and magnetic hyperthermia (MHT) have emerged as innovative and selective treatments, for which plasmonic-magnetic NPs would be used²⁰³. In the following section, PTT and MHT produced by AuNPs and IONPs will be discussed, highlighting the advantages and disadvantages of using hybrid NPs to enhance such effects.

1.4.1 Magnetic hyperthermia

MHT exploits heat generated by magnetic NPs, usually for oncology treatments. Upon excitation with an alternating current (AC) magnetic field, tumour-localized magnetic NPs generate localized heat that strongly depends on the concentration, but also on the size, composition, shape and anisotropy of the magnetic NPs^{204,205}. The main drawback of MHT is that most magnetic NPs have a rather poor heating efficiency, so large amounts of NPs should be directly injected for effective therapeutic performance, which may in turn induce cytotoxicity issues. Additionally, NPs often lose some of their heating efficiency in biological environments as a consequence of aggregation and the subsequent decrease in interparticle distance²⁰⁶. For this reason, an increased NP heating efficiency is still highly desired, which could be obtained by modifying the degree of mutual interaction between magnetic NPs in close contact, such as in multicore IONPs²⁰⁷. More recently, the heating properties of IONFs have been analysed for application in MHT, concluding that a larger number of cores favours MHT performance²⁰⁸. On the other hand, a greater heating performance has been demonstrated for IONCs under MHT, in comparison with various other shapes^{73,209}. Both IONCs and IONFs with larger NP volume and high concentration of defects have also been shown to display suitable properties, not only for their use in MHT but also as PTT heaters thanks to the efficient absorption of light when irradiated at 808 and 1064 nm wavelengths, respectively^{208,210}.

1.4.2 Photothermal therapy

PTT is based on the photothermal conversion of absorbed light into heat, i.e. dissipation of an electromagnetic radiation absorbed at a certain location, in the form of heat to the surrounding environment. This process requires the presence of light absorbing “sensitizers”, such as molecular dyes or small NPs (in larger particles light scattering is the preferred mechanism, thus reducing heating efficiency). AuNPs are efficient in converting light into heat. This conversion occurs when NPs are irradiated with a laser, in this process, resonant irradiation induces an excitation of the free electrons of metal NPs leading to a quick non-equilibrium heating²¹¹. Electrons jump to an excited energy state followed by a relaxation process consisting of electron-electron scattering that produces an increase of temperature on the surface. One of the processes used to decrease this temperature consists of phonon-phonon interactions with the surrounding media. The phonon-phonon interactions dissipate heat across a particle-matrix interface until the NPs return to their initial electron temperature¹⁷⁶. The main advantages of this technique include low cost (no major equipment needed), minimum invasiveness (extremely small amounts of sensitizers are needed and the light stimulus can be applied remotely), and high specificity (heating is confined to the irradiated area where the sensitizers are located). These properties render PTT highly suitable to selectively kill diseased cells, with negligible harm to healthy ones, which is of particular interest in cancer therapy²¹². The applied local heat causes irreversible damage to cell membranes leading to necrosis. The heating efficiency of the AuNPs themselves is directly related to their plasmonic response, i.e. the specific LSPR mode²¹³. The selection of preferred AuNPs in terms of size and shape will thus depend on the desired optical properties, which should match the laser wavelength to be applied, usually within the NIR range, from 650 to 1359 nm. In this range, deeper light penetration is achieved due to minimum scattering by tissue and light absorption by haemoglobin (<650 nm) and water (>900 nm) (see **Figure 1.6**).

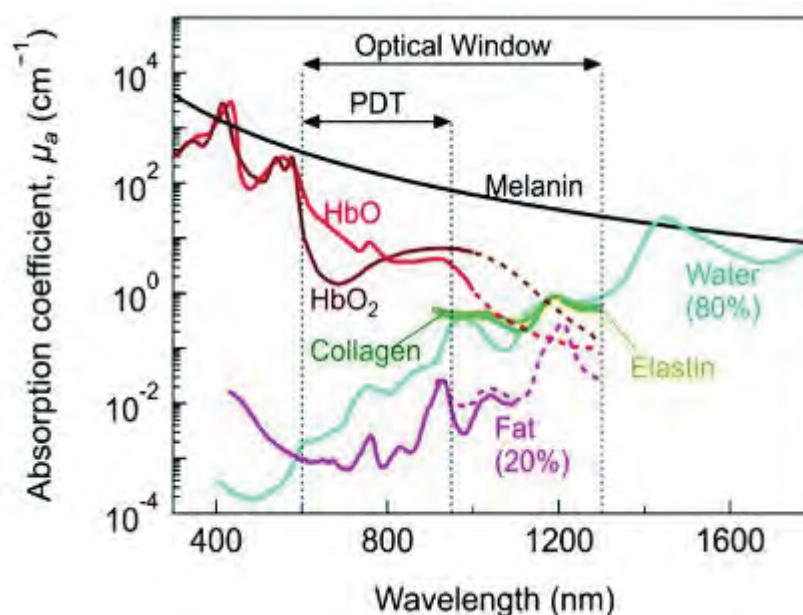


Figure 1.6. Main biological molecules and their absorbances in the Vis-NIR electromagnetic range²¹⁴.

Anisotropic AuNPs are thus ideal candidates as nanoheaters for photothermal therapy, as their LSPR in the NIR can be effectively tuned. Given the wide variety of available AuNP shapes, different possibilities have been explored for this purpose. Gold nanoshells (AuNSHs) have been studied for both *in vitro* and *in vivo* PTT, achieving irreversible photothermal ablation of tumour tissue²¹⁵, and this was the first AuNP shape that found application in clinical trials²¹⁶. AuNRs have also been used for *in vitro* PTT²¹⁷. Experimental demonstration was subsequently reported using smaller AuNRs (D = 10 nm), with LSPRs around 800 nm, for *in vivo* treatment²¹⁸. Another preferred morphology is that of spiky nanostars; AuNSs with sizes of 30 and 60 nm proved effective for tumour ablation upon PTT, with smaller ones reaching a deeper penetration depth into the tumour interstitial space²¹⁹. Gold nanocages (AuNCs) have also been shown to be effective; e.g. AuNCs with 45 nm edge-length and LSPR at 810 nm led to *in vitro* targeted photothermal destruction of breast cancer cells²²⁰. The efficacy of AuNCs for *in vivo* photothermal treatment of a bilateral tumour was subsequently demonstrated by the same authors²²¹. More recently, a nanoprobe based on a silica core covered by a gold shell has been applied for localized photothermal ablation of prostate tumours in a clinical trial, demonstrating the potential of Au nanoprobe for clinical treatment²¹⁶.

1.4.3 Towards multitherapy: *photothermal therapy + magnetic hyperthermia*

As discussed above, external stimuli such as light or magnetic fields, are required to generate heat using AuNPs or IONPs as sensitizers²⁰⁹. Magnetic NPs present a low molar absorption coefficient in the NIR region and consequently have poor photothermal effects. On the other hand, plasmonic NPs do not possess magnetic properties, and thus cannot be applied in MHT. Thus, by combining IONPs and AuNPs into hybrid nanostructures, hybrid nanoheaters with PTT and MHT properties should be able to form²²². Such dual-nanoheaters have shown improved hyperthermal performance, as the temperature increment reached by PTT is supplemented by that induced by MHT²²³. Hybrid NPs have been successfully demonstrated to detain tumour growth in cancer cells, both using *in vitro* and *in vivo* models, thanks to combined PTT and MHT treatments²²⁴. However, even though the combination of PTT and MHT appears as an interesting approach for novel and effective cancer treatments, such a combination is still rare and only a few examples are found in literature where hybrid NPs were used²²⁵⁻²²⁷ (see **Figure 1.7**). This slow development may be related to the concentration differences required for each heating technique.

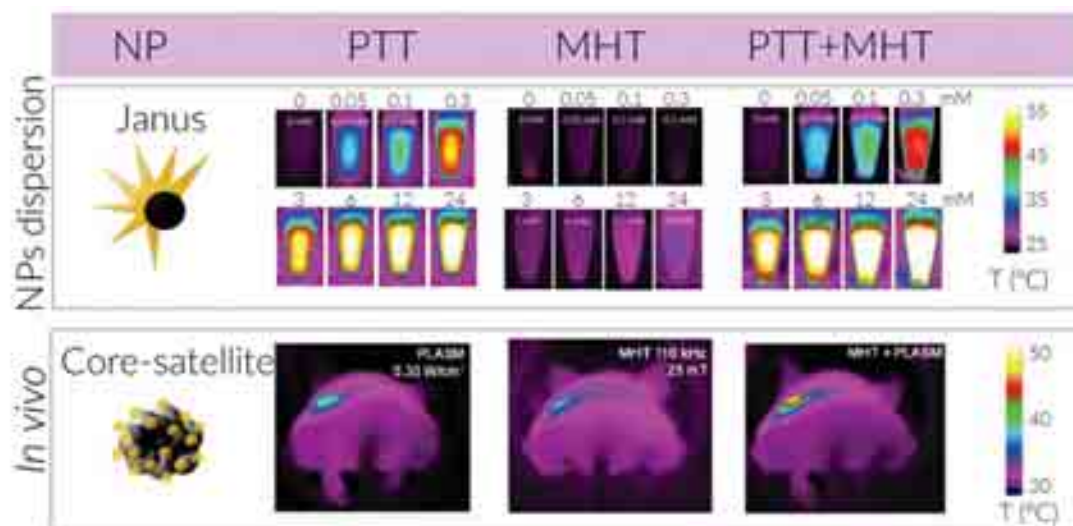


Figure 1.7. PTT, MHT and dual PTT+MHT experiments using colloidal dispersions of Janus NPs in water, at different concentrations. The measurements were carried out in Eppendorf tubes, using a volume of 150 μL and a 680 nm laser working at 0.5 W/cm^2 during 5 min for PTT and 470 kHz and 18 mT for MHT (upper panel). In the lower panel, PTT, MHT and dual PTT+MHT *in vivo* experiments are illustrated. A volume of 100 μL of core-satellite NP solution at $[\text{Fe}] = 150 \text{ mM}$ was directly injected into tumors produced from human prostate adenocarcinoma cells (PC3), in a mouse animal model. Irradiation conditions were: 680 nm, 0.3 W/cm^2 for PTT; AC magnetic field at 110 kHz, 25 mT, for MHT. Reproduced from^{223,224}. Copyright (2020) John Wiley and Sons, (2017) Royal Society of Chemistry.

Even if multitherapy combining PTT and MHT remains largely unexplored, the use of hybrid NPs for image-guided hyperthermia is increasing exponentially and has been described by a number of authors²²⁸⁻²³². Since PTT is easier to implement and more efficient than MHT²³³, recent studies have reported the use of the plasmonic domain of hybrid NPs for PTT while the magnetic domain was employed for imaging, so that a single nanostructure becomes an interesting tool for image-guided phototherapy^{186,234,235}. This combination has shown interesting results in both *in vitro* and *in vivo* experiments, achieving complete tumour ablation and cell death. Interestingly, the use of magnets during the incubation of NPs with cells has also been used to enhance internalization, again leading to more effective therapies²⁰⁹.

One of the most common combinations of imaging + treatment involves the use of hybrid NPs as contrast agents for MRI/CT, followed by PTT after tumour localization¹⁸⁵. Notwithstanding, NP systems that combine multimodal imaging such as SERS, MRI and PAI²³⁶, or MRI, CT and PAI¹⁸⁴, with PTT treatment have also been reported. Hybrid $\text{Fe}_2\text{O}_3@Au$ magnetic gold nanoflowers have been described for cancer theranostics using MRI to first localize the tumour, followed by PAI for deep tumour localization, and finally SERS to allow the detection of tumour margins. This method results in a precise localization of the tumour over various orders of magnitude. Having specific information regarding the position of the tumour, efficient ablation under NIR irradiation can be achieved using the photothermal effect of the Au component²³⁶.

Moreover, magnetic targeting can improve the therapeutic response of PTT by enhancing thermal damage. In a recent study, hybrid NPs were injected intravenously and magnets were used for accumulation of the NPs. The results showed that the temperature increment in the tumour was 16.7 °C, as compared to 8.5 °C in the absence of the guiding magnets. This result confirmed that intravenous injection followed by magnetic accumulation is more efficient than even intratumoral injection, which reported a temperature increment of 12 °C²³⁰.

Considering all this information, the development of novel theranostics agents is highly desirable. The study of new hybrid NPs that combine magnetic and plasmonic properties with innovative structures and configurations is rapidly increasing. The combination of emerging techniques such as SERS with conventional ones like MRI and/or fluorescence imaging will provide an interesting approach towards complementary multimodal bioimaging that would represent an important tool for diagnosis. These observations, alongside the progress in the development of novel hyperthermia treatments, make hybrid NPs suitable candidates as theranostics agents. Hence, in this thesis, we have explored new approaches to obtain hybrid NPs with different configurations as novel theranostics agents.

Thesis contents

The term "theranostics" refers to the smart integration of therapy and diagnostics. Such an ability to simultaneously image and treat tumors with NPs may prove advantageous over conventional techniques for individual diagnosis or therapy. Thus, a further advantage for both imaging and treatment is to be able to study diseases *in vitro* by means of a variety of imaging methods and combining them with novel treatments.

This thesis is divided in 4 additional chapters. In chapter II, the synthesis and optimization of hybrid NPs are described. The arrangement of the hybrids consists of a core made of a IONP covered by a spiky gold shell. The hybrid NPs were then further functionalized with Raman-active molecules and fluorescent dyes) for their use in multimodal bioimaging. In particular, SERS, MRI and fluorescence imaging were combined and studied in 2D, 3D *in vitro* cell models and *ex vivo* models. In chapter III, the hybrid nanostructures were further optimized for their use in hyperthermia. The size of the IOAuNS was decreased and the properties of the NPs for photothermal therapy was studied in 2D and 3D cell models.

In chapter IV, a new hybrid system was developed, comprising AuNRs covered by a silica shell, on which IONPs were subsequently grown using thermal decomposition cycles. Additionally, the hybrids were functionalized with antibodies. The application of the hybrid NPs for photothermal therapy was studied in 2D and 3D cell models and the IOAuNS were functionalized with antibodies for specific targeting of cells.

Hence, the multifunctional hybrid systems that were prepared and characterized in this thesis represent an interesting multimodal approach towards the development of novel theranostic platforms. Additionally, in chapter V, a guide of factors to consider when conducting photothermal experiments is presented. Based on our experience, we have studied the effect of some parameters such as the use of a collimator and/or the importance of a proper calibration in the

photothermal measurements. The results demonstrate the importance of controlling and reporting all the details of a set-up for reproducing and comparing experiments using NPs as nanoheaters.

References

- (1) Cooper, G. M. The Development and Causes of Cancer. *Cell A Mol. approach; Assoc. S., Ed.; Sinauer Assoc.* **2000**.
- (2) Sung, H.; Ferlay, J.; Siegel, R. L.; Laversanne, M.; Soerjomataram, I.; Jemal, A.; Bray, F. Global Cancer Statistics 2020: GLOBOCAN Estimates of Incidence and Mortality Worldwide for 36 Cancers in 185 Countries. *CA. Cancer J. Clin.* **2021**, *71* (3), 209–249. <https://doi.org/10.3322/caac.21660>.
- (3) Welch, D. R.; Hurst, D. R. Defining the Hallmarks of Metastasis. *Cancer Res.* **2019**, *79*(12), 3011–3028. <https://doi.org/10.1158/0008-5472.CAN-19-0458>.
- (4) Guan, X. Cancer Metastases: Challenges and Opportunities. *Acta Pharm. Sin. B* **2015**, *5* (5), 402–418. <https://doi.org/10.1016/j.apsb.2015.07.005>.
- (5) Schiffman, J. D.; Fisher, P. G.; Gibbs, P. Early Detection of Cancer : Past , Present , and Future. *ASCO Educ. B.* **2015**.
- (6) Miller, K. D.; Nogueira, L.; Mariotto, A. B.; Rowland, J. H.; Yabroff, K. R.; Jemal, A.; Kramer, J. L.; Siegel, R. L. Cancer Treatment and Survivorship Statistics , 2019. **2019**, *0* (0), 1–23. <https://doi.org/10.3322/caac.21565>.
- (7) <https://www.who.int/news-room/fact-sheets/detail/cancer>.
- (8) <https://www.cdc.gov/cancer/dcpc/prevention/screening.htm>.
- (9) Blumen, H., Fitch, K., & Polkus, V. Comparison of Treatment Costs for Breast Cancer, by Tumor Stage and Type of Service. *Am. Heal. drug benefits* **2016**, *9* (1), 23–32.
- (10) Cipriano, L. E.; Romanus, D.; Earle, C. C.; Neville, B. A.; Halpern, E. F.; Scott Gazelle, G.; McMahon, P. M. Lung Cancer Treatment Costs, Including Patient Responsibility, by Disease Stage and Treatment Modality, 1992 to 2003. *Value Heal.* **2011**, *14* (1), 41–52. <https://doi.org/10.1016/j.jval.2010.10.006>.
- (11) Chen, M.; Zhao, H. Next-Generation Sequencing in Liquid Biopsy: Cancer Screening and Early Detection. *Hum. Genomics* **2019**, *13* (1), 34. <https://doi.org/10.1186/s40246-019-0220-8>.
- (12) Pansare, V. J.; Hejazi, S.; Faenza, W. J.; Prud, R. K. Review of Long-Wavelength Optical and NIR Imaging Materials : Contrast Agents , Fluorophores , and Multifunctional Nano Carriers. *Chem. Mater.* **2012**, *24*, 812–827.
- (13) Ray, P. Multimodality Molecular Imaging of Disease Progression in Living Subjects. *J. Biosci.* **2011**, *36* (3), 499–504. <https://doi.org/10.1007/s12038-011-9079-0>.
- (14) Barentsz, J.; Takahashi, S.; Oyen, W.; Mus, R.; De Mulder, P.; Reznik, R.; Oudkerk, M.; Mali, W. Commonly Used Imaging Techniques for Diagnosis and Staging. *J. Clin. Oncol.* **2006**, *24* (20), 3234–3244. <https://doi.org/10.1200/JCO.2006.06.5946>.
- (15) Tichauer, K. M.; Wang, Y.; Pogue, B. W.; Liu, J. T. C. Quantitative in Vivo Cell-Surface

- Receptor Imaging in Oncology: Kinetic Modeling and Paired-Agent Principles from Nuclear Medicine and Optical Imaging. *Phys. Med. Biol.* **2015**, *60* (14), R239–R269. <https://doi.org/10.1088/0031-9155/60/14/R239>.
- (16) Zhou, Z.; Yang, L.; Gao, J.; Chen, X. Structure–Relaxivity Relationships of Magnetic Nanoparticles for Magnetic Resonance Imaging. *Adv. Mater.* **2019**, *31* (8), 1804567. <https://doi.org/10.1002/adma.201804567>.
- (17) Van Geuns, R. J. M.; Wielopolski, P. A.; De Bruin, H. G.; Rensing, B. J.; Van Ooijen, P. M. A.; Hulshoff, M.; Oudkerk, M.; De Feyter, P. J. Basic Principles of Magnetic Resonance Imaging. *Prog. Cardiovasc. Dis.* **1999**, *42* (2), 149–156. [https://doi.org/10.1016/S0033-0620\(99\)70014-9](https://doi.org/10.1016/S0033-0620(99)70014-9).
- (18) Clough, T. J.; Jiang, L.; Wong, K. L.; Long, N. J. Ligand Design Strategies to Increase Stability of Gadolinium-Based Magnetic Resonance Imaging Contrast Agents. *Nat. Commun.* **2019**, *10* (1), 1–14. <https://doi.org/10.1038/s41467-019-09342-3>.
- (19) Margolis, D. J. A.; Hoffman, J. M.; Herfkens, R. J.; Jeffrey, R. B.; Quon, A. Molecular Imaging Techniques in Body Imaging. *Radiology* **2007**, *245* (2), 333–356.
- (20) Li, X.; Kim, J.; Yoon, J.; Chen, X. Cancer-Associated, Stimuli-Driven, Turn on Theranostics for Multimodality Imaging and Therapy. *Adv. Mater.* **2017**, *29* (23), 1606857. <https://doi.org/10.1002/adma.201606857>.
- (21) Yang, Q.; Ma, Z.; Wang, H.; Zhou, B.; Zhu, S.; Zhong, Y.; Wang, J.; Wan, H.; Antaris, A.; Ma, R.; Zhang, X.; Yang, J. Rational Design of Molecular Fluorophores for Biological Imaging in the NIR-II Window. *Adv. Mater.* **2017**, *1605497*. <https://doi.org/10.1002/adma.201605497>.
- (22) Yan, C.; Zhang, Y.; Guo, Z. Recent Progress on Molecularly Near-Infrared Fluorescent Probes for Chemotherapy and Phototherapy. *Coord. Chem. Rev.* **2021**, *427*, 213556. <https://doi.org/10.1016/j.ccr.2020.213556>.
- (23) Li, C.; Wang, Q. Challenges and Opportunities for Intravital Near-Infrared Fluorescence Imaging Technology in the Second Transparency Window. *ACS Nano* **2018**, *12*(10), 9654–9659. <https://doi.org/10.1021/acsnano.8b07536>.
- (24) Beard, P. Biomedical Photoacoustic Imaging. *Interface Focus* **2011**, *1* (4), 602–631. <https://doi.org/10.1098/rsfs.2011.0028>.
- (25) Gröhl, J.; Schellenberg, M.; Dreher, K.; Maier-Hein, L. Deep Learning for Biomedical Photoacoustic Imaging: A Review. *Photoacoustics* **2021**, *22*, 100241. <https://doi.org/10.1016/j.pacs.2021.100241>.
- (26) Ly, C. D.; Nguyen, V. T.; Vo, T. H.; Mondal, S.; Park, S.; Choi, J.; Vu, T. T. H.; Kim, C. S.; Oh, J. Full-View in Vivo Skin and Blood Vessels Profile Segmentation in Photoacoustic Imaging Based on Deep Learning. *Photoacoustics* **2022**, *25* (September 2021), 100310. <https://doi.org/10.1016/j.pacs.2021.100310>.

- (27) Gleich, B.; Weizenecker, J. Tomographic Imaging Using the Nonlinear Response of Magnetic Particles. *Nature* **2005**, *435* (7046), 1214–1217. <https://doi.org/10.1038/nature03808>.
- (28) Borgert, J.; Schmidt, J. D.; Schmale, I.; Rahmer, J.; Bontus, C.; Gleich, B.; David, B.; Eckart, R.; Woywode, O.; Weizenecker, J.; Schnorr, J.; Taupitz, M.; Haegele, J.; Vogt, F. M.; Barkhausen, J. Fundamentals and Applications of Magnetic Particle Imaging. *J. Cardiovasc. Comput. Tomogr.* **2012**, *6* (3), 149–153. <https://doi.org/10.1016/j.jcct.2012.04.007>.
- (29) Raman, C. V.; Krishnan, K. S. A New Type of Secondary Radiation. *Nature* **1928**, *121* (3048), 501–502. <https://doi.org/10.1038/121501c0>.
- (30) Abramczyk, H.; Brozek-Pluska, B. Raman Imaging in Biochemical and Biomedical Applications. Diagnosis and Treatment of Breast Cancer. *Chem. Rev.* **2013**, *113* (8), 5766–5781. <https://doi.org/10.1021/cr300147r>.
- (31) Wang, W.; Wang, W.; Liu, L.; Xu, L.; Kuang, H.; Zhu, J.; Xu, C. Raman Spectra of Pyridine Adsorbed at Silver Electrode. *Chem. Phys. Lett.* **1974**, *26* (2), 163–166. <https://doi.org/10.1021/acsami.6b02905>.
- (32) Langer, J.; Jimenez de Aberasturi, D.; Aizpurua, J.; Alvarez-Puebla, R. A.; Auguie, B.; Baumberg, J. J.; Bazan, G. C.; Bell, S. E. J.; Boisen, A.; Brolo, A. G.; Choo, J.; Cialla-May, D.; Deckert, V.; Fabris, L.; Faulds, K.; Javier García de Abajo, F.; Goodacre, R.; Graham, D.; Haes, A. J.; Haynes, C. L.; Huck, C.; Itoh, T.; Käll, M.; Kneipp, J.; Kotov, N. A.; Kuang, H.; Le Ru, E. C.; Lee, H. K.; Li, J. F.; Ling, X. Y.; Maier, S. A.; Mayerhöfer, T.; Moskovits, M.; Murakoshi, K.; Nam, J. M.; Nie, S.; Ozaki, Y.; Pastoriza-Santos, I.; Perez-Juste, J.; Popp, J.; Pucci, A.; Reich, S.; Ren, B.; Schatz, G. C.; Shegai, T.; Schlücker, S.; Tay, L. L.; George Thomas, K.; Tian, Z. Q.; van Duyne, R. P.; Vo-Dinh, T.; Wang, Y.; Willets, K. A.; Xu, C.; Xu, H.; Xu, Y.; Yamamoto, Y. S.; Zhao, B.; Liz-Marzán, L. M. Present and Future of Surface-Enhanced Raman Scattering. *ACS Nano* **2020**, *14* (1), 28–117. <https://doi.org/10.1021/acsnano.9b04224>.
- (33) Jimenez de Aberasturi, D.; Henriksen-Lacey, M.; Litti, L.; Langer, J.; Liz-Marzán, L. M. Using SERS Tags to Image the Three-Dimensional Structure of Complex Cell Models. *Adv. Funct. Mater.* **2020**, *30* (14), 1909655. <https://doi.org/10.1002/adfm.201909655>.
- (34) Indrasekara, A. S. D. S.; Meyers, S.; Shubeita, S.; Feldman, L. C.; Gustafsson, T.; Fabris, L. Gold Nanostar Substrates for SERS-Based Chemical Sensing in the Femtomolar Regime. *Nanoscale* **2014**, *6* (15), 8891–8899. <https://doi.org/10.1039/c4nr02513j>.
- (35) Willets, K. A.; Van Duyne, R. P. Localized Surface Plasmon Resonance Spectroscopy and Sensing. *Annu. Rev. Phys. Chem.* **2007**, *58*, 267–297. <https://doi.org/10.1146/annurev.physchem.58.032806.104607>.
- (36) Scarabelli, L.; Grzelczak, M. Tuning Gold Nanorod Synthesis through Prereduction with Salicylic Acid. **2013**. <https://doi.org/10.1021/cm402177b>.
- (37) Jimenez de Aberasturi, D.; Serrano-Montes, A. B.; Langer, J.; Henriksen-Lacey, M.; Parak,

- W. J.; Liz-Marzán, L. M. Surface Enhanced Raman Scattering Encoded Gold Nanostars for Multiplexed Cell Discrimination. *Chem. Mater.* **2016**, *28* (18), 6779–6790. <https://doi.org/10.1021/acs.chemmater.6b03349>.
- (38) Fernández-Suárez, M.; Ting, A. Y. Fluorescent Probes for Super-Resolution Imaging in Living Cells. *Nat. Rev. Mol. Cell Biol.* **2008**, *9* (12), 929–943. <https://doi.org/10.1038/nrm2531>.
- (39) Sharma, P.; Brown, S.; Walter, G.; Santra, S.; Moudgil, B. Nanoparticles for Bioimaging. *Adv. Colloid Interface Sci.* **2006**, *123–126*, 471–485. <https://doi.org/10.1016/j.cis.2006.05.026>.
- (40) Tsang, M. K.; Wong, Y. T.; Hao, J. Cutting-Edge Nanomaterials for Advanced Multimodal Bioimaging Applications. *Small Methods* **2018**, *2* (1), 1–14. <https://doi.org/10.1002/smt.201700265>.
- (41) Liu, Y.; Jia, Q.; Zhou, J. Recent Advance in Near-Infrared (NIR) Imaging Probes for Cancer Theranostics. *Adv. Ther.* **2018**, *1* (8), 1800055. <https://doi.org/10.1002/adtp.201800055>.
- (42) Reguera, J.; Jimenez de Aberasturi, D.; Henriksen-Lacey, M.; Langer, J.; Espinosa, A.; Szczupak, B.; Wilhelm, C.; Liz-Marzán, L. M. Janus Plasmonic-Magnetic Gold-Iron Oxide Nanoparticles as Contrast Agents for Multimodal Imaging. *Nanoscale* **2017**, *9* (27), 9467–9480. <https://doi.org/10.1039/c7nr01406f>.
- (43) Foulkes, R.; Man, E.; Thind, J.; Yeung, S.; Joy, A.; Hoskins, C. The Regulation of Nanomaterials and Nanomedicines for Clinical Application: Current and Future Perspectives. *Biomater. Sci.* **2020**, *8* (17), 4653–4664. <https://doi.org/10.1039/d0bm00558d>.
- (44) Giner-Casares, J. J.; Henriksen-Lacey, M.; Coronado-Puchau, M.; Liz-Marzán, L. M. Inorganic Nanoparticles for Biomedicine: Where Materials Scientists Meet Medical Research. *Mater. Today* **2016**, *19* (1), 19–28. <https://doi.org/10.1016/j.mattod.2015.07.004>.
- (45) De, M.; Ghosh, P. S.; Rotello, V. M. Applications of Nanoparticles in Biology. *Adv. Mater.* **2008**, *20* (22), 4225–4241. <https://doi.org/10.1002/adma.200703183>.
- (46) Stark, W. J.; Stoessel, P. R.; Wohlleben, W.; Hafner, A. Industrial Applications of Nanoparticles. *Chem. Soc. Rev.* **2015**, *44* (16), 5793–5805. <https://doi.org/10.1039/c4cs00362d>.
- (47) Langer, J.; Novikov, S. M.; Liz-Marzán, L. M. Sensing Using Plasmonic Nanostructures and Nanoparticles. *Nanotechnology* **2015**, *26* (32), 322001. <https://doi.org/10.1088/0957-4484/26/32/322001>.
- (48) Pellico, J.; Gawne, P. J.; T. M. De Rosales, R. Radiolabelling of Nanomaterials for Medical Imaging and Therapy. *Chem. Soc. Rev.* **2021**, *50* (5), 3355–3423. <https://doi.org/10.1039/d0cs00384k>.

- (49) de la Encarnación, C.; Jimenez de Aberasturi, D.; Liz-Marzán, L. M. Multifunctional Plasmonic-Magnetic Nanoparticles for Bioimaging and Hyperthermia. *Adv. Drug Deliv. Rev.* **2022**, *189*, 114484. <https://doi.org/10.1016/j.addr.2022.114484>.
- (50) Dadfar, S. M.; Roemhild, K.; Drude, N. I.; von Stillfried, S.; Knüchel, R.; Kiessling, F.; Lammers, T. Iron Oxide Nanoparticles: Diagnostic, Therapeutic and Theranostic Applications. *Adv. Drug Deliv. Rev.* **2019**, *138*, 302–325. <https://doi.org/10.1016/j.addr.2019.01.005>.
- (51) Hu, F.; Jia, Q.; Li, Y.; Gao, M. Facile Synthesis of Ultrasmall PEGylated Iron Oxide Nanoparticles for Dual-Contrast T1-and T2-Weighted Magnetic Resonance Imaging. *Nanotechnology* **2011**, *22* (24), 245604. <https://doi.org/10.1088/0957-4484/22/24/245604>.
- (52) Sibuyi, N. R. S.; Moabelo, K. L.; Fadaka, A. O.; Meyer, S.; Onani, M. O.; Madiehe, A. M.; Meyer, M. Multifunctional Gold Nanoparticles for Improved Diagnostic and Therapeutic Applications: A Review. *Nanoscale Res. Lett.* **2021**, *16* (1), 174. <https://doi.org/10.1186/s11671-021-03632-w>.
- (53) Wang, L.; Hasanzadeh Kafshgari, M.; Meunier, M. Optical Properties and Applications of Plasmonic-Metal Nanoparticles. *Adv. Funct. Mater.* **2020**, 2005400. <https://doi.org/10.1002/adfm.202005400>.
- (54) Bansal, S. A.; Kumar, V.; Karimi, J.; Singh, A. P.; Kumar, S. Role of Gold Nanoparticles in Advanced Biomedical Applications. *Nanoscale Adv.* **2020**, *2* (9), 3764–3787. <https://doi.org/10.1039/d0na00472c>.
- (55) Jeong, H. H.; Choi, E.; Ellis, E.; Lee, T. C. Recent Advances in Gold Nanoparticles for Biomedical Applications: From Hybrid Structures to Multi-Functionality. *J. Mater. Chem. B* **2019**, *7*(22), 3480–3496. <https://doi.org/10.1039/c9tb00557a>.
- (56) Laurent, S.; Forge, D.; Port, M.; Roch, A.; Robic, C.; Vander Elst, L.; Muller, R. N. Magnetic Iron Oxide Nanoparticles: Synthesis, Stabilization, Vectorization, Physicochemical Characterizations and Biological Applications. *Chem. Rev.* **2008**, *108* (6), 2064–2110. <https://doi.org/10.1021/cr068445e>.
- (57) Guo, X.; Wu, Z.; Li, W.; Wang, Z.; Li, Q.; Kong, F.; Zhang, H.; Zhu, X.; Du, Y. P.; Jin, Y.; Du, Y.; You, J. Appropriate Size of Magnetic Nanoparticles for Various Bioapplications in Cancer Diagnostics and Therapy. *ACS Appl. Mater. Interfaces* **2016**, *8* (5), 3092–3106. <https://doi.org/10.1021/acsami.5b10352>.
- (58) Kouhpanji, M. R. Z.; Stadler, B. J. H. A Guideline for Effectively Synthesizing and Characterizing Magnetic Nanoparticles for Advancing Nanobiotechnology: A Review. *Sensors (Switzerland)* **2020**, *20* (9), 2554. <https://doi.org/10.3390/s20092554>.
- (59) Ahn, T.; Kim, J. H.; Yang, H. M.; Lee, J. W.; Kim, J. D. Formation Pathways of Magnetite Nanoparticles by Coprecipitation Method. *J. Phys. Chem. C* **2012**, *116* (10), 6069–6076. <https://doi.org/10.1021/jp211843g>.

- (60) Liu, X.; Qiu, G.; Yan, A.; Wang, Z.; Li, X. Hydrothermal Synthesis and Characterization of α -FeOOH and α -Fe₂O₃ Uniform Nanocrystallines. *J. Alloys Compd.* **2007**, *433* (1–2), 216–220. <https://doi.org/10.1016/j.jallcom.2006.06.029>.
- (61) Ge, S.; Shi, X.; Sun, K.; Li, C.; Uher, C.; Baker, J. R.; Banaszak Holl, M. M.; Orr, B. G. Facile Hydrothermal Synthesis of Iron Oxide Nanoparticles with Tunable Magnetic Properties. *J. Phys. Chem. C* **2009**, *113* (31), 13593–13599. <https://doi.org/10.1021/jp902953t>.
- (62) Wu, W.; He, Q.; Jiang, C. Magnetic Iron Oxide Nanoparticles: Synthesis and Surface Functionalization Strategies. *Nanoscale Res. Lett.* **2008**, *3* (11), 397–415. <https://doi.org/10.1007/s11671-008-9174-9>.
- (63) Sun, S.; Zeng, H. Size-Controlled Synthesis of Magnetite Nanoparticles. *J. Am. Chem. Soc.* **2002**, *124* (28), 8204–8205. <https://doi.org/10.1021/ja026501x>.
- (64) Mahdavi, M.; Ahmad, M. Bin; Haron, M. J.; Namvar, F.; Nadi, B.; Ab Rahman, M. Z.; Amin, J. Synthesis, Surface Modification and Characterisation of Biocompatible Magnetic Iron Oxide Nanoparticles for Biomedical Applications. *Molecules* **2013**, *18* (7), 7533–7548. <https://doi.org/10.3390/molecules18077533>.
- (65) Roca, A. G.; Marco, J. F.; Del Puerto Morales, M.; Serna, C. J. Effect of Nature and Particle Size on Properties of Uniform Magnetite and Maghemite Nanoparticles. *J. Phys. Chem. C* **2007**, *111* (50), 18577–18584. <https://doi.org/10.1021/jp075133m>.
- (66) Zhou, Z.; Zhu, X.; Wu, D.; Chen, Q.; Huang, D.; Sun, C.; Xin, J.; Ni, K.; Gao, J. Anisotropic Shaped Iron Oxide Nanostructures: Controlled Synthesis and Proton Relaxation Shortening Effects. *Chem. Mater.* **2015**, *27* (9), 3505–3515. <https://doi.org/10.1021/acs.chemmater.5b00944>.
- (67) Roca, A. G.; Gutiérrez, L.; Gavilán, H.; Fortes Brollo, M. E.; Veintemillas-Verdaguer, S.; Morales, M. del P. Design Strategies for Shape-Controlled Magnetic Iron Oxide Nanoparticles. *Adv. Drug Deliv. Rev.* **2019**, *138*, 68–104. <https://doi.org/10.1016/j.addr.2018.12.008>.
- (68) Smolensky, E. D.; Park, H. Y. E.; Zhou, Y.; Rolla, G. A.; Marjańska, M.; Botta, M.; Pierre, V. C. Scaling Laws at the Nanosize: The Effect of Particle Size and Shape on the Magnetism and Relaxivity of Iron Oxide Nanoparticle Contrast Agents. *J. Mater. Chem. B* **2013**, *1* (22), 2818–2828. <https://doi.org/10.1039/c3tb00369h>.
- (69) Gutiérrez, L.; Costo, R.; Grüttner, C.; Westphal, F.; Gehrke, N.; Heinke, D.; Fornara, A.; Pankhurst, Q. A.; Johansson, C.; Veintemillas-Verdaguer, S.; Morales, M. P. Synthesis Methods to Prepare Single- and Multi-Core Iron Oxide Nanoparticles for Biomedical Applications. *Dalt. Trans.* **2015**, *44* (7), 2943–2952. <https://doi.org/10.1039/c4dt03013c>.
- (70) Hemery, G.; Keyes, A. C.; Garaio, E.; Rodrigo, I.; Garcia, J. A.; Plazaola, F.; Garanger, E.; Sandre, O. Tuning Sizes, Morphologies, and Magnetic Properties of Monocore versus Multicore Iron Oxide Nanoparticles through the Controlled Addition of Water in the Polyol Synthesis. *Inorg. Chem.* **2017**, *56* (14), 8232–8243.

<https://doi.org/10.1021/acs.inorgchem.7b00956>.

- (71) Guardia, P.; Corato, R. Di; Lartigue, L.; Wilhelm, C.; Espinosa, A.; Garcia-hernandez, M.; Gazeau, F.; Manna, L.; Pellegrino, T. Water-Soluble Iron Oxide Nanocubes with High Values of Specific Absorption Rate for Cancer Cell Hyperthermia Treatment. *ACS Nano* **2012**, *6* (4), 3080–3091. <https://doi.org/10.1021/nn2048137>.
- (72) Hu, X.; Yu, J. C. Continuous Aspect-Ratio Tuning and Fine Shape Control of Monodisperse α -Fe₂O₃ Nanocrystals by a Programmed Microwave-Hydrothermal Method. *Adv. Funct. Mater.* **2008**, *18* (6), 880–887. <https://doi.org/10.1002/adfm.200700671>.
- (73) Nemati, Z.; Alonso, J.; Rodrigo, I.; Das, R.; Garaio, E.; García, J. Á.; Orue, I.; Phan, M. H.; Srikanth, H. Improving the Heating Efficiency of Iron Oxide Nanoparticles by Tuning Their Shape and Size. *J. Phys. Chem. C* **2018**, *122* (4), 2367–2381. <https://doi.org/10.1021/acs.jpcc.7b10528>.
- (74) Storozhuk, L.; Besenhard, M. O.; Mourdikoudis, S.; LaGrow, A. P.; Lees, M. R.; Tung, L. D.; Gavriilidis, A.; Thanh, N. T. K. Stable Iron Oxide Nanoflowers with Exceptional Magnetic Heating Efficiency: Simple and Fast Polyol Synthesis. *ACS Appl. Mater. Interfaces* **2021**, *13* (38), 45870–45880. <https://doi.org/10.1021/acsami.1c12323>.
- (75) Lu, X.; Rycenga, M.; Skrabalak, S. E.; Wiley, B.; Xia, Y. Chemical Synthesis of Novel Plasmonic Nanoparticles. *Annu. Rev. Phys. Chem.* **2009**, *60*, 167–192. <https://doi.org/10.1146/annurev.physchem.040808.090434>.
- (76) Duan, H.; Wang, D.; Li, Y. Green Chemistry for Nanoparticle Synthesis. *Chem. Soc. Rev.* **2015**, *44* (16), 5778–5792. <https://doi.org/10.1039/c4cs00363b>.
- (77) Thakkar, K. N.; Mhatre, S. S.; Parikh, R. Y. Biological Synthesis of Metallic Nanoparticles. *Nanomedicine Nanotechnology, Biol. Med.* **2010**, *6* (2), 257–262. <https://doi.org/10.1016/j.nano.2009.07.002>.
- (78) Turkevich, J.; Stevenson, P. C.; Hillier, J. A Study of the Nucleation and Growth Processes in the Synthesis of Colloidal Gold. *Discuss. Faraday Soc.* **1951**, *11*, 55–75. <https://doi.org/10.1039/DF9511100055>.
- (79) Reguera, J.; Langer, J.; Jimenez de Aberasturi, D.; Liz-Marzán, L. M. Anisotropic Metal Nanoparticles for Surface Enhanced Raman Scattering. *Chem. Soc. Rev.* **2017**, *46* (13), 3866–3885. <https://doi.org/10.1039/c7cs00158d>.
- (80) Hemmer, E.; Benayas, A.; Légaré, F.; Vetrone, F. Exploiting the Biological Windows: Current Perspectives on Fluorescent Bioprobes Emitting above 1000 Nm. *Nanoscale Horizons* **2016**, *1* (3), 168–184. <https://doi.org/10.1039/c5nh00073d>.
- (81) Liz-Marzán, L. M.; Grzelczak, M. Growing Anisotropic Crystals at the Nanoscale. *Science (80-)* **2017**, *356* (6343), 1120–1121. <https://doi.org/10.1126/science.aam8774>.
- (82) Sánchez-iglesias, A.; Winckelmans, N.; Bals, S.; Grzelczak, M.; Liz-marzán, L. M. High-Yield Seeded Growth of Monodisperse Pentatwinned Gold Nanoparticles through Thermally

- Induced Seed Twinning. *J. Am. Chem. Soc.* **2017**, *139* (1), 107–110. <https://doi.org/https://doi.org/10.1021/jacs.6b12143>.
- (83) González-Rubio, G.; Kumar, V.; Llombart, P.; Díaz-Núñez, P.; Bladt, E.; Altantzis, T.; Bals, S.; Peña-Rodríguez, O.; Noya, E. G.; Macdowell, L. G.; Guerrero-Martínez, A.; Liz-Marzán, L. M. Disconnecting Symmetry Breaking from Seeded Growth for the Reproducible Synthesis of High Quality Gold Nanorods. *ACS Nano* **2019**, *13* (4), 4424–4435. <https://doi.org/10.1021/acsnano.8b09658>.
- (84) Scarabelli, L.; Coronado-Puchau, M.; Giner-Casares, J. J.; Langer, J.; Liz-Marzán, L. M. Monodisperse Gold Nanotriangles: Size Control, Large-Scale Self-Assembly, and Performance in Surface-Enhanced Raman Scattering. *ACS Nano* **2014**, *8* (6), 5833–5842. <https://doi.org/10.1021/nn500727w>.
- (85) Hanske, C.; González-Rubio, G.; Hamon, C.; Formentín, P.; Modin, E.; Chuvilin, A.; Guerrero-Martínez, A.; Marsal, L. F.; Liz-Marzán, L. M. Large-Scale Plasmonic Pyramidal Supercrystals via Templated Self-Assembly of Monodisperse Gold Nanospheres. *J. Phys. Chem. C* **2017**, *121* (20), 10899–10906. <https://doi.org/10.1021/acs.jpcc.6b12161>.
- (86) Wu, H. L.; Kuo, C. H.; Huang, M. H. Seed-Mediated Synthesis of Gold Nanocrystals with Systematic Shape Evolution from Cubic to Trisoctahedral and Rhombic Dodecahedral Structures. *Langmuir* **2010**, *26* (14), 12307–12313. <https://doi.org/10.1021/la1015065>.
- (87) Cho, S. J.; Idrobo, J. C.; Olamit, J.; Liu, K.; Browning, N. D.; Kauzlarich, S. M. Growth Mechanisms and Oxidation Resistance of Gold-Coated Iron Nanoparticles. *Chem. Mater.* **2005**, *17* (12), 3181–3186. <https://doi.org/10.1021/cm0500713>.
- (88) Chiang, I. C.; Chen, D. H. Structural Characterization and Self-Assembly into Superlattices of Iron Oxide-Gold Core-Shell Nanoparticles Synthesized via a High-Temperature Organometallic Route. *Nanotechnology* **2009**, *20* (1), 015602. <https://doi.org/10.1088/0957-4484/20/1/015602>.
- (89) Wang, L.; Luo, J.; Fan, Q.; Suzuki, M.; Suzuki, I. S.; Engelhard, M. H.; Lin, Y.; Kim, N.; Wang, J. Q.; Zhong, C. J. Monodispersed Core-Shell Fe₃O₄@Au Nanoparticles. *J. Phys. Chem. B* **2005**, *109* (46), 21593–21601. <https://doi.org/10.1021/jp0543429>.
- (90) Billen, A.; de Cattelle, A.; Jochum, J. K.; Van Bael, M. J.; Billen, J.; Seo, J. W.; Brullot, W.; Koeckelberghs, G.; Verbiest, T. Novel Synthesis of Superparamagnetic Plasmonic Core-Shell Iron Oxide-Gold Nanoparticles. *Phys. B Condens. Matter* **2019**, *560*, 85–90. <https://doi.org/10.1016/j.physb.2019.02.009>.
- (91) Ji, X.; Shao, R.; Elliott, A. M.; Jason Stafford, R.; Esparza-Coss, E.; Bankson, J. A.; Liang, G.; Luo, Z. P.; Park, K.; Markert, J. T.; Li, C. Bifunctional Gold Nanoshells with a Superparamagnetic Iron Oxide-Silica Core Suitable for Both MR Imaging and Photothermal Therapy. *J. Phys. Chem. C* **2007**, *111* (17), 6245–6251. <https://doi.org/10.1021/jp0702245>.
- (92) Jin, C.; Qu, Y.; Wang, M.; Han, J.; Hu, Y.; Guo, R. Aqueous Solution-Based Fe₃O₄ Seed-

Mediated Route to Hydrophilic Fe₃O₄-Au Janus Nanoparticles. *Langmuir* **2016**, *32* (18), 4595–4601. <https://doi.org/10.1021/acs.langmuir.6b01269>.

- (93) Goon, I. Y.; Lai, L. M. H.; Lim, M.; Munroe, P.; Gooding, J. J.; Amal, R. Fabrication and Dispersion of Gold-Shell-Protected Magnetite Nanoparticles: Systematic Control Using Polyethyleneimine. *Chem. Mater.* **2009**, *21* (4), 673–681. <https://doi.org/10.1021/cm8025329>.
- (94) Barrow, M.; Taylor, A.; Murray, P.; Rosseinsky, M. J.; Adams, D. J. Design Considerations for the Synthesis of Polymer Coated Iron Oxide Nanoparticles for Stem Cell Labelling and Tracking Using MRI. *Chem. Soc. Rev.* **2015**, *44* (19), 6733–6748. <https://doi.org/10.1039/c5cs00331h>.
- (95) Xiao, S.; Yu, X.; Zhang, L.; Zhang, Y.; Fan, W.; Sun, T.; Zhou, C.; Liu, Y.; Liu, Y.; Gong, M.; Zhang, D. Synthesis of Peg-Coated, Ultrasmall, Manganese-Doped Iron Oxide Nanoparticles with High Relaxivity for T1 /T2 Dual-Contrast Magnetic Resonance Imaging. *Int. J. Nanomedicine* **2019**, *14*, 8499–8507. <https://doi.org/10.2147/IJN.S219749>.
- (96) Amara, D.; Grinblat, J.; Margel, S. Solventless Thermal Decomposition of Ferrocene as a New Approach for One-Step Synthesis of Magnetite Nanocubes and Nanospheres. *J. Mater. Chem.* **2012**, *22* (5), 2188–2195. <https://doi.org/10.1039/c1jm13942h>.
- (97) Demirer, G. S.; Okur, A. C.; Kizilel, S. Synthesis and Design of Biologically Inspired Biocompatible Iron Oxide Nanoparticles for Biomedical Applications. *J. Mater. Chem. B* **2015**, *3* (40), 7831–7849. <https://doi.org/10.1039/c5tb00931f>.
- (98) Panda, J.; Satapathy, B. S.; Majumder, S.; Sarkar, R.; Mukherjee, B.; Tudu, B. Engineered Polymeric Iron Oxide Nanoparticles as Potential Drug Carrier for Targeted Delivery of Docetaxel to Breast Cancer Cells. *J. Magn. Magn. Mater.* **2019**, *485* (August 2018), 165–173. <https://doi.org/10.1016/j.jmmm.2019.04.058>.
- (99) Arias, L. S.; Pessan, J. P.; de Souza Neto, F. N.; Lima, B. H. R.; de Camargo, E. R.; Ramage, G.; Delbem, A. C. B.; Monteiro, D. R. Novel Nanocarrier of Miconazole Based on Chitosan-Coated Iron Oxide Nanoparticles as a Nanotherapy to Fight Candida Biofilms. *Colloids Surfaces B Biointerfaces* **2020**, *192* (February), 111080. <https://doi.org/10.1016/j.colsurfb.2020.111080>.
- (100) Xia, T.; Wang, J.; Wu, C.; Meng, F.; Shi, Z.; Lian, J.; Feng, J.; Meng, J. Novel Complex-Coprecipitation Route to Form High Quality Triethanolamine-Coated Fe₃O₄ Nanocrystals: Their High Saturation Magnetizations and Excellent Water Treatment Properties. *CrystEngComm* **2012**, *14* (18), 5741–5744. <https://doi.org/10.1039/c2ce25813g>.
- (101) Nosrati, H.; Salehiabar, M.; Davaran, S.; Ramazani, A.; Manjili, H. K.; Danafar, H. New Advances Strategies for Surface Functionalization of Iron Oxide Magnetic Nano Particles (IONPs). *Res. Chem. Intermed.* **2017**, *43* (12), 7423–7442. <https://doi.org/10.1007/s11164-017-3084-3>.

- (102) Korpany, K. V.; Mottillo, C.; Bachelder, J.; Cross, S. N.; Dong, P.; Trudel, S.; Friščić, T.; Blum, A. S. One-Step Ligand Exchange and Switching from Hydrophobic to Water-Stable Hydrophilic Superparamagnetic Iron Oxide Nanoparticles by Mechanochemical Milling. *Chem. Commun.* **2016**, *52* (14), 3054–3057. <https://doi.org/10.1039/c5cc07107k>.
- (103) Wu, W.; Wu, Z.; Yu, T.; Jiang, C.; Kim, W. S. Recent Progress on Magnetic Iron Oxide Nanoparticles: Synthesis, Surface Functional Strategies and Biomedical Applications. *Sci. Technol. Adv. Mater.* **2015**, *16* (2), 23501. <https://doi.org/10.1088/1468-6996/16/2/023501>.
- (104) Iwaki, Y.; Kawasaki, H.; Arakawa, R. Human Serum Albumin-Modified Fe₃O₄ Magnetic Nanoparticles for Affinity-SALDI-MS of Small-Molecule Drugs in Biological Liquids. *Anal. Sci.* **2012**, *28* (9), 893–900. <https://doi.org/10.2116/analsci.28.893>.
- (105) Samanta, B.; Yan, H.; Fischer, N. O.; Shi, J.; Jerry, D. J.; Rotello, V. M. Protein-Passivated Fe₃O₄ Nanoparticles: Low Toxicity and Rapid Heating for Thermal Therapy. *J. Mater. Chem.* **2008**, *18* (11), 1204–1208. <https://doi.org/10.1039/b718745a>.
- (106) Bhattacharya, D.; Chakraborty, S. P.; Pramanik, A.; Baksi, A.; Roy, S.; Maiti, T. K.; Ghosh, S. K.; Pramanik, P. Detection of Total Count of Staphylococcus Aureus Using Anti-Toxin Antibody Labelled Gold Magnetite Nanocomposites: A Novel Tool for Capture, Detection and Bacterial Separation. *J. Mater. Chem.* **2011**, *21* (43), 17273–17282. <https://doi.org/10.1039/c1jm12076j>.
- (107) More, M. P.; Deshmukh, P. K. Development of Amine-Functionalized Superparamagnetic Iron Oxide Nanoparticles Anchored Graphene Nanosheets as a Possible Theranostic Agent in Cancer Metastasis. *Drug Deliv. Transl. Res.* **2020**, *10* (4), 862–877. <https://doi.org/10.1007/s13346-020-00729-0>.
- (108) Mout, R.; Moyano, D. F.; Rana, S.; Rotello, V. M. Surface Functionalization of Nanoparticles for Nanomedicine. *Chem. Soc. Rev.* **2012**, *41* (7), 2539–2544. <https://doi.org/10.1039/c2cs15294k>.
- (109) Laing, S.; Gracie, K.; Faulds, K. Multiplex in Vitro Detection Using SERS. *Chem. Soc. Rev.* **2016**, *45* (7), 1901–1918. <https://doi.org/10.1039/c5cs00644a>.
- (110) Sztandera, K.; Gorzkiewicz, M.; Klajnert-Maculewicz, B. Gold Nanoparticles in Cancer Treatment. *Mol. Pharm.* **2019**, *16* (1), 1–23. <https://doi.org/10.1021/acs.molpharmaceut.8b00810>.
- (111) Mahato, K.; Nagpal, S.; Shah, M. A.; Srivastava, A.; Maurya, P. K.; Roy, S.; Jaiswal, A.; Singh, R.; Chandra, P. Gold Nanoparticle Surface Engineering Strategies and Their Applications in Biomedicine and Diagnostics. *3 Biotech* **2019**, *9* (2), 57. <https://doi.org/10.1007/s13205-019-1577-z>.
- (112) Sánchez, A.; Ovejero Paredes, K.; Ruiz-Cabello, J.; Martínez-Ruiz, P.; Pingarrón, J. M.; Villalonga, R.; Filice, M. Hybrid Decorated Core@shell Janus Nanoparticles as a Flexible Platform for Targeted Multimodal Molecular Bioimaging of Cancer. *ACS Appl. Mater.*

Interfaces **2018**, *10* (37), 31032–31043. <https://doi.org/10.1021/acsami.8b10452>.

- (113) Bouché, M.; Hsu, J. C.; Dong, Y. C.; Kim, J.; Taing, K.; Cormode, D. P. Recent Advances in Molecular Imaging with Gold Nanoparticles. *Bioconjug. Chem.* **2020**, *31* (2), 303–314. <https://doi.org/10.1021/acs.bioconjchem.9b00669>.
- (114) Liu, X.; Song, X.; Luan, D.; Hu, B.; Xu, K.; Tang, B. Real-Time in Situ Visualizing of the Sequential Activation of Caspase Cascade Using a Multicolor Gold-Selenium Bonding Fluorescent Nanoprobe. *Anal. Chem.* **2019**, *91* (9), 5994–6002. <https://doi.org/10.1021/acs.analchem.9b00452>.
- (115) Hu, X.; Zhang, Y.; Ding, T.; Liu, J.; Zhao, H. Multifunctional Gold Nanoparticles: A Novel Nanomaterial for Various Medical Applications and Biological Activities. *Front. Bioeng. Biotechnol.* **2020**, *8* (August), 1–17. <https://doi.org/10.3389/fbioe.2020.00990>.
- (116) Liu, S.; Han, M. Y. Silica-Coated Metal Nanoparticles. *Chem. - An Asian J.* **2010**, *5* (1), 36–45. <https://doi.org/10.1002/asia.200900228>.
- (117) Halas, N. J. Nanoscience under Glass: The Versatile Chemistry of Silica Nanostructures. *ACS Nano* **2008**, *2* (2), 179–183. <https://doi.org/10.1021/nn800052e>.
- (118) Luke, G. P.; Bashyam, A.; Homan, K. A.; Makhija, S.; Chen, Y. S.; Emelianov, S. Y. Silica-Coated Gold Nanoplates as Stable Photoacoustic Contrast Agents for Sentinel Lymph Node Imaging. *Nanotechnology* **2013**, *24* (45). <https://doi.org/10.1088/0957-4484/24/45/455101>.
- (119) Terentyuk, G.; Panfilova, E.; Khanadeev, V.; Chumakov, D.; Genina, E.; Bashkatov, A.; Tuchin, V.; Bucharskaya, A.; Maslyakova, G.; Khlebtsov, N.; Khlebtsov, B. Gold Nanorods with a Hematoporphyrin-Loaded Silica Shell for Dual-Modality Photodynamic and Photothermal Treatment of Tumors in Vivo. *Nano Res.* **2014**, *7* (3), 325–337. <https://doi.org/10.1007/s12274-013-0398-3>.
- (120) Cai, C.; Li, X.; Wang, Y.; Liu, M.; Shi, X.; Xia, J.; Shen, M. Polydopamine-Coated Gold Core/Hollow Mesoporous Silica Shell Particles as a NanoplatforM for Multimode Imaging and Photothermal Therapy of Tumors. *Chem. Eng. J.* **2019**, *362* (December 2018), 842–850. <https://doi.org/10.1016/j.cej.2019.01.072>.
- (121) Carrasco, S.; Benito-Peña, E.; Navarro-Villoslada, F.; Langer, J.; Sanz-Ortiz, M. N.; Reguera, J.; Liz-Marzán, L. M.; Moreno-Bondi, M. C. Multibranching Gold-Mesoporous Silica Nanoparticles Coated with a Molecularly Imprinted Polymer for Label-Free Antibiotic Surface-Enhanced Raman Scattering Analysis. *Chem. Mater.* **2016**, *28* (21), 7947–7954. <https://doi.org/10.1021/acs.chemmater.6b03613>.
- (122) Levin, C. S.; Hofmann, C.; Ali, T. A.; Kelly, A. T.; Morosan, E.; Nordlander, P.; Whitmire, K. H.; Halas, N. J. Magnetic-Plasmonic Core-Shell Nanoparticles. *ACS Nano* **2009**, *3* (6), 1379–1388. <https://doi.org/10.1021/nn900118a>.
- (123) Quaresma, P.; Osório, I.; Dória, G.; Carvalho, P. A.; Pereira, A.; Langer, J.; Araújo, J. P.;

- Pastoriza-Santos, I.; Liz-Marzán, L. M.; Franco, R.; Baptista, P. V.; Pereira, E. Star-Shaped Magnetite@gold Nanoparticles for Protein Magnetic Separation and SERS Detection. *RSC Adv.* **2014**, *4* (8), 3659–3667. <https://doi.org/10.1039/c3ra46762g>.
- (124) LaConte, L. E. W.; Nitin, N.; Zurkiya, O.; Caruntu, D.; O'Connor, C. J.; Hu, X.; Bao, G. Coating Thickness of Magnetic Iron Oxide Nanoparticles Affects R₂ Relaxivity. *J. Magn. Reson. Imaging* **2007**, *26* (6), 1634–1641. <https://doi.org/10.1002/jmri.21194>.
- (125) Cortie, M. B.; McDonagh, A. M. Synthesis and Optical Properties of Hybrid and Alloy Plasmonic Nanoparticles. *Chem. Rev.* **2011**, *111* (6), 3713–3735. <https://doi.org/10.1021/cr1002529>.
- (126) Ha, M.; Kim, J. H.; You, M.; Li, Q.; Fan, C.; Nam, J. M. Multicomponent Plasmonic Nanoparticles: From Heterostructured Nanoparticles to Colloidal Composite Nanostructures. *Chem. Rev.* **2019**, *119* (24), 12208–12278. <https://doi.org/10.1021/acs.chemrev.9b00234>.
- (127) Das, P.; Fatehbasharadz, P.; Colombo, M.; Fiandra, L.; Prospero, D. Multifunctional Magnetic Gold Nanomaterials for Cancer. *Trends Biotechnol.* **2019**, *37* (9), 995–1010. <https://doi.org/10.1016/j.tibtech.2019.02.005>.
- (128) Nguyen Tri, P.; Ouellet-Plamondon, C.; Rtimi, S.; Assadi, A. A.; Nguyen, T. A. *Noble Metal-Metal Oxide Hybrid Nanoparticles. Chapter 3: Methods for Synthesis of Hybrid Nanoparticles*; 2019. <https://doi.org/10.1016/B978-0-12-814134-2.00003-6>.
- (129) Lim, J.; Majetich, S. A. Composite Magnetic-Plasmonic Nanoparticles for Biomedicine: Manipulation and Imaging. *Nano Today* **2013**, *8* (1), 98–113. <https://doi.org/10.1016/j.nantod.2012.12.010>.
- (130) Stafford, S.; Garcia, R. S.; Gun'ko, Y. K. Multimodal Magnetic-Plasmonic Nanoparticles for Biomedical Applications. *Appl. Sci.* **2018**, *8*, 97. <https://doi.org/10.3390/app8010097>.
- (131) M. Tréguer-Delapierre, J. Majimel, S. Mornet, E. Duguet, S. R. Synthesis of Non-Spherical Gold Nanoparticles. *Gold Bull.* **2008**, *41* (2), 195–207. <https://doi.org/10.1166/jnn.2011.4339>.
- (132) Arenas-Guerrero, P.; Delgado, Á. V.; Donovan, K. J.; Scott, K.; Bellini, T.; Mantegazza, F.; Jiménez, M. L. Determination of the Size Distribution of Non-Spherical Nanoparticles by Electric Birefringence-Based Methods. *Sci. Rep.* **2018**, *8* (1), 9502. <https://doi.org/10.1038/s41598-018-27840-0>.
- (133) Bhattacharjee, S. DLS and Zeta Potential - What They Are and What They Are Not? *J. Control. Release* **2016**, *235*, 337–351. <https://doi.org/10.1016/j.jconrel.2016.06.017>.
- (134) Winsett, J.; Moilanen, A.; Paudel, K.; Kamali, S.; Ding, K.; Cribb, W.; Seifu, D.; Neupane, S. Quantitative Determination of Magnetite and Maghemite in Iron Oxide Nanoparticles Using Mössbauer Spectroscopy. *SN Appl. Sci.* **2019**, *1*, 1636. <https://doi.org/10.1007/s42452-019-1699-2>.

- (135) Yadav, B. Sen; Singh, R.; Vishwakarma, A. K.; Kumar, N. Facile Synthesis of Substantially Magnetic Hollow Nanospheres of Maghemite ($\gamma\text{-Fe}_2\text{O}_3$) Originated from Magnetite (Fe_3O_4) via Solvothermal Method. *J. Supercond. Nov. Magn.* **2020**, *33* (7), 2199–2208. <https://doi.org/10.1007/s10948-020-05481-7>.
- (136) Lee, N.; Hyeon, T. Designed Synthesis of Uniformly Sized Iron Oxide Nanoparticles for Efficient Magnetic Resonance Imaging Contrast Agents. *Chem. Soc. Rev.* **2012**, *41* (7), 2575–2589. <https://doi.org/10.1039/c1cs15248c>.
- (137) Wu, K.; Liu, J.; Saha, R.; Peng, C.; Su, D.; Wang, Y. A.; Wang, J. P. Investigation of Commercial Iron Oxide Nanoparticles: Structural and Magnetic Property Characterization. *ACS Omega* **2021**, *6* (9), 6274–6283. <https://doi.org/10.1021/acsomega.0c05845>.
- (138) Mychinko, M.; Skorikov, A.; Albrecht, W.; Sánchez-Iglesias, A.; Zhuo, X.; Kumar, V.; Liz-Marzán, L. M.; Bals, S. The Influence of Size, Shape, and Twin Boundaries on Heat-Induced Alloying in Individual Au@Ag Core–Shell Nanoparticles. *Small* **2021**, *17* (34), 2102348. <https://doi.org/10.1002/sml.202102348>.
- (139) Sánchez-Iglesias, A.; Zhuo, X.; Albrecht, W.; Bals, S.; Liz-Marzán, L. M. Tuning Size and Seed Position in Small Silver Nanorods. *ACS Mater. Lett.* **2020**, *2* (9), 1246–1250. <https://doi.org/10.1021/acsmaterialslett.0c00388>.
- (140) Estradé, S.; Yedra, L.; López-Ortega, A.; Estrader, M.; Salazar-Alvarez, G.; Baró, M. D.; Nogués, J.; Peiró, F. Distinguishing the Core from the Shell in $\text{MnO}_x/\text{MnO}_y$ and $\text{FeO}_x/\text{MnO}_x$ Core/Shell Nanoparticles through Quantitative Electron Energy Loss Spectroscopy (EELS) Analysis. *Micron* **2012**, *43* (1), 30–36. <https://doi.org/10.1016/j.micron.2011.04.002>.
- (141) Wagener, P.; Jakobi, J.; Rehbock, C.; Chakravadhanula, V. S. K.; Thede, C.; Wiedwald, U.; Bartsch, M.; Kienle, L.; Barcikowski, S. Solvent-Surface Interactions Control the Phase Structure in Laser-Generated Iron-Gold Core-Shell Nanoparticles. *Sci. Rep.* **2016**, *6*, 23352. <https://doi.org/10.1038/srep23352>.
- (142) Kattan, N.; Hou, B.; Fermín, D. J.; Cherns, D. Crystal Structure and Defects Visualization of $\text{Cu}_2\text{ZnSnS}_4$ Nanoparticles Employing Transmission Electron Microscopy and Electron Diffraction. *Appl. Mater. Today* **2015**, *1* (1), 52–59. <https://doi.org/10.1016/j.apmt.2015.08.004>.
- (143) Bals, S.; Goris, B.; Liz-Marzán, L. M.; Van Tendeloo, G. Three-Dimensional Characterization of Noble-Metal Nanoparticles and Their Assemblies by Electron Tomography. *Angew. Chemie - Int. Ed.* **2014**, *53* (40), 10600–10610. <https://doi.org/10.1002/anie.201401059>.
- (144) Winckelmans, N.; Altantzis, T.; Grzelczak, M.; Sánchez-Iglesias, A.; Liz-Marzán, L. M.; Bals, S. Multimode Electron Tomography as a Tool to Characterize the Internal Structure and Morphology of Gold Nanoparticles. *J. Phys. Chem. C* **2018**, *122* (25), 13522–13528. <https://doi.org/10.1021/acs.jpcc.7b12379>.
- (145) Rogosnitzky, M.; Branch, S. Gadolinium-Based Contrast Agent Toxicity: A Review of

- Known and Proposed Mechanisms. *BioMetals*. 2016, pp 365–376. <https://doi.org/10.1007/s10534-016-9931-7>.
- (146) Cho, S. J.; Jarrett, B. R.; Louie, A. Y.; Kauzlarich, S. M. Gold-Coated Iron Nanoparticles: A Novel Magnetic Resonance Agent for T₁ and T₂ Weighted Imaging. *Nanotechnology* **2006**, *17* (3), 640–644. <https://doi.org/10.1088/0957-4484/17/3/004>.
- (147) Jung, H.; Park, B.; Lee, C.; Cho, J.; Suh, J.; Park, J. Y.; Kim, Y. R.; Kim, J.; Cho, G.; Cho, H. J. Dual MRI T₁ and T₂(*) Contrast with Size-Controlled Iron Oxide Nanoparticles. *Nanomedicine Nanotechnology, Biol. Med.* **2014**, *10* (8), 1679–1689. <https://doi.org/10.1016/j.nano.2014.05.003>.
- (148) Gallo, J.; Long, N. J.; Aboagye, E. O. Magnetic Nanoparticles as Contrast Agents in the Diagnosis and Treatment of Cancer. *Chem. Soc. Rev.* **2013**, *42* (19), 7816–7833. <https://doi.org/10.1039/c3cs60149h>.
- (149) Peng, Y. K.; Tsang, S. C. E.; Chou, P. T. Chemical Design of Nanoprobes for T₁-Weighted Magnetic Resonance Imaging. *Mater. Today* **2016**, *19* (6), 336–348. <https://doi.org/10.1016/j.mattod.2015.11.006>.
- (150) Fernández-Barahona, I.; Muñoz-Hernando, M.; Ruiz-Cabello, J.; Herranz, F.; Pellico, J. Iron Oxide Nanoparticles: An Alternative for Positive Contrast in Magnetic Resonance Imaging. *Inorganics* **2020**, *8* (4), 28. <https://doi.org/10.3390/inorganics8040028>.
- (151) Zhu, X.; Li, J.; Peng, P.; Hosseini Nassab, N.; Smith, B. R. Quantitative Drug Release Monitoring in Tumors of Living Subjects by Magnetic Particle Imaging Nanocomposite. *Nano Lett.* **2019**, *19* (10), 6725–6733. <https://doi.org/10.1021/acs.nanolett.9b01202>.
- (152) Zheng, B.; Yu, E.; Orendorff, R.; Lu, K.; Konkle, J. J.; Tay, Z. W.; Hensley, D.; Zhou, X. Y.; Chandrasekharan, P.; Saritas, E. U.; Goodwill, P. W.; Hazle, J. D.; Conolly, S. M. Seeing SPIOs Directly In Vivo with Magnetic Particle Imaging. *Mol. Imaging Biol.* **2017**, *19* (3), 385–390. <https://doi.org/10.1007/s11307-017-1081-y>.
- (153) Tay, Z. W.; Chandrasekharan, P.; Chiu-Lam, A.; Hensley, D. W.; Dhavalikar, R.; Zhou, X. Y.; Yu, E. Y.; Goodwill, P. W.; Zheng, B.; Rinaldi, C.; Conolly, S. M. Magnetic Particle Imaging-Guided Heating in Vivo Using Gradient Fields for Arbitrary Localization of Magnetic Hyperthermia Therapy. *ACS Nano* **2018**, *12* (4), 3699–3713. <https://doi.org/10.1021/acsnano.8b00893>.
- (154) Ludewig, P.; Gdaniec, N.; Sedlacik, J.; Forkert, N. D.; Szwargulski, P.; Graeser, M.; Adam, G.; Kaul, M. G.; Krishnan, K. M.; Ferguson, R. M.; Khandhar, A. P.; Walczak, P.; Fiehler, J.; Thomalla, G.; Gerloff, C.; Knopp, T.; Magnus, T. Magnetic Particle Imaging for Real-Time Perfusion Imaging in Acute Stroke. *ACS Nano* **2017**, *11* (10), 10480–10488. <https://doi.org/10.1021/acsnano.7b05784>.
- (155) Bulte, J. W. M. Superparamagnetic Iron Oxides as MPI Tracers: A Primer and Review of Early Applications. *Adv. Drug Deliv. Rev.* **2019**, *138*, 293–301. <https://doi.org/10.1016/j.addr.2018.12.007>.

- (156) Graeser, M.; Thieben, F.; Szwargulski, P.; Werner, F.; Gdaniec, N.; Boberg, M.; Griese, F.; Möddel, M.; Ludewig, P.; van de Ven, D.; Weber, O. M.; Woywode, O.; Gleich, B.; Knopp, T. Human-Sized Magnetic Particle Imaging for Brain Applications. *Nat. Commun.* **2019**, *10* (1), 1936. <https://doi.org/10.1038/s41467-019-09704-x>.
- (157) Lu, C.; Han, L.; Wang, J.; Wan, J.; Song, G.; Rao, J. Engineering of Magnetic Nanoparticles as Magnetic Particle Imaging Tracers. *Chem. Soc. Rev.* **2021**, *50* (14), 8102–8146. <https://doi.org/10.1039/d0cs00260g>.
- (158) Panagiotopoulos, N.; Duschka, R. L.; Ahlborg, M.; Bringout, G.; Debbeler, C.; Graeser, M.; Kaethner, C.; Lüdtke-Buzug, K.; Medimagh, H.; Stelzner, J.; Buzug, T. M.; Barkhausen, J.; Vogt, F. M.; Haegele, J. Magnetic Particle Imaging: Current Developments and Future Directions. *Int. J. Nanomedicine* **2015**, *10*, 3097–3114. <https://doi.org/10.2147/IJN.S70488>.
- (159) Kim, D.; Yu, M. K.; Lee, T. S.; Park, J. J.; Jeong, Y. Y.; Jon, S. Amphiphilic Polymer-Coated Hybrid Nanoparticles as CT/MRI Dual Contrast Agents. *Nanotechnology* **2011**, *22* (15), 155101. <https://doi.org/10.1088/0957-4484/22/15/155101>.
- (160) Cormode, D. P.; Naha, P. C.; Fayad, Z. A. Nanoparticle Contrast Agents for Computed Tomography: A Focus on Micelles. *Contrast Media Mol. Imaging* **2014**, *9* (1), 37–52. <https://doi.org/10.1002/cmml.1551>.
- (161) Dong, Y. C.; Hajfathalian, M.; Maidment, P. S. N.; Hsu, J. C.; Naha, P. C.; Si-Mohamed, S.; Breuilly, M.; Kim, J.; Chhour, P.; Douek, P.; Litt, H. I.; Cormode, D. P. Effect of Gold Nanoparticle Size on Their Properties as Contrast Agents for Computed Tomography. *Sci. Rep.* **2019**, *9* (1), 141912. <https://doi.org/10.1038/s41598-019-50332-8>.
- (162) Mantri, Y.; Jokerst, J. V. Engineering Plasmonic Nanoparticles for Enhanced Photoacoustic Imaging. *ACS Nano* **2020**, *14* (8), 9408–9422. <https://doi.org/10.1021/acsnano.0c05215>.
- (163) Eggeling, C.; Widengren, J.; Rigler, R.; Seidel, C. A. M. Photobleaching of Fluorescent Dyes under Conditions Used for Single-Molecule Detection: Evidence of Two-Step Photolysis. *Anal. Chem.* **1998**, *70* (13), 2651–2659. <https://doi.org/10.1021/ac980027p>.
- (164) Bao, C.; Beziere, N.; Del Pino, P.; Pelaz, B.; Estrada, G.; Tian, F.; Ntziachristos, V.; De La Fuente, J. M.; Cui, D. Gold Nanoprisms as Optoacoustic Signal Nanoamplifiers for in Vivo Bioimaging of Gastrointestinal Cancers. *Small* **2013**, *9* (1), 68–74. <https://doi.org/10.1002/smll.201201779>.
- (165) Song, K. H.; Kim, C.; Cogley, C. M.; Xia, Y.; Wang, L. V. Near-Infrared Gold Nanocages as a New Class of Tracers for Photoacoustic Sentinel Lymph Node Mapping on a Rat Model. *Nano Lett.* **2009**, *9* (1), 183–188. <https://doi.org/10.1021/nl802746w>.
- (166) Lu, W.; Huang, Q.; Ku, G.; Wen, X.; Zhou, M.; Guzatov, D.; Brecht, P.; Su, R.; Oraevsky, A.; Wang, L. V.; Li, C. Photoacoustic Imaging of Living Mouse Brain Vasculature Using Hollow Gold Nanospheres. *Biomaterials* **2010**, *31* (9), 2617–2626. <https://doi.org/10.1016/j.biomaterials.2009.12.007>.

- (167) Huang, P.; Lin, J.; Li, W.; Rong, P.; Wang, Z.; Wang, S.; Wang, X.; Sun, X.; Aronova, M.; Niu, G.; Leapman, R. D.; Nie, Z.; Chen, X. Biodegradable Gold Nanovesicles with an Ultrastrong Plasmonic Coupling Effect for Photoacoustic Imaging and Photothermal Therapy. *Angew. Chemie - Int. Ed.* **2013**, *52* (52), 13958–13964. <https://doi.org/10.1002/anie.201308986>.
- (168) Raghavan, V.; O'Flatharta, C.; Dwyer, R.; Breathnach, A.; Zafar, H.; Dockery, P.; Wheatley, A.; Keogh, I.; Leahy, M.; Olivo, M. Dual Plasmonic Gold Nanostars for Photoacoustic Imaging and Photothermal Therapy. *Nanomedicine* **2017**, *12* (5), 457–471. <https://doi.org/10.2217/nnm-2016-0318>.
- (169) Cai, K.; Zhang, W.; Foda, M. F.; Li, X.; Zhang, J.; Zhong, Y.; Liang, H.; Li, H.; Han, H.; Zhai, T. Miniature Hollow Gold Nanorods with Enhanced Effect for in Vivo Photoacoustic Imaging in the NIR-II Window. *Small* **2020**, *16* (37), 2002748. <https://doi.org/10.1002/sml.202002748>.
- (170) García-Álvarez, R.; Chen, L.; Nedilko, A.; Sánchez-Iglesias, A.; Rix, A.; Lederle, W.; Pathak, V.; Lammers, T.; Von Plessen, G.; Kostarelos, K.; Liz-Marzán, L. M.; Kuehne, A. J. C.; Chigrin, D. N. Optimizing the Geometry of Photoacoustically Active Gold Nanoparticles for Biomedical Imaging. *ACS Photonics* **2020**, *7* (3), 646–652. <https://doi.org/10.1021/acsp Photonics.9b01418>.
- (171) Lenzi, E.; Jimenez de Aberasturi, D. Surface-Enhanced Raman Scattering Tags for Three-Dimensional Bioimaging and Biomarker Detection. *ACS sensors* **2019**, *4* (5), 1126–1137. <https://doi.org/10.1021/acssensors.9b00321>.
- (172) Huynh, E.; Zheng, G. Engineering Multifunctional Nanoparticles: All-in-One versus One-for-All. *Wiley Interdiscip. Rev. Nanomedicine Nanobiotechnology* **2013**, *5* (3), 250–265. <https://doi.org/10.1002/wnan.1217>.
- (173) Fabris, L. SERS Tags: The next Promising Tool for Personalized Cancer Detection? *ChemNanoMat* **2016**, *2* (4), 249–258. <https://doi.org/10.1002/cnma.201500221>.
- (174) Rodal-Cedeira, S.; Vazquez-Arias, A.; Bodelon, G.; Skorikov, A.; ez-Sanchez, S. N.; Laporta, A.; Polavarapu, L.; Bals, S.; Liz-Marzán, L. M.; Perez-Juste, J.; Pastoriza-Santos, I. An Expanded Surface-Enhanced Raman Scattering Tags Library by Combinatorial Encapsulation of Reporter Molecules in Metal Nanoshells. *ACS Nano* **2020**, *14* (11), 14655–14664. <https://doi.org/10.1021/acsnano.0c04368>.
- (175) Ali, M. R. K.; Wu, Y.; El-Sayed, M. A. Gold-Nanoparticle-Assisted Plasmonic Photothermal Therapy Advances toward Clinical Application. *J. Phys. Chem. C* **2019**, *123* (25), 15375–15393. <https://doi.org/10.1021/acs.jpcc.9b01961>.
- (176) Webb, J. A.; Bardhan, R. Emerging Advances in Nanomedicine with Engineered Gold Nanostructures. *Nanoscale* **2014**, *6* (5), 2502–2530. <https://doi.org/10.1039/c3nr05112a>.
- (177) Jokerst, J. V.; Cole, A. J.; Van De Sompel, D.; Gambhir, S. S. Gold Nanorods for Ovarian Cancer Detection with Photoacoustic Imaging and Resection Guidance via Raman Imaging

in Living Mice. *ACS Nano* **2012**, *6* (11), 10366–10377.
<https://doi.org/10.1021/nn304347g>.

- (178) Wang, Y. W.; Kang, S.; Khan, A.; Bao, P. Q.; Liu, J. T. C. In Vivo Multiplexed Molecular Imaging of Esophageal Cancer via Spectral Endoscopy of Topically Applied SERS Nanoparticles. *Biomed. Opt. Express* **2015**, *6* (10), 3714–3723.
<https://doi.org/10.1364/boe.6.003714>.
- (179) Wang, Y.; Kang, S.; Khan, A.; Ruttner, G.; Leigh, S. Y.; Murray, M.; Abeytunge, S.; Peterson, G.; Rajadhyaksha, M.; Dintzis, S.; Javid, S.; Liu, J. T. C. Quantitative Molecular Phenotyping with Topically Applied SERS Nanoparticles for Intraoperative Guidance of Breast Cancer Lumpectomy. *Sci. Rep.* **2016**, *6*, 21242. <https://doi.org/10.1038/srep21242>.
- (180) Wang, J.; Wu, X.; Wang, C.; Shao, N.; Dong, P.; Xiao, R.; Wang, S. Magnetically Assisted Surface-Enhanced Raman Spectroscopy for the Detection of Staphylococcus Aureus Based on Aptamer Recognition. *ACS Appl. Mater. Interfaces* **2015**, *7* (37), 20919–20929.
<https://doi.org/10.1021/acsami.5b06446>.
- (181) Sun, C.; Zhang, R.; Gao, M.; Zhang, X. A Rapid and Simple Method for Efficient Capture and Accurate Discrimination of Circulating Tumor Cells Using Aptamer Conjugated Magnetic Beads and Surface-Enhanced Raman Scattering Imaging. *Anal. Bioanal. Chem.* **2015**, *407* (29), 8883–8892. <https://doi.org/10.1007/s00216-015-9049-8>.
- (182) Wang, M.; Yang, Q.; Li, M.; Zou, H.; Wang, Z.; Ran, H.; Zheng, Y.; Jian, J.; Zhou, Y.; Luo, Y.; Ran, Y.; Jiang, S.; Zhou, X. Multifunctional Nanoparticles for Multimodal Imaging-Guided Low-Intensity Focused Ultrasound/Immunosynergistic Retinoblastoma Therapy. *ACS Appl. Mater. Interfaces* **2020**, *12* (5), 5642–5657. <https://doi.org/10.1021/acsami.9b22072>.
- (183) Zeng, J.; Gong, M.; Wang, D.; Li, M.; Xu, W.; Li, Z.; Li, S.; Zhang, D.; Yan, Z.; Yin, Y. Direct Synthesis of Water-Dispersible Magnetic/Plasmonic Heteronanostructures for Multimodality Biomedical Imaging. *Nano Lett.* **2019**, *19* (5), 3011–3018.
<https://doi.org/10.1021/acs.nanolett.9b00171>.
- (184) Wang, W.; Hao, C.; Sun, M.; Xu, L.; Xu, C.; Kuang, H. Spiky Fe₃O₄@Au Supraparticles for Multimodal in Vivo Imaging. *Adv. Funct. Mater.* **2018**, *28* (22), 1800310.
<https://doi.org/10.1002/adfm.201800310>.
- (185) Hou, X.; Wang, X.; Liu, R.; Zhang, H.; Liu, X.; Zhang, Y. Facile Synthesis of Multifunctional Fe₃O₄@SiO₂@Au Magneto-Plasmonic Nanoparticles for MR/CT Dual Imaging and Photothermal Therapy. *RSC Adv.* **2017**, *7* (31), 18844–18850.
<https://doi.org/10.1039/c7ra00925a>.
- (186) Tomitaka, A.; Arami, H.; Ahmadvand, A.; Pala, N.; McGoron, A. J.; Takemura, Y.; Febo, M.; Nair, M. Magneto-Plasmonic Nanostars for Image-Guided and NIR-Triggered Drug Delivery. *Sci. Rep.* **2020**, *10* (1), 10115. <https://doi.org/10.1038/s41598-020-66706-2>.
- (187) Amendola, V.; Scaramuzza, S.; Litti, L.; Meneghetti, M.; Zuccolotto, G.; Rosato, A.; Nicolato, E.; Marzola, P.; Fracasso, G.; Anselmi, C.; Pinto, M.; Colombatti, M. Magneto-Plasmonic

- Au-Fe Alloy Nanoparticles Designed for Multimodal SERS-MRI-CT Imaging. *Small* **2014**, *10*(12), 2476–2486. <https://doi.org/10.1002/smll.201303372>.
- (188) Feng, W.; Zhou, X.; Nie, W.; Chen, L.; Qiu, K. Au/Polypyrrole@Fe₃O₄ Nanocomposites for MR/CT Dual-Modal Imaging Guided-Photothermal Therapy : An in Vitro Study. *ACS Appl. Mater. Interfaces* **2015**, *7*(7), 4354–4367.
- (189) Tomitaka, A.; Arami, H.; Raymond, A.; Yndart, A.; Kaushik, A.; Jayant, R. D.; Takemura, Y.; Cai, Y.; Toborek, M.; Nair, M. Development of Magneto-Plasmonic Nanoparticles for Multimodal Image-Guided Therapy to the Brain. *Nanoscale* **2017**, *9* (2), 764–773. <https://doi.org/10.1039/c6nr07520g>.
- (190) Wang, G.; Gao, W.; Zhang, X.; Mei, X. Au Nanocage Functionalized with Ultra-Small Fe₃O₄ Nanoparticles for Targeting T1-T2 Dual MRI and CT Imaging of Tumor. *Sci. Rep.* **2016**, *6*, 28258. <https://doi.org/10.1038/srep28258>.
- (191) Tomitaka, A.; Ota, S.; Nishimoto, K.; Arami, H.; Takemura, Y.; Nair, M. Dynamic Magnetic Characterization and Magnetic Particle Imaging Enhancement of Magnetic-Gold Core-Shell Nanoparticles. *Nanoscale* **2019**, *11* (13), 6489–6496. <https://doi.org/10.1039/C9NR00242A>.
- (192) Zhu, J.; Lu, Y.; Li, Y.; Jiang, J.; Cheng, L.; Liu, Z.; Guo, L.; Pan, Y.; Gu, H. Synthesis of Au-Fe₃O₄ Heterostructured Nanoparticles for in Vivo Computed Tomography and Magnetic Resonance Dual Modal Imaging. *Nanoscale* **2014**, *6* (1), 199–202. <https://doi.org/10.1039/c3nr04730j>.
- (193) Zhao, H. Y.; Liu, S.; He, J.; Pan, C. C.; Li, H.; Zhou, Z. Y.; Ding, Y.; Huo, D.; Hu, Y. Synthesis and Application of Strawberry-like Fe₃O₄-Au Nanoparticles as CT-MR Dual-Modality Contrast Agents in Accurate Detection of the Progressive Liver Disease. *Biomaterials* **2015**, *57*, 194–207. <https://doi.org/10.1016/j.biomaterials.2015.02.019>.
- (194) Li, J.; Zheng, L.; Cai, H.; Sun, W.; Shen, M.; Zhang, G.; Shi, X. Facile One-Pot Synthesis of Fe₃O₄@Au Composite Nanoparticles for Dual-Mode MR/CT Imaging Applications. *ACS Appl. Mater. Interfaces* **2013**, *5*(20), 10357–10366. <https://doi.org/10.1021/am4034526>.
- (195) Zhou, T.; Wu, B.; Xing, D. Bio-Modified Fe₃O₄ Core/Au Shell Nanoparticles for Targeting and Multimodal Imaging of Cancer Cells. *J. Mater. Chem.* **2012**, *22* (2), 470–477. <https://doi.org/10.1039/c1jm13692e>.
- (196) Liu, Y.; Yang, X.; Huang, Z.; Huang, P.; Zhang, Y.; Deng, L.; Wang, Z.; Zhou, Z.; Liu, Y.; Kalish, H.; Khachab, N. M.; Chen, X.; Nie, Z. Magneto-Plasmonic Janus Vesicles for Magnetic Field-Enhanced Photoacoustic and Magnetic Resonance Imaging of Tumors. *Angew. Chemie - Int. Ed.* **2016**, *55*(49), 15297–15300. <https://doi.org/10.1002/anie.201608338>.
- (197) Motiei, M.; Dreifuss, T.; Sadan, T.; Omer, N.; Blumenfeld-Katzir, T.; Fragogeorgi, E.; Loudos, G.; Popovtzer, R.; Ben-Eliezer, N. Trimodal Nanoparticle Contrast Agent for CT, MRI and SPECT Imaging: Synthesis and Characterization of Radiolabeled Core/Shell Iron Oxide@gold Nanoparticles. *Chem. Lett.* **2019**, *48* (3), 291–294.

<https://doi.org/10.1246/cl.180780>.

- (198) Li, J.; Hu, Y.; Yang, J.; Wei, P.; Sun, W.; Shen, M.; Zhang, G.; Shi, X. Hyaluronic Acid-Modified Fe₃O₄ at Au Core/Shell Nanostars for Multimodal Imaging and Photothermal Therapy of Tumors. *Biomaterials* **2015**, *38*, 10–21. <https://doi.org/10.1016/j.biomaterials.2014.10.065>.
- (199) Senapati, S.; Mahanta, A. K.; Kumar, S.; Maiti, P. Controlled Drug Delivery Vehicles for Cancer Treatment and Their Performance. *Signal Transduct. Target. Ther.* **2018**, *3* (7). <https://doi.org/10.1038/s41392-017-0004-3>.
- (200) Wagner, A.; Hempel, G.; Boos, J. Paclitaxel: A Review of Its Pharmacodynamic and Pharmacokinetic Properties and Therapeutic Potential in the Oral Treatment of Cancer. *Anticancer. Drugs* **1997**, *48* (5), 794–847. <https://doi.org/10.1097/00001813-199706000-00002>.
- (201) Richter, K.; Haslbeck, M.; Buchner, J. The Heat Shock Response: Life on the Verge of Death. *Mol. Cell* **2010**, *40* (2), 253–266. <https://doi.org/10.1016/j.molcel.2010.10.006>.
- (202) Zhang, Y.; Zhan, X.; Xiong, J.; Peng, S.; Huang, W.; Joshi, R.; Cai, Y.; Liu, Y.; Li, R.; Yuan, K.; Zhou, N.; Min, W. Temperature-Dependent Cell Death Patterns Induced by Functionalized Gold Nanoparticle Photothermal Therapy in Melanoma Cells. *Sci. Rep.* **2018**, *8* (1), 8720. <https://doi.org/10.1038/s41598-018-26978-1>.
- (203) Oluwasanmi, A.; Malekigorji, M.; Jones, S.; Curtis, A.; Hoskins, C. Potential of Hybrid Iron Oxide-Gold Nanoparticles as Thermal Triggers for Pancreatic Cancer Therapy. *RSC Adv.* **2016**, *6* (97), 95044–95054. <https://doi.org/10.1039/c6ra20552f>.
- (204) Mehdaoui, B.; Meffre, A.; Carrey, J.; Lachaize, S.; Lacroix, L. M.; Gougeon, M.; Chaudret, B.; Respaud, M. Optimal Size of Nanoparticles for Magnetic Hyperthermia: A Combined Theoretical and Experimental Study. *Adv. Funct. Mater.* **2011**, *21* (23), 4573–4581. <https://doi.org/10.1002/adfm.201101243>.
- (205) De La Presa, P.; Luengo, Y.; Multigner, M.; Costo, R.; Morales, M. P.; Rivero, G.; Hernando, A. Study of Heating Efficiency as a Function of Concentration, Size, and Applied Field in γ -Fe₂O₃ Nanoparticles. *J. Phys. Chem. C* **2012**, *116* (48), 25602–25610. <https://doi.org/10.1021/jp310771p>.
- (206) Di Corato, R.; Espinosa, A.; Lartigue, L.; Tharaud, M.; Chat, S.; Pellegrino, T.; Ménager, C.; Gazeau, F.; Wilhelm, C. Magnetic Hyperthermia Efficiency in the Cellular Environment For different Nanoparticle Designs. *Biomaterials* **2014**, *35* (24), 6400–6411. <https://doi.org/10.1016/j.biomaterials.2014.04.036>.
- (207) Lartigue, L.; Hugounenq, P.; Alloyeau, D.; Clarke, S. P.; Lévy, M.; Bacri, J. C.; Bazzi, R.; Brougham, D. F.; Wilhelm, C.; Gazeau, F. Cooperative Organization in Iron Oxide Multi-Core Nanoparticles Potentiates Their Efficiency as Heating Mediators and MRI Contrast Agents. *ACS Nano* **2012**, *6* (12), 10935–10949. <https://doi.org/10.1021/nn304477s>.

- (208) Bertuit, E.; Benassai, E.; Meriguet, G.; Greneche, J. M.; Baptiste, B.; Neveu, S.; Wilhelm, C.; Abou-Hassan, A. Structure-Property-Function Relationships of Iron Oxide Multicore Nanoflowers in Magnetic Hyperthermia and Photothermia. *ACS Nano* **2022**, *16*, 271–284. <https://doi.org/10.1021/acsnano.1c06212>.
- (209) Espinosa, A.; Kolosnjaj-Tabi, J.; Abou-Hassan, A.; Plan Sangnier, A.; Curcio, A.; Silva, A. K. A.; Di Corato, R.; Neveu, S.; Pellegrino, T.; Liz-Marzán, L. M.; Wilhelm, C. Magnetic (Hyper)Thermia or Photothermia? Progressive Comparison of Iron Oxide and Gold Nanoparticles Heating in Water, in Cells, and in Vivo. *Adv. Funct. Mater.* **2018**, *28* (37), 1803660. <https://doi.org/10.1002/adfm.201803660>.
- (210) Espinosa, A.; Di Corato, R.; Kolosnjaj-Tabi, J.; Flaud, P.; Pellegrino, T.; Wilhelm, C. Duality of Iron Oxide Nanoparticles in Cancer Therapy: Amplification of Heating Efficiency by Magnetic Hyperthermia and Photothermal Bimodal Treatment. *ACS Nano* **2016**, *10* (2), 2436–2446. <https://doi.org/10.1021/acsnano.5b07249>.
- (211) Link, S.; El-Sayed, M. A. *Shape and Size Dependence of Radiative, Non-Radiative and Photothermal Properties of Gold Nanocrystals*; 2000; Vol. 19. <https://doi.org/10.1080/01442350050034180>.
- (212) Datta, N. R.; Ordóñez, S. G.; Gaip, U. S.; Paulides, M. M.; Crezee, H.; Gellermann, J.; Marder, D.; Puric, E.; Bodis, S. Local Hyperthermia Combined with Radiotherapy And/or Chemotherapy: Recent Advances and Promises for the Future. *Cancer Treat. Rev.* **2015**, *41* (9), 742–753. <https://doi.org/10.1016/j.ctrv.2015.05.009>.
- (213) Baffou, G.; Quidant, R. Thermo-Plasmonics: Using Metallic Nanostructures as Nano-Sources of Heat. *Laser Photonics Rev.* **2013**, *7* (2), 171–187. <https://doi.org/10.1002/lpor.201200003>.
- (214) Quintanilla, M.; Henriksen-lacey, M.; Renero-Lecuna, C.; Liz-marza, L. M.; Renero-lecuna, C. Challenges for Optical Nanothermometry in Biological Environments. *Chem. Soc. Rev.* **2022**. <https://doi.org/10.1039/d2cs00069e>.
- (215) Hirsch, L. R.; Stafford, R. J.; Bankson, J. A.; Sershen, S. R.; Rivera, B.; Price, R. E.; Hazle, J. D.; Halas, N. J.; West, J. L. Nanoshell-Mediated near-Infrared Thermal Therapy of Tumors under Magnetic Resonance Guidance. *Proc. Natl. Acad. Sci. U. S. A.* **2003**, *100*(23), 13549–13554. <https://doi.org/10.1073/pnas.2232479100>.
- (216) Rastinehad, A. R.; Anastos, H.; Wajswol, E.; Winoker, J. S.; Sfakianos, J. P.; Doppalapudi, S. K.; Carrick, M. R.; Knauer, C. J.; Taouli, B.; Lewis, S. C.; Tewari, A. K.; Schwartz, J. A.; Canfield, S. E.; George, A. K.; West, J. L.; Halas, N. J. Gold Nanoshell-Localized Photothermal Ablation of Prostate Tumors in a Clinical Pilot Device Study. *Proc. Natl. Acad. Sci. U. S. A.* **2019**, *116*(37), 18590–18596. <https://doi.org/10.1073/pnas.1906929116>.
- (217) Huang, X.; El-Sayed, I. H.; Qian, W.; El-Sayed, M. A. Cancer Cell Imaging and Photothermal Therapy in the Near-Infrared Region by Using Gold Nanorods. *J. Am. Chem. Soc.* **2006**, *128*(6), 2115–2120. <https://doi.org/10.1021/ja057254a>.

- (218) Morales-Dalmau, J.; Vilches, C.; De Miguel, I.; Sanz, V.; Quidant, R. Optimum Morphology of Gold Nanorods for Light-Induced Hyperthermia. *Nanoscale* **2018**, *10* (5), 2632–2638. <https://doi.org/10.1039/c7nr06825e>.
- (219) Liu, Y.; Ashton, J. R.; Moding, E. J.; Yuan, H.; Register, J. K.; Fales, A. M.; Choi, J.; Whitley, M. J.; Zhao, X.; Qi, Y.; Ma, Y.; Vaidyanathan, G.; Zalutsky, M. R.; Kirsch, D. G.; Badea, C. T.; Vo-Dinh, T. A Plasmonic Gold Nanostar Theranostic Probe for in Vivo Tumor Imaging and Photothermal Therapy. *Theranostics* **2015**, *5* (9), 946–960. <https://doi.org/10.7150/thno.11974>.
- (220) Skrabalak, S. E.; Chen, J.; Sun, Y.; Lu, X.; Au, L.; Cobley, C. M.; Xia, Y. Gold Nanocages: Synthesis, Properties, and Applications. *Acc. Chem. Res.* **2008**, *41* (12), 1587–1595. <https://doi.org/10.1002/9783527809080.catatz11280>.
- (221) Chen, J.; Glaus, C.; Laforest, R.; Zhang, Q.; Yang, M.; Gidding, M.; Welch, M. J.; Xia, Y. Gold Nanocages as Photothermal Transducers for Cancer Treatment. *Small* **2010**, *6* (7), 811–817. <https://doi.org/10.1002/smll.200902216>.
- (222) Lavorato, G. C.; Das, R.; Alonso Masa, J.; Phan, M. H.; Srikanth, H. Hybrid Magnetic Nanoparticles as Efficient Nanoheaters in Biomedical Applications. *Nanoscale Adv.* **2021**, *3* (4), 867–888. <https://doi.org/10.1039/d0na00828a>.
- (223) Espinosa, A.; Bugnet, M.; Radtke, G.; Neveu, S.; Botton, G. A.; Wilhelm, C.; Abou-Hassan, A. Can Magneto-Plasmonic Nanohybrids Efficiently Combine Photothermia with Magnetic Hyperthermia? *Nanoscale* **2015**, *7* (45), 18872–18877. <https://doi.org/10.1039/c5nr06168g>.
- (224) Espinosa, A.; Reguera, J.; Curcio, A.; Muñoz-Noval, Á.; Kuttner, C.; Van de Walle, A.; Liz-Marzán, L. M.; Wilhelm, C. Janus Magnetic-Plasmonic Nanoparticles for Magnetically Guided and Thermally Activated Cancer Therapy. *Small* **2020**, *16* (11), 1904960. <https://doi.org/10.1002/smll.201904960>.
- (225) Ma, X.; Wang, Y.; Liu, X. L.; Ma, H.; Li, G.; Li, Y.; Gao, F.; Peng, M.; Fan, H. M.; Liang, X. J. Fe₃O₄-Pd Janus Nanoparticles with Amplified Dual-Mode Hyperthermia and Enhanced ROS Generation for Breast Cancer Treatment. *Nanoscale Horizons* **2019**, *4* (6), 1450–1459. <https://doi.org/10.1039/c9nh00233b>.
- (226) Curcio, A.; Silva, A. K. A.; Cabana, S.; Espinosa, A.; Baptiste, B.; Menguy, N.; Wilhelm, C.; Abou-Hassan, A. Iron Oxide Nanoflowers@CuS Hybrids for Cancer Tri-Therapy: Interplay of Photothermal Therapy, Magnetic Hyperthermia and Photodynamic Therapy. *Theranostics* **2019**, *9* (5), 1288–1302. <https://doi.org/10.7150/thno.30238>.
- (227) Abdulla-Al-Mamun, M.; Kusumoto, Y.; Zannat, T.; Horie, Y.; Manaka, H. Au-Ultrathin Functionalized Core-Shell (Fe₃O₄@Au) Monodispersed Nanocubes for a Combination of Magnetic/Plasmonic Photothermal Cancer Cell Killing. *RSC Adv.* **2013**, *3* (21), 7816–7827. <https://doi.org/10.1039/c3ra21479f>.
- (228) Li, Z.; Aranda-Ramos, A.; Güell-Grau, P.; Tajada, J. L.; Pou-Macayo, L.; Lope Piedrafita, S.;

- Pi, F.; G. Roca, A.; Baró, M. D.; Sort, J.; Nogués, C.; Nogués, J.; Sepúlveda, B. Magnetically Amplified Photothermal Therapies and Multimodal Imaging with Magneto-Plasmonic Nanodomains. *Appl. Mater. Today* **2018**, *12*, 430–440. <https://doi.org/10.1016/j.apmt.2018.07.008>.
- (229) Hu, Y.; Hu, H.; Yan, J.; Zhang, C.; Li, Y.; Wang, M.; Tan, W.; Liu, J.; Pan, Y. Multifunctional Porous Iron Oxide Nanoagents for MRI and Photothermal/Chemo Synergistic Therapy. *Bioconjug. Chem.* **2018**, *29* (4), 1283–1290. <https://doi.org/10.1021/acs.bioconjchem.8b00052>.
- (230) Abed, Z.; Beik, J.; Laurent, S.; Eslahi, N.; Khani, T.; Davani, E. S.; Ghaznavi, H.; Shakeri-Zadeh, A. Iron Oxide–Gold Core–Shell Nano-Theranostic for Magnetically Targeted Photothermal Therapy under Magnetic Resonance Imaging Guidance. *J. Cancer Res. Clin. Oncol.* **2019**, *145* (5), 1213–1219. <https://doi.org/10.1007/s00432-019-02870-x>.
- (231) Lin, A. Y.; Young, J. K.; Nixon, A. V.; Drezek, R. A. Encapsulated Fe₃O₄/Ag Complexed Cores in Hollow Gold Nanoshells for Enhanced Theranostic Magnetic Resonance Imaging and Photothermal Therapy. *Small* **2014**, *10* (16), 3246–3251. <https://doi.org/10.1002/sml.201303593>.
- (232) Nan, X.; Zhang, X.; Liu, Y.; Zhou, M.; Chen, X.; Zhang, X. Dual-Targeted Multifunctional Nanoparticles for Magnetic Resonance Imaging Guided Cancer Diagnosis and Therapy. *ACS Appl. Mater. Interfaces* **2017**, *9* (11), 9986–9995. <https://doi.org/10.1021/acsami.6b16486>.
- (233) Plan Sangnier, A.; Preveral, S.; Curcio, A.; K. A. Silva, A.; Lefèvre, C. T.; Pignol, D.; Lalatonne, Y.; Wilhelm, C. Targeted Thermal Therapy with Genetically Engineered Magnetite Magnetosomes@RGD: Photothermia Is Far More Efficient than Magnetic Hyperthermia. *J. Control. Release* **2018**, *279*, 271–281. <https://doi.org/10.1016/j.jconrel.2018.04.036>.
- (234) Bai, L. Y.; Yang, X. Q.; An, J.; Zhang, L.; Zhao, K.; Qin, M. Y.; Fang, B. Y.; Li, C.; Xuan, Y.; Zhang, X. S.; Zhao, Y. Di; Ma, Z. Y. Multifunctional Magnetic-Hollow Gold Nanospheres for Bimodal Cancer Cell Imaging and Photothermal Therapy. *Nanotechnology* **2015**, *26* (31), 315701. <https://doi.org/10.1088/0957-4484/26/31/315701>.
- (235) Brennan, G.; Bergamino, S.; Pescio, M.; Tofail, S. A. M.; Silien, C. The Effects of a Varied Gold Shell Thickness on Iron Oxide Nanoparticle Cores in Magnetic Manipulation, T1 and T2 MRI Contrasting, and Magnetic Hyperthermia. *Nanomaterials* **2020**, *10* (12), 2424. <https://doi.org/10.3390/nano10122424>.
- (236) Huang, J.; Guo, M.; Ke, H.; Zong, C.; Ren, B.; Liu, G.; Shen, H.; Ma, Y.; Wang, X.; Zhang, H.; Deng, Z.; Chen, H.; Zhang, Z. Rational Design and Synthesis of Fe₂O₃@Au Magnetic Gold Nanoflowers for Efficient Cancer Theranostics. *Adv. Mater.* **2015**, *27* (34), 5049–5056. <https://doi.org/10.1002/adma.201501942>.
- (237) Tarkistani, M. A. M.; Komalla, V.; Kayser, V. Recent Advances in the Use of Iron–Gold Hybrid Nanoparticles for Biomedical Applications. *Nanomaterials* **2021**, *11* (5), 1227.

<https://doi.org/10.3390/nano11051227>.

- (238) Zhou, H.; Kim, J. P.; Bahng, J. H.; Kotov, N. A.; Lee, J. Self-Assembly Mechanism of Spiky Magnetoplasmonic Supraparticles. *Adv. Funct. Mater.* **2014**, *24* (10), 1439–1448. <https://doi.org/10.1002/adfm.201302405>.
- (239) Efremova, M. V; Naumenko, V. A.; Spasova, M.; Garanina, A. S.; Abakumov, M. A.; Blokhina, A. D.; Melnikov, P. A.; Alexandra, O. P.; Heidelmann, M.; Li, Z.; Ma, Z.; Shchetinin, I. V; Golovin, Y. I.; Kireev, I. I.; Savchenko, A. G.; Chekhonin, V. P.; Klyachko, N. L.; Farle, M.; Majouga, A. G.; Wiedwald, U. Magnetite-Gold Nanohybrids as Ideal All-in-One Platforms for Theranostics. *Sci. Rep.* **2018**, *8*, 11295. <https://doi.org/10.1038/s41598-018-29618-w>.
- (240) Li, Y.; Zhao, J.; You, W.; Cheng, D.; Ni, W. Gold Nanorod@iron Oxide Core-Shell Heterostructures: Synthesis, Characterization, and Photocatalytic Performance. *Nanoscale* **2017**, *9*(11), 3925–3933. <https://doi.org/10.1039/c7nr00141j>.
- (241) Kwizera, E. A.; Chaffin, E.; Shen, X.; Chen, J.; Zou, Q.; Wu, Z.; Gai, Z.; Bhana, S.; Oconnor, R.; Wang, L.; Adhikari, H.; Mishra, S. R.; Wang, Y.; Huang, X. Size- and Shape-Controlled Synthesis and Properties of Magnetic-Plasmonic Core-Shell Nanoparticles. *J. Phys. Chem. C* **2016**, *120*(19), 10530–10546. <https://doi.org/10.1021/acs.jpcc.6b00875>.

Chapter II



2. Synthesis of hybrid nanostars for multimodal bioimaging

Contents

| | |
|---|-----|
| 2.1 Introduction..... | 70 |
| 2.2 Synthesis of magnetic nanoparticles | 71 |
| 2.2.1 Magnetic characterization..... | 71 |
| 2.3 Synthesis of plasmonic nanoparticles..... | 72 |
| 2.4 Synthesis of hybrid iron oxide-gold nanoparticles.... | 73 |
| 2.4.1 Decoration of iron oxide nanoparticles with gold nanoparticles..... | 73 |
| 2.4.2 Optimization of iron oxide-gold nanostars: <i>controlling the size and the branching degree</i> | 74 |
| 2.5 Functionalization..... | 78 |
| 2.5.1 SERS encoding | 81 |
| 2.5.1.1 SERS characterization | 83 |
| 2.5.2 Fluorescent dyes | 84 |
| 2.6 Application of nanoparticles for imaging..... | 87 |
| 2.6.1 2D cell model | 87 |
| 2.6.1.1 SERS imaging..... | 89 |
| 2.6.1.2 Magnetic resonance imaging | 90 |
| 2.6.1.3 Confocal fluorescence imaging | 92 |
| 2.6.2 3D cell model | 93 |
| 2.6.2.1 Multimodal imaging in 3D..... | 95 |
| 2.6.3 Multimodal imaging <i>ex vivo</i> | 98 |
| 2.7 Conclusions | 100 |
| 2.8 Experimental Section | 101 |
| 2.8.1 Materials | 101 |
| 2.8.2 Nanoparticle synthesis methods | 102 |
| 2.8.3 Functionalization | 104 |
| 2.8.4 Characterization..... | 105 |
| 2.8.5 Cell culture | 107 |
| 2.8.6 Multimodal imaging..... | 108 |
| References | 113 |

2.1 Introduction

In this chapter, the synthesis and optimization protocols of hybrid magnetic-plasmonic NPs are discussed with emphasis on their application as contrast agents in multimodal bioimaging. Multimodal contrast agents, which take advantage of multiple imaging modalities, have emerged as an interesting approach to overcome the technical limitations of individual techniques¹. As has been discussed in Chapter I, although many efforts have been made in the development of hybrid NPs with new configurations and properties, for example, hybrid NPs with suitable plasmonic properties for SERS are still needed. In this chapter, a new strategy for the fabrication of multifunctional nanohybrids is addressed.

Core-shell IOAuNPs composed of an iron oxide (IO) core surrounded by an outer gold shell layer, are an example of contrast agents, often used in combined MRI/CT imaging^{2,3}. The use of such NPs with alternative techniques such as SERS, surgical guidance, or detection of metabolites, is still its infancy but presents great potential⁴.

Regarding the development of core-shell hybrid NPs, the coating gold shell is usually designed to protect the IO cores from oxidation and degradation in cellular media, thereby improving their long-term stability. Reports suggest this protective effect depends strongly on the morphology and thickness of the gold shell, being most efficient when a continuous (hole-free) shell is formed^{5,6}. This double role of the Au component, not only as an inert protective material to IONPs, but also as a chemical component sensitive to alternative imaging techniques such as SERS, merits further investigation to determine whether either property can be improved upon.

In the first experimental chapter of this thesis, we have focussed on the fabrication of a novel hybrid iron oxide-gold system by the adsorption of small gold nanoparticles (AuNPs) onto pre-made IO cores⁷, followed by the controlled growth of spiky gold shells. We determined that the gold layer thickness and branching degree (tip sharpness) can be controlled by modifying both the density of AuNPs on the cores (IONPs) and the conditions of subsequent nanostar growth. In the synthesis of IOAuNSs, each step was optimized to maximize the potential of the NPs for the desired applications. As shown in chapter I, hybrid NPs can be functionalized with different molecules, thereby allowing functionalization of IOAuNSs with Raman-active molecules and fluorescent dyes. The procedures for synthesis and functionalization are detailed in the Experimental section. All hybrid NPs were fully characterized, including electron tomography, STEM, 3D reconstructions, EELS and EDX analysis, in collaboration with the Electron microscopy for Materials Science (EMAT) group led by Prof. Sara Bals in the University of Antwerp (Belgium). Additionally, the performance of the IOAuNSs as multimodal contrast agents for correlative imaging of *in vitro* 2D and 3D cell models, as well as *ex vivo* tissue samples, were studied. In particular, NPs were applied in MRI, SERS, and fluorescence imaging, showing remarkable performance as contrast agents in all three imaging techniques. These findings represent a step forward in the fabrication of hybrid materials for their use as novel contrast agents for multimodal bioimaging.

2.2 Synthesis of magnetic nanoparticles

The first step for the synthesis of our hybrid NPs was the synthesis of a magnetic core. For this purpose, multicore IONPs were prepared by means of a polyol-mediated solvothermal synthesis approach⁸, with slight modifications. Briefly, iron (III) chloride was dissolved in ethylene glycol, a short-chain polyol, followed by addition of poly(vinylpyrrolidone) (PVP) as a capping agent. Next, sodium acetate (NaAc) was incorporated to the reaction mixture to promote the hydrolysis of Fe³⁺ ions, thereby controlling both nucleation and the final particle morphology. After exposing the mixture to high temperature (200 °C) for 8 hours in an autoclave, the formation of hollow maghemite (γ -Fe₂O₃) IONPs composed of multiple crystallites is observed. The UV-Vis-NIR spectrum of the obtained IONPs is shown in **Figure 2.1A**. Using this procedure, we have fabricated IONPs of 119 ± 25 nm that appeared homogeneous and presented a narrow size distribution, as shown in the TEM image (**Figure 2.1B**). Using annular dark field STEM (ADF-STEM), it could be observed that IONPs cores presented a hollow structure in middle of around 39 nm (see **Figure 2.1C**). The size of the crystallites that make up the multicore structure, were measured by high resolution STEM (HRSTEM) and resulted in 5 nm.

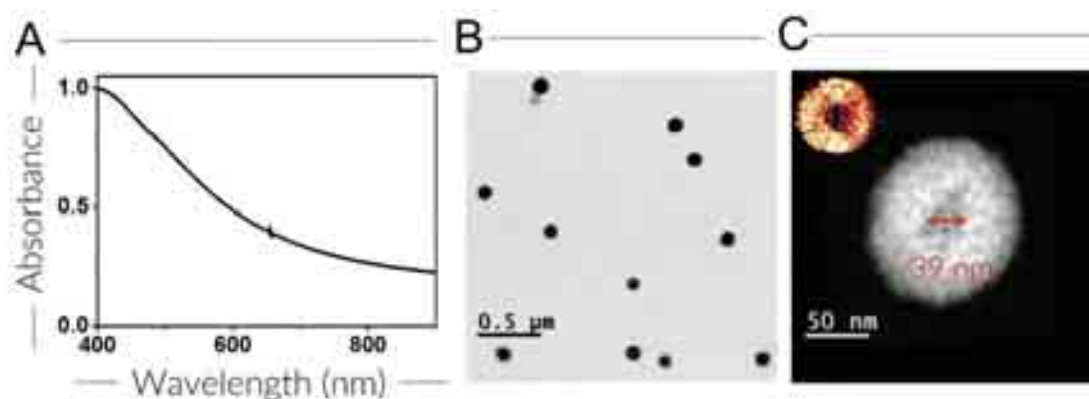


Figure 2.1. (A) Normalized UV-Vis-NIR spectra of IONPs. (B) TEM images of homogeneous and polydisperse IONPs. (C) ADF-STEM image of a IONP showing a hollow core of 39 nm, an electron tomography reconstruction of the IONP is shown (top-left).

2.2.1 Magnetic characterization

The magnetic properties of the IONPs were studied using the various techniques described in Chapter I, section 1.2.6. We recorded zero-field cooled (ZFC) and field cooled (FC) magnetization curves, as well as magnetic hysteresis loops, to obtain information about the iron phase and to confirm that the magnetic properties of aged and freshly prepared IONPs did not change with time. Electron energy loss spectroscopy (EELS) was used to confirm the Fe₂O₃ composition of the cores (**Figure 2.2A,B**). To test for potential oxidation over time, which would have an important effect on the magnetic properties, hysteresis loops were recorded for both freshly prepared and aged (6 months post-synthesis) IONPs. A saturation magnetization of 50 Am²/kg was measured in both cases (**Figure 2.2C**), which is slightly lower than the saturation magnetization of bulk maghemite (74 Am²/kg)⁹, likely due to surface disorder effects on the synthesized IONPs¹⁰. Additionally, a near-superparamagnetic behavior characterized by low remanence and coercivity

can be observed in the intersection of the loop with the axes. Additionally, ZFC/FC curves for IONPs also confirm a maghemite phase of IONPs with only negligible traces of the Verwey transition (Figure 2.2D)¹¹.

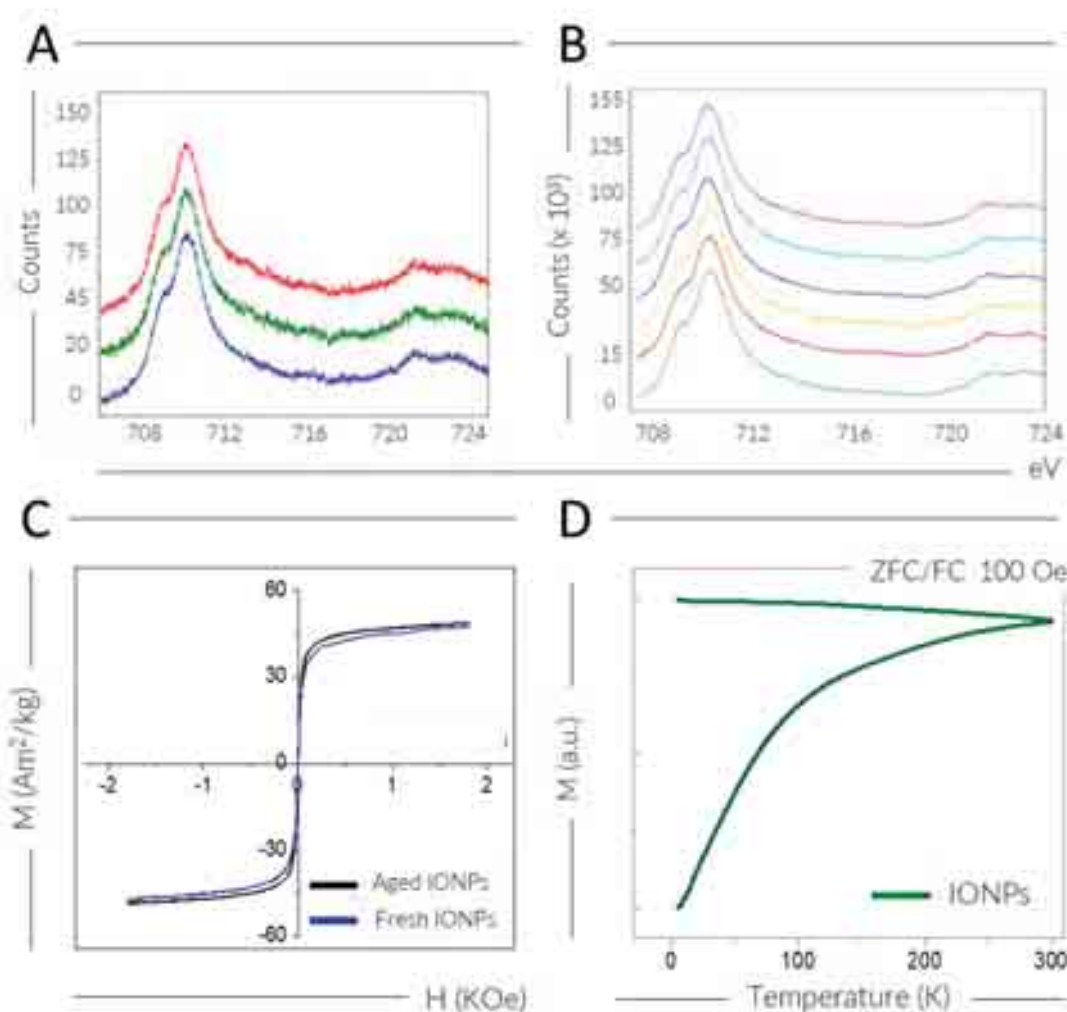


Figure 2.2 (A) EELS spectra of freshly prepared IONPs, showing a small shoulder centred at 710.8 eV, assigned to Fe^{3+} . (B) EELS spectra of IONPs that were aged for 6 months. The different spectra in (A) and (B) correspond to measurements of different IONPs of the same sample. (C) Hysteresis loops for freshly made (blue) and aged (black) IONPs. (D) ZFC/FC curves for IONPs recorded at a magnetic field of 100 Oe.

2.3 Synthesis of plasmonic nanoparticles

The process for growing a Au shell surrounding the IONP core involves the synthesis of AuNPs, which are used to decorate pre-made IONPs. The synthesis was performed by means of previously described methods^{12,13}. Briefly, for both methods, citrate is added to a HAuCl_4 solution. For the synthesis of 4 nm AuNPs, citrate acts as a capping agent, while reduction with NaBH_4 under vigorous stirring allows the formation of small spherical particles. By contrast, for the synthesis of 15 nm AuNPs, citrate acts as both capping and reducing agent at high temperature (boiling), promoting the formation of bigger AuNPs. Thus, homogeneous AuNPs with a narrow size distribution were obtained and the diameters were calculated from TEM images

(see Figure 2.3). UV-Vis-NIR spectroscopy confirmed the non-aggregated nature of the AuNPs, exhibiting a characteristic peak at 520 nm for 4 nm AuNPs, whereas that for the larger 15 nm AuNPs was located at 524 nm, in agreement with previous literature¹⁴.

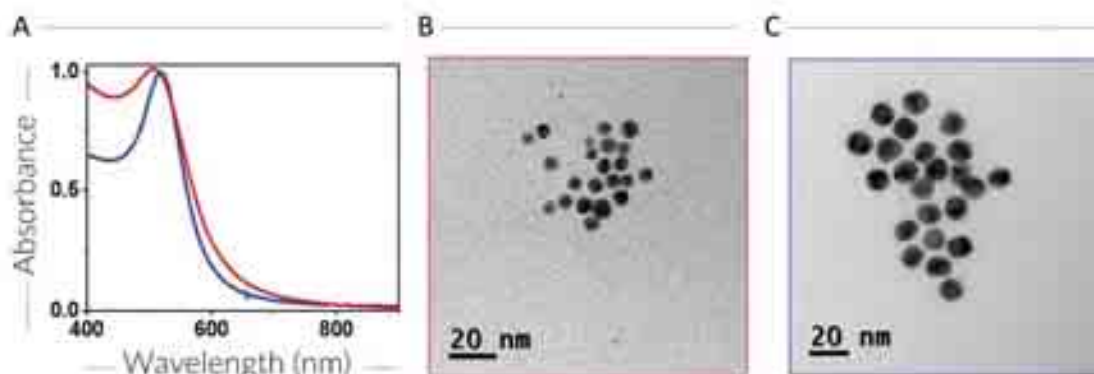


Figure 2.3. (A) Normalized UV-Vis-NIR spectra (400 nm) for 4 nm AuNPs (red) and 15 nm AuNPs (blue), and representative TEM images of (B) 4 nm AuNPs and (C) 15 nm AuNPs.

2.4 Synthesis of hybrid iron oxide-gold nanoparticles

2.4.1 Decoration of iron oxide nanoparticles with gold nanoparticles

In order to obtain hybrid NPs, previously synthesized AuNPs were spontaneously adsorbed onto the IONPs surface by the simple addition of the AuNP solution to dried IONPs, under sonication. We investigated the attachment of both 4 and 15 nm AuNPs, and whereas uniform surface adsorption was observed for both NP types, a higher density of AuNPs was achieved using 4 nm AuNPs (Figure 2.4).

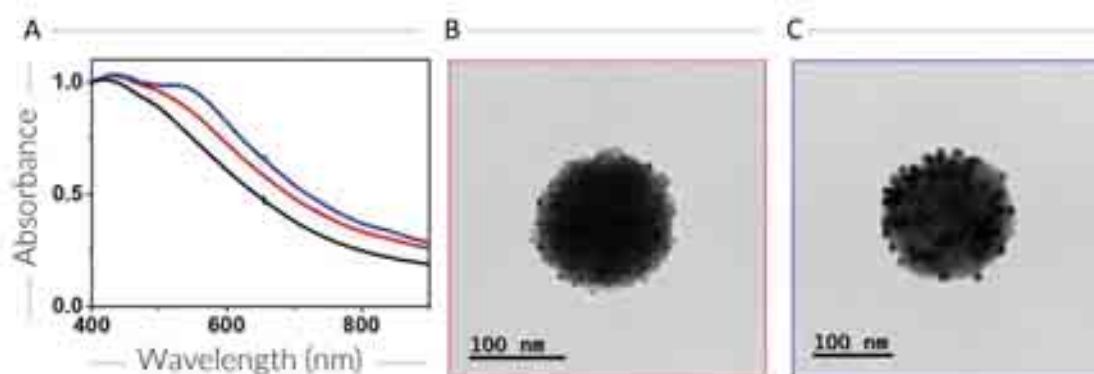


Figure 2.4. (A) Normalized UV-Vis-NIR spectra (400 nm) of IONPs decorated with 4 nm AuNPs (red) and 15 nm AuNPs (blue). The black spectrum corresponds to IONPs as a control. (B) TEM images of IONPs decorated with 4 nm and (C) 15 nm AuNPs.

We subsequently focused on the characterization of IONPs decorated with 4 nm AuNPs. We first conducted ADF-STEM imaging to attempt to determine the spatial distribution of the two metallic components. The successful and homogeneous decoration of AuNPs along the IONPs outer surface was confirmed. HRSTEM was used and allowed to perfectly distinguish the AuNPs

(Figure 2.5A). Then, using 3D reconstructions from electron tomography images we were able to clearly resolve the AuNPs that attached to the IONPs surface (Figure 2.5B).

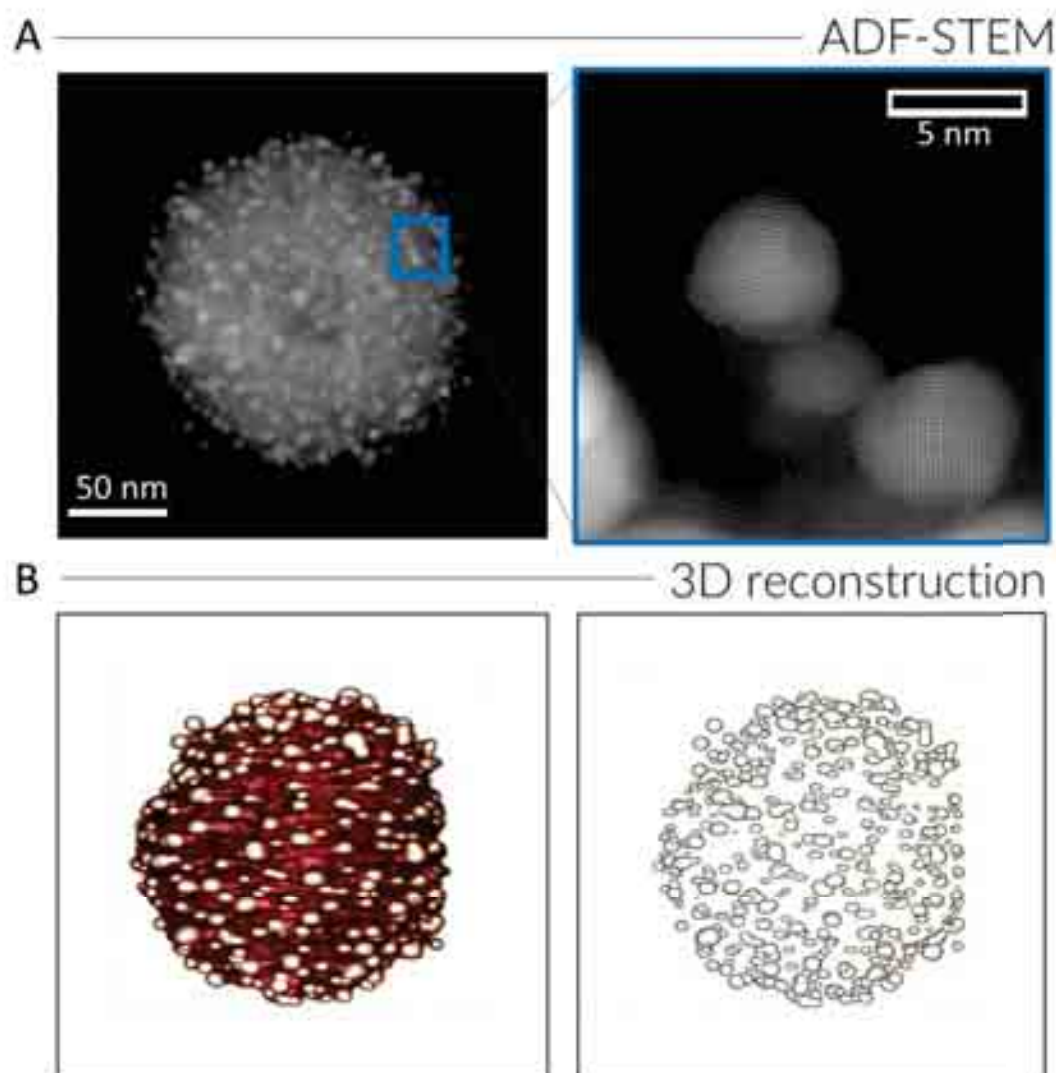


Figure 2.5. (A) ADF-STEM images of IONPs decorated with 4nm AuNPs. A HRSTEM image showing the 4nm AuNPs is shown in the blue box (upper-right). (B) Electron tomography reconstruction in 3D of IOAuNPs and isolated AuNPs.

2.4.2 Optimization of iron oxide-gold nanostars: *controlling the size and the branching degree*

It was important to determine the AuNP density on IONPs as the AuNPs act as nucleation points for growth and branching of the final outer Au shell. Therefore, the procedure was optimized to obtain IONPs decorated with different densities of 4 nm AuNP on the surface. We observed that by varying the relative concentration of AuNPs with respect to that of IONPs, the amount of AuNPs that attach to the IONPs surface can be controlled. Specifically, with decreasing AuNP concentration, a decreasing surface coverage was observed (herein termed Series a-c). As can be observed in Figure 2.6, TEM images confirmed the decrease in the density of AuNPs from series a to series c.

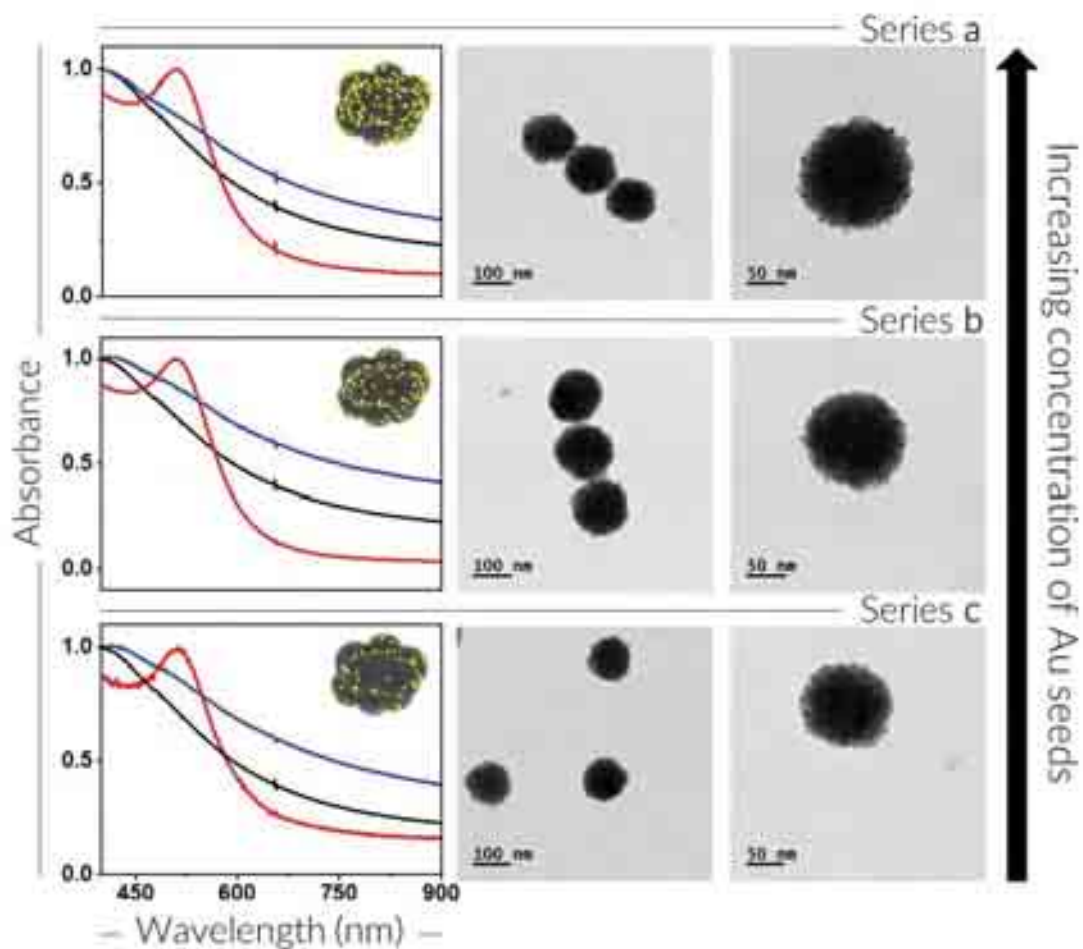


Figure 2.6. Normalized UV-Vis-NIR spectra and TEM images of series a-c of 4 nm AuNPs (red), IONPs (black), and IONPs decorated with AuNPs (IOAuNPs) (blue). The insets in the left column depict the schematic representation of each nanostructure. The [Au]/[Fe] ratio decreases from series a = 3.7×10^{-2} to series b = 1.1×10^{-2} to series c = 2.3×10^{-3} . All spectra were normalized at 400 nm.

In a final step, the growth of Au tips protruding from AuNPs was achieved by adapting a reported procedure for surfactant-free AuNS¹⁵. The conditions were varied to explore the effect of branch length and density on the physico-chemical characteristics of the final NPs, and thus their performance as contrast agents. Two approaches were used for the variation of the nanostructures: (1) the previously described decrease in concentration of AuNPs attached to the IONPs, and (2), an increase of the concentration of HAuCl₄ in the tip-formation reaction. As shown in **Figure 2.7** below, low and high magnification TEM images clearly show homogeneous and monodispersed nanoparticles with notable differences in tip length and density. Specifically, longer tips and hence overall larger IOAuNSs were grown when increasing the amount of HAuCl₄ added in the growth step (sequence I-IV), whereas IOAuNSs with smaller overall diameters were obtained from IO cores with a lower density of AuNPs (series a-c).

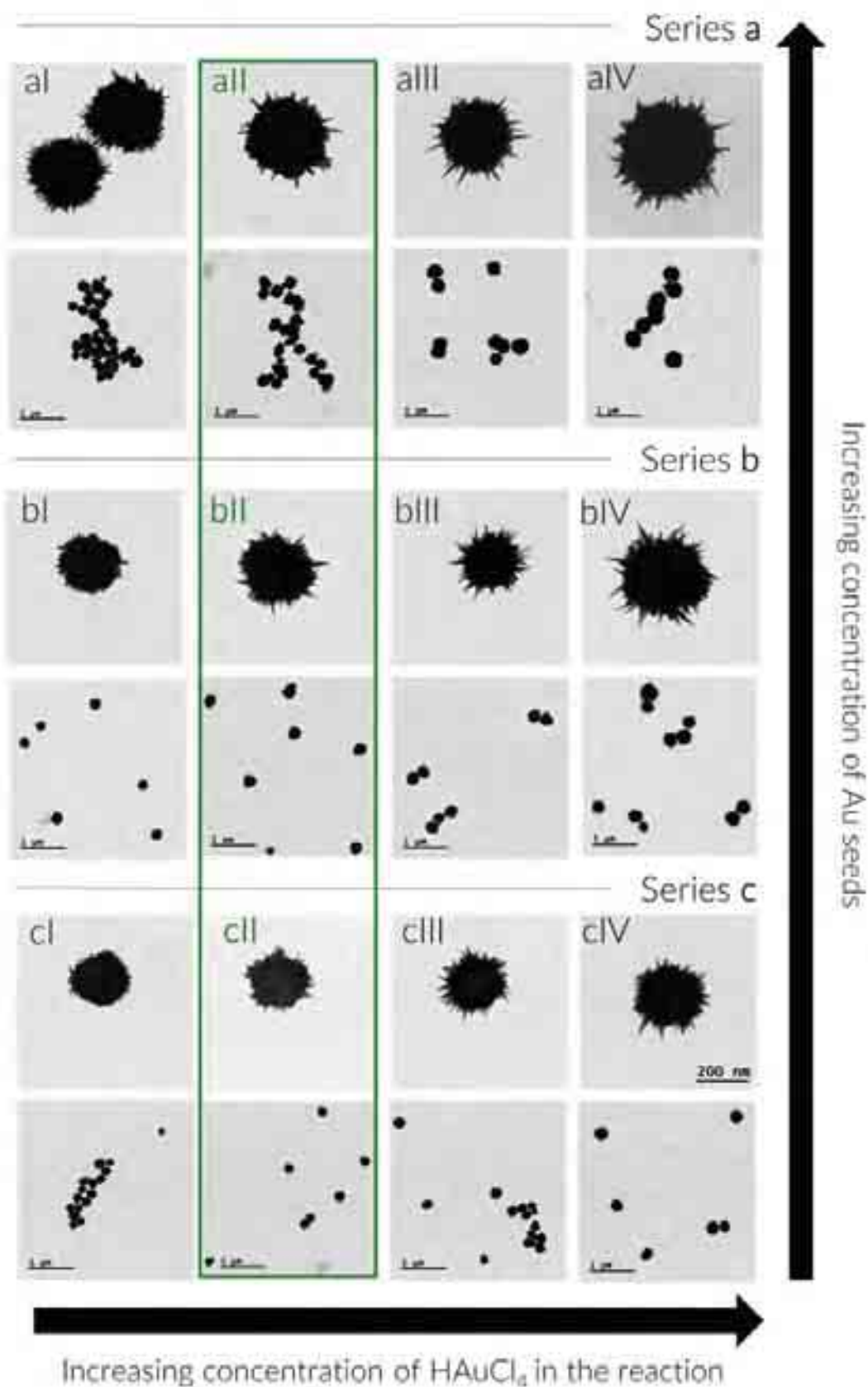


Figure 2.7. Low and high magnification TEM images of IOAuNSs obtained from series a-c (increasing AuNPs coverage), and I-IV (increasing added HAuCl_4). Series II (highlighted in a green box) was selected for further experiments. All the images are at the same magnification. The $[\text{Au}]/[\text{Fe}]$ molar ratios, measured by ICP-MS, were: aI = 3.6, aII = 2.7, aIII = 2.6, aIV = 0.97, bI = 1.7, bII = 1.2, bIII = 1.0, bIV = 0.2, cI = 0.58, cII = 0.35, cIII = 0.25, cIV = 0.13.

From TEM images, we measured the overall diameter of the IOAuNSs, measuring from outer tip-to-tip. As shown in **Table 2.1** and **Figure 2.8**, the diameter decreases, as expected, along **series a** to **b** to **c**, and increases along **series I** to **IV**.

Table 2.1. Diameter of IOAuNSs measured from TEM images.

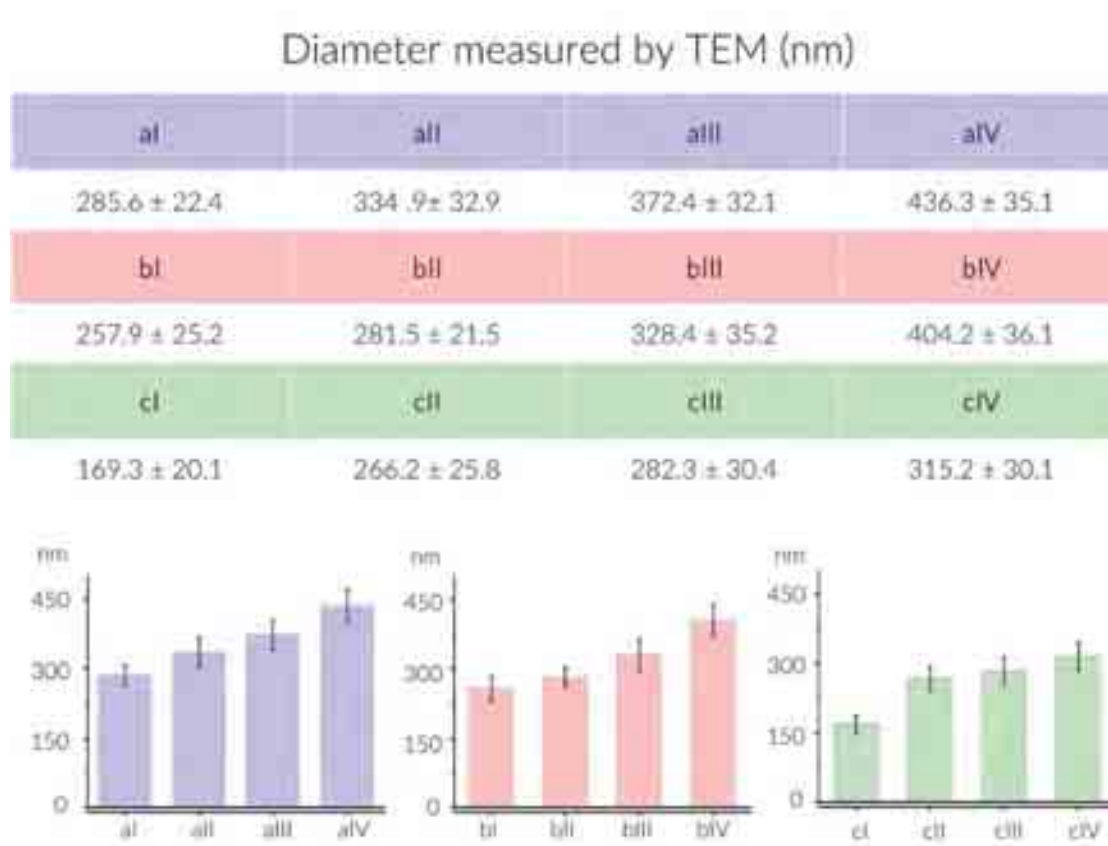


Figure 2.8. Graphical representation of the results from TEM determination of particle diameter, listed in **Table 2.1**.

In order to have a more detailed analysis of the thickness and structure of the Au shell, further characterization by electron microscopy and electron tomography was carried out for the NPs highlighted in green in **Figure 2.7**. As shown in this same figure, for a fixed amount of added HAuCl₄, thicker gold shells were obtained when increasing the initial coverage of IONP cores with AuNPs. Representative 3D visualizations of the structures retrieved by high-angle annular dark field (HAADF) electron tomography are shown in **Figure 2.9**. The results showed complete gold shell formation for samples aIII and bIII, but defects were observed for cII (**Figure 2.9A**). Careful inspection of orthoslices through 3D reconstructed data sets yielded the average gold shell thickness for samples aIII (75 ± 15 nm), bIII (66 ± 12 nm) and cII (24 ± 5 nm), as illustrated in **Figure 2.9B**.

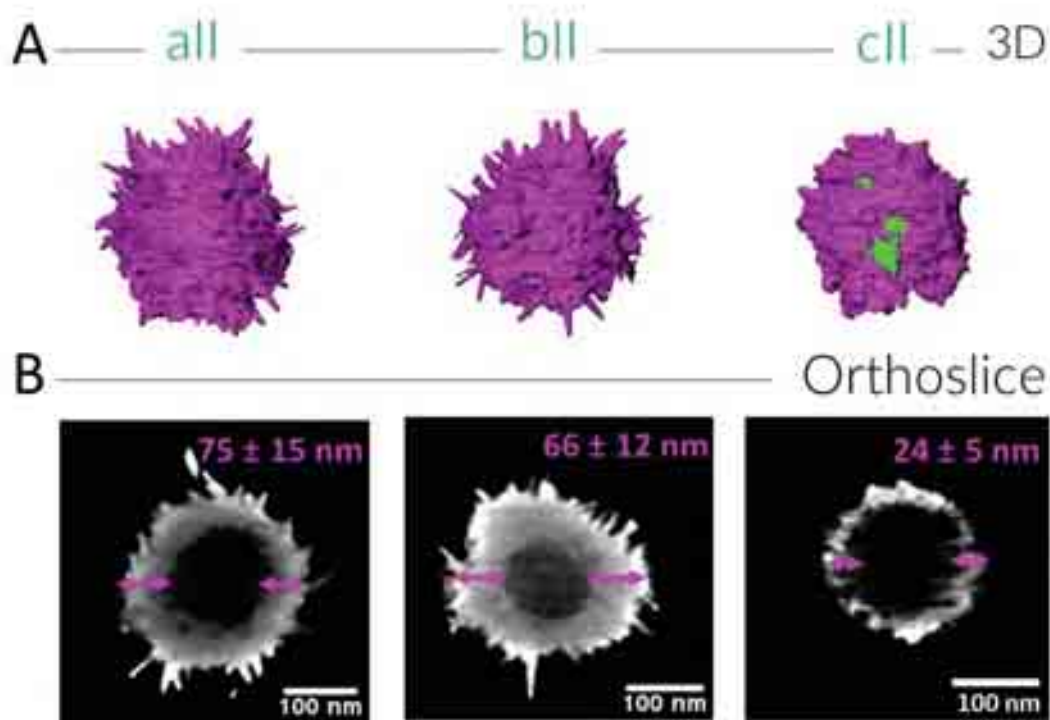


Figure 2.9. (A) Representative 3D visualizations of electron tomography reconstructions corresponding to particles all, bll and cII. (B) Orthoslices through the 3D electron tomography reconstructions shown in (A). The double-head arrows indicate the thickness of the gold shells.

In addition, EDX analysis was performed to distinguish the spatial distribution of both metals in the IOAuNSs. As shown in **Figure 2.10**, Fe in the IO core (shown in red) could be easily distinguished from the Au shell (shown in green). Additionally, a hollow core in the IONP can also be observed in the Fe mapping.

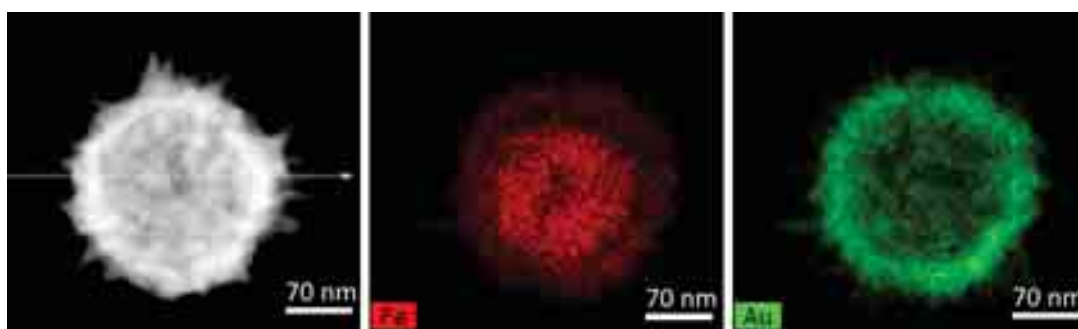


Figure 2.10. ADF-STEM and EDX analysis of IOAuNS. The hollow IO core can be seen in red and the Au spiky shell is shown in green.

2.5 Functionalization

The functionalization of the NPs with different molecules was carried out to provide the IOAuNSs with specific properties to act as contrast agents for SERS and fluorescence imaging. One important concern is the control over the number of functional molecules that can be attached to the Au surface. In this regard, previous methods to calculate the surface area of AuNSs typically assumed an area equivalent to a sphere, taking the outer tip-to-tip diameter of the NP as the

overall sphere diameter¹⁶. In this thesis we developed a geometric model to better simulate the surface area, thus being more accurate in calculating the concentration of molecules required for efficient NP functionalization. As shown in **Figure 2.11A**, three scenarios for the random distribution of spikes were considered (see details in Experimental section), and the surface area and the estimated number of spikes were calculated from this theoretical model. Subsequently, we validated the model with real data obtained from electron tomography, thus providing real values for the surface area. Using a manual segmentation process and a surface generation module, boundary surfaces were extracted for Au surface area determination (**Figure 2.11B**). Data regarding the surface area were also acquired (**Figure 2.11C**) and a study of the length of the spikes was also performed to validate the geometrical model (**Figure 2.11D**). This study was also performed in collaboration with the Electron microscopy for Materials Science group.

Remarkably, the experimental values were in agreement with the geometrical model based on a hexagonal arrangement of spikes with randomly assigned lengths. Thus, the theoretical model was validated with real data and could be used for a more accurate calculation of the surface area of nanostars.

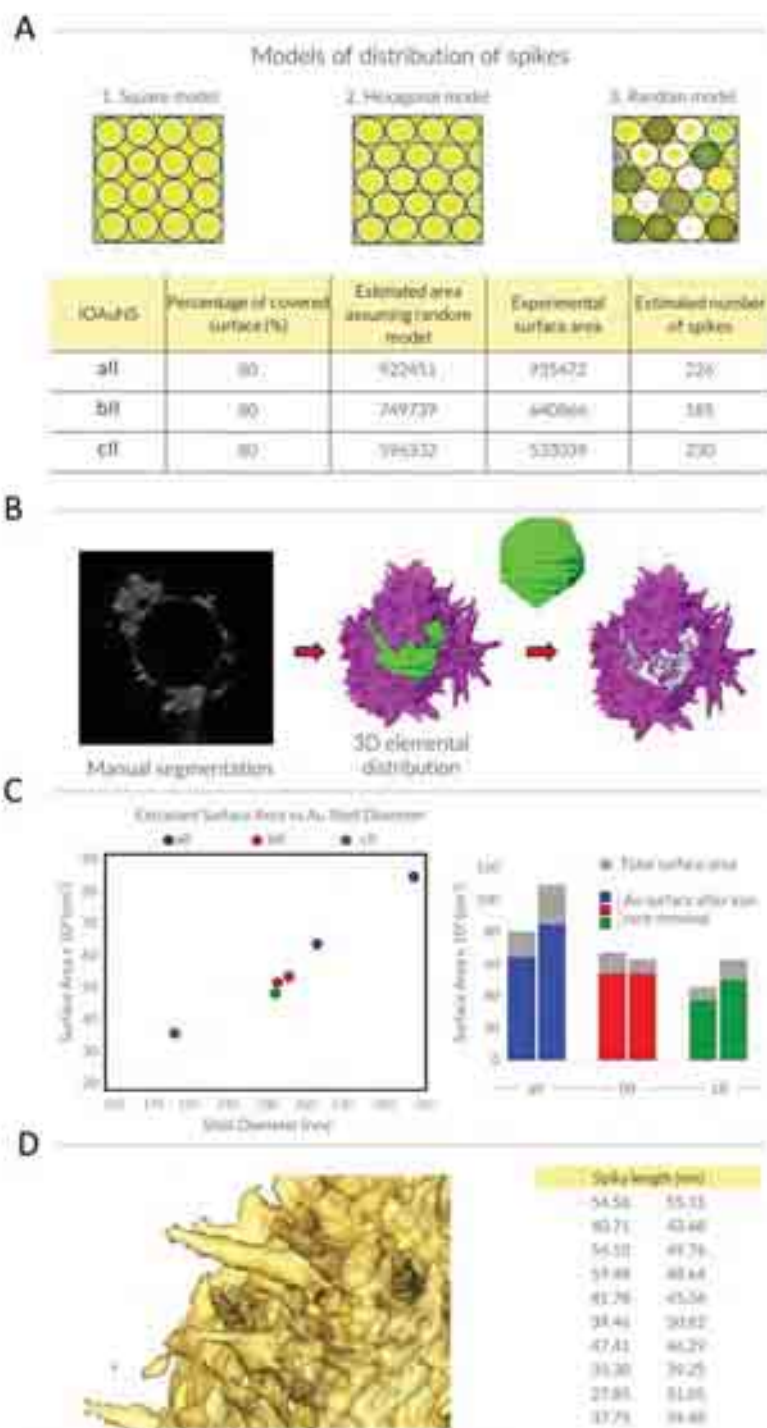


Figure 2.11. (A) Three scenarios for spike distribution, modelled as fully ordered circles (base of conical spikes) on a surface, assuming that the cone radius is much smaller than the radius of the core sphere. In the table, the data obtained from the theoretical models are compared to the experimental data. All the area values are given in nm². (B) Sketch of the procedure to calculate Au coverage, comprising removal of the iron core by manual segmentation in 3D ADF-STEM images (see Experimental section). (C) Analysis of shell diameter and total Au surface area for the particles in series II. (D) Spike length distribution for particle bII, obtained from the 3D reconstruction of a single NP.

2.5.1 SERS encoding

As required for the use of the NPs as contrast agents in SERS imaging, Raman-active molecules were attached to the Au surface. It is well-known that AuNPs can be readily functionalized with thiolated molecules, due to the stability of thiol-metal bonding¹⁷. We therefore selected two standard thiolated RaRs, namely biphenyl-4-thiol (4-BPT) and naphthalene-2-thiol (2-NAT), for surface functionalization and encoding of IOAuNSs.

We selected 4-BPT and 2-NAT because they offer clearly distinguishable fingerprints so is easy to differentiate precisely between both molecules in a mixed population. The chemical structures of the molecules and the characteristic SERS spectra are shown in **Figure 2.12**. The characteristic Raman vibrations of the molecules in solution and in cells as well as the assignment of their vibrational modes are listed in **Table 2.2**.

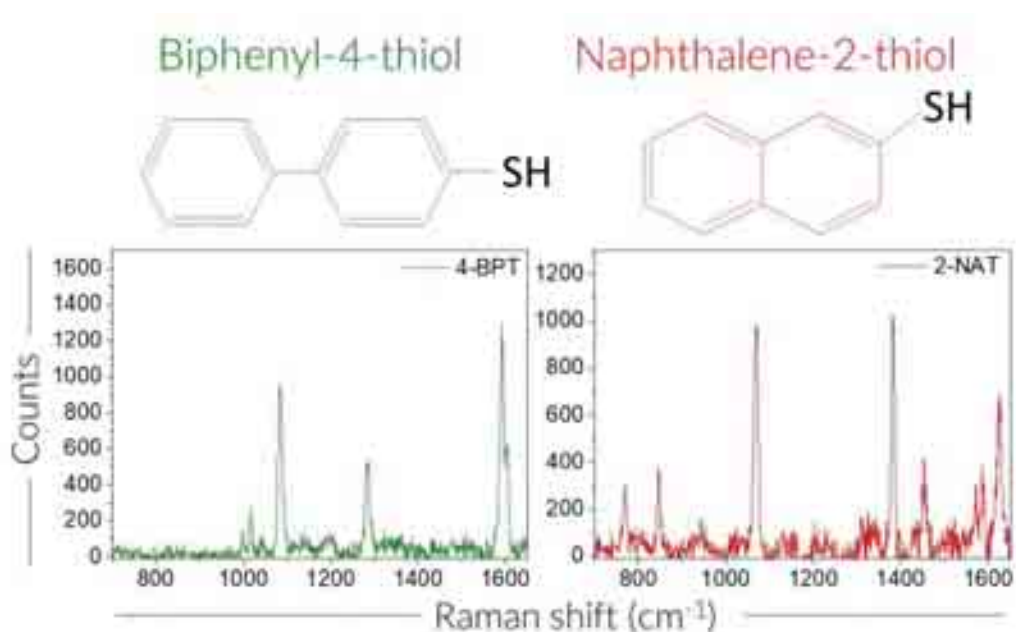


Figure 2.12. Molecular structures of 4-BPT and 2-NAT and SERS spectra with the characteristic peaks for these molecules.

Table 2.2. Characteristic Raman vibrations of 4-BPT and 2-NAT in solution and in cells, and assignment of their Raman-active vibrational modes as reported in the literature.

| RaR | vib ν ~ / cm^{-1} (in solution) | vib ν ~ / cm^{-1} (in cell) | mode assignment |
|-------|---|---|-----------------------------------|
| 4-BPT | 1084 | 1083 | ring C-H bend ^{18,19} |
| | 1285 | 1284 | ring C-H bend ^{18,19} |
| | 1593/1604 | 1593/1603 | ring C-C stretch ^{18,19} |

| | | | |
|-------|------|------|---|
| 2-NAT | 640 | 641 | ring deformation ²⁰ ring deformation ²⁰ C-H twist ²⁰ ring C-H bend (in plane) ²⁰ ring C-C stretch ²⁰ ring C-C stretch ²⁰ ring C-C stretch ²⁰ ring C-C stretch ²⁰ |
| | 769 | 770 | |
| | 846 | 850 | |
| | 1070 | 1070 | |
| | 1383 | 1382 | |
| | 1453 | 1454 | |
| | 1586 | 1587 | |
| | 1626 | 1625 | |

RaR adsorption onto IOAuNSs was achieved by means of a previously reported phase-transfer method in which the NPs were transferred to an organic solvent (chloroform) containing the Raman reporter²¹. A schematic representation of the phase transfer is shown in **Figure 2.13**.

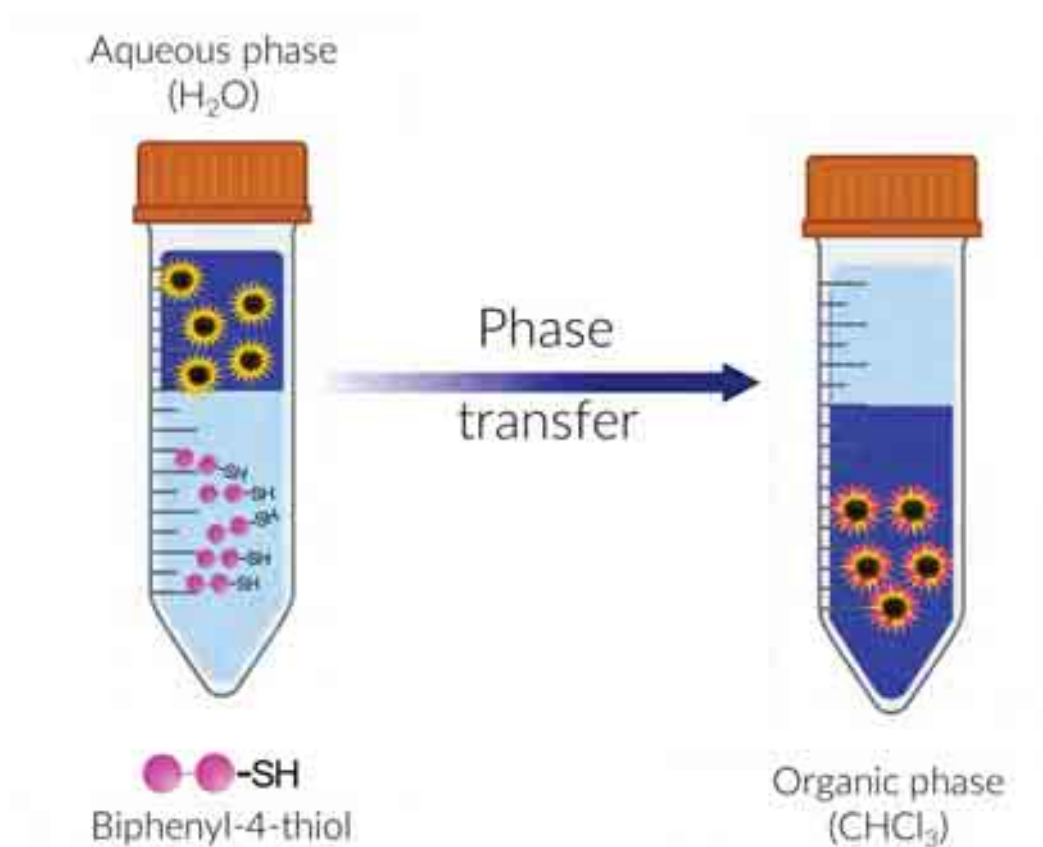


Figure 2.13. Schematic representation of the phase transfer process. Both solutions were placed in the same tube, NPs are initially located in the aqueous phase (H_2O) whereas 4-BPT molecules are located in the organic phase (chloroform). After shaking vigorously, 4-BPT molecules start binding onto the NPs, which get functionalized and diffuse into the organic phase (CHCl_3).

The RaR-functionalized NPs (in chloroform) were subsequently coated with the amphiphilic dodecylamine-modified polyisobutylene-alt-maleic anhydride amphiphilic polymer (PMA), resulting in their subsequent phase transfer, back to aqueous solvents²¹. Finally, the remaining

organic solvent was removed in a rotary evaporator and the particles were washed and recovered by centrifugation (full details in the Experimental section). The addition of the external PMA layer renders IOAuNSs hydrophilic, thus allowing their redispersion in water for further use in biological environments. The structure of the polymer is shown in **Figure 2.14**.

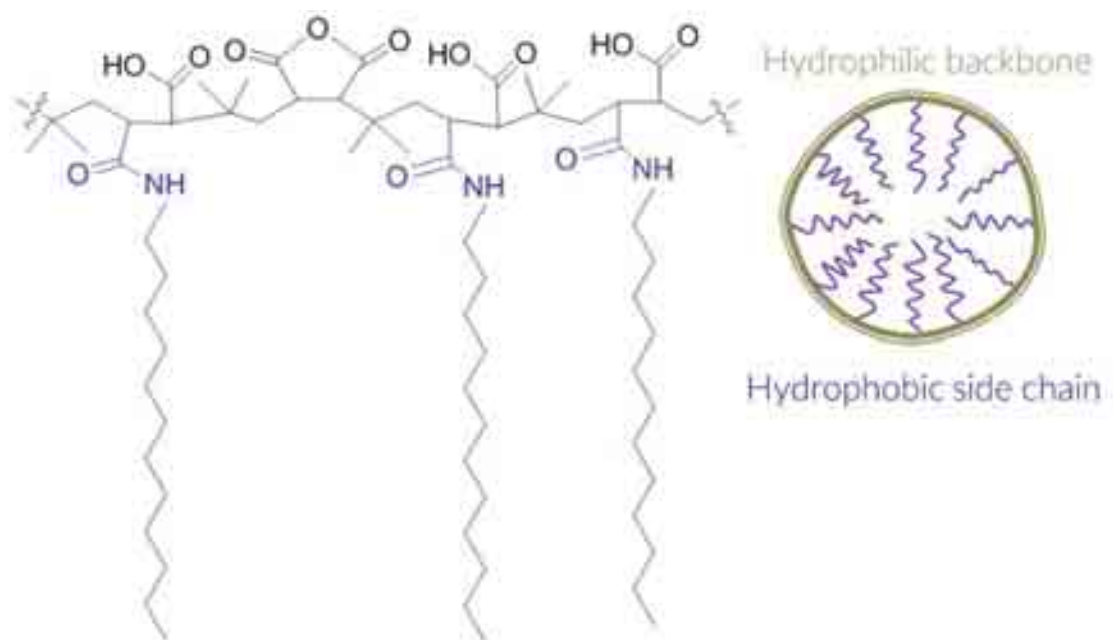


Figure 2.14. Structure of the amphiphilic polymer (PMA). The hydrophilic backbone of polyisobutylene-alt-maleic anhydride (black) is modified via amide bonds with hydrophobic dodecylamine side chains (blue). A sketch of the amphiphilic polymer is shown in the right panel. Figure modified from¹⁶.

2.5.1.1 SERS characterization

All IOAuNSs samples (series a-c and I – IV) were successfully encoded with Raman reporter 4-BPT molecules, using the phase transfer procedure and PMA coating (see Experimental section). Considering that biological tissues are particularly transparent at wavelengths between 650 and 950 nm (first biological window, BW-I) and that IOAuNSs were selected to display LSPR within the NIR range, a 785 nm laser was used for all SERS measurements. UV-Vis-NIR and SERS spectra are shown in **Figure 2.15**. The characteristic vibrational fingerprints of 4-BPT could be clearly observed for all the encoded NPs, however, changes in the intensity of the spectra were observed due to the different morphologies of the NPs. SERS measurements were performed by fixing the NP concentration based on iron content ($[Fe] = 0.1 \text{ mM}$), thus allowing us to solely study the effect of the gold shell thickness and morphology on the SERS intensity. It has been widely reported that the presence of well-defined spikes on AuNSs can strongly contribute to the enhancement of the Raman signal of adsorbed molecules, acting as intrinsic hotspots²². In this regard, the significantly lower SERS intensity recorded for particles cII is likely due to the less defined and more polydisperse spikes, as reflected by broader LSPR bands²³. In contrast, the high SERS signal is reflected by the high level of tip branching and tip definition.

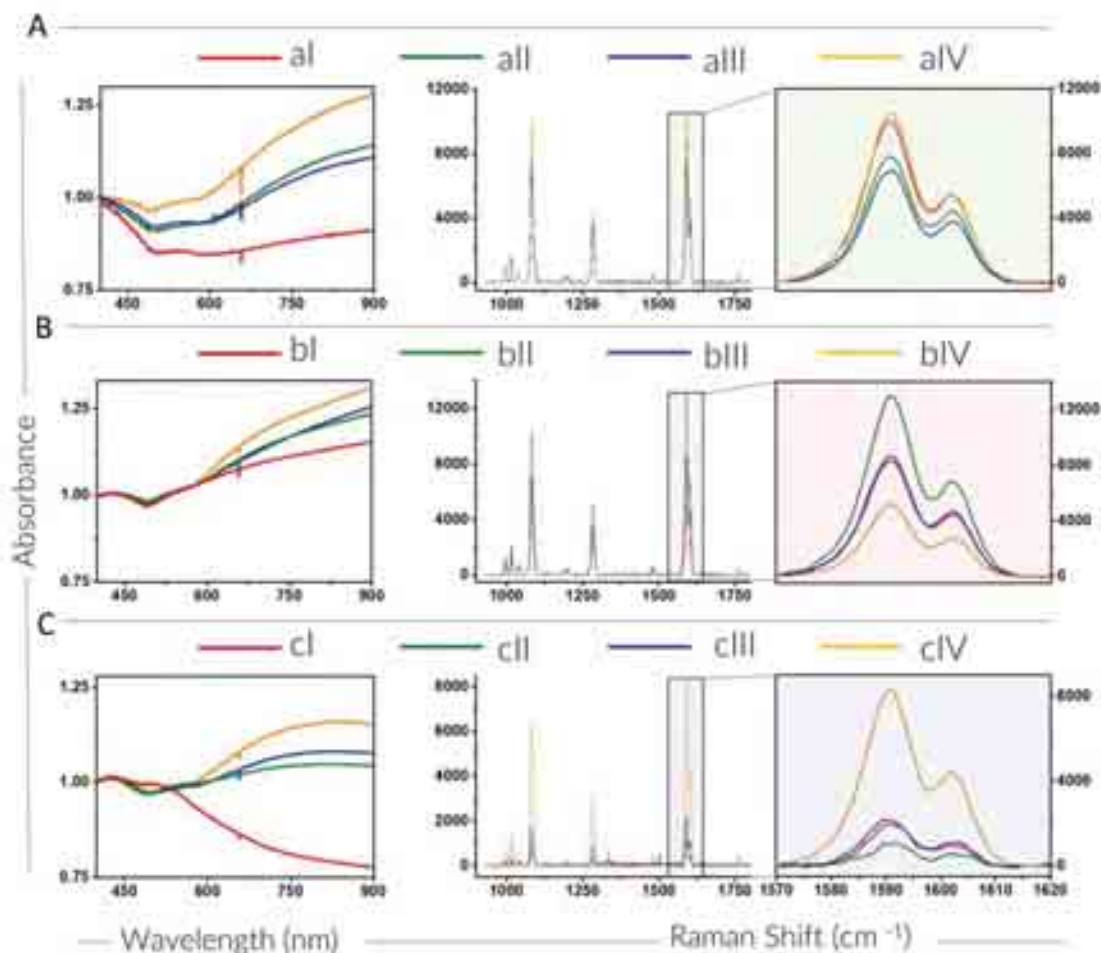


Figure 2.15. Normalized UV-Vis-NIR spectra (left) for IOAuNSs after coating with 4-BPT and SERS spectra (centre and right) of PMA-encapsulated IOAuNSs of **(A)** series a **(B)** series b and **(C)** series c. Colour scheme for all IOAuNSs: series I (red), series II (green), series III (blue), and series IV (yellow). All samples were measured in solution and at the same iron concentration [$[\text{Fe}] = 0.1 \text{ mM}$].

2.5.2 Fluorescent dyes

To incorporate fluorescent molecules to the structure, the PMA used to encapsulate IOAuNSs was chemically modified with 5-Carboxytetramethylrhodamine (TAMRA) and 2-(3-{2-tert-butyl-7-[ethyl(3-sulfonatopropyl)amino]chromenium-4-yl}prop-2-en-1-ylidene)-1-(5-carboxypentyl)-3,3-dimethylindoline-5-sulfonate (DY633) fluorescent dyes (See **Figure 2.16** for a schematic representation). Briefly, the dyes were attached via amide bonds to the carboxylic group of the hydrophilic backbone of the PMA using N-ethyl-N'-(3-(dimethylamino)propyl) carbodiimide/N-Hydroxysulfosuccinimide (EDC/NHS) chemistry. **Figure 2.17** shows the optical characterization with the specific excitation and emission bands for the dyes and for the PMA modified with the dyes

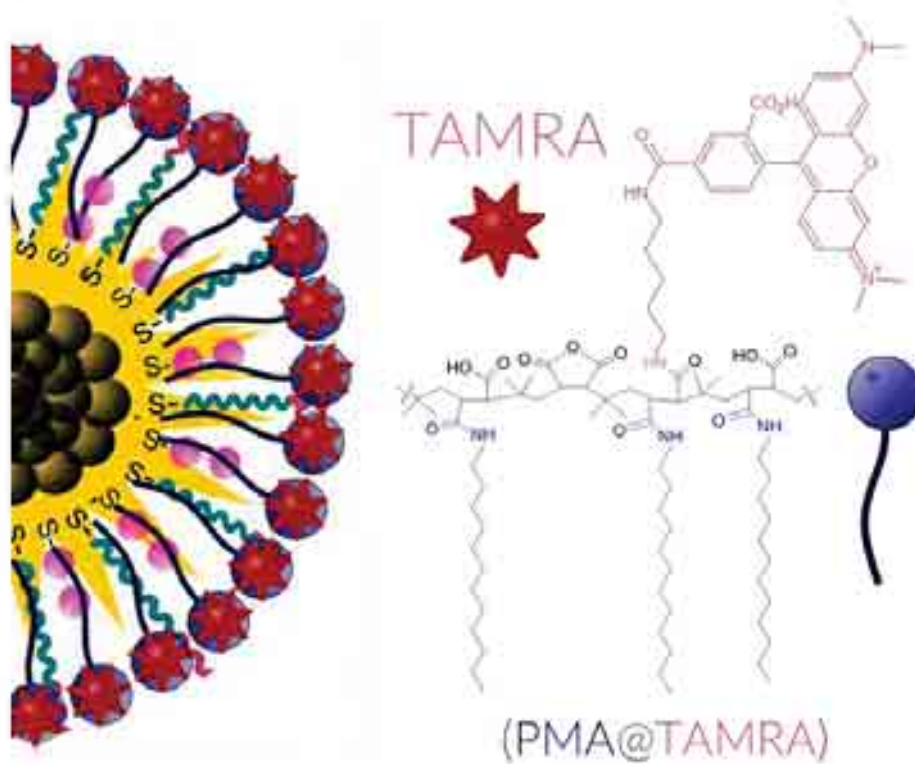
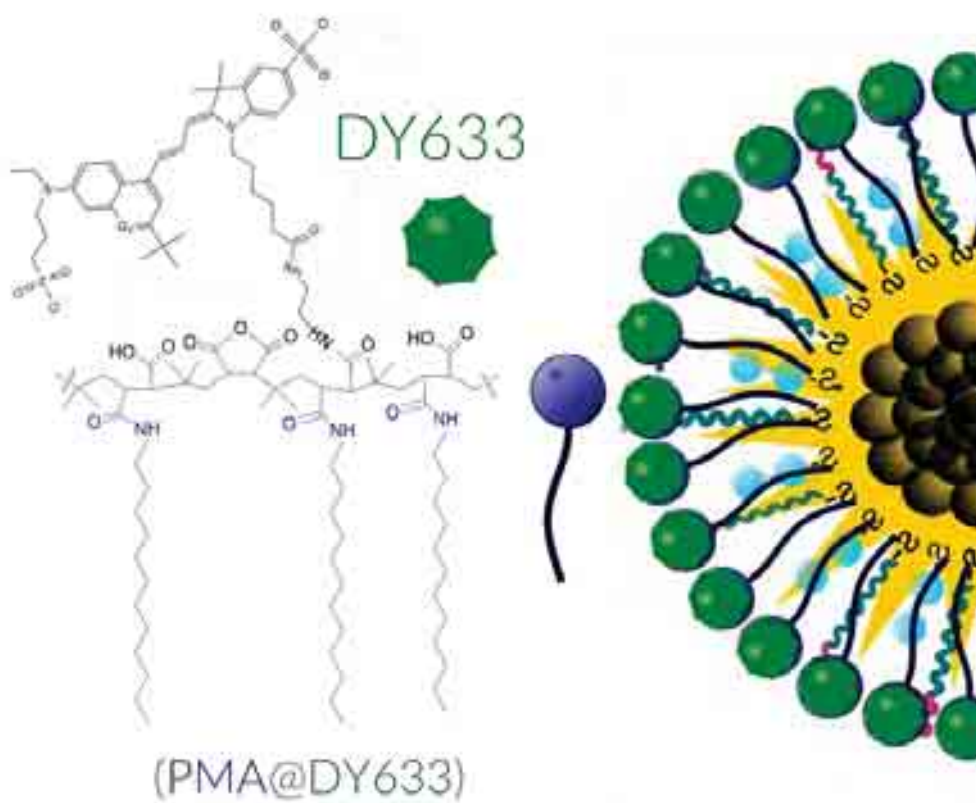
A**B**

Figure 2.16. Structure of PMA-modified TAMRA (A) and DY633 (B), also showing a schematic representation of their incorporation into IOAuNSs. Figure modified from¹⁵.

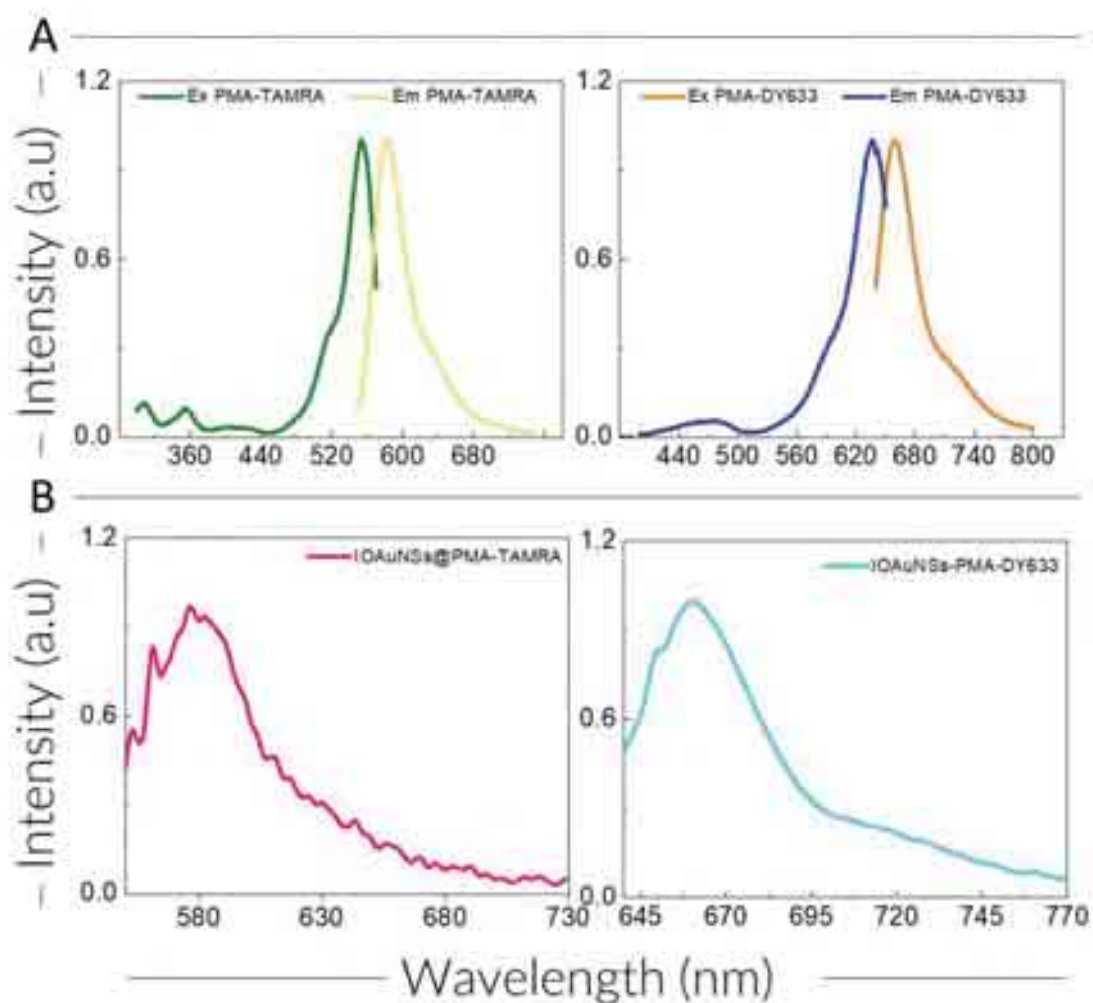


Figure 2.17. (A) Normalized fluorescence excitation and emission spectra of PMA-TAMRA micelles and normalized fluorescence emission of IOAuNSs@4-BPT@TAMRA (pink). (B) Normalized fluorescence excitation and emission spectra of PMA-DY633 micelles and normalized fluorescence emission IOAuNSs@2-NAT@DY633 (blue).

Labelling the PMA structures with the fluorescent dyes allowed in turn the functionalization of IOAuNSs with both RaR molecules (4-BPT and 2-NAT) and fluorescent dyes (TAMRA and DY633). SERS spectra were recorded to check that the signal of the Raman reporter was not affected by the functionalization with fluorescent molecules. As shown in **Figure 2.18**, no significant changes in the intensity and the fingerprint of their SERS spectra were detected in the presence of the dyes.

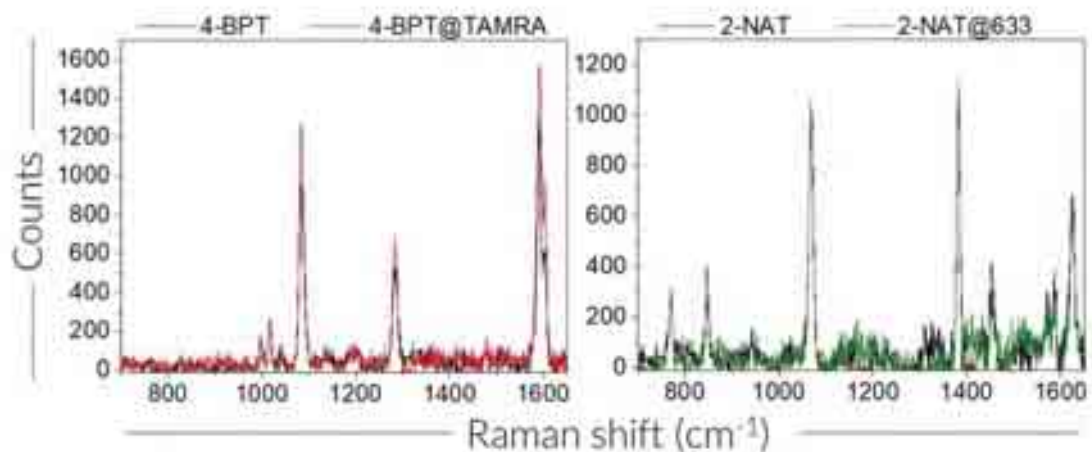


Figure 2.18. SERS spectra of IOAuNSs labelled with Raman reporters and fluorescent dyes, compared to those of IOAuNSs labelled with Raman reporters only. The concentration was fixed to $[Au+Fe] = 0.5 \text{ mM}$. No significant changes were observed, neither in the vibrational fingerprint of the Raman tags nor in the signal intensity. A 785 nm laser was used for the measurements.

2.6 Application of nanoparticles for imaging

2.6.1 2D cell model

The use of NPs as contrast agents in any biological application requires biocompatibility, stability and, in cases where cell-internalization is required, efficient cellular uptake. Human breast cancer MCF7 cells were chosen for the biological experiments, thanks to their frequent use in research and various characteristics such as uncomplicated maintenance, normal division times (ca. 1 day), adherent nature when grown in traditional cell culture, and size (typically ca. $30 \mu\text{m}$, with high circularity). Additionally, they exhibit active endocytosis, which results in high amounts of nanoparticle internalization without inhibition of normal cellular features (growth, proliferation, etc.). We first conducted cell viability and NP uptake studies to confirm the biocompatible nature of IOAuNSs. We incubated adhered MCF7 cells with various concentrations of IOAuNSs (up to 0.25 mM of $[Au + Fe]$) and after 24 h we measured the cell viability using the commercial lactate dehydrogenase (LDH assay) (**Figure 2.19A**). No signs of cytotoxicity were observed. TEM imaging of fixed and resin-embedded MCF7 cells exposed to IOAuNSs showed that IOAuNSs were internalized by the cells and organized inside vesicles, suggestive of endosomes, throughout the volume of the cell (**Figure 2.19B**).

Importantly, no sign of cytotoxicity was observed, which was confirmed by exposing MCF7 cells to different concentrations of IOAuNSs up to for 24 h, followed by cytotoxicity analysis.

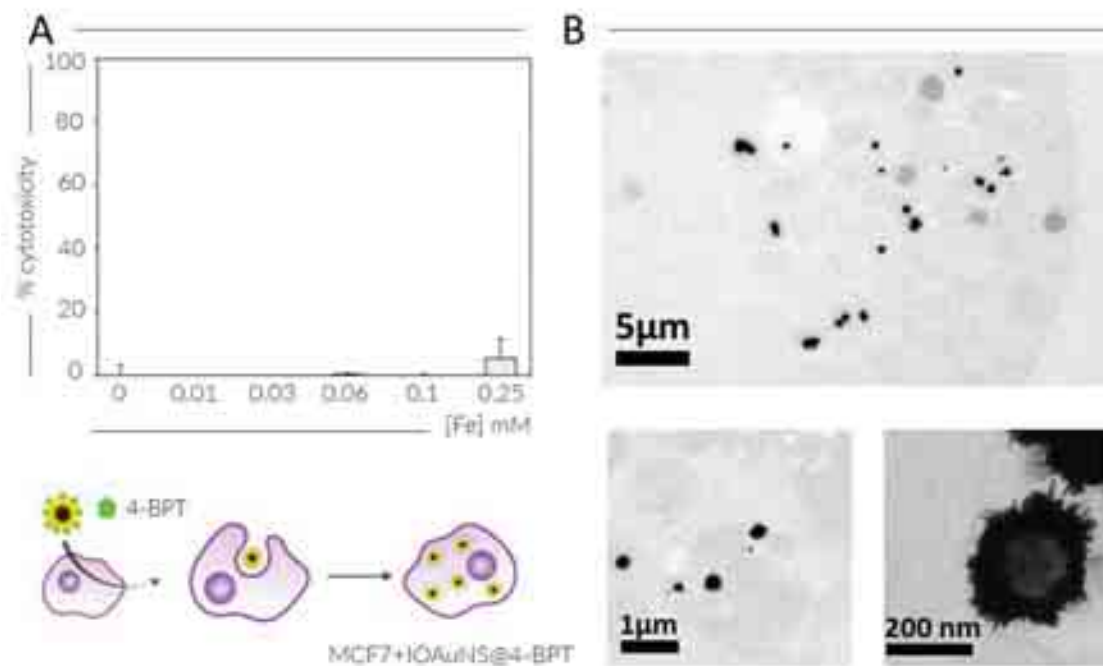


Figure 2.19. (A) Results of LDH tests after incubation of MCF7 cells with IOAuNS-bII, for 24 hours. (B) TEM images of ultramicrotomed MCF7 cells containing IOAuNSs confined in endosomes. A schematic representation of the incubation process is shown in the bottom-left part.

Additionally, we verified the uptake of IOAuNSs by conducting SERS mappings of a single MCF7 cell after incubation with IOAuNSs@4-BPT. The results are shown in **Figure 2.20A** and confirmed the colocalization of IOAuNSs with MCF7 cells. Additional high resolution 3D SERS maps of MCF7 cells incubated with IOAuNSs@4-BPT-bII were also conducted to better determine their spatial distribution (**Figure 2.20B**). As the 2D image and the 3D reconstruction from confocal Raman microscopy indicates, IOAuNSs@4-BPT seems to be organized and distributed in vesicles inside the cell, in agreement with TEM results in **Figure 2.19B**.

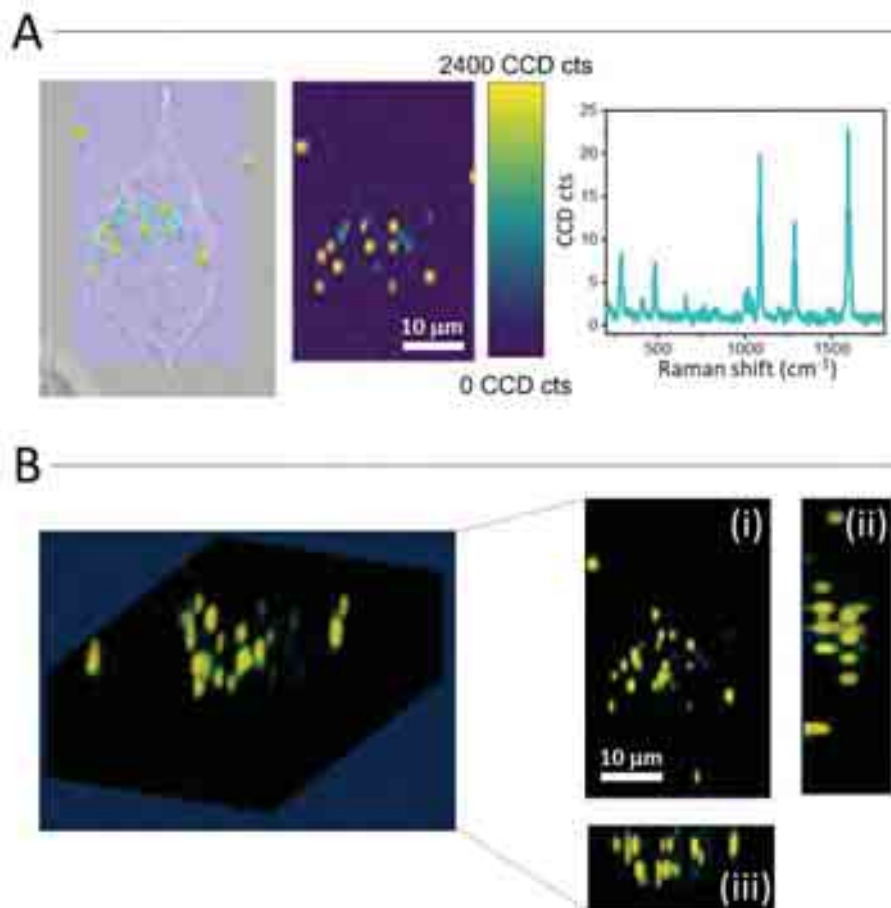


Figure 2.20. (A) SERS map (left) analysed with true component analysis, which evidences in an intensity colour code the presence of the NPs, and representative SERS spectrum (right) of a single cell pre-loaded with IOAuNSs@4-BPT-bil. (B) 3D Reconstruction of the measurement shown in (A). Orthogonal projections of a z-stack are shown in the right panel, including *xy* projection (i) *yz* projection (ii) and *xz* projection (iii).

2.6.1.1 SERS imaging

Again, in order to study the role that the gold shell thickness and morphology have on the overall SERS intensity, SERS measurements were performed on cells labelled (see details in Experimental section) with the different SERS encoded NPs, fixing the iron concentration of the NPs ($[\text{Fe}] = 0.1 \text{ mM}$), as opposed to the gold or the overall metal or NP concentration. The results for SERS imaging in 2D cell cultures showed that all the IOAuNSs could act as contrast agents for SERS (**Figure 2.21**). However, it was previously commented that the presence of well-defined spikes can strongly contribute to the enhancement of the Raman signal of the adsorbed RaR molecules. In this regard, IOAuNSs cI and cII showed poor SERS signal in solution (**Figure 2.15**) and in cell uptake studies, related to the less defined and more polydisperse Au spikes and their broader LSPR bands.

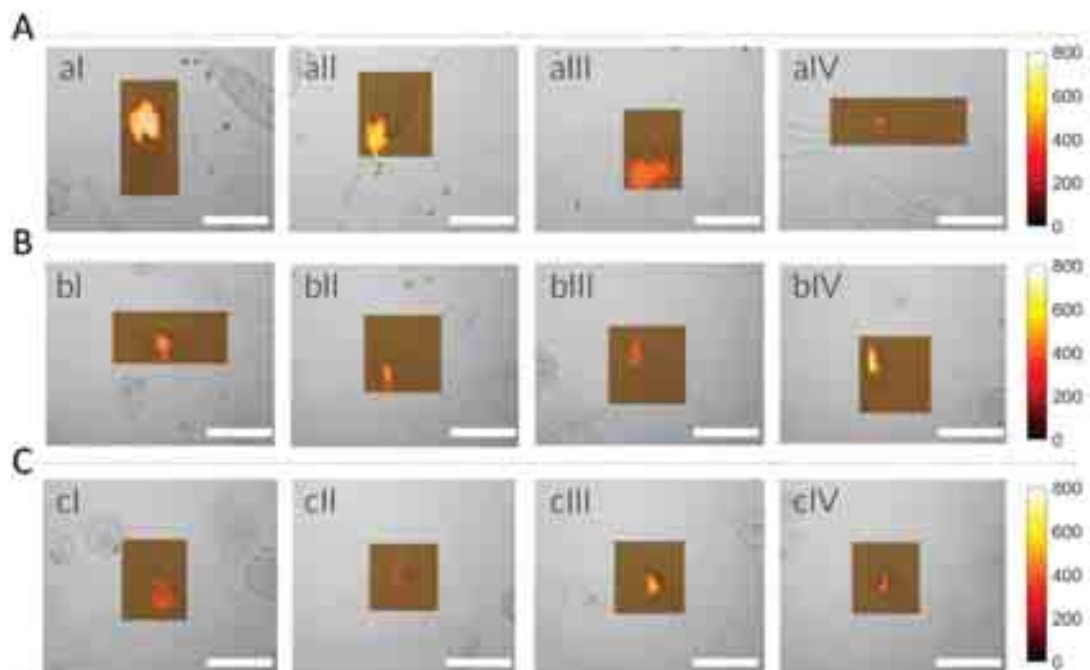


Figure 2.21. SERS maps of MCF7 cells, pre-loaded with IOAuNSs@4-BPT from series a, b and c, and I-IV. Multiple Linear Regression analysis (MLRA) was performed on the data to obtain the regression coefficient calculated as the b-values, whose intensities indicate the presence of the IOAuNSs inside the cell and the intensity differences represents the difference between the intensity of the signal that was acquired. More details about the procedure are provided in the Experimental section. The scale bars correspond to 20 μm .

2.6.1.2 Magnetic resonance imaging

Prior to analyse the use of IOAuNSs as contrast agents for MRI in cells, ZFC/FC measurements were performed to confirm that the magnetic properties of the IONPs did not change when coated with the gold shell (see **Figure 2.22**). Considering that there are no differences between the IO cores of all the IOAuNSs, the gold shell was confirmed not to affect the magnetic properties of the cores and thus, the contrast capacity for all the NPs should be the same.

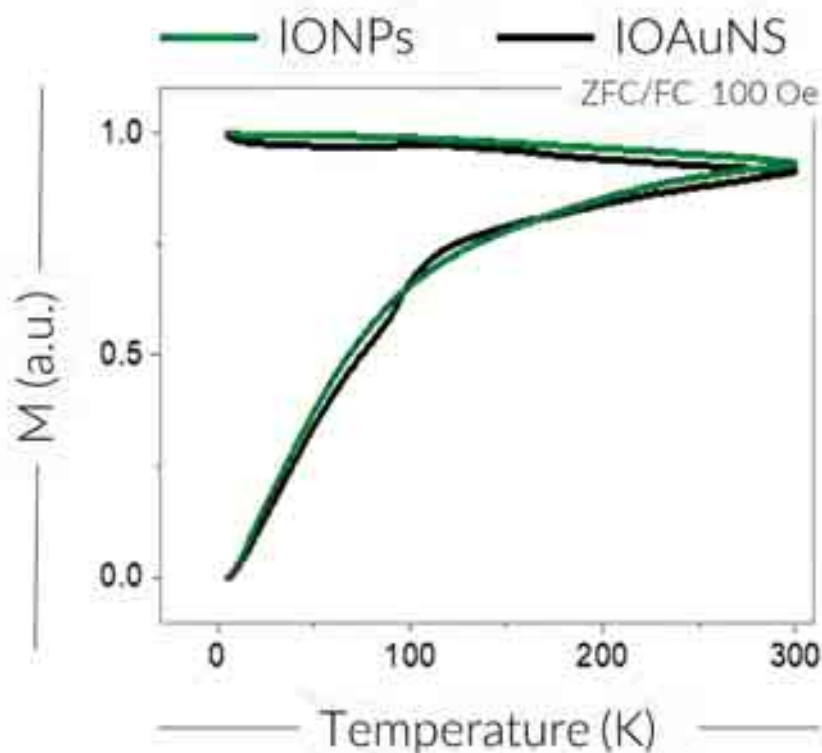
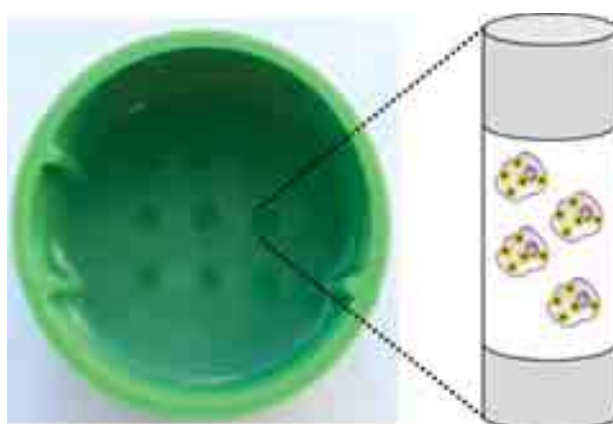


Figure 2.22. ZFC/FC curves for IONPs recorded at a magnetic field of 100 Oe for IONPs (green line) and IOAuNSs (black line).

We proceeded next to analyse the use of IOAuNSs as T2 contrast agents for MRI in cells. To do so, an agarose phantom was made by filling a 40 mm mold with agarose (1%). After cooling down to harden the agarose, small holes (2 mm) were carefully drilled into the agarose resulting in cylinders of equal size. Due to the pointed nature of the drill bit, we observed that the bottom of the cylinder was not completely flat. Hence, 20 μ L of a 0.4 % agarose solution was pipetted into the bottom of each cylinder, thus achieving a flat base. Cells incubated with the different IOAuNSs



(50 μ L) were subsequently placed in the cylinders with special care to avoid the formation of air bubbles, which produce strong noise and will appear as dark spots in the MRI. Finally, a 0.9% agarose solution was used to seal the cylinders. Using this procedure, the NP dispersion remains encapsulated in a matrix of agarose which allows minimal interference in MRI signals (**Figure 2.23**).

Figure 2.23. Image of the agarose phantom and scheme of the cell+IOAuNSs-containing cavities.

As the IO core size plays a major role in these experiments, IOAuNSs concentrations were adjusted based on the total metal (Fe + Au) concentration. Compared to SERS imaging, a lower IOAuNSs concentration was chosen (0.05 mM) because of the increased sensitivity of the

technique at these settings. Phantoms were prepared as previously described and cells, pre-incubated with IOAuNSs, were subsequently placed in the pre-made agarose holes. A schematic of the MRI phantom preparation is shown in **Figure 2.24**. Each agarose phantom contained enough holes to accommodate also appropriate controls, including cell media, water, IONP, and cells with IOAuNSs. As can be observed in **Figure 2.24A, B, C** dark contrast (typical for T2 contrast agents) appeared only in those samples containing IONP and cells incubated with IOAuNSs. As expected, higher concentrations of Fe in IOAuNSs ($c > b > a$) resulted in higher contrast. It is interesting to observe that more concentrated, darker contrast was observed in the cell containing sample. This is possibly due to the close packing of IOAuNSs in cellular endosomes, essentially mimicking NP aggregation, leading to MRI intensities similar to those of considerably larger NPs²⁴.

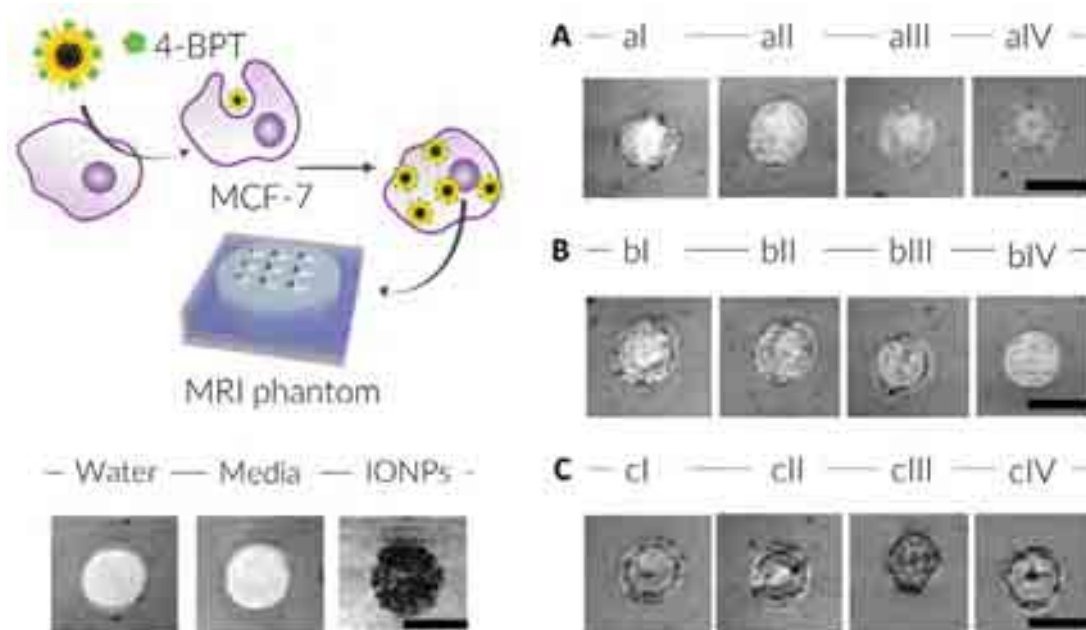


Figure 2.24. MRI experiments in 2D using agarose phantoms (see methods). IOAuNSs (I, II, III and IV) of **(A)** series a, **(B)** series b and **(C)** series c, internalized in MCF7 cells, were placed in the holes. Water, cell media and IONPs were also introduced in the agarose phantom as controls. Scale bars: 2 mm.

2.6.1.3 Confocal Fluorescence imaging

In order to provide an alternative imaging modality which offers relatively high spatial resolution, IOAuNSs were labelled with fluorescence molecules and added to cells to conduct confocal fluorescence imaging. IOAuNSs@4-BPT@TAMRA and IOAuNSs@2-NAT@DY633 were added to MCF7 cells and imaged after 24 h (**Figure 2.25**). As can be observed, fluorescent signal was recorded from the cell area, in agreement with previous SERS studies. This therefore suggests that multifunctional IOAuNSs are able to act as contrast agents for SERS, MRI and fluorescence imaging in 2D.

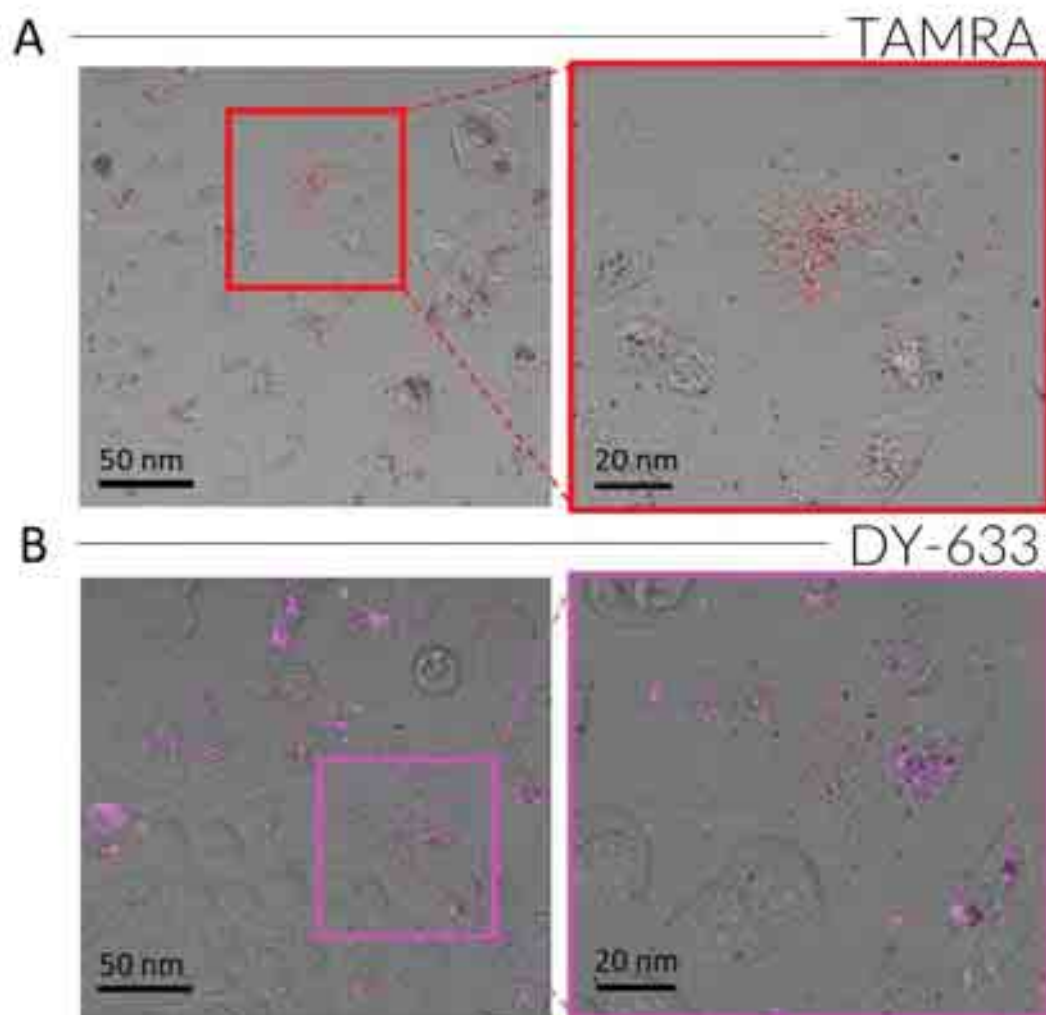


Figure 2.25. Fluorescence microscopy images of MCF7 cells incubated with (A) with IOAuNSs@4-BPT@TAMRA (B) IOAuNSs@2-NAT@DY633.

2.6.2 3D cell model

To test the particles in 3D, we chose to focus solely on the IOAuNSs bII because these NPs had good SERS and MRI properties and therefore were of interest for multimodal imaging applications.

We decided to test the capability of IOAuNSs to act as contrast agents for MRI, SERS and fluorescence imaging in a 3D cell model. Spheroids constitute an excellent and accessible alternative model to more traditional 2D cell culture studies, as they better represent the complex 3D environment occurring *in vivo*, often incorporating mixed cell types and gradients in nutrients and waste products²⁵. Furthermore, the complications involved in NP delivery due to the presence of an extracellular matrix (ECM) or poor NP penetration are better mimicked in spheroids compared to 2D cell experiments²⁶. We thus explored the use of spheroids comprising MCF7 cancer cells and fibroblasts (HDF), as a 3D model for multimodal imaging with IOAuNSs. HDF cells are known to aid in improving intercellular adhesions and thus spheroid formation with certain cell types²⁷.

We initially pre-labelled the separate cell populations with two different RaR-labelled IOAuNS-bII which were also fluorescently labelled to allow correlative confocal fluorescence microscopy.

IOAuNSs-containing cells were detached from the surface and mixed in a 1:1 ratio (IOAuNSs@4BPT and IOAuNSs@2NAT) to form spheroids. A scheme of the procedure can be seen in **Figure 2.26** as well as an optical image in which a dark area appeared after the incubation of the spheroids with NPs, confirming the internalization of the NPs by the cells that pre-formed the spheroid.

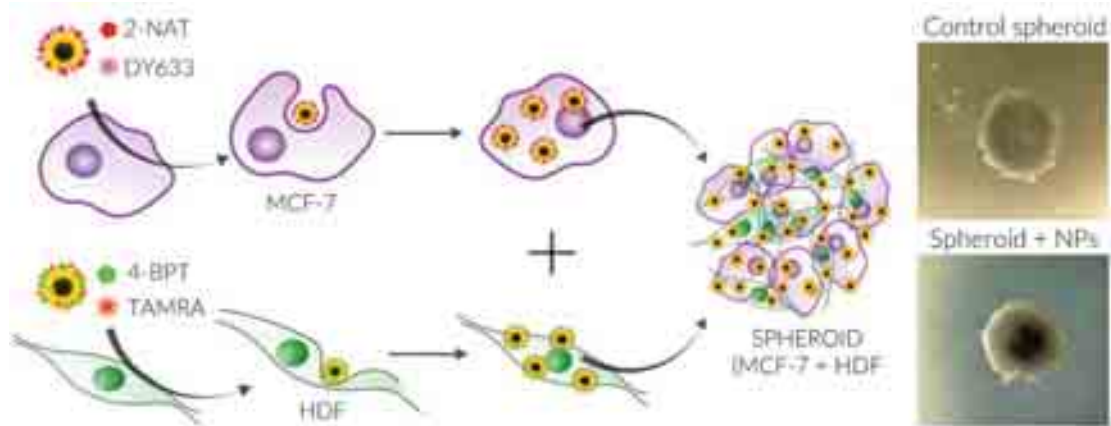


Figure 2.26. Schematic illustration of spheroid preparation. MCF7 and HDF cells were pre-incubated with IOAuNSs@4-BPT@TAMRA and IOAuNSs@2-NAT@DY633, respectively, prior to co-culture into the spheroid. Optical images of the spheroids with and without NPs are shown in the right part.

Additional characterization was carried out for MCF7 and HDF cells in 2D pre-loaded with NPs that were then used to form the spheroids. Both cells were immunostained with E-cadherin and TE-7 and fluorescence imaging was used to confirm that both cells were present and that the internalized NPs can be detected inside each cell through the fluorescent dyes (**Figure 2.27**).

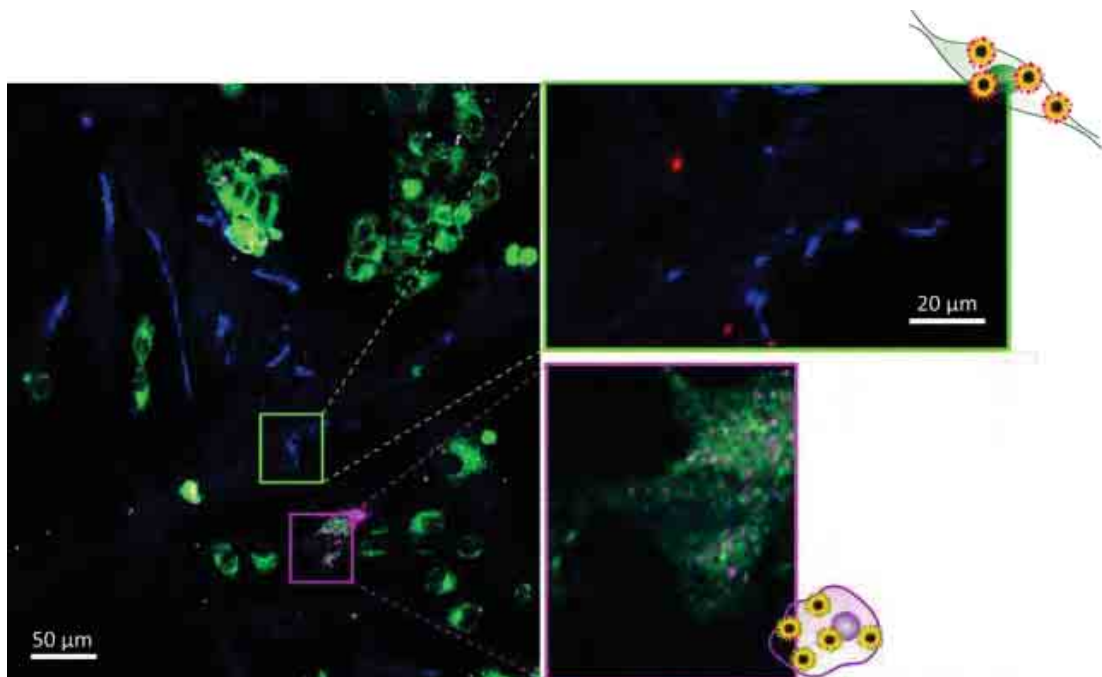


Figure 2.27. Cellular uptake of IOAuNSs. Immunostaining of MCF7 (E-cadherin, green) and HDF (TE-7, blue) cells previously incubated with IOAuNSs@4-BPT@TAMRA (red) and IOAuNSs@2-NAT@DY633 (pink), respectively.

2.6.2.1 Multimodal imaging in 3D

We proceeded to image the 3D spheroid using all three imaging techniques. Live SERS imaging of the whole spheroid was first carried out to probe the overall location of the multimodal NPs. As shown in **Figure 2.28A, B**, whereas both RaRs can be clearly identified in the SERS maps, and 3D reconstructions can be obtained, IOAuNSs appear to be located only at the outer layer of the spheroid. Considering that spheroid-containing cells were pre-labelled with IOAuNSs, this result was unexpected – IOAuNSs should have been distributed throughout the entire spheroid volume. We thus examined a slice of the spheroid after fixation and microtome cutting, conducting SERS mapping and fluorescence confocal imaging on the central part of the spheroid. As can be observed in **Figure 2.28C, D**, this measurement confirmed the presence of both types of SERS-encoded NPs throughout the *xy* plane, suggesting that the lack of SERS signal in the center of the spheroid in live samples stemmed from limitations in the penetration depth of the incident or outbound laser, and extensive backscattered signal, principally due to the large amount of IOAuNSs in the sample, which can cause absorption and multiple scattering of light. We subsequently examined the spheroids using MRI, by placing 5 spheroids per hole in the agarose phantoms. Contrast was clearly observed for the spheroids containing IOAuNSs, with intense dark areas corresponding to the spheroids (**Figure 2.28E**).

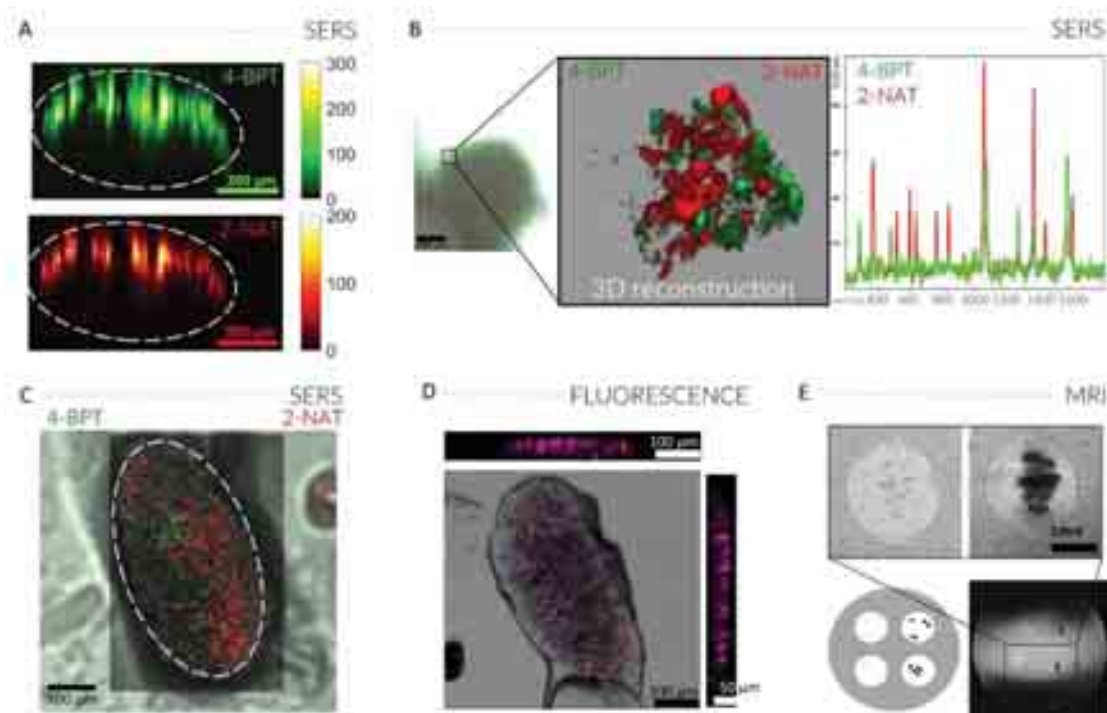


Figure 2.28. (A) SERS mapping along the xz plane, of live spheroids showing pixels corresponding to 4-BPT (green) and 2-NAT (red). A total area of $800 \times 430 \mu\text{m}^2$ was imaged, with a resolution of $5 \times 10 \mu\text{m}^2$. Data were analysed by MLRA. In this analysis for each x - y point on the map, the entire SERS spectrum is used to determine statistically how well it matches the reference spectrum. Thus, the intensity map is given by the differences in the spectra comparison. The white dotted line highlights the edge of the spheroid. (B) SERS mapping and 3D reconstruction of a selected volume at the outer edge of a live spheroid (brightfield image also shown). A total volume of $84 \times 84 \times 70 \mu\text{m}^3$ (xyz) was probed, with a resolution of $2 \times 2 \times 5 \mu\text{m}^3$ (xyz). Data were analysed by TCA. (C) SERS map of a transversal cut (area $360 \times 560 \mu\text{m}^2$, $50 \mu\text{m}$ in thickness) of a fixed and embedded spheroid, showing the presence of 4-BPT and 2-NAT positive pixels throughout the xy plane. Data were analysed by MLRA. (D) Orthogonal projection collected by confocal fluorescence imaging of a transversal cut ($50 \mu\text{m}$ in thickness) through a fixed and embedded spheroid. (E) MRI images from spheroids, with (right-hand side circles) and without (left-hand side circles) IOAuNSs, planted in a phantom.

To mimic a more realistic situation, a second model of IOAuNS-spheroid interaction was developed. When NPs are administered *in vivo* for imaging purposes, NP penetration into the site of interest is determined by various factors, including the enhanced permeation and retention (EPR) effect, the tumor microvasculature, and potential spatial inhomogeneities in the NP delivery. We thus formed the spheroids first (again comprising MCF7 and HDF cells) and subsequently exposed them to a mixture of IOAuNSs@4-BPT@TAMRA and IOAuNSs@2-NAT@DY633. A scheme of the procedure can be seen in **Figure 2.29**.

Due to the size of IOAuNSs, some sedimentation was observed during the incubation period with the spheroids. To avoid this issue, we incubated IOAuNSs with spheroids inside Eppendorf tubes, in a rotisserie rotator stored in an incubator at 37°C overnight.

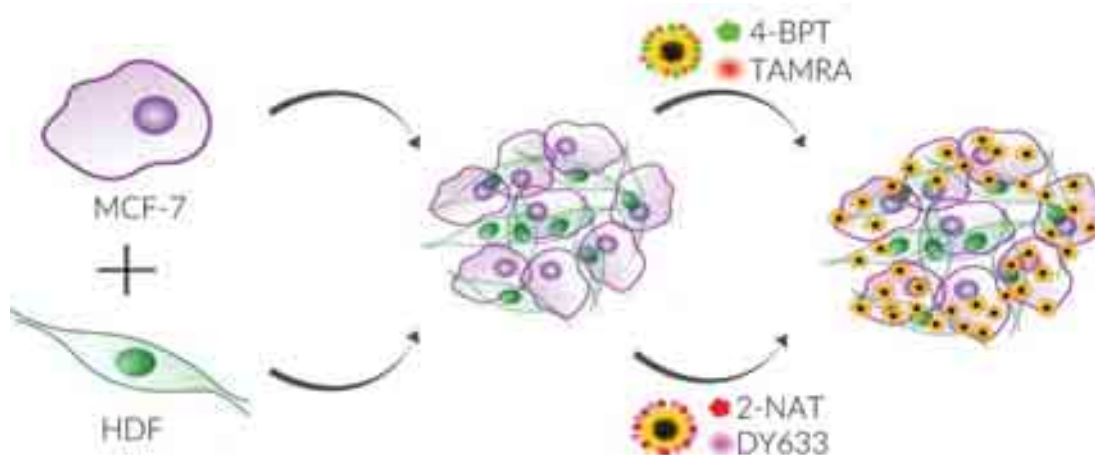


Figure 2.29. Illustration of spheroid formation. MCF7 and HDF cells were used to pre-form spheroids and then, IOAuNSs@4-BPT@TAMRA and IOAuNSs@2-NAT@DY633, were added for incubation.

We first conducted confocal and SERS imaging of the whole live spheroid, again to determine IOAuNSs distribution (**Figure 2.30A, B**). Similar results were observed as in the previous experiment, with limited capacity to determine the distribution of the NPs in deeper buried layers. Although it appeared that NPs were only located at the outer edge of the spheroids, this could only be confirmed by fixing and making a transversal cut along the *xy* plane. Indeed, SERS imaging clearly showed the presence of IOAuNSs at the outer 100 μm layer of the spheroid, with no signal recorded from the inner core (**Figure 2.30C**). Thus, we proved that IOAuNSs are suitable contrast agents for spheroid imaging, and although they do penetrate the complex 3D model, a certain limitation was found in the light penetration depth that can be achieved.

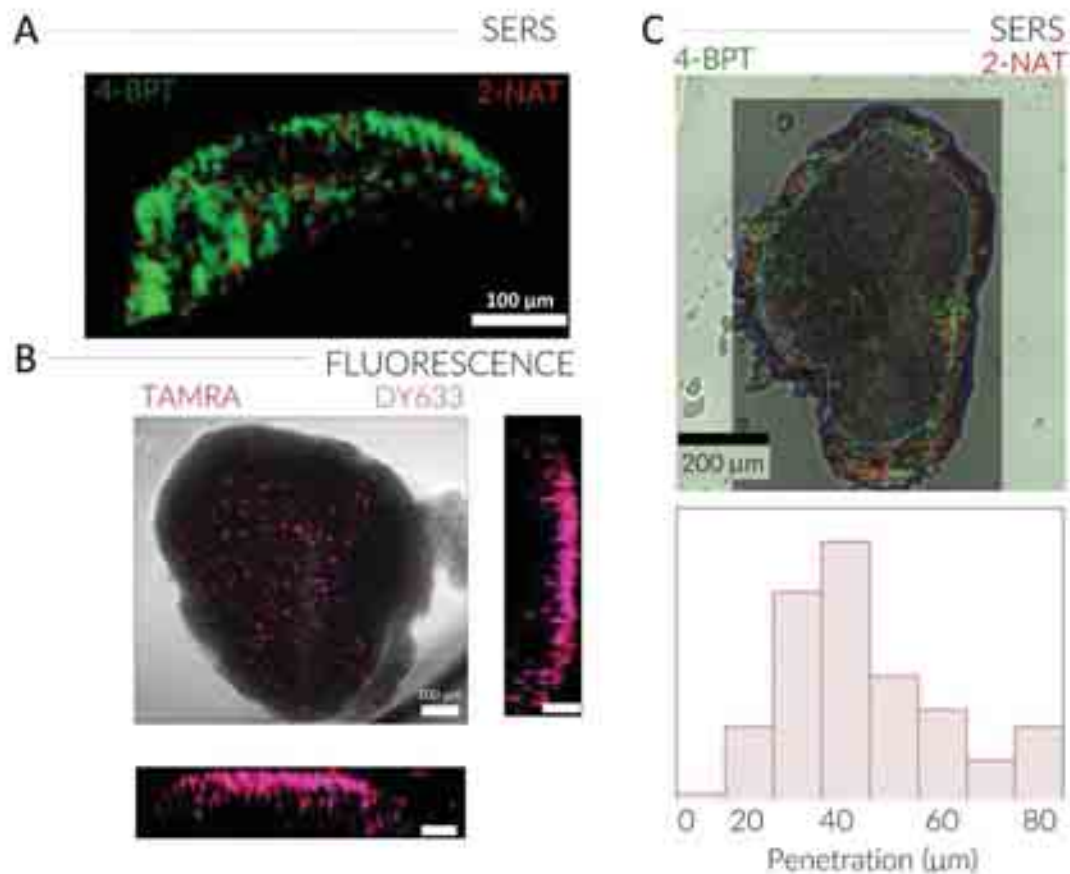


Figure 2.30. (A) SERS imaging of a MCF7:HDF spheroid incubated with IOAuNSs@4-BPT@TAMRA (in green) and IOAuNSs@2-NAT@DY633 (in red) NPs. A volume of $400 \times 380 \times 150 \mu\text{m}^3$ was mapped and MLRA used to obtain b-values whose intensities are shown. Scale bar, $100 \mu\text{m}$ (B) Orthogonal projection captured using confocal fluorescence imaging of a z-stack of a MCF7:HDF spheroid incubated with IOAuNSs@4-BPT@TAMRA (in red) and IOAuNSs@2-NAT@DY633 (in pink) NPs. Scale bars correspond to $100 \mu\text{m}$ (C) Brightfield image with overlaid SERS map of IOAuNSs@4-BPT@TAMRA (in green) and IOAuNSs@2-NAT@DY633 (in red) NPs, detected in an OCT-embedded slice ($635 \times 875 \mu\text{m}^2$) of MCF7:HDF spheroid. MLRA used to obtain b-values whose intensities are shown. The blue dotted lines represent the spheroid edge and approximate maximum penetration depth of IOAuNSs, used to calculate the bottom graph.

2.6.3 Multimodal imaging *ex vivo*

In our pursuit of increasing complexity of the biological model, the next step comprised implementing the NP contrast agents for multimodal imaging in *ex vivo* models. For this purpose, we chose to conduct intracerebral injections into an excised mouse brain. The brain is an organ that provides a tissue with homogenous, low-level background contrast in MRI and which is sufficiently large to apply multiple injections of different materials for comparison. Considering that we aimed at conducting SERS and fluorescence imaging on sliced tissue measuring a few tens of microns in thickness, MCF7 cells were chosen as the carriers of IOAuNSs (using IOAuNSs functionalized with 2-NAT and DY633 for SERS and fluorescence microscopy, respectively), because the injection of free IOAuNSs posed the problem of NPs diffusing into the tissue, inducing

a significant reduction in SERS and fluorescence signals. First, MCF7 cells were incubated overnight with IOAuNSs@2-NAT@DY633, at a final total metal (Fe + Au) concentration of 0.05 mM, previously shown to be suitable for MRI imaging. Cells were trypsinized and concentrated to 2×10^6 cells/mL before injecting 5 μ L into the right brain hemisphere. A second injection of IOAuNSs@2-NAT@DY633, at the same estimated concentration in the cell-containing sample, was injected into the left hemisphere as a NP control. PBS buffer was also injected in the upper part of the brain as a media control. A schematic view of the layout is shown in **Figure 2.31**.

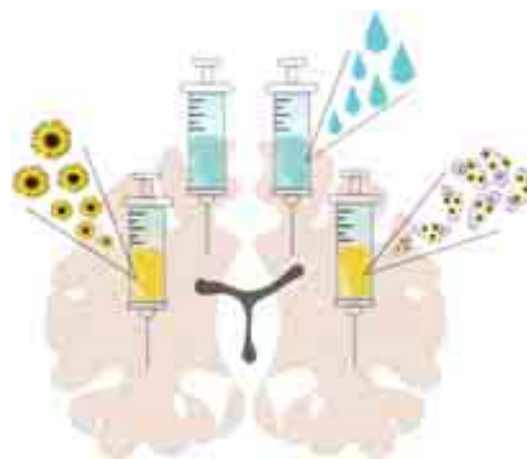


Figure 2.31. Schematic illustration of different injections into a mouse brain, both with (right hemisphere) and without cells (left hemisphere), as well as a PBS buffer control (top part of both left and right hemispheres).

For MRI measurements, the entire brain was placed in the MRI scanner for imaging, whereas SERS and fluorescence images were obtained a posteriori, using the same brain tissue cut with a microtome. As can be clearly observed in **Figure 2.32**, MRI imaging shows dark contrast where the injections were performed and both free IOAuNSs and IOAuNSs-endocytosed MCF7 cells were visible in multiple slices. Subsequently, correlated SERS and fluorescence imaging of brain tissue cuts were analysed and the suitability of these techniques for IOAuNSs detection and mapping in whole tissue samples was demonstrated (**Figure 2.33A, B**). Whereas sample processing was arguably more complicated and laborious due to the numerous cuts to be made and sequential verification of positive signal, both techniques proved suitable for imaging of these multimodal NPs at different spatial resolutions and concentrations.

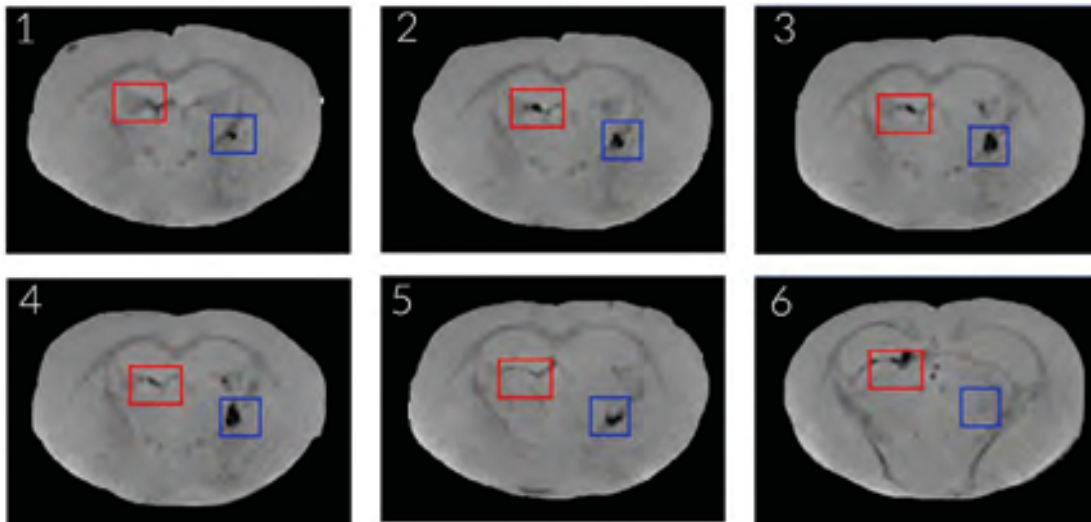


Figure 2.32. MRI of consecutive brain slices after injection of cells incubated with IOAuNSs@2-NAT@DY633 (right hemisphere; shown by blue boxes) and IOAuNSs@2-NAT@DY633 (left hemisphere; shown by red boxes). PBS buffer was injected as control (top part of both left and right hemispheres).

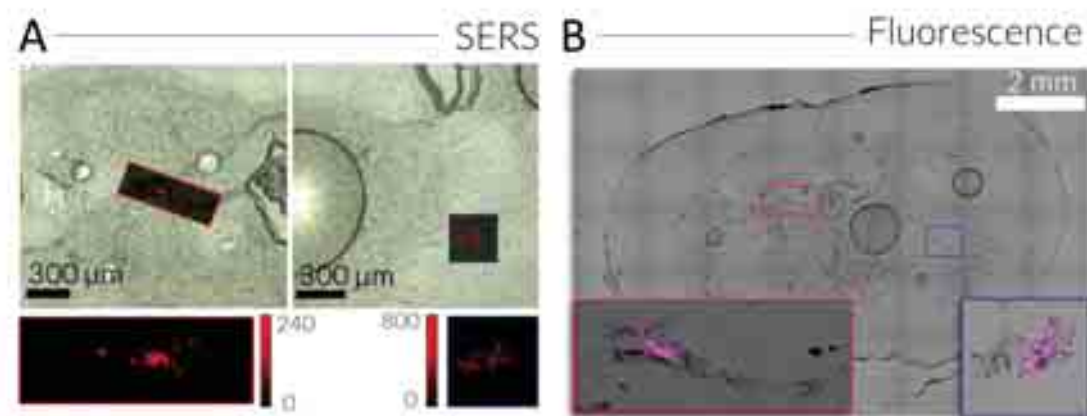


Figure 2.33. Images from a brain slice containing IOAuNSs@2-NAT@DY633 and cells + IOAuNSs@2-NAT@DY633 (A) SERS imaging in which 2-NAT of IOAuNSs@2-NAT@DY633 appears as a red signal. (B) Fluorescence imaging of IOAuNSs@2-NAT@DY633 in which the signal of DY633 appears as a pink signal.

2.7 Conclusions

We have developed a colloidal system comprising hybrid NPs with magnetic and plasmonic components, which can act as contrast agents for multimodal imaging, combining SERS, MRI, and fluorescence imaging. The NPs showed high versatility for imaging biological samples, ranging from 2D cell cultures to *ex vivo* models. We demonstrated that the overall particle size can be tuned by varying two key synthesis parameters, namely the concentration of gold spheres used as the nucleation points upon adsorption on IO cores, and the concentration of added gold precursor for seeded growth of spikes. Through variation of these parameters, we succeeded in fabricating particles with different morphologies and sizes, which therefore displayed different optical properties. Whereas a low density of gold spheres on the surface of IONP cores leads to

smaller final particles with incomplete gold shells and short tips, a higher Au NP density and higher concentration of HAuCl_4 in the seeded-growth reaction resulted in complete shell formation with well-defined spikes. The morphology of IOAuNSs can thus be tuned accordingly and was optimized to obtain NPs with suitable properties for applications in bioimaging. Whereas most published studies calculate the surface area of complex NPs for subsequent functionalization by assuming the volume of a sphere while using stars, we showed here a simple geometry model for realistic estimation of the surface area, which is more accurate toward efficient NP functionalization, while a better description of the surface morphology can be reached in compliment with 3D tomography data. We applied the results of this model to the surface functionalization of IOAuNSs with Raman-active molecules and fluorescent dyes, and then demonstrated their non-cytotoxic nature in MCF7 breast cancer and fibroblast cells. With regards to the multimodal imaging properties of the IOAuNSs, SERS signal enhancement was found to be largely dependent on their absorbance and the density of hotspots (tips), so that the best candidates for SERS were smaller NPs with complete gold shells and well-defined spikes (IOAuNSs sample bII). MRI experiments demonstrated that all particles provided T2 contrast due to the γ - Fe_2O_3 magnetic cores, regardless of the presence of any further SERS or fluorescence functionalization. Furthermore, magnetic characterization of the NPs showed that the gold shell thickness did not affect the magnetic properties of the IO cores. Both these aspects are particularly important for multimodal contrast agents, where the addition of one extra imaging component may hinder the efficacy of another. In summary, iron oxide-gold hybrid nanoparticles with controlled sizes were employed for SERS, MRI and fluorescence imaging within complex biological models. The synthesized IOAuNSs can thus be used as an interesting alternative to conventional contrast agents, achieving valuable information from each imaging technique that could improve the accuracy of the actual diagnostic methods. These findings open up the possibility of expanding the use of multimodal NPs for combination of imaging with other bioapplications such as photothermal therapy and/or magnetic targeting of cells and tissues.

2.8 Experimental Section

2.8.1 Materials

Ferric chloride hexahydrate ($\text{FeCl}_3 \cdot 6\text{H}_2\text{O}$, $\geq 98\%$ Sigma-Aldrich), poly(vinylpyrrolidone) (PVP360; Sigma-Aldrich), sodium acetate anhydrous (ReagentPlus $\geq 99.0\%$ Sigma-Aldrich), ethylene glycol (ReagentPlus, $\geq 99\%$ Sigma-Aldrich), absolute ethanol ($\text{CH}_3\text{CH}_2\text{OH}$, Sigma-Aldrich), hydrogen tetrachloroaurate trihydrate ($\text{HAuCl}_4 \cdot 3\text{H}_2\text{O}$, $\geq 99.9\%$ Sigma-Aldrich), sodium citrate tribasic dihydrate ($\geq 98\%$ Sigma-Aldrich), sodium borohydride (NaBH_4 , ReagentPlus, 99%, Sigma-Aldrich), silver nitrate (AgNO_3 , $\geq 99\%$ Sigma-Aldrich), L-ascorbic acid (AA, $\geq 99\%$ Sigma-Aldrich), hydrochloric acid solution (HCl 37 wt% Panreac), poly (isobutylene-alt-maleic anhydride) (Mw 6.000 Da, Sigma-Aldrich), dodecylamine ($\text{CH}_3(\text{CH}_2)_{11}\text{NH}_2$ $\geq 99.9\%$, Sigma-Aldrich), Tetrahydrofuran (THF, $\text{C}_4\text{H}_8\text{O}$, anhydrous $\geq 99.9\%$, Sigma-Aldrich), naphthalene-2-thiol (2-NAT, 99% Sigma-Aldrich), biphenyl-4-thiol (4-BPT, 97% Sigma-Aldrich), chloroform (CHCl_3 , $\geq 99.8\%$ Sigma-Aldrich), HS-PEG-COOH (Mw 3.000 Dalton, Iris Biotech), DY633 ($\lambda_{\text{ex}} = 637 \text{ nm}$, $\lambda_{\text{em}} = 657$

nm, Dyomics,) and TAMRA (Molecular Probes, Life Technologies, #A1318, $\lambda_{\text{ex}} = 544$ nm, $\lambda_{\text{em}} = 571$ nm, Fisher scientific) were prepared and used without further treatment. Milli-Q water was used for all the experiments.

2.8.2 Nanoparticle synthesis methods

Multicore IONPs Synthesis. For the preparation of multicore IONPs, a previously reported synthetic procedure was followed.²⁶ Briefly, 0.21 mmol of iron chloride hexahydrate was dissolved in 36.3 mL of ethylene glycol under stirring. Then, 516.6 μmol of PVP360 was slowly added to the solution under vigorous stirring and the solution was heated (< 100 °C). When the reactants were completely dissolved, 5.2 mmol of sodium acetate was added to the solution. The mixture was placed in a Teflon autoclave and heated in a drying oven for 4 h at 200 °C. Finally, the solution was cooled down and the particles were washed twice by centrifugation (9000 rpm, 20 min) with ethanol and one additional wash with milli-Q water.

AuNP Synthesis (4nm). For the synthesis of 4 nm Au seeds, a previously reported method was used.²⁷ In brief, 0.6 mL of freshly prepared 0.1 M NaBH_4 solution was quickly added under vigorous stirring to a 20 mL of solution containing 2.5×10^{-4} M HAuCl_4 and 2.5×10^{-4} M sodium citrate. The formation of Au NPs was immediately observed by a color change. The colloidal dispersion was stored at 4 °C and used as seeds within 2-5 h.

AuNP Synthesis (15nm). For the synthesis of 15 nm Au seeds, 95 mL of 0.5 mM HAuCl_4 was mixed under vigorous stirring and heated until boiling and then 5 mL of 34 mM citrate solution was added. After 15 min of boiling, the solution was cooled down and stored at 4 °C.

IOAuNP Synthesis. For the decoration of IONPs with 4 nm AuNPs,²⁸ 5 mL of iron oxide nanoparticles [Fe] = 14 mM (Z-potential: -2 mV) was placed in a 40 mL glass vial and separated using a magnet, followed by removal of the solution and addition of 25 mL of gold nanospheres at the desired concentration (Table 2.3). The mixture was left under sonication for 30 min and stirred in a vortex mixer for 1.5 h. The product was washed several times with the help of a magnet, to ensure complete removal of the gold nanospheres that were not attached to IONPs. The final gold concentration of IOAuNP was analysed by ICP-MS.

Table 2.3. Concentration of AuNPs solution (25 mL) used for the fabrication of the IOAuNPs used as seeds for the tip's growth

| [Au] of AuNPs solution | Seeds for IOAuNSs |
|------------------------|-------------------|
| 0.1 mM | a; I, II, III, IV |
| 0.05 mM | b; I, II, III, IV |
| 0.02 mM | c; I, II, III, IV |

IOAuNS Synthesis. Typically, 10 mL of HAuCl₄ at different concentrations were placed in a 20 mL glass vial. Then, HCl was added and immediately after, a solution containing the IOAuNSs was incorporated as seeds, the concentration of gold being varied as shown in **Table 2.4**. Then, AgNO₃ and ascorbic acid were simultaneously and quickly added to the solution. A fast change from brown to blue indicates gold nanostar formation. Subsequently, HS-PEG-COOH was added to stabilize the final particles. The different amounts and concentrations of the reactants used for the fabrication of IOAuNSs are summarised in **Table 2.4**. The solution was stored at 4 °C until further use. Due to the magnetic nature of the IOAuNSs, for all the reactions a specially designed stirrer made of polylactic acid (PLA) was 3D-printed and connected to a mechanical stirrer to ensure effective mixing of the reactants (**Figure 2.34**).

Table 2.4. Summary of the reactants used for the synthesis of IOAuNSs

| Sample | Total Vol. (mL) | HAuCl ₄ (μL) (0.129 M) | HCl (μL) (1 M) | IOAuNPs (μL) [Au] = 0.30 mM | AgNO ₃ (μL) (3 mM) | Ascorbic acid (μL) (100 mM) | PEG (μL) (1 mM) |
|-------------|-----------------|-----------------------------------|----------------|-----------------------------|-------------------------------|-----------------------------|-----------------|
| aI | 10 | 5 | 2.5 | 25 | 175 | 25 | 30 |
| aII | 10 | 10 | 5.0 | 25 | 350 | 50 | 30 |
| aIII | 10 | 15 | 7.5 | 25 | 525 | 75 | 30 |
| aIV | 10 | 20 | 10 | 25 | 700 | 100 | 30 |

| Sample | Total Vol. (mL) | HAuCl ₄ (μL) (0.129 M) | HCl (μL) (1 M) | IOAuNPs (μL) [Au] = 0.20 mM | AgNO ₃ (μL) (3 mM) | Ascorbic acid (μL) (100 mM) | PEG (μL) (1 mM) |
|-------------|-----------------|-----------------------------------|----------------|-----------------------------|-------------------------------|-----------------------------|-----------------|
| bI | 10 | 5 | 2.5 | 35 | 175 | 25 | 30 |
| bII | 10 | 10 | 5.0 | 35 | 350 | 50 | 30 |
| bIII | 10 | 15 | 7.5 | 35 | 525 | 75 | 30 |
| bIV | 10 | 20 | 10 | 35 | 700 | 100 | 30 |

| Sample | Total Vol. (mL) | HAuCl ₄ (μL) (0.129 M) | HCl (μL) (1 M) | IOAuNPs (μL) [Au] = 0.10 mM | AgNO ₃ (μL) (3 mM) | Ascorbic acid (μL) (100 mM) | PEG (μL) (1 mM) |
|-------------|-----------------|-----------------------------------|----------------|-----------------------------|-------------------------------|-----------------------------|-----------------|
| cI | 10 | 5 | 2.5 | 70 | 175 | 25 | 30 |
| cII | 10 | 10 | 5.0 | 70 | 350 | 50 | 30 |
| cIII | 10 | 15 | 7.5 | 70 | 525 | 75 | 30 |
| cIV | 10 | 20 | 10 | 70 | 700 | 100 | 30 |



Figure 2.34. Polylactic acid (PLA) 3D printed stirrer that worked attached to a mechanical stirrer

PMA synthesis. For the preparation of the PMA a previously published protocol was followed²⁸. Typically, 3.1 g of poly (isobutylene-alt-maleic anhydride) and 2.7 g of dodecylamine were mixed with 100 mL of THF in a 250 round bottom flask. The yellow-pale mixture was then placed in a ultrasonic bath for 30 min and then stirred for 3 h. Afterwards, the mixture total volume was reduced to 40 mL in a rotary evaporator. The solution was then left with reflux overnight. Then, the THF was completely removed in the rotavapor, and the PMA was redissolved in 40 mL of chloroform and was storage in the freezer until use. The final concentration of the PMA is 0.5 M.

2.8.3 Functionalization

Description of geometrical model. We assumed spikes with conical shape (height L ; base radius B), much smaller than the radius of the spherical core R_{core} . We can thus assume the core as a flat surface, with area $A_{core} = 4\pi R_{core}^2 = l_{core}^2$ ($l_{core} = 2R_{core}\sqrt{\pi}$ is the side of a square with the same area as the sphere). The area of the conical spike is $A_{spike} = \pi B(\sqrt{L^2 + B^2})$.

Three different arrangements were considered: first, a square array of n circles with equal radius (Figure 2.11), $n = N^2 = \left(\frac{l_{core}}{2B}\right)^2 = \pi \left(\frac{R_{core}}{B}\right)^2$. The total surface area is the sum of the cones (spikes) plus the total free area, given by:

$$A_{TNS} = N \left[\pi B \sqrt{L^2 + B^2} + l_{squa}^2 - \pi B^2 \right]$$

A second case comprises a hexagonal arrangement of identical conical spikes on a planar area, covering an area φ of ca. 0.9069. The area occupied by the circular bases of the spikes is

$4\pi R_{core}^2 \varphi = n\pi B^2$, so that: $n = \frac{4\pi\varphi R_{core}^2}{\pi B^2} = 4\varphi \left(\frac{R_{core}}{B}\right)^2$. Hence, the total area of an IOAuNSs with a hexagonal surface arrangement of conical spikes is:

$$A_{TNS} = 4\pi R_{core}^2(1 - \varphi) + n \left[\pi B(\sqrt{L^2 + B^2}) \right]$$

The third model involves a hexagonal arrangement of conical spikes with a random distribution of lengths fitting the experimental data for IOAuNSs surface (from electron tomography). The number and area of the spikes, as well as the total IOAuNSs surface area, was estimated from all three models, the random model being the most realistic one.

SERS encoding of IOAuNSs. The probes were encoded using different Raman-active molecules, following an established protocol based on successive phase transfer.¹⁰ Briefly, 5 mL of IOAuNPs (total concentration of metals [Au + Fe] = 1.5 mM) was placed in a test tube. 2 mL of 4-BPT 10 mM in chloroform and 16 μ L of HCl were added and the mixture was stirred for 2 h to enable phase transfer. Finally, the particles located in the organic phase (bottom phase) were recovered and washed twice with chloroform by centrifugation (9000 rpm, 5 min).

PMA functionalization of IOAuNSs. The dispersion of IOAuNSs@4-BPT or IOAuNSs@2-NAT was placed in a round-bottom flask and 100 μ L 0.05M of dodecylamine-modified polyisobutylene-alt-maleic anhydride amphiphilic polymer (PMA) was added and stirred. The solvent was evaporated in a rotary evaporator and the particles redispersed in 5 mL of water and 1 mL of NaOH pH = 12. The particles were washed three-fold by centrifugation (9000 rpm, 5 min) or until neutralization. The PMA used to wrap the Raman-encoded IOAuNSs was prepared following previous reports.^{10,29} PMA comprises polyisobutylene-alt-maleic anhydride (hydrophilic backbone) on which 75% of the anhydride rings have been reacted with dodecylamine (hydrophobic chain).

PMA functionalization with fluorescent dyes. Labelling of NPs with fluorophores was performed on PMA functionalized with TAMRA dye and DY633 dye. The procedure was conducted as previously reported.³⁰ The excitation and emission spectra of the particles coated with the dye- modified polymer are shown in **Figure 2.16**.

2.8.4 Characterization

Standard characterization. All NPs were characterized using TEM, ICP-MS, and UV-Vis-NIR. UV-vis-NIR extinction spectra were recorded using an Agilent 8453 UV-Vis diode array spectrophotometer, normalizing spectra at 400 nm. ICP-MS analysis was conducted using an ICP-MS Agilent 7500 ce to determine the concentration of Au and Fe. Samples containing biological material (cells or spheroids) were digested in *aqua regia* during 48 h, followed by addition of H₂O₂ and continued heating until a clear and transparent solution was observed. The samples were cooled down to RT and subsequently measured. TEM images were collected with a JEOL JEM-1400PLUS transmission electron microscope operating at 120 kV, using carbon-coated 400 square mesh Cu grids.

Z-Sizer measurements. A Malvern Zetasizer 3000 HS particle size analyser (Malvern Instruments, UK) was used to measure zeta-potential and dynamic light scattering (DLS), from which hydrodynamic diameter distributions were obtained. Samples were placed in disposable cuvettes of 1 cm optical path length using a diluted (1:100) NP solution, using distilled water as solvent. The width of the DLS hydrodynamic diameter distribution is characterized by the polydispersity index (Pdl). In the case of a monomodal distribution (Gaussian) calculated by means of cumulant analysis, $Pdl = (\sigma/Z_{avg})^2$, where σ is the width of the distribution and Z_{avg} the average diameter of the particle's population, respectively.

Electron Tomography. IOAuNSs were diluted in H₂O to a final concentration of 0.05 mM, and drop-cast on a carbon-coated 400 square mesh Cu grid. The samples were then left to dry at ambient temperature. TEM images were acquired using an aberration-corrected 'cubed' Thermo Fisher Scientific-Titan electron microscope operated at an acceleration voltage of 300 kV, with a camera length of 58 - 105 mm. STEM HAADF images were acquired using a convergence angle of 20 mrad. Tomography tilt series were acquired using a Fischione 2020 tomography holder over $\pm 76^\circ$ with tilt increments of 2° . Typically, each angle consisted of a 1k x 1k STEM HAADF image using 12 ms dwell time. The images acquired manually at each angle were aligned with respect to each other and the tomograms rotation axis was determined with mathematical precision through phase correlation. Finally, the 3D reconstruction was achieved using 25 SIRT cycles. A bandwidth limit was also applied to the SIRT reconstruction in real and Fourier space to achieve a high-quality reconstruction with minimized missing wedge artefacts.

EDX Analysis. Energy dispersive X-ray (EDX) measurements were acquired every 10° with an acquisition time of 10 minutes per angle and 150 pA screen current using a SuperX detector. The resulting data was reconstructed using an Expectation Maximisation (EM) reconstruction algorithm using a STEM HAADF signal for accurate alignment.

STEM EELS Imaging. Fe oxidation state was determined by electron energy loss spectroscopy (EELS) using an aberration-corrected 'cubed' FEI-Titan electron microscope operated at an acceleration voltage of 200 kV. Lower acceleration voltages were tried, however this led to significant cupping artefacts. The energy resolution provided by the electron monochromator, as measured from the full-width at half maximum of acquired zero-loss peaks was 0.2 eV, the dispersion of the spectrometer was set to 0.01 eV/ch and 2000 channels are used to cover an energy range from 704 eV to 724 eV, being the entire Fe L_{2,3} edge. The pixel size equals 1.8 nm (65x65 pixels) for higher magnification single-particle EELS mapping, which is sufficient to distinguish any variation in oxidation state throughout the nanoflower's sub-structure. Lower magnification EELS maps with a pixel size of 20 nm² was used to determine oxidation state variation within different nanoflowers from both samples.

Surface Area Measurement. To extract the accessible and external Au surface area relevant for further functionalization, Fe and Au phases were identified by a manual segmentation process using Amira software. As the Au surface contained voids and areas of exposed Fe₂O₃ core, the total Fe surface could not be directly subtracted from the total surface (internal and external Au

surface) of Au. Rather, the Fe surface in contact with Au must be calculated first, so that accurate accessible Au surface areas could be derived. Using a surface generation module, boundary surfaces can be extracted and later removed for a final Au surface area.

SERS. Characterization of the SERS signal of IOAuNSs@4-BPT and IOAuNSs@2-NAT was performed with a Raman microscope (inVia Reflex, Renishaw, Wotton-under-Edge, U.K.) equipped with a $-60\text{ }^{\circ}\text{C}$ Peltier-cooled front-illuminated CCD detector ($1024 \times 512\text{ pixel}^2$ chip), using a 785 nm laser excitation source (maximum output 270 mW) and a 1200 lines/mm diffraction grating. For the experiments 300 μL of each aqueous solutions was placed in a glass vial. SERS spectra were collected using a 10 \times objective (NA = 0.25; Leica Microsystems, Wetzlar, Germany) in expanded scan mode, with an integration time of 10 s and at a laser power of 52.5 mW. All the spectra were analysed using the WiRE4.4 software (Renishaw, Wotton-under Edge, U.K.) to eliminate cosmic rays and the correction of the baseline in the spectra was performed on Matlab, using the Beads function.

Magnetism. ZFC/FC measurements were performed at 100 Oe and within a temperature range of 5-300 K, using a Quantum Design MPMS3 VSM-SQUID magnetometer with a sensitivity of 10^{-8} emu up to a maximum field of 7 T. The hysteresis loops were measured in a Vibrating Sample Magnetometer (VSM) with a sensitivity of $5 \cdot 10^{-6}$ emu, up to a maximum field of 18 kOe working at room temperature.

2.8.5 Cell culture

MCF7 cells were purchased from the ATCC. Human Dermal Fibroblasts (HDF), fetal bovine serum (FBS), penicillin-streptomycin (PS), DMEM, lactate dehydrogenase (LDH) assay, and NucBlue were purchased from Invitrogen. Propidium iodide (PI) was purchased from Sigma. MCF7 and HDF cells were grown in DMEM supplemented with 10% FBS and 1% PS (herein termed complete DMEM, cDMEM).

IOAuNSs cytotoxicity tests. The cytotoxicity of IOAuNSs in MCF7 cells was evaluated using the LDH assay and PI staining. Cells were seeded at 1.6×10^5 cells/cm² in 96-well plates to analyse the cytotoxicity by LDH assay, and at 9×10^4 cells/cm² in 96-well imaging plates (Ibidi) for characterization by microscopy. The following day, IOAuNSs were added at concentrations ranging from 0.25 mM to 0.031 mM (total metal ion concentration). After 24 h, the NP solution was removed and rinsed with media. The media was renewed again 6 h later to remove IOAuNSs in suspension and on the bottom of the plate. The presence of aggregated NPs was monitored daily by optical microscopy. The LDH test was performed using the standard protocol 48 h post addition of IOAuNSs. For analysis via imaging, PI was added to a final concentration of 500 nM, and nuclei stained using NucBlue. Images of $1 \times 1.3\text{ mm}^2$ were acquired with a Cell Observer microscope (Axio Observer, Zeiss) 48 h after the addition of IOAuNSs. Post-processing and quantification of cells were conducted with ImageJ, and data represented as a percentage of dead cells.

Spheroids formation. Spheroids were formed from cells, with and without pre-incubation steps with IOAuNSs. In the case of spheroids which were exposed to IOAuNSs post formation, MCF7 and HDF cells were mixed in a 1:1 ratio using a final cell number of 1.7×10^4 cells/spheroid (μ -shaped plate growth method) and left for 3 days to form the spheroid. A 25 μ L dispersion of IOAuNSs (1:1 mix of IOAuNSs@4-BPT@TAMRA and IOAuNSs@2-NAT@DY633, final ion concentration 0.05 mM) in cDMEM was made in a 500 μ L Eppendorf and ca. 5 spheroids added. Using a rotisserie rotator placed in an incubator at 37 °C, 5% CO₂, spheroids were rotated during 24 h to help achieve an even distribution of IOAuNSs around spheroids. Spheroids were subsequently retrieved and used for imaging studies or fixed using 4% formaldehyde for later imaging and embedding in OCT freezing media.

For spheroids exposed to IOAuNSs pre-formation, MCF7 and HDF cells were seeded in 12-well plates (8×10^4 MCF and 6×10^4 HDF cells/mL) and once adhered, IOAuNSs@4-BPT@TAMRA and IOAuNSs@2-NAT@DY633 were added to MCF7 and HDF cells, respectively, at a final concentration of 0.05 mM. After 24h, non-endocytosed IOAuNSs were removed via washing, and cells detached using trypsin-EDTA. Cells were readjusted to 8.6×10^4 cells/mL and mixed in a 1:1 ratio. Cells (1.7×10^4 cells, 200 μ L) were added to μ -shaped 96-well plates and incubated at 37 °C, 5% CO₂ for 3 days for spheroid formation to occur. Spheroids were subsequently retrieved and used for imaging studies or fixed using 4% formaldehyde for later imaging and embedding in OCT freezing media.

2.8.6 Multimodal imaging

Cell preparation. 2D SERS mapping was conducted using MCF7 cells preincubated with IOAuNSs from series a, b and c. In brief, MCF7 cells were seeded at 2.8×10^4 cells/cm² in 12-well plates and allowed to adhere. The following day, IOAuNSs diluted in cDMEM were added (0.05 mM final total ion concentration) and after 24 h, non-endocytosed IOAuNSs were removed, and cells detached using trypsin-EDTA. For SERS imaging, cells were seeded in 35 mm glass-bottomed dishes (5×10^4 cells/dish) and after 2-3 h of incubation, SERS mapping undertaken using the settings described below. For MRI, a volume containing 2×10^5 cells was centrifuged and resuspended to 400 μ L of PBS. Subsequently, 100 μ L (containing 5×10^4 cells) was dispersed into each well of the phantom for MRI imaging. For ICP measurements, a volume of cell solution containing 5×10^4 cells was centrifuged, concentrated in 50 μ L PBS, and frozen at -20 °C. To promote cell lysis, three freeze-thaw cycles were performed. The samples were subsequently digested using aqua regia, aided by microwave digestion (**Table 2.5**). For fluorescence confocal imaging, 1.3×10^4 cells (1:1 mix of HDF and MCF7 cells previously exposed to IOAuNSs@4-BPT@TAMRA and IOAuNSs@2-NAT@DY633, respectively) were seeded in 35 mm glass-bottomed dishes with a 500 μ m etched grid (Ibidi) and allowed to adhere. The following day the media was removed, and samples fixed and permeabilized using 4% formaldehyde and TritonX-100. Immunostaining to identify MCF7 and HDF cells was carried out using antibodies against E-cadherin and TE7 (both Novusbio), respectively. Appropriate matching secondary antibodies with

AlexaFluor 405 and 633 fluorescent labels were used at a 1/400 dilution. Samples were stored in PBS at 4 °C until imaged.

Table 2.5. Concentrations used for the preparations of phantoms for MRI, measured by ICP-MS.

| IOAuNSs | IOAuNSs [Au] μM | Cells + IOAuNSs [Au] μM |
|---------|----------------------------|------------------------------------|
| aI | 47 | 9 |
| aII | 48 | 8 |
| aIII | 35 | 40 |
| aIV | 33 | 10 |
| bI | 28 | 26 |
| bII | 49 | 32 |
| bIII | 36 | 38 |
| bIV | 35 | 17 |
| cI | 29 | 36 |
| cII | 38 | 31 |
| cIII | 23 | 7 |
| cIV | 25 | 7 |

SERS imaging of cells. SERS measurements were performed with a Raman microscope (inVia Reflex, Renishaw, Wotton-under-Edge, U.K.) equipped with a -60 °C Peltier-cooled front-illuminated CCD detector ($1024 \times 512 \text{ pixel}^2$), using a 785 nm laser excitation source (maximum output 270 mW) and a 1200 lines/mm diffraction grating. SERS maps were recorded in static mode (centered of scattered wavenumber 1450 cm^{-1}) using a 40 \times dip-in water immersion objective (numerical aperture, NA = 0.8; Nikon Corporation, Tokyo, Japan). For single cell measurements, areas of ca. $30 \times 30 \text{ }\mu\text{m}^2$ containing one single cell, were imaged with 0.5 s integration time, at 12.08 mW laser power at the surface and a step size of 2 μm . All the spectra were first analysed using the WiRE 4.4 software (Renishaw, Wotton-under Edge, U.K.) to correct the baseline in the spectra (intelligent 11th polynomial order) and eliminate cosmic rays. Then, the maps were analysed with a MLRA-based supervised algorithm developed in a previous work²⁹, to represent in the cellular images only the spectra similar to the SERS signal of the corresponding nanoparticles.

SERS imaging of spheroids. SERS mapping of spheroids involved placing individual spheroids inside a home-made holder,³¹ on top of a small drop of dental glue to fix the spheroid position.

SERS mapping along xz was performed in a Renishaw Raman microscope (inVia Reflex, Renishaw, Wotton-under-Edge, U.K.). An area of $800 \times 430 \text{ }\mu\text{m}^2$ was imaged with 0.7 s integration time, 12.08 mW laser power at the surface and a step size of 6 μm and 10 μm in x and z directions, respectively.

Additional SERS measurements of the spheroids were performed with a WITec confocal Raman microscope (Alpha300R, WITec GmbH, Ulm, Germany) equipped with a -60 °C Peltier-cooled

CCD detector (1024×128 pixel² chip), using a 785 nm laser excitation source (maximum output 83 mW) and a 300 lines/mm diffraction grating. The center of scattered wavenumber was set to 1450 cm^{-1} , and the signal was recorded using a N-achroplan 20× dip-in water immersion objective (NA = 0.5; Zeiss, Jena, Germany). For the measurement of the outer edge of a live spheroid, a volume of $84 \times 84 \times 70\text{ }\mu\text{m}^3$ was imaged with a 5 mW laser power, 0.01 s integration time, and step size of 2 μm in xy and 5 μm in z directions. For the transversal cut, an area of $360 \times 560\text{ }\mu\text{m}^2$ was imaged with a 10 mW laser power, 0.1 s integration time, and step size of 5 μm . For post-incubated spheroids a volume of $400 \times 380 \times 150\text{ }\mu\text{m}^3$ containing a quarter of the spheroid, was imaged with a 10 mW laser power, 0.1 s integration time, and step size of 5 μm in xy and 10 μm in z . For the measurement of the spheroid slice, an area of $635 \times 875\text{ }\mu\text{m}^2$ was imaged with a 10 mW laser power, 0.1 s integration time, and step size of 5 μm . Prior to data analysis, SERS spectra were pre-treated by cosmic ray removal and background subtraction (Shape 100), both implemented in the Project FIVE plus software (WITec, Um, Germany). To identify the known Raman reporter spectrum, the TrueComponent tool, also embedded in the same software package, was applied.

Ex-vivo sample preparation. A mouse brain was extracted from a cadaveric specimen provided by our animal facility (no animals were expressly used for this study) and casted in a falcon tube with 15 mL of agarose solution (1.6% w/v). Then, 5 μL of IOAuNSs@2-NAT@DY633, cells incubated with IOAuNSs@2-NAT@DY633 and PBS were injected in the tissue with the help of a stereotaxic frame and a Hamilton syringe. After MRI imaging studies, the brain was extracted from the agarose, and then it was immersed in formalin 10% overnight and posteriorly in sucrose (30%) in PBS solution for two days, for fixation and cryopreservation of the tissue. Finally, the brain was frozen and kept at -80°C until posterior use.

SERS imaging of brain slices. SERS imaging of brain histology slices was carried out on top of a quartz slide. SERS measurements were performed with a confocal Raman microscope (Alpha300R, WITec GmbH, Ulm, Germany) equipped with a $-60\text{ }^\circ\text{C}$ Peltier-cooled CCD detector (1024×128 pixel² chip), using a 785 nm laser excitation source (maximum output 83 mW) and a 300 lines/mm diffraction grating. The center of scattered wavenumber was set to 1450 cm^{-1} , and the signal was recorded using a 20× objective (NA = 0.4; Nikon Corporation, Tokyo, Japan). For SERS measurements of brain samples, two areas of $680 \times 250\text{ }\mu\text{m}^2$ and $350 \times 350\text{ }\mu\text{m}^2$ were imaged with a 5 mW laser power, 0.05 s integration time, and step size of 3 μm . Prior to data analysis, SERS spectra were pre-treated by cosmic ray removal and background subtraction (Shape 100), both implemented in the Project FIVE plus software (WITec, Um, Germany). To identify the known Raman reporter spectrum, the TrueComponent tool, also embedded in the same software package, was applied.

Confocal fluorescence microscopy. Fluorescence images of biological samples were obtained with a Zeiss 880 confocal microscope. To image whole spheroids, the sample was immobilized in a 0.5 cm silicon well printed on a coverslip (total volume ca. 50 μL), with a 1 cm circular glass cover slip placed on top to avoid evaporation. TAMRA- and DY633-containing IOAuNSs were

imaged using 561 and 633 nm laser sources, with detectors set to ca. 595 ± 25 nm and 680 ± 25 nm, respectively. A Plan-apochromat x10 objective (NA = 0.45, Zeiss) was used to obtain z-stacks of ca. 200 μ m. A 3-pixel mean filter was applied prior to obtaining Maximum Intensity Projections (MIP). 2D images of co-cultured HDF and MCF7 cells, pre-incubated with IOAuNSs@4-BPT@TAMRA and IOAuNSs@2-NAT@DY633, respectively, were also obtained using a Plan-apochromat x20 objective (NA = 0.8, Zeiss) and 405, 488, 561, and 633 laser excitation sources. For brain imaging, slices were cut using a cryotome and collected on quartz slides. A Plan-apochromat x10 objective (NA = 0.45, Zeiss) was used with 633 nm excitation. The tile-feature of the ZEN software was used to produce an overview of the whole brain slice.

MRI Phantom imaging. Agar was solved in hot water (15 mL, 1.6% w/v), placed in a plastic mold and left to solidify at room temperature. Once hardened, 32 wells of 2 mm of diameter were drilled in the gel. To have a perfectly flat bottom in each well, 20 μ L of 0.4% agar solution was pipetted into the base of each well and left to solidify. Then, 50 μ L of the desired sample was deposited in each well and completely covered with 0.9% agar solution. A scheme of the phantoms containing the distribution of the holes and the concentrations of the samples is shown for cells in **Figure 2.35A** and for spheroids in **Figure 2.35B**.

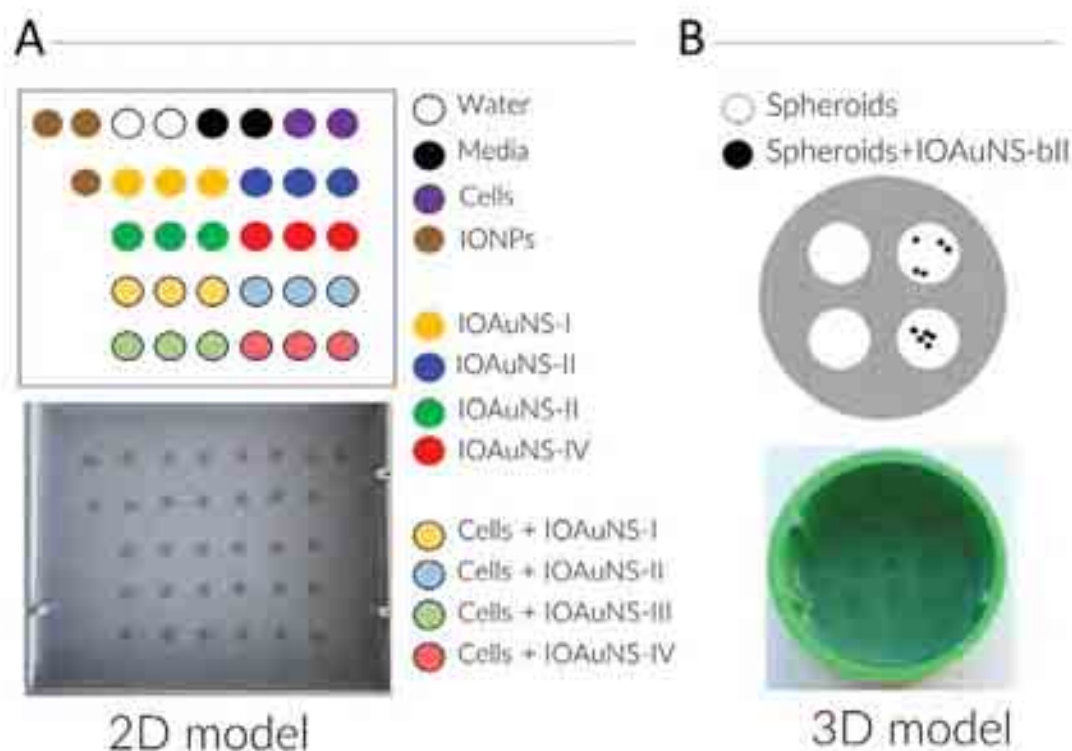


Figure 2.35. Scheme of the phantom model and distribution of samples and controls used in the phantom model for MRI measurements on 2D **(A)** and 3D **(B)** cell models.

MRI imaging of brain slices. The brain images were performed in a 11.7 T horizontal bore Bruker Biospec 117/16 USR scanner (Bruker Biospin, Ettlingen, Germany).

Biological TEM Cells and spheroids were prepared for TEM imaging by first fixing the sample with 2% formaldehyde / 2.5% glutaraldehyde in Sorensen's buffer, followed by OsO₄ fixation/staining and dehydration in an ethanol series. Finally, samples were embedded in Spurr's resin, followed by cutting 100 nm thick slices using an ultramicrotome.

References

- (1) Louie, A. Multimodality Imaging Probes: Design and Challenges. *Chem. Rev.* **2010**, *110*(5), 3146–3195. <https://doi.org/10.1021/cr9003538>.
- (2) Zhu, J.; Lu, Y.; Li, Y.; Jiang, J.; Cheng, L.; Liu, Z.; Guo, L.; Pan, Y.; Gu, H. Synthesis of Au-Fe₃O₄ Heterostructured Nanoparticles for in Vivo Computed Tomography and Magnetic Resonance Dual Model Imaging. *Nanoscale* **2014**, *6* (1), 199–202. <https://doi.org/10.1039/c3nr04730j>.
- (3) Zhao, H. Y.; Liu, S.; He, J.; Pan, C. C.; Li, H.; Zhou, Z. Y.; Ding, Y.; Huo, D.; Hu, Y. Synthesis and Application of Strawberry-like Fe₃O₄-Au Nanoparticles as CT-MR Dual-Modality Contrast Agents in Accurate Detection of the Progressive Liver Disease. *Biomaterials* **2015**, *57*, 194–207. <https://doi.org/10.1016/j.biomaterials.2015.02.019>.
- (4) Miyasato, D. L.; Mohamed, A. W.; Zavaleta, C. A Path toward the Clinical Translation of Nano-Based Imaging Contrast Agents. *Wiley Interdiscip. Rev. Nanomedicine Nanobiotechnology* **2021**, *13*(6), e1721. <https://doi.org/10.1002/wnan.1721>.
- (5) Han, Y.; Lei, S. L.; Lu, J. H.; He, Y.; Chen, Z. W.; Ren, L.; Zhou, X. Potential Use of SERS-Assisted Theranostic Strategy Based on Fe₃O₄/Au Cluster/Shell Nanocomposites for Bio-Detection, MRI, and Magnetic Hyperthermia. *Mater. Sci. Eng. C* **2016**, *64*, 199–207. <https://doi.org/10.1016/j.msec.2016.03.090>.
- (6) Lasserus, M.; Knez, D.; Schnedlitz, M.; Hauser, A. W.; Hofer, F.; Ernst, W. E. On the Passivation of Iron Particles at the Nanoscale. *Nanoscale Adv.* **2019**, *1* (6), 2276–2283. <https://doi.org/10.1039/c9na00161a>.
- (7) Zou, F.; Ding, Q.; Tran, V. T.; Wang, G.; Zhang, Y.; Kang, S.; Lee, J.; Zhou, H. Magnetically Recyclable Catalytic Activity of Spiky Magneto-Plasmonic Nanoparticles. *RSC Adv.* **2015**, *5* (70), 56653–56657. <https://doi.org/10.1039/c5ra08425c>.
- (8) Gavilán, H.; Sánchez, E. H.; Brollo, M. E. F.; Asín, L.; Moerner, K. K.; Frandsen, C.; Lázaro, F. J.; Serna, C. J.; Veintemillas-Verdaguer, S.; Morales, M. P.; Gutiérrez, L. Formation Mechanism of Maghemite Nanoflowers Synthesized by a Polyol-Mediated Process. *ACS Omega* **2017**, *2*(10), 7172–7184. <https://doi.org/10.1021/acsomega.7b00975>.
- (9) Shafi, K. V. P. M.; Ulman, A.; Dyal, A.; Yan, X.; Yang, N. L.; Estournès, C.; Fournès, L.; Wattiaux, A.; White, H.; Rafailovich, M. Magnetic Enhancement of γ -Fe₂O₃ Nanoparticles by Sonochemical Coating. *Chem. Mater.* **2002**, *14* (4), 1778–1787. <https://doi.org/10.1021/cm011535+>.
- (10) Kucheryavy, P.; He, J.; John, V. T.; Maharjan, P.; Spinu, L.; Goloverda, G. Z.; Kolesnichenko, V. L. Superparamagnetic Iron Oxide Nanoparticles with Variable Size and an Iron Oxidation State as Prospective Imaging Agents. *Langmuir* **2013**, *29* (2), 710–716. <https://doi.org/10.1021/la3037007>.
- (11) Yadav, B. Sen; Singh, R.; Vishwakarma, A. K.; Kumar, N. Facile Synthesis of Substantially

Magnetic Hollow Nanospheres of Maghemite ($\gamma\text{-Fe}_2\text{O}_3$) Originated from Magnetite (Fe_3O_4) via Solvothermal Method. *J. Supercond. Nov. Magn.* **2020**, *33* (7), 2199–2208. <https://doi.org/10.1007/s10948-020-05481-7>.

- (12) Jana, N. R.; Gearheart, L.; Murphy, C. J. Seeding Growth for Size Control of 5–40 Nm Diameter Gold Nanoparticles. *Langmuir* **2001**, *17* (22), 6782–6786. <https://doi.org/10.1021/la0104323>.
- (13) Turkevich, J. Colloidal Gold. Part I - Historical and Preparative Aspects, Morphology and Structure. *Gold Bull.* **1985**, *18* (3), 86–91. <https://doi.org/10.1007/BF03214690>.
- (14) Hanske, C.; González-Rubio, G.; Hamon, C.; Formentín, P.; Modin, E.; Chuvilin, A.; Guerrero-Martínez, A.; Marsal, L. F.; Liz-Marzán, L. M. Large-Scale Plasmonic Pyramidal Supercrystals via Templated Self-Assembly of Monodisperse Gold Nanospheres. *J. Phys. Chem. C* **2017**, *121* (20), 10899–10906. <https://doi.org/10.1021/acs.jpcc.6b12161>.
- (15) Jimenez de Aberasturi, D.; Henriksen-Lacey, M.; Litti, L.; Langer, J.; Liz-Marzán, L. M. Using SERS Tags to Image the Three-Dimensional Structure of Complex Cell Models. *Adv. Funct. Mater.* **2020**, *30* (14), 1909655. <https://doi.org/10.1002/adfm.201909655>.
- (16) Jimenez de Aberasturi, D.; Serrano-Montes, A. B.; Langer, J.; Henriksen-Lacey, M.; Parak, W. J.; Liz-Marzán, L. M. Surface Enhanced Raman Scattering Encoded Gold Nanostars for Multiplexed Cell Discrimination. *Chem. Mater.* **2016**, *28* (18), 6779–6790. <https://doi.org/10.1021/acs.chemmater.6b03349>.
- (17) Lenzi, E.; Jimenez de Aberasturi, D. Surface-Enhanced Raman Scattering Tags for Three-Dimensional Bioimaging and Biomarker Detection. *ACS sensors* **2019**, *4* (5), 1126–1137. <https://doi.org/10.1021/acssensors.9b00321>.
- (18) El-Khoury, P. Z.; Hu, D.; Apkarian, V. A.; Hess, W. P. Raman Scattering at Plasmonic Junctions Shorted by Conductive Molecular Bridges. *Nano Lett.* **2013**, *13* (4), 1858–1861. <https://doi.org/10.1021/nl400733r>.
- (19) Kalbacova, J.; Rodriguez, R. D.; Desale, V.; Schneider, M.; Amin, I.; Jordan, R.; Zahn, D. R. T. Chemical Stability of Plasmon-Active Silver Tips for Tip-Enhanced Raman Spectroscopy. *Nanospectroscopy* **2015**, *1* (1), 12–18. <https://doi.org/10.2478/nansp-2014-0002>.
- (20) Alvarez-Puebla, R. A.; Dos Santos, D. S.; Aroca, R. F. Surface-Enhanced Raman Scattering for Ultrasensitive Chemical Analysis of 1 and 2-Naphthalenethiols. *Analyst* **2004**, *129* (12), 1251–1256. <https://doi.org/10.1039/b410488a>.
- (21) Serrano-Montes, A. B.; De Aberasturi, D. J.; Langer, J.; Giner-Casares, J. J.; Scarabelli, L.; Herrero, A.; Liz-Marzán, L. M. A General Method for Solvent Exchange of Plasmonic Nanoparticles and Self-Assembly into SERS-Active Monolayers. *Langmuir* **2015**, *31* (33), 9205–9213. <https://doi.org/10.1021/acs.langmuir.5b01838>.
- (22) Reguera, J.; Langer, J.; Jimenez de Aberasturi, D.; Liz-Marzán, L. M. Anisotropic Metal Nanoparticles for Surface Enhanced Raman Scattering. *Chem. Soc. Rev.* **2017**, *46* (13),

3866–3885. <https://doi.org/10.1039/c7cs00158d>.

- (23) Rodríguez-Lorenzo, L.; Álvarez-Puebla, R. A.; Pastoriza-Santos, I.; Mazzucco, S.; Stéphan, O.; Kociak, M.; Liz-Marzán, L. M.; De Abajo, F. J. G. Zeptomol Detection through Controlled Ultrasensitive Surface-Enhanced Raman Scattering. *J. Am. Chem. Soc.* **2009**, *131* (13), 4616–4618. <https://doi.org/10.1021/ja809418t>.
- (24) Lee, N.; Hyeon, T. Designed Synthesis of Uniformly Sized Iron Oxide Nanoparticles for Efficient Magnetic Resonance Imaging Contrast Agents. *Chem. Soc. Rev.* **2012**, *41* (7), 2575–2589. <https://doi.org/10.1039/c1cs15248c>.
- (25) Costa, E. C.; Moreira, A. F.; de Melo-Diogo, D.; Gaspar, V. M.; Carvalho, M. P.; Correia, I. J. 3D Tumor Spheroids: An Overview on the Tools and Techniques Used for Their Analysis. *Biotechnol. Adv.* **2016**, *34* (8), 1427–1441. <https://doi.org/10.1016/j.biotechadv.2016.11.002>.
- (26) Pulagam, K. R.; Henriksen-Lacey, M.; B. Uribe, K.; Renero-Lecuna, C.; Kumar, J.; Charalampopoulou, A.; Facchetti, A.; Protti, N.; Gómez-Vallejo, V.; Baz, Z.; Kumar, V.; Sánchez-Iglesias, A.; Altieri, S.; Cossío, U.; Di Silvio, D.; Martínez-Villacorta, A. M.; Ruiz De Angulo, A.; Rejc, L.; Liz-Marzán, L. M.; Llop, J. In Vivo Evaluation of Multifunctional Gold Nanorods for Boron Neutron Capture and Photothermal Therapies. *ACS Appl. Mater. Interfaces* **2021**, *13* (42), 49589–49601. <https://doi.org/10.1021/acscami.0c17575>.
- (27) Olsen, C. J.; Moreira, J.; Lukanidin, E. M.; Ambartsumian, N. S. Human Mammary Fibroblasts Stimulate Invasion of Breast Cancer Cells in a Three-Dimensional Culture and Increase Stroma Development in Mouse Xenografts. *BMC Cancer* **2010**, *10*, 444. <https://doi.org/10.1186/1471-2407-10-444>.
- (28) Teresa pellegrino Manna Liberato Stefan Kudera; Tim Liedl; Dmitry Koktysh; Andrey L. Rogach; Simon Keller; Joachim Radler; Giovanni Natile; Wolfgang J. Hydrophobic Nanocrystals Coated with an Amphiphilic Polymer Shell: A General Route to Water Soluble Nanocrystals. *Nano Lett.* **2004**, *4* (4), 703–707.
- (29) Lenzi, E.; Henriksen-lacey, M.; Molina, B.; Langer, J.; Albuquerque, C. D. L. De; Aberasturi, D. J. De; Liz-marz, L. M. Combination of Live Cell Surface-Enhanced Raman Scattering Imaging with Chemometrics to Study Intracellular Nanoparticle Dynamics. *ACS sensors* **2022**. <https://doi.org/10.1021/acssensors.2c00610>.

Chapter III



3. Synthesis of hybrid nanostars for hyperthermia

Contents

| | |
|--|-----|
| 3.1 Introduction..... | 120 |
| 3.2 Optimization of hybrid nanoparticles for hyperthermia..... | 121 |
| 3.2.1 Iron oxide nanoparticles: <i>Influence of water on particle size</i> | 121 |
| 3.2.2 Decoration of iron oxide nanoparticles with gold nanoparticles | 123 |
| 3.2.3 Synthesis of hybrid iron oxide-gold nanostars | 124 |
| 3.3 Photothermal characterization | 126 |
| 3.4 Hyperthermia in 2D cell cultures | 134 |
| 3.5 Hyperthermia in 3D cell spheroids | 135 |
| 3.6 Conclusions | 136 |
| 3.7 Experimental Section | 137 |
| 3.7.1 Materials | 137 |
| 3.7.2 Nanoparticle synthesis..... | 138 |
| 3.7.3 Nanoparticles characterization | 139 |
| 3.7.4 Photothermal heating experiments | 140 |
| References | 142 |

3.1 Introduction

We have described in Chapter II the synthesis of hybrid magnetic-plasmonic nanoparticles – consisting of a multicore iron oxide core covered by a plasmonic spiky gold shell – for their use in multimodal bioimaging applications. We have shown that the dimensions and branching degree of the tips can be varied through the density of AuNP seeds and the amount of gold precursor used for tip growth.

In the present Chapter III, we have used the same protocol for the synthesis of hybrid NPs, but further optimization was implemented to pay special attention to their potential use as sensitizers for photothermal therapy (PTT). PTT has emerged as an efficient therapeutic tool that allows localized cancer treatment by means of a controlled and targeted heating of malignant cells¹. It is based on the capacity of NPs to convert light energy into heat, thereby inducing a local increase of temperature. The photothermal effect induced upon laser irradiation is an interesting method to produce local and rapid temperature increments in a controlled manner². The ultimate goal is the generation of a local increase of temperature above 42° C, which would result in the selective destruction of cancer cells while avoiding damage to healthy tissue³.

Noble metal nanoparticles, which present unique optical properties such as strong LSPR absorption in the NIR, can be used as photosensitisers⁴. In particular, AuNPs have shown their potential as promising heating agents because they are highly efficient at light to heat conversion. By irradiating AuNPs with a laser, which emits a coherent and focused beam of photons at a specific wavelength, a rapid non-equilibrium heating process takes place which starts with an excitation of free electrons on the metallic NPs⁵. Electrons subsequently jump into an excited energy state, followed by a relaxation process comprising electron-electron scattering, which ultimately leads to an increase of temperature on the surface. One of the processes used to stabilize and decrease the temperature back to equilibrium consists of phonon-phonon interactions with the surrounding medium. Such phonon-phonon interactions dissipate heat across a particle-medium interface, until the NPs return to their initial surface temperature⁶.

The photothermal efficiency of NPs as photosensitisers strongly depends on the morphology and size of the particles⁷. In terms of efficiency, it is preferable that AuNPs present low scattering and strong absorption at the emission wavelength of the laser used for irradiation⁸. Thus, the size- and shape-dependent spectral tuning of AuNPs allows one to select the most suitable morphology for the desired laser wavelength⁹, typically using anisotropic AuNPs that maximally absorb NIR light (650-1350 nm)^{10,11}. This wavelength range is particularly interesting for PTT due to the transparency of tissues such as the dermis and underlying hypodermis, which represent the first barrier for light penetration upon application of externally applied light sources (see **Figure 3.1**) Indeed, the limit of penetration has been shown to be directly related to the incident light wavelength, therefore efforts to maximise this should always be taken into account for light to penetrate tissues and reach the NPs¹².

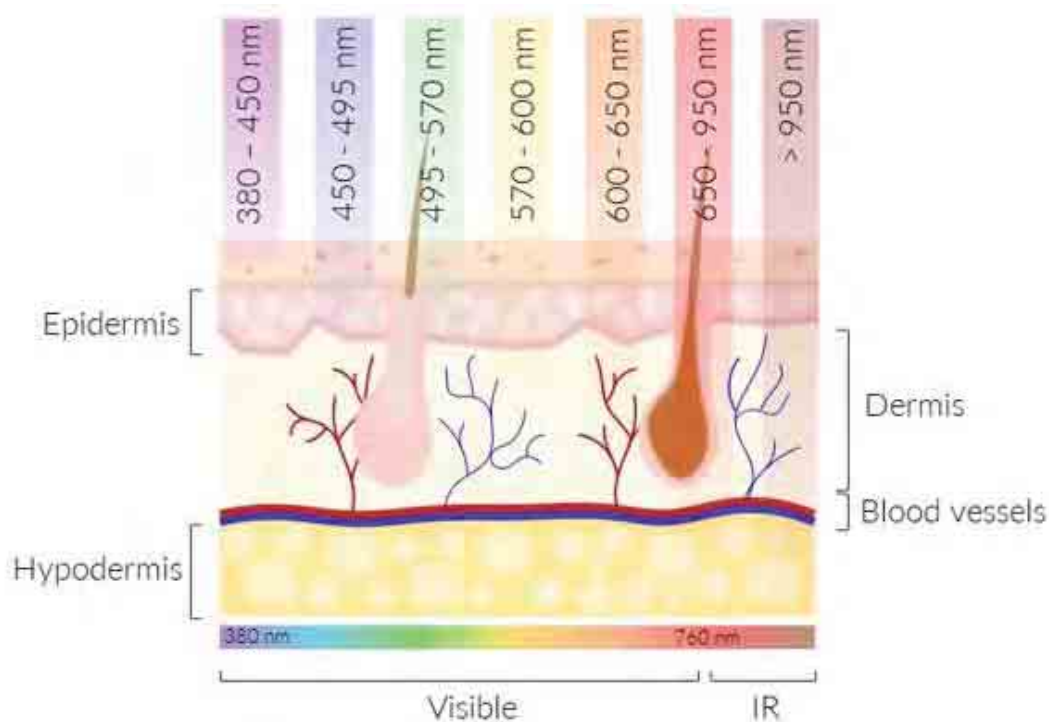


Figure 3.1. Scheme showing the different penetration depth through the skin, for light with different wavelengths.

In this Chapter, we further optimized the synthesis of IOAuNSs with different core size and gold coverage, and characterized their efficiency as nanoheaters for PTT, using both 2D and 3D cell models. The photothermal heating (PTH) experiments that are described in this chapter were mainly performed during a short research (5 weeks) stay at the Macromolecules and Microsystems in Biology and Medicine (MMBM) group, within the Institut Pierre Gilles de Gennes (IPGG, Paris), under the supervision of Dr. Claire Wilhelm. During this secondment I investigated and characterized the photothermal properties of IOAuNSs, while also developing 2D and 3D cellular models for PTH.

3.2 Optimization of hybrid nanoparticles for hyperthermia

3.2.1 Iron oxide nanoparticles: *Influence of water on particle size*

Through experimental variation of the synthetic process, we observed that the IONPs diameter, and the size of IO crystallites making up the core, can be tuned by varying the amount of water in the solvothermal process employed for the formation of multicore NPs. According to literature, the effect of water on the resulting IONPs size is related to the hydrolysis of the iron precursors, with smaller particles being obtained when the hydrolysis process is faster because the solvent becomes less viscous¹³. Hydrolysis is the first step in IONP synthesis, generally using polyethylene glycol as the reaction medium, so that its highly viscous nature controls the hydrolysis rate. Therefore, addition of water to alter the solvent viscosity can ultimately be used to control the reaction rate. Thus, we studied the effect of increasing amounts of water on the morphology and size of the obtained IONPs. The effect of varying the amount of water from 200 μ L to 5 mL while maintaining constant the volume of ethylene glycol (36.3 mL) is summarised in **Figure 3.2**. We

observed that, upon addition of small volumes of water, large particles made of small crystallites were obtained, whereas increasing volumes of water resulted in a decrease of the total diameter of the IONPs but the size for the crystallites increased. When adding volumes above 1.5 mL, the NPs appeared to be formed of single crystallites that did not aggregate. One important factor that was not varied in these experiments was the reaction time, which may play a role in the aggregation of crystallites. We observed that, when the amount of water was higher than 1 mL, a high proportion of isolated crystallites were found in the TEM images of the samples. In this case, by increasing the reaction time and employing high temperatures, complete aggregation of the cores could be observed. Nevertheless, such isolated crystallites could be easily removed by washing cycles using magnetic separation of larger particles, which were more strongly attracted to the magnet in comparison to the smaller ones.

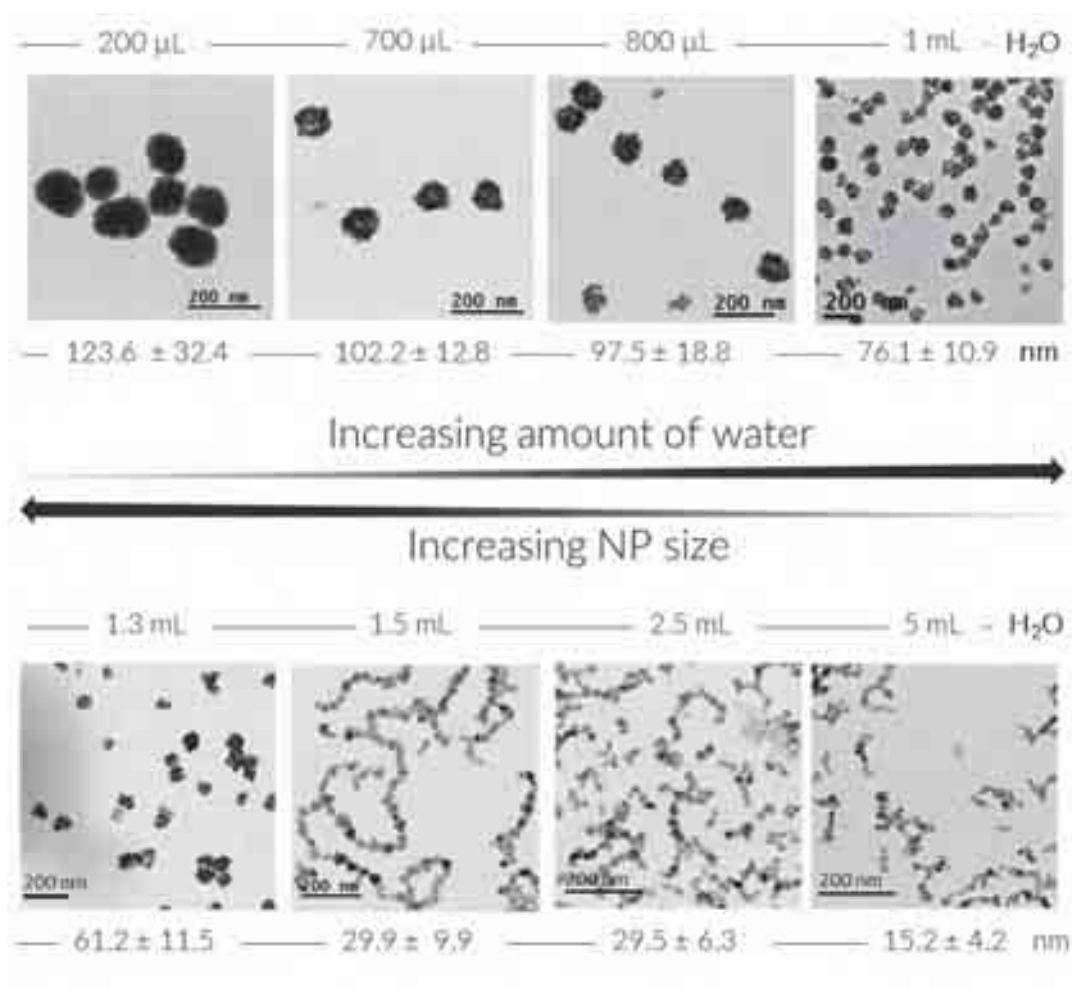


Figure 3.2. TEM images of IONPs with different sizes, obtained by varying the amount of water in the reaction solvent.

Among the different sizes obtained (see **Figure 3.2**), IONPs of 102.2 ± 12.8 nm (herein termed NP “A”), and IONPs of 76.1 ± 10.9 nm (herein termed NP “B”), were chosen for further study due their better reproducibility. The TEM and optical characterisation of these IONPs is shown in **Figure 3.3**. In the previous chapter we have shown that 5 nm crystallites were measured when synthesizing IONPs with no water in the reaction medium. We observed that, when adding water,

the total diameter of the IONPs decreased but the size of the crystallites increased. High magnification TEM images of single NPs are shown in **Figure 3.3**, from which crystallites of 15.3 ± 4.2 nm were measured.

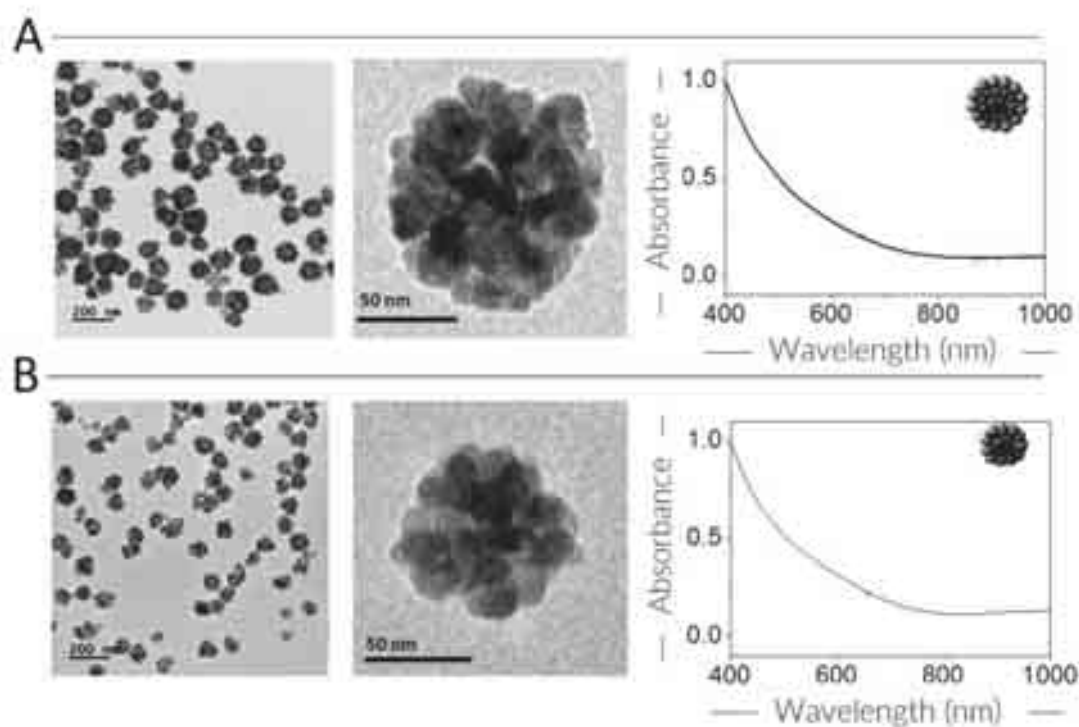


Figure 3.3. TEM images and normalized UV-Vis-NIR spectra (400 nm) of **(A)** 102.2 ± 12.8 nm IONPs and **(B)** 76.1 ± 10.9 IONPs.

3.2.2 Decoration of iron oxide nanoparticles with gold nanoparticles

Following the same strategy as in Chapter II, the IONPs were decorated with AuNPs at different concentrations. As already demonstrated in Chapter II, 4 nm and 15 nm AuNPs can be used for IONPs decoration. However, a higher number of AuNPs were adsorbed onto the IONPs surface when using smaller AuNPs. Thus, 4 nm AuNPs were used for these experiments due to their high level of adsorption and their easy and quick synthesis¹⁴. The concentration of Fe was fixed for all the samples and a decreasing concentration of AuNPs was added (herein termed series 1-3) to obtain IONPs decorated with a decreasing AuNP density on the surface.

The obtained IOAuNPs were characterized using TEM and UV-Vis-NIR spectroscopy. A decreasing density of AuNPs is clearly visible in TEM images, from IONPs A1/B1 to A3/B3 (**Figure 3.4**). The UV-Vis-NIR spectra show the characteristic shoulder at ca. 530 nm corresponding to the 4 nm AuNPs attached to the IONPs surface.

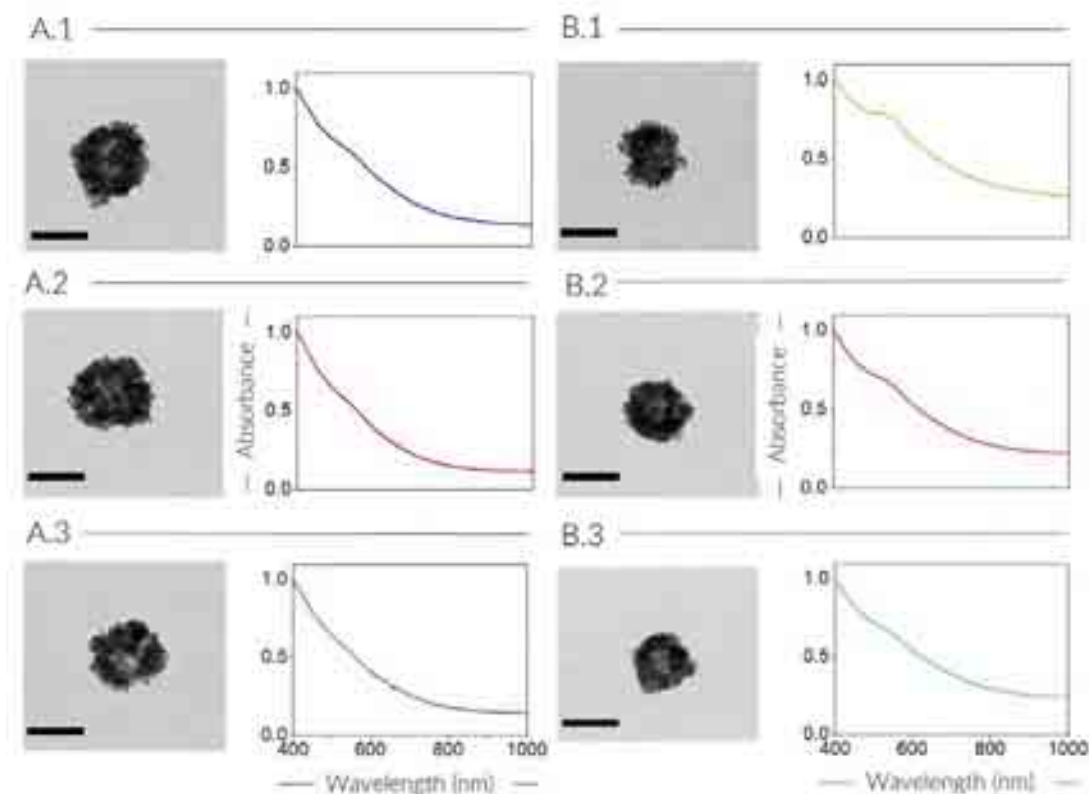


Figure 3.4. TEM images and normalized (400 nm) UV-Vis-NIR spectra of IONPs decorated with AuNPs. The highest concentrations of AuNPs were found for A.1 and B.1 and the density decreased from A.1 to A.2 to A.3 and from B.1 to B.2 to B.3. The [Au]/[Fe] ratios for the NPs were measured by ICP, as **A.1** = 0.25, **A.2** = 0.20, **A.3** = 0.14, **B.1** = 0.35, **B.2** = 0.28, **B.3** = 0.18. Scale bars correspond to 100 nm.

Because an excess of AuNPs were added to a fixed Fe concentration of IONPs (as opposed to a fixed NP concentration), and that the “B” IONPs, although smaller than the “A” IONPs, had an overall larger surface area, a higher [Au]/[Fe] ratio was observed.

3.2.3 Synthesis of hybrid iron oxide-gold nanostars

The synthesized IOAuNPs (A.1, A.2, A.3, B.1, B.2 and B.3) were used as seeds for subsequent gold overgrowth. The reaction was carried out as previously described in Chapter II. To calculate the amount of IOAuNPs required for tip growth, the concentration of Au in samples A.1, A.2 and A.3, and B.1, B.2 and B.3 was measured by ICP-MS. The conditions for the tip growth reaction were then calculated for a fixed [Au] = 0.3 mM measured directly from IOAuNPs (A.1, A.2, A.3, B.1, B.2 and B.3 in **Figure 3.5**). Thus, to maintain the same amount of gold it is necessary to modify the number of IOAuNPs in the reaction mixture. Therefore, the concentration of Fe increases from A.1 to A.3 and from B.1 to B.3. As the amount of IOAuNPs (used as seeds) was higher, the resulting NPs were smaller. So, two approaches were used to decrease the size of the particles: firstly, the thickness of the spiky gold shell was varied, as in Chapter II, by using IONPs decorated with a lower density of gold NPs because of the decreasing [Au]/[Fe] ratio (less gold per IO particle). Second, by using smaller IONPs as cores (IOAuNSs obtained from IONPs **A** are bigger than those obtained from IONPs **B**). A schematic representation of the synthesized NPs and the

characterization of the obtained IOAuNSs is shown in **Figure 3.5**, while the TEM and UV-Vis-NIR characterization of the final IOAuNSs is shown in **Figure 3.6**. Details are provided in the Experimental section.

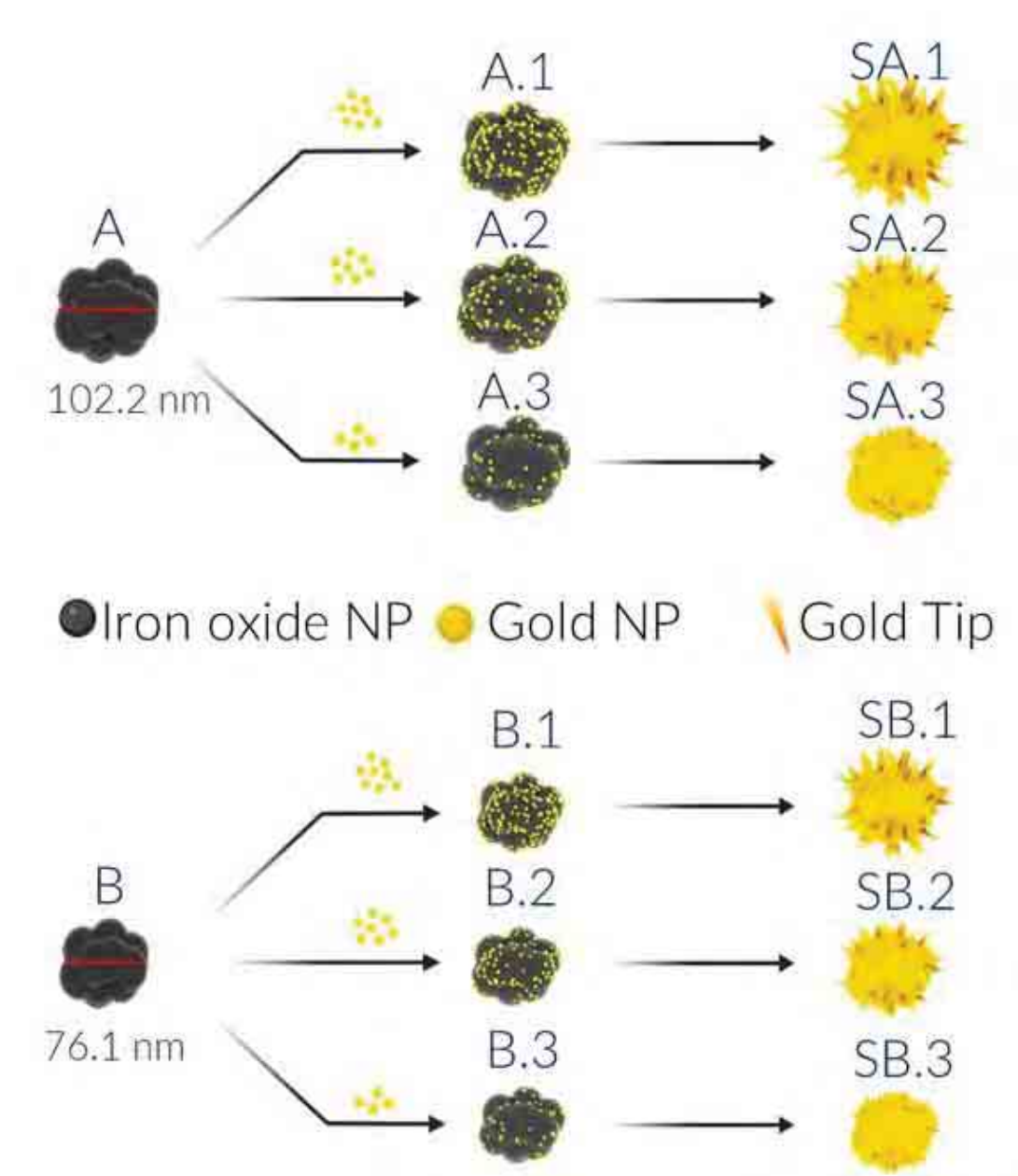


Figure 3.5. Schematic representation of different steps in the synthesis of IOAuNSs with different cores and final sizes.

We recorded the UV-Vis-NIR spectra of the different NPs and observed that, for the smallest stars (**SB.2** and **SB.3** in **Figure 3.6**), the spectra showed a slight red-shift and a sharper band in comparison with larger IOAuNSs. This effect was expected to be beneficial from the point of view of the efficiency of the NPs for their performance in photothermal heating because the absorbance maximum is closer to the laser wavelength used, i.e. 808 nm¹⁵. The final sizes of the IOAuNSs were measured using TEM images, obtaining the following average diameters (from tip to tip): **SA.1** = 396.1 ± 23.7 nm, **SA.2** = 302.2 ± 17.1 nm, **SA.3** = 220.8 ± 21.4 nm, **SB.1** = 370.0 ± 21.7 nm, **SB.2** = 210.5 ± 19.9 nm and **SB.3** = 194.4 ± 18.3 nm.

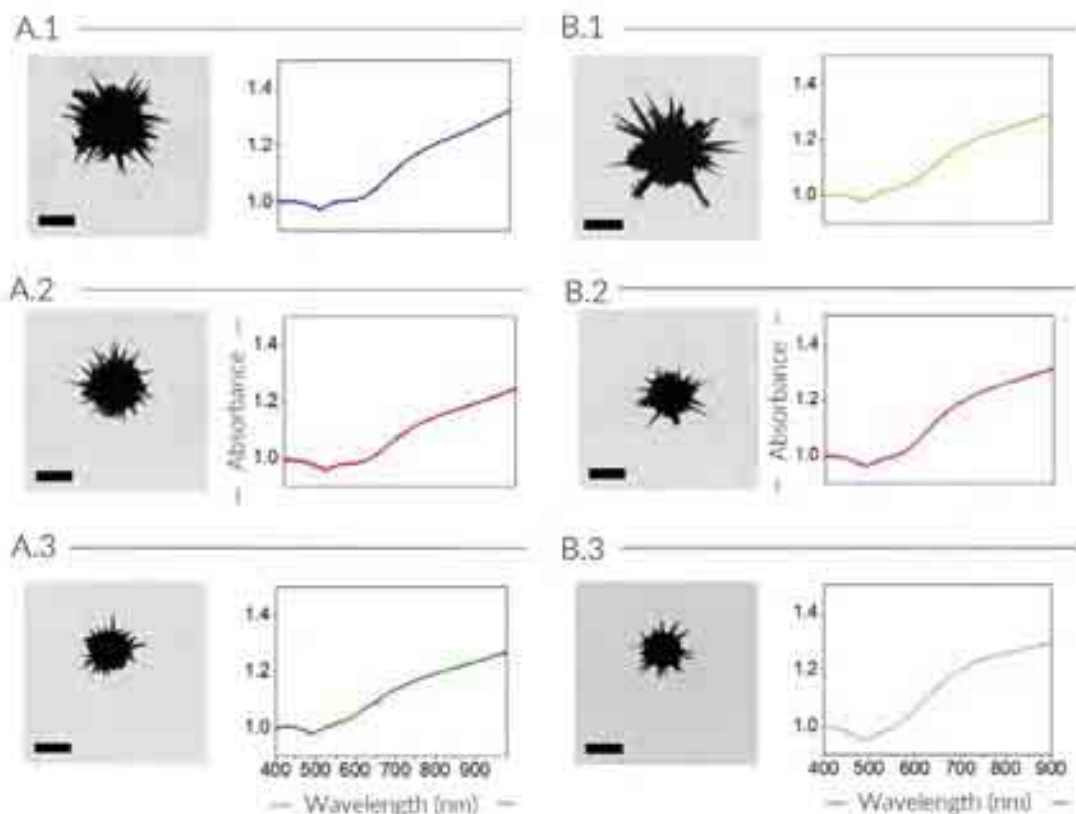


Figure 3.6. TEM images and normalized (at 400 nm) UV-vis-NIR spectra of the obtained IOAuNSs. The spectra were normalized at 400 nm because there is a minimum in the absorbance of IOAuNSs at this wavelength and above 400 nm the absorbance is increasingly influenced by the LSPR. The final gold concentration in IOAuNSs was analysed by ICP-MS and the resulting [Au]/[Fe] ratios were: **SA.1** = 11.6, **SA.2** = 9.3, **SA.3** = 7.8, **SB.1** = 12.5, **SB.2** = 10.6 and **SB.3** = 7.6. Scale bars correspond to 200 nm.

In conclusion, the size of IOAuNSs could be decreased by decreasing the concentration of AuNPs used as nucleation points for gold overgrowth and by decreasing the size of the iron oxide cores with the aim of obtaining smaller stars that displayed optimal properties for photothermal applications.

3.3 Photothermal characterization

To compare the properties of the different NPs as nanoheaters, first, the optical density of the IOAuNSs was measured. The spectra were recorded at different concentrations that ranged from [Au] = 0.1 to 2 mM using a UV-Vis-NIR spectrometer. The results are shown in **Table 3.1**. The optical density was measured at the same wavelength of the laser that will be used for the photothermal heating experiments (808 nm). For the IOAuNSs with smaller sizes (SA.3 and SB.3) the optical density at the given concentrations is higher. Thus, higher increments of temperature for these IOAuNSs were expected.

Table 3.1. Optical density at 808 nm for the IOAuNSs at the concentrations used for the photothermal characterization of the NPs in solution.

| [Au] mM | Optical density | | | | | |
|---------|-----------------|-------|-------|-------|-------|-------|
| | SA.1 | SA.2 | SA.3 | SB.1 | SB.2 | SB.3 |
| 0.1 | 0.006 | 0.005 | 0.050 | 0.016 | 0.021 | 0.027 |
| 0.2 | 0.016 | 0.020 | 0.034 | 0.025 | 0.029 | 0.036 |
| 0.5 | 0.057 | 0.044 | 0.055 | 0.050 | 0.063 | 0.085 |
| 1 | 0.104 | 0.100 | 0.128 | 0.124 | 0.102 | 0.180 |
| 2 | 0.193 | 0.163 | 0.276 | 0.214 | 0.274 | 0.352 |

Then, a standard photothermal characterization of IOAuNSs in solution was performed. We studied the effect of changing the IOAuNSs concentration whilst using a fixed power density. Aliquots of 50 μL from the IOAuNSs dispersion at different particle concentrations from $[\text{Au}] = 0.1$ to 2 mM, were placed in Eppendorf tubes (0.5 mL) and subsequently irradiated using an 808 nm single mode laser for 5 min, with a power density of 1 W/cm^2 . The temperature increments were registered using a thermal camera focused on the region of interest (ROI); the temperature was first registered and then the corresponding temperature increment was calculated by subtracting the initial temperature (time = 0) from the final temperature (time = 5 min). A schematic representation of the set-up is shown in **Figure 3.7**.

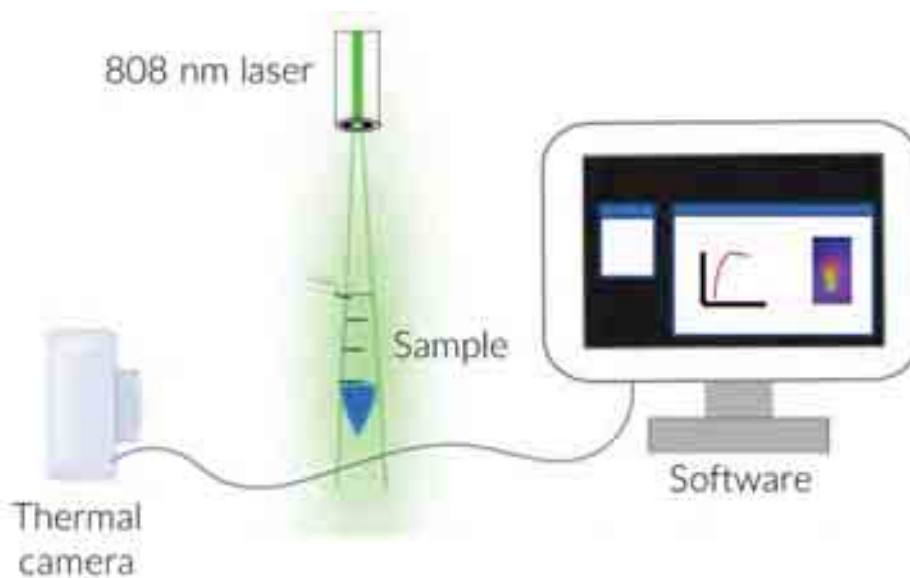


Figure 3.7. Schematic representation of the photothermal setup. The camera is located at one side and the samples are irradiated from the top. During irradiation, the temperature of the IOAuNSs solution is measured using a thermal camera and registered using a software (FLIR ResearchIR Standard Software)

As can be observed in **Figure 3.8**, all IOAuNSs showed concentration-dependent heating upon laser irradiation, with a clear trend of higher overall changes in temperature observed for

decreasing IOAuNSs size. Of note, to conduct these experiments the Au concentration was fixed (and not the Fe or NP concentration), and therefore with decreasing IOAuNSs size, there was an increase in the IO component of the NP. This suggests that the IO component may also play a role in the heating properties, albeit not as strong as the Au component.

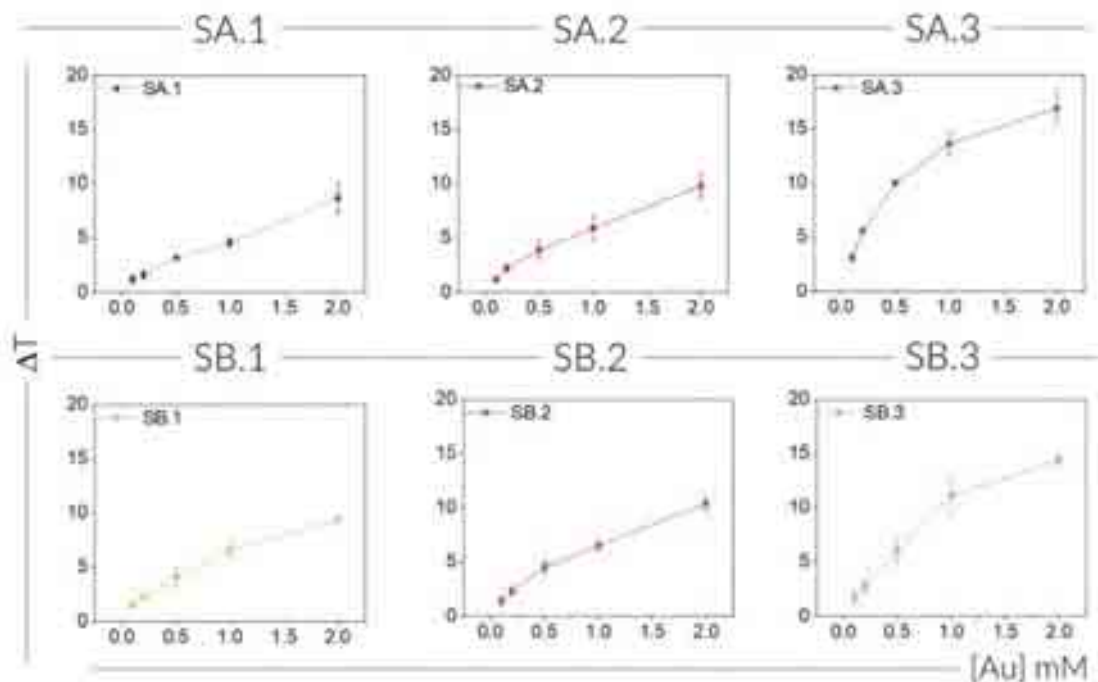


Figure 3.8. Average temperature change (ΔT , in $^{\circ}\text{C}$) of IOAuNSs in solution. Different concentrations of IOAuNSs, ranging from $[\text{Au}] = 0.1$ to 2 mM, were irradiated for 5 min at 1 W/cm^2 .

The increase of temperature achieved at this power density (1 W/cm^2) was not very high at relatively low concentrations. Only with the highest concentration ($[\text{Au}] = 2$ mM) temperature increments above 10 - 15 $^{\circ}\text{C}$ were achieved. Thus, we decided to repeat the irradiation at all concentrations but increasing the power density from 1 to 2.5 W/cm^2 . As expected, the overall changes in temperature were considerably higher at all concentrations studied (**Figure 3.9**). We thus investigated the photothermal effect of the IOAuNSs in a cellular environment. We chose a human glioblastoma cell line (U87) for photothermal characterization. The cells were first incubated at a fixed concentration ($[\text{Au}] = 0.1$ mM) of IOAuNPs for 24 h. Subsequently, the cells were recovered, and their volume adjusted to 50 μL , to match previous PTH experiments. This cell pellet represented the most concentrated stock solution (the concentration of which was measured using ICP-MS) and successive dilutions were made to obtain different points representing the different cell+IOAuNPs concentrations. In addition, the specific absorption rate was calculated as previously reported¹⁶ for IOAuNSs and cells+IOAuNSs (**Figure 3.9**).

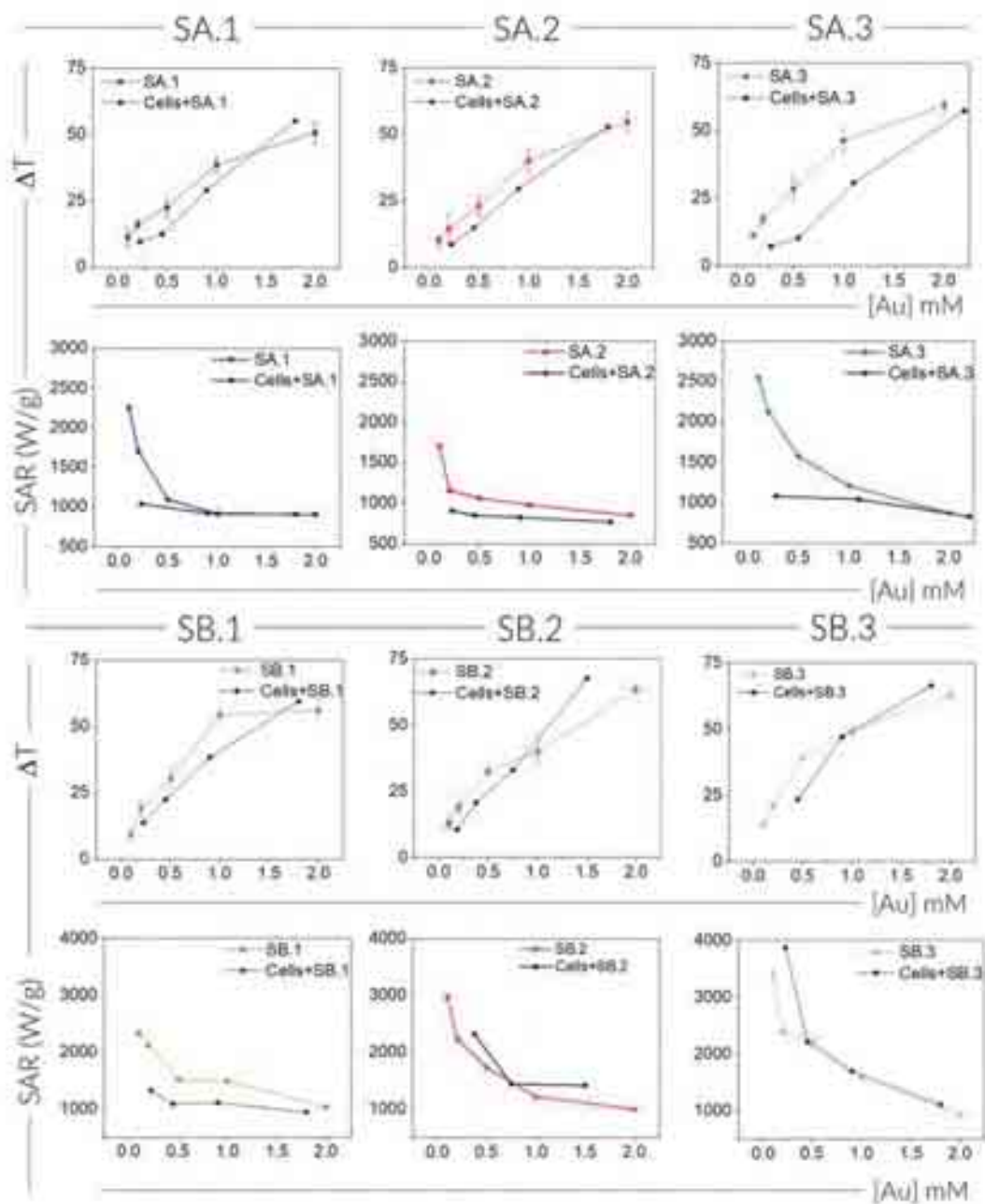


Figure 3.9. Average temperature change (ΔT , in $^{\circ}\text{C}$), and specific absorption rate (SAR) for IOAuNSs in solution (color line) and in cells incubated with IOAuNSs (black line). A fixed laser power density of 2.5 W/cm^2 was used throughout. Triplicates were done for the IOAuNSs in solution whereas cells+IOAuNSs were measured once at each concentration.

We observed that the heating profiles, overall temperature change, and SAR values were similar for IOAuNSs in solution and internalized in U87 cells. According to the literature, at a fixed NP concentration, the capacity of the NPs to heat when aggregated inside cells is higher than in solution¹⁶⁻¹⁸. Indeed, from **Figure 3.9** it appears that this is the case at the highest concentration tested, but at lower concentrations IOAuNSs in solution heat more than in cells. The variation in results between IOAuNS types, concentrations, and conditions (solution vs cell) may be due to experimental inaccuracies during the dilution of cell+IOAuNSs samples, because mistakes would have been carried over during sequential dilutions, from one concentration to the next. Nevertheless, the photothermal characterization of IOAuNSs in both conditions allowed us to

check the heating capacity of the NPs and this information was considered to estimate the concentrations that would be needed for the application for PTH in other cellular models.

Regarding the results, as can be seen in **Figure 3.10** and **Table 3.2** the differences between various particles are not remarkable. Notwithstanding, a tendency that is in agreement with the values of the optical density (**Table 3.1**) could be appreciated. The results demonstrate that bigger particles had a lower heating capacity than smaller ones, likely due to their red shifted absorption maxima, which matched better the laser wavelength, making them more efficiently light absorbers, although the better heating efficiency could also be due to the higher concentration of IONPs. At the same concentration of Au, smaller IOAuNSs contain more IONPs that would contribute to the total heating.

Thus, in the series SA, comprising the bigger cores, particles SA.1 can heat less than SA.2 and the heating capacity is further increased for SA.3. Likewise, for series SB, which showed the same trend, a higher increase of temperature in solution was achieved when decreasing the gold coverage and thus the total size of the NP. If we compare particles with different core sizes that were synthesized using the same amount of HAuCl_4 for tip growth, such as SA.1 and SB.1, SA.2 with SB.2 and SA.3 with SB.3, the results again suggest that particles with smaller cores and thinner Au coverage, leading to IOAuNSs with a smaller total diameter, showed a better performance for photothermal heating.

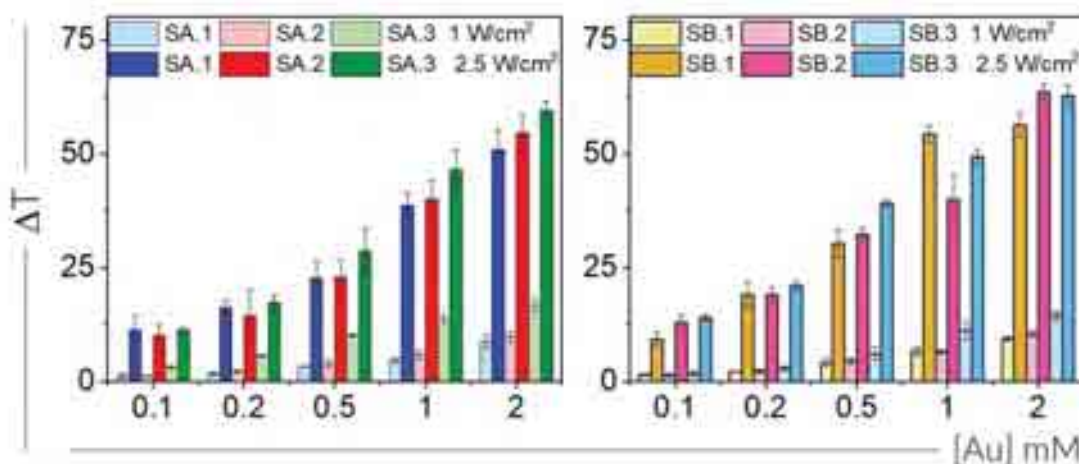


Figure 3.10. Average temperature increment (ΔT , in $^{\circ}\text{C}$) upon irradiation for 5 min at 2.5 W/cm^2 of IOAuNS in solution at different concentrations.

Table 3.2. Average temperature elevation (ΔT , in $^{\circ}\text{C}$) for PTH at 1 and 2.5 W/cm^2 in solution at different concentrations of IOAuNSs.

| | | SA.1 | | | | SA.2 | | | | SA.3 | | | |
|------------|--------------------------|------|--------------------------|-----|--------------------------|------|--------------------------|-----|--------------------------|------|--------------------------|-----|--|
| [Au] mM | 1 W/cm^2 | | 2 W/cm^2 | | 1 W/cm^2 | | 2 W/cm^2 | | 1 W/cm^2 | | 2 W/cm^2 | | |
| | ΔT | SD | ΔT | SD | ΔT | SD | ΔT | SD | ΔT | SD | ΔT | SD | |
| 0.1 | 1.2 | 0.4 | 11.2 | 3.3 | 1.2 | 0.1 | 10.1 | 2.3 | 3.1 | 0.3 | 11.2 | 0.7 | |
| 0.2 | 1.6 | 0.4 | 16.1 | 1.7 | 2.2 | 0.3 | 14.4 | 5.7 | 5.6 | 0.2 | 17.3 | 1.7 | |
| 0.5 | 3.2 | 0.1 | 22.7 | 3.7 | 3.9 | 0.8 | 22.9 | 3.8 | 10.0 | 0.3 | 28.6 | 4.9 | |
| 1 | 4.6 | 0.5 | 38.6 | 2.8 | 5.9 | 1.1 | 40.1 | 4.1 | 13.6 | 1.1 | 46.4 | 4.4 | |
| 2 | 8.7 | 1.4 | 50.9 | 4.2 | 9.8 | 1.1 | 54.6 | 3.9 | 16.9 | 1.6 | 59.4 | 2.0 | |

| | | SB.1 | | | | SB.2 | | | | SB.3 | | | |
|------------|--------------------------|------|--------------------------|-----|--------------------------|------|--------------------------|-----|--------------------------|------|--------------------------|-----|--|
| [Au] mM | 1 W/cm^2 | | 2 W/cm^2 | | 1 W/cm^2 | | 2 W/cm^2 | | 1 W/cm^2 | | 2 W/cm^2 | | |
| | ΔT | SD | ΔT | SD | ΔT | SD | ΔT | SD | ΔT | SD | ΔT | SD | |
| 0.1 | 1.5 | 0.2 | 9.2 | 1.5 | 1.4 | 0.4 | 12.9 | 1.7 | 1.8 | 0.6 | 14.0 | 0.7 | |
| 0.2 | 2.2 | 0.1 | 19.1 | 2.8 | 2.3 | 0.4 | 19.0 | 1.7 | 2.8 | 0.6 | 21.0 | 1.0 | |
| 0.5 | 4.1 | 0.8 | 30.3 | 3.0 | 4.5 | 0.7 | 32.3 | 1.4 | 6.1 | 1.4 | 39.1 | 0.6 | |
| 1 | 6.6 | 0.9 | 54.3 | 1.9 | 6.5 | 0.5 | 40.0 | 5.4 | 11.1 | 2.1 | 49.3 | 1.6 | |
| 2 | 9.4 | 0.4 | 56.2 | 2.6 | 10.4 | 0.6 | 63.5 | 1.7 | 14.4 | 1.0 | 62.7 | 2.3 | |

To check the role of the IO core in the overall heating, an additional experiment using IONPs **A** and **B** was carried out as control. The IONPs were irradiated under the same laser conditions as the IOAuNSs, using a Fe concentration 3-5 times higher ($[\text{Fe}] = 0.5 \text{ mM}$) than that estimated to be present in the IOAuNSs ($[\text{Fe}] = 0.1 - 0.2 \text{ mM}$). The results showed that, even at high concentrations, the IO cores had a lower heating efficiency, with an average increase in temperature of 12°C (**Figure 3.11**). Additionally, there were no differences in the heating capacity of the cores depending on their size. Considering that the iron concentration in IOAuNSs is much lower than the Fe concentration used in these controls, we can confirm that the cores are hardly affecting or contributing to the total heating.

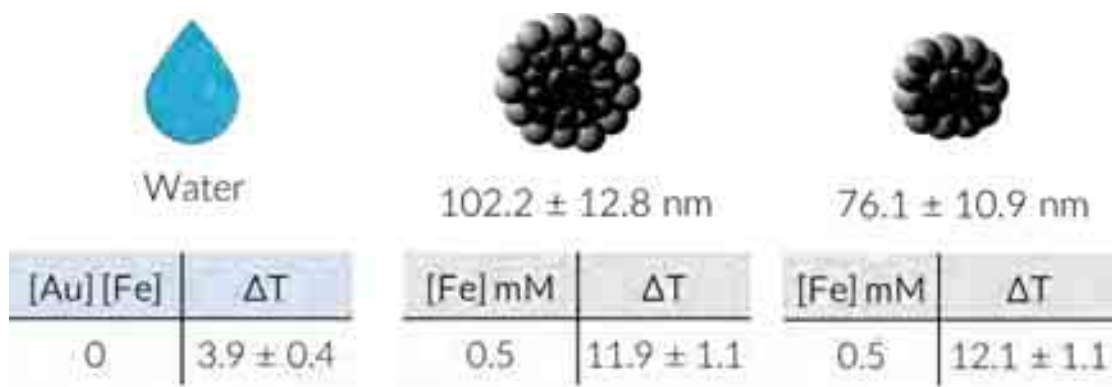


Figure 3.11. Average temperature elevation (ΔT , in $^{\circ}\text{C}$) upon irradiation during 5 min at 2.5 W/cm^2 in solution for water and both IONPs that were used as cores for the IOAuNSs. These samples were used as controls for the experiments.

From these findings we can conclude that all IOAuNSs tested have a great capacity to heat in solution, and that no significant differences between the different IOAuNSs were found for their

capability to heat in solution. Upon addition to cells, similar heating trends were observed, reaching a sufficiently high temperature that would cause hyperthermia in PTT applications.

With the aim to better understand the heating mechanism of IOAuNSs, and how the properties and the morphology of the particles affect the heating efficiency, we prepared various additional control samples. The first control consisted of a polystyrene bead (PS-bead) covered by a spiky gold shell that was synthesized using the same conditions as those for IOAuNSs. Thus, PS-Beads ($D = 200$ nm) were first decorated with 4 nm AuNPs. For the attachment of AuNPs on the PS surface, a layer-by-layer assembly procedure was applied using polyelectrolytes (PE) with opposite charges, the details of which are fully explained in the Experimental section. Citrate coated (negatively charged) AuNPs, were added to PS-beads with an outer positively charged layer of polyallylamine hydrochloride (PAA(+)), which promoted their decoration by electrostatic attraction. Subsequently, the previously described procedure was used to grow Au tips from AuNPs adhered to the PS bead (resulting in PSAuNSs). A scheme of the procedure can be seen in **Figure 3.12A**. PSAuNSs were characterized using TEM and elemental analysis (EDX) of Au and Carbon (C), to confirm the core-shell distribution of PS and Au components (**Figure 3.12B**).

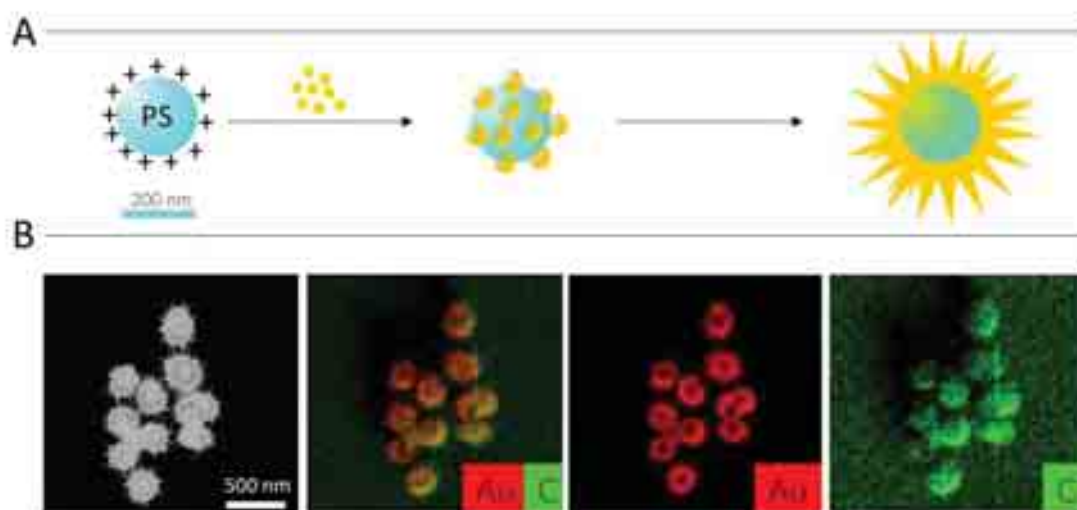


Figure 3.12. (A) Schematic illustration of the synthesis of PSAuNSs. (B) Dark field TEM image and EDX analysis of Au (red) and C (green) confirming that both elements are present in PSAuNSs and Au is located at the external (spiky) shell.

From TEM/EDX images we confirmed the expected distribution of both elements (high C-content PS core surrounding by Au shell and tips), and the overall size (364.3 ± 24.6 nm) which was found to be similar to SA.1 IOAuNSs. We then irradiated PSAuNSs using the same laser parameters and the same Au concentration as those in the experiments with IOAuNSs. The results show that both PSAuNS and SA.1 IOAuNSs have very similar maximum heating at all the analysed concentrations, confirming that the core is not affecting nor contributing to the total heating by the hybrid nanoparticles (**Figure 3.13**). A further non-Au containing control (PS-beads alone) was also irradiated at the same PS-bead concentration used for the PSAuNSs, observing no significant temperature increase (3.1 ± 0.3 °C, similar to pure water).

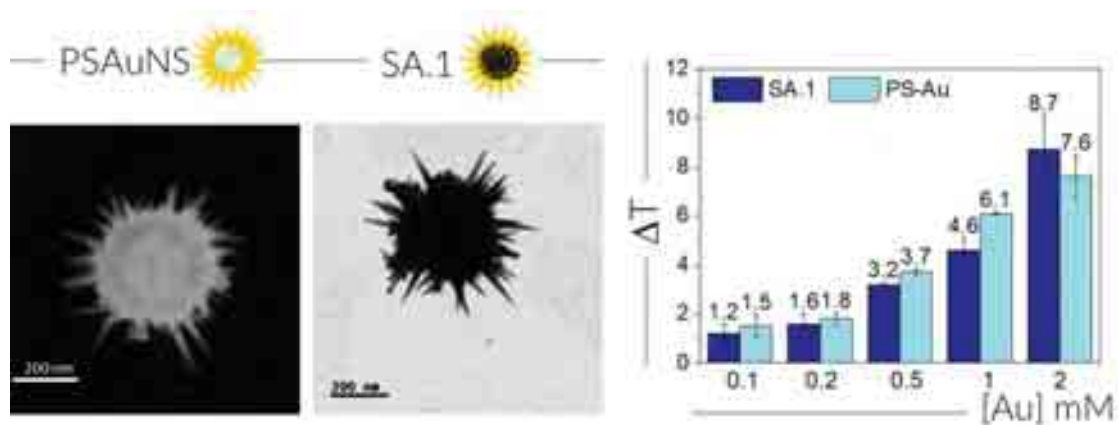


Figure 3.13. TEM images of SA.1 IOAuNSs and PSAuNSs and comparison of the average temperature change (ΔT , in $^{\circ}\text{C}$) upon irradiation in solution for 5 min at $2.5 \text{ W}/\text{cm}^2$.

To further verify that heating was due to the Au component, a further non-IO containing AuNSs control, of similar size to IOAuNSs, was synthesized. AuNSs measured $230.6 \pm 20.1 \text{ nm}$ in diameter, similar to SA.3 IOAuNSs. Considering that we previously observed that the heating of IOAuNSs was due to the gold shell (because the IO core alone did not heat significantly even at higher concentrations than those found in IOAuNSs), we measured the heating profiles for AuNSs with a solid gold core. For a proper comparison between AuNSs and IOAuNSs, we fixed NP concentration as opposed to Au concentration, The results showed that AuNSs and similarly sized IOAuNSs were able to heat up to similar temperatures ($15.7 \pm 2.1 \text{ }^{\circ}\text{C}$ vs $13.2 \pm 1.6 \text{ }^{\circ}\text{C}$; Figure 3.14). The combination of all these results suggests that the photothermal conversion of light into heat that occurs when irradiating the NPs with a laser is a surface effect that is not affected by the core, regardless of the material comprising the core.

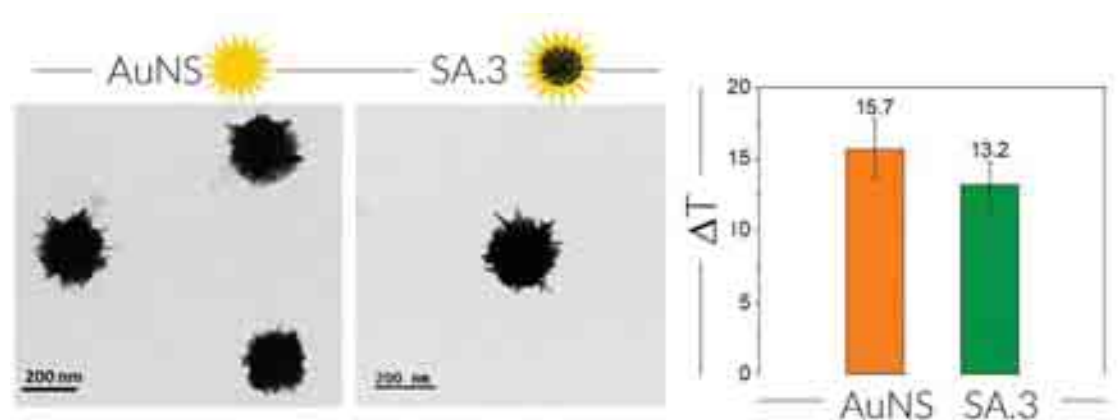


Figure 3.14. TEM images of AuNSs and SA.3 IOAuNSs and the comparison of the average temperature change (ΔT , in $^{\circ}\text{C}$) upon irradiation at $1 \text{ W}/\text{cm}^2$ in solution.

3.4 Hyperthermia in 2D cell cultures

Up to this point, we have shown that all NPs tested show a significant heating efficiency, both in solution and after internalization in cells. However, conducting PTH with a cell pellet is not a realistic biological model, and therefore we studied PTH in adherent cells, grown in the traditional 96-well plate format. We followed the same laser set-up as shown in **Figure 3.7**, changing the Eppendorf tube for a 96-well plate containing the samples. We used the results obtained for the increase of temperature at different concentrations (**Figure 3.9**) as a guide to decide which IOAuNSs concentration to apply. Again, U87 cells were used, initially adding SB.3 at low concentrations (<1 mM). The cell viability was measured using the AlamarBlue assay, which is based on the natural reducing power of living cells to convert resazurin (blue) to fluorescent resorufin (pink). As observed in **Figure 3.15A**, upon irradiation with a power density of 1 W/cm² for 5 min, no significant changes in cell viability were observed. We thus decided to increase the power density to 2 W/cm² while maintaining the same IOAuNSs concentrations. As can be observed in **Figure 3.15B**, cell viability reaches almost zero (100% cytotoxicity) when using the highest IOAuNSs concentration of 0.8 mM. From these experiments we deduced the optimal conditions for irradiation in cells, the incubation of U87 cells with IOAuNSs at 0.4 mM for 24 h results in an increase of temperature that is high enough to kill 75-80% of cells. We then chose to perform a comparative study between all the different IOAuNSs (SA.1, SA.2, SA.3, SB.1, SB.2 and SB.3). U87 cells were incubated overnight with 0.4 mM of each IOAuNS sample, followed by irradiation at 2 W/cm² using the same laser setup as previously described. The results confirmed the same tendency of smaller NPs showing higher overall changes in temperature and thus cytotoxicity (**Figure 3.15C**). It should be considered that the concentration in cells is lower than the one added for incubation because not all the NP are internalized in the cells during the incubation. To check the real concentration, ICP-MS was required but it was not possible to use it in this occasion.

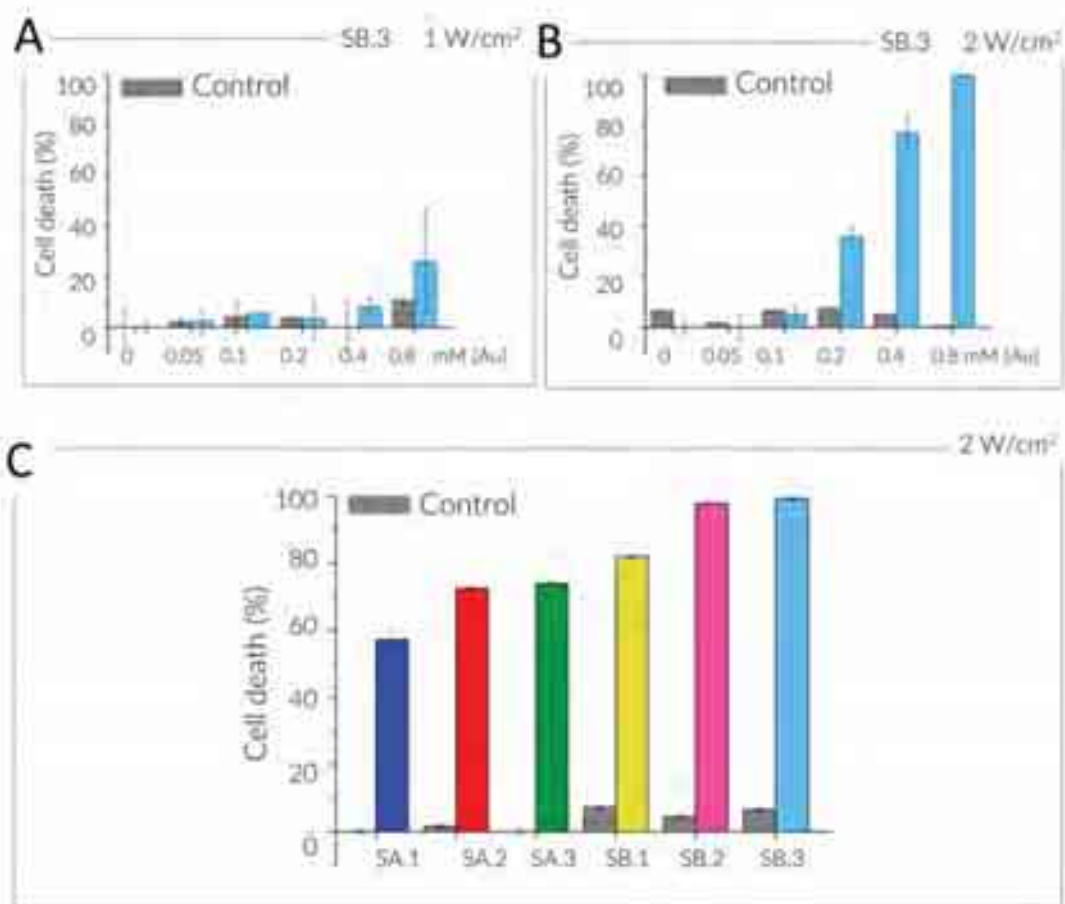


Figure 3.15. Cell death (%) calculated using AlamarBlue cell viability reagent after heating in a cellular environment. U87 cells were incubated with IOAuNPs **SB.3** at increasing concentrations ([Au] = 0.05-0.8 mM), then the cells were irradiated for 5 min at **(A)** 1 W/cm² and **(B)** 2 W/cm². **(C)** U87 cells were incubated with different IOAuNSs at [Au] = 0.4 mM, followed by irradiation at 2 W/cm² for 5 min. All the irradiations were performed in a 96-well plate containing 100 μ L/well. Controls were incubated at the same conditions, but laser irradiation was not applied. For all the experiments, an 808 nm laser was used.

3.5 Hyperthermia in 3D cell spheroids

We subsequently studied the ability to apply PTH to 3D cell models. Under certain growth conditions, U87 cells spontaneously form cell aggregates, also termed spheroids, which serve as miniaturized 3D models for high-throughput testing. In this study, we formed spheroids using micro-moulds in 96-well plates which inhibit cell interactions with the underlying surface, thus promoting cell-cell adhesion and spheroid growth. U87 cells were incubated for 24 h with IOAuNSs SA.3 at [Au] = 0.1 mM in normal 2D cell growth substrates, and then transferred to micro-moulds to allow the growth of an array of spheroids in the same imaging plane. We selected IOAuNSs SA.3 because they showed the best performance for PTH, achieving the highest percentage of dead cells in 2D studies. After formation of the spheroids, the media was changed prior to irradiation experiments, to remove any NPs that may have been exocytosed from the cells. We applied different power densities ranging from 0.5 to 2 W/cm². Our results suggest that

a gradual power-density-dependent cytotoxic effect can be achieved with maximal cell death occurring when using 2 W/cm² (Figure 3.16). This is in agreement with the results obtained for cells in 2D and in solution. Thus, when increasing the concentration and/or the power density, the capacity to kill cells also increases. Besides, lower concentrations can be used when using 3D cell models in comparison with 2D models, being able to kill the cells in spheroids while using lower concentrations ([Au] = 0.1 mM) and lower power densities (1.5 W/cm²).

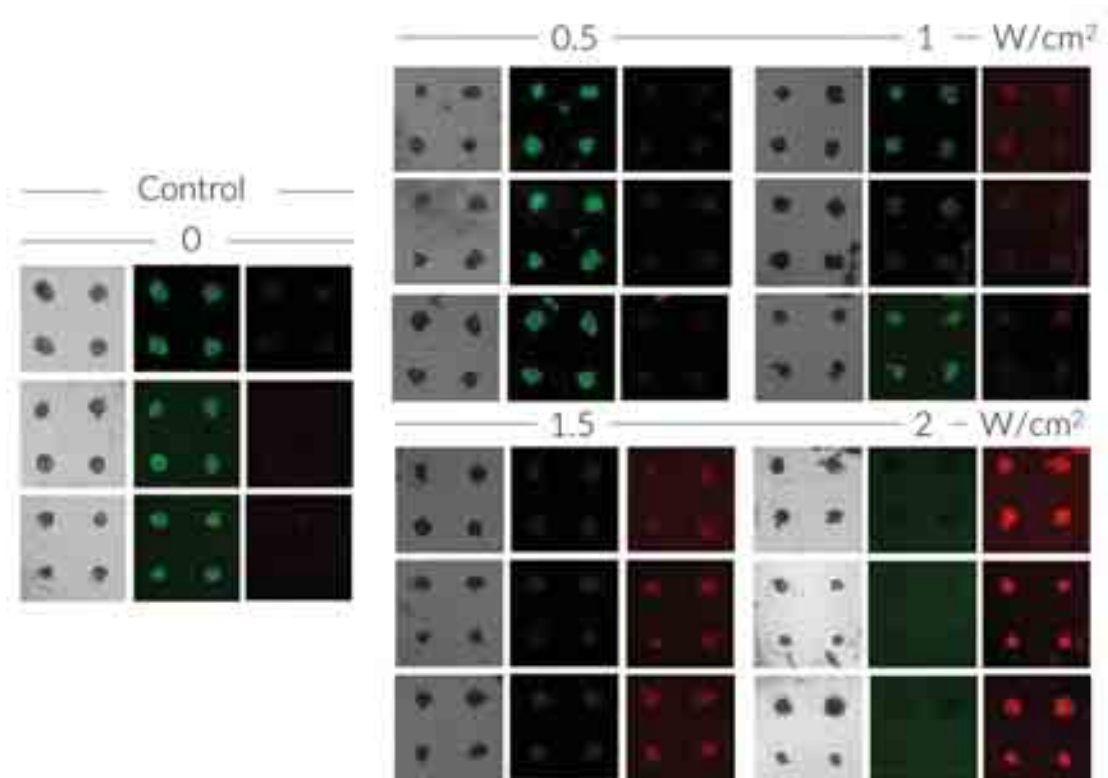


Figure 3.16. Optical and live/dead images of spheroids pre-loaded with 0.1 mM of IOAuNSs SA.3 and irradiated for 5 min at increasing power densities (from 0.5 to 2 W/cm²). The control corresponds to spheroids that were incubated with the IOAuNSs at the same concentration but were not irradiated (0 W/cm²).

3.6 Conclusions

We have developed biocompatible magneto-plasmonic nanohybrids composed of an IO multi-core and Au shell with tunable plasmonic properties in the NIR region, as efficient nanoheaters for PTH. We have demonstrated that the size of the IO core was tunable through the amount of water in the solvothermal synthesis. Hence, a library of IOAuNSs particles with different Au shells were synthesized by decreasing the density of AuNPs on the surface (strategy developed and explained in Chapter II), and two different IO core sizes. IOAuNSs were characterized by UV-Vis-NIR, showing a red-shifting of the LSPR band with decreasing IOAuNSs size.

A complete comparative study of the photothermal efficiency of NPs in solution and in 2D cell cultures was undertaken. We demonstrated the capacity of the formulation to generate heat through irradiation with a 808 nm laser. We compared particles with different morphologies and sizes, and we found that the heating capacity (expressed as SAR in W/g) increases when

decreasing the size of the NPs, either via decreasing the gold coverage or when decreasing the diameter of the IO core.

Additionally, we have demonstrated that the IO core does not contribute to the total heating because the cores themselves, even when heated at higher Fe concentrations, do not heat significantly. An additional control to determine the relevance of the metal core was developed using PS beads. The PS beads were successfully covered with AuNPs and a gold shell was synthesized around the PS, demonstrating the versatility of the optimized method. The heating experiments comparing the PSAuNSs control (364.3 ± 24.6 nm) with the most similar IOAuNSs SA.1 (396 ± 23.7 nm) showed that the iron core does not affect the heating properties of the gold shell. A further control using pure AuNSs was used to evaluate if the presence of a solid Au core can contribute to increasing the total heating. Thus, AuNSs measuring 230.6 ± 20.1 nm in diameter were synthesized and compared with SA.3 IOAuNSs (220.8 ± 21.4 nm). After adjusting the solutions to the same number of NPs, both particles showed essentially the same increase of temperature upon irradiation. We thus concluded that the heating of NPs is a surface/tip effect and that the core of the NP is not heating regardless of its material.

With regards to the application of IOAuNSs in biological environments, we applied various concentrations of the different IOAuNSs to U87 cells and observed nearly zero cytotoxicity from the IOAuNSs at concentrations up to $[\text{Au}] = 0.8$ mM. Application of PTH through laser irradiation reduced the dose needed to inhibit 100% of cell activity (IC100) in 2D to $[\text{Au}] = 0.4$ mM when using power densities of 2 W/cm^2 for 5 min. The results of calculating the heating efficiency (SAR) of the NPs internalized in cells resulted in similar values compared to those in solution. A 3D cell model consisting of arrays of spheroids made of cells pre-loaded with NPs were also successfully developed. Improved results were found for the efficiency of the NPs to kill the cells in 3D. In these models, we were able to reach an IC100 with a lower dose $[\text{Au}] = 0.1$ mM in comparison to the experiments in 2D and lower power density of $1.5 - 2 \text{ W/cm}^2$ applied for a shorter time (3 min).

3.7 Experimental Section

3.7.1 Materials

Ferric chloride hexahydrate ($\text{FeCl}_3 \cdot 6\text{H}_2\text{O}$, $\geq 98\%$ Sigma-Aldrich), poly(vinylpyrrolidone) (PVP360; Sigma-Aldrich), sodium acetate anhydrous (ReagentPlus $\geq 99.0\%$ Sigma-Aldrich), ethylene glycol (ReagentPlus, $\geq 99\%$ Sigma-Aldrich), absolute ethanol ($\text{CH}_3\text{CH}_2\text{OH}$, Sigma-Aldrich), hydrogen tetrachloroaurate trihydrate ($\text{HAuCl}_4 \cdot 3\text{H}_2\text{O}$, $\geq 99.9\%$ Sigma-Aldrich), sodium citrate tribasic dihydrate ($\geq 98\%$ Sigma-Aldrich), sodium borohydride (NaBH_4 , ReagentPlus, 99%, Sigma-Aldrich), silver nitrate (AgNO_3 , $\geq 99\%$ Sigma-Aldrich), L-ascorbic acid (AA, $\geq 99\%$ Sigma-Aldrich), hydrochloric acid solution (HCl 37 wt% Panreac), biphenyl-4-thiol (4-BPT, 97% Sigma-Aldrich), chloroform (CHCl_3 , $\geq 99.8\%$ Sigma-Aldrich), HS-PEG-COOH (Mw 3.000 Dalton, Iris Biotech), HS-PEH (Mw 3.000 Dalton, Sigma-Aldrich), PS-beads (AJ20SO_3 , Ikerlat polymers), polyallylamine hydrochloride (Mw 50.000, Sigma-Aldrich) and poly (sodium-4-styrenesulfonate) (Mw 70.000,

Sigma-Aldrich) were prepared and used without further treatment. Milli-Q water was used for all the experiments.

3.7.2 Nanoparticle synthesis

IONPs Synthesis. For the synthesis of 102.2 nm IONPs, 0.21 mmol of iron chloride hexahydrate was dissolved in 36.3 mL of ethylene glycol under stirring. Then, 516.6 μ mol of PVP360 was slowly added to the solution under vigorous stirring and the solution was heated (< 100 °C). When the reactants were completely dissolved, 5.2 mmol of sodium acetate was added to the solution. The mixture was placed in a Teflon autoclave and heated in a drying oven for 4 h at 200 °C. Finally, the solution was cooled down and the particles were washed twice by centrifugation (9000 rpm, 20 min) with ethanol and one additional wash with milli-Q water.

For the synthesis of 76.1 nm IONPs the procedure was the same but 1 mL of water was added to the ethylene glycol in the first step of the synthesis.

IOAuNPs Synthesis. The protocol for the synthesis of IONPs decorated with AuNPs of chapter II was used to synthesize the IOAuNSs with both iron cores. Then, 4 nm seeds were attached at different concentrations by adding 25 mL of the AuNPs to 5 mL of dried IONPs (**Table 3.3**)

Table 3.3. Concentration of AuNPs solution (25 mL) used for the fabrication of the IOAuNPs used as seeds for the tip's growth.

| [Au] of AuNPs solution | Seeds for IOAuNSs |
|------------------------|-------------------|
| 0.1 mM | A.1, B.1 |
| 0.05 mM | A.2, B.2. |
| 0.02 mM | A.3, B.3 |

Then, spiky gold shells were grown using the protocol explained in chapter II for IOAuNSs-bll. Briefly, 10 μ L of HAuCl₄ (0.129 M) were added to 10mL of water, in a 20 mL glass vial. Then, 10 μ L of HCl 1M was added and immediately after, 35 μ L of IOAuNSs at [Au]=0.3 mM of each IOAuNPs (**A.1, A.2, A.3, B.1, B.2, B.3**) was incorporated as seeds. Then, 350 μ L of AgNO₃ 3 mM and 50 μ L of ascorbic acid 100 mM were simultaneously and quickly added to the solution. A fast change from brown to blue indicates IOAuNSs formation. Subsequently, 30 μ L HS-PEG-COOH 1 mM was added to stabilize the final particles. The solution was stored at 4 °C until further use. The designed mechanical stirrer was used during all the synthesis for mixing the reactants.

Polyelectrolyte solutions. for the preparation of PAH (+) and PSS(-), 100 mL of a solution 2 mg/mL of polyallylamine hydrochloride and poly (Sodium-4-styrenesulfonate) respectively in 0.5 M NaCl was prepared. Then, using a buffer solution, the pH was adjusted to 6.

PSAuNPs Synthesis. 50 μ L of PS beads (10% solids) were solved in 500 μ L of H₂O. To remove the stabilizing agents the samples were washed twice by centrifugation (14000 rpm-30 min).

Then, 500 μL of PE solution and 500 μL PS-Beads were added in a 1.5 mL Eppendorf under sonication for 2 min, then the sample was placed in a shaker for 20 min. Then particles were recovered by centrifugation and washed twice with 1 mL of water (8500 rpm-25 min). This procedure was repeated three times (PAH/PSS/PAH) to prepare the beads for the adsorption of negatively charged AuNP. 4nm AuNP were synthesized as reported in the experimental section of Chapter II. 5 mL of 4nm AuNP [Au]=0.1 mM were added under sonication for 2 min and then, the Eppendorf was placed in a shaker for 20 min. The particles then were washed twice with 1 mL of water and redispersed in 500 μL of water. The final gold concentration of PSAuNPs was analysed by ICP-MS.

PSAuNSs Synthesis. Typically, 10 μL of HAuCl_4 (0.129 M) were dissolved in 10mL of H_2O in a 20 mL glass vial. Then, 5 μL of HCl 1 M was added and immediately after, 35 μL of PSAuNPs was incorporated as seeds, the concentration of gold was [Au]=0.3 mM. Then, 350 μL of AgNO_3 (3 mM) and 50 μL of ascorbic acid (100 mM) were simultaneously and quickly added to the solution. A fast change from brown to blue indicates AuNS formation. Subsequently, 30 μL of HS-PEG-COOH (1 M) was added to stabilize the final particles. The particles were washed twice by centrifugation (2000 rpm-10 min) and redispersed in water. The solution was stored at 4 $^\circ\text{C}$ until further use. The final gold concentration of PSAuNS was analysed by ICP-MS.

AuNSs Synthesis. A seed mediated procedure was used for the synthesis of AuNSs¹⁹. Thus, 15 nm AuNPs were grown as AuNSs.

-Synthesis of 15 nm AuNPs. 95 mL of 0.5 mM HAuCl_4 was mixed under vigorous stirring and heated until boiling under vigorous stirring. Then 5 mL of 34 mM citrate solution was added. After 15 min of boiling, the solution was cooled down and stored at 4 $^\circ\text{C}$. The formation of Au seeds is evidenced by a change in the color solution from pale yellow to red.

-Synthesis of 230 nm AuNSs. 15 nm AuNPs (50 μL , [Au] = 0.5 mM) were added to 10 mL of water containing HAuCl_4 (50 μL , 50 mM) and HCl (10 μL , 1 M) followed by a simultaneous and fast addition of AgNO_3 (30 μL , 10 mM) and AA (50 μL , 100 mM). After 30 seconds, 100 μL , of PEG-SH 0.1 mM was added as a stabilizer for the AuNSs. The sample was centrifuged twice (3500 rpm, 30 min) and dispersed in water. The average diameter (230.6 ± 20.1 nm) was measured from TEM images.

SERS encoding and coating with PMA. The SERS encoding and the PMA encapsulation of the IOAuNSs, PSAuNSs and AuNSs were done following the previously reported protocol (See experimental section Chapter II).

3.7.3 Nanoparticles characterization

NPs standard characterization. All NPs were characterized using TEM, ICP-MS, and UV-Vis-NIR. TEM images were collected with a JEOL JEM-1400PLUS transmission electron microscope operating at 120 kV, using carbon-coated 400 square mesh Cu grids. ICP-MS analysis was conducted using an ICP-MS Agilent 7500ce to determine the concentration of Au and Fe. Samples

containing biological material (i.e. cells or spheroids) were digested in aqua regia during 48 h followed by addition of H₂O₂ and continued heating until a clear and transparent solution was observed. The samples were cooled down to RT and subsequently measured. UV-vis optical extinction spectra were recorded using an Agilent 8453 UV-Vis diode array spectrophotometer, normalizing spectra at 400 nm.

3.7.4 Photothermal heating experiments

Photothermal heating in solution. Photothermal measurements of nanomaterials in aqueous dispersion were performed in Eppendorf tubes (0.5 mL) containing 50 µL of the sample. Each sample was irradiated for 5 min from the top with a single mode NIR laser (808 nm) coupled to an optic fibre (Laser Components SAS, France) at 1 or 2.5 W/cm² and imaged with an infrared camera (FLIR SC7000) in order to measure the temperature increase. Triplicates were done for all the measurements for statistics.

SAR calculation. SAR was calculated as reported in previously studies¹⁶

The temperature elevation was measured as a function of time (dT/dt) at the initial linear slope (t = 30 s) to evaluate the heating effect in terms of SAR, power dissipation per unit mass of iron + gold (W/g). SAR was calculated using the following formula where m_{Fe+Au} is the total mass of iron and gold in the sample, m_i is the nanoparticle element mass, and C_i the specific heat capacity of the component i:

$$SAR = \sum \frac{m_i \cdot C_i}{m_{mFe+Au}} \frac{dT}{dt}$$

Since the mass of the heating element (IOAuNSs) is significantly lower than those of water (C_w = 4.18 J g⁻¹ K⁻¹, C_{cell} = 4.125 J g⁻¹ K⁻¹), the initial equation can be written as:

$$SAR = \sum \frac{m_w \cdot C_w}{m_{Au}} \frac{dT}{dt}$$

Cell preparation 2D. U-87 MG human glioblastoma cells (ATCC) were cultured in Dulbecco's Modified Eagle Medium (DMEM, Gibco) supplemented with 10% fetal bovine serum (Gibco) and 1% penicillin-streptomycin (Gibco) and grown at 37 °C in a humidified incubator with 5% CO₂. Then, the NPs resuspended in cell media were added at the desired concentration and left for incubation 24h. Afterwards, the media was changed to remove from the media the NPs that were not been internalized by the cells and fresh new media was added to the cells.

Cell viability. The AlamarBlue metabolic assay (DAL1100, Invitrogen) was used to control the cell viability. Briefly, following the vendor's protocol, AlamarBlue reagent was added to the 96-well plate containing the cells, after an incubation time of 2 h, the fluorescence was recorded in a EnSpire Multimode Plate Reader (PerkinElmer), using a fluorescence excitation and emission wavelength of 570 and 585 nm, respectively.

Spheroids formation. U87 glioblastoma cells were incubated with SA.3 [Au] = 0.1mM following the same protocol than before. After 24 h incubation, the U87 glioblastoma cells were detached (trypsin) and counted. A 3D printed stamp with micropillars of 200 μm diameter and 200 μm in height was used to print molds into the wells of a 96-well plate containing 50 μL of 2% agarose (AO576, Sigma Aldrich) in PBS. The agarose was then left to solidify between one and two minutes and the stamp was removed, leaving an array of molds in the wells. The 96-well plate was then sterilized in UV light for 30 min before cell seeding (15000 cells per well) and centrifugation. Cells were allowed to mature for 48 h before photothermal irradiation. Imaging was performed on an EnSight Multimode Microplate Reader (Perkin Elmer), and ImageJ software was used for processing the acquired images and for fluorescence quantification.

Photothermal heating in 2D. Photothermal measurements of cells incubated with NPs were performed in a 96-well-plate containing 100 μL of the solution of cells + NPs. Each sample was irradiated during 5 min from the top with a single mode NIR laser (808 nm) coupled to an optic fiber (Laser Components SAS, France) at 1 and 2 W/cm^2 . The cell viability was checked using AlamarBlue assay. As shown in **Figure 3.17**, triplicates were done for all the experiments and an empty well was left between samples to avoid that the laser arrives the adjacent well while irradiating.

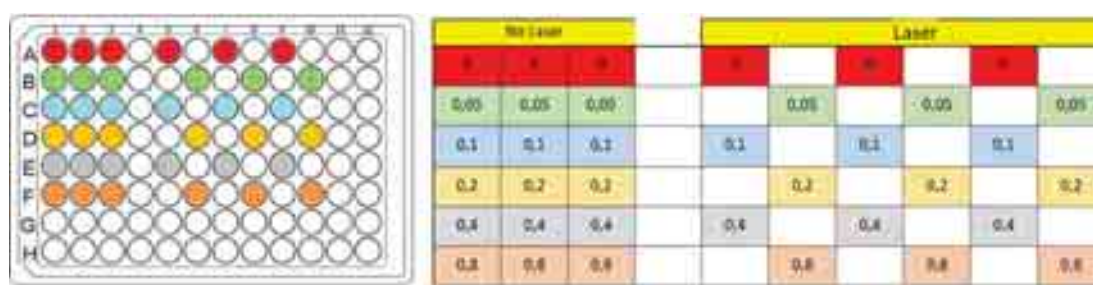


Figure 3.17. Schematic representation of the distribution of the samples and the controls in a 96-well plate for the photothermal experiments in 2D.

Photothermal heating in 3D. Photothermal measurements of 3D spheroids incubated with IOAuNSs were performed in a 96-well-plate containing the spheroids. Each sample was irradiated for 3 min from the top with a single mode NIR laser (808 nm) coupled to an optic fibre (Laser Components SAS, France) at power densities that ranged from 0.5 to 2 W/cm^2 . The viability of the spheroids was done using live/dead cell images.

Live/dead staining and visualization. The Live/dead Cell Imaging Kit (R37601, Invitrogen) was used to check the cell viability in spheroids. Following the protocol, spheroids at day 3 of maturation were stained with Live Green/Dead Red staining solution in non-adherent dishes for 2 h at 37 $^{\circ}\text{C}$ in a humidified incubator with 5% CO_2 . Then, the staining solution was removed and the spheroids were imaged using an Olympus IX81F-3 inverted microscope (Olympus) coupled with a laser dual spinning disc unit (Yokogawa CSU-X1) and an Andor iXonEM + CDD camera (Andor Technology), with a 10x objective. Images were processed using ImageJ.

References

- (1) Hwang, S.; Nam, J.; Jung, S.; Song, J.; Doh, H.; Kim, S. Gold Nanoparticle-Mediated Photothermal Therapy: Current Status and Future Perspective. *Nanomedicine* **2014**, *9*(13), 2003–2022. <https://doi.org/10.2217/nnm.14.147>.
- (2) Pissuwan, D.; Valenzuela, S. M.; Cortie, M. B. Therapeutic Possibilities of Plasmonically Heated Gold Nanoparticles. *Trends Biotechnol.* **2006**, *24* (2), 62–67. <https://doi.org/10.1016/j.tibtech.2005.12.004>.
- (3) Zou, L.; Wang, H.; He, B.; Zeng, L.; Tan, T.; Cao, H.; He, X.; Zhang, Z.; Guo, S.; Li, Y. Current Approaches of Photothermal Therapy in Treating Cancer Metastasis with Nanotherapeutics. *Theranostics* **2016**, *6* (6), 762–772. <https://doi.org/10.7150/thno.14988>.
- (4) Lv, Z.; He, S.; Wang, Y.; Zhu, X. Noble Metal Nanomaterials for NIR-Triggered Photothermal Therapy in Cancer. *Adv. Healthc. Mater.* **2021**, *10* (6), 2001806. <https://doi.org/10.1002/adhm.202001806>.
- (5) Link, S.; El-Sayed, M. A. *Shape and Size Dependence of Radiative, Non-Radiative and Photothermal Properties of Gold Nanocrystals*, 2000; Vol. 19. <https://doi.org/10.1080/01442350050034180>.
- (6) Webb, J. A.; Bardhan, R. Emerging Advances in Nanomedicine with Engineered Gold Nanostructures. *Nanoscale* **2014**, *6* (5), 2502–2530. <https://doi.org/10.1039/c3nr05112a>.
- (7) Jimenez de Aberasturi, D.; Serrano-Montes, A. B.; Liz-Marzán, L. M. Modern Applications of Plasmonic Nanoparticles: From Energy to Health. *Adv. Opt. Mater.* **2015**, *3* (5), 602–617. <https://doi.org/10.1002/adom.201500053>.
- (8) Khlebtsov, B.; Zharov, V.; Melnikov, A.; Tuchin, V.; Khlebtsov, N. Optical Amplification of Photothermal Therapy with Gold Nanoparticles and Nanoclusters. *Nanotechnology* **2006**, *17*(20), 5167–5179. <https://doi.org/10.1088/0957-4484/17/20/022>.
- (9) Trigari, S.; Rindi, A.; Margheri, G.; Sottini, S.; Dellepiane, G.; Giorgetti, E. Synthesis and Modelling of Gold Nanostars with Tunable Morphology and Extinction Spectrum. *J. Mater. Chem.* **2011**, *21* (18), 6531–6540. <https://doi.org/10.1039/c0jm04519e>.
- (10) Tsai, M. F.; Chang, S. H. G.; Cheng, F. Y.; Shanmugam, V.; Cheng, Y. S.; Su, C. H.; Yeh, C. S. Au Nanorod Design as Light-Absorber in the First and Second Biological near-Infrared Windows for in Vivo Photothermal Therapy. *ACS Nano* **2013**, *7* (6), 5330–5342. <https://doi.org/10.1021/nn401187c>.
- (11) Morales-Dalmau, J.; Vilches, C.; De Miguel, I.; Sanz, V.; Quidant, R. Optimum Morphology of Gold Nanorods for Light-Induced Hyperthermia. *Nanoscale* **2018**, *10* (5), 2632–2638. <https://doi.org/10.1039/c7nr06825e>.
- (12) Yang, W.; Liang, H.; Ma, S.; Wang, D.; Huang, J. Gold Nanoparticle Based Photothermal Therapy: Development and Application for Effective Cancer Treatment. *Sustain. Mater. Technol.* **2019**, *22*, e00109. <https://doi.org/10.1016/j.susmat.2019.e00109>.
- (13) Xiao, Z.; Zhang, Q.; Guo, X.; Villanova, J.; Hu, Y.; Külaots, I.; Garcia-Rojas, D.; Guo, W.;

- Colvin, V. L. Libraries of Uniform Magnetic Multicore Nanoparticles with Tunable Dimensions for Biomedical and Photonic Applications. *ACS Appl. Mater. Interfaces* **2020**, *12* (37), 41932–41941. <https://doi.org/10.1021/acscami.0c09778>.
- (14) Jana, N. R.; Gearheart, L.; Murphy, C. J. Seeding Growth for Size Control of 5-40 Nm Diameter Gold Nanoparticles. *Langmuir* **2001**, *17* (22), 6782–6786. <https://doi.org/10.1021/la0104323>.
- (15) Kim, M.; Lee, J. H.; Nam, J. M. Plasmonic Photothermal Nanoparticles for Biomedical Applications. *Adv. Sci.* **2019**, *6* (17), 1900471. <https://doi.org/10.1002/advs.201900471>.
- (16) Espinosa, A.; Kolosnjaj-Tabi, J.; Abou-Hassan, A.; Plan Sangnier, A.; Curcio, A.; Silva, A. K. A.; Di Corato, R.; Neveu, S.; Pellegrino, T.; Liz-Marzán, L. M.; Wilhelm, C. Magnetic (Hyper)Thermia or Photothermia? Progressive Comparison of Iron Oxide and Gold Nanoparticles Heating in Water, in Cells, and in Vivo. *Adv. Funct. Mater.* **2018**, *28* (37), 1803660. <https://doi.org/10.1002/adfm.201803660>.
- (17) Espinosa, A.; Silva, A. K. A.; Sánchez-Iglesias, A.; Grzelczak, M.; Péchoux, C.; Desboeufs, K.; Liz-Marzán, L. M.; Wilhelm, C. Cancer Cell Internalization of Gold Nanostars Impacts Their Photothermal Efficiency In Vitro and In Vivo: Toward a Plasmonic Thermal Fingerprint in Tumoral Environment. *Adv. Healthc. Mater.* **2016**, *5* (9), 1040–1048. <https://doi.org/10.1002/adhm.201501035>.
- (18) Espinosa, A.; Reguera, J.; Curcio, A.; Muñoz-Noval, Á.; Kuttner, C.; Van de Walle, A.; Liz-Marzán, L. M.; Wilhelm, C. Janus Magnetic-Plasmonic Nanoparticles for Magnetically Guided and Thermally Activated Cancer Therapy. *Small* **2020**, *16* (11), 1904960. <https://doi.org/10.1002/sml.201904960>.
- (19) Vanrompay, H.; Bladt, E.; Albrecht, W.; Béché, A.; Zakhosheva, M.; Sánchez-Iglesias, A.; Liz-Marzán, L. M.; Bals, S. 3D Characterization of Heat-Induced Morphological Changes of Au Nanostars by Fast: In Situ Electron Tomography. *Nanoscale* **2018**, *10* (48), 22792–22801. <https://doi.org/10.1039/c8nr08376b>.

Chapter IV



4. Synthesis of hybrid core-shell nanoparticles for hyperthermia

Contents

| | |
|---|-----|
| 4.1 Introduction..... | 148 |
| 4.2 Synthesis of hybrid nanoparticles: <i>a new approach</i> | 149 |
| 4.2.1 Silica@iron oxide nanoparticles | 149 |
| 4.2.2 Gold nanorods@silica@iron oxide nanoparticles | 152 |
| 4.2.2.1 The golden core: Synthesis of gold nanorods | 152 |
| 4.2.2.2 Synthesis of silica-coated gold nanorods | 153 |
| 4.2.2.3 Growth of iron oxide on gold nanorod@silica nanoparticles | 154 |
| 4.2.2.4 Biocompatibility | 155 |
| 4.2.2.5 Characterization | 156 |
| 4.2.2.6 Fast magnetic separation | 157 |
| 4.3 Photothermal characterization of hybrid nanoparticles..... | 157 |
| 4.4 Hyperthermia in 2D cell cultures | 160 |
| 4.5 Hyperthermia in 3D cell cultures | 162 |
| 4.6 Selective hyperthermia through cell targeting..... | 163 |
| 4.6.1 Functionalization with antibodies | 163 |
| 4.7 Conclusions | 164 |
| 4.8 Experimental Section | 165 |
| 4.8.1 Materials | 165 |
| 4.8.2 Nanoparticle synthesis..... | 166 |
| 4.8.3 Functionalization | 168 |
| 4.8.4 Nanoparticles characterization | 168 |
| 4.8.5 Cell culture..... | 170 |
| 4.8.6 Hyperthermia | 171 |
| References | 173 |

4.1 Introduction

In this chapter, a novel approach to the synthesis of hybrid magnetic-plasmonic nanoparticles is presented. In Chapter II multicore IONPs were coated by a spiky gold shell to obtain hybrid IOAuNPs with magnetic and plasmonic properties, and eventually functionalized with RAR molecules and fluorescent dyes for multimodal bioimaging and photothermal heating. In the actual Chapter IV, we proposed different combination of the gold and iron oxide components with the objective of achieving optimal conditions for hyperthermia and improved magnetic properties for fast magnetic separation in solution. As explained in Chapter III, therapeutic hyperthermia conditions are reached at temperatures above 42 °C. To obtain the best heating performance, ideally the maximum plasmon band position should be close to the incident light wavelength. However, even if IOAuNSs presented nice PTH performance, they showed broad plasmon bands without a well-defined maximum. Therefore, herein we have chosen AuNRs as cores for our hybrid system that in comparison with the IOAuNSs described in Chapter III, present sharper LSPR absorbance bands in the NIR, at wavelengths that can be tailored through their aspect ratio and can fit with the irradiation laser wavelength at 808 nm^{1,2}. Moreover, AuNRs have been already reported to show excellent PTH performance with high biocompatibility³. Therefore, the aim of this chapter is to improve the light-to-heat conversion for PTH, trying to optimize and improve the performance of the hybrid systems by reducing either the concentration of NPs or the applied power density.

On the other hand, magnetic separation is an effective method for the sensitive and reliable capture of specific biomolecules. This technique, which consists of the use of a magnetic gradient to separate, sort and/or label cells, proteins and other molecules⁴⁻⁶, has been widely used for water purification, sensing and biological analysis^{7,8}. The process involves two-steps, first labelling the chosen biological entity with a magnetic material and then, separation of these targeted moieties using magnets. In this novel system, IONPs were grown by a thermal decomposition process on the outer part of the hybrid NPs, thereby achieving a high magnetic response. Indeed, successive thermal decomposition steps allowed us to increase the density and size of the obtained IONPs. Therefore, magnetic shells with improved magnetic response, in comparison with IOAuNSs, were obtained, which can be used for fast magnetic separation of specific molecules or malignant cells such as circulating tumour cells.

Specifically, for the fabrication of these hybrid structures we first synthesized AuNRs by means of a seeded-growth method,⁹ which would serve as the cores for hybrid NPs. The AuNRs were subsequently covered with mesoporous silica,¹⁰ which provided stability and silanol groups at the outer surface that could be used for further functionalization. Then, the magnetic component was deposited by directly growing IONPs onto the silica shells, using thermal decomposition steps of organometallic iron precursors¹¹. This step of the synthesis was optimized to control the density of IONPs grown on the silica surface, through the number of thermal decomposition steps. A schematic representation of the NPs obtained at each synthetic step is provided in **Figure 4.1**.



Figure 4.1. Schematic representation of the NPs obtained at each synthetic step. In this process, AuNRs were synthesized, covered by mesoporous silica (AuNR@SiO₂) and IONPs were finally grown onto the silica shell to obtain AuNR@SiO₂@IONPs.

The application of these hybrid NPs as nanoheaters for PTH was studied as previously described in chapter III, using both 2D and 3D cell models. Additionally, the hybrid NPs were functionalized with antibodies (CD44+) to implement selective binding onto a target cell type for specific PTH treatment^{12,13}. In our study, an antibody selective for the CD44 antigen was selected because this cell-surface glycoprotein is involved in a wide range of biological processes such as cell-cell interactions, cell adhesion, migration and thus, is related to tumour metastasis¹⁴. Additionally, we aimed for magnetic separation of the cells that have been labelled with magnetic NPs using an external magnetic field for accurate cell discrimination and specific irradiation to induce cell death.

4.2 Synthesis of hybrid nanoparticles: *a new approach*

In this section, we discuss in detail the synthesis of hybrid nanostructures following the new method introduced above. The various steps involved in the process were optimized to obtain NPs with the desired optical and magnetic properties. The characterization of the NPs at each synthetic step was performed in collaboration with the Electron microscopy for Materials Science group led by Prof. Sara Bals at the University of Antwerp (Belgium).

4.2.1 Silica@iron oxide nanoparticles

For a simpler optimization of the process, the deposition of IONPs was first performed and optimized on the surface of pure SiO₂ NPs. Therefore, mesoporous silica particles with diameters of 150 and 240 nm were synthesized by a modified Stöber method, according to the protocol reported by Sanz-Ortiz *et al.*¹⁰. Then, IONPs were directly grown on the surface of the SiO₂ NPs by means of a protocol for the thermal decomposition of iron oleate, as reported by Nistler *et al.*⁹. A schematic representation of the process is shown in **Figure 4.2**.

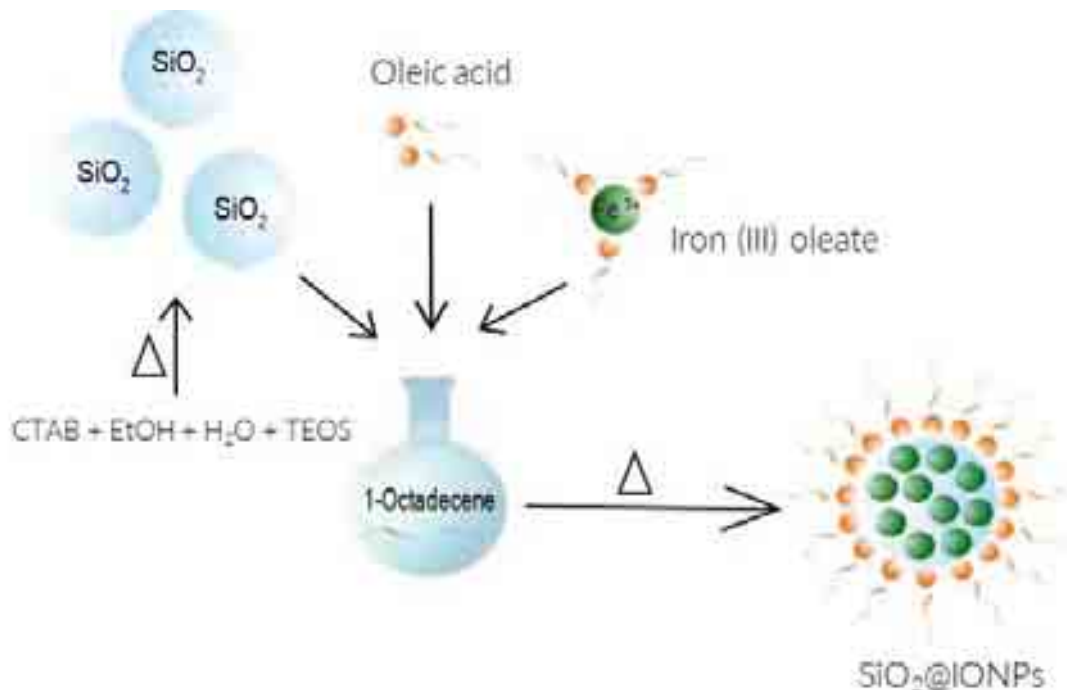


Figure 4.2. Schematic representation of the synthesis of SiO₂@IONPs.

Briefly, 100 mg of mesoporous silica particles was dispersed in 3 mL of ethanol, placed in a round bottom flask and then mixed with 3 g of iron (III) oleate dispersed in 21 mL of 1-octadecene. Afterwards, oleic acid, which acts as a stabilizing agent, was added and the mixture was heated at a controlled rate for 30 min, during which time the iron oleate decomposed, forming IONPs. To obtain the final product, the reaction mixture was centrifuged to separate the decorated SiO₂@IONPs from free IONPs in the reaction medium.

The coverage of SiO₂ particles by IONPs can be controlled through the number of thermal decomposition steps. Up to five steps were performed and the obtained SiO₂@IONPs were characterized by TEM (Figure 4.3). It can be observed that the density and the size of IONPs on the SiO₂ surface increased gradually from the first to the fifth step, for SiO₂ NPs of both sizes.

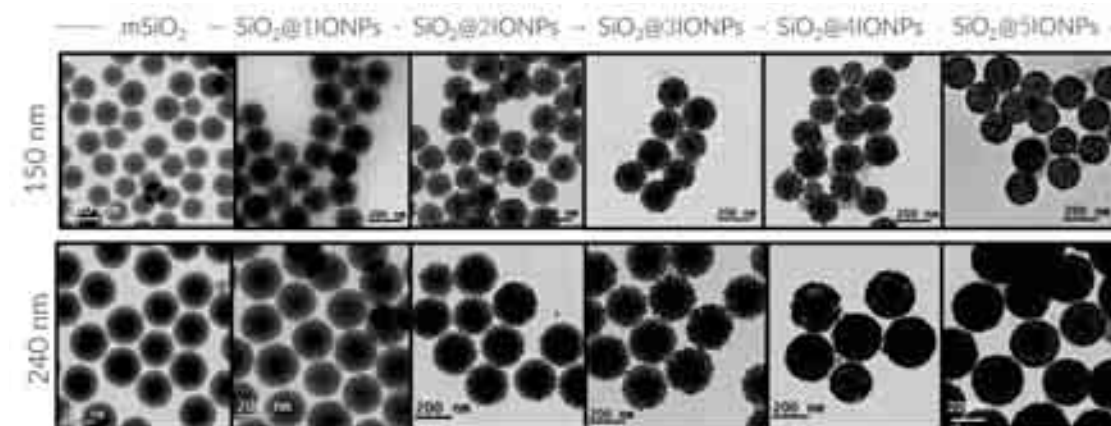


Figure 4.3. TEM images of 150 and 240 nm SiO₂@IONPs after subsequent thermal decomposition steps. The number in green indicates the number of thermal decomposition steps for each sample. An increasing density and size of IONPs at the SiO₂ surface can be observed from step 1 to step 5. The initial SiO₂ NPs are also shown as a reference in the left part of the figure.

The magnetic properties of the obtained hybrid NPs are provided by the outer IONPs. The 150 nm SiO₂ NPs were selected for the study of the magnetic properties due to their higher surface area in comparison with the 240 nm SiO₂ NPs. To study the magnetic properties of the hybrid system, a hysteresis loop as well as ZFC/FC steps of representative SiO₂@IONPs NPs were recorded and the results are shown in **Figure 4.4**. In order to confirm that IONPs were nucleating and growing as NPs on top of the silica shell, we first measured the magnetic properties of the SiO₂@1IONPs. The hysteresis loop (M(H)) (**Figure 4.4A**) showed a saturation magnetization of 75 emu/g, in agreement with values reported in the literature for IONPs²⁰. The results suggested a superparamagnetic behaviour for the SiO₂@1IONPs, with low remanence and coercivity, which was confirmed by the ZFC/FC curves (**Figure 4.4B**). The blocking temperature, estimated as the point where the ZFC curve exhibits an apex, was determined to be T_B = 100 K. Analysis of the normalized magnetization M/M_s (H) at 300 K according to the Langevin model²¹ (see Experimental section) and fitting of ZFC/FC measurements yield both a size distribution centred around 10 nm for the first grown IONPs. For SiO₂@4IONPs, when the silica shell seems to be fully covered, ZFC/FC curves were also measured (**Figure 4.4C**). The blocking temperature was in this case shifted from T_B = 100 K to T_B = 225 K. The fitting of the ZFC/FC measurements was performed using the same parameters (magnetization, thermal dependence etc.) as for the first growth sample to make them comparable. The size distribution in this case was around 15 nm, which confirms NP growth as can be seen by TEM (**Figure 4.5**) and also in agreement with sizes measured by HRSTEM (**Figure 4.5**), which show a more precise value of 19.5 nm.

Additionally, the ZFC curve indicated that the synthesized IONPs were made of maghemite (Fe₂O₃), due to the absence of a hump near 110 K, which is known to be a peculiar metal-insulator transition in Fe₃O₄²².

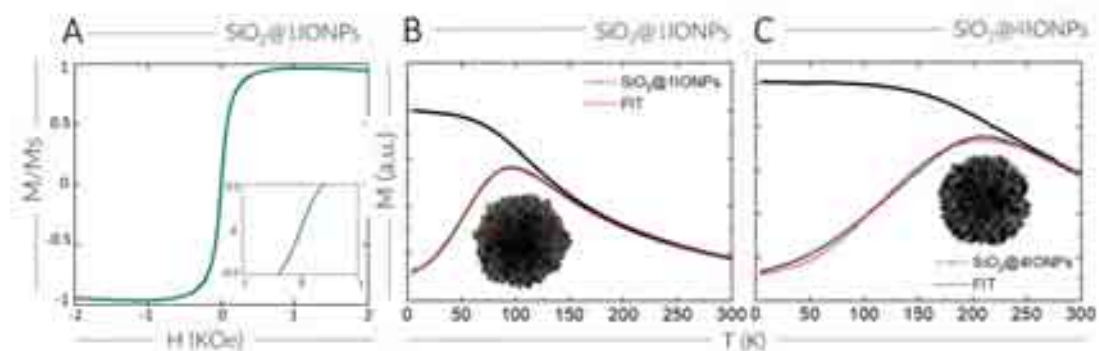


Figure 4.4. (A) Hysteresis loop for SiO₂@1IONPs. (B) ZFC/FC curves and TEM image for SiO₂@1IONPs and (C) SiO₂@4IONPs and TEM image of a single NP. The difference in the size and density of the IONPs can be noted.

Additional characterization including HAADF-STEM, HRSTEM and electron diffraction was performed for SiO₂@4IONPs. The results in **Figure 4.5A** show the structure of SiO₂@4IONPs with IONPs observed around the silica surface. Additionally, an orthoslice from a 3D electron tomography reconstruction showed that single IONPs were not nucleating nor growing inside the

pores of the SiO₂ NPs but at the surface (Figure 4.5B). HRSTEM images confirmed an average size of the IONPs around 19.4 nm (Figure 4.5C).

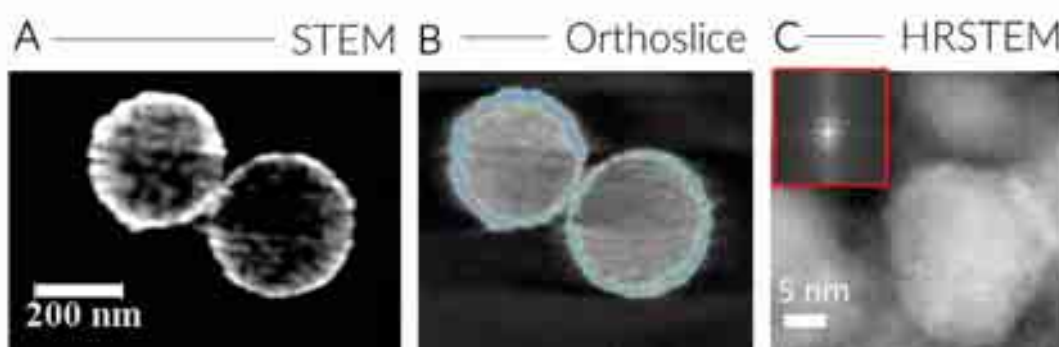


Figure 4.5. (A) HAADF-STEM image of SiO₂@4IONPs. (B) Orthoslice of a 3D electron tomography reconstruction of SiO₂@4IONPs; the area in blue indicates the IONPs. (C) HRSTEM image of IONPs grown around the silica surface and electron diffraction analysis showing the crystallographic structure of the IONPs (red box).

4.2.2 Gold nanorods@silica@iron oxide nanoparticles

Once the growth of IONPs onto silica particles was optimized, the method was implemented for hybrid NPs including AuNRs as plasmonic cores, for improved PTH.

4.2.2.1 The golden core: Synthesis of gold nanorods

AuNRs were synthesized using a seed-mediated method⁹. Briefly, AuNRs of 21 nm in length and 7.5 nm in width with a longitudinal LSPR band located at 725-730 nm were first synthesized and subsequently used as seeds for further overgrowth into AuNRs of 66.5 ± 5.7 nm in length and 16.4 ± 2.7 nm in width. The obtained AuNRs showed a maximum in absorbance at 790 nm. The particles were finally purified by centrifugation and redispersion in a 2 mM CTAB solution. The normalized UV-Vis spectra and a representative TEM image of the AuNRs are shown in Figure 4.6. Well-dispersed AuNRs were obtained, indicating that there was no aggregation in solution.

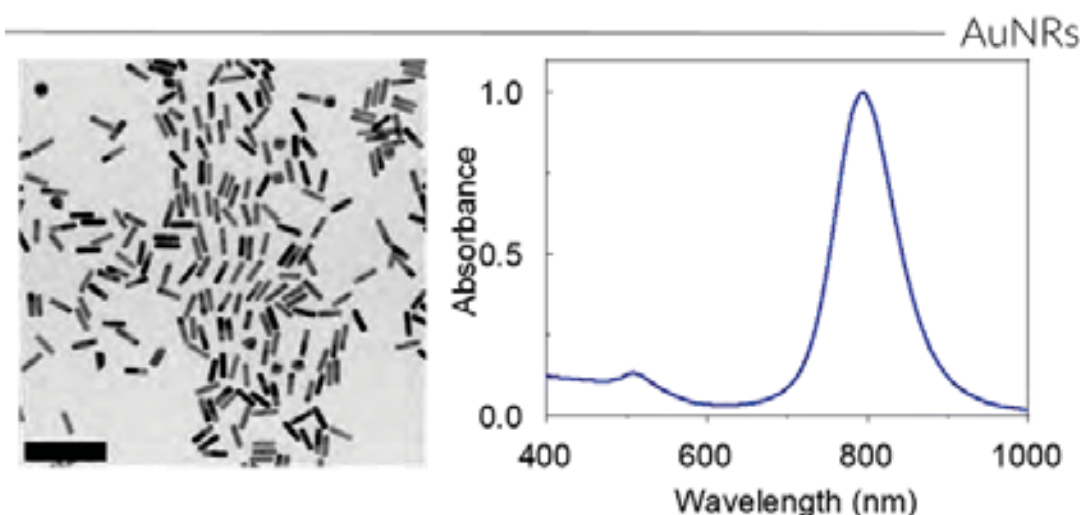


Figure 4.6. TEM image and normalized (at the LSPR maximum) UV-Vis spectrum of AuNRs. The scale bar corresponds to 200 nm.

4.2.2.2 Synthesis of silica-coated gold nanorods

Afterwards, the AuNRs were coated by a mesoporous silica shell. For the coating of AuNRs, a previously published protocol was used¹⁰. Briefly, a colloidal dispersion containing AuNRs, CTAB, ethanol, and water was prepared. After adjusting the pH to 9 by addition of aqueous ammonia, 200 μL of tetraethyl orthosilicate (TEOS) were added dropwise under strong stirring to trigger the silica formation through hydrolysis and condensation. After TEOS addition, the temperature was increased to 60 $^{\circ}\text{C}$ and the mixture was stirred for three days. Then, the particles were recovered by centrifugation and thoroughly washed with ethanol and diluted HCl, to remove the surfactant (CTAB). Normalized UV-vis spectra and a TEM image of AuNR@SiO₂ are shown in **Figure 4.7**. The TEM image shows that the AuNRs were uniformly encapsulated by a silica shell with a thickness of 70.8 ± 8.2 nm, while the UV-Vis spectrum showed no changes in the shape and peak position of the longitudinal LSPR, compared to uncoated AuNRs (blue spectrum in **Figure 4.7**). Therefore, the AuNRs are not found to be optically affected by the silica coating process.

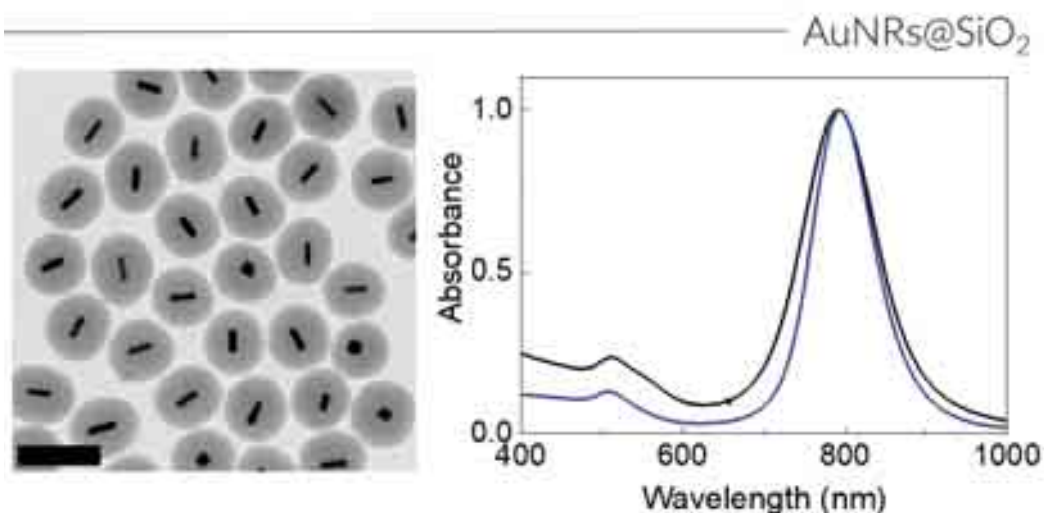


Figure 4.7. TEM image and normalized (at the LSPR maximum) UV-Vis spectra of AuNRs@SiO₂ (black) and uncoated AuNRs (blue). The scale bar corresponds to 200 nm.

4.2.2.3 Growth of iron oxide nanoparticles on gold nanorods@silica nanoparticles

For the growth of IONPs on top of AuNRs@SiO₂, the optimized protocol developed for SiO₂ NPs was used. Briefly, AuNRs@SiO₂ NPs were added to a mixture of oleic acid, 1-octadecene and iron (III) oleate, which then was decomposed by a controlled increase of temperature, to obtain AuNRs@SiO₂@IONPs, which were then recovered and washed *via* centrifugation. A schematic illustration of the full synthetic process is shown in **Figure 4.8**.

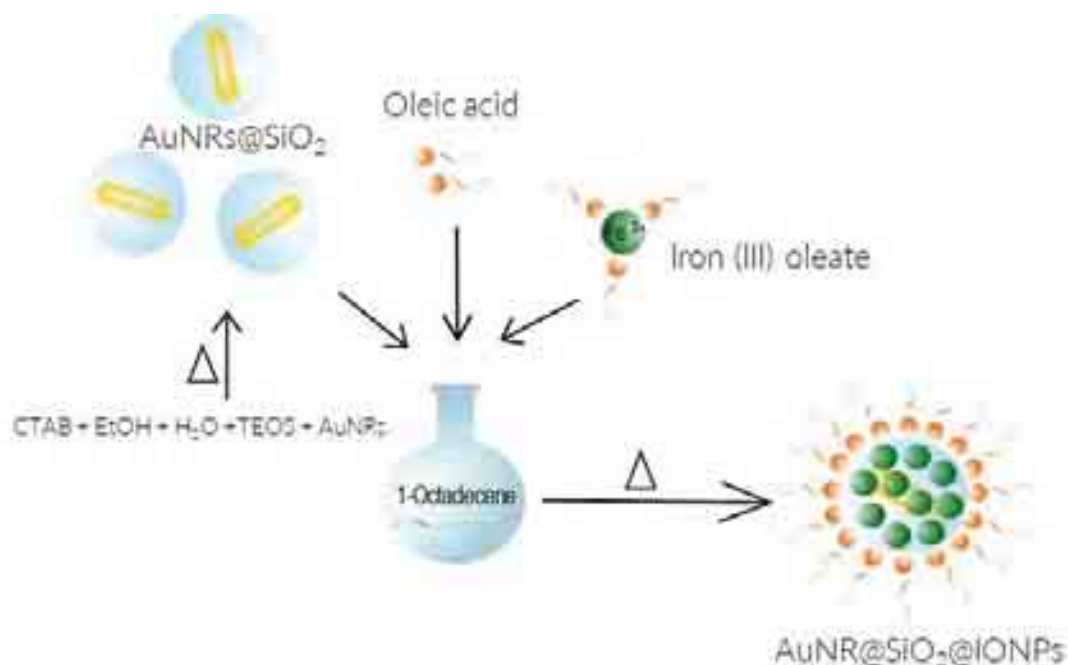


Figure 4.8. Schematic representation of the synthesis of AuNRs@SiO₂@IONPs

Since the first step resulted in a poor surface coverage, the decomposition procedure was repeated up to three times, yielding densely covered hybrid NPs. The number of steps was reduced from five, performed for SiO₂ NPs, to three decomposition steps of 30 min because

enough density of IONPs was achieved after these steps. Thus, homogeneous and fully covered AuNRs@SiO₂@IONPs were obtained and characterized by TEM and UV-vis spectroscopy (Figure 4.9).

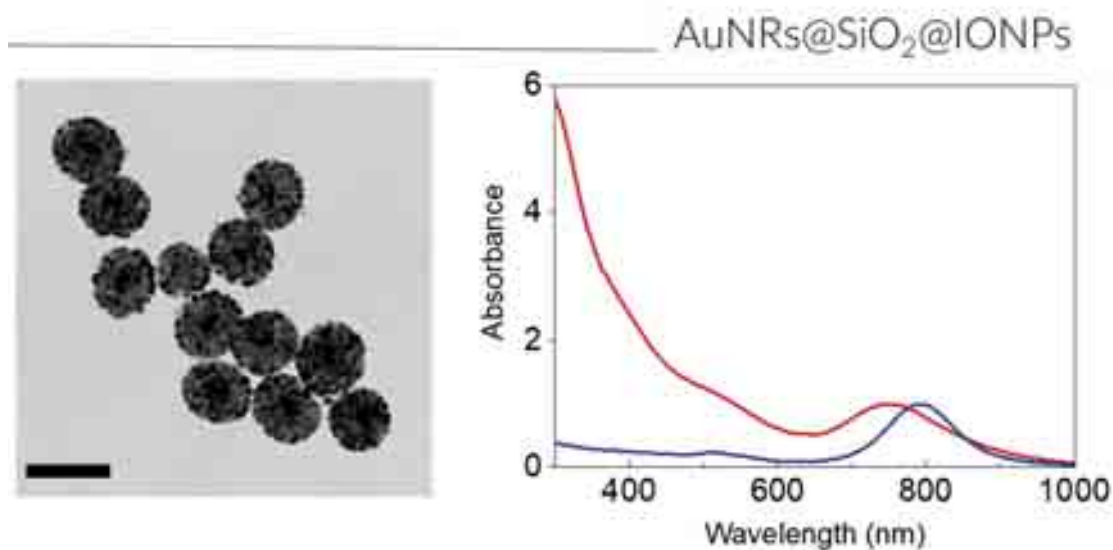


Figure 4.9. Representative TEM image and normalized UV-Vis spectra of the obtained AuNRs@SiO₂@IONPs (red) and AuNRs@SiO₂ as a control (blue).

When comparing the UV-vis spectra of AuNRs or AuNRs@SiO₂ (Figure 4.8) with AuNRs@SiO₂@IONPs (Figure 4.9) a blue shift of the longitudinal LSPR band from 790 to 760 nm can be observed. This shift may result from a partial thermal reshaping of AuNRs during the decomposition steps due to the high temperature employed²³, into a less anisotropic shape²⁴. After this effect was observed, the steps were reduced to three, which was the minimum number of decomposition steps yielding fully covered AuNRs@SiO₂. The effect on the particle size becomes also apparent when comparing AuNRs measured directly from TEM images. The initial AuNRs (Figure 4.6) appeared longer (66.5 ± 5.7 nm in length and 16.4 ± 2.7 nm in width) than the final AuNRs (Figure 4.9), which were shorter and thicker (58.3 ± 5.1 nm in length and 15.1 ± 2.4 nm in width). However, the two characteristic plasmon bands (the longitudinal and the less prominent transversal band at roughly 520 nm) are still clearly seen, as well as a higher background produced by the contribution of the IONPs, which appears as a broad shoulder²⁵.

4.2.2.4 Biocompatibility

For their use in biomedical environments, NPs must be stable in aqueous media. Therefore, transfer of the obtained AuNRs@SiO₂@IONPs (covered by oleic acid) into water required encapsulation with PMA, using the same strategy as described in Chapters II and III.

Functionalization with PMA was thus performed for both AuNRs@SiO₂@IONPs and SiO₂@IONPs, which were also functionalized for use as controls in future experiments. By contrast, AuNRs@SiO₂, also used as a control in applications, were already soluble in polar solvents after synthesis. These NPs were functionalized with a PEG-silane of a similar size as PMA, to enhance their stability and to mimic the coating of AuNRs@SiO₂@IONPs. These coatings allowed us to

study the hybrid NPs and their controls (AuNRs@SiO₂ and SiO₂@IONPs) under similar conditions, ensuring that changes in their properties are not due to different coatings.

4.2.2.5 Characterization

A thorough characterization of the hybrid system was carried out. HAADF-STEM and EDX analysis were performed to achieve information of Au, Silica (Si), and Fe components. As can be seen in **Figure 4.10A**, AuNRs are still located inside the silica shell after the thermal decomposition procedure and IONPs are surrounding the silica shell. Furthermore, Si, Au and Fe were analysed by EDX to confirm the morphology and distribution of all the components within the hybrid NPs. (**Figure 4.10B**).

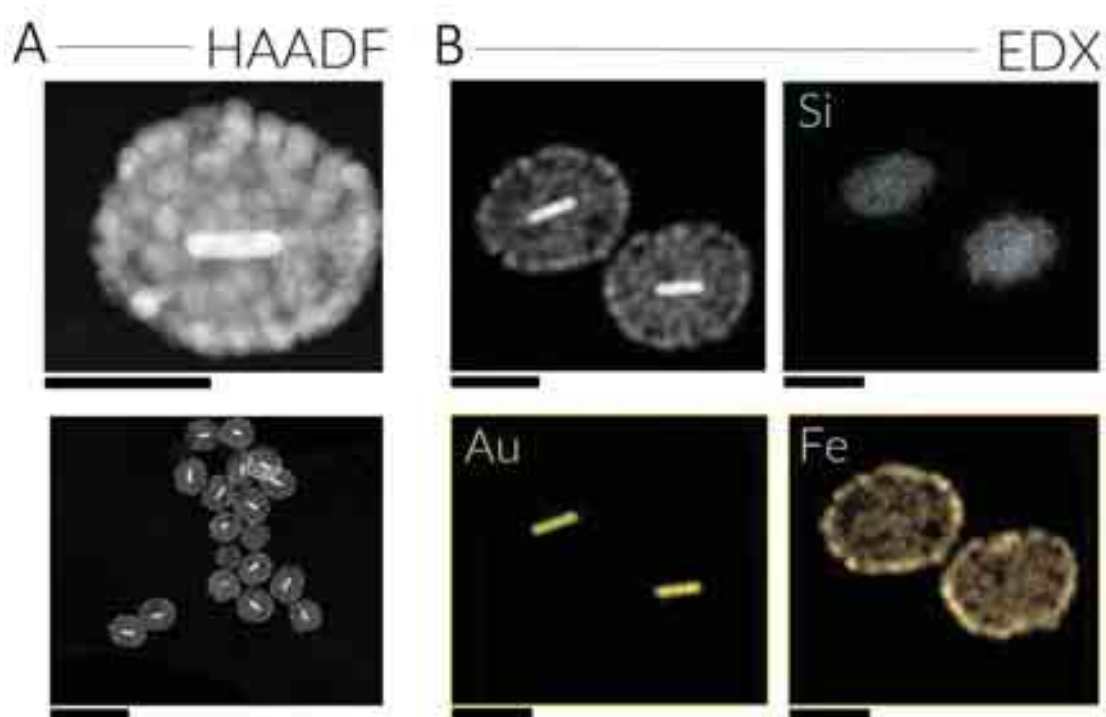


Figure 4.10. (A) HAADF-STEM images of AuNRs@SiO₂@IONPs. (B) EDX mapping of AuNRs@SiO₂@IONPs showing the distribution of Au, Fe and Si within the hybrid NPs. Scale bars correspond to 100 nm.

The final NPs were also characterized to acquire information about the magnetic properties of the hybrid system. The corresponding hysteresis loop and the ZFC/FC curves were therefore recorded (**Figure 4.11**), and again the hysteresis loop revealed superparamagnetic behaviour of the AuNRs@SiO₂@IONPs at room temperature with no remanence and low coercivity (**Figure 4.11A**). Besides, the ZFC/FC step showed a blocking temperature of 250 K, similar to the blocking temperature obtained for the SiO₂@IONPs (**Figure 4.4C**).

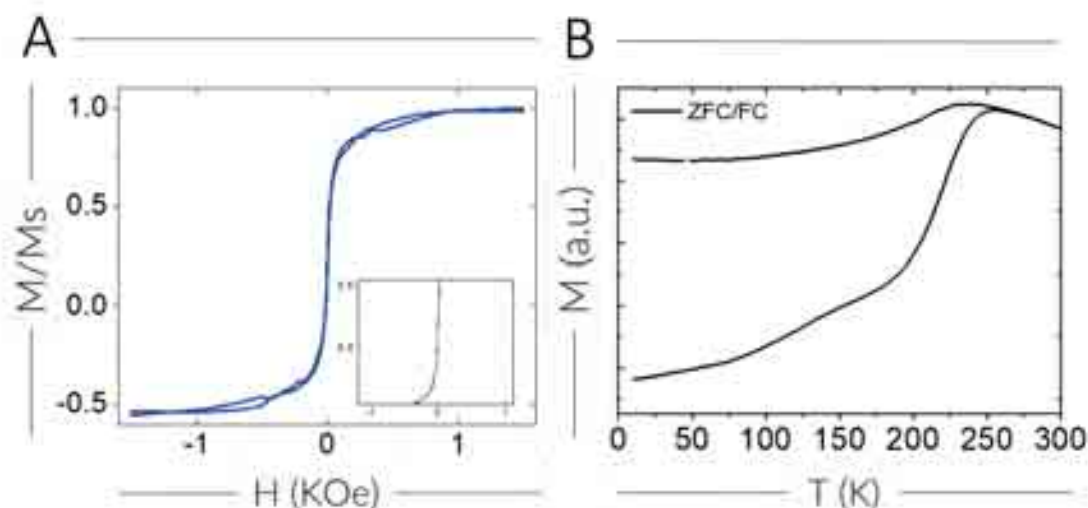


Figure 4.11. (A) Hysteresis loop and (B) ZFC/FC curves for AuNRs@SiO₂@IONPs.

4.2.2.6 Fast magnetic separation

The response of the AuNRs@SiO₂@IONPs to an external magnetic field can be used for fast separation. This magnetic behaviour was characterized using a simple setup schematically shown in Figure 4.12.

A dispersion of AuNRs@SiO₂@IONPs was placed in a plastic vial and then, a permanent magnet was attached to the side. After 20 s the particles were magnetically separated and remained concentrated in a pellet. After removing the magnet, the NPs could be redispersed again in water and remained stable. The separation process could be repeated for the desired number of times.

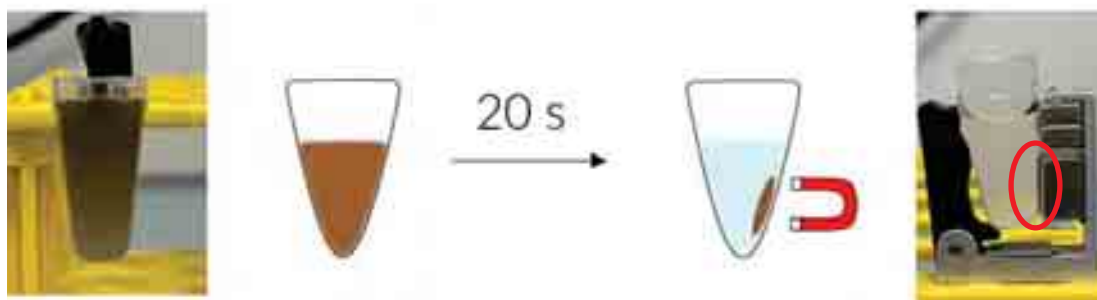


Figure 4.12. Schematic representation and real pictures showing magnetic separation. The AuNRs@SiO₂@IONPs aqueous dispersion was placed in a plastic vial (left) and a permanent magnet was placed on the side of the vial. The AuNRs@SiO₂@IONPs were magnetically separated and concentrated into a brown pellet (right).

4.3 Photothermal characterization of hybrid nanoparticles

The photothermal characterization of the NPs was carried out using an 808 nm laser. The samples were irradiated in solution for 5 min with a power density of 2.5 W/cm². As in Chapter III, AuNRs@SiO₂@IONPs in solution at different concentrations were irradiated and the temperature increase was registered using a thermal camera focused on the ROI; the temperature change was

first measured and then the corresponding temperature increment was calculated by subtracting the initial temperature (time = 0) from the final temperature (time = 5 min) (Figure 4.13A). Likewise, AuNRs@SiO₂ (Figure 4.13B) and SiO₂@4IONPs (Figure 4.13C) were also measured as controls. The SAR for the final NPs and the controls were calculated as previously reported in Chapter III, and the results are shown in the right part of Figure 4.13.

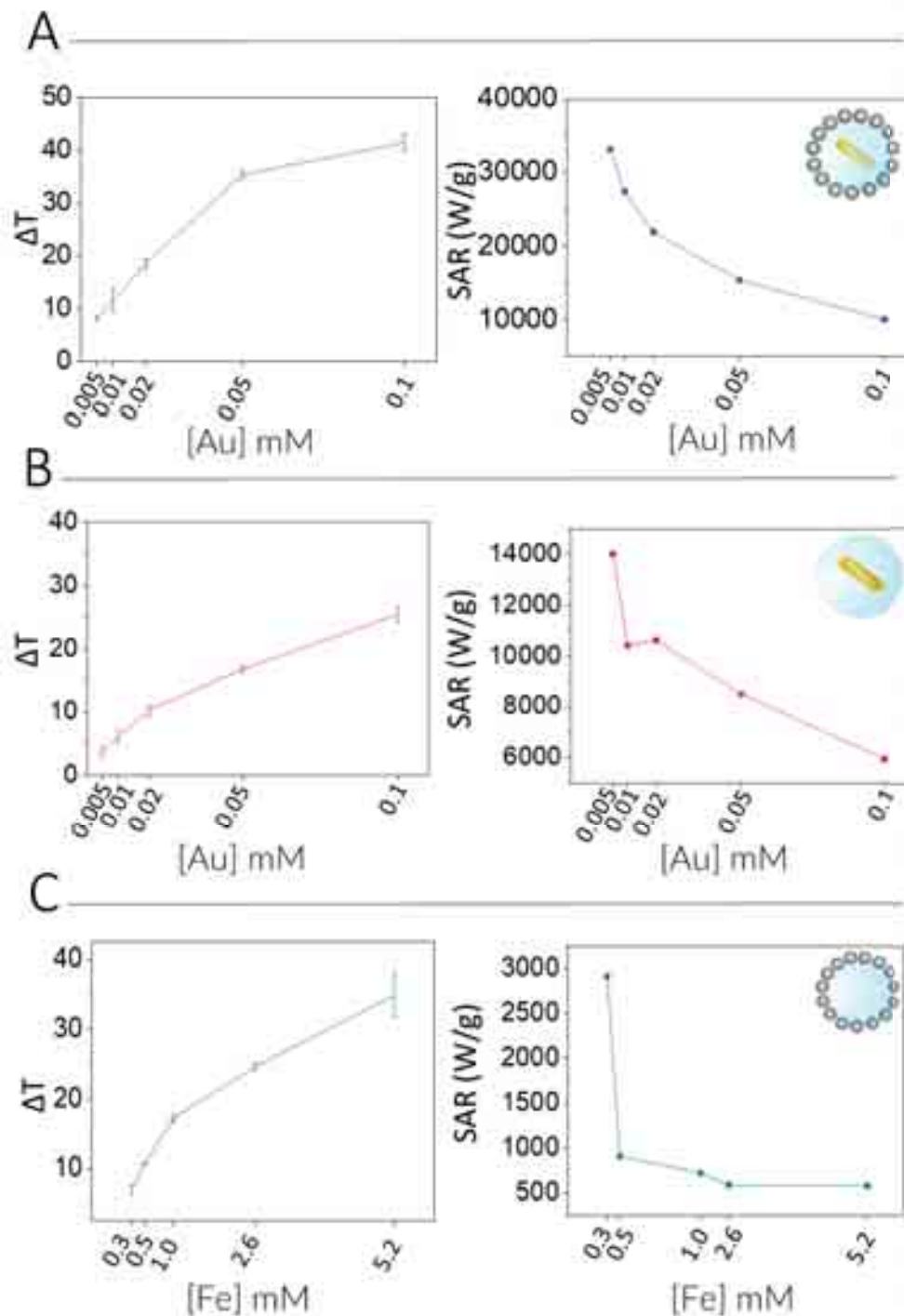


Figure 4.13. Average temperature increment (ΔT , °C) for PTH during 5 min at 2.5 W/cm² in solution, at different concentrations of (A) AuNRs@SiO₂@IONPs (B) AuNRs@SiO₂ and (C) SiO₂@4IONPs, and calculation of the SAR for each NP. For all the experiments, an 808 nm laser was used.

To determine the combined effect of Au and Fe in the heating ability of the NPs, the concentrations of Au and Fe in the control samples were compared with the equivalent concentrations of Au and Fe in AuNRs@SiO₂@IONPs, as calculated from ICP-MS (Table 4.1, Figure 4.14). We observed that, for a certain concentration of AuNR@SiO₂@IONPs, the equivalent control samples resulted in less heating, and that the AuNR@SiO₂ control heated less than the SiO₂@4IONP sample. In other words, at comparable concentrations, the presence of both metals always resulted in the highest heating, and when comparing the contribution of each metallic component, Fe results in a higher heating than gold under the conditions studied. However, if the concentrations of Fe and Au in the control samples are compared like-for-like, fixing absolute concentration (i.e., 0.5 mM Au vs. 0.5 mM Fe), Au remains a much more effective heater thanks to its plasmonic properties, leading to strong absorption of light with the laser wavelength (808 nm vs LSPR@760 nm). This is clearly shown by the fact that 25 times more Fe in SiO₂@4IONPs compared to Au in AuNRs@SiO₂ was needed to reach the same levels of temperature change.

Table 4.1. Average temperature increment (ΔT , °C) for PTH at 2.5 W/cm² in solution, at different concentrations of AuNRs@SiO₂ (red), SiO₂@4IONPs (green), and AuNRs@SiO₂@IONPs (blue).

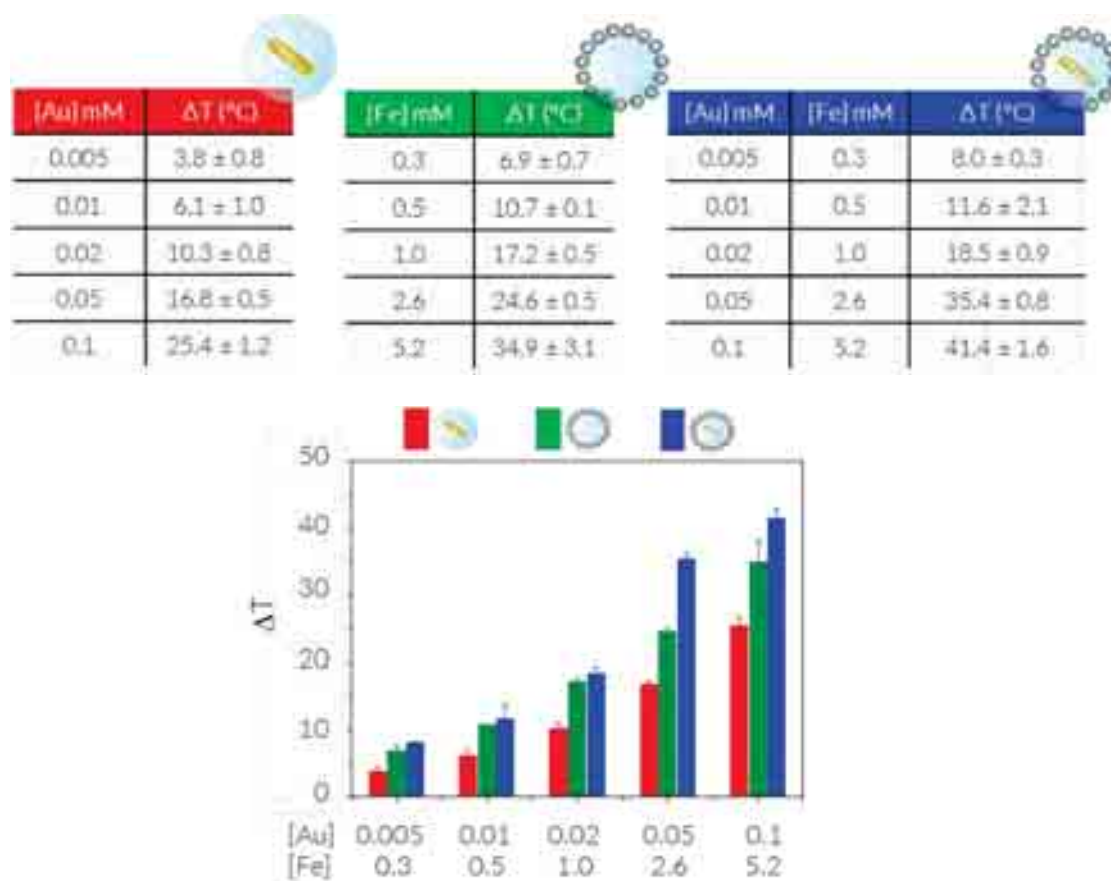


Figure 4.14. Average temperature increment (ΔT , °C) for PTH at 2.5 W/cm² in solution, at different concentrations of AuNRs@SiO₂ (red), SiO₂@4IONPs (green) and AuNRs@SiO₂@IONPs (blue).

The optical density of the samples at 808 nm was measured at the concentrations used for the irradiation and the results are shown in **Table 4.2**.

Table 4.2 Optical density at 808 nm of AuNRs@SiO₂ (**red**), SiO₂@4IONPs (**green**) and AuNRs@SiO₂@IONPs (**blue**) measured using a UV-Vis-NIR spectrometer.

Optical density

| [Au]mM | | [Fe]mM | | [Au]mM [Fe]mM OD ₈₀₈ | | |
|--------|-------|--------|------|---------------------------------|-----|------|
| 0.005 | 0.007 | 0.3 | 0.04 | 0.005 | 0.3 | 0.15 |
| 0.01 | 0.009 | 0.5 | 0.06 | 0.01 | 0.5 | 0.24 |
| 0.02 | 0.03 | 1.0 | 0.09 | 0.02 | 1.0 | 0.42 |
| 0.05 | 0.1 | 2.6 | 0.27 | 0.05 | 2.6 | 0.77 |
| 0.1 | 0.34 | 5.2 | 1.12 | 0.1 | 5.2 | 1.46 |

The results of the optical density agreed with the heating values obtained in the photothermal characterization (**Figure 4.14**) i.e., the higher the optical density of the samples at 808 nm the higher the increment of temperature.

4.4 Hyperthermia in 2D cell cultures

Biological experiments were carried out using the same human glioblastoma cell line as that used in Chapter III. Thus, U87 cells were incubated with AuNRs@SiO₂@IONPs, and after 24h of incubation, NP uptake was studied. TEM imaging showed that AuNRs@SiO₂@IONPs were successfully uptaken by the cells and confined in endosomes, i.e., not bound to the cell surface (**Figure 4.15**).

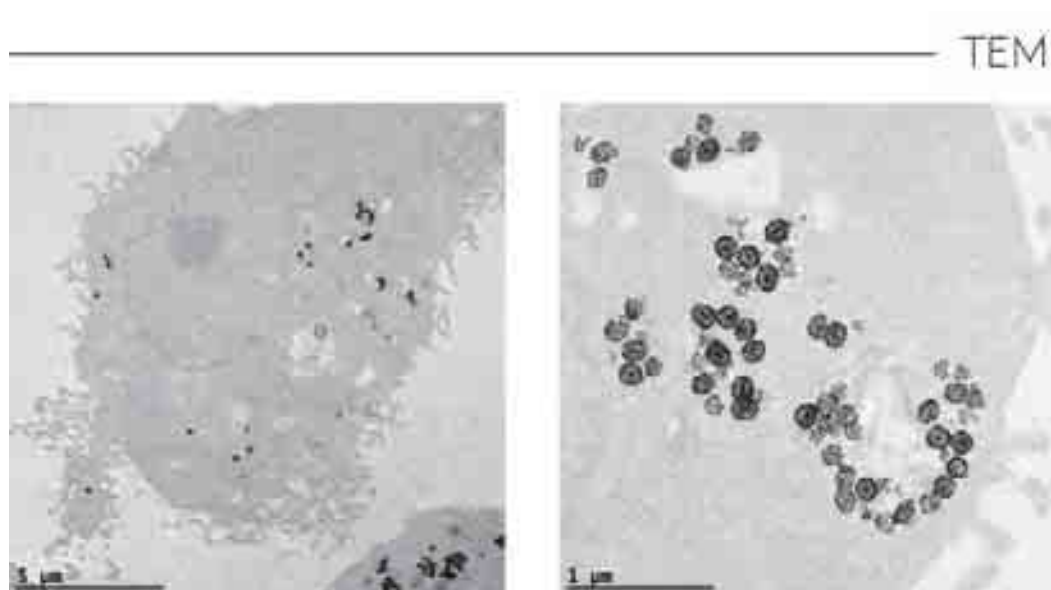


Figure 4.15. TEM images of ultramicrotomed cells after incubation with AuNRs@SiO₂@IONPs. The NPs are clearly internalized in the cell and inside endosomes.

We subsequently studied the heating capacity of AuNRs@SiO₂@IONPs once internalized inside cells. Considering that we observed in Chapter III higher heating profiles for uptaken NPs compared to those in solution at the same NP concentration, we studied AuNRs@SiO₂@IONPs in cells at lower concentrations and power densities than those used for the photothermal characterization in solution. U87 cells were seeded in 96-well plates, allowed to adhere, and then incubated with AuNRs@SiO₂@IONPs at concentrations ranging from 0.0125 to 0.05 mM. After 24 h, samples were irradiated from the top using a NIR laser (808 nm) at 1 and 2 W/cm² during 5 min. Cell death in each well was calculated using the AlamarBlue kit, as explained in Chapter III, and the data processed as a percentage of cell death (Figure 4.16).

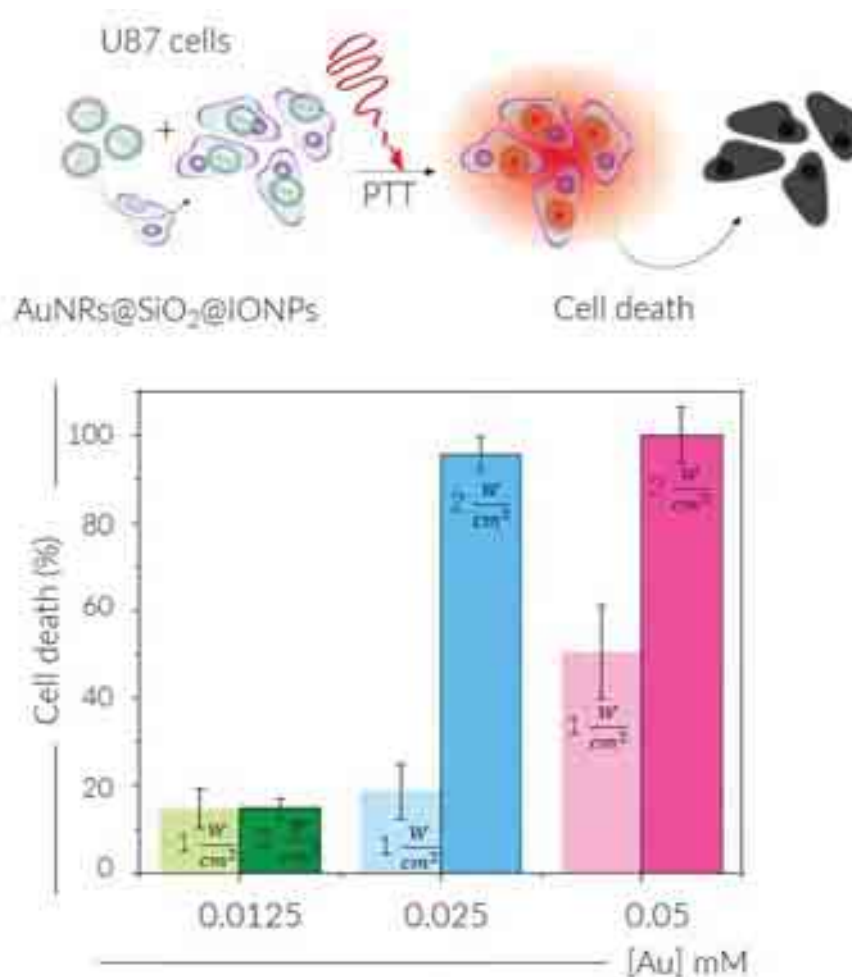


Figure 4.16. Schematic illustration of U87 cells incubated with NPs and graphical representation of the cell death (%) calculated using AlamarBlue cell viability reagent, after heating in the cellular environment. Viability was calculated as a proportion of 100% viable (healthy control cells with NPs but without irradiation).

The results showed that, at 1 W/cm² high NP concentrations were required to cause significant levels of cell death (e.g., 50% when using [Au] = 0.05 mM). By increasing the laser power density to 2 W/cm², not only could 100% cell death be achieved, but lower NP concentrations ([Au] = 0.025 mM) could also be used to achieve similar levels of cell death. Unfortunately, we could not determine the concentration of NPs actually internalized by the cells, and therefore we are only

presenting instead the results as the concentration added to the cells. Thus, whereas we can conclude that the hybrid NPs can act as efficient nanoheaters for photothermal heating in 2D cultures, we could not determine a reliable value of the relationship between NP concentration and % cell death due to PTT.

4.5 Hyperthermia in 3D cell cultures

We next developed a 3D model to study the heating properties of the NPs for PTH in a more realistic manner. Spheroids were grown as explained in Chapter III and incubated with AuNRs@SiO₂@IONPs ([Au] = 0.01 mM), without washing non-endocytosed NP prior to irradiation during 3 min, at laser power densities ranging from 0 to 2 W/cm². According to the results in Chapter III and to the literature²⁶, we chose to lower the NP dose because of the observed increase of cell death when NPs are internalized in cells or spheroids, as compared to a solution of NPs at the same final concentration. After the irradiation experiments, live/dead images were acquired to evaluate the extent of cell death (Figure 4.17). We confirmed the non-toxic nature of the NPs when added to spheroids at a concentration of [Au] = 0.01 mM and without irradiation (control). Upon irradiation, we observed an increase in spheroid cell death when increasing laser power density. Unfortunately, we do not have a control sample of spheroid irradiation without NP incubation but considering the laser wavelength used for irradiation (808 nm), no laser-induced cytotoxicity was expected.

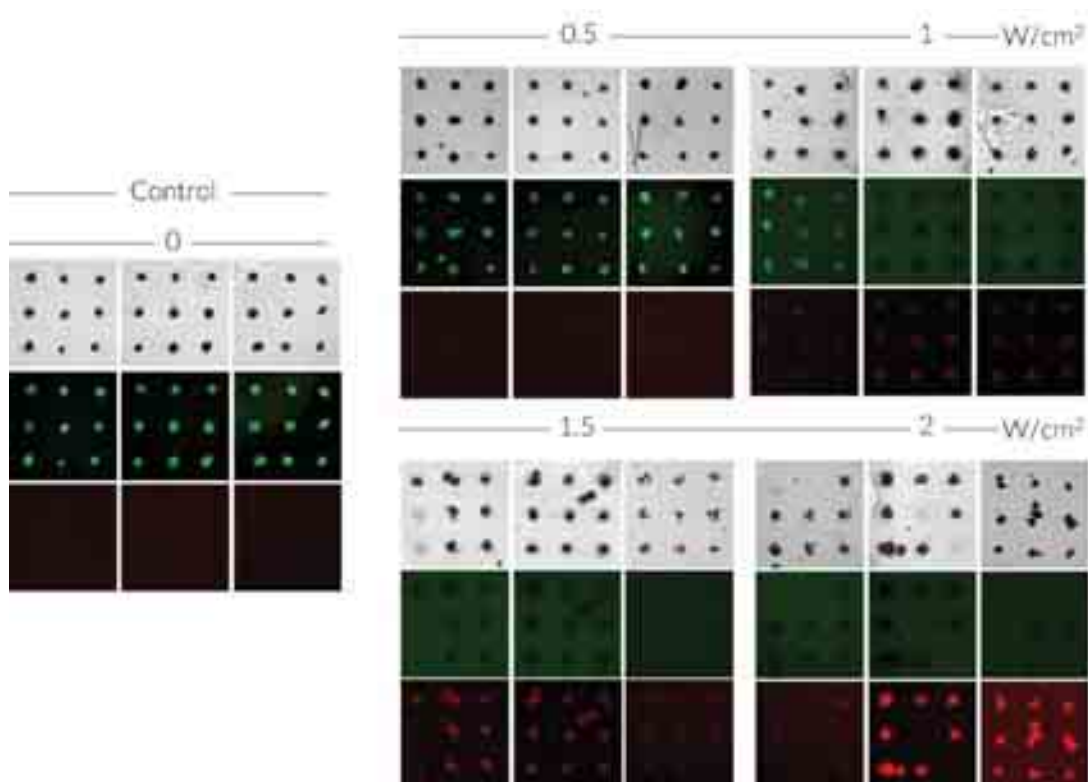


Figure 4.17. Optical and live/dead images of spheroids pre-loaded with AuNRs@SiO₂@IONPs (0.01mM [Au]) and irradiated for 3 min at increasing power densities (from 0.5 to 2 W/cm²). Incubated but non-irradiated (0 W/cm²) spheroids were used as a control for the experiments.

4.6 Selective hyperthermia through cell targeting

4.6.1 Functionalization with antibodies

The lack of specific binding of NPs to cancer cells is a serious concern in applications of NPs for cancer treatment. As shown in Chapter II and Chapter III, on certain occasions, hybrid NPs can be internalized by MCF7 and U87 cells without incorporating any surface functionalization targeting specific receptors. In order to achieve cancer cell specific targeting, NPs can be conjugated with antibodies, so that the intracellular uptake of such conjugated NPs would be limited by the specific antibody-antigen receptor interaction taking place on the cell membrane²⁷. The objective of such targeting is focused on inducing cell death of cancerous cells only, thus avoiding damage to healthy cells. As discussed in the Introduction, for this study we chose to target the CD44 receptor due to its role in metastatic processes²⁸. The CD44 receptor is a cell membrane receptor expressed by various cells of epithelial lineage, such as the human breast cancer cell line MDA.MB.231²⁹.

The functionalization of AuNRs@SiO₂@IONPs with antibodies was performed using an extended protocol based on the activation of free carboxylic groups in the PMA structure, via EDC/NHS chemistry³⁰. Thus, AuNRs@SiO₂@IONPs were labelled with an anti-human anti-CD44 unlabelled antibody, using protein G that was previously bonded to the PMA structure. The carboxylic groups in PMA were functionalized *via* amide bonds with protein G. Briefly, EDC is a water-soluble carbodiimide that is used to bind carboxyl and phosphate groups to amines. EDC reacts with the carboxyl groups of PMA on the surface of NPs, allowing bioconjugation with the carboxylic moiety. In the process, an unstable amine-reactive intermediate (O-acylisourea ester) is created. Then, NHS turns this amine-reactive ester into a semi-stable active ester to stabilize this intermediate. The amine groups on the protein G are reactive with NHS esters, releasing the NHS group and generating stable amide bonds. Then, the antibody is added and its fragment crystallizable region (Fc region) is attached to the protein G *via* non-covalent interaction. Thus, the use of the protein G allowed the correct orientation of the antibody that maintained its fragment antigen-binding region (Fab region) free to interact with the antigens for the correct targeting of cells.

First, indirect immunostaining was used to verify that MDA.MB.231 cells were positive for the expression of CD44. Cells were grown as an adherent culture and fixed prior to normal immunostaining protocols, using a primary anti-CD44 and a secondary fluorescently labelled antibody. As a negative control, we used the human breast cancer cell line MCF7, which is described to be low-on CD44 expression, only upregulating expression in metastatic situations of expressed by MCF7 cancer stem cells.³¹ As can be observed in **Figure 4.18A**, MDA.MB.231 cells show significantly higher levels of CD44 expression. We thus added AuNRs@SiO₂@IONPs to cells and then the cells were washed and fixed after 2h, prior to addition of the same secondary fluorescently labelled antibody. We examined the presence of NPs using both fluorescence confocal microscopy and multiphoton (MP) confocal microscopy. As shown in **Figure 4.18B**, both the fluorescence and multiphoton signals correlated perfectly, suggesting that MP confocal microscopy can be used to image NPs in live cells, avoiding the requirement to fix and locate the NP using immunostaining protocols. The results also suggest that NPs could bind to the cell

surface CD44 receptor, but that the NP concentration should be optimized to avoid overloading cells. Additionally, NPs also showed unexpected binding to the MCF7 cell membrane, which was surprising considering that the immunostaining test itself showed relatively low levels of CD44.

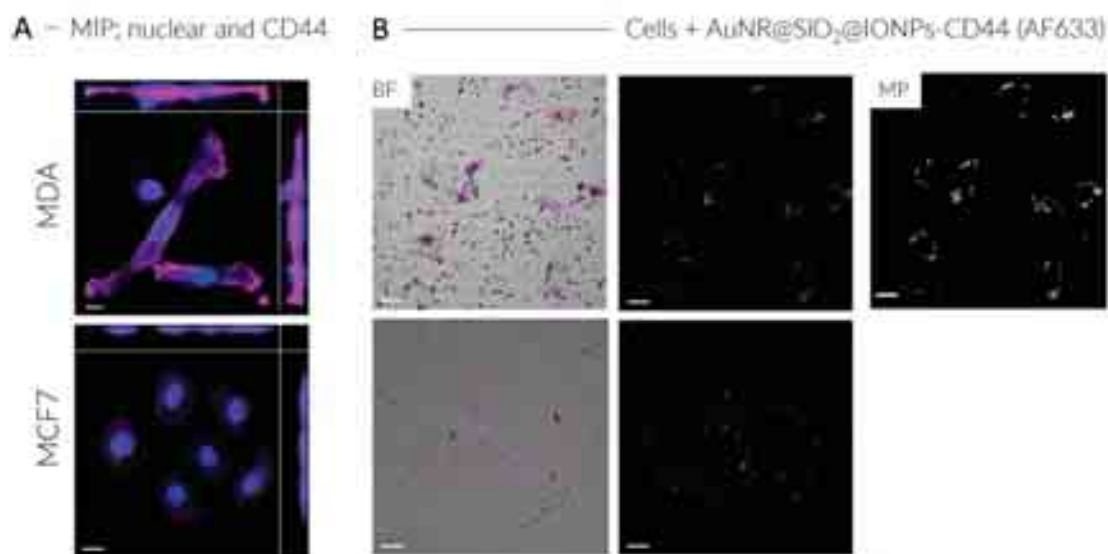


Figure 4.18. (A) Maximum intensity projections (MIP) of MDA.MB.231 and MCF7 cells stained for CD44, using an indirect immunostaining protocol. The nuclei are shown in blue and CD44 in pink (the intensity is comparable between images). (B) MDA.MB.231 and MCF7 cells incubated with NPs conjugated with an anti-CD44 receptor antibody. Brightfield, fluorescence (NPs-CD44 is shown in pink), and multiphoton (NPs shown in white) images are shown. No images were obtained for MCF7 cells incubated with NPs because of failure of the laser. Scale bars correspond to 20 μm .

4.7 Conclusions

A new method for the synthesis of hybrid NPs has been reported in this chapter. Starting from AuNRs, we were able to cover them with a silica shell, on which IONPs were grown using thermal decomposition of iron oleate. It was found that the density of IONPs can be increased by performing multiple thermal decomposition steps. The number of steps was first optimized using SiO₂ NPs and the methodology was subsequently applied to the synthesis of hybrid NPs containing AuNRs, with the desired IONPs coverage. It was observed in TEM images that, by increasing the number of steps, we could increase not only the coverage but also the size of the IONPs reaching around 19 nm after 3 steps of thermal decomposition. A possible explanation for this process is that, in the first step IONPs are formed and then, these IONPs act as nucleation spots and preferential growth sites for subsequent steps. It could also be observed that IONPs did not nucleate or grow inside the pores of the silica shell, but on its surface.

The obtained AuNRs@SiO₂@IONPs were characterized by TEM, HAADF and EDX, thereby confirming the structure and composition of the hybrid NPs. UV-Vis spectra were also recorded, showing partial reshaping of AuNRs due to the high temperature used during IONPs synthesis. Magnetic characterization showed promising magnetic properties with superparamagnetic behaviour characterized by low remanence and coercivity.

The photothermal characterization of the NPs displayed promising properties as nanoheaters, achieving high temperature increments with low concentrations of Au. AuNRs covered by silica and silica covered by IONPs were used as controls for the heating experiments, showing that also the IONPs are contributing to the total heating due to the high concentration of this metal in the final NPs. Notwithstanding, the heating capacity of AuNRs is much better, because a similar temperature increment can be achieved when using concentrations 25 times lower.

The NPs were used for photothermal heating in 2D and 3D cultures, being able to kill U87 cells using low concentrations and low power densities. In addition, it was demonstrated again that the capacity of the NPs to heat is increased when the NPs are internalized by cells. This phenomenon, which was already observed in Chapter III, is further enhanced when the cells are aggregated forming spheroids. It should be taken into account that we were working with significantly lower Au concentrations, compared to those used in Chapter III, meaning that AuNRs@SiO₂@IONPs resulted to be more efficient nanoheaters than IOAuNSs.

The conjugation of AuNRs@SiO₂@IONPs with antibodies was successfully performed using EDC/NHS chemistry and the capacity of the NPs to bind specific cells that expressed the CD44 antigen was studied, using MDA as a positive control and MCF7 cells not expressing the antigen as a negative control. We can conclude that antibody-labelled nanohybrids provide specific targeting of MCF7 cells.

4.8 Experimental Section

4.8.1 Materials

Ferric chloride hexahydrate (FeCl₃·6H₂O, ≥98% Sigma-Aldrich), sodium oleate (≥99% Sigma-Aldrich), ammonia (≥99.5% Sigma-Aldrich), absolute ethanol (CH₃CH₂OH, Sigma-Aldrich), tetraethyl orthosilicate (TEOS) (Sigma-Aldrich), hexane (≥95% Sigma-Aldrich), 1-octadecene (≥90% Sigma-Aldrich), hexadecyltrimethylammonium bromide (CTAB, ≥99% Sigma-Aldrich), 1-decanol (98% Sigma-Aldrich), hydrogen tetrachloroaurate trihydrate (HAuCl₄·3H₂O, ≥99.9% Sigma-Aldrich), sodium citrate tribasic dihydrate (≥98% Sigma-Aldrich), silver nitrate (AgNO₃, ≥99% Sigma-Aldrich), L-ascorbic acid (AA, ≥99% Sigma-Aldrich), O-[2-(3-mercaptopropionylamino)ethyl]-O'-methylpolyethylene glycol (SH-PEH, Sigma-Aldrich), 1-Ethyl-3-(3-dimethylaminopropyl)-carbodiimide (EDC, ≥98% Sigma-Aldrich), N-Hydroxysuccinimide (NHS, ≥98% Sigma-Aldrich), COOH-PEG-silane (Mw 5000 Da, Nanocs), Phosphate buffered saline (PBS, Sigma-Aldrich), Phosphate buffer (PB, Sigma-Aldrich), 2-(N-morpholino)ethanesulfonic acid (MES buffer, Sigma-Aldrich), Anti-CD44 antibody (ab157107, Abcam), Donkey anti-Rabbit IgG (H+L) Highly Cross-Adsorbed Secondary Antibody, Alexa Fluor™ Plus 647 (Thermo Fisher) were prepared and used without further treatments. Milli-Q water was used for all the experiments.

4.8.2 Nanoparticle synthesis

Synthesis of AuNRs. For the preparation of AuNRs, a seed-mediated method was used. Thus, first we have synthesized small AuNRs as seeds that were subsequently overgrown as bigger AuNRs.

Synthesis of Small Anisotropic Seeds ($L=21$ nm $W= 7.5$ nm). Typically, 2400 μ L of 0.01 M AgNO_3 , 21 mL of 1 M HCl, 3000 μ L of 0.05 M HAuCl_4 , and 3900 μ L of 0.1 M ascorbic acid were added to 300 mL of a 50 mM CTAB and 11 mM *n*-decanol solution at 25 °C. Then, 18 mL of the seed solution was added under stirring. The mixture was left undisturbed for at least 4 h at 25 °C. The obtained small anisotropic seeds displaying an LSPRs band located at 725-730 nm were centrifuged at 14000-15000 rpm for 45 – 60 min in 2 mL tubes. The precipitates were collected and diluted with 20 mL of a 10 mM CTAB solution. The AuNRs dispersion was centrifuged twice under the same conditions. The final volume of small AuNRs dispersion was fixed to $[\text{Au}] = 4.6$ mM.

Synthesis of AuNRs with LSPRs at 790 nm. In a typical synthesis, 2500 μ L of a 0.01 M AgNO_3 solution, 1000 μ L of 0.05 M HAuCl_4 , 800 μ L of a 0.1 M ascorbic acid solution and 3000 μ L of HCl 1M were added under stirring to 100 mL of a 50 mM CTAB and 11 mM *n*-decanol solution at 28 °C. Then, 650 μ L of the small anisotropic seed suspension was added. The mixture was left undisturbed for 12 h. The obtained AuNRs were centrifuged at 7000 rpm and dispersed in 10 mL of 2 mM CTAB solution. This process was repeated twice. AuNRs of 58 ± 5.1 nm in length and 15 ± 2.4 nm in width were obtained. The dimensions were directly measured by TEM and a maximum absorbance at 790 nm was determined from UV-Vis spectra.

Synthesis of core-shell AuNRs@SiO₂. The reaction was performed according a reported protocol¹⁰. 170 mL of a 6 mM CTAB solution and 75 mL of ethanol were mixed at a temperature between 30 and 35 °C in a 500 mL round beaker. Then, 100 μ L of NH_3 (25 vol %) was added to the mixture, followed by addition of 5 mL of AuNRs 5 mM. Thereafter, 200 μ L of TEOS was added dropwise under vigorous stirring. For the rest of the reaction time, the temperature was fixed at 60 °C. After 2–3 hours, the sample became gradually turbid indicating the formation of the silica shell. The final AuNRs@SiO₂ were recovered by centrifugation (9000 rpm, 20 min, 35 °C) and washed twice with ethanol.

Synthesis of SiO₂ NPs. 350 mL of 6 mM CTAB and 150 mL of ethanol were mixed in a 1 L round bottom flask under mechanical stirring at 35 °C. Then, the pH was adjusted to 9.5 by addition of NH_3 (5 wt%) and the mixture was stirred for 30 min. Afterwards, 3 mL of TEOS was added dropwise under vigorous stirring, thus, primary nucleation clusters are formed, then, the mixture turned turbid indicating the formation of the NPs. After 5 min, the temperature was set at 60 °C and the reaction mixture was left for three days. The product was recovered by centrifugation (9000 rpm, 30 min, 35 °C), washed twice with ethanol and dried at 60 °C in the oven. Finally, the NPs were calcined (4 h – 600 °C) to clean completely the surface and to increase the stability.

Synthesis of SiO₂@IONPs. The obtained mesoporous silica NPs were covered with IONPs *via* thermal decomposition of iron (III) oleate, according to a protocol published by Park *et al.*¹. First, iron (III) oleate was prepared by dissolving 36.5 g sodium oleate and 10.8 g FeCl₃ · 6 H₂O in a mixture of 60 mL water, 80 mL ethanol and 140 mL hexane and heating to reflux (ca. 70 °C) for 4 h. After cooling down, the organic layer was separated and washed four times with 60 mL water, the solvent was then evaporated and the product was dried, first using a rotary evaporator and then using a high vacuum line. After drying for 12 h, a dark orange viscous product was obtained, which was stored under argon and light exclusion.

To perform the thermal decomposition, 3 g of iron(III) oleate was dissolved in 21 mL of 1-octadecene in a 3 neck 150 mL round bottom flask equipped with a magnetic stirring bar. The reaction vessel was connected to a vacuum line and the mixture was degassed at 70 °C in a bath for 30 min. Afterwards, the water bath was removed, and the flask was equipped with a reflux condenser, a thermocouple and a septum while applying a N₂-flow. 130 mg of mesoporous silica was dispersed in 3 mL of ethanol using a sonication bath and then added to the reaction mixture together with 535 µL of oleic acid. The flask was equipped with a septum and a thermocouple and the reaction mixture was heated to 317 °C with a heating ramp of 200 °C/h and a holding time at 317 °C of 30 min. During the whole heating process, a gentle N₂-flow was applied, furthermore the water cooling for the reflux condenser was only switched on when the reaction reached a temperature of 200 °C, ensuring that all ethanol was removed from the reaction, which otherwise could drip back into the hot solvent causing splashing of the reaction mixture due to spontaneous evaporation. After cooling to room temperature, hexane was added and the product was recovered by centrifugation (9000 rpm, 10 min, 20 °C). The product was washed several times with hexane to remove unbound IONPs.

For overgrowth, the same process was employed. First 130 mg of the prepared NPs was dissolved in 7 mL of 1-octadecene and then added to 3 g iron(III) oleate dissolved in 14 mL 1-octadecene. The mixture was degassed for 30 min, the flask was equipped with a reflux condenser and 535 µL of oleic acid was added. Then the same heating ramp was used, and the product was collected *via* centrifugation (9000 rpm, 10 min, 20 °C) and washed several times with hexane. This process was repeated until the desired coverage was obtained.

Synthesis of AuNR@SiO₂@IONPs. The growth of IONPs onto silica shells was performed through thermal decomposition. For this process, 1.2 g iron(III) oleate, prepared as described above, was dissolved in 10 mL of 1-octadecene in a 50 mL 3 neck round bottom flask equipped with magnetic stirring. The flask was connected to the high vacuum line and degassed at 70 °C bath temperature for 30 min. Afterwards the flask was equipped with a reflux condenser, a thermocouple and a septum while applying a N₂-flow. 15 mg AuNRs@SiO₂ in 1 mL ethanol and 267.5 µL oleic acid were added and the reaction mixture was heated to 317 °C with a rate of 200 °C/h under a weak N₂-flow, where it was held for 10 min. After cooling, hexane was added to the reaction mixture and the particles were recovered by centrifugation (9000 rpm, 10 min, 20 °C). The obtained product was washed several times with hexane yielding a slightly reddish dispersion.

For overgrowth, the same process was employed. The dried particles were first dispersed in 5 mL of 1-octadecene which was added to 1.2 g iron(III) oleate. When drying the particles, precaution must be taken to not leave them without solvent for too long since the particles then become hard to disperse again. The obtained mixture was degassed at 70 °C bath temperature for 30 min. Afterwards 267.5 µL oleic acid was added and the reaction mixture was heated to 317 °C with a ramp of 200 °C/h under a weak N₂-flow. After cooling, hexane was added and the product was recovered by centrifugation (9000 rpm, 10 min, 20 °C). The obtained product was washed several times with hexane until the supernatant remained clear. This process was repeated until the desired coverage was obtained.

4.8.3 Functionalization

Functionalization with PMA. For the functionalization with PMA, 100 µL 0.05M of PMA was added to 2 mL of AuNRs@SiO₂@IONPs ([Au] = 1mM). The solvent was evaporated in a rotary evaporator and the particles were redispersed in 1 mL of water and 100 µL of NaOH at pH = 12. The particles were washed several times until neutralization, using a magnet for separation.

Functionalization with antibodies. First, 100 µL of AuNRs@SiO₂@IONPs was placed in a glass vial and washed with water using a magnet for separation. Then, 200 µL of EDC (10 mM) and 100 µL (20 mM) of NHS in MES buffer were added to the NPs under sonication in a glass vial. The particles were then left for 30 min under stirring before washing twice using a magnet. Then, 10 µL of protein G (1 mg/mL) and 200 µL of PB were added and the mixture were left while stirring for 30 min; then, the NPs were washed again twice and 5 µL of the AB (5 µg) and 200 µL of PB were added. The particles were washed twice again and finally redispersed in 100 µL of PBS.

Functionalization with COOH-PEG-silane. For the functionalization with COOH-PEG-silane, 1 mL of COOH-PEG-silane 1 mM was added to 2 mL of AuNRs@SiO₂ ([Au] = 1mM). The particles were then recovered by centrifugation and washed twice (9000 rpm – 20 min). The AuNRs@SiO₂ were redispersed in water.

4.8.4 Nanoparticles characterization

Standard characterization. All NPs were characterized using TEM, ICP-MS, and UV-Vis. TEM images were collected with a JEOL JEM-1400PLUS transmission electron microscope operating at 120 kV, using carbon-coated 400 square mesh Cu grids. ICP-MS analysis was conducted using an ICP-MS Agilent 7500ce to determine the concentration of Au and Fe. Samples containing biological material (i.e., cells or spheroids) were digested in aqua regia during 48 h, followed by addition of H₂O₂ and continued heating until a clear and transparent solution was observed. The samples were cooled down to RT and subsequently measured. UV-vis optical extinction spectra were recorded using an Agilent 8453 UV-Vis diode array spectrophotometer, normalizing spectra at 400 nm or at maximum peaks.

EDX analysis. EDX measurements were acquired at different tilt angles, every 10°, with an acquisition time of 10 minutes per angle and 150 pA screen current using a SuperX detector. The resulting data was reconstructed using an Expectation Maximisation (EM) reconstruction algorithm using a STEM HAADF signal for accurate alignment

STEM Characterization for SiO₂@IONPs. Samples were drop casted on an amorphous carbon coated Cu TEM grid. A Thermo Fisher Scientific Themis Z electron microscope operated at a voltage of 300 kV was used, for imaging in ADF STEM mode. Hereby, the probe convergence semiangle was 20.6 mrad, and the camera length was selected to be 73 mm resulting in inner and outer collection semiangles of 19 and 74 mrad, respectively. Tilt series were acquired using a Fischione model 2020 tomography holder over an angular range of -75° to 60° with a 3° tilt increment. The tilt series were reconstructed using the expectation-maximization (EM) algorithm as implemented in the ASTRA tomography toolbox³².

STEM Characterization of AuNR@SiO₂@IONPs. Samples were drop casted on an amorphous carbon coated Cu TEM grid. A Thermo Fisher Scientific Themis Z electron microscope operated at a voltage of 300 kV was used at EMAT for imaging in HAADF STEM mode. Hereby, the probe convergence semiangle was 20.6 mrad, and the camera length was selected to be 73 mm resulting in inner and outer collection semiangles of 79 and 200 mrad respectively for HAADF STEM and 19 and 74 mrad for ADF STEM. Tilt series were simultaneously acquired in HAADF and ADF mode using a Fischione model 2020 tomography holder over an angular range of -70° to 66° with a 2° tilt increment. The reconstruction of the Au NR was based on HAADF STEM tilt series and the reconstruction was performed using the expectation-maximization (EM) algorithm as implemented in the ASTRA tomography toolbox³². To obtain a 3D reconstruction of the AuNR@SiO₂@IONPs, inpainting as explained by Sentosun *et al.*³³, was applied to ADF STEM projection images. During this process, the pixels of AuNRs were removed from the ADF STEM data and replaced by the surrounding texture corresponding to SiO₂. The processed tilt series were then reconstructed using the EM algorithm. The 3D reconstructions of HAADF STEM and ADF STEM tilt series were then combined by using Amira software.

Magnetism. ZFC/FC measurements were performed at 100 Oe and within a temperature range of 5-300 K, using a Quantum Design MPMS3 VSM-SQUID magnetometer with a sensitivity of 10⁻⁸ emu up to a maximum field of 7 T. The hysteresis loops were measured in a Vibrating Sample Magnetometer (VSM) with a sensitivity of 5·10⁻⁶ emu, up to a maximum field of 18 kOe working at room temperature.

Langevin and non-interacting models fitting. The standard Langevin approach to the superparamagnetism (ideal SPM model) was used to provide quantitative information about the size of the particles from the hysteresis loops. Besides, a non-interacting model was used to fit the obtained experimental measurements of the ZFC/FC curves. These fittings were performed as reported in previous studies³⁴.

4.8.5 Cell culture

2D Cell culture. U87 human glioblastoma cells (ATCC) were cultured in Dulbecco's Modified Eagle Medium (DMEM, Gibco) supplemented with 10% fetal bovine serum (FBS, Gibco) and 1% penicillin-streptomycin (Gibco) and grown at 37 °C in a humidified incubator with 5% CO₂. Then, the NPs resuspended in cell media at different concentrations ([Au] = 0.0125, 0.025 and 0.05 mM) were added and incubated with cells during 24h. Afterwards, the media was changed to remove the NPs that had not been internalized by the cells and fresh media was added to the cells. Cells were subsequently treated for PTH (see below).

2D Cell culture with NPs conjugated with antibodies (MDA and MCF7). Cells were seeded in a 96-well optical imaging plate and allowed to adhere. Subsequently, wells were set aside for addition of NPs (pre-conjugated with anti-CD44 antibody), or for indirect immunostaining. In the case of the NP-incubation wells, NPs were added at [Au] = 0.01 mM for 2h, followed by washing with PBS to remove unbound NPs. Of note, in the images in Figure 18, many non-endocytosed NP can be observed, presumably sticking to the underlying cell treated plastic in a non-specific manner. All cells were subsequently fixed using 4% formaldehyde in PBS, followed by a 30 min blocking step incubating cells in 1% bovine serum albumin (BSA) in PBS. Subsequently, non-NP samples were incubated with Rabbit anti-human anti-CD44 (1/100) for 1h, followed by washing with PBS. Then, all wells (NP incubated and non-NP incubated) were incubated with an anti-rabbit AF647 labelled secondary antibody (1/1000) in PBS for 1h. All samples were washed thoroughly and, in some cases, counterstained with DAPI. Images were taken with a Zeiss LSM 880 confocal microscope equipped with a 633 nm laser line (AF647 ex) and a multiphoton laser set at 780 nm for NP detection. For imaging, a x40 oil immersion EC Plan-Neofluar objective was used and, in some cases, maximum intensity profiles (MIP) of z-stack images obtained to show XY, XZ, and YZ profiles of the cells.

Cell viability. The AlamarBlue metabolic assay (DAL1100, Invitrogen) was used to measure cell viability. Briefly, following the commercial protocol, AlamarBlue reagent was added to the 96-well plate containing the cells, and after an incubation time of 2 h, fluorescence was recorded using an EnSpire Multimode Plate Reader (PerkinElmer) with fluorescence excitation and emission wavelengths of 570 and 585 nm, respectively.

Spheroids formation. U87 glioblastoma cells were incubated with AuNRs@SiO₂@IONPs ([Au] = 0.01mM) following the same protocol as described in Chapter III. Briefly, U87 cells were seeded and once adhered, NPs were added. After 24 h incubation, the U87 cells were detached (trypsin) and counted. A 3D printed stamp with micropillars of 200 μm diameter and 200 μm in height was used to print moulds into the wells of a 96-well plate containing 50 μL of 2% agarose (A0576, Sigma Aldrich) in PBS. The agarose was then left to solidify between one and two minutes and the stamp was removed, leaving an array of moulds in the wells. The 96-well plate was then sterilized in UV light for 30 minutes before cell seeding (15,000 cells per well) and centrifugation. Cells were allowed to mature for 48 hours before photothermal irradiation. Imaging was

performed on an EnSight Multimode Microplate Reader (Perkin Elmer), and ImageJ software was used for processing the acquired images and for fluorescence quantification.

4.8.6 Hyperthermia

Photothermal measurements in solution. 50 μL of AuNRs@SiO₂@IONPs, SiO₂@4IONPs and AuNRs@SiO₂ at different concentrations ranging from [Au] = 0.005 - 0.1 mM and [Fe] = 0.3 - 5.2 mM was placed in a 1.5 mL Eppendorf tube. Subsequently, it was irradiated during 5 min at 2.5 W/cm² and the sample was left 2 min for cooling down. The heating step including heating and cooling was recorded by a thermal camera and the data were used for calculations. The procedure was repeated 3 times per sample and concentration.

For PTT, each sample was illuminated from the side with a NIR laser (808 nm) coupled to an optical fibre (Laser Components SAS, France) at 2.5 W/cm⁻² and imaged with an infrared camera (FLIR SC7000) to measure the temperature increase.

SAR calculation. SAR was calculated as reported in chapter III²⁶

Briefly, the temperature elevation was measured as a function of time (dT/dt) at the initial linear slope (t = 30 s) to evaluate the heating effect in terms of SAR, power dissipation per unit mass of element, Fe or Au (W/g). SAR was calculated using the following formula where $m_{\text{Fe/Au}}$ is the total mass of iron and gold in the sample, m_i is the nanoparticle element mass, and C_i to the specific heat capacity of the component i:

$$\text{SAR} = \sum \frac{m_i \cdot C_i}{m_{\text{Fe or Au}}} \frac{dT}{dt}$$

Since the mass of Fe and Au are significantly lower than those of water ($C_w = 4.18 \text{ J g}^{-1} \text{ K}^{-1}$, $C_{\text{cell}} = 4.125 \text{ J g}^{-1} \text{ K}^{-1}$), the initial equation can be written as:

$$\text{SAR} = \sum \frac{m_w \cdot C_w}{m_{\text{Fe or Au}}} \frac{dT}{dt}$$

Photothermal measurements in cells. PTT measurements of cells incubated with NPs were performed in a 96-well-plate containing 100 μL of the solution of cells+AuNRs@SiO₂@IONPs. Each sample was irradiated during 5 min from the top with a single mode NIR laser (808 nm) coupled to an optical fibre (Laser Components SAS, France) at 1 and 2 W/cm⁻². Cell viability was checked using the AlamarBlue assay. As explained in Chapter III, triplicates were performed for all the experiments and an empty well was left between samples to avoid that the laser caused heating of adjacent wells during irradiation (**Figure 4.19**).

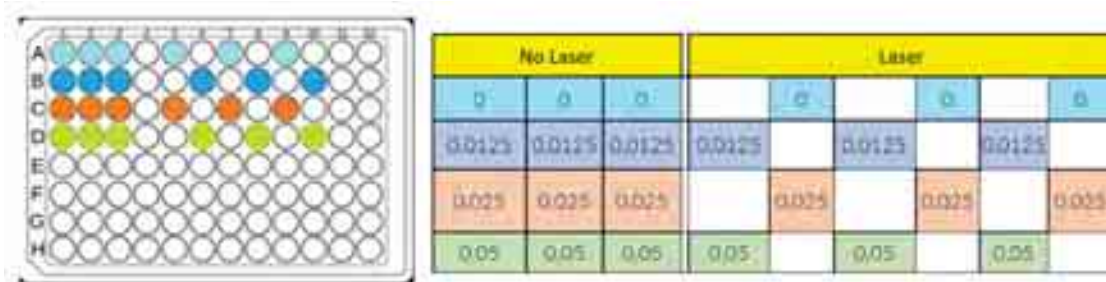


Figure 4.19. Scheme of the distribution of cells in a 96-well plate for irradiation.

Photothermal measurements in spheroids. PTT measurements of 3D spheroids incubated with AuNRs@SiO₂@IONPs were performed in a 96-well-plate containing the spheroids. Each sample was irradiated for 3 min from the top with a single-mode NIR laser (808 nm) coupled to an optical fibre (Laser Components SAS, France) at power densities ranging from 0.5 to 2 W/cm⁻². The viability of the spheroids was studied using live/dead cell images.

Live/dead staining and visualization. The Live/dead Cell Imaging Kit (R37601, Invitrogen) was used to check the cell viability in spheroids. Following the protocol, spheroids at day 3 of maturation were stained with Live Green/Dead Red staining solution in non-adherent dishes for 2 h at 37 °C in a humidified incubator with 5% CO₂. Then, the staining solution was removed, and the spheroids were imaged using an Olympus IX81F-3 inverted microscope coupled with a laser dual spinning disc unit (Yokogawa CSU-X1) and an Andor iXonEM + CDD camera, with a 10x objective. Images were processed using ImageJ.

References

- (1) Zhou, B.; Song, J.; Wang, M.; Wang, X.; Wang, J.; Howard, E. W.; Zhou, F.; Qu, J.; Chen, W. R. BSA-Bioinspired Gold Nanorods Loaded with Immunoadjuvant for the Treatment of Melanoma by Combined Photothermal Therapy and Immunotherapy. *Nanoscale* **2018**, *10* (46), 21640–21647. <https://doi.org/10.1039/c8nr05323e>.
- (2) Huang, X.; El-Sayed, I. H.; Qian, W.; El-Sayed, M. A. Cancer Cell Imaging and Photothermal Therapy in the Near-Infrared Region by Using Gold Nanorods. *J. Am. Chem. Soc.* **2006**, *128* (6), 2115–2120. <https://doi.org/10.1021/ja057254a>.
- (3) Zhou, R.; Zhang, M.; Xi, J.; Li, J.; Ma, R.; Ren, L.; Bai, Z.; Qi, K.; Li, X. Gold Nanorods-Based Photothermal Therapy: Interactions Between Biostructure, Nanomaterial, and Near-Infrared Irradiation. *Nanoscale Res. Lett.* **2022**, *17* (1). <https://doi.org/10.1186/s11671-022-03706-3>.
- (4) You, S. M.; Luo, K.; Jung, J. Y.; Jeong, K. B.; Lee, E. S.; Oh, M. H.; Kim, Y. R. Gold Nanoparticle-Coated Starch Magnetic Beads for the Separation, Concentration, and SERS-Based Detection of E. Coli O157:H7. *ACS Appl. Mater. Interfaces* **2020**, *12* (16), 18292–18300. <https://doi.org/10.1021/acscami.0c00418>.
- (5) Huergo, L. F.; Selim, K. A.; Conzentino, M. S.; Gerhardt, E. C. M.; Santos, A. R. S.; Wagner, B.; Alford, J. T.; Deobald, N.; Pedrosa, F. O.; De Souza, E. M.; Nogueira, M. B.; Raboni, S. M.; Souto, D.; Rego, F. G. M.; Zanette, D. L.; Aoki, M. N.; Nardin, J. M.; Fornazari, B.; Morales, H. M. P.; Borges, V. A.; Nelde, A.; Walz, J. S.; Becker, M.; Schneiderhan-Marra, N.; Rothbauer, U.; Reis, R. A.; Forchhammer, K. Magnetic Bead-Based Immunoassay Allows Rapid, Inexpensive, and Quantitative Detection of Human SARS-CoV-2 Antibodies. *ACS Sensors* **2021**, *6* (3), 703–708. <https://doi.org/10.1021/acssensors.0c02544>.
- (6) Iranmanesh, M.; Hulliger, J. Magnetic Separation: Its Application in Mining, Waste Purification, Medicine, Biochemistry and Chemistry. *Chem. Soc. Rev.* **2017**, *46* (19), 5925–5934. <https://doi.org/10.1039/c7cs00230k>.
- (7) Gloag, L.; Mehdipour, M.; Chen, D.; Tilley, R. D.; Gooding, J. J. Advances in the Application of Magnetic Nanoparticles for Sensing. *Adv. Mater.* **2019**, *31* (48), 1–26. <https://doi.org/10.1002/adma.201904385>.
- (8) Hao, L.; Leng, Y.; Zeng, L.; Chen, X.; Chen, J.; Duan, H.; Huang, X.; Xiong, Y.; Chen, X. Core-Shell-Heterostructured Magnetic-Plasmonic Nanoassemblies with Highly Retained Magnetic-Plasmonic Activities for Ultrasensitive Bioanalysis in Complex Matrix. *Adv. Sci.* **2020**, *7* (2), 1902433. <https://doi.org/10.1002/advs.201902433>.
- (9) González-Rubio, G.; Kumar, V.; Llombart, P.; Díaz-Núñez, P.; Bladt, E.; Altantzis, T.; Bals, S.; Peña-Rodríguez, O.; Noya, E. G.; Macdowell, L. G.; Guerrero-Martínez, A.; Liz-Marzán, L. M. Disconnecting Symmetry Breaking from Seeded Growth for the Reproducible

- Synthesis of High Quality Gold Nanorods. *ACS Nano* **2019**, *13* (4), 4424–4435. <https://doi.org/10.1021/acsnano.8b09658>.
- (10) Sanz-ortiz, M. N.; Sentosun, K.; Bals, S.; Liz-marzan, L. M. Templated Growth of Surface Enhanced Raman Scattering-Active Branched Gold Nanoparticles within Radial Mesoporous Silica Shells. *ACS Nano* **2015**, *9* (10), 10489–10497. <https://doi.org/10.1021/acsnano.5b04744>.
- (11) Park, J.; An, K.; Hwang, Y.; Park, J. E. G.; Noh, H. J.; Kim, J. Y.; Park, J. H.; Hwang, N. M.; Hyeon, T. Ultra-Large-Scale Syntheses of Monodisperse Nanocrystals. *Nat. Mater.* **2004**, *3*(12), 891–895. <https://doi.org/10.1038/nmat1251>.
- (12) Goddard, Z. R.; Marín, M. J.; Russell, D. A.; Searcey, M. Active Targeting of Gold Nanoparticles as Cancer Therapeutics. *Chem. Soc. Rev.* **2020**, *49* (23), 8774–8789. <https://doi.org/10.1039/d0cs01121e>.
- (13) Pramanik, A.; Gao, Y.; Patibandla, S.; Mitra, D.; McCandless, M. G.; Fassero, L. A.; Gates, K.; Tandon, R.; Chandra Ray, P. The Rapid Diagnosis and Effective Inhibition of Coronavirus Using Spike Antibody Attached Gold Nanoparticles. *Nanoscale Adv.* **2021**, *3* (6), 1588–1596. <https://doi.org/10.1039/d0na01007c>.
- (14) Endo, K.; Terada, T. Protein Expression of CD44 (Standard and Variant Isoforms) in Hepatocellular Carcinoma: Relationships with Tumor Grade, Clinicopathologic Parameters, P53 Expression, and Patient Survival. *J. Hepatol.* **2000**, *32* (1), 78–84. [https://doi.org/10.1016/S0168-8278\(00\)80192-0](https://doi.org/10.1016/S0168-8278(00)80192-0).
- (15) Espinosa, A.; Reguera, J.; Curcio, A.; Muñoz-Noval, Á.; Kuttner, C.; Van de Walle, A.; Liz-Marzán, L. M.; Wilhelm, C. Janus Magnetic-Plasmonic Nanoparticles for Magnetically Guided and Thermally Activated Cancer Therapy. *Small* **2020**, *16* (11), 1904960. <https://doi.org/10.1002/smll.201904960>.
- (16) Abed, Z.; Beik, J.; Laurent, S.; Eslahi, N.; Khani, T.; Davani, E. S.; Ghaznavi, H.; Shakeri-Zadeh, A. Iron Oxide–Gold Core–Shell Nano-Theranostic for Magnetically Targeted Photothermal Therapy under Magnetic Resonance Imaging Guidance. *J. Cancer Res. Clin. Oncol.* **2019**, *145* (5), 1213–1219. <https://doi.org/10.1007/s00432-019-02870-x>.
- (17) Wang, J.; Wu, X.; Wang, C.; Shao, N.; Dong, P.; Xiao, R.; Wang, S. Magnetically Assisted Surface-Enhanced Raman Spectroscopy for the Detection of Staphylococcus Aureus Based on Aptamer Recognition. *ACS Appl. Mater. Interfaces* **2015**, *7* (37), 20919–20929. <https://doi.org/10.1021/acsam.5b06446>.
- (18) Sun, C.; Zhang, R.; Gao, M.; Zhang, X. A Rapid and Simple Method for Efficient Capture and Accurate Discrimination of Circulating Tumor Cells Using Aptamer Conjugated Magnetic Beads and Surface-Enhanced Raman Scattering Imaging. *Anal. Bioanal. Chem.* **2015**, *407*(29), 8883–8892. <https://doi.org/10.1007/s00216-015-9049-8>.

- (19) Nistler, A.; Hartmann, C.; Rügenapp, C.; Opel, M.; Gleich, B.; Ivleva, N. P.; Niessner, R.; Seidel, M. Production and Characterization of Long-Term Stable Superparamagnetic Iron Oxide-Shell Silica-Core Nanocomposites. *J. Magn. Magn. Mater.* **2017**, *442*, 497–503. <https://doi.org/10.1016/j.jmmm.2017.07.005>.
- (20) Lee, N.; Hyeon, T. Designed Synthesis of Uniformly Sized Iron Oxide Nanoparticles for Efficient Magnetic Resonance Imaging Contrast Agents. *Chem. Soc. Rev.* **2012**, *41* (7), 2575–2589. <https://doi.org/10.1039/c1cs15248c>.
- (21) Knobel, M.; Nunes, W. C.; Socolovsky, L. M.; De Biasi, E.; Vargas, J. M.; Denardin, J. C. Superparamagnetism and Other Magnetic Features in Granular Materials: A Review on Ideal and Real Systems. *J. Nanosci. Nanotechnol.* **2008**, *8* (6), 2836–2857. <https://doi.org/10.1166/jnn.2008.15348>.
- (22) Yadav, B. Sen; Singh, R.; Vishwakarma, A. K.; Kumar, N. Facile Synthesis of Substantially Magnetite-Hollow Nanospheres of Maghemite (γ - Fe_2O_3) Originated from Magnetite (Fe_3O_4) via Solvothermal Method. *J. Supercond. Nov. Magn.* **2020**, *33* (7), 2199–2208. <https://doi.org/10.1007/s10948-020-05481-7>.
- (23) Mohamed, M. B.; Ismail, K. Z.; Link, S.; El-Sayed, M. A. Thermal Reshaping of Gold Nanorods in Micelles. *J. Phys. Chem. B* **1998**, *102* (47), 9370–9374. <https://doi.org/10.1021/jp9831482>.
- (24) Kennedy, W. J.; Izor, S.; Anderson, B. D.; Frank, G.; Varshney, V.; Ehlert, G. J. Thermal Reshaping Dynamics of Gold Nanorods: Influence of Size, Shape, and Local Environment. *ACS Appl. Mater. Interfaces* **2018**, *10* (50), 43865–43873. <https://doi.org/10.1021/acsami.8b12965>.
- (25) Tang, J.; Myers, M.; Bosnick, K. A.; Brus, L. E. Magnetite Fe_3O_4 Nanocrystals: Spectroscopic Observation of Aqueous Oxidation Kinetics. *J. Phys. Chem. B* **2003**, *107*(30), 7501–7506. <https://doi.org/10.1021/jp027048e>.
- (26) Espinosa, A.; Kolosnjaj-Tabi, J.; Abou-Hassan, A.; Plan Sangnier, A.; Curcio, A.; Silva, A. K. A.; Di Corato, R.; Neveu, S.; Pellegrino, T.; Liz-Marzán, L. M.; Wilhelm, C. Magnetic (Hyper)Thermia or Photothermia? Progressive Comparison of Iron Oxide and Gold Nanoparticles Heating in Water, in Cells, and in Vivo. *Adv. Funct. Mater.* **2018**, *28* (37), 1803660. <https://doi.org/10.1002/adfm.201803660>.
- (27) Majumder, J.; Taratula, O.; Minko, T. Nanocarrier-Based Systems for Targeted and Site Specific Therapeutic Delivery. *Adv. Drug Deliv. Rev.* **2019**, *144*, 57–77. <https://doi.org/10.1016/j.addr.2019.07.010>.
- (28) Chen, C.; Zhao, S.; Karnad, A.; Freeman, J. W. The Biology and Role of CD44 in Cancer Progression: Therapeutic Implications. *J. Hematol. Oncol.* **2018**, *11* (1), 1–23. <https://doi.org/10.1186/s13045-018-0605-5>.

- (29) Pramanik, A.; Xu, Z.; Ingram, N.; Coletta, P. L.; Millner, P. A.; Tyler, A. I. I.; Hughes, T. A. Hyaluronic-Acid-Tagged Cubosomes Deliver Cytotoxics Specifically to CD44-Positive Cancer Cells. **2022**. <https://doi.org/10.1021/acs.molpharmaceut.2c00439>.
- (30) Marques, A. C.; Costa, P. J.; Velho, S.; Amaral, M. H. Functionalizing Nanoparticles with Cancer-Targeting Antibodies: A Comparison of Strategies. *J. Control. Release* **2020**, *320* (January), 180–200. <https://doi.org/10.1016/j.jconrel.2020.01.035>.
- (31) Yan, W.; Chen, Y.; Yao, Y.; Zhang, H.; Wang, T. Increased Invasion and Tumorigenicity Capacity of CD44 + / CD24 - Breast Cancer MCF7 Cells in Vitro and in Nude Mice. **2013**, No. 13, 62.
- (32) van Aarle, W.; Palenstijn, W. J.; De Beenhouwer, J.; Altantzis, T.; Bals, S.; Batenburg, K. J.; Sijbers, J. The ASTRA Toolbox: A Platform for Advanced Algorithm Development in Electron Tomography. *Ultramicroscopy* **2015**, *157*, 35–47. <https://doi.org/10.1016/j.ultramic.2015.05.002>.
- (33) Sentosun, K.; Sanz Ortiz, M. N.; Batenburg, K. J.; Liz-Marzán, L. M.; Bals, S. Combination of HAADF-STEM and ADF-STEM Tomography for Core-Shell Hybrid Materials. *Part. Part. Syst. Charact.* **2015**, *32* (12), 1063–1067. <https://doi.org/10.1002/ppsc.201500097>.
- (34) Reguera, J.; Jiménez De Aberasturi, D.; Henriksen-Lacey, M.; Langer, J.; Espinosa, A.; Szczupak, B.; Wilhelm, C.; Liz-Marzán, L. M. Janus Plasmonic-Magnetic Gold-Iron Oxide Nanoparticles as Contrast Agents for Multimodal Imaging. *Nanoscale* **2017**, *9* (27), 9467–9480. <https://doi.org/10.1039/c7nr01406f>.

Chapter V



5. Guidelines on reporting the photothermal effect of plasmonic nanoheaters

Contents

| | |
|--|-----|
| 5.1 Introduction..... | 182 |
| 5.2 Synthesis and characterization of gold nanostars... | 184 |
| 5.3 Photothermal measurements | 185 |
| 5.3.1 Importance of collimating the laser beam..... | 186 |
| 5.3.2 Importance of a correct calibration | 188 |
| 5.3.3 Importance of the use of a multimode or a single mode laser..... | 188 |
| 5.4 Results | 190 |
| 5.5 Conclusions | 191 |
| 5.6 Experimental Section | 193 |
| 5.6.1 Materials | 193 |
| 5.6.2 Nanoparticle synthesis..... | 193 |
| 5.6.3 Nanoparticle characterization | 193 |
| References | 194 |

5.1 Introduction

In this final chapter we address the importance of providing a complete report of the conditions used for photothermal measurements, as well as the potential consequences of undefined conditions on the reproducibility and comparability of different systems and their measurements.

Along this thesis, we focused on the application of hybrid IOAuNPs for photothermal heating. Within our aim to learn about the photothermal effect and the techniques that are used to measure and evaluate the performance of NPs as nanoheaters, as discussed in chapter III, a short stay in the group of Prof. Claire Wilhelm was carried out to gain knowledge from a group with extensive expertise in the study of the photothermal properties of colloidal systems. After that stay, we attempted to implement their protocols in our laboratory and reproduce the methods they use.

However, we noticed that even when performing the measurements under the same conditions and carefully reproducing the same set-up, we were unable to obtain the same results. Consequently, we started analysing those parameters that could affect the measurements, so as to understand where the differences might come from. After an extensive study, we found that some parameters that are rarely reported or considered when performing photothermal measurements, are however key toward the reproducibility of the measurements. In this chapter V, we report how the components of the laser heating set-up can affect the results and we present some guidelines that we consider should be followed when reporting on the photothermal effect of plasmonic nanoheaters.

As explained in Chapters III and IV, the photothermal effect induced upon laser irradiation is an interesting method to produce local and rapid temperature increments in a controlled manner, which in turn allow destroying cancer cells selectively¹. Therefore, several *in vitro* and *in vivo* studies has been carried out^{2,3} and the technique has been employed in clinical trials for prostate tumour ablation⁴ and head and neck cancer⁵.

We demonstrated in Chapter III that AuNPs can act as efficient local heating agents because they feature suitable optical properties for their use as photosensitizers^{6,7}. The photothermal efficiency of NPs as photosensitisers strongly depends on the morphology and size of the particles⁸ and AuNPs should present low scattering and strong absorption cross sections within the region around the irradiation laser wavelength⁹.

To understand the efficiency of AuNPs as nanoheaters, an important concern is how these photothermal agents are characterized. In the design of PTH experiments using AuNPs, prior to application in cells or *in vivo* studies, the first step generally includes the irradiation of a dispersion of AuNPs at a certain laser power to study their heating efficiency, occasionally described as the Specific Absorption Rate (SAR)^{10,11}. Consequently, besides from laser wavelength and power (and thus, power density), sample volume and concentration are also crucial aspects affecting the overall heating efficiency.

In many cases, the reported data on the application of PTH are far from following a standard protocol. A literature search of the most relevant hybrid NPs for PTH was carried out and is summarized in **Table 5.1**. It can be readily noticed that different conditions are reported for each system, in terms of laser power, irradiation time and NP concentration. Therefore, benchmarking of the efficiency of different particles remains largely challenging and unclear. In most cases, even key parameters such as the temperature increase, irradiation time of NP concentrations are missing or unclear. Concentrations of hybrid NPs expressed as mg/mL are not informative enough, specific information about the concentration of each metal component, should be provided for a fair comparison to be made. Additionally, the achieved temperature increment (ΔT), irradiation time (min), as well as information of the power density of the laser used for the PTH experiments (expressed in W/cm²) are key aspects when trying to compare and reproduce experiments.

Table 5.1. Summary of hybrid nanoparticles for PTH.

| Hybrid NP | Concentration | Treatment | Laser λ (nm) | Power density W/cm ² | Time (min) | ΔT (°C) | Ref. |
|------------------|------------------------------|------------------------|----------------------|---------------------------------|------------|-----------------|------|
| Core-shell | [Au] 1 mM [Fe] 2 mM | PTT <i>in vivo</i> | 808 | 1.4 | 15 | 16.7 | 18 |
| Core-shell | [Fe] 160 $\mu\text{g/mL}$ | PTT <i>in vitro</i> | 808 | 2 | 10 | 40 | 19 |
| Core-shell | [Au] 1.25mM | PTT <i>in vitro</i> | 808 | 1.5 | 5 | 49 | 20 |
| Nano-domes | [Fe] 100 $\mu\text{g/mL}$ | PTT <i>in vitro</i> | 808 | 5 | 0.5 | - | 21 |
| Core-shell | [Fe] 40 $\mu\text{mol/L}$ | PTT <i>in vitro</i> | 808 | 1 | 10 | 30 | 22 |
| Spiky core-shell | [Fe] 4 nM | PTT <i>in vivo</i> | 808 | 0.5 | 6 | 65.7 | 23 |
| Nano popcorns | [NPs] 4 $\mu\text{g/mL}$ | PTT <i>in vitro</i> | 808 | 0.55 | 10 | 21.4 | 24 |
| Janus | [Fe] 6 mM | PPT <i>in vitro</i> | 680 | 0.5 | 5 | 32.3 | 11 |
| Core-satellite | [Fe] 150 mM | PTT <i>in vivo</i> | 680 | 0.3 | 5 | 20 | 3 |

Additionally, in the majority of published reports, there is a lack of information related to the equipment configuration, irradiation conditions, and laser calibration, all of which hinder the reproducibility of the measurements and limit reliable comparisons between different nanoheaters¹²⁻¹⁷.

In this study, we highlight important parameters that influence the increase of temperature produced by AuNPs under laser irradiation. Additionally, we have identified lesser discussed aspects such as the use of a laser beam collimator, the laser position during calibration, and the use of multimode or single-mode lasers, as crucial parameters toward the reproducibility of experimental findings (Figure 5.1). Consequently, we propose the standardization of protocols to thoroughly report all experimental parameters, should we aim to advance the application of PTH.

We thus present the importance of the mentioned parameters and how the obtained heating values are affected when measuring the same sample under different conditions.

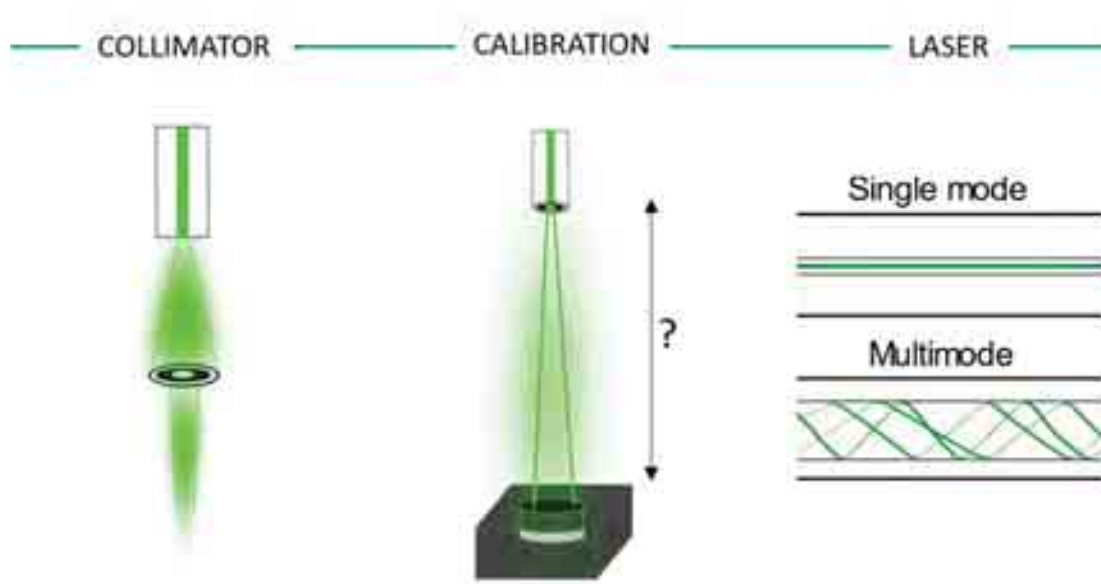


Figure 5.1. Scheme of the parameters that were studied regarding their effect in photothermal measurements.

5.2 Synthesis and characterization of gold nanostars

For this study, AuNSs were synthesized using a seed-mediated surfactant-free method²⁵, with slight modifications. Briefly, 15 nm Au seeds were added to 10 mL of water containing H₂AuCl₄ and HCl, followed by a simultaneous and fast addition of AgNO₃ and ascorbic acid (AA), which promotes the growth of Au seeds into AuNSs. Thus, the amount of seeds that was added to the reaction as nucleation points was adjusted to obtain AuNSs with an LSPR centred at ca. 813 nm, in close resonance with the laser wavelength used in this work (808 nm). The average diameter (tip to tip) of the obtained AuNSs (117.3 ± 10.3 nm) was measured from TEM images. Further details on the preparation can be found in the Experimental section (5.6.2), while the

characterization of the AuNSs is shown in **Figure 5.2**. These AuNSs were used for all the heating experiments that are discussed in this chapter.

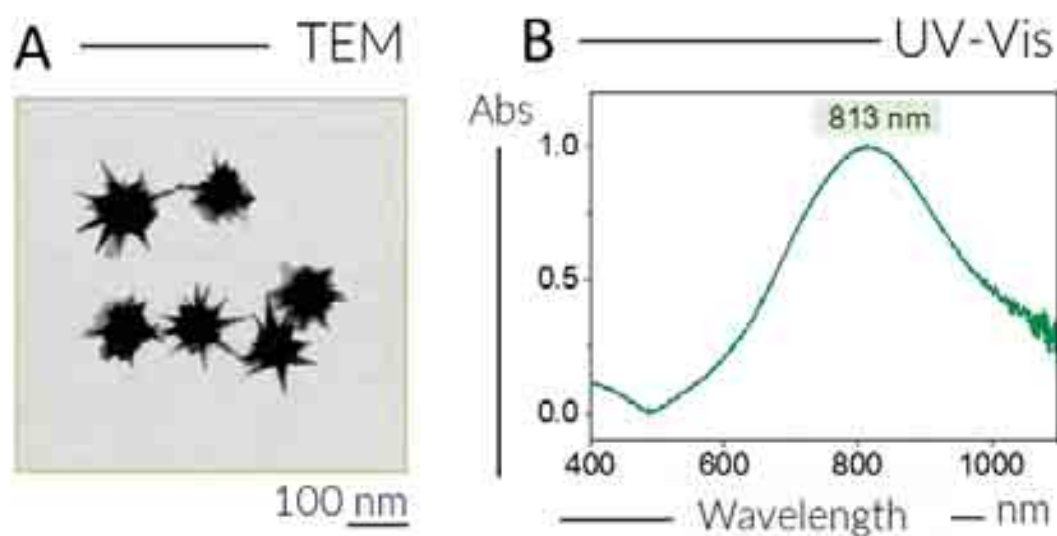


Figure 5.2. (A) Representative TEM image of the synthesized AuNSs. (B) UV-vis spectra of AuNSs normalized at the LSPR maximum (813 nm).

5.3 Photothermal measurements

All the AuNSs photothermal measurements were performed in aqueous dispersion, using a fixed concentration ($[Au] = 0.1 \text{ mM}$) and volume ($50 \mu\text{L}$). Samples were placed in a 0.5 mL Eppendorf tube, thus always maintaining the same geometrical conditions such as sample volume in the laser beam path. The Eppendorf tube was held in a purposefully 3D-printed support at controlled distances from the exit of the laser optical fibre. The sample was suspended in air, at a distance of ca. 5 cm from the benchtop and thus was not in contact with any material underneath which may have affected heat absorption or light reflection. Each sample was then irradiated for 5 min using a vertical setup with the laser, coupled to an optic fibre, shining downwards on top of the Eppendorf tube. Two types of lasers were used for comparison: a single-mode (Laser components SAS, France) and a multimode (Lumics GmbH IR; LU0808T040) diode laser. Both lasers were applied at a power density of 1 W/cm^2 . Prior to all experiments, both lasers were calibrated to determine the power needed to achieve a power density of 1 W/cm^2 . The use of a non-collimated beam required the use of a mask during calibration. A square mask, with a centred hole measuring 4 mm in diameter, was 3D-printed using a photopolymer resin. The mask was then covered with aluminium foil, keeping the hole in the centre free. This mask allowed us to block light that does not interact with the sample and therefore to determine the power required to achieve a power density of 1 W/cm^2 . The diameter of the mask must be properly chosen to make it match the diameter of the sample irradiation area. In this study, 0.5 mL Eppendorf tubes containing the sample solution were used, and the diameter of the upper solution surface was measured to be 4 mm. It should be noted that the irradiation area will change when using other volumes or tubes, and consequently the hole in the mask should be adjusted to ensure a correct calculation of the

output power during calibration. After irradiation for 5 min, the samples were allowed to cool down for 2 min. An infrared camera (FLIR A35) was used to register temperature changes during the experiments; in order to do so, a region of interest (ROI) was drawn equivalent to the surface area of the AuNP solution in the Eppendorf ($D = 4$ mm), and a further ROI outside of the sample was used as a background control. Temperature increments were calculated from the acquired data by subtracting the initial temperature (time = 0) from the final temperature (time = 5 min). All experiments were conducted in triplicate with fresh, non-irradiated AuNSs solutions. Additionally, the experiments were performed in a closed room under controlled temperature.

5.3.1 Importance of collimating the laser beam

Fibre-coupled lasers emit strongly diverging light that has not parallel rays but scattered angles. In order to avoid this divergence, a collimator can be used, which improves the directionality of the beam leaving the optical fibre, resulting in parallel rays with low beam divergence. The resulting effect is that the beam diameter along its path (once outside the optical fibre, also known as the spot size) does not increase significantly, and thus, the power density reaching a sample at different distances from the laser will remain constant. In contrast, due to the divergence of a non-collimated beam, a significant increase in the spot size and thus decrease in the power density will result upon small changes in the distance between the laser and the sample. To prove the importance of collimating a laser source in PTH experiments, two different conditions were tested. In the first one, no collimator was applied and both single and multimode lasers were compared (experiments 1 and 2, respectively). The experimental setup was the same for both measurements, in that the laser was placed at a distance of 4 cm from the sample, resulting in a spot size that was slightly bigger ($D = 6$ mm, area = 28.3 mm²) than the sample area ($D = 4$ mm, area = 12.6 mm²) due to the lack of beam collimation. In order to calibrate both lasers to determine the power density actually reaching the sample, a mask was required to black out all illumination not reaching the samples. The mask was removed for the actual measurement. A schematic representation of the set-up is shown in **Figure 5.3**. In the second condition (experiments 3 and 4), a collimator was applied and, therefore, the distance between laser and sample was increased to achieve a spot size of the same diameter ($D = 6$ mm) as in the first experimental condition. Again, in order to block out light not interacting with the sample, a mask was applied for the calibration step.



Figure 5.3. Scheme of the set-up for the calibration and irradiation of samples when measuring with a non-collimated beam or a collimated beam with a spot size bigger than the irradiation area.

The design of this experiment allowed us to study the effect of the laser profile on the overall heating of AuNss. As previously mentioned, whereas single-mode lasers emit light of low divergence and low light output modes, multimode lasers emit light of multiple modes which forms a Gaussian-curve in its intensity. As such, it is reasonable to expect that the homogeneity of irradiation intensity of a single-mode laser is higher than that for a multimode laser. Taking into consideration the increasing beam divergence with increasing the distance between laser and sample in cases where no collimation is applied, it is also expected that multimodal lasers will lose more laser intensity.

The results of the experiments showed that, for experiments 1 and 2 in which the beam was not collimated, huge differences were found between the results when using a single-mode (23.2 ± 1.4) and a multimode laser (9.9 ± 1.1), but such differences are not significant when the beam is collimated, obtaining temperature increments of (10.1 ± 0.3) and (9.2 ± 0.1), for single-mode and multimode lasers, respectively.

5.3.2 Importance of a correct calibration

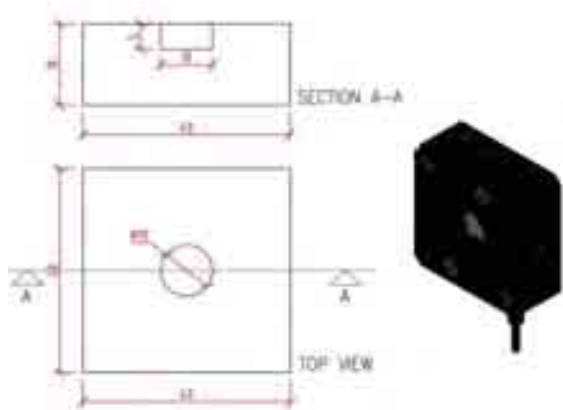


Figure 5.4. Design of a conventional power meter, in which the detector is located inside the case at a different level.

As in all quantitative techniques, a correct calibration is crucial to achieve precise results. Often, the importance of the distance between laser and sample is taken for granted, or poorly characterized. However, considering that the power and modal profile reaching a sample is directly related to the spot size, it is understandable that a correct comparison between samples requires maintaining the exact same laser-sample distance. Additionally, not only for different samples but also for different sample and calibration measurement setups, should the

laser-sample distance remain the same. A standard power meter configuration is shown in **Figure 5.4**. Of note, the detector itself is slightly offset from the outer casing, lying at a distance of ca. 5 mm inside the casing. Thus, we chose to repeat the initial experimental conditions (single vs. multimode without collimation) but to factor in this a difference of 5 mm between calibration and experimental setups. The experimental set-up is the same as in **Figure 5.3** but changing the distance from 4 to 4.5 cm in the calibration.

The results showed a temperature increment of 19.9 ± 2.3 °C for the single-mode laser (experiment 5) and 26.5 ± 1.1 °C for the multimode laser (experiment 6). To see the effect of a wrong calibration, we compared these results with those obtained in experiment 1 (23.2 ± 1.4 °C) and experiment 2 (9.9 ± 1.1 °C). It can be noticed that, for a non-collimated beam, the effect of a 5 mm error in the calibration position remarkably affects the temperature increment when using a multimode laser, in which a difference of 16.6 °C was recorded. By contrast, this effect was not appreciated when using a single mode laser.

5.3.3 Importance of the use of a multimode or a single mode laser

The mode of the beam has been found to be a factor that could affect the results when measuring colloidal NPs. The essential difference between a single mode and a multimode laser is related to changes in the spatial distribution of energy. Single mode lasers display a Gaussian distribution, whereas multimode lasers present a flat-type distribution which energy is averaged. Thus, the energy of a single mode laser is relatively concentrated, the core is thin, and the 3D map is represented by a circle. By contrast, the multimode laser core is thicker, the energy distribution is wider than in the single mode laser, and the 3D map corresponds to an inverted cup²⁶. A schematic representation of laser types and their energy distributions can be seen in **Figure 5.5**.

In general terms, the choice of single-mode or multimode laser mainly depends on the user needs. Thus, it is not known a priori, which kind of laser is better for each particular application. However,

the differences when using a single-mode or a multimode laser must be considered when measuring NPs for PTH.

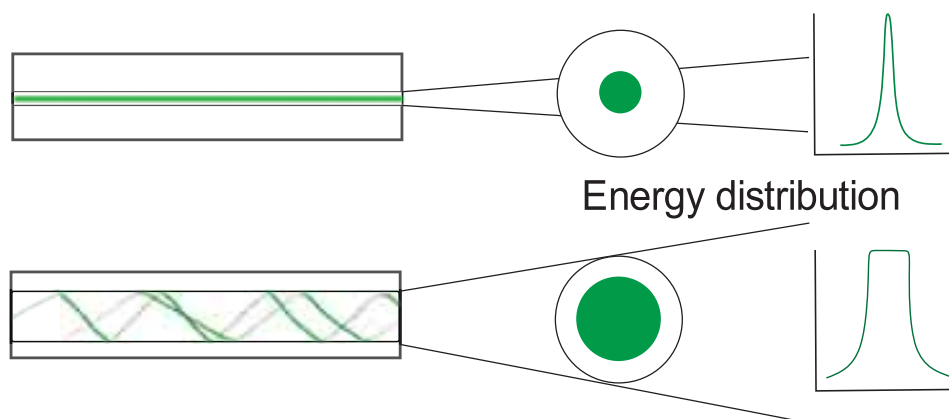


Figure 5.5. Scheme of the energy distributions for a single-mode laser (upper panel) and a multimode laser (lower panel).

Two additional experiments were performed using the single-mode and the multimode lasers, to study the influence of the type of laser on photothermal measurements. Thus, samples were irradiated using a collimated beam with a spot size matching the irradiation area ($D = 4$ mm), both with a single-mode laser (experiment 7) and a multimode laser (experiment 8). A schematic representation of the set-up is shown in **Figure 5.6**.



Figure 5.6. Schematic representation of the laser configuration when calibrating and measuring using a collimator with a beam spot size of equal area as the irradiation area.

The results showed that, when collimating the beam and adjusting the spot size to the irradiation area, the results are similar for single-mode (8.6 ± 0.3 °C) and multimode (8.3 ± 0.5 °C) laser.

Besides, when comparing the results with experiment 3 ($10.1 \pm 0.3 \text{ }^\circ\text{C}$) and experiment 4 ($9.2 \pm 0.1 \text{ }^\circ\text{C}$), in which we have used a collimator without adjusting the spot size, the results are slightly higher but still similar. The single-mode and multimode lasers work similarly when using a collimator but when the beam is not collimated significant differences are registered between them as shown in the two first experiments ($23.2 \pm 1.4 \text{ }^\circ\text{C}$) vs ($9.9 \pm 1.1 \text{ }^\circ\text{C}$).

5.4 Results

The results demonstrated that the details of the set-up and the experimental conditions are crucial for a reliable data output. The average temperature increments are shown as heating curves for all the experiments in **Figure 5.7**. The plots represent the temperature increase during 5 minutes of heating at 1 W/cm^2 and 2 min of cooling for all the experiments, in triplicate.

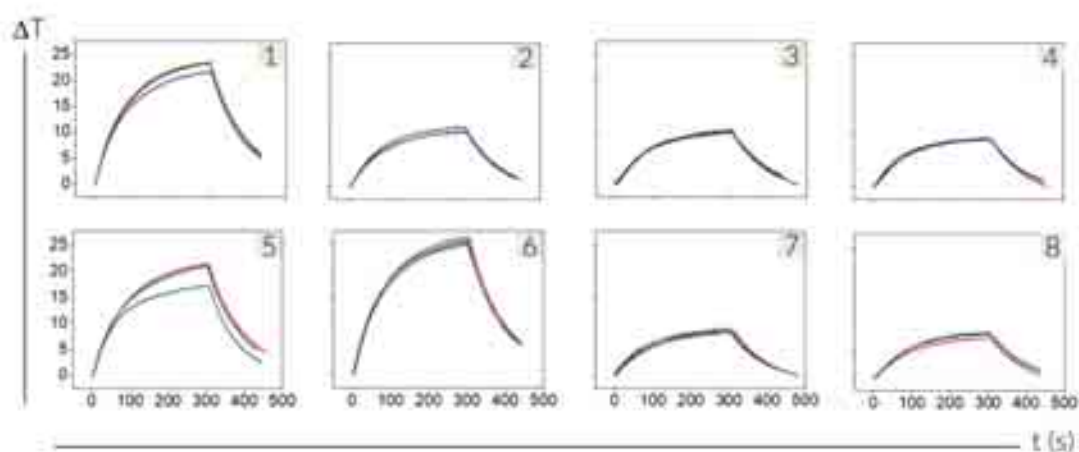


Figure 5.7. Temperature increment curves (ΔT , in $^\circ\text{C}$) during 5 min of irradiation at 1 W/cm^2 using AuNSs colloidal dispersion ($50 \mu\text{L}$, 0.1 mM).

A summary of the experimental conditions for all the experiments is shown in **Table 5.2**. Summary of the experimental conditions for the irradiation experiments 1-8. the results is represented in **Figure 5.8**.

Table 5.2. Summary of the experimental conditions for the irradiation experiments 1-8.

| Experiment | Laser | Collimator | Spot size | Distance detector (Calibration) | Distance sample (Irradiation) | ΔT |
|------------|--------|------------|-----------|---------------------------------|-------------------------------|----------------|
| 1 | Single | No | >4 mm | 4 cm | 4 cm | 23.2 ± 1.4 |
| 2 | Multi | No | >4 mm | 4 cm | 4 cm | 9.9 ± 1.1 |
| 3 | Single | Yes | >4 mm | 21 cm | 21 cm | 10.1 ± 0.3 |
| 4 | Multi | Yes | >4 mm | 21 cm | 21 cm | 9.2 ± 0.1 |
| 5 | Single | No | >4 mm | 4.5 cm | 4 cm | 19.9 ± 2.3 |
| 6 | Multi | No | >4 mm | 4.5 cm | 4 cm | 26.5 ± 1.1 |
| 7 | Single | Yes | 4 mm | 10 cm | 10 cm | 8.6 ± 0.3 |
| 8 | Multi | Yes | 4 mm | 10 cm | 10 cm | 8.3 ± 0.5 |

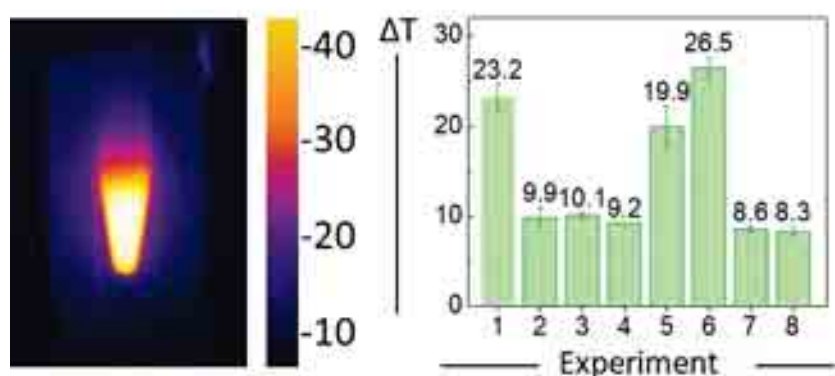


Figure 5.8. PTH results representing the experimental increase of temperature. A real image acquired with the thermal camera upon irradiation of one of the samples is shown in the left panel.

5.5 Conclusion

We have demonstrated that giving precise information about the specific photothermal heating set-up and operation conditions is crucial for the reproducibility of PTH results and therefore should be mandatory in related scientific reports. The combination of a wide variety of factors may easily yield different results, which should be considered not only from the point of view of establishing guidelines for measuring the PTH efficiency of NP sensitizers and obtaining a reliable benchmarking, but also because it provides valuable information toward selecting the most suitable set-up for a desired application. For example, when a higher temperature increment is needed, the use of a single-mode laser without collimator should be considered. We have also proven that a lower variability in the results is obtained when using a collimator of the beam because, even when changing the laser spot size, consistent results were obtained.

Besides, the importance of a proper calibration has been also demonstrated. In particular, special care should be taken when using a multimode without collimator of the beam because even slight mistakes may lead to wrong results.

Additionally, to prove that PTH results can be reproduced when all the details of the set-up are provided, we have reproduced the PTH measurements of AuNSs that were previously reported by our group¹⁰. The temperature increase was the same as in the published article, as shown in **Figure 5.9**.

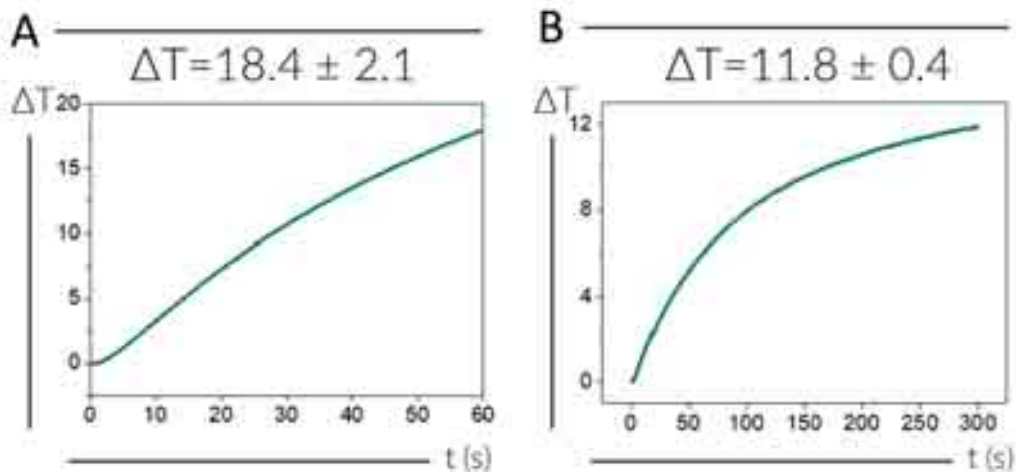


Figure 5.9. Average temperature increment (ΔT in $^{\circ}\text{C}$) over time for 150 μL of AuNSs solution ($[\text{Au}] = 0.75 \text{ mM}$) irradiated for (A) 1 min at 1 W/cm^2 and (B) 5 min at 0.3 W/cm^2 .

The reported configuration was employed for the measurements¹⁰. Thus, 150 μL of 85 nm AuNSs at $[\text{Au}] = 0.75 \text{ mM}$ were placed in a 0.5 mL Eppendorf tube. A single-mode laser working at 1 W/cm^2 was used without collimator. The spot size was bigger than the irradiation area ($D = 5.5 \text{ mm}$, area = 23.7 mm^2), a mask of 5.5 mm was used for the calibration, to adjust the output power to 1 W/cm^2 at 4 cm distance. Since the volume of the irradiated sample was increased, the size of the hole in the mask was accordingly adjusted, in this case to the irradiation area. When 50 μL of the dispersion were introduced inside an Eppendorf tube, the diameter at the height of the solution was 4 mm, which changes to 5.5 mm when 150 μL are introduced in the same Eppendorf tube (see **Figure 5.10**). As reported in the publication, the irradiation laser was placed at the same distance to the sample and the temperature was registered during 1 min. Then, the power density was lowered to 0.3 W/cm^2 and the samples were irradiated for 5 min to see the increase in the temperature profile. The previously reported results showed the same results as those acquired in these experiments, with a temperature increase of $17 \text{ }^{\circ}\text{C}$ for 1 W/cm^2 and $10 \text{ }^{\circ}\text{C}$ for 0.3 W/cm^2 .

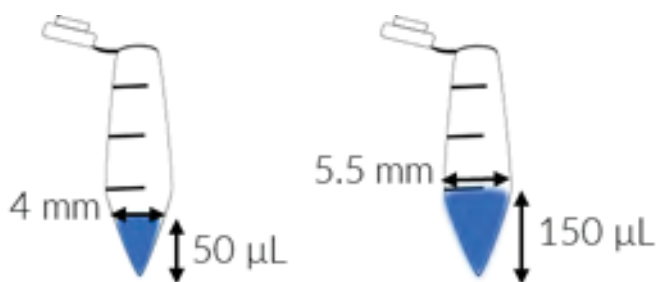


Figure 5.10. Schematic representation of the height of different volumes in an Eppendorf.

Taking all this information into account, we have demonstrated that clear differences can be appreciated between experiments carried out with different set-ups, evidencing an effect of the studied parameters on the results. We can thus conclude that the set-up conditions must be accurately described to avoid reporting incomplete and unreliable data from the point of view of reproducibility and efficiency of nanoheaters.

5.6 Experimental Section

5.6.1 Materials

Hydrogen tetrachloroaurate trihydrate ($\text{HAuCl}_4 \cdot 3 \text{H}_2\text{O}$, $\geq 99.9\%$), sodium citrate tribasic dihydrate ($\geq 98\%$), silver nitrate (AgNO_3 , $\geq 99.0\%$), hydrochloric acid (HCl, 37%), L-ascorbic acid (AA, $\geq 99\%$) and O-[2-(3-mercaptopropionylamino) ethyl]-O'-methylpolyethylene glycol (PEG, Mw 5.000 Da) were purchased from Sigma-Aldrich. Milli-Q water was used for all experiments. All glassware was washed with aqua regia before use.

5.6.2 Nanoparticle synthesis

Synthesis of 15 nm Au seeds. 95 mL of 0.5 mM HAuCl_4 was mixed under vigorous stirring and heated until boiling under vigorous stirring. Then 5 mL of 34 mM citrate solution was added. After 15 min of boiling, the solution was cooled down and stored at 4 °C. The formation of Au seeds is evidenced by a change in the solution colour, from pale yellow to red.

Synthesis of AuNSss²⁵. 50 μL of 15 nm Au seeds $[\text{Au}] = 0.5 \text{ mM}$ were added to 10 mL of water containing 50 μL HAuCl_4 (50 mM) and 10 μL of HCl 1 M followed by a simultaneous and fast addition of 30 μL of AgNO_3 10 mM and 50 μL AA 100 mM. After 30 seconds, 100 μL of PEG-SH 0.1 mM was added as a stabilizer for the AuNSss. The sample was centrifuged twice (3500 rpm, 30 min) and dispersed in water. The resulting average tip-to-tip diameter ($117.3 \pm 10.3 \text{ nm}$) was measured from TEM images.

5.6.3 Nanoparticle characterization

NPs standard characterization. The synthesized AuNSss were characterized using TEM and UV-Vis. UV-vis optical extinction spectra were recorded using an Agilent 8453 UV-Vis diode array spectrophotometer, normalizing spectra at the LSPR maximum (813 nm). TEM images were collected with a JEOL JEM-1400PLUS transmission electron microscope operating at 120 kV, using carbon-coated 400 square mesh Cu grids.

References

- (1) Zou, L.; Wang, H.; He, B.; Zeng, L.; Tan, T.; Cao, H.; He, X.; Zhang, Z.; Guo, S.; Li, Y. Current Approaches of Photothermal Therapy in Treating Cancer Metastasis with Nanotherapeutics. *Theranostics* **2016**, *6* (6), 762–772. <https://doi.org/10.7150/thno.14988>.
- (2) Kim, M.; Lee, J. H.; Nam, J. M. Plasmonic Photothermal Nanoparticles for Biomedical Applications. *Adv. Sci.* **2019**, *6* (17), 1900471. <https://doi.org/10.1002/adv.201900471>.
- (3) Espinosa, A.; Bugnet, M.; Radtke, G.; Neveu, S.; Botton, G. A.; Wilhelm, C.; Abou-Hassan, A. Can Magneto-Plasmonic Nanohybrids Efficiently Combine Photothermia with Magnetic Hyperthermia? *Nanoscale* **2015**, *7* (45), 18872–18877. <https://doi.org/10.1039/c5nr06168g>.
- (4) Rastinehad, A. R.; Anastos, H.; Wajswol, E.; Winoker, J. S.; Sfakianos, J. P.; Doppalapudi, S. K.; Carrick, M. R.; Knauer, C. J.; Taouli, B.; Lewis, S. C.; Tewari, A. K.; Schwartz, J. A.; Canfield, S. E.; George, A. K.; West, J. L.; Halas, N. J. Gold Nanoshell-Localized Photothermal Ablation of Prostate Tumors in a Clinical Pilot Device Study. *Proc. Natl. Acad. Sci. U. S. A.* **2019**, *116* (37), 18590–18596. <https://doi.org/10.1073/pnas.1906929116>.
- (5) ClinicalTrials.gov. <https://clinicaltrials.gov/ct2/show/study/NCT00848042?term=photothermal+therapy&draw=3&rank=11>.
- (6) Baffou, G.; Quidant, R. Thermo-Plasmonics: Using Metallic Nanostructures as Nano-Sources of Heat. *Laser Photonics Rev.* **2013**, *7* (2), 171–187. <https://doi.org/10.1002/lpor.201200003>.
- (7) Lv, Z.; He, S.; Wang, Y.; Zhu, X. Noble Metal Nanomaterials for NIR-Triggered Photothermal Therapy in Cancer. *Adv. Healthc. Mater.* **2021**, *10* (6), 2001806. <https://doi.org/10.1002/adhm.202001806>.
- (8) Jimenez de Aberasturi, D.; Serrano-Montes, A. B.; Liz-Marzán, L. M. Modern Applications of Plasmonic Nanoparticles: From Energy to Health. *Adv. Opt. Mater.* **2015**, *3* (5), 602–617. <https://doi.org/10.1002/adom.201500053>.
- (9) Khlebtsov, B.; Zharov, V.; Melnikov, A.; Tuchin, V.; Khlebtsov, N. Optical Amplification of Photothermal Therapy with Gold Nanoparticles and Nanoclusters. *Nanotechnology* **2006**, *17* (20), 5167–5179. <https://doi.org/10.1088/0957-4484/17/20/022>.
- (10) Espinosa, A.; Kolosnjaj-Tabi, J.; Abou-Hassan, A.; Plan Sangnier, A.; Curcio, A.; Silva, A. K. A.; Di Corato, R.; Neveu, S.; Pellegrino, T.; Liz-Marzán, L. M.; Wilhelm, C. Magnetic (Hyper)Thermia or Photothermia? Progressive Comparison of Iron Oxide and Gold Nanoparticles Heating in Water, in Cells, and in Vivo. *Adv. Funct. Mater.* **2018**, *28* (37), 1803660. <https://doi.org/10.1002/adfm.201803660>.

- (11) Espinosa, A.; Reguera, J.; Curcio, A.; Muñoz-Noval, Á.; Kuttner, C.; Van de Walle, A.; Liz-Marzán, L. M.; Wilhelm, C. Janus Magnetic-Plasmonic Nanoparticles for Magnetically Guided and Thermally Activated Cancer Therapy. *Small* **2020**, *16* (11), 1904960. <https://doi.org/10.1002/sml.201904960>.
- (12) Dai, X.; Zhao, X.; Liu, Y.; Chen, B.; Ding, X.; Zhao, N.; Xu, F. J. Controlled Synthesis and Surface Engineering of Janus Chitosan-Gold Nanoparticles for Photoacoustic Imaging-Guided Synergistic Gene/Photothermal Therapy. *Small* **2021**, *17*, 2006004. <https://doi.org/10.1002/sml.202006004>.
- (13) Riley, R. S.; Day, E. S. Gold Nanoparticle-Mediated Photothermal Therapy: Applications and Opportunities for Multimodal Cancer Treatment. *Wiley Interdiscip. Rev. Nanomedicine Nanobiotechnology* **2017**, *9*(4), e1449. <https://doi.org/10.1002/wnan.1449>.
- (14) Xia, H.; Gao, Y.; Yin, L.; Cheng, X.; Wang, A.; Zhao, M.; Ding, J.; Shi, H. Light-Triggered Covalent Coupling of Gold Nanoparticles for Photothermal Cancer Therapy. *ChemBioChem* **2019**, *20*(5), 667–671. <https://doi.org/10.1002/cbic.201800648>.
- (15) Park, S.; Lee, W. J.; Park, S.; Choi, D.; Kim, S.; Park, N. Reversibly PH-Responsive Gold Nanoparticles and Their Applications for Photothermal Cancer Therapy. *Sci. Rep.* **2019**, *9*, 20180. <https://doi.org/10.1038/s41598-019-56754-8>.
- (16) Ong, C.; Cha, B. G.; Kim, J. Mesoporous Silica Nanoparticles Doped with Gold Nanoparticles for Combined Cancer Immunotherapy and Photothermal Therapy. *ACS Appl. Bio Mater.* **2019**, *2*(8), 3630–3638. <https://doi.org/10.1021/acsabm.9b00483>.
- (17) Zhang, Y.; Zhan, X.; Xiong, J.; Peng, S.; Huang, W.; Joshi, R.; Cai, Y.; Liu, Y.; Li, R.; Yuan, K.; Zhou, N.; Min, W. Temperature-Dependent Cell Death Patterns Induced by Functionalized Gold Nanoparticle Photothermal Therapy in Melanoma Cells. *Sci. Rep.* **2018**, *8*(1), 8720. <https://doi.org/10.1038/s41598-018-26978-1>.
- (18) Abed, Z.; Beik, J.; Laurent, S.; Eslahi, N.; Khani, T.; Davani, E. S.; Ghaznavi, H.; Shakeri-Zadeh, A. Iron Oxide–Gold Core–Shell Nano-Theranostic for Magnetically Targeted Photothermal Therapy under Magnetic Resonance Imaging Guidance. *J. Cancer Res. Clin. Oncol.* **2019**, *145*(5), 1213–1219. <https://doi.org/10.1007/s00432-019-02870-x>.
- (19) Hou, X.; Wang, X.; Liu, R.; Zhang, H.; Liu, X.; Zhang, Y. Facile Synthesis of Multifunctional Fe₃O₄@SiO₂@Au Magneto-Plasmonic Nanoparticles for MR/CT Dual Imaging and Photothermal Therapy. *RSC Adv.* **2017**, *7* (31), 18844–18850. <https://doi.org/10.1039/c7ra00925a>.
- (20) Huang, J.; Guo, M.; Ke, H.; Zong, C.; Ren, B.; Liu, G.; Shen, H.; Ma, Y.; Wang, X.; Zhang, H.; Deng, Z.; Chen, H.; Zhang, Z. Rational Design and Synthesis of Fe₂O₃@Au Magnetic Gold Nanoflowers for Efficient Cancer Theranostics. *Adv. Mater.* **2015**, *27* (34), 5049–5056. <https://doi.org/10.1002/adma.201501942>.

- (21) Li, Z.; Aranda-Ramos, A.; Güell-Grau, P.; Tajada, J. L.; Pou-Macayo, L.; Lope Piedrafita, S.; Pi, F.; G. Roca, A.; Baró, M. D.; Sort, J.; Nogués, C.; Nogués, J.; Sepúlveda, B. Magnetically Amplified Photothermal Therapies and Multimodal Imaging with Magneto-Plasmonic Nanodomes. *Appl. Mater. Today* **2018**, *12*, 430–440. <https://doi.org/10.1016/j.apmt.2018.07.008>.
- (22) Nan, X.; Zhang, X.; Liu, Y.; Zhou, M.; Chen, X.; Zhang, X. Dual-Targeted Multifunctional Nanoparticles for Magnetic Resonance Imaging Guided Cancer Diagnosis and Therapy. *ACS Appl. Mater. Interfaces* **2017**, *9* (11), 9986–9995. <https://doi.org/10.1021/acsami.6b16486>.
- (23) Wang, W.; Hao, C.; Sun, M.; Xu, L.; Xu, C.; Kuang, H. Spiky Fe₃O₄@Au Supraparticles for Multimodal in Vivo Imaging. *Adv. Funct. Mater.* **2018**, *28* (22), 1800310. <https://doi.org/10.1002/adfm.201800310>.
- (24) Bhana, S.; Lin, G.; Wang, L.; Starring, H.; Mishra, S. R.; Liu, G.; Huang, X. Near-Infrared-Absorbing Gold Nanopopcorns with Iron Oxide Cluster Core for Magnetically Amplified Photothermal and Photodynamic Cancer Therapy. *ACS Appl. Mater. Interfaces* **2015**, *7* (21), 11637–11647. <https://doi.org/10.1021/acsami.5b02741>.
- (25) Jimenez de Aberasturi, D.; Serrano-Montes, A. B.; Langer, J.; Henriksen-Lacey, M.; Parak, W. J.; Liz-Marzán, L. M. Surface Enhanced Raman Scattering Encoded Gold Nanostars for Multiplexed Cell Discrimination. *Chem. Mater.* **2016**, *28* (18), 6779–6790. <https://doi.org/10.1021/acs.chemmater.6b03349>.
- (26) Lednev, V.; Pershin, S. M.; Bunkin, A. F. Laser Beam Profile Influence on LIBS Analytical Capabilities: Single vs. Multimode Beam. *J. Anal. At. Spectrom.* **2010**, *25* (11), 1745–1757. <https://doi.org/10.1039/c0ja00017e>.

6. Conclusions

This thesis has introduced new methods for synthesizing multifunctional hybrid nanoparticles based on iron oxide and gold for their use as contrast agents for multimodal bioimaging and their potential application as nanoheaters for photothermal heating.

A first approach was introduced in **Chapter II**. Therein, iron oxide NPs were synthesized and covered by AuNPs, which subsequently act as nucleation points for overgrowth into a spiky gold coating shell. We named these NPs as iron oxide-gold nanostars (IOAuNSs). We demonstrated that the total particle size can be tailored by adjusting two synthetic parameters 1) the concentration of gold spheres employed as nucleation sites and 2) the concentration of additional gold precursor for the spiky gold shell formation reaction. Thus, particles with different morphologies and sizes, as well as different optical characteristics can be obtained by varying these factors. Additionally, we demonstrated that these IOAuNSs can be functionalized with molecular or polymeric ligands, to obtain additional characteristics for the desired bioimaging applications. The use of the IOAuNSs as contrast agents for MRI, SERS and fluorescence imaging has been proven in 2D, 3D cell models and an *ex-vivo* animal tissue model. In this regard, SERS signal enhancement was discovered to be largely dependent on the absorbance and density of hotspots (spikes) of the IOAuNSs, while MRI measurements revealed that all particles, regardless of their functionalization for SERS or fluorescence, generated T2 contrast due to the IONP cores. In summary, hybrid IOAuNSs were shown to act as efficient contrast agents for multimodal bioimaging in complex biological models. Therefore, the synthesised IOAuNSs can be exploited as an attractive alternative to standard contrast agents, providing multifunctionality with the goal of improving the accuracy of current diagnostic procedures.

In **Chapter III** it has been demonstrated that the size of IOAuNSs can be further decreased by optimization of the protocol presented in Chapter II. The decrease of the overall particle size was achieved by two alternative approaches: 1) lowering the concentration of AuNPs used as nucleation sites for gold overgrowth (strategy developed in Chapter II) and 2) by reducing the diameter of the iron oxide cores through addition of increased amounts of water to the synthesis. Thus, smaller IOAuNSs with optimized photothermal characteristics were obtained for their use as nanoheaters for photothermal heating. Controls consisting of IONPs, AuNSs, and PS-beads covered by a spiky gold shell, were developed to determine the relevance of the metal shell and the dielectric core in the heating properties. The results showed that heating provided by IONPs upon laser irradiation at low concentrations was negligible. Besides, AuNSs and PSAuNSs showed a heating performance similar to that of IOAuNPs, thus indicating that PTH is a surface/tip effect, whereas the core of the NPs does not contribute, regardless of its material composition. In addition, the synthesis of PSAuNSs by the same method developed for IOAuNSs proved the versatility of this method to grow spiky shells around a material with arbitrary composition. Regarding the use of the IOAuNSs for photothermal heating in cell models (2D and 3D), it was demonstrated the biocompatibility of the NPs and the capability of the NPs to heat and successfully induce cell death by achieving hyperthermia conditions in both cell cultures.

Additionally, it was demonstrated that the concentration of NPs or the applied power density can be lowered when the complexity of the model is increased, i.e., the efficiency is higher in 3D models than in 2D models.

In **Chapter IV** a second approach was presented for the synthesis of hybrid NPs with better capacity for PTH and improved magnetic susceptibility for their potential use in magnetic separation. We demonstrated the ability to grow IONPs on top of AuNRs covered by a mesoporous silica shell. Additionally, by carrying out several IONP growth cycles, the density and size of the obtained IONPs could be increased. The NPs revealed remarkable photothermal heating performance, with high temperature increments achieved, even with relatively low Au concentrations. However, the high concentration of Fe in the final hybrid NPs was found to contribute to the overall heating. We demonstrated the ability of these hybrid NPs to act as nanoheaters in 2D and 3D cell models, killing cells with low concentrations and power densities. Furthermore, it was proven, as previously concluded in Chapter III, that the heating capacity of NPs was increased when internalised by cells and the effect is even amplified when cells aggregate to form spheroids. The lower concentrations of Au used for these experiments confirmed that AuNRs@SiO₂@IONPs were more efficient nanoheaters than IOAuNSs. Additionally, EDC/NHS chemistry was successfully used to effectively conjugate AuNRs@SiO₂@IONPs with antibodies. The ability of the NPs to bind targeted cells expressing the CD44 antigen was demonstrated by using MDA cells as a positive control and MCF7 cells as a negative control. Thus, we proved that MCF7 cells could be specifically targeted by antibody-labelled hybrid NPs.

In **Chapter V** we showed it is essential to provide detailed information of the heating set-up, toward the reproducibility of PTH measurements. In this chapter, we have studied different parameters having a high impact on heating, such as the effect of beam collimation, the use of multi- or single-mode lasers, and a proper calibration on the measurements. We concluded that, establishing guidelines for measuring the PTH efficiency of NPs as nanoheaters and making reliable comparisons, a wide range of factors are to be taken into consideration. We demonstrated that using a collimator leads to lesser variability when the laser spot size is changed, and that special care should be taken during the calibration of a multimode, non-collimated laser. In addition, we have demonstrated that PTH results are reproducible when all the set-up and laser beam specifications are known. In conclusion, we showed that different parameters influence the PTH results, and that the setup must be precisely specified to prevent reporting incorrect data. Despite of these results, more parameters and detailed information about the laser are required and further experiments should be carried out to fully understand the variability of heating results.

Overall, we presented in this thesis two novel hybrid systems based on iron oxide and gold NPs that revealed remarkable properties as contrast agents for multimodal bioimaging and as nanoheaters for PTH. The synthetic methods and functionalization of hybrid NPs presented are useful for the synthesis of nanohybrids with desired properties for specific applications and they represent a step forward towards the development of novel theranostic platforms.

Publications

- (1) **De la Encarnación, C.**; Jimenez de Aberasturi D.; Liz-Marzán, L.M. Multifunctional plasmonic-magnetic nanoparticles for bioimaging and hyperthermia. *Advanced Drug Delivery Reviews*, **2022**, 189, 114484. <https://doi.org/10.1016/j.addr.2022.114484>.
- (2) **De la Encarnación, C.**; Lenzi, E.; Henriksen-Lacey, M.; Molina, B.; Jenkinson, K.; Herrero, A.; Colás, L.; Ramos-Cabrer, P.; Toro-Mendoza, J.; Orue, I.; Langer, J.; Bals, S.; Jimenez de Aberasturi, D.; and Liz-Marzán, L.M. Hybrid Magnetic–Plasmonic Nanoparticle Probes for Multimodal Bioimaging. *The Journal of Physical Chemistry C*. **2022**, 126 (45), 19519-19531. [10.1021/acs.jpcc.2c06299](https://doi.org/10.1021/acs.jpcc.2c06299)

The full publications are reported in **Appendix A**.

In preparation

- (1) Hybrid core-shell nanoparticles for photothermal therapy and magnetic targeting. **De la Encarnación C.**; Jungwirth F.; Fromain, A.; Vila-Liarte, D.; Renero-Lecuna, C.; Wilhelm, C.; Bals, S.; Jimenez de Aberasturi, D.; Liz-Marzán, L.M.
- (2) Guidelines on reporting the photothermal effects of plasmonic nanoheaters. **De la Encarnación, C.**; Renero-Lecuna, C.; Henriksen-Lacey, M.; Cavaniol, C.; Wilhelm, C.; Jimenez de Aberasturi, D.; and Liz-Marzán, L.M.

Contents

A.1 **De la Encarnación, C.;** Jimenez de Aberasturi D.; Liz-Marzán, L.M. Multifunctional plasmonic-magnetic nanoparticles for bioimaging and hyperthermia. *Advanced Drug Delivery Reviews*, **2022**, 189, 114484. <https://doi.org/10.1016/j.addr.2022.114484>.

A.2 **De la Encarnación, C.;** Lenzi, E.; Henriksen-Lacey, M.; Molina, B.; Jenkinson, K.; Herrero, A.; Colás, L.; Ramos-Cabrer, P.; Toro-Mendoza, J.; Orue, I.; Langer, J.; Bals, S.; Jimenez de Aberasturi, D.; and Liz-Marzán, L.M. Hybrid Magnetic–Plasmonic Nanoparticle Probes for Multimodal Bioimaging. *The Journal of Physical Chemistry C*. **2022**, 126 (45), 19519-19531. [10.1021/acs.jpcc.2c06299](https://doi.org/10.1021/acs.jpcc.2c06299)



Multifunctional plasmonic-magnetic nanoparticles for bioimaging and hyperthermia



Cristina de la Encarnación^{a,d}, Dorleta Jimenez de Aberasturi^{a,b,c,*}, Luis M. Liz-Marzán^{a,b,c,*}

^a CIC biomAGUNE, Basque Research and Technology Alliance (BRTA), Paseo de Miramón 194, 20014 Donostia-San Sebastián, Spain

^b CIBER-BBN, ISCIII, 20014 Donostia-San Sebastián, Spain

^c Ikerbasque, Basque Foundation for Science, 48009 Bilbao, Spain

^d Department of Applied Chemistry, University of the Basque Country, 20018 Donostia-San Sebastián, Spain

ARTICLE INFO

Article history:

Received 30 March 2022

Revised 28 June 2022

Accepted 3 August 2022

Available online 6 August 2022

Keywords:

Multifunctional nanoparticles

Multimodal bioimaging

Photothermal therapy

Magnetic hyperthermia

Theranostics

ABSTRACT

Multicompartment nanoparticles have raised great interest for different biomedical applications, thanks to the combined properties of different materials within a single entity. These hybrid systems have opened new avenues toward diagnosis and combination therapies, thus becoming preferred theranostic agents. When hybrid nanoparticles comprise magnetic and plasmonic components, both magnetic and optical properties can be achieved, which are potentially useful for multimodal bioimaging, hyperthermal therapies and magnetically driven selective delivery. Nanostructures comprising iron oxide and gold are usually selected for biomedical applications, as they display size-dependent properties, biocompatibility, and unique physical and chemical characteristics that can be tuned through highly precise synthetic protocols. We provide herein an overview of the most recent synthetic protocols to prepare magnetic-plasmonic nanostructures made of iron oxide and gold, to then highlight the progress made on multifunctional magnetic-plasmonic bioimaging and heating-based therapies. We discuss the advantages and limitations of the various systems in these directions.

© 2022 Elsevier B.V. All rights reserved.

Contents

| | |
|--|----|
| 1. Introduction | 2 |
| 2. Plasmonic and magnetic NPs: synthesis and characterization of hybrid nanostructures | 3 |
| 2.1. Synthesis of hybrid nanoparticles | 3 |
| 2.2. Characterization of hybrid systems | 5 |
| 3. Biomedical applications | 5 |
| 3.1. AuNPs and IONPs for bioimaging | 5 |
| 3.1.1. AuNPs for computed tomography | 6 |
| 3.1.2. AuNPs for photoacoustic imaging | 6 |
| 3.1.3. AuNPs for surface-enhanced Raman scattering imaging | 6 |
| 3.1.4. IONPs for magnetic resonance imaging | 6 |
| 3.1.5. IONPs for magnetic particle imaging | 7 |
| 3.2. Multimodal bioimaging | 7 |
| 3.2.1. Hybrid plasmonic-magnetic nanoparticles for multimodal bioimaging | 7 |
| 3.3. Plasmonic-magnetic nanoparticles for hyperthermia | 7 |
| 3.3.1. Plasmonic nanoparticles for photothermal therapy | 7 |
| 3.3.2. Magnetic nanoparticles for magnetic hyperthermia | 9 |
| 3.3.3. Plasmonic-magnetic nanoparticles for magnetic and photothermal therapy | 9 |
| 3.4. Plasmonic-magnetic nanoparticles for combined imaging and hyperthermia | 10 |
| 3.5. Light and magnetically driven drug delivery | 11 |
| 4. Conclusions and outlook | 11 |

* Corresponding authors.

E-mail addresses: djimenezdeaberasturi@bicbiomagune.es (D. Jimenez de Aberasturi), llizmarzan@bicbiomagune.es (L.M. Liz-Marzán).

| | |
|---|----|
| Declaration of Competing Interest | 13 |
| Acknowledgments | 13 |
| References | 13 |

1. Introduction

Early diagnosis and effective therapies are undoubtedly of major concern when aiming to improve global health, as they can efficiently prevent patient worsening while increasing the chances for successful treatment and survival [1]. The development of advanced methodologies that provide fast and accurate readouts is thus required, including minimally-invasive imaging techniques [2]. Unfortunately, a single imaging technique often does not provide the information needed for a precise diagnosis. Therefore, multimodal imaging techniques based on the combination of different imaging modalities provide advantages over the limitations of the individual techniques [3]. However, such a combination of techniques also requires contrast agents that can enhance the imaging resolution of the various techniques involved. In addition, multimodal bioimaging can be combined with novel hyperthermia treatments. Hyperthermia, from *hyper*-'beyond' + *thermē* 'heat', consists of heating a lesion site above 45 °C to induce cell death and has been shown to provide high efficacy in cancer treatment [4,5].

Nanomaterials are especially suited to play an important role toward these challenges. In particular, nanoparticles (NPs) based on different metals or metal oxides can act as dual contrast agents, thanks to the specific properties of each component, thus rendering them excellent candidates for application in multimodal bioimaging [6,7]. One of the most popular materials combinations comprises gold and iron oxide, resulting in so-called plasmonic-magnetic nanostructures [8]. On one hand, plasmonic NPs – mainly gold and silver but also other metals – have been shown to excel in various biomedical applications, such as sensing, diagnosis and therapy [9–11], on account of their characteristic optical properties, which can be readily tuned by adjusting synthetic parameters to obtain the desired size, shape and composition [12]. In brief, plasmonic nanoparticles are characterized by so-called localized surface plasmon resonances (LSPR) [13,14], occurring when conductive electrons undergo collective oscillations in resonance with an external electromagnetic field (incident light in the visible or near-IR). As a result, plasmonic NPs can efficiently absorb and scatter light of a specific wavelength, as light is confined at nanoscale dimensions. Such a light confinement leads to surface-localized electric field enhancements, which can largely affect the spectroscopy of nearby molecules. A characteristic example is the enhancement of Raman scattering by molecules, which is known as surface-enhanced Raman spectroscopy (SERS) and has been demonstrated as a powerful analytical technique for ultrasensitive (bio)sensing [15]. In addition to biosensing, SERS bioimaging has also been implemented, by means of contrast agents (SERS tags) comprising AuNPs that carry a molecular label (Raman reporter, RaR) typically featuring a high Raman cross section and an easily recognizable vibrational fingerprint [16]. SERS tags present long-term stability, biocompatibility and negligible photobleaching, which are essential features for long-term *in vivo* imaging of 3D complex cellular structures [17,18]. Apart from the amplification of spectroscopic events, plasmonic NPs additionally release part of the absorbed light in the form of heat, which is efficiently transmitted to the local environment upon irradiation with resonant light. This phenomenon, usually known as the photothermal effect or plasmonic heating, is related to a relaxation by electron–electron scattering when electrons have been promoted to an excited

energy state by resonant photons, in turn translating into an increase of surface temperature [19,20]. The subsequent dissipation of thermal energy into the surrounding medium has been exploited in therapeutic approaches causing local thermal damage, for example, of malignant cells, toward cancer therapy and tumor depletion [21].

On the other hand, magnetic NPs have also been extensively studied, in the form of metals such as iron, cobalt, and nickel, or metal oxides such as ferrites, cobaltites, or mixed oxides. Iron oxide NPs (IONPs) can act by shortening the longitudinal and transverse relaxation times of nearby water protons. Thus, IONPs have been highly regarded as contrast agents for MRI and can be classified as T1 (positive) or T2 (negative) contrast agents, depending on the relaxation process that is more significantly altered [22]. In general, IONPs have been extensively utilized as T2 contrast agents, but more recently they have also been exploited as T1 contrast agents [23], which requires small IONPs (<5 nm) with medium size coatings (hydrodynamic sizes of 10–20 nm) [24]. Importantly, IONPs have been approved by the U.S. Food and Drug Administration (FDA) [25] for bioapplications such as iron replacement therapies or tumor ablation therapies through local hyperthermia [26,27]. The grand advances in the preparation of IONPs have resulted in a rigorous control over their size and shape, which in turn affect the resulting magnetic response [28–30]. In addition, since their movement can be manipulated using external magnetic fields, they have a high potential for magnetic targeting of cells or tissue [30] and have also been used to mechanically stimulate stem cell differentiation [31].

Despite the excellent performance of single-component NPs, the presence of different materials within a single NP offers further opportunities by combining the physical and chemical characteristics of both components. For example, whereas AuNPs are excellent plasmonic materials and IONPs are exemplary magnetic materials, by combining them into the same NP (AuIONPs) their respective properties, e.g. as contrast agents in SERS and MRI, can be retained, which is known as multimodal imaging [32]. Additionally, the use of plasmonic and magnetic NPs as nanoheaters has become attractive toward combined therapies, together with conventional cancer treatments such as chemotherapy and radiotherapy [33]. Gold and iron oxide moieties can be used to release heat upon appropriate stimulation, i.e. magnetic (hyperthermia) and photothermal heating [34], and the combination of both heating modalities can be applied when both materials are used in conjunction [35].

These novel cancer treatments can be further improved, in terms of specificity and selectivity, by using the magnetic domain for light driven delivery and magnetically targeted drug delivery. For these techniques, an external magnetic field is used to drag the nanoparticles, which have been pre-loaded with specific drugs, to a desired site where drug release is triggered by the photothermal response of the gold component [36] or by the magnetic component, thus combining hyperthermia and targeted chemotherapy [37–39].

In this review, we highlight recent advances in the design of AuIONPs and focus on their applications, specifically in the fields of multimodal imaging for diagnosis and hyperthermia as therapeutic agents. In the following sections we thus summarize recently reported results, aiming at providing an overview of the advantages and limitations of these hybrid systems.

2. Plasmonic and magnetic NPs: synthesis and characterization of hybrid nanostructures

2.1. Synthesis of hybrid nanoparticles

Synthesis of plasmonic NPs has been achieved by means of a wide variety of chemical [40], physical [41] and biological [42] methods. After several decades of research on spherical Au nanoparticles (AuNPs) [43], the colloidal synthesis of anisotropic NPs has gained huge interest, mainly driven by their finely tunable optical properties. Anisotropic nanoparticles can accommodate multiple plasmon modes, related to the nanoparticle morphology and its orientation with respect to the polarization of incident light. Additionally, elongated nanoparticles can display LSPRs at lower energies, down to the near-IR (NIR). Such an optical tunability is particularly relevant for biological applications [44,45] because maximum light transmission through tissue and minimized autofluorescence are obtained in the NIR [46]. Nanorods (AuNRs), nanostars (AuNSs), or nanotriangles (AuNTs) are some examples of AuNPs that can reach high anisotropy and tunable LSPR properties [47]. The most widely applied approach for the fabrication of anisotropic NPs is based on seed-mediated growth, comprising an initial step in which metal ions are reduced to form small metal nuclei, which are subsequently used as seeds for the growth of larger NPs with morphologies determined by the seed structure, surfactant (and other additives), and reaction kinetics. Selected AuNP morphologies for application in imaging and hyperthermia are summarized in Fig. 1.

Regarding magnetic NPs, IONPs in particular, colloidal synthesis has also been studied extensively [53]. Methods for IONP fabrication can be selected to ensure control over size, shape and composition [54]. Co-precipitation, thermal decomposition and hydrothermal processes are the most common synthesis methods [55]. Co-precipitation comprises the simultaneous precipitation of Fe^{2+} and Fe^{3+} ions in a highly basic solution, usually under inert atmosphere (N_2 or Ar), either at room temperature or at higher temperatures (above 70 °C); particles with sizes ranging from 5 to 20 nm are usually obtained with this method [56]. In the

hydrothermal procedure, IONPs are obtained by treating iron salt precursors at high temperature (130–250 °C) in an autoclave, at pressures ranging from 0.3 to 4 MPa [57–59]. By contrast, using the thermal decomposition method, IONPs are obtained through the decomposition of organometallic iron precursors, followed by oxidation in a high boiling point organic solvent containing surfactants. Monodisperse particles can be obtained with high reproducibility by using this method, but its main drawback is that biological applications require a post-synthesis phase transfer into a polar solvent [60]. Dadfar *et al.* [61] have classified the synthetic methods for IONPs and coatings needed for different applications in diagnosis and therapy, on the basis of their stability and non-toxic nature. Magnetite (Fe_3O_4) and its oxidized form maghemite ($\gamma\text{-Fe}_2\text{O}_3$) are the most widely used IONPs for biomedical applications [62]. Both iron oxides present structural similarity comprising a cubic inverse spinel, the main difference being that magnetite is made of both Fe(II) and Fe(III) whereas maghemite contains ferric Fe(III) ions only, and shows higher thermal and chemical stability. Both materials are metastable oxides, show size-dependent magnetic properties, [63] and are easily magnetized, thus showing a magnetic response in the presence of an external magnetic field (see Fig. 2).

The magnetic properties of IONPs are directly related to their size and morphology. Particle size determines the paramagnetic or superparamagnetic response of the nanostructures, in connection to the size-dependent spin exchange effect. On the other hand, the morphology of the particles is involved through shape-induced magnetic anisotropy [64]. Thus, the development of anisotropic and faceted IONPs, such as iron oxide nanocubes (IONCs) or nanoflowers (IONFs), have been studied in connection with their use for both magnetic resonance imaging (MRI) and magnetic hyperthermia [65].

The effect of particle size and shape on the relaxivity has also been reported. Several studies have demonstrated that faceted nanoparticles provide improved magnetism and relaxivity, as compared to spherical nanoparticles of similar size, with an increase in the relaxation rates when increasing particle size [66]. It has also been established that, the shape of the hysteresis loops for IONPs

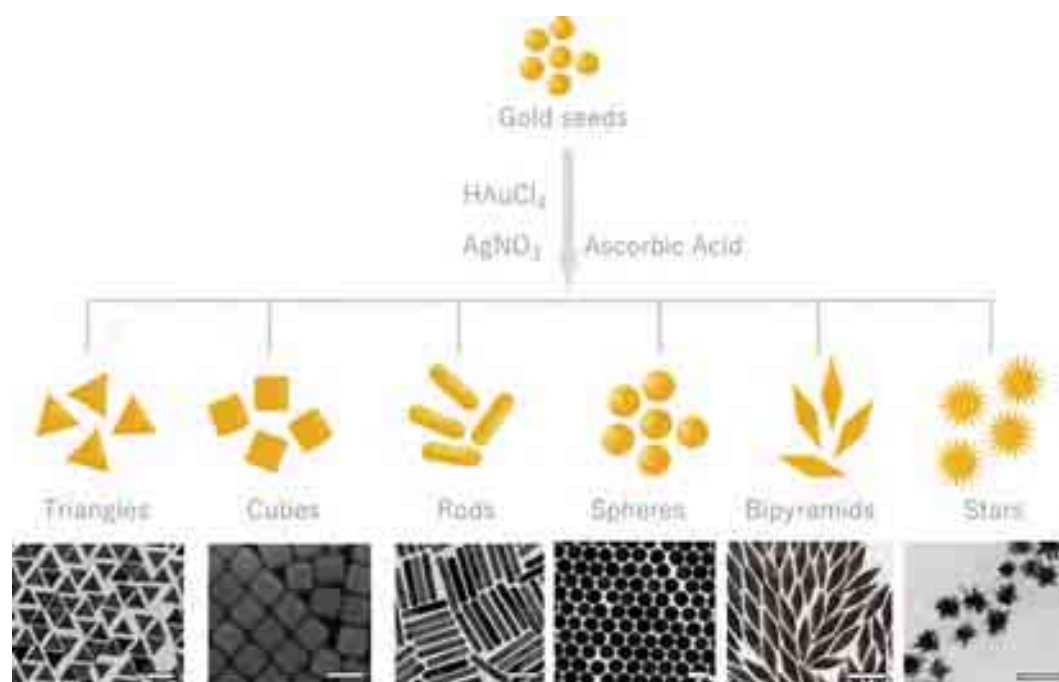


Fig. 1. Most common morphologies obtained by seed mediated growth of gold NPs, for imaging and hyperthermia applications. Scale bars correspond to 100 nm. Modified and reproduced from [16,48–52]. Copyright (2010) (2014) (2016) (2017) (2019) American Chemical Society.

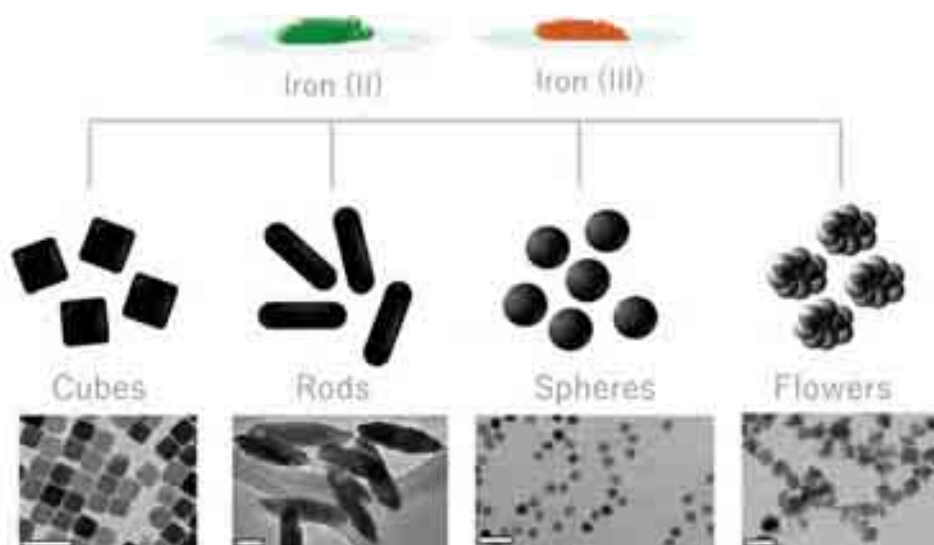


Fig. 2. Most common morphologies of IONPs made of magnetite or maghemite, for imaging and hyperthermia applications. Scale bars correspond to 50 nm. Modified and reproduced from [67,70-72]. Copyright (2012) (2018) (2021) American Chemical Society, (2008) John Wiley and Sons.

is regulated by their magnetic anisotropy. Therefore, IONCs with a low magnetic anisotropy show improved heating efficiency, which is preferred for hyperthermia treatments, compared to spheres [67]. Additionally, multicore systems show an improved magnetic response in comparison to single-core NPs of similar size. While dipole-dipole interactions arise in single-core particles, exchange coupling occurs among individual grains in multi-core systems due to the short distance between them, thus leading to strong magnetic interactions [68]. These assemblies represent a situation where aggregation of IONPs is controlled, so that no changes occur in the number of cores per particle. This system is advantageous for biomedical applications such as MRI and MHT, because of high saturation magnetization values and colloidal stability [69].

Considering the above introduced synthesis methods for both AuNPs and IONPs, novel approaches for the fabrication of hybrid NPs that combine both magnetic and plasmonic nanostructures have been reported (Fig. 3). Aqueous syntheses have naturally become most valuable when nanomaterials are considered for bioapplications. Most of the plasmonic-magnetic NPs reported in literature are made of an iron oxide core surrounded by an outer plasmonic gold layer (AuIONPs). The coating shell is meant to enhance the stability of the IONPs and allow more diverse functionalization [73]. The synthetic process comprises the reduction of Au precursors in the presence of IONPs, which act as seeds and become inner cores upon gold shell formation. For this purpose, two principal strategies have been used. On the one hand,

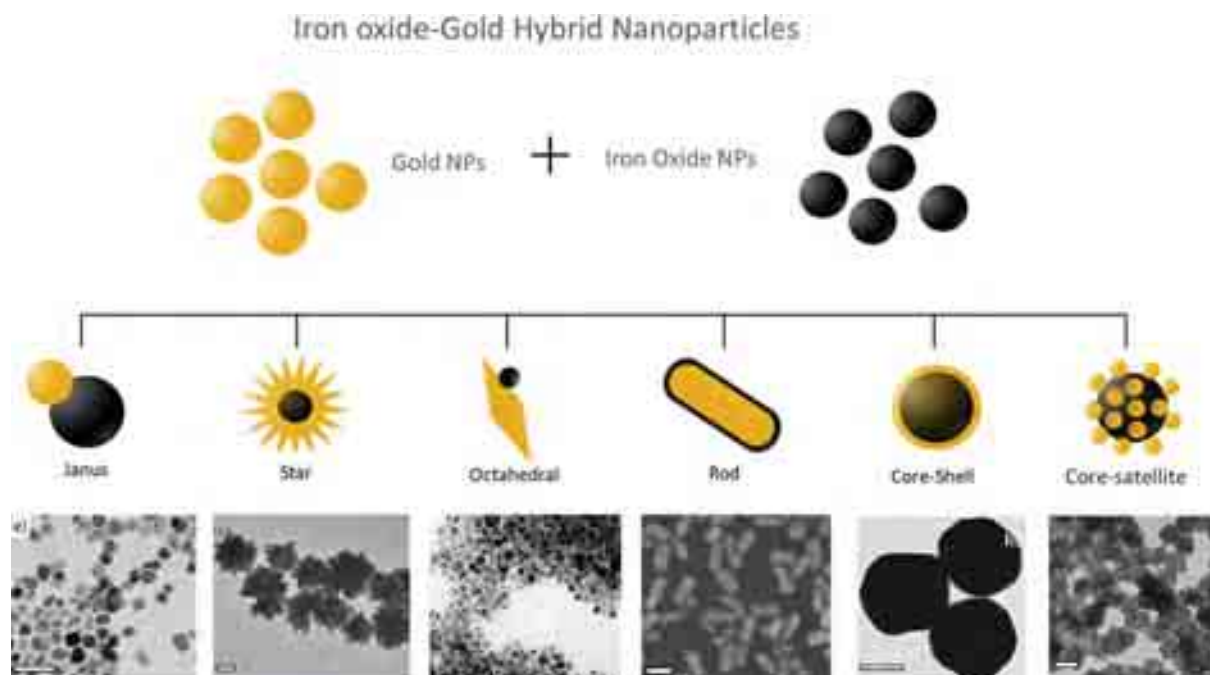


Fig. 3. Schematic illustration and TEM images of common combinations of iron oxide and gold into hybrid NPs. Scale bars correspond to 50 nm. Adapted from refs.[32,81-86]. Copyright (2009) (2016) (2017) American Chemical Society, (2017) Royal Society of Chemistry, (2013) John Wiley and Sons, (2018) Springer Nature.

the direct synthesis of the gold layer can be performed by adding gold precursors and a reducing agent to the dispersion of IONPs [74,75]. This process is however hindered by a complicated control over the thickness and geometry of the gold shell. On the other hand, hybrid particles can also be achieved by first depositing an intermediate layer, which provides a suitable surface charge, facilitating the decoration with gold seeds. The density of seeds can subsequently determine the thickness and geometry of the gold shell, obtained upon reduction of gold ions [76]. The intermediate layer usually comprises either silica [77] or polymers such as polyvinylpyrrolidone (PVP) [78] or polyethyleneimine (PEI) [79]. A different approach to obtain plasmonic-magnetic NPs is the fabrication of Janus NPs, with two distinct surface regions, made of Au and IONPs [80]. Examples of common AuIONPs are summarized in Fig. 3.

One important concern during the synthesis of hybrid plasmonic-magnetic particles is the potential influence of the gold layer on the magnetic cores, thus, a meticulous characterization of their properties is crucial. In this respect, it has been shown with wide generality, that magnetic properties remain unchanged after growing Au around IONPs [32,85,87]. However, any coatings or shells can affect their performance as contrast agents for bioimaging. Coatings may reduce, for example, the accessibility of water protons to IONPs cores, which can be detrimental to their effect on the relaxation times and thus compromise the application of hybrid NPs for MRI [88]. The various synthetic protocols for the fabrication of plasmonic-magnetic NPs and functionalization strategies have been reported in detail [89–92] as well as the biomedical application of these hybrid nanostructures [93,94], even though, we found insufficient description of the relevant characterization techniques, and their connection with bioapplications. Therefore, we restrict ourselves in this review to describing characterization methods for AuIONPs, and their use as contrast agents for multimodal imaging, as specific heaters for hyperthermia and controlled drug delivery treatments.

2.2. Characterization of hybrid systems

From both the synthetic and applied points of view, appropriate analysis of the prepared nanostructures is essential. Characterization of plasmonic NPs necessarily requires UV–visible-NIR spectroscopy, which provides information about the plasmon modes excited upon irradiation of the NPs, such that the extinction bands can usually be correlated to their size, shape, or aspect ratio [95]. Transmission electron microscopy (TEM) and scanning electron microscopy (SEM) are widely used to retrieve NP morphological and structural characterization, with precise information regarding size distribution, morphology, crystalline phase, elemental composition, etc. Dynamic light scattering (DLS) is typically used to measure the hydrodynamic diameter and polydispersity of NPs in a colloidal dispersion. Whereas characterization of anisotropic NPs requires a more complex analysis [59], reliable results are often obtained when working with spherical NPs [96,97].

Regarding the characterization of magnetic NPs, apart from the above-mentioned techniques for morphological characterization, spectroscopic methods are used to collect information on their chemical composition for a correct identification of metal oxide phases. For this purpose, X-ray diffraction (XRD), Mössbauer spectroscopy [98], or X-ray photoelectron spectroscopy (XPS) can be used to identify crystalline structures and composition. Understanding the magnetic response of IONPs requires more specific characterization. Superconducting quantum interference device (SQUID) is used as a magnetometer, to measure the response of IONPs under external magnetic fields, from which information can also be obtained regarding size distribution and blocking temperature, T_B (below T_B magnetic ordering occurs; above T_B thermal

energy dominates the NPs response to the applied magnetic field). Magnetic hysteresis loops at room temperature can be obtained by vibrating sample magnetometry (VSM), from which the saturation magnetization, M_S , can be determined. For IONPs, M_S values typically range from 45 to 80 emu/g-Fe and give information about their magnetic response [99,100]. Additionally, magnetic relaxivity (r) and relaxation time shortening values (T_1 and T_2) can be determined using a contrast agent analyzer or an MRI scanner [32].

Characterization of hybrid AuIONPs should be possible by using the same methods as for the single components. However, it may be complicated to distinguish both metals within the same nanostructure. Thus, more sophisticated methods should be applied for a complete characterization of hybrid NPs. For example, in core-shell type AuIONPs it is usually difficult to distinguish the core from the shell using conventional electron microscopy techniques such as SEM or TEM. In this respect, identification of the presence of both domains in single NPs can be made by using energy dispersive X-ray spectroscopy (EDXS). When the electron beam hits the sample, it produces electron transitions from a high-energy (outer) shell to a lower-energy (inner) shell of the atom, the energy difference produced by the electron displacement is released as X-rays and is characteristic for each element [101], so different metals within the same nanostructure can be identified [102]. Another useful tool is electron energy loss spectroscopy (EELS) coupled to TEM. In EELS, one measures the distribution of electron energies that have been inelastically scattered while passing through the sample, due to interactions of primary beam electrons with the electrons in the sample. Thus, information about electronic structures, bonding states or coordination number can be acquired by looking at the characteristic energy loss spectra [103]. Differentiation of metals can also be achieved by high-angle annular dark field scanning transmission electron microscopy (HAADF-STEM), as the contrast of the images depends on the atomic mass of the elements [104]. Electron diffraction techniques are also readily available on any TEM, by which the interaction between electrons and crystalline materials produces patterns that allow characterization of the crystalline structure. For example, specific information related to structural determination or determination of the growth direction can be acquired by using selected area electron diffraction (SAED), while symmetry, thickness and unit-cell parameters can be studied using convergent beam electron diffraction (CBED) [105]. High-resolution TEM (HRTEM) can also provide precise information, even about atomic distribution in complex systems.

Although the previously described techniques can only provide information in 2D, electron tomography can be used to achieve quantitative three-dimensional (3D) information of nanostructures [106]. In electron tomography, multiple images are acquired at different angles and, by applying mathematical algorithms, 3D volumetric reconstructions of the NPs can be retrieved. This versatile tool, with resolution from the nanometer to the atomic level, provides a better understanding of the structure and composition of NPs, even allowing the distinction between different elements at different depths when combined with EDXS or EELS analysis [107].

3. Biomedical applications

3.1. AuNPs and IONPs for bioimaging

Non-invasive imaging techniques are of high importance in medicine for fast disease diagnosis and continuous evaluation and follow-up of the therapeutic effects after treatment, while keeping an eye on undesired side-effects. Even though, in most cases, different techniques are complementary to each other, there are important differences in terms of sensitivity, resolution, as well

as acquisition time and cost [108]. Bioimaging techniques typically require the use of contrast agents to enhance the signal from selected structures or fluids within the body. In this line, both AuNPs [17] and IONPs [99,109] have been used as contrast agents for the different clinical imaging techniques. Having the characteristics of both components in a single NP would obviously allow their use as multimodal contrast agents for correlative imaging. Before analyzing the use of plasmonic-magnetic NPs in bioimaging and their multimodality potential, we briefly describe below the most relevant imaging techniques in which either plasmonic or magnetic NPs individually play an important role.

3.1.1. AuNPs for computed tomography

Computed tomography (CT), is a non-invasive technique that features high spatial resolution and tissue penetration depth. In this technique an ionizing radiation, specifically X-ray radiation, is used to obtain cross-sectional images of the internal organs, bones, soft tissues, vessels, etc., by differences in the absorption and attenuation of the radiation when passing through the different tissues. X-ray images are recorded while the detector moves around and a reconstruction of the individual images into cross-sectional images or "slices" is performed. A drawback of the technique is the high radiation dose required to reconstruct the images from those individual X-ray projections.

Iodinated contrast media are commonly used in CT due to its high X-ray absorption coefficient, which enhances the quality of the images [110]. In this regard, the use of AuNPs as contrast agents has been proposed as an interesting possibility, since it allows to reduce the overall radiation exposure thanks to their significantly improved contrast efficiency and accumulation time in tissues, as compared to conventional iodine contrast agents, thereby reducing the imaging time and, as a result, the risk of acute kidney injury [111]. Several examples have been reported on the use of AuNPs as contrast agents for CT [112]. Although in principle one may think that the contrast properties may vary depending on the NP properties, a study by Dong et al. on the CT contrast capacity of AuNPs with different sizes, from 4 to 152 nm, did not show meaningful differences in terms of signal contrast [113].

3.1.2. AuNPs for photoacoustic imaging

Photoacoustic imaging (PAI) is an emerging hybrid imaging technique, which combines optical imaging and ultrasound detection with a relatively deep tissue imaging capability [114]. In PAI, tissues are irradiated with non-ionizing laser pulses, light is absorbed by chromophores and converted into heat, producing a time variant thermoelastic expansion. This expansion process generates pressure changes in the tissues that result in the emission of acoustic waves. By using laser pulses for irradiation, this process is repeated with each pulse, thereby generating multiple waves that constitute the PA signals that are recorded by an ultrasound transducer. The signal is then measured and amplified to reconstruct a sonogram image [115]. When using plasmonic AuNPs, which can effectively absorb and scatter light, a difference in the PA signal is registered allowing the acquisition of images with improved contrast. Thus, anisotropic AuNPs are excellent contrast agents for PAI, which allows obtaining information in real time, with high spatial resolution and deep penetration when using NIR wavelengths. Therefore, for the optimal amplification of the photoacoustic signal, it is important to control the morphological and optical properties of the NPs [116]. Another important feature of AuNPs is the absence of photobleaching, which may readily occur when using other molecules as contrast agents, e.g. fluorescent dyes [117]. AuNPs with different geometries, including nanoprisms [118], nanocages [119], nanospheres [120], nanovesicles [121] and nanostars [122] have been studied, but AuNRs are still the preferred geometry for use as contrast agents in PAI [123]. A theoret-

ical study on the optimal geometry and size for AuNRs and AuNSs proposed AuNSs with small cores (30 nm) and relatively long tips (17 nm) as the optimum NP geometry toward the development of biocompatible PAI contrast agents [124].

3.1.3. AuNPs for surface-enhanced Raman scattering imaging

Surface-enhanced Raman scattering (SERS) is an emerging imaging tool, which relies on the enhancement of the Raman signal of molecules attached to the surface of plasmonic NPs [15]. Apart from the high sensitivity provided by the plasmonic enhancement, down to single molecule detection, the narrow bandwidth of the detected spectral peaks (vibrational molecular fingerprint) largely facilitates multiplexing, which is highly attractive for bioimaging [16]. The contrast agents in SERS bioimaging are encoded plasmonic NPs, typically AuNPs labeled with Raman-active molecules, known as Raman reporters (RaR). Such encoded AuNPs are commonly known as SERS tags [18,125,126], and different designs have demonstrated the possibility of creating large libraries of SERS barcodes [127]. Another key advantage of SERS tags is their stability against photobleaching [19,20], which renders them excellent candidates for long-term bioimaging experiments. SERS imaging has been used for live imaging of *in vitro* complex cell systems [17], as well as *in vivo* imaging, e.g. for visualization of the boundaries between tumor and normal tissues in mice [128], or the detection of gastrointestinal tumors in rats [129]. In a further development, the use of SERS tags for image-guided surgery is gaining interest, for example toward improving intraoperative tumor-resection procedures, in which SERS tags have been used to detect residual tumors at the margins of freshly resected tissue [130].

3.1.4. IONPs for magnetic resonance imaging

Magnetic resonance imaging (MRI) is a non-invasive and non-ionizing imaging technique with relatively high spatial resolution [131]. In MRI, an external magnetic field is used to align atomic nuclei, i.e. water protons (^1H), which are the most abundant magnetic nuclei in our body. Such an alignment creates a magnetization vector that is parallel to the applied magnetic field. To generate images, radiofrequency energy pulses at the resonance frequency are applied and energy is absorbed by the protons, which then change their orientation by rotating toward the transverse plane. When the pulse ends, the protons return to their equilibrium state and the accumulated energy is delivered as an alternating current that will be different depending on the molecular environment of the protons. This current will be measured in a receiver coil and used for image construction. The time that the proton needs to return to its initial state is called relaxation time and can be divided into T1, which depends on the interaction between atoms and their environment, and T2, related to the interaction of atoms with each other. MRI relies on the differences in tissue proton density and relaxation times to generate contrast. T1 is given by the time required for the excited ^1H to return to their original position, causing some energy loss into surrounding nuclei (spin-lattice relaxation). On the other hand, T2, also known as spin-spin relaxation, is the exchange of energy between high and low energy nuclei, without loss of energy to surrounding nuclei [132]. That said, discrimination of certain tissues gets complicated when the relaxation differences do not generate enough contrast. To improve that, Gd-contrast agents have been most commonly used to enhance the contrast in the regions of interest. The majority of clinically available T1 contrast agents are paramagnetic metal-chelates comprising Gd, which acts by shortening the relaxation time of protons, producing a bright contrast that improves the quality of the images. Unfortunately, it has been demonstrated that Gd^{3+} complexes may cause renal toxicity [133], hence the development of efficient and safer contrast agents for MRI is essential. Magnetic NPs are great candidates as contrast agents for MRI, as

they produce a magnetic field that alter the relaxation time of water protons resulting in an enhancement of the contrast between the background and the region of interest where the NPs are incorporated [134,135]. In particular, IONPs have been widely used as negative (T₂) contrast agents in magnetic resonance imaging. IONPs reduce magnetic relaxation times, thereby inducing a hyperintense change of the resonance signal in MRI and providing a so-called negative contrast. Magnetic mono-domains at the nanometer scale in the appropriate iron oxide phase, together with appropriate saturation magnetization values, provide IONPs with excellent T₂ contrast. Additionally, superparamagnetic IONPs present strong magnetic response under external magnetic fields, turning back to zero when the magnetic field is off. IONPs can thus act as “magnets” and yield signal suppression during MRI, appearing as dark spots (negative contrast) [109]. Notwithstanding, due to the limitations of T₂-driven diagnosis, research nowadays focuses mainly on the development of T₁ contrast agents based on small IONPs (<5 nm) with medium size coatings (hydrodynamic sizes of 10–20 nm), which display high water exchange rate, so they may eventually replace the current Gd-based contrast agents and provide positive contrast (brighter images) while avoiding kidney toxicity [136]. Coatings on NPs play an important role, as bulkier coatings (i.e., hydrodynamic diameter > 30–40 nm) restrict water access to the nanoparticle core, increasing the outer-sphere contribution to the relaxation mechanism and limiting the T₁ effect. Coatings leading to small hydrodynamic diameters (<7 nm) do not provide enough stability to the particles, resulting in aggregates that may increase the T₂ effect [24].

3.1.5. IONPs for magnetic particle imaging

Magnetic particle imaging (MPI) is an emerging pre-clinical imaging system that was developed in the early 2000s. [137]. MPI is a quantitative 3D imaging technique that enables real-time imaging with high sensitivity and spatial resolution. Static and oscillating magnetic fields combined with particles, as the name indicates, are applied in this technique. Thus, MPI measures changes produced due to the magnetization of IONPs, resulting in an image that can be reconstructed considering the spatial distribution of the NPs. Hence, there is no background, and as the NPs are the only source of signal, this will be proportional to their concentration [138]. IONPs have been optimized for their use as tracers for MPI [139] and have provided promising results for vascular imaging, oncology, inflammation and cell tracking [140,141].

3.2. Multimodal bioimaging

Having discussed the various techniques where AuNPs and IONPs can be used as highly efficient contrast agents, we review in what follows the application of magnetic-plasmonic NPs for combined analysis based on multiple bioimaging techniques. Multimodal imaging has indeed emerged as a suitable approach to overcome the limitations of individual imaging modalities. We summarize in the following section recent examples of the use of hybrid NPs as versatile contrast agents for combined imaging techniques.

3.2.1. Hybrid plasmonic-magnetic nanoparticles for multimodal bioimaging

The development of NPs that can provide contrast simultaneously for different techniques has largely advanced, hand-by-hand with the general progress on colloidal synthesis methods. The potential of such plasmonic-magnetic NPs as multimodal imaging probes has now been sufficiently demonstrated [142,143], as well as the resulting imaging combinations. As shown in Fig. 3 above, the most common application of hybrid AuNPs and

IONPs is for their use as contrast agent for multimodal imaging. Examples include hydrophilic and biocompatible Au-Fe₂O₃ heterodimers for MRI, CT and PAI [144], plasmonic AuIONPs obtained by laser ablation of a bulk Au-Fe alloy for MRI, CT, and SERS [145], Au-IO Janus NPs for MRI, CT, SERS, and PAI [32], IONPs and AuNRs as contrast agents for dual MRI/CT [146], and hybrid star-shape NPs for MPI, MRI and PAI [36]. In Fig. 4, we collected selected images that illustrate the use of plasmonic-magnetic NPs in different imaging modalities. PAI, SERS and CT imaging modalities can be applied thanks to the gold component, whereas MPI and MRI rely on the iron oxide part.

In addition to these examples, an extensive literature search of the most relevant plasmonic-magnetic NPs for multimodal imaging is summarized in Table 1, highlighting the morphology, the imaging modalities, the target disease and the harmless maximum concentration that was used for each system.

In general, it can be observed that core-shell NPs are the most frequently used structures, in which the magnetic core is commonly synthesized by co-precipitation and subsequently covered with a gold layer by seeded-growth. This choice is likely due to the availability of simple synthesis methods for IONPs, as well as optimized methods for gold encapsulation, which then also enable surface biofunctionalization. In terms of imaging, the most extended combination is MRI + CT, using the magnetic and plasmonic domains, respectively, to obtain high spatial resolution images of soft tissue using MRI and real-time 3D images of hard tissues by CT [160] or PAI [161,162]. However, the thickness of the gold shell may affect the properties of the IONPs for MRI, hindering their contrast efficiency due to the decrease on the accessibility of water protons to the iron cores. Therefore, thin shells are usually preferred for this specific technique [163]. In addition, it can be observed that studies reported for various hybrid NPs have focused on different types of cancer and other diseases, such as HIV and neurological disorders, for which both *in vitro* and *in vivo* models have been tested. We indicate the maximum concentrations that were identified in each study as non-toxic for the corresponding *in vitro* or *in vivo* model.

3.3. Plasmonic-magnetic nanoparticles for hyperthermia

Plasmonic-magnetic nanoparticles can also be used as therapeutic agents. Hyperthermia refers to a condition in which the temperature is abnormally increased, causing cell damage. In biological environments the hyperthermia temperature threshold is set at 42 °C. Above this temperature, various processes including protein denaturation, cytoskeleton disruption, or changes in the signal transduction, are triggered in the cells and promote the activation of cell death mechanisms [164]. In this context, a recent study showed that cell death patterns depend on the specific temperature reached, so that apoptosis prevails at temperatures between 43 and 49 °C, whereas necrosis dominates above 49 °C [165]. However, application of hyperthermia as a therapeutic technique has the drawback that it can affect both diseased and healthy cells, thereby resulting in unwanted side-effects. Therefore, localized hyperthermia, including photothermal therapy (PTT) and magnetic hyperthermia (MHT), has emerged as an innovative and selective treatment, for which plasmonic-magnetic nanoparticles would be used as the therapeutic agents [166]. In the following section, magnetic hyperthermia and photothermal therapy produced by AuNPs and IONPs will be discussed, highlighting the advantages and disadvantages of using hybrid NPs to enhance such effects.

3.3.1. Plasmonic nanoparticles for photothermal therapy

PTT is based on the photothermal conversion of absorbed light into heat, i.e. dissipation of an electromagnetic radiation absorbed at a certain location, in the form of heat to the surrounding

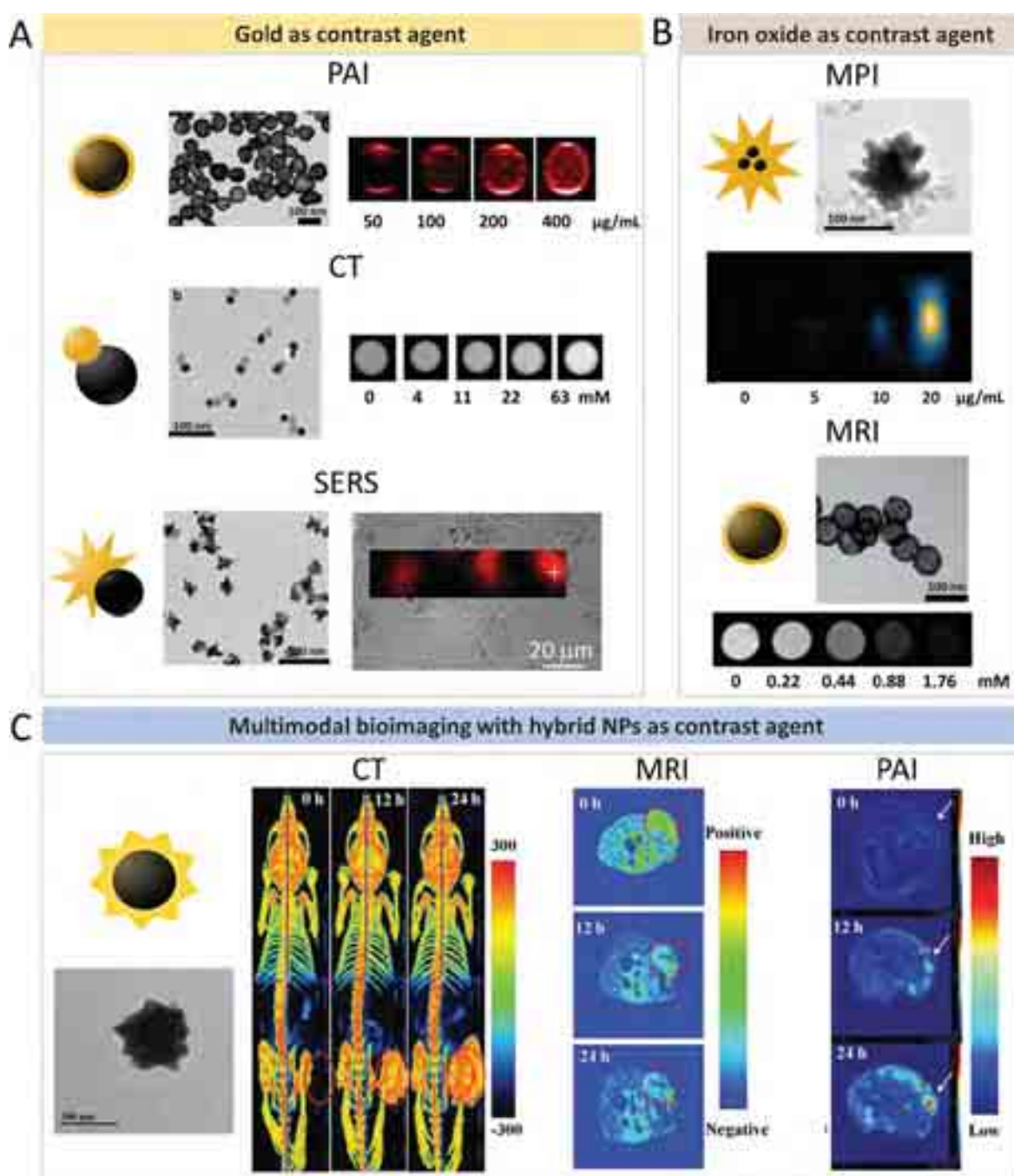


Fig. 4. (A) Hybrid NPs as contrast agents for PAI, CT and SERS. Core-shell, spherical Janus NPs and star-like Janus NPs are used respectively for each technique. The gold component is involved in the capacity of the hybrid NPs to act as contrast agents for these techniques. (B) Core-shell NPs containing either smaller iron oxide cores or a unique big core, have been used as contrast agents for MPI and MRI due to the magnetic component. (C) CT, MRI and PAI of a HeLa tumour in a mouse model, at different points after injection of 200 μL , 40 nM of star-like hybrid NPs. Both components are exploited for multimodal imaging. Graphical representations and representative TEM images are shown for the various NPs, next to corresponding images generated from the different techniques. Increasing contrast can be observed when increasing the dose concentration of gold or iron oxide in each case. Adapted from [7,32,36,144,147,148]. Copyright (2019) (2020) American Chemical Society, (2017) Royal Society of Chemistry, (2020) Springer Nature, (2018) John Wiley and Sons.

environment. This process requires the presence of light absorbing “sensitizers”, such as molecular dyes or small NPs (in larger particles light scattering would be the preferred mechanism, so heating efficiency would be hindered). Among the advantages of this technique, we can mention low cost (no major equipment needed), minimum invasiveness (extremely small amounts of sensitizers are needed and the light stimulus can be applied remotely), and high specificity (heating is confined to the irradiated area where the sensitizers are located). These properties render PTT highly suitable to selectively kill diseased cells, with negligible harm to

the healthy ones, which is of particular interest in cancer therapy [167]. The applied local heat causes irreversible damage to cell membranes, thereby leading to necrosis. The heating efficiency of AuNPs is directly related to their plasmonic response, i.e. to their specific LSPR modes [168]. The selection of the preferred AuNPs in terms of size and shape will thus depend on the desired optical properties, which should match with the laser wavelength to be applied, usually within the near-infrared (NIR) range, from 650 to 1359 nm. In this range the so-called biological transparency window is located, where deeper light penetration is achieved due to

Table 1
Summary of plasmonic-magnetic nanoparticles for multimodal bioimaging.

| Nanostructure | Type | Synthesis of the magnetic NP | Imaging modalities | Target disease | Model | Harmless (up to) | Ref |
|---|----------------|------------------------------|--------------------|--|-----------------------------------|--|-----------|
| M – Fe ₃ O ₄ (M = Au, Ag, and Pd) | Hetero-dymers | Laser-pyrolisis | MRI, CT, PAI | Lung cancer | <i>in vivo</i> | 0.5 µg/mL | [144] |
| Au-Fe NPs | Alloy | Laser ablation | MRI, CT, SERS | Breast, prostate cancer and hystiocytic lymphoma | <i>in vivo</i> | 290 µg/mL Au 10 µg/mL Fe | [145] |
| Fe ₃ O ₄ @Au | Core-shell | Co-precipitation | MRI, CT | Brain diseases | <i>in vitro</i> | 100 µg/mL | [149,150] |
| Fe ₃ O ₄ @AuNPs | Janus | Co-precipitation | MRI, CT, PAI, SERS | Lung cancer Adenocarcinoma | <i>in vivo</i> <i>in vitro</i> | [Au] = 50 µM | [32] |
| Fe ₃ O ₄ @Au | Core-shell | Co-precipitation | MPI | Glioblastoma | <i>in vitro</i> | 50 µg/mL | [151] |
| Fe ₃ O ₄ -AuNSs | Core-shell | Co precipitation | MRI, MPI, PAI | HIV | <i>in vitro</i> | 50 µg/mL | [36] |
| Fe ₃ O ₄ @SiO ₂ @Au | Core-shell | Thermal decomposition | MRI, CT | Liver cancer | <i>in vitro</i> | 200 µg/mL | [148] |
| spiky Fe ₃ O ₄ @Au | Core-shell | Co-precipitation | MRI, PAI, CT | Cervical carcinoma | <i>in vivo</i> | 200 µg/mL | [7] |
| Fe ₃ O ₄ @ SiO ₂ @Au | Core-shell | Thermal decomposition | MRI, CT, FI | Cervical carcinoma | <i>in vitro</i> | 350 µg/mL | [152] |
| Fe ₃ O ₄ @AuNPs | Janus | Thermal decomposition | MRI, CT | Liver cancer | <i>in vivo</i> | [Fe] 3.2 mM | [153] |
| Fe ₃ O ₄ @AuNPs | Core-satellite | Co-precipitation | MRI, CT | Liver cancer | <i>in vivo</i> | 1 mg/mL | [154] |
| Fe ₃ O ₄ @AuNPs | Core-satellite | Hydrothermal | MRI, CT | Epithelial carcinoma | <i>in vivo</i> | 100 µg/mL | [155] |
| Fe ₃ O ₄ @Au | Core-shell | Co-precipitation | MRI, PAI | Glioblastoma and breast cancer | <i>in vitro</i> | [Fe] 2.5–20 mM | [156] |
| Fe ₃ O ₄ @AuNPs | Dumbbell | Thermal decomposition | MRI, CT | Liver cancer | <i>in vivo</i> | Au 48 mg kg ⁻¹ Fe 36 mg kg ⁻¹ | [111] |
| Fe ₃ O ₄ @BCP@AuNPs | Janus Vesicle | Thermal decomposition | MRI, PAI | Glioblastoma | <i>in vivo</i> | [Fe] 0.125 mM | [157] |
| Fe ₃ O ₄ @AuNPs | Core-shell | Co-precipitation | MRI, CT, SPECT | – | NPs in solution | – | [158] |
| Fe ₃ O ₄ @AuNSs | Core-shell | Hydrothermal | MRI, CT | Cervical canrcinoma and glioblastoma | <i>in vitro</i> | [Au] = 2 mM | [159] |

minimum scattering by tissue and light absorption by hemoglobin (<650 nm) and water (>900 nm). Therefore, anisotropic AuNPs turn out to be the ideal candidates as nanoheaters for photothermal therapy, as LSPR in the NIR can be obtained for large enough aspect ratios. Given the wide variety of available AuNP shapes, different possibilities have been explored for this purpose. Gold nanoshells (AuNSHs) have been studied for both *in vitro* and *in vivo* PTT achieving irreversible photothermal ablation of tumor tissue [169], and this was the first AuNP shape that found application in clinical trials [170]. AuNRs have also been used for *in vitro* PTT [171]. Experimental demonstration was subsequently reported using smaller AuNRs (D = 10 nm), with LSPR around 800 nm, for *in vivo* treatment [172]. Another preferred morphology is that of spiky nanostars; AuNSs with sizes of 30 and 60 nm proved effective for tumor ablation upon PTT, the smaller ones reaching a deeper penetration depth into the tumor interstitial space [173]. Gold nanocages (AuNCs) should also be mentioned, e.g. AuNCs with 45 nm edge-length and LSPR at 810 nm led to *in vitro* photothermal destruction of targeted breast cancer cells [174]. The efficacy of AuNCs for *in vivo* photothermal treatment of a bilateral tumor was subsequently demonstrated by the same authors [175]. More recently, a nanoprobe based on a silica core covered by a gold shell has been applied for localized photothermal ablation of prostate tumors in a clinical trial, demonstrating the potential of Au nanoprobes for clinical treatment. In this novel therapy, the nanoprobes were accumulated in the tumor and irradiated with NIR light. Hence, hyperthermia conditions were reached, inducing selective cell death. [170].

3.3.2. Magnetic nanoparticles for magnetic hyperthermia

MHT is a different hyperthermia modality, which exploits heat generated by magnetic NPs, usually for oncology treatments. Upon excitation with an alternating current (AC) magnetic field, tumor-

localized magnetic NPs generate localized heat that strongly depends on the concentration, but also on the size, composition, shape and anisotropy of the magnetic NPs [176,177]. The main drawback of MHT is that most magnetic NPs have a rather poor heating efficiency, so large amounts of NPs should be directly injected for effective therapeutic performance, which may in turn induce cytotoxicity issues. Additionally, the NPs often lose some of their heating efficiency in cell environments, as a consequence of aggregation and decrease of interparticle distance [178]. For this reason, an increased NP heating efficiency is still highly desired, which could be obtained by modifying the degree of mutual interaction between magnetic NPs in close contact, such as in multicore IONPs [179]. More recently, the heating properties of IONFs have been analyzed for application in MHT, concluding that a larger number or cores favors MHT performance [180]. On the other hand, a greater heating performance has been demonstrated for IONCs under MHT, in comparison with various other shapes [34]. Both IONCs and IONFs with larger volume and high concentration of defects, have also been shown to display suitable properties, not only for their use in MHT but also as PTT heaters (they efficiently absorb laser light when irradiated at 808 and 1064 nm wavelengths respectively) [180,181].

3.3.3. Plasmonic-magnetic nanoparticles for magnetic and photothermal therapy

As discussed above, external stimuli such as light or magnetic fields, are required to generate heat using AuNPs or IONPs as sensitizers [34]. Magnetic NPs present a low molar absorption coefficient in the NIR region, consequently they have poor photothermal effects. On the other hand, plasmonic NPs do not possess magnetic properties, and thus cannot be applied in MHT. Thus, by combining IONPs and AuNPs into hybrid nanostructures

as schematically represented in Fig. 5, we should be on track to develop efficient hybrid nanoheaters [182].

Such dual-nanoheaters have shown improved hyperthermal performance, as the temperature increment reached by PTT is supplemented by that induced by MHT [183]. Hybrid NPs have been successfully demonstrated to detain tumor growth in cancer cells, both using *in vitro* and *in vivo* models, thanks to combined PTT and MHT treatments [35]. However, even though the combination of

PTT and MHT appears as an interesting approach for novel and effective cancer treatments, such a combination is still rare and only a few examples are found in literature where hybrid NPs were used [184–186] (see Fig. 6). This slow development may be related to the concentration differences required for each heating technique.

As can be observed in Table 2, the reported data on the application of PTT and MHT treatments are far from following a standard protocol. Different conditions are reported for each system, in terms of laser power, irradiation time, magnetic field frequency, and NP concentrations. Therefore, benchmarking of the efficiency of different particles remains largely challenging and unclear. In many cases, even key parameters such as the temperature increase, irradiation time of NP concentrations are missing or unclear. Concentrations of hybrid NPs expressed as mg/mL are not informative enough, specific information about the concentration of each metal component, i.e. Au for PTT or Fe for MHT, should be provided for a fair comparison to be made. Additionally, the achieved temperature increment (ΔT), irradiation time (min), as well as information of the power density of the laser used for the PTT experiments (expressed in W/cm^2) and of the frequency (Hz) and intensity (kA/m) of the magnetic field for MHT, are key aspects when trying to compare and reproduce reported experiments.

3.4. Plasmonic-magnetic nanoparticles for combined imaging and hyperthermia

Even if multitherapy combining PTT and MHT remains largely unexplored, the use of hybrid NPs for image-guided hyperthermia is increasing rapidly and has been described by a number of authors [187,189,190,193,194]. Since PTT is easier to implement and more efficient than MHT [195], recent studies have reported the use of the plasmonic domain of hybrid NPs for PTT while the magnetic domain was employed for imaging, so that a single nanostructure becomes an interesting tool for image-guided phototherapy [36,162,163]. This combination has shown interesting results in both *in vitro* and *in vivo* experiments, achieving complete

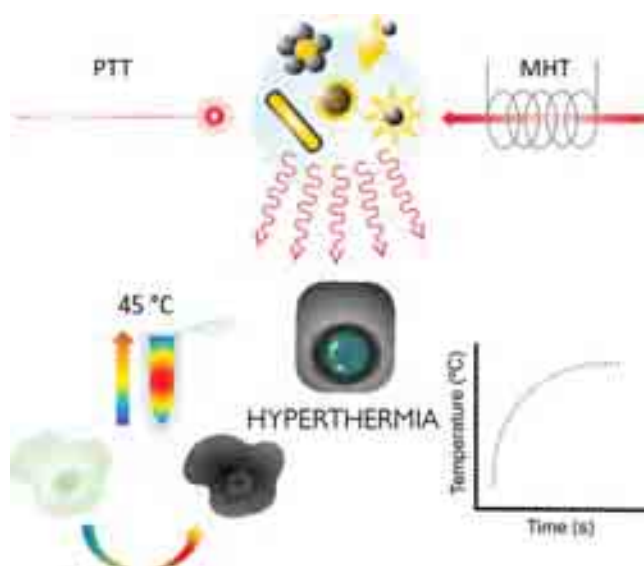


Fig. 5. Sketch of PTT and MHT experiments using hybrid NPs. The difference between the techniques is mainly related to the power source: For PTT a NIR laser is used, whereas for MHT an alternating magnetic field is required. Hybrid nanoparticles can absorb the energy from both laser light and magnetic fields, and subsequently release it as heat. The lower panel illustrates the conditions required for hyperthermia to be achieved, i.e. heating above 45 °C with a typical profile of temperature increase over time.

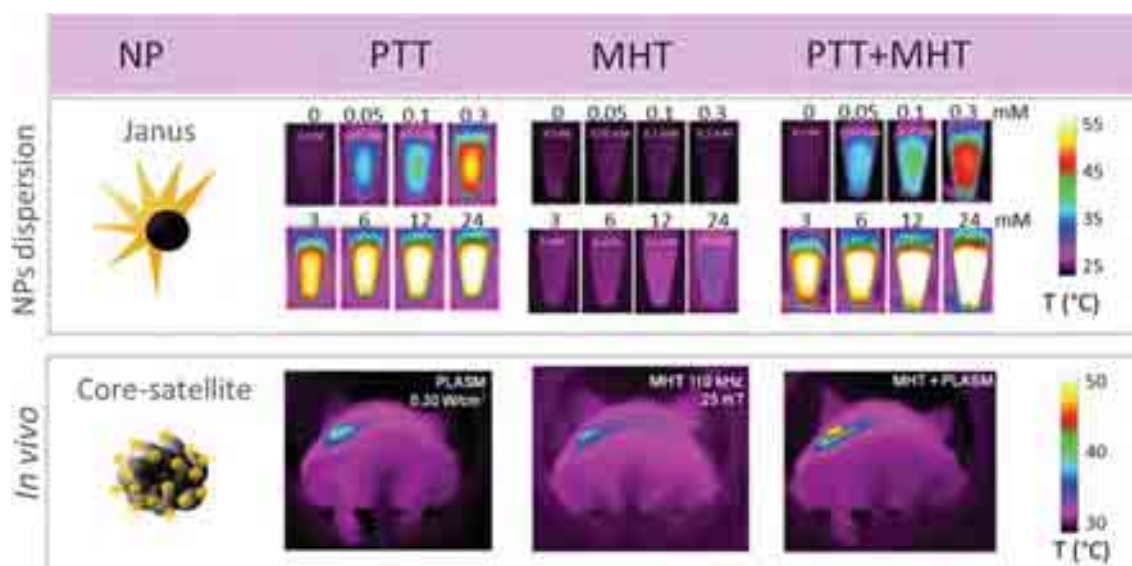


Fig. 6. PTT, MHT and dual PTT + MHT experiments using colloidal dispersions of Janus NPs in water, at different concentrations. The measurements were carried out in Eppendorf tubes, using a volume of 150 μL and a 680 nm laser working at 0.5 W/cm^2 during 5 min for PTT and 470 kHz and 18 mT for MHT (upper panel). In the lower panel, PTT, MHT and dual PTT + MHT *in vivo* experiments are illustrated. A volume of 100 μL of core-satellite NP solution at $[Fe] = 150$ mM was directly injected into tumors produced from human prostate adenocarcinoma cells (PC3), in a mouse animal model. Irradiation conditions were: 680 nm, 0.3 W/cm^2 for PTT; AC magnetic field at 110 kHz, 25 mT, for MHT. Reproduced from [35,183]. Copyright (2020) John Wiley and Sons, (2017) Royal Society of Chemistry. In addition to these examples, a literature search of the most relevant hybrid NPs for PTT and MHT and dual treatment is summarized in Table 2, highlighting the morphology, treatment, if the model is *in vitro* or *in vivo* and the specific conditions for PTT and MHT on each system. Besides, efficiency of the treatment is given by the increase of temperature.

Table 2
Summary of hybrid nanoparticles for PTT and MHT.

| Hybrid NP | Concentration | Treatment | Laser λ (nm) | Power density (W/cm ²) | Magnetic field Frequency Intensity (kHz) (kA/m) | | Time (min) | ΔT (°C) | Ref. |
|------------------|------------------------|------------------------------------|----------------------|------------------------------------|---|-----------|------------|-----------------------|-------|
| Core-shell | [Au] 1 mM [Fe] 2 mM | PTT <i>in vivo</i> | 808 | 1.4 | - | - | 15 | 16.7 | [187] |
| Core-shell | [Fe] 160 μ g/mL | PTT <i>in vitro</i> | 808 | 2 | - | - | 10 | 40 | [148] |
| Core-shell | [Au] 1.25 mM | PTT <i>in vitro</i> | 808 | 1.5 | - | - | 5 | 49 | [188] |
| Nano-domes | [Fe] 100 μ g/mL | PTT <i>in vitro</i> | 808 | 5 | - | - | 0.5 | - | [189] |
| Core-shell | [Fe] 40 μ mol/L | PTT <i>in vitro</i> | 808 | 1 | - | - | 10 | 30 | [190] |
| Spiky core-shell | [Fe] 4 nM | PTT <i>in vivo</i> | 808 | 0.5 | - | - | 6 | 65.7 | [7] |
| Nano popcorns | [NPs] 4 μ g/mL | PTT <i>in vitro</i> | 808 | 0.55 | - | - | 10 | 21.4 | [191] |
| Core-satellite | [Fe] 1.66 mg/mL | MHT <i>in vitro</i> | - | - | 571 | 19.9–23.9 | - | - | [192] |
| Janus | [Fe] 6 mM | PPT + MHT <i>in vitro</i> | 680 | 0.5 | 470 | 14.32 | 5 | 32.3 PTT 1.1 MHT | [35] |
| Core-satellite | [Fe] 150 mM | PTT + MHT <i>in vivo</i> | 680 | 0.3 | 110 | 19.89 | 5 | 20 PTT + MHT | [183] |

tumor ablation and cell death. Interestingly, the use of magnets during the incubation of NPs with cells has also been used to enhance internalization, again leading to more effective therapies [34].

One of the most common combinations involves the use of hybrid NPs as contrast agents for MRI/CT, followed by PTT after tumor localization [148]. Notwithstanding, NP systems that combine multimodal imaging such as SERS, MRI and PAI [188], or MRI, CT and PAI [7], with PTT treatment have also been reported. Hybrid γ -Fe₂O₃@Au magnetic gold nanoflowers were described for cancer theranostics, using MRI to first localize the tumor, then PAI for deep tumor localization, and SERS allowing the detection of tumor margins, overall resulting in a precise localization of the tumor. Having specific information regarding the position of the tumor, efficient ablation under NIR irradiation can be achieved using the photothermal effect of the Au component [188].

Moreover, magnetic targeting can improve the therapeutic response of PTT by enhancing thermal damage. In a recent study, hybrid NPs were injected intravenously and magnets were used for accumulation of the NPs. The results showed that the temperature increment in the tumor was 16.7 °C, as compared to 8.5 °C in the absence of the guiding magnets. This result confirmed that intravenous injection followed by magnetic accumulation is more efficient than even intratumoral injection, which reported a temperature increment of 12 °C [187].

3.5. Light and magnetically driven drug delivery

One of the main concerns about chemotherapy and radiotherapy treatments is that they are unspecific treatments and thus cause damage to the surrounding healthy tissue. Thus, another promising therapeutic application of plasmonic-magnetic NPs is the magnetically targeted, selective light-driven drug delivery. The basis of this method is the release of a drug loaded on anisotropic AuNPs, when triggered by application of NIR light. This phenomenon can be achieved through the incorporation of photolabile molecules [196] or thermoresponsive molecules, which will

undergo molecular changes or dissociation when irradiated. The main advantage of using hybrid NPs for such an application is that selective drug delivery can be achieved upon illumination, after the particles have been directed to the desired site under the effect of magnets [197]. Once successful magnetic accumulation or guidance has been achieved, selective drug delivery can be activated by irradiating the site with an appropriate light source [198]. An example comprises the use of IONPs and AuNSHs to combine MRI, magnetic-targeted drug delivery, light-triggered drug release and PTT, thereby providing a multifunctional system for effective cancer diagnosis and therapy [199]. On a different configuration, oval hybrid NPs loaded with an anticancer drug were imaged by MRI and subsequently drug release was triggered using hyperthermia [200]. A multifunctional system based on AuNPs and IONPs embedded in porous silica was preloaded with a fluorescent anticancer drug and then encapsulated with a temperature- and pH-sensitive polymer, so the release of the drug inside cells was controlled by applying heat and a magnetic field, as demonstrated using *in vitro* models for human cells and neurons.

Such novel therapies highlight the potential clinical application of hybrid NPs in targeted drug delivery and on-demand drug release, while representing a significant development toward personalized medicine [201].

4. Conclusions and outlook

Hybrid NPs provide important advantages in biomedicine due to their multifunctionality. In particular, a great interest has been shown toward the use of different types of NPs within a single platform for theranostics. Magnetic NPs combined with gold plasmonic NPs are a paradigmatic example of such emerging hybrids. Thus, much effort has been made on the development of plasmonic-magnetic NPs with different size, shape, composition, and arrangement of the magnetic and the plasmonic domains, so as to obtain the ideal next-generation contrast agents for multimodal bioimaging and nanoheaters for hyperthermia and photothermia treatments at early disease stages. However, for their use as a clinical

tool, the dose of NPs administered needs to be low enough to avoid toxicity problems and side-effects, while maintaining the desired contrast and thermal effects. One concern in this regard is the long-term cytotoxicity, which may be caused by the bioaccumulation of NPs after injection in the body. Several studies have shown the harmless nature of most NPs and the different pathways of elimination, depending on particle size. It has been proven that small NPs (<10 nm) are effectively removed by the kidneys [202], while larger particles tend to accumulate in the liver and the spleen [203,204].

Due to their easy synthesis and functionalization, magnetic NPs fully coated with a gold shell are the most extended conformation of hybrid NPs. These core-shell systems display the magnetic properties of the iron oxide core, which is protected from oxidation and aggregation by the gold shell, which additionally provides them with plasmonic properties, to be exploited in bioimaging or photothermal treatments.

Regarding the stability and degradation of NPs in biological environments, most studies focus on the biological effects caused by NPs [205]. However, information about how NPs behave inside the organism, including reshaping of the nanostructures potentially inducing changes in their properties, NPs distribution and accumulation, biotransformation, or degradation, is still scarce. Understanding the behaviour of NPs and how the organism may transform them from initial exposure to complete removal, is crucial to evaluate their efficacy for biological applications. In this regard, it has been demonstrated that AuNPs are considered bioinert and resistant to degradation in cellular media, a property that is further improved for increasing particle sizes [206]. In contrast, IONPs tend to degrade faster and their biodegradation depends on the clustering state and the nature of the capping agent, the degradation process is thus especially noticeable when the coating is missing or less dense [207,208]. IONPs can be processed and assimilated by the organism due to the iron metabolism. The degradation of IONPs in acidic biological media may induce the loss of the required magnetic properties, thereby compromising long-term application. Therefore, the development of coating gold shells is meant to protect the iron oxide cores from oxidation and degradation in cellular media, thereby improving their long-term stability. This protective effect depends strongly on the morphology and thickness of the gold shell, being most efficient when a continuous (hole-free) shell is formed [209].

Other metals, such as silver, have also been studied as plasmonic shells covering magnetic cores. Unfortunately, fast degradation and quick alteration of the iron oxide cores inside cellular endosomes has been identified [210]. Thus, the development of nanohybrids containing a magnetic core protected by a gold shell becomes particularly interesting, not only for their potential use as a combined diagnostic and therapeutic tool, but also for the improvement of chemical stability and performance in biological environments, which is crucial for applications requiring long-term activity.

Related to bioimaging, core-shell AuIONPs are also commonly used hybrid NPs as contrast agents, most often for application in combined MRI/CT imaging. The use of such NPs with alternative techniques such as SERS, which is gradually being demonstrated to have excellent features for bioimaging, surgical guidance [211], or detection of metabolites, is still its infancy but presents a great potential.

By contrast, the optimal shapes for PPT are AuNRs, AuNSHs, AuNSs and AuNCs, which aspect-ratio can be optimized to obtain a suitable LSPR matching the incident laser wavelength. The reason why Au nanospheres are not used for PTT is related to their LSPR ranging from 520 to 550 nm, thus falling outside of the biological transparency windows [212]. Magnetic NPs with cubic (IONCs) and flower-like (IONFs) shapes were demonstrated to be optimum

heaters for MHT, but also with activity in PTT. The mechanism of heating by IONPs, as well as the relationship between structure and properties for PPT and MHT of IONPs, have been recently reported. IONFs with a total size of 24 nm, each multicore assembly being composed of 15 grains but with a low density of crystalline defects, were identified as the most efficient characteristics for the efficient design of nanoheaters [180].

It should be noted that, only IONPs are commercially available and have found their way into clinical routine so far. Sinerem[®], Clariscan[®], Endorem[®], Resovist[®], Abdoscan[®], Feridex[®], and Lumirem[®] are commercially available IONPs to be used as contrast agents for MRI, with sizes ranging from 4 nm to 3 μm [213]. The company Magforce (1997, Berlin, Germany) developed NanoTherm[®], an IONP solution to be injected in brain tumors to destroy cancer cells using MHT [214]. Since November 2021, NanoTherm[®] is in the recruiting phase of a second clinical trial for the application in focal ablation of prostate cancer [215]. Even if some NPs are already being used for clinical applications, some challenges are still unresolved regarding efficient translation of hybrid nanoparticles to the clinic. Most currently existing procedures for the fabrication of hybrid NPs are still complex and therefore efforts are being made toward developing large-scale, low-cost production of IONPs [216] and hybrid NPs [217]. Co-precipitation is known as one of the methods for mass production of IONPs, but it yields rather polydisperse NPs within a restricted size range. Other synthetic approaches, including polyol methods assisted by microwave and thermal decomposition of iron oleates, are thus considered for the large-scale, inexpensive production of monodisperse metal NPs [218]. It should be noted that, some of the proposed NP structures are even more complex and expensive than conventional drugs, which poses additional difficulties toward their incorporation in the pharmaceutical industry, from the cost-effectiveness point of view [219]. In this context, flow reactors and microfluidic devices have emerged as a promising alternative to address the challenges for mass production and cost reduction in conventional synthetic methods [220,221]. The production of NPs at high temperature in continuous flow reactors has been demonstrated to reduce production costs and improve the reproducibility of the obtained products [222]. Still, the issues listed above should be taken into consideration and carefully resolved from a clinical perspective. In this context, appropriate drug testing models *in vitro* and/or *in vivo* are needed, which properly mimic the targeted diseases. Specific accumulation at the target tissue is highly desirable and the protocols and dosage for administration of NPs to humans should be clarified, prior to translation of hybrid NPs into the clinic.

Even if promising results for photothermal experiments are shown in most studies, the efficiency of NPs for heating is difficult to evaluate. Different concentrations of metals are used, power densities range from 0.1 to 6 W/cm², irradiation times vary from a few seconds to minutes and, in many cases, the heating capacity is not given by a temperature increase but in terms of cell death or tumor depletion. Besides, one of the most challenging problems is still the measurement of local temperature at the surface of NPs and the associated heat transfer. Hence, almost all hybrid NPs appear to be convenient as nanoheaters for a given application, but is impossible to reliably compare different hybrid NPs due to measurement difficulties, variability of parameters and different set-ups being used [223]. Standardization of the protocols for the measurement of the heating capacity of NPs is thus urgently needed. A better understanding of the behavior of NPs during MHT measurements is also required. As in PPT, standardization of the method to understand and compare hyperthermia efficiencies is mandatory, as well as establishing the most suitable magnetic field excitation conditions, in accordance with clinical aspects and patients' safety. One additional problem of MHT is that

high concentrations of IONPs are needed, which may be toxic for biological systems. A concentration of 25 mM is considered as a low Fe dose for MHT, whereas 0.1–1.0 mM AuNPs is used for similar temperature increments in PTT [34].

Finally, new applications are emerging to exploit the potential of hybrid NPs, such as magnetically amplified PTT by which the concentration of hybrid NPs is increased by using external magnetic fields, to enhance the localized PTT effect [191]. Finally, the combination of thermal therapies with conventional cancer therapies such as radiotherapy and chemotherapy is proposed as a promising approach for cancer multitherapy [224].

Declaration of Competing Interest

The authors declare that they have no known competing financial interests or personal relationships that could have appeared to influence the work reported in this paper.

Acknowledgments

Financial support is acknowledged from the European Research Council (ERC Advanced Grant 787510, 4DbioSERS), and MCIN/AEI/10.13039/501100011033 through grants # PID2019-108854RA-I00 and Maria de Maeztu Unit of Excellence No. MDM-2017-0720.

References

- [1] A. Mahasneh, F. Al-Shaheri, E. Jamal, Molecular biomarkers for an early diagnosis, effective treatment and prognosis of colorectal cancer: Current updates, *Exp. Mol. Pathol.* 102 (3) (2017) 475–483, <https://doi.org/10.1016/j.yexmp.2017.05.005>.
- [2] N. Ashammakhi, S. Ahadian, M.A. Darabi, M. El Tahchi, J. Lee, K. Suthiwanich, A. Sheikhi, M.R. Dokmeci, R. Oklu, A. Khademhosseini, Minimally Invasive and Regenerative Therapeutics, *Adv. Mater.* 31 (1) (2019) 1804041, <https://doi.org/10.1002/adma.201804041>.
- [3] D. Kim, K. Shin, S.G. Kwon, T. Hyeon, Synthesis and biomedical applications of multifunctional nanoparticles, *Adv. Mater.* 30 (49) (2018) 1802309, <https://doi.org/10.1002/adma.201802309>.
- [4] P. Vaupel, F. Kallinowski, Physiological effects of hyperthermia, *Recent Results Cancer Res.* 104 (1987) 71–109, https://doi.org/10.1007/978-3-642-82955-0_3.
- [5] H.I. Bicher, F.W. Hetzel, T.S. Sandhu, S. Frinak, P. Vaupel, M.D. O'Hara, T. O'Brien, Effects of hyperthermia on normal and tumor microenvironment, *Radiology.* 137 (2) (1980) 523–530, <https://doi.org/10.1148/radiology.137.2.7433686>.
- [6] S.K. Mishra, S. Kannan, A bimetallic silver-neodymium theranostic nanoparticle with multimodal NIR/MRI/CT imaging and combined chemophotothermal therapy, *Inorg. Chem.* 56 (19) (2017) 12054–12066, <https://doi.org/10.1021/acs.inorgchem.7b02103>.
- [7] W. Wang, C. Hao, M. Sun, L. Xu, C. Xu, H. Kuang, Spiky Fe₃O₄@Au supraparticles for multimodal in vivo imaging, *Adv. Funct. Mater.* 28 (22) (2018) 1800310, <https://doi.org/10.1002/adfm.201800310>.
- [8] T.T. Nguyen, F. Mammeri, S. Ammar, Iron oxide and gold based magneto-plasmonic nanostructures for medical applications: A review, *Nanomaterials.* 8 (2018) 149, <https://doi.org/10.3390/nano8030149>.
- [9] S. Jiang, K.Y. Win, S. Liu, C.P. Teng, Y. Zheng, M.Y. Han, Surface-functionalized nanoparticles for biosensing and imaging-guided therapeutics, *Nanoscale.* 5 (2013) 3127–3148, <https://doi.org/10.1039/c3nr34005h>.
- [10] Y.-C. Yeh, B. Creran, V.M. Rotello, Gold nanoparticles: Preparation, properties, and applications in bionanotechnology, *Nanoscale.* 4 (6) (2012) 1871–1880, <https://doi.org/10.1039/c1nr11188d>.
- [11] D. Giljohann, D. Seferos, W. Daniel, M. Massich, P. Patel, C. Mirkin, Gold nanoparticles for biology and medicine, *Angew. Chem. Int. Ed.* 49 (19) (2010) 3280–3294, <https://doi.org/10.1002/anie.200904359>.
- [12] M. Grzelczak, J. Pérez-Juste, P. Mulvaney, L.M. Liz-Marzán, Shape control in gold nanoparticle synthesis, *Chem. Soc. Rev.* 37 (2008) 1783–1791, <https://doi.org/10.1039/b711490g>.
- [13] G. Bauer, G. Borstel, H.J. Falge, A. Otto *Solid-State Physics*, Springer Tracts in Modern Physics, Vol. 74. 1974.
- [14] C.F. Bohren, D.R. Huffman, *Absorption and scattering of light by small particles*, John Wiley, 1983.
- [15] J. Langer, D. Jimenez de Aberasturi, J. Aizpurua, R.A. Alvarez-Puebla, B. Auguie, J.J. Baumberg, G.C. Bazan, S.E.J. Bell, A. Boisen, A.G. Brolo, J. Choo, D. Ciialla-May, V. Deckert, L. Fabris, K. Faulds, F.J. Garcia de Abajo, R. Goodacre, D. Graham, A.J. Haes, C.L. Haynes, C. Huck, T. Itoh, M. Käll, J. Kneipp, N.A. Kotov, H. Kuang, E.C. Le Ru, H.K. Lee, J.-F. Li, X.Y. Ling, S.A. Maier, T. Mayerhöfer, M. Moskovits, K. Murakoshi, J.-M. Nam, S. Nie, Y. Ozaki, I. Pastoriza-Santos, J. Perez-Juste, J. Popp, A. Pucci, S. Reich, B. Ren, G.C. Schatz, T. Shegai, S. Schlücker, L.-L. Tay, K.G. Thomas, Z.-Q. Tian, R.P. Van Duyne, T. Vo-Dinh, Y. Wang, K.A. Willets, C. Xu, H. Xu, Y. Xu, Y.S. Yamamoto, B. Zhao, L.M. Liz-Marzán, Present and future of surface-enhanced Raman scattering, *ACS Nano.* 14 (1) (2020) 28–117, <https://doi.org/10.1021/acsnano.9b04224>.
- [16] D. Jimenez de Aberasturi, A.B. Serrano-Montes, J. Langer, M. Henriksen-Lacey, W.J. Parak, L.M. Liz-Marzán, Surface enhanced Raman scattering encoded gold nanostars for multiplexed cell discrimination, *Chem. Mater.* 28 (18) (2016) 6779–6790, <https://doi.org/10.1021/acs.chemmater.6b03349>.
- [17] D. Jimenez de Aberasturi, M. Henriksen-Lacey, L. Litti, J. Langer, L.M. Liz-Marzán, Using SERS tags to image the three-dimensional structure of complex cell models, *Adv. Funct. Mater.* 30 (14) (2020) 1909655, <https://doi.org/10.1002/adfm.201909655>.
- [18] E. Lenzi, D. Jimenez de Aberasturi, L.M. Liz-Marzán, Surface-enhanced Raman scattering tags for three-dimensional bioimaging and biomarker detection, *ACS Sens.* 4 (5) (2019) 1126–1137, <https://doi.org/10.1021/acssensors.9b00321>.
- [19] M.R.K. Ali, Y. Wu, M.A. El-Sayed, Gold-nanoparticle-assisted plasmonic photothermal therapy advances toward clinical application, *J. Phys. Chem. C.* 123 (25) (2019) 15375–15393, <https://doi.org/10.1021/acs.jpcc.9b01961>.
- [20] J.A. Webb, R. Bardhan, Emerging advances in nanomedicine with engineered gold nanostructures, *Nanoscale.* 6 (2014) 2502–2530, <https://doi.org/10.1039/c3nr05112a>.
- [21] D.J. de Aberasturi, A.B. Serrano-Montes, L.M. Liz-Marzán, Modern applications of plasmonic nanoparticles: From energy to health, *Adv. Optical Mater.* 3 (5) (2015) 602–617, <https://doi.org/10.1002/adom.201500053>.
- [22] M.F. Casula, P. Floris, C. Innocenti, A. Lascialfari, M. Marinone, M. Corti, R.A. Sperling, W.J. Parak, C. Sangregorio, Magnetic resonance imaging contrast agents based on iron oxide superparamagnetic ferrofluids, *Chem. Mater.* 22 (5) (2010) 1739–1748, <https://doi.org/10.1021/cm9031557>.
- [23] M. Jeon, M.V. Halbert, Z.R. Stephen, M. Zhang, Iron Oxide Nanoparticles as T1 Contrast Agents for Magnetic Resonance Imaging: Fundamentals, Challenges, Applications, and Prospectives, *Adv. Mater.* 33 (23) (2021) 1906539, <https://doi.org/10.1002/adma.201906539>.
- [24] I. Fernández-Barahona, M. Muñoz-Hernando, J. Ruiz-Cabello, F. Herranz, J. Pellico, Iron oxide nanoparticles: An alternative for positive contrast in magnetic resonance imaging, *Inorganics.* 8 (2020) 28, <https://doi.org/10.3390/inorganics8040028>.
- [25] D. Bobo, K.J. Robinson, J. Islam, K.J. Thurecht, S.R. Corrie, Nanoparticle-based medicines: A review of FDA-approved materials and clinical trials to date, *Pharmaceutical Res.* 33 (10) (2016) 2373–2387, <https://doi.org/10.1007/s11095-016-1958-5>.
- [26] A. Figuerola, R. Di Corato, L. Manna, T. Pellegrino, From iron oxide nanoparticles towards advanced iron-based inorganic materials designed for biomedical applications, *Pharmacol. Res.* 62 (2) (2010) 126–143, <https://doi.org/10.1016/j.phrs.2009.12.012>.
- [27] M. Colombo, S. Carregal-Romero, M.F. Casula, L. Gutiérrez, M.P. Morales, I.B. Böhm, J.T. Heverhagen, D. Prospero, W.J. Parak, Biological applications of magnetic nanoparticles, *Chem. Soc. Rev.* 41 (2012) 4306–4334, <https://doi.org/10.1039/c2cs15337h>.
- [28] P. Guardia, A. Labarta, X. Batlle, Tuning the size, the shape, and the magnetic properties of iron oxide nanoparticles, *J. Phys. Chem. C.* 115 (2) (2011) 390–396, <https://doi.org/10.1021/jp1084982>.
- [29] P. Tartaj, M.A.D.P. Morales, S. Veintemillas-Verdaguer, T. Gonz lez-Carre o, C.J. Serna, The preparation of magnetic nanoparticles for applications in biomedicine, *J. Phys. D Appl. Phys.* 36 (13) (2003) R182–R197, <https://doi.org/10.1088/0022-3727/36/13/202>.
- [30] K. Marathe, P. Doshi, Magnetic nanoparticles: preparation, physical properties, and applications in biomedicine, *Nanoscale Res. Lett.* 7 (2012) 144, <https://doi.org/10.1109/IRLOS.2015.7353724>.
- [31] S.K. Boda, G. Thrikaraman, B. Basu, Magnetic field assisted stem cell differentiation - Role of substrate magnetization in osteogenesis, *J. Mater. Chem. B.* 3 (16) (2015) 3150–3168, <https://doi.org/10.1039/c5tb00118h>.
- [32] J. Reguera, D. Jiménez de Aberasturi, M. Henriksen-Lacey, J. Langer, A. Espinosa, B. Szczupak, C. Wilhelm, L.M. Liz-Marzán, Janus plasmonic-magnetic gold-iron oxide nanoparticles as contrast agents for multimodal imaging, *Nanoscale.* 9 (27) (2017) 9467–9480, <https://doi.org/10.1039/c7nr01406f>.
- [33] N.S. Abadeer, C.J. Murphy, Recent progress in cancer thermal therapy using gold nanoparticles, *J. Phys. Chem. C.* 120 (9) (2016) 4691–4716, <https://doi.org/10.1021/acs.jpcc.5b11232>.
- [34] A. Espinosa, J. Kolosnjaj-Tabi, A. Abou-Hassan, A. Plan Sangnier, A. Curcio, A.K. A. Silva, R. Di Corato, S. Neveu, T. Pellegrino, L.M. Liz-Marzán, C. Wilhelm, Magnetic (hyper)thermia or photothermia? progressive comparison of iron oxide and gold nanoparticles heating in water, in cells, and in vivo, *Adv. Funct. Mater.* 28 (37) (2018) 1803660, <https://doi.org/10.1002/adfm.201803660>.
- [35] A. Espinosa, J. Reguera, A. Curcio, Á. Muñoz-Noval, C. Kuttner, A. Van de Walle, L.M. Liz-Marzán, C. Wilhelm, Janus magnetic-plasmonic nanoparticles for magnetically guided and thermally activated cancer therapy, *Small.* 16 (11) (2020) 1904960, <https://doi.org/10.1002/sml.201904960>.
- [36] A. Tomitaka, H. Arami, A. Ahmadivand, N. Pala, A.J. McGoron, Y. Takemura, M. Febo, M. Nair, Magneto-plasmonic nanostars for image-guided and NIR-triggered drug delivery, *Sci. Rep.* 10 (2020) 10115, <https://doi.org/10.1038/s41598-020-66706-2>.
- [37] F. Oltolina, A. Peigneux, D. Colangelo, N. Clemente, A. D'Urso, G. Valente, G.R. Iglesias, C. Jiménez-Lopez, M. Prat, Biomimetic magnetite nanoparticles as

- targeted drug nanocarriers and mediators of hyperthermia in an experimental cancer model, *Cancers (Basel)* 12 (9) (2020) 2564, <https://doi.org/10.3390/cancers12092564>.
- [38] K. Hayashi, M. Nakamura, H. Miki, S. Ozaki, M. Abe, T. Matsumoto, W. Sakamoto, T. Yogo, K. Ishimura, Magnetically responsive smart nanoparticles for cancer treatment with a combination of magnetic hyperthermia and remote-control drug release, *Theranostics* 4 (8) (2014) 834–844, <https://doi.org/10.1016/j.thno.2014.07.002>.
- [39] J. Estelrich, E. Escribano, J. Queralt, M.A. Busquets, Iron oxide nanoparticles for magnetically-guided and magnetically-responsive drug delivery, *Int. J. Mol. Sci.* 16 (2015) 8070–8101, <https://doi.org/10.3390/ijms16048070>.
- [40] X. Lu, M. Rycenga, S.E. Skrabalak, B. Wiley, Y. Xia, Chemical synthesis of novel plasmonic nanoparticles, *Annu. Rev. Phys. Chem.* 60 (1) (2009) 167–192, <https://doi.org/10.1146/annurev.physchem.040808.090434>.
- [41] H. Duan, D. Wang, Y. Li, Green chemistry for nanoparticle synthesis, *Chem. Soc. Rev.* 44 (16) (2015) 5778–5792, <https://doi.org/10.1039/c4cs00363b>.
- [42] K.N. Thakkar, S.S. Mhatre, R.Y. Parikh, Biological synthesis of metallic nanoparticles, *Nanomedicine Nanotechnology, Biol. Med.* 6 (2) (2010) 257–262, <https://doi.org/10.1016/j.nano.2009.07.002>.
- [43] J. Turkevich, P.C. Stevenson, J. Hillier, A study of the nucleation and growth processes in the synthesis of colloidal gold, *Discuss. Faraday Soc.* 11 (1951) 55–75, <https://doi.org/10.1039/DF9511100055>.
- [44] J.J. Giner-Casares, M. Henriksen-Lacey, M. Coronado-Puchau, L.M. Liz-Marzán, Inorganic nanoparticles for biomedicine: Where materials scientists meet medical research, *Mater. Today* 19 (1) (2016) 19–28, <https://doi.org/10.1016/j.mattod.2015.07.004>.
- [45] J. Reguera, J. Langer, D. Jiménez de Aberasturi, L.M. Liz-Marzán, Anisotropic metal nanoparticles for surface enhanced Raman scattering, *Chem. Soc. Rev.* 46 (13) (2017) 3866–3885, <https://doi.org/10.1021/acs.langmuir.5b01838>.
- [46] E. Hemmer, A. Benayas, F. Légaré, F. Vetrone, Exploiting the biological windows: Current perspectives on fluorescent bioprobes emitting above 1000 nm, *Nanoscale Horiz.* 1 (3) (2016) 168–184, <https://doi.org/10.1039/c5nh00073d>.
- [47] L.M. Liz-Marzán, M. Grzelczak, Growing anisotropic crystals at the nanoscale, *Science* 356 (6343) (2017) 1120–1121, <https://doi.org/10.1126/science.aam8774>.
- [48] A. Sánchez-Iglesias, N. Winckelmans, T. Altantzis, S. Bals, M. Grzelczak, L.M. Liz-Marzán, High-Yield Seeded Growth of Monodisperse Pentatwinned Gold Nanoparticles through Thermally Induced Seed Twinning, *J. Am. Chem. Soc.* 139 (1) (2017) 107–110, <https://doi.org/10.1021/jacs.6b12143>.
- [49] G. González-Rubio, V. Kumar, P. Lombart, P. Díaz-Núñez, E. Bladt, T. Altantzis, S. Bals, O. Peña-Rodríguez, E.G. Noya, L.G. MacDowell, A. Guerrero-Martínez, L.M. Liz-Marzán, Disconnecting symmetry breaking from seeded growth for the reproducible synthesis of high quality gold nanorods, *ACS Nano* 13 (4) (2019) 4424–4435, <https://doi.org/10.1021/acsnano.8b09658>.
- [50] L. Scarabelli, M. Coronado-Puchau, J.J. Giner-Casares, J. Langer, L.M. Liz-Marzán, Monodisperse gold nanotriangles: Size control, large-scale self-assembly, and performance in surface-enhanced Raman scattering, *ACS Nano* 8 (6) (2014) 5833–5842, <https://doi.org/10.1021/nn500727w>.
- [51] C. Hanske, G. González-Rubio, C. Hamon, P. Formentín, E. Modin, A. Chuvilin, A. Guerrero-Martínez, L.F. Marsal, L.M. Liz-Marzán, Large-scale plasmonic pyramidal supercrystals via templated self-assembly of monodisperse gold nanospheres, *J. Phys. Chem. C* 121 (20) (2017) 10899–10906, <https://doi.org/10.1021/acs.jpcc.6b12161>.
- [52] H.-L. Wu, C.-H. Kuo, M.H. Huang, Seed-mediated synthesis of gold nanocrystals with systematic shape evolution from cubic to trisoctahedral and rhombic dodecahedral structures, *Langmuir* 26 (14) (2010) 12307–12313, <https://doi.org/10.1021/la1015065>.
- [53] S. Laurent, D. Forge, M. Port, A. Roch, C. Robic, L. Vander Elst, R.N. Muller, Magnetic iron oxide nanoparticles: Synthesis, stabilization, vectorization, physicochemical characterizations and biological applications, *Chem. Rev.* 108 (6) (2008) 2064–2110, <https://doi.org/10.1021/cr068445e>.
- [54] X. Guo, Z. Wu, W. Li, Z. Wang, Q. Li, F. Kong, H. Zhang, X. Zhu, Y.P. Du, Y.i. Jin, Y. Du, J. You, Appropriate size of magnetic nanoparticles for various bioapplications in cancer diagnostics and therapy, *ACS Appl. Mater. Interfaces* 8 (5) (2016) 3092–3106, <https://doi.org/10.1021/acsami.5b10352>.
- [55] M.R.Z. Kouhpanji, B.J.H. Stadler, A guideline for effectively synthesizing and characterizing magnetic nanoparticles for advancing nanobiotechnology: A review, *Sensors* 20 (2020) 2554, <https://doi.org/10.3390/s20092554>.
- [56] T. Ahn, J.H. Kim, H.-M. Yang, J.W. Lee, J.-D. Kim, Formation pathways of magnetite nanoparticles by coprecipitation method, *J. Phys. Chem. C* 116 (10) (2012) 6069–6076, <https://doi.org/10.1021/jp211843g>.
- [57] X. Liu, G. Qiu, A. Yan, Z. Wang, X. Li, Hydrothermal synthesis and characterization of α -FeOOH and α -Fe₂O₃ uniform nanocrystallines, *J. Alloys Compd.* 433 (1–2) (2007) 216–220, <https://doi.org/10.1016/j.jallcom.2006.06.029>.
- [58] S. Ge, X. Shi, K. Sun, C. Li, C. Uher, J.R. Baker, M.M. Banaszak Holl, B.G. Orr, Facile hydrothermal synthesis of iron oxide nanoparticles with tunable magnetic properties, *J. Phys. Chem. C* 113 (31) (2009) 13593–13599, <https://doi.org/10.1021/jp902953t>.
- [59] W. Wu, Q. He, C. Jiang, Magnetic iron oxide nanoparticles: Synthesis and surface functionalization strategies, *Nanoscale Res. Lett.* 3 (2008) 397–415, <https://doi.org/10.1007/s11671-008-9174-9>.
- [60] S. Sun, H. Zeng, Size-controlled synthesis of magnetite nanoparticles, *J. Am. Chem. Soc.* 124 (28) (2002) 8204–8205, <https://doi.org/10.1021/ja026501x>.
- [61] S.M. Dadfar, K. Roemhild, N.J. Drude, S. von Stillfried, R. Knüchel, F. Kiessling, T. Lammers, Iron oxide nanoparticles: Diagnostic, therapeutic and theranostic applications, *Adv. Drug Deliv. Rev.* 138 (2019) 302–325, <https://doi.org/10.1016/j.addr.2019.01.005>.
- [62] M. Mahdavi, M. Bin Ahmad, M.J. Haron, F. Namvar, B. Nadi, M.Z. Ab Rahman, J. Amin, Synthesis, surface modification and characterisation of biocompatible magnetic iron oxide nanoparticles for biomedical applications, *Molecules* 18 (2013) 7533–7548, <https://doi.org/10.3390/molecules18077533>.
- [63] A.G. Roca, J.F. Marco, M.D.P. Morales, C.J. Serna, Effect of nature and particle size on properties of uniform magnetite and maghemite nanoparticles, *J. Phys. Chem. C* 111 (50) (2007) 18577–18584, <https://doi.org/10.1021/jp075133m>.
- [64] Z. Zhou, X. Zhu, D. Wu, Q. Chen, D. Huang, C. Sun, J. Xin, K. Ni, J. Gao, Anisotropic shaped iron oxide nanostructures: Controlled synthesis and proton relaxation shortening effects, *Chem. Mater.* 27 (9) (2015) 3505–3515, <https://doi.org/10.1021/acs.chemmater.5b00944>.
- [65] A.G. Roca, L. Gutiérrez, H. Gavián, M.E. Fortes Brollo, S. Veintemillas-Verdaguer, M. del P. Morales, Design strategies for shape-controlled magnetic iron oxide nanoparticles, *Adv. Drug Deliv. Rev.* 138 (2019) 68–104, <https://doi.org/10.1016/j.addr.2018.12.008>.
- [66] E.D. Smolensky, H.Y.E. Park, Y. Zhou, G.A. Rolla, M. Marjańska, M. Botta, V.C. Pierre, Scaling laws at the nanosize: The effect of particle size and shape on the magnetism and relaxivity of iron oxide nanoparticle contrast agents, *J. Mater. Chem. B* 1 (2013) 2818–2828, <https://doi.org/10.1039/c3tb00369h>.
- [67] Z. Nemati, J. Alonso, I. Rodrigo, R. Das, E. Garaio, J.A. García, I. Orue, M.-H. Phan, H. Srikanth, Improving the Heating Efficiency of Iron Oxide Nanoparticles by Tuning Their Shape and Size, *J. Phys. Chem. C* 122 (4) (2018) 2367–2381, <https://doi.org/10.1021/acs.jpcc.7b10528>.
- [68] L. Gutiérrez, R. Costo, C. Grüttner, F. Westphal, N. Gehrke, D. Heinke, A. Fornara, Q.A. Pankhurst, C. Johansson, S. Veintemillas-Verdaguer, M.P. Morales, Synthesis methods to prepare single- and multi-core iron oxide nanoparticles for biomedical applications, *Dalt. Trans.* 44 (7) (2015) 2943–2952.
- [69] G. Hemery, A.C. Keyes, E. Garaio, I. Rodrigo, J.A. Garcia, F. Plazaola, E. Garanger, O. Sandre, Tuning sizes, morphologies, and magnetic properties of monocoreshell versus multicore iron oxide nanoparticles through the controlled addition of water in the polyol synthesis, *Inorg. Chem.* 56 (14) (2017) 8232–8243, <https://doi.org/10.1021/acs.inorgchem.7b00956>.
- [70] P. Guardia, R. Di Corato, L. Lartigue, C. Wilhelm, A. Espinosa, M. Garcia-Hernandez, F. Gazeau, L. Manna, T. Pellegrino, Water-soluble iron oxide nanocubes with high values of specific absorption rate for cancer cell hyperthermia treatment, *ACS Nano* 6 (4) (2012) 3080–3091, <https://doi.org/10.1021/nn2048137>.
- [71] X. Hu, J.C. Yu, Continuous aspect-ratio tuning and fine shape control of monodisperse α -Fe₂O₃ nanocrystals by a programmed microwave-hydrothermal method, *Adv. Funct. Mater.* 18 (6) (2008) 880–887, <https://doi.org/10.1002/adfm.200700671>.
- [72] L. Storzuk, M.O. Besenhard, S. Mourdikoudis, A.P. LaGrow, M.R. Lees, L.D. Tung, A. Gavriilidis, N.T.K. Thanh, Stable iron oxide nanoflowers with exceptional magnetic heating efficiency: Simple and fast polyol synthesis, *ACS Appl. Mater. Interfaces* 13 (38) (2021) 45870–45880, <https://doi.org/10.1021/acsaami.1c12323>.
- [73] S.-J. Cho, J.-C. Idrobo, J. Olamit, K. Liu, N.D. Browning, S.M. Kauzlarich, Growth mechanisms and oxidation resistance of gold-coated iron nanoparticles, *Chem. Mater.* 17 (12) (2005) 3181–3186, <https://doi.org/10.1021/cm0500713>.
- [74] I.-C. Chiang, D.-H. Chen, Structural characterization and self-assembly into superlattices of iron oxide-gold core-shell nanoparticles synthesized via a high-temperature organometallic route, *Nanotechnology* 20 (1) (2009) 015602, <https://doi.org/10.1088/0957-4484/20/1/015602>.
- [75] L. Wang, J. Luo, Q. Fan, M. Suzuki, I.S. Suzuki, M.H. Engelhard, Y. Lin, N. Kim, J.Q. Wang, C.J. Zhong, Monodispersed core-shell Fe₃O₄@Au nanoparticles, *J. Phys. Chem. B* 109 (2005) 21593–21601, <https://doi.org/10.1021/jp0543429>.
- [76] A. Billen, A. de Cattelle, J.K. Jochum, M.J. Van Bael, J. Billen, J.W. Seo, W. Brullot, G. Koeckelberghs, T. Verbiest, Novel synthesis of superparamagnetic plasmonic core-shell iron oxide-gold nanoparticles, *Phys. B Condens. Matter* 560 (2019) 85–90, <https://doi.org/10.1016/j.physb.2019.02.009>.
- [77] X. Ji, R. Shao, A.M. Elliott, R.J. Stafford, E. Esparza-Coss, J.A. Bankson, G. Liang, Z.-P. Luo, K. Park, J.T. Markert, C. Li, Bifunctional Gold Nanoshells with a Superparamagnetic Iron Oxide–Silica Core Suitable for Both MR Imaging and Photothermal Therapy, *J. Phys. Chem. C* 111 (17) (2007) 6245–6251, <https://doi.org/10.1021/jp0702245>.
- [78] C. Jin, Y. Qu, M. Wang, J. Han, Y. Hu, R. Guo, Aqueous solution-based Fe₃O₄ seed-mediated route to hydrophilic Fe₃O₄-Au janus nanoparticles, *Langmuir* 32 (18) (2016) 4595–4601, <https://doi.org/10.1021/acs.langmuir.6b01269>.
- [79] I.Y. Goon, L.M.H. Lai, M. Lim, P. Munroe, J.J. Gooding, R. Amal, Fabrication and dispersion of gold-shell-protected magnetite nanoparticles: Systematic control using polyethyleneimine, *Chem. Mater.* 21 (4) (2009) 673–681, <https://doi.org/10.1021/cm8025329>.
- [80] J. Reguera, D. Jimenez de Aberasturi, N. Winckelmans, J. Langer, S. Bals, L.M. Liz-Marzán, Synthesis of Janus plasmonic-magnetic, star-sphere nanoparticles, and their application in SERS detection, *Faraday Discuss.* 191 (2016) 47–59, <https://doi.org/10.1039/c6fd00012f>.

- [81] M.A.M. Tarkistani, V. Komalla, V. Kayser, Recent advances in the use of iron-gold hybrid nanoparticles for biomedical applications, *Nanomaterials*. 11 (2021) 1227, <https://doi.org/10.3390/nano11051227>.
- [82] H. Zhou, J.-P. Kim, J.H. Bahng, N.A. Kotov, J. Lee, Self-assembly mechanism of spiky magnetoplasmonic supraparticles, *Adv. Funct. Mater.* 24 (10) (2014) 1439–1448, <https://doi.org/10.1002/adfm.201302405>.
- [83] M.V. Efremova, V.A. Naumenko, M. Spasova, A.S. Garanina, M.A. Abakumov, A. D. Blokhina, P.A. Melnikov, O.P. Alexandra, M. Heidelmann, Z. Li, Z. Ma, I.V. Shchetinin, Y.I. Golovin, I.I. Kireev, A.G. Savchenko, V.P. Chekhonin, N.L. Klyachko, M. Farle, A.G. Majouga, U. Wiedwald, Magnetite-Gold nano hybrids as ideal all-in-one platforms for theranostics, *Sci. Rep.* 8 (2018) 11295, <https://doi.org/10.1038/s41598-018-29618-w>.
- [84] Y. Li, J. Zhao, W. You, D. Cheng, W. Ni, Gold nanorod@iron oxide core-shell heterostructures: Synthesis, characterization, and photocatalytic performance, *Nanoscale*. 9 (11) (2017) 3925–3933, <https://doi.org/10.1039/c7nr00141j>.
- [85] C.S. Levin, C. Hofmann, T.A. Ali, A.T. Kelly, E. Morosan, P. Nordlander, K.H. Whitmire, N.J. Halas, Magnetic-plasmonic core-shell nanoparticles, *ACS Nano*. 3 (6) (2009) 1379–1388, <https://doi.org/10.1021/nn900118a>.
- [86] E.A. Kwizera, E. Chaffin, X. Shen, J. Chen, Q. Zou, Z. Wu, Z. Gai, S. Bhana, R. O'Connor, L. Wang, H. Adhikari, S.R. Mishra, Y. Wang, X. Huang, Size- and shape-controlled synthesis and properties of magnetic-plasmonic core-shell nanoparticles, *J. Phys. Chem. C*. 120 (19) (2016) 10530–10546, <https://doi.org/10.1021/acs.jpcc.6b00875>.
- [87] P. Quaresima, I. Osório, G. Dória, P.A. Carvalho, A. Pereira, J. Langer, J.P. Araújo, I. Pastoriza-Santos, L.M. Liz-Marzán, R. Franco, P.V. Baptista, E. Pereira, Star-shaped magnetite@gold nanoparticles for protein magnetic separation and SERS detection, *RSC Adv.* 4 (8) (2014) 3690–3698, <https://doi.org/10.1039/c3ra46762g>.
- [88] L.E.W. LaConte, N. Nitin, O. Zurkiya, D. Caruntu, C.J. O'Connor, X. Hu, G. Bao, Coating thickness of magnetic iron oxide nanoparticles affects R 2 relaxivity, *J. Magn. Reson. Imaging*. 26 (6) (2007) 1634–1641, <https://doi.org/10.1002/jmri.21194>.
- [89] M.B. Cortie, A.M. McDonagh, Synthesis and optical properties of hybrid and alloy plasmonic nanoparticles, *Chem. Rev.* 111 (6) (2011) 3713–3735, <https://doi.org/10.1021/cr1002529>.
- [90] M. Ha, J.-H. Kim, M. You, Q. Li, C. Fan, J.-M. Nam, Multicomponent plasmonic nanostructures: From heterostructured nanoparticles to colloidal composite nanostructures, *Chem. Rev.* 119 (24) (2019) 12208–12278, <https://doi.org/10.1021/acs.chemrev.9b00234>.
- [91] P. Das, P. Fatehbasharizad, M. Colombo, L. Fiandra, D. Prosperi, Multifunctional magnetic gold nanomaterials for cancer, *Trends Biotechnol.* 37 (9) (2019) 995–1010, <https://doi.org/10.1016/j.tibtech.2019.02.005>.
- [92] P. Nguyen Tri, C. Ouellet-Plamondon, S. Rtimi, A.A. Assadi, T.A. Nguyen, Noble Metal-Metal Oxide Hybrid Nanoparticles, in: *Noble Metal-Metal Oxide Hybrid Nanoparticles*, Elsevier, 2019, pp. 51–63, <https://doi.org/10.1016/B978-0-12-814134-2.00003-6>.
- [93] JitKang Lim, S.A. Majetich, Composite magnetic-plasmonic nanoparticles for biomedicine: Manipulation and imaging, *Nano Today*. 8 (1) (2013) 98–113, <https://doi.org/10.1016/j.nantod.2012.12.010>.
- [94] S. Stafford, R.S. Garcia, Y.K. Gun'ko, Multimodal magnetic-plasmonic nanoparticles for biomedical applications, *Appl. Sci.* 8 (2018) 97, <https://doi.org/10.3390/app8010097>.
- [95] S.R.M. Tréguer-Delapierre, J. Majimel, S. Mornet, E. Duguet, Synthesis of non-spherical gold nanoparticles, *Gold Bull.* 41 (2008) 195–207, <https://doi.org/10.1166/jnm.2011.4339>.
- [96] P. Arenas-Guerrero, Á.V. Delgado, K.J. Donovan, K. Scott, T. Bellini, F. Mantegazza, M.L. Jiménez, Determination of the size distribution of non-spherical nanoparticles by electric birefringence-based methods, *Sci. Rep.* 8 (2018) 9502, <https://doi.org/10.1038/s41598-018-27840-0>.
- [97] S. Bhattacharjee, DLS and zeta potential - What they are and what they are not?, *J. Control. Release*. 235 (2016) 337–351, <https://doi.org/10.1016/j.jconrel.2016.06.017>.
- [98] J. Winsett, A. Moilanen, K. Paudel, S. Kamali, K. Ding, W. Cribb, D. Seifu, S. Neupane, Quantitative determination of magnetite and maghemite in iron oxide nanoparticles using Mössbauer spectroscopy, *SN Appl. Sci.* 1 (2019) 1636, <https://doi.org/10.1007/s42452-019-1699-2>.
- [99] N. Lee, T. Hyeon, Designed synthesis of uniformly sized iron oxide nanoparticles for efficient magnetic resonance imaging contrast agents, *Chem. Soc. Rev.* 41 (7) (2012) 2575–2589, <https://doi.org/10.1039/c1cs15248c>.
- [100] K. Wu, J. Liu, R. Saha, C. Peng, D. Su, Y.A. Wang, J.-P. Wang, Investigation of commercial iron oxide nanoparticles: Structural and magnetic property characterization, *ACS Omega*. 6 (9) (2021) 6274–6283, <https://doi.org/10.1021/acsomega.0c05845>.
- [101] M. Mychinko, A. Skorikov, W. Albrecht, A. Sánchez-Iglesias, X. Zhuo, V. Kumar, L.M. Liz-Marzán, S. Bals, The Influence of size, shape, and twin boundaries on heat-induced alloying in individual Au@Ag core-shell nanoparticles, *Small*. 17 (34) (2021) 2102348, <https://doi.org/10.1002/sml.202102348>.
- [102] A. Sánchez-Iglesias, X. Zhuo, W. Albrecht, S. Bals, L.M. Liz-Marzán, Tuning size and seed position in small silver nanorods, *ACS Mater. Lett.* 2 (2020) 1246–1250, <https://doi.org/10.1021/acsmaterlett.0c00388>.
- [103] S. Estradé, L.I. Yedra, A. López-Ortega, M. Estrader, G. Salazar-Alvarez, M.D. Baró, J. Nogués, F. Peiró, Distinguishing the core from the shell in MnO x/MnO y and FeO x/MnO x core/shell nanoparticles through quantitative electron energy loss spectroscopy (EELS) analysis, *Micron*. 43 (1) (2012) 30–36, <https://doi.org/10.1016/j.micron.2011.04.002>.
- [104] P. Wagener, J. Jakobi, C. Rehbock, V.S.K. Chakravadhanula, C. Thede, U. Wiedwald, M. Bartsch, L. Kienle, S. Barcikowski, Solvent-surface interactions control the phase structure in laser-generated iron-gold core-shell nanoparticles, *Sci. Rep.* 6 (2016) 23352, <https://doi.org/10.1038/srep23352>.
- [105] N. Kattan, B.o. Hou, D.J. Fermín, D. Cherns, Crystal structure and defects visualization of Cu2ZnSnS4 nanoparticles employing transmission electron microscopy and electron diffraction, *Appl. Mater. Today*. 1 (1) (2015) 52–59, <https://doi.org/10.1016/j.apmt.2015.08.004>.
- [106] S. Bals, B. Goris, L.M. Liz-Marzán, G. Van Tendeloo, Three-dimensional characterization of noble-metal nanoparticles and their assemblies by electron tomography, *Angew. Chem. Int. Ed.* 53 (40) (2014) 10600–10610, <https://doi.org/10.1002/anie.201401059>.
- [107] N. Winckelmans, T. Altantzis, M. Grzelczak, A. Sánchez-Iglesias, L.M. Liz-Marzán, S. Bals, Multimode electron tomography as a tool to characterize the internal structure and morphology of gold nanoparticles, *J. Phys. Chem. C*. 122 (25) (2018) 13522–13528, <https://doi.org/10.1021/acs.jpcc.7b12379>.
- [108] P. Sharma, S. Brown, G. Walter, S. Santra, B. Moudgil, Nanoparticles for bioimaging, *Adv. Colloid Interface Sci.* 123–126 (2006) 471–485, <https://doi.org/10.1016/j.cis.2006.05.026>.
- [109] J. Gallo, N.J. Long, E.O. Aboagye, Magnetic nanoparticles as contrast agents in the diagnosis and treatment of cancer, *Chem. Soc. Rev.* 42 (2013) 7816–7833, <https://doi.org/10.1039/c3cs60149h>.
- [110] D.J.A. Margolis, J.M. Hoffman, R.J. Herfkens, R.B. Jeffrey, A. Quon, S.S. Gambhir, Molecular imaging techniques in body imaging, *Radiology*. 245 (2) (2007) 333–356, <https://doi.org/10.1148/radiol.2452061117>.
- [111] D. Kim, M.K. Yu, T.S. Lee, J.J. Park, Y.Y. Jeong, S. Jon, Amphiphilic polymer-coated hybrid nanoparticles as CT/MRI dual contrast agents, *Nanotechnology*. 22 (15) (2011) 155101, <https://doi.org/10.1088/0957-4484/22/15/155101>.
- [112] D.P. Cormode, P.C. Naha, Z.A. Fayad, Nanoparticle contrast agents for computed tomography: A focus on micelles, *Contrast Media Mol. Imaging*. 9 (2014) 37–52, <https://doi.org/10.1002/cmmi.1551>.
- [113] Y.C. Dong, M. Hajfathalian, P.S.N. Maidment, J.C. Hsu, P.C. Naha, S. Si-Mohamed, M. Breuilly, J. Kim, P. Chhour, P. Douek, H.I. Litt, D.P. Cormode, Effect of gold nanoparticle size on their properties as contrast agents for computed tomography, *Sci. Rep.* 9 (2019) 141912, <https://doi.org/10.1038/s41598-019-50332-8>.
- [114] P. Beard, Biomedical photoacoustic imaging, *Interface, Focus*. 1 (4) (2011) 602–631, <https://doi.org/10.1098/rsfs.2011.0028>.
- [115] J. Gröhl, M. Schellenberg, K. Dreher, L. Maier-Hein, Deep learning for biomedical photoacoustic imaging: A review, *Photoacoustics*. 22 (2021) 100241, <https://doi.org/10.1016/j.pacs.2021.100241>.
- [116] Y. Mantri, J.V. Jokerst, Engineering plasmonic nanoparticles for enhanced photoacoustic imaging, *ACS Nano*. 14 (8) (2020) 9408–9422, <https://doi.org/10.1021/acsnano.0c05215>.
- [117] C. Eggeling, J. Widengren, R. Rigler, C.A.M. Seidel, Photobleaching of fluorescent dyes under conditions used for single-molecule detection: Evidence of two-step photolysis, *Anal. Chem.* 70 (1998) 2651–2659, <https://doi.org/10.1021/ac980027p>.
- [118] C. Bao, N. Beziere, P. del Pino, B. Pelaz, G. Estrada, F. Tian, V. Ntziachristos, J.M. de la Fuente, D. Cui, Gold nanoprism as optoacoustic signal nanoamplifiers for in vivo bioimaging of gastrointestinal cancers, *Small*. 9 (1) (2013) 68–74, <https://doi.org/10.1002/sml.201201779>.
- [119] K.H. Song, C. Kim, C.M. Cobley, Y. Xia, L.V. Wang, Near-infrared gold nanocages as a new class of tracers for photoacoustic sentinel lymph node mapping on a rat model, *Nano Lett.* 9 (1) (2009) 183–188, <https://doi.org/10.1021/nl802746w>.
- [120] W. Lu, Q. Huang, G. Ku, X. Wen, M. Zhou, D. Guzatov, P. Brecht, R. Su, A. Oraevsky, L.V. Wang, C. Li, Photoacoustic imaging of living mouse brain vasculature using hollow gold nanospheres, *Biomaterials*. 31 (9) (2010) 2617–2626, <https://doi.org/10.1016/j.biomaterials.2009.12.007>.
- [121] P. Huang, J. Lin, W. Li, P. Rong, Z. Chen, S. Wang, X. Wang, X. Sun, M. Aronova, G. Niu, R.D. Leapman, Z. Nie, X. Chen, Biodegradable gold nanovesicles with an ultralong plasmonic coupling effect for photoacoustic imaging and photothermal therapy, *Angew. Chem. Int. Ed.* 52 (52) (2013) 13958–13964, <https://doi.org/10.1002/anie.201308986>.
- [122] V. Raghavan, C. O'Flatharta, R. Dwyer, A. Breathnach, H. Zafar, P. Dockery, A. Wheatley, I. Keogh, M. Leahy, M. Olivo, Dual plasmonic gold nanostars for photoacoustic imaging and photothermal therapy, *Nanomedicine*. 12 (5) (2017) 457–471, <https://doi.org/10.2217/nnm-2016-0318>.
- [123] K. Cai, W. Zhang, M.F. Foda, X. Li, J. Zhang, Y. Zhong, H. Liang, H. Li, H. Han, T. Zhai, Miniature hollow gold nanorods with enhanced effect for in vivo photoacoustic imaging in the NIR-II window, *Small*. 16 (37) (2020) 2002748, <https://doi.org/10.1002/sml.202002748>.
- [124] R. García-Álvarez, L. Chen, A. Nedilko, A. Sánchez-Iglesias, A. Rix, W. Lederle, V. Pathak, T. Lammers, G. von Plessen, K. Kostarelos, L.M. Liz-Marzán, A.J.C. Kuehne, D.N. Chigrin, Optimizing the geometry of photoacoustically active gold nanoparticles for biomedical imaging, *ACS Photonics*. 7 (3) (2020) 646–652, <https://doi.org/10.1021/acsp Photonics.9b01418>.
- [125] E. Huynh, G. Zheng, Engineering multifunctional nanoparticles: All-in-one versus one-for-all, *Wiley Interdiscip. Rev. Nanomed. Nanobiotech.* 5 (3) (2013) 250–265, <https://doi.org/10.1002/wnan.1217>.
- [126] L. Fabris, SERS tags: The next promising tool for personalized cancer detection?, *ChemNanoMat* 2 (4) (2016) 249–258, <https://doi.org/10.1002/cnma.201500221>.

- [127] S. Rodal-Cedeira, A. Vázquez-Arias, G. Bodelón, A. Skorikov, S. Núñez-Sánchez, A. Laporta, L. Polavarapu, S. Bals, L.M. Liz-Marzán, J. Pérez-Juste, I. Pastoriza-Santos, An expanded surface-enhanced Raman scattering tags library by combinatorial encapsulation of reporter molecules in metal nanoshells, *ACS Nano*. 14 (11) (2020) 14655–14664, <https://doi.org/10.1021/acsnano.0c04368>.
- [128] J.V. Jokerst, A.J. Cole, D. Van de Sompel, S.S. Gambhir, Gold nanorods for ovarian cancer detection with photoacoustic imaging and resection guidance via Raman imaging in living mice, *ACS Nano*. 6 (11) (2012) 10366–10377, <https://doi.org/10.1021/nn304347g>.
- [129] Y.W. Wang, S. Kang, A. Khan, P.Q. Bao, J.T.C. Liu, In vivo multiplexed molecular imaging of esophageal cancer via spectral endoscopy of topically applied SERS nanoparticles, *Biomed. Opt. Express*. 6 (2015) 3714–3723, <https://doi.org/10.1364/boe.6.003714>.
- [130] Y. Wang, S. Kang, A. Khan, G. Ruttner, S.Y. Leigh, M. Murray, S. Abeytunge, G. Peterson, M. Rajadhyaksha, S. Dintzis, S. Javid, J.T.C. Liu, Quantitative molecular phenotyping with topically applied SERS nanoparticles for intraoperative guidance of breast cancer lumpectomy, *Sci. Rep.* 6 (2016) 21242, <https://doi.org/10.1038/srep21242>.
- [131] Z. Zhou, L. Yang, J. Gao, X. Chen, Structure–relaxivity relationships of magnetic nanoparticles for magnetic resonance imaging, *Adv. Mater.* 31 (8) (2019) 1804567, <https://doi.org/10.1002/adma.201804567>.
- [132] R.-J. van Geuns, P.A. Wielopolski, H.G. de Bruin, B.J. Rensing, P.M.A. van Ooijen, M. Hulshoff, M. Oudkerk, P.J. de Feyter, Basic principles of magnetic resonance imaging, *Prog. Cardiovasc. Dis.* 42 (2) (1999) 149–156, [https://doi.org/10.1016/S0033-0620\(99\)70014-9](https://doi.org/10.1016/S0033-0620(99)70014-9).
- [133] M. Rogosnitzky, S. Branch, Gadolinium-based contrast agent toxicity: a review of known and proposed mechanisms, *BioMetals*. 29 (3) (2016) 365–376, <https://doi.org/10.1007/s10534-016-9931-7>.
- [134] S.-J. Cho, B.R. Jarrett, A.Y. Louie, S.M. Kauzlarich, Gold-coated iron nanoparticles: A novel magnetic resonance agent for T1 and T2 weighted imaging, *Nanotechnology*. 17 (3) (2006) 640–644, <https://doi.org/10.1088/0957-4484/17/3/004>.
- [135] H. Jung, B. Park, C. Lee, J. Cho, J. Suh, JangYeon Park, YoungRo Kim, J. Kim, G. Cho, HyungJoon Cho, Dual MRI T1 and T2(*) contrast with size-controlled iron oxide nanoparticles, *Nanomedicine Nanotechnology, Biol. Med.* 10 (8) (2014) 1679–1689, <https://doi.org/10.1016/j.nano.2014.05.003>.
- [136] Y.-K. Peng, S.C.E. Tsang, P.-T. Chou, Chemical design of nanoprobe for T1-weighted magnetic resonance imaging, *Mater. Today*. 19 (6) (2016) 336–348, <https://doi.org/10.1016/j.mattod.2015.11.006>.
- [137] B. Gleich, J. Weizenecker, Tomographic imaging using the nonlinear response of magnetic particles, *Nature*. 435 (7046) (2005) 1214–1217, <https://doi.org/10.1038/nature03808>.
- [138] J. Borgert, J.D. Schmidt, I. Schmale, J. Rahmer, C. Bontus, B. Gleich, B. David, R. Eckart, O. Woywode, J. Weizenecker, J. Schnorr, M. Taupitz, J. Haegeler, F.M. Vogt, J. Barkhausen, Fundamentals and applications of magnetic particle imaging, *J. Cardiovasc. Comput. Tomogr.* 6 (3) (2012) 149–153, <https://doi.org/10.1016/j.jcct.2012.04.007>.
- [139] C. Lu, L. Han, J. Wang, J. Wan, G. Song, J. Rao, Engineering of magnetic nanoparticles as magnetic particle imaging tracers, *Chem. Soc. Rev.* 50 (14) (2021) 8102–8146, <https://doi.org/10.1039/d0cs00260g>.
- [140] P. Ludewig, N. Gdaniec, J. Sedlaczek, N.D. Forkert, P. Szwargulski, M. Graeser, G. Adam, M.G. Kaul, K.M. Krishnan, R.M. Ferguson, A.P. Khandhar, P. Walczak, J. Fiehler, G. Thomalla, C. Gerloff, T. Knopp, T. Magnus, Magnetic particle imaging for real-time perfusion imaging in acute stroke, *ACS Nano*. 11 (10) (2017) 10480–10488, <https://doi.org/10.1021/acsnano.7b05784>.
- [141] J.W.M. Bulte, Superparamagnetic iron oxides as MRI tracers: A primer and review of early applications, *Adv. Drug Deliv. Rev.* 138 (2019) 293–301, <https://doi.org/10.1016/j.addr.2018.12.007>.
- [142] J. Wang, X. Wu, C. Wang, N. Shao, P. Dong, R. Xiao, S. Wang, Magnetically assisted surface-enhanced Raman spectroscopy for the detection of staphylococcus aureus based on aptamer recognition, *ACS Appl. Mater. Interfaces*. 7 (37) (2015) 20919–20929, <https://doi.org/10.1021/acsnano.5b06446>.
- [143] C. Sun, R. Zhang, M. Gao, X. Zhang, A rapid and simple method for efficient capture and accurate discrimination of circulating tumor cells using aptamer conjugated magnetic beads and surface-enhanced Raman scattering imaging, *Anal. Bioanal. Chem.* 407 (29) (2015) 8883–8892, <https://doi.org/10.1007/s00216-015-9049-8>.
- [144] J. Zeng, M. Gong, D. Wang, M. Li, W. Xu, Z. Li, S. Li, D. Zhang, Z. Yan, Y. Yin, Direct synthesis of water-dispersible magnetic/plasmonic heteronanostructures for multimodality biomedical imaging, *Nano Lett.* 19 (5) (2019) 3011–3018, <https://doi.org/10.1021/acs.nanolett.9b00171>.
- [145] V. Amendola, S. Scaramuzza, L. Litti, M. Meneghetti, G. Zuccolotto, A. Rosato, E. Nicolato, P. Marzola, G. Fracasso, C. Anselmi, M. Pinto, M. Colombatti, Magneto-plasmonic Au-Fe alloy nanoparticles designed for multimodal SERS-MRI-CT imaging, *Small*. 10 (12) (2014) 2476–2486, <https://doi.org/10.1002/smll.201303372>.
- [146] W. Feng, X. Zhou, W. Nie, L. Chen, K. Qiu, Au/Polypyrrole@Fe₃O₄ nanocomposites for MR/CT dual-modal imaging guided-photothermal therapy: An in vitro study, *ACS Appl. Mater. Interfaces*. 7 (2015) 4354–4367, <https://doi.org/10.1021/am508837v>.
- [147] M. Wang, Q. Yang, M. Li, H. Zou, Z. Wang, H. Ran, Y. Zheng, J. Jian, Y. Zhou, Y. Luo, Y. Qan, S. Jiang, X. Zhou, Multifunctional nanoparticles for multimodal imaging-guided low-intensity focused ultrasound/immunotherapeutic retinoblastoma therapy, *ACS Appl. Mater. Interfaces*. 12 (5) (2020) 5642–5657, <https://doi.org/10.1021/acsnano.9b22072>.
- [148] X. Hou, X. Wang, R. Liu, H. Zhang, X. Liu, Y. Zhang, Facile synthesis of multifunctional Fe₃O₄@SiO₂@Au magneto-plasmonic nanoparticles for MR/CT dual imaging and photothermal therapy, *RSC Adv.* 7 (31) (2017) 18844–18850, <https://doi.org/10.1039/c7ra00925a>.
- [149] A. Tomitaka, H. Arami, A. Raymond, A. Yndart, A. Kaushik, R.D. Jayant, Y. Takemura, Y. Cai, M. Toborek, M. Nair, Development of magneto-plasmonic nanoparticles for multimodal image-guided therapy to the brain, *Nanoscale*. 9 (2) (2017) 764–773, <https://doi.org/10.1039/c6nr07520g>.
- [150] G. Wang, W. Gao, X. Zhang, X. Mei, Au nanocage functionalized with ultra-small Fe₃O₄ nanoparticles for targeting T1–T2 dual MRI and CT imaging of tumor, *Sci. Rep.* 6 (2016) 28258, <https://doi.org/10.1038/srep28258>.
- [151] A. Tomitaka, S. Ota, K. Nishimoto, H. Arami, Y. Takemura, M. Nair, Dynamic magnetic characterization and magnetic particle imaging enhancement of magnetic-gold core-shell nanoparticles, *Nanoscale*. 11 (13) (2019) 6489–6496, <https://doi.org/10.1039/C9NR00242A>.
- [152] A. Sánchez, K. Ovejero Paredes, J. Ruiz-Cabello, P. Martínez-Ruiz, J.M. Pingarrón, R. Villalonga, M. Filice, Hybrid decorated core/shell janus nanoparticles as a flexible platform for targeted multimodal molecular bioimaging of cancer, *ACS Appl. Mater. Interfaces*. 10 (37) (2018) 31032–31043, <https://doi.org/10.1021/acsnano.8b10452>.
- [153] J. Zhu, Y. Lu, Y. Li, J. Jiang, L. Cheng, Z. Liu, L. Guo, Y. Pan, H. Gu, Synthesis of Au-Fe₃O₄ heterostructured nanoparticles for in vivo computed tomography and magnetic resonance dual model imaging, *Nanoscale*. 6 (1) (2014) 199–202, <https://doi.org/10.1039/c3nr04730j>.
- [154] H.Y. Zhao, S. Liu, J. He, C.C. Pan, H. Li, Z.Y. Zhou, Y. Ding, D. Huo, Y. Hu, Synthesis and application of strawberry-like Fe₃O₄-Au nanoparticles as CT-MR dual-modality contrast agents in accurate detection of the progressive liver disease, *Biomaterials*. 51 (2015) 194–207, <https://doi.org/10.1016/j.biomaterials.2015.02.019>.
- [155] J. Li, L. Zheng, H. Cai, W. Sun, M. Shen, G. Zhang, X. Shi, Facile one-pot synthesis of Fe₃O₄@Au composite nanoparticles for dual-mode MR/CT imaging applications, *ACS Appl. Mater. Interfaces*. 5 (20) (2013) 10357–10366, <https://doi.org/10.1021/am4034526>.
- [156] T. Zhou, B. Wu, D.a. Xing, Bio-modified Fe₃O₄ core/Au shell nanoparticles for targeting and multimodal imaging of cancer cells, *J. Mater. Chem.* 22 (2) (2012) 470–477, <https://doi.org/10.1039/c1jm13692e>.
- [157] Y. Liu, X. Yang, Z. Huang, P. Huang, Y. Zhang, L. Deng, Z. Wang, Z. Zhou, Y.i. Liu, H. Kalish, N.M. Khachab, X. Chen, Z. Nie, Magneto-plasmonic janus vesicles for magnetic field-enhanced photoacoustic and magnetic resonance imaging of tumors, *Angew. Chem. Int. Ed.* 55 (49) (2016) 15297–15300, <https://doi.org/10.1002/anie.201608338>.
- [158] M. Motiei, T. Dreifuss, T. Sadan, N. Omer, T. Blumenfeld-Katzir, E. Fragogeorgi, G. Loudos, R. Popovtzer, N. Ben-Eliezer, Trimodal nanoparticle contrast agent for CT, MRI and SPECT imaging: Synthesis and characterization of radiolabeled core/shell iron oxide@gold nanoparticles, *Chem. Lett.* 48 (3) (2019) 291–294, <https://doi.org/10.1246/cl.180780>.
- [159] J. Li, Y. Hu, J. Yang, P. Wei, W. Sun, M. Shen, G. Zhang, X. Shi, Hyaluronic acid-modified Fe₃O₄ at Au core/shell nanostars for multimodal imaging and photothermal therapy of tumors, *Biomaterials*. 38 (2015) 10–21, <https://doi.org/10.1016/j.biomaterials.2014.10.065>.
- [160] S. Narayanan, B.N. Sathy, U. Mony, M. Koyakutty, S.V. Nair, D. Menon, Biocompatible magnetite/gold nanohybrid contrast agents via green chemistry for MRI and CT bioimaging, *ACS Appl. Mater. Interfaces*. 4 (1) (2012) 251–260, <https://doi.org/10.1021/am201311c>.
- [161] J. Sun, X. Li, A. Chen, W. Cai, X. Peng, L. Li, B. Fan, L. Wang, H. Zhang, R. Zhang, A dual-modality MR/PA imaging contrast agent based on ultrasmall biopolymer nanoparticles for orthotopic hepatocellular carcinoma imaging, *Int. J. Nanomedicine*. 14 (2019) 9893–9904, <https://doi.org/10.2147/IJN.S219794>.
- [162] L.-Y. Bai, X.-Q. Yang, J. An, L. Zhang, K. Zhao, M.-Y. Qin, B.-Y. Fang, C. Li, Y. Xuan, X.-S. Zhang, Y.-D. Zhao, Z.-Y. Ma, Multifunctional magnetic-hollow gold nanospheres for bimodal cancer cell imaging and photothermal therapy, *Nanotechnology*. 26 (31) (2015) 315701, <https://doi.org/10.1088/0957-4484/26/31/315701>.
- [163] G. Brennan, S. Bergamino, M. Pescio, S.A.M. Tofail, C. Silien, The effects of a varied gold shell thickness on iron oxide nanoparticle cores in magnetic manipulation, T1 and T2 MRI contrasting, and magnetic hyperthermia, *Nanomaterials*. 10 (2020) 2424, <https://doi.org/10.3390/nano10122424>.
- [164] K. Richter, M. Haslbeck, J. Buchner, The heat shock response: life on the verge of death, *Mol. Cell*. 40 (2) (2010) 253–266, <https://doi.org/10.1016/j.molcel.2010.10.006>.
- [165] Y. Zhang, X. Zhan, J. Xiong, S. Peng, W. Huang, R. Joshi, Y. Cai, Y. Liu, R. Li, K. Yuan, N. Zhou, W. Min, Temperature-dependent cell death patterns induced by functionalized gold nanoparticle photothermal therapy in melanoma cells, *Sci. Rep.* 8 (2018) 8720, <https://doi.org/10.1038/s41598-018-26978-1>.
- [166] A. Oluwasanmi, M. Malekigorji, S. Jones, A. Curtis, C. Hoskins, Potential of hybrid iron oxide-gold nanoparticles as thermal triggers for pancreatic cancer therapy, *RSC Adv.* 6 (97) (2016) 95044–95054, <https://doi.org/10.1039/c6ra20552f>.
- [167] N.R. Datta, S.G. Ordóñez, U.S. Gaipal, M.M. Paulides, H. Crezee, J. Gellermann, D. Marder, E. Puric, S. Bodis, Local hyperthermia combined with radiotherapy and/or chemotherapy: Recent advances and promises for the future, *Cancer Treat. Rev.* 41 (9) (2015) 742–753, <https://doi.org/10.1016/j.ctrv.2015.05.009>.

- [168] G. Baffou, R. Quidant, Thermo-plasmonics: Using metallic nanostructures as nano-sources of heat, *Laser Photonics Rev.* 7 (2) (2013) 171–187, <https://doi.org/10.1002/lpor.201200003>.
- [169] L.R. Hirsch, R.J. Stafford, J.A. Bankson, S.R. Sershen, B. Rivera, R.E. Price, J.D. Hazle, N.J. Halas, J.L. West, Nanoshell-mediated near-infrared thermal therapy of tumors under magnetic resonance guidance, *Proc. Natl. Acad. Sci. USA* 100 (23) (2003) 13549–13554, <https://doi.org/10.1073/pnas.2232479100>.
- [170] A.R. Rastinehad, H. Anastos, E. Wajswol, J.S. Winoker, J.P. Sfakianos, S.K. Doppalapudi, M.R. Carrick, C.J. Knauer, B. Taouli, S.C. Lewis, A.K. Tewari, J.A. Schwartz, S.E. Canfield, A.K. George, J.L. West, N.J. Halas, Gold nanoshell-localized photothermal ablation of prostate tumors in a clinical pilot device study, *Proc. Natl. Acad. Sci. USA* 116 (37) (2019) 18590–18596, <https://doi.org/10.1073/pnas.1906929116>.
- [171] X. Huang, I.H. El-Sayed, W. Qian, M.A. El-Sayed, Cancer cell imaging and photothermal therapy in the near-infrared region by using gold nanorods, *J. Am. Chem. Soc.* 128 (6) (2006) 2115–2120, <https://doi.org/10.1021/ja057254a>.
- [172] J. Morales-Dalmau, C. Vilches, I. de Miguel, V. Sanz, R. Quidant, Optimum morphology of gold nanorods for light-induced hyperthermia, *Nanoscale* 10 (5) (2018) 2632–2638, <https://doi.org/10.1039/c6ra20552f>.
- [173] Y. Liu, J.R. Ashton, E.J. Moding, H. Yuan, J.K. Register, A.M. Fales, J. Choi, M.J. Whitley, X. Zhao, Y.i. Qi, Y. Ma, G. Vaidyanathan, M.R. Zalutsky, D.G. Kirsch, C. T. Badea, T. Vo-Dinh, A plasmonic gold nanostar theranostic probe for in vivo tumor imaging and photothermal therapy, *Theranostics* 5 (9) (2015) 946–960, <https://doi.org/10.7150/thno.11974>.
- [174] S.E. Skrabalak, J. Chen, Y. Sun, X. Lu, L. Au, C.M. Cobley, Y. Xia, Gold nanocages: synthesis, properties, and applications, *Acc. Chem. Res.* 41 (2008) 1587–1595, <https://doi.org/10.1002/9783527809080.catanz11280>.
- [175] J. Chen, C. Glaus, R. Laforest, Q. Zhang, M. Yang, M. Gidding, M.J. Welch, Y. Xia, Gold nanocages as photothermal transducers for cancer treatment, *Small* 6 (7) (2010) 811–817, <https://doi.org/10.1002/sml.200902216>.
- [176] B. Mehdou, A. Meffre, J. Carrey, S. Lachaize, L.-M. Lacroix, M. Gougeon, B. Chaudret, M. Respaud, Optimal size of nanoparticles for magnetic hyperthermia: A combined theoretical and experimental study, *Adv. Funct. Mater.* 21 (23) (2011) 4573–4581, <https://doi.org/10.1002/adfm.201101243>.
- [177] P. de la Presa, Y. Luengo, M. Multigner, R. Costo, M.P. Morales, G. Rivero, A. Hernando, Study of heating efficiency as a function of concentration, size, and applied field in γ -Fe₂O₃ nanoparticles, *J. Phys. Chem. C* 116 (48) (2012) 25602–25610, <https://doi.org/10.1021/jp310771p>.
- [178] R. Di Corato, A. Espinosa, L. Lartigue, M. Tharaud, S. Chat, T. Pellegrino, C. Ménager, F. Gazeau, C. Wilhelm, Magnetic hyperthermia efficiency in the cellular environment for different nanoparticle designs, *Biomaterials* 35 (2014) 6400–6411, <https://doi.org/10.1016/j.biomaterials.2014.04.036>.
- [179] L. Lartigue, P. Hugounenq, D. Alloeyau, S.P. Clarke, M. Lévy, J.-C. Bacri, R. Bazzi, D.F. Brougham, C. Wilhelm, F. Gazeau, Cooperative organization in iron oxide multi-core nanoparticles potentiates their efficiency as heating mediators and MRI contrast agents, *ACS Nano* 6 (12) (2012) 10935–10949, <https://doi.org/10.1021/nn304477s>.
- [180] E. Bertuit, E. Benassai, G. Méridet, J.-M. Gréneche, B. Baptiste, S. Neveu, C. Wilhelm, A. Abou-Hassan, Structure-property-function relationships of iron oxide multicore nanoflowers in magnetic hyperthermia and photothermal, *ACS Nano* 16 (1) (2022) 271–284, <https://doi.org/10.1021/acsnano.1c06212>.
- [181] A. Espinosa, R. Di Corato, J. Kolosnjaj-Tabi, P. Flaud, T. Pellegrino, C. Wilhelm, Duality of iron oxide nanoparticles in cancer therapy: Amplification of heating efficiency by magnetic hyperthermia and photothermal bimodal treatment, *ACS Nano* 10 (2) (2016) 2436–2446, <https://doi.org/10.1021/acsnano.5b07249>.
- [182] G.C. Lavorato, R. Das, J. Alonso Masa, M.-H. Phan, H. Srikanth, Hybrid magnetic nanoparticles as efficient nanoheaters in biomedical applications, *Nanoscale Adv.* 3 (4) (2021) 867–888, <https://doi.org/10.1039/d0na00828a>.
- [183] A. Espinosa, M. Bugnet, G. Radtke, S. Neveu, G.A. Botton, C. Wilhelm, A. Abou-Hassan, Can magneto-plasmonic nanohybrids efficiently combine photothermal with magnetic hyperthermia?, *Nanoscale* 7 (45) (2015) 18872–18877, <https://doi.org/10.1039/c5nr06168g>.
- [184] X. Ma, Y. Wang, X.-L. Liu, H. Ma, G. Li, Y. Li, F. Gao, M. Peng, H.M. Fan, X.-J. Liang, Fe₃O₄-Pd Janus nanoparticles with amplified dual-mode hyperthermia and enhanced ROS generation for breast cancer treatment, *Nanoscale Horiz.* 4 (6) (2019) 1450–1459, <https://doi.org/10.1039/c9nh00233b>.
- [185] A. Curcio, A.K.A. Silva, S. Cabana, A. Espinosa, B. Baptiste, N. Menguy, C. Wilhelm, A. Abou-Hassan, Iron oxide nanoflowers@CuS hybrids for cancer tri-therapy: Interplay of photothermal therapy, magnetic hyperthermia and photodynamic therapy, *Theranostics* 9 (5) (2019) 1288–1302, <https://doi.org/10.7150/thno.30238>.
- [186] M. Abdulla-Al-Mamun, Y. Kusumoto, T. Zannat, Y. Horie, H. Manaka, Au-ultrathin functionalized core-shell (Fe₃O₄@Au) monodispersed nanocubes for a combination of magnetic/plasmonic photothermal cancer cell killing, *RSC Adv.* 3 (2013) 7816–7827, <https://doi.org/10.1039/c3ra21479f>.
- [187] Z. Abed, J. Beik, S. Laurent, N. Eslahi, T. Khani, E.S. Davani, H. Ghaznavi, A. Shakeri-Zadeh, Iron oxide-gold core-shell nano-theranostic for magnetically targeted photothermal therapy under magnetic resonance imaging guidance, *J. Cancer Res. Clin. Oncol.* 145 (5) (2019) 1213–1219, <https://doi.org/10.1007/s00432-019-02870-x>.
- [188] J. Huang, M. Guo, H. Ke, C. Zong, B. Ren, G. Liu, H.e. Shen, Y. Ma, X. Wang, H. Zhang, Z. Deng, H. Chen, Z. Zhang, Rational design and synthesis of γ -Fe₂O₃@Au magnetic gold nanoflowers for efficient cancer theranostics, *Adv. Mater.* 27 (34) (2015) 5049–5056, <https://doi.org/10.1002/adma.201501942>.
- [189] Z. Li, A. Aranda-Ramos, P. Güell-Grau, J.L. Tajada, L. Pou-Macayo, S. Lope Piedrafita, F. Pi, A.G. Roca, M.D. Baró, J. Sort, C. Nogués, J. Nogués, B. Sepúlveda, Magnetically amplified photothermal therapies and multimodal imaging with magneto-plasmonic nanodomes, *Appl. Mater. Today* 12 (2018) 430–440, <https://doi.org/10.1016/j.apmt.2018.07.008>.
- [190] X. Nan, X. Zhang, Y. Liu, M. Zhou, X. Chen, X. Zhang, Dual-targeted multifunctional nanoparticles for magnetic resonance imaging guided cancer diagnosis and therapy, *ACS Appl. Mater. Interfaces* 9 (11) (2017) 9986–9995, <https://doi.org/10.1021/acsami.6b16486>.
- [191] S. Bhana, G. Lin, L. Wang, H. Starring, S.R. Mishra, G. Liu, X. Huang, Near-infrared-absorbing gold nanopopcorns with iron oxide cluster core for magnetically amplified photothermal and photodynamic cancer therapy, *ACS Appl. Mater. Interfaces* 7 (21) (2015) 11637–11647, <https://doi.org/10.1021/acsami.5b02741>.
- [192] L. León Félix, B. Sanz, V. Sebastián, T.E. Torres, M.H. Sousa, J.A.H. Coaquira, M. R. Ibarra, G.F. Goya, Gold-decorated magnetic nanoparticles design for hyperthermia applications and as a potential platform for their surface-functionalization, *Sci. Rep.* 9 (2019) 4185, <https://doi.org/10.1038/s41598-019-40769-2>.
- [193] Y. Hu, H. Hu, J. Yan, C. Zhang, Y. Li, M. Wang, W. Tan, J. Liu, Y. Pan, Multifunctional porous iron oxide nanoagents for MRI and photothermal/chemo synergistic therapy, *Bioconjugate Chem.* 29 (4) (2018) 1283–1290, <https://doi.org/10.1021/acs.bioconjug.8b00052>.
- [194] A.Y. Lin, J.K. Young, A.V. Nixon, R.A. Drezek, Encapsulated Fe₃O₄/Ag complexed cores in hollow gold nanoshells for enhanced theranostic magnetic resonance imaging and photothermal therapy, *Small* 10 (16) (2014) 3246–3251, <https://doi.org/10.1002/sml.201303593>.
- [195] A. Plan Sanguier, S. Preveral, A. Curcio, A.K.A. Silva, C.T. Lefèvre, D. Pignol, Y. Lalatonne, C. Wilhelm, Targeted thermal therapy with genetically engineered magnetite magnetosomes@RGD: Photothermia is far more efficient than magnetic hyperthermia, *J. Control. Release* 279 (2018) 271–281, <https://doi.org/10.1016/j.jconrel.2018.04.036>.
- [196] A. Hernández-Montoto, M. Gorbe, A. Llopis-Lorente, J.M. Terrés, R. Montes, R. Cao-Milán, B. Díaz de Greñu, M. Alfonso, M. Orzaez, M.D. Marcos, R. Martínez-Máñez, F. Sancenón, A NIR light-triggered drug delivery system using core-shell gold nanostars-mesoporous silica nanoparticles based on multiphoton absorption photo-dissociation of 2-nitrobenzyl PEG, *Chem. Commun.* 55 (61) (2019) 9039–9042, <https://doi.org/10.1039/c9cc04260a>.
- [197] M.M. Yallapu, S.F. Othman, E.T. Curtis, B.K. Gupta, M. Jaggi, S.C. Chauhan, Multi-functional magnetic nanoparticles for magnetic resonance imaging and cancer therapy, *Biomaterials* 32 (7) (2011) 1890–1905, <https://doi.org/10.1016/j.biomaterials.2010.11.028>.
- [198] D. Zhou, L. Ren, Y.C. Li, P. Xu, Y. Gao, G. Zhang, W. Wang, T.E. Mallouk, L. Li, Visible light-driven, magnetically steerable gold/iron oxide nanomotors, *Chem. Commun.* 53 (83) (2017) 11465–11468, <https://doi.org/10.1039/c7cc06327j>.
- [199] Y. Ma, X. Liang, S. Tong, G. Bao, Q. Ren, Z. Dai, Gold nanoshell nanomicelles for potential magnetic resonance imaging, light-triggered drug release, and photothermal therapy, *Adv. Funct. Mater.* 23 (7) (2013) 815–822, <https://doi.org/10.1002/adfm.201201663>.
- [200] Y. Li, U. Dhawan, H.-Y. Wang, X. Liu, H.-H. Ku, M.-T. Tsai, H.-W. Yen, R.-J. Chung, Theranostic iron@gold core-shell nanoparticles for simultaneous hyperthermia-chemotherapy upon photo-stimulation, *Part. Part. Syst. Charact.* 36 (6) (2019) 1800419, <https://doi.org/10.1002/ppsc.201800419>.
- [201] L. Wang, G. Jang, D.K. Ban, V. Sant, J. Seth, S. Kazmi, N. Patel, Q. Yang, J. Lee, W. Janetanakit, S. Wang, B.P. Head, G. Glinisky, R. Lal, Multifunctional stimuli responsive polymer-gated iron and gold-embedded silica nano golf balls: Nanoshuttles for targeted on-demand theranostics, *Bone Res.* 5 (2017) 17051, <https://doi.org/10.1038/boneres.2017.51>.
- [202] J.F. Hainfeld, D.N. Slatkin, T.M. Focella, H.M. Smilowitz, Gold nanoparticles: A new X-ray contrast agent, *Br. J. Radiol.* 79 (939) (2006) 248–253, <https://doi.org/10.1259/bjr/13169882>.
- [203] C. Pe, S.E. Moya, R.F. Ziolo, T. Reese, J. Llop, T. Calvo-ferna, Biodistribution of different sized nanoparticles assessed by positron emission tomography: A general strategy for direct activation of metal oxide nanoparticles, *ACS Nano* (2013) 3498–3505, <https://doi.org/10.1021/nn400450p>.
- [204] Y. Ding, S. Li, G. Nie, Nanotechnological strategies for therapeutic targeting of tumor vasculature, *Nanomedicine* 8 (7) (2013) 1209–1222, <https://doi.org/10.2217/nnm.13.106>.
- [205] N. Khebtsov, L. Dykman, Biodistribution and toxicity of engineered gold nanoparticles: A review of in vitro and in vivo studies, *Chem. Soc. Rev.* 40 (3) (2011) 1647–1671, <https://doi.org/10.1039/c0cs00018c>.
- [206] F. Mazuel, A. Espinosa, G. Radtke, M. Bugnet, S. Neveu, Y. Lalatonne, G.A. Botton, A. Abou-Hassan, C. Wilhelm, Magneto-Thermal Metrics Can Mirror the Long-Term Intracellular Fate of Magneto-Plasmonic Nanohybrids and Reveal the Remarkable Shielding Effect of Gold, *Adv. Funct. Mater.* 27 (9) (2017) 1605997, <https://doi.org/10.1002/adfm.201605997>.
- [207] G. Stepien, M. Moros, M. Pérez-Hernández, M. Monge, L. Gutiérrez, R.M. Fratila, M.d. Ias Heras, S. Menaó Guillén, J.J. Puente Lanzarote, C. Solans, J. Pardo, J.M. de la Fuente, De La Fuente, Effect of surface chemistry and associated protein corona on the long-term biodegradation of iron oxide nanoparticles in Vivo, *ACS Appl. Mater. Interfaces* 10 (5) (2018) 4548–4560, <https://doi.org/10.1021/acsami.7b18648>.

- [208] J. Kolosnjaj-Tabi, L. Lartigue, Y. Javed, N. Luciani, T. Pellegrino, C. Wilhelm, D. Alloyeau, F. Gazeau, Biotransformations of magnetic nanoparticles in the body, *Nano Today*. 11 (3) (2016) 280–284, <https://doi.org/10.1016/j.nantod.2015.10.001>.
- [209] J. Kolosnjaj-Tabi, Y. Javed, L. Lartigue, J. Volatron, D. Elgrabli, I. Marangon, G. Pugliese, B. Caron, A. Figuerola, N. Luciani, T. Pellegrino, D. Alloyeau, F. Gazeau, The one year fate of iron oxide coated gold nanoparticles in mice, *ACS Nano*. 9 (8) (2015) 7925–7939, <https://doi.org/10.1021/acsnano.5b00042>.
- [210] A. Curcio, A.V. de Walle, E. Benassai, A. Serrano, N. Luciani, N. Menguy, B.B. Manshian, A. Sargsian, S. Soenen, A. Espinosa, A. Abou-Hassan, C. Wilhelm, Massive Intracellular Remodeling of CuS Nanomaterials Produces Nontoxic Bioengineered Structures with Preserved Photothermal Potential, *ACS Nano*. 15 (6) (2021) 9782–9795, <https://doi.org/10.1021/acsnano.1c00567>.
- [211] D.L. Miyasato, A.W. Mohamed, C. Zavaleta, A path toward the clinical translation of nano-based imaging contrast agents, *Wiley Interdiscip. Rev. Nanomed. Nanobiotech.* 13 (6) (2021), <https://doi.org/10.1002/wnan.1721>.
- [212] Y. Zheng, X. Zhong, Z. Li, Y. Xia, Successive, seed-mediated growth for the synthesis of single-crystal gold nanospheres with uniform diameters controlled in the range of 5–150 nm, *Part. Part. Syst. Charact.* 31 (2) (2014) 266–273, <https://doi.org/10.1002/ppsc.201300256>.
- [213] C.F.G.C. Geraldes, S. Laurent, Classification and basic properties of contrast agents for magnetic resonance imaging, *Contrast Media Mol. Imaging*. 4 (1) (2009) 1–23, <https://doi.org/10.1002/cmml.265>.
- [214] Magforce: Für Patienten, (n.d.). <https://magforce.com/home>.
- [215] Study of focal ablation of the prostate with NanoTherm® therapy system for intermediate-risk prostate cancer, (n.d.). <https://clinicaltrials.gov/ct2/show/NCT05010759?term=magforce&draw=2&rank=1>.
- [216] Y.-P. Rui, B.o. Liang, F. Hu, J. Xu, Y.-F. Peng, P.-H. Yin, Y. Duan, C. Zhang, H. Gu, Ultra-large-scale production of ultrasmall superparamagnetic iron oxide nanoparticles for T1-weighted MRI, *RSC Adv.* 6 (27) (2016) 22575–22585, <https://doi.org/10.1039/c6ra00347h>.
- [217] S. Ji, C. Miao, H. Liu, L. Feng, X. Yang, H. Guo, A Hydrothermal Synthesis of Fe₃O₄@C Hybrid Nanoparticle and Magnetic Adsorptive Performance to Remove Heavy Metal Ions in Aqueous Solution, *Nanoscale Res. Lett.* 13 (2018) 178, <https://doi.org/10.1186/s11671-018-2580-8>.
- [218] H.J. Kwon, K. Shin, M. Soh, H. Chang, J. Kim, J. Lee, G. Ko, B.H. Kim, D. Kim, T. Hyeon, Large-scale synthesis and medical applications of uniform-sized metal oxide nanoparticles, *Adv. Mater.* 30 (42) (2018) 1704290, <https://doi.org/10.1002/adma.201704290>.
- [219] S. Hua, M.B.C. de Matos, J.M. Metselaar, G. Storm, Current trends and challenges in the clinical translation of nanoparticulate nanomedicines: Pathways for translational development and commercialization, *Front. Pharmacol.* 9 (2018) 790, <https://doi.org/10.3389/fphar.2018.00790>.
- [220] H.L. Hellstern, J. Becker, P. Hald, M. Bremholm, A. Mamakhel, B.B. Iversen, Development of a Dual-Stage Continuous Flow Reactor for Hydrothermal Synthesis of Hybrid Nanoparticles, *Ind. Eng. Chem. Res.* 54 (34) (2015) 8500–8508, <https://doi.org/10.1021/acs.iecr.5b02899>.
- [221] Z. Han, X. Jiang, Microfluidic Synthesis of Functional Nanoparticles, *Nanotechnol. Microfluid.* (2019) 319–345, <https://doi.org/10.1002/9783527818341.ch10>.
- [222] M.O. Besenhard, A.P. LaGrow, S. Famiani, M. Pucciarelli, P. Lettieri, N.T.K. Thanh, A. Gavriilidis, Continuous production of iron oxide nanoparticles: Via fast and economical high temperature synthesis, *React. Chem. Eng.* 5 (8) (2020) 1474–1483, <https://doi.org/10.1039/d0re00078g>.
- [223] A. Paściak, A. Pilch-Wróbel, Ł. Marciniak, P.J. Schuck, A. Bednarkiewicz, Standardization of methodology of light-to-heat conversion efficiency determination for colloidal nanoheaters, *ACS Appl. Mater. Interfaces*. 13 (37) (2021) 44556–44567, <https://doi.org/10.1021/acsami.1c12409>.
- [224] V. Hosseini, M. Mirrahimi, A. Shakeri-Zadeh, F. Koosha, B. Ghalandari, S. Maleki, A. Komeili, S.K. Kamrava, Multimodal cancer cell therapy using Au@Fe₂O₃ core-shell nanoparticles in combination with photo-thermo-radiotherapy, *Photodiagnosis Photodyn. Ther.* 24 (2018) 129–135, <https://doi.org/10.1016/j.pdpdt.2018.08.003>.

Hybrid Magnetic–Plasmonic Nanoparticle Probes for Multimodal Bioimaging

Published as part of *The Journal of Physical Chemistry virtual special issue “Horst Weller Festschrift”*.

Cristina de la Encarnación, Elisa Lenzi, Malou Henriksen-Lacey, Beatriz Molina, Kellie Jenkinson, Ada Herrero, Lorena Colás, Pedro Ramos-Cabrer, Jhoan Toro-Mendoza, Iñaki Orue, Judith Langer, Sara Bals, Dorleta Jimenez de Aberasturi,* and Luis M. Liz-Marzán*

 Cite This: *J. Phys. Chem. C* 2022, 126, 19519–19531

 Read Online

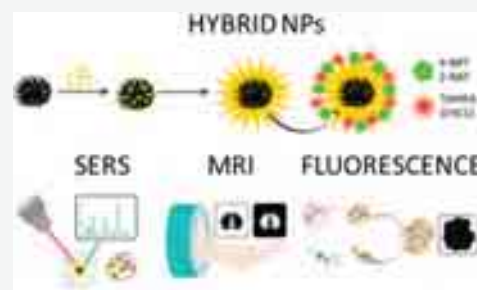
ACCESS |

 Metrics & More

 Article Recommendations

 Supporting Information

ABSTRACT: Multimodal contrast agents, which take advantage of different imaging modalities, have emerged as an interesting approach to overcome the technical limitations of individual techniques. We developed hybrid nanoparticles comprising an iron oxide core and an outer gold spiky layer, stabilized by a biocompatible polymeric shell. The combined magnetic and optical properties of the different components provide the required functionalities for magnetic resonance imaging (MRI), surface-enhanced Raman scattering (SERS), and fluorescence imaging. The fabrication of such hybrid nanoprobe comprised the adsorption of small gold nanoparticles onto premade iron oxide cores, followed by controlled growth of spiky gold shells. The gold layer thickness and branching degree (tip sharpness) can be controlled by modifying both the density of Au nanoparticle seeds on the iron oxide cores and the subsequent nanostar growth conditions. We additionally demonstrated the performance of these hybrid multifunctional nanoparticles as multimodal contrast agents for correlative imaging of *in vitro* cell models and *ex vivo* tissues.



INTRODUCTION

Early disease diagnosis is essential to increasing the chances of successful treatment. In this regard, advances in minimally invasive imaging techniques, from the single cell to the whole-body level, are essential in biomedicine.¹ However, one realistic concern is that a single imaging technique does not provide sufficient information for a precise diagnosis, and thus multimodal imaging techniques should provide advantages over each individual modality on its own.^{2,3}

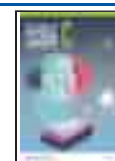
Most bioimaging techniques require the use of molecular or nanoparticulate contrast agents to improve the visualization of detailed features in tissues⁴ or to selectively recognize a specific component of particular relevance to the final diagnosis, for example, regions with inflammation or cancerous cells.⁵ In particular, gold nanoparticles (AuNPs) have shown great potential in the detection, diagnosis, and/or treatment of diseases.^{6–8} AuNPs feature excellent plasmonic properties related to the interaction of their conduction electrons with incident light, yielding localized surface plasmon resonances (LSPRs). Therefore, AuNPs act as antennas for light, driving the amplification of the Raman signal of molecules in close proximity to their surface, a phenomenon known as surface-enhanced Raman scattering (SERS).⁹ The anisotropic and pointed nature of Au nanostars (AuNSs) has been shown to render them excellent Raman enhancers because of the

particularly efficient electromagnetic field enhancement at their tips, which results in intrinsic hot spots. Consequently, AuNSs combined with Raman reporters (RaRs, i.e., molecules of high Raman cross section with well-defined characteristic vibrational fingerprints) have been extensively explored as labels for SERS bioimaging, both *in vitro* and *in vivo*.^{10,11} In terms of clinically relevant imaging techniques, AuNSs have found application in photoacoustic, SERS, and computed tomography (CT) imaging,¹² but the diamagnetic nature of gold does not make it useful for more common nuclear magnetic resonance (NMR)-based techniques, most often used for whole-body imaging in clinical settings. In particular, magnetic resonance imaging (MRI) plays an important role in the clinical diagnosis of many diseases because of its noninvasive nature and excellent safety profile.¹³ Therefore, many attempts have been made toward combining Au with magnetic NPs, namely iron oxide NPs (IONPs), to conduct

Received: September 2, 2022

Revised: October 21, 2022

Published: November 4, 2022



simultaneous imaging by MRI, CT, and SERS, among other modalities.^{14–16}

For example, the combination of MRI and SERS offers the fast operation and deep-tissue penetration of MRI to obtain a global picture of the tissue,¹⁷ combined with the high sensitivity of SERS that allows more detailed structures to be resolved.¹⁸ This multimodal imaging, however, requires the use of multifunctional NPs, which must be synthesized with accurate control over the various synthesis parameters. Most of the studies found in the literature focus on the fabrication of core–shell hybrid NPs comprising a magnetic core encapsulated by an Au-based plasmonic shell. This is partly due to the availability of simple and reliable synthesis methods for IONPs, such as coprecipitation or thermal decomposition,¹⁹ as well as optimized protocols for gold encapsulation.^{20–22} However, anisotropic NPs featuring spikes or edges that can act as hot spots for SERS are preferred for signal enhancement, especially in biological samples where high background values require strong SERS intensities. One such example is the synthesis of magnetic–plasmonic Janus NPs comprising a single magnetic core and a spiky gold region.¹² However, this system is restricted to magnetic cores of ~10–20 nm in diameter and is only partially covered by Au. In this study, we prepared magnetic–plasmonic NPs by growing a spiky gold shell on premade multicore iron oxide nanoflowers. Magnetic iron oxide nanoflowers comprise multiple crystallites and therefore show an improved magnetic response as compared to single-core NPs of similar size. The reason is exchange coupling occurring among individual crystallites in multicore systems due to the short distances between them, thus leading to strong magnetic interaction.²³ The Au surface of the spiky outer shell additionally enables surface functionalization (through thiol chemistry) and acts as an efficient SERS substrate. Additionally, the formation of a complete gold shell around the iron oxide core prevents oxidation and degradation of IONPs in biological environments, which has been shown in previous studies.^{24,25} In this configuration, the magnetic iron oxide core acts as an effective T2 negative contrast agent, whereas the outer gold shell is functionalized with RaRs for SERS and can be subsequently wrapped with biocompatible polymers, labeled (or not) with fluorescent dyes. The plasmonic (SERS) response of these hybrid NPs, which we herein denote IOAuNS, is defined by the morphology of the spiky gold shell, with tip-localized plasmon modes within the first biological transparency window (NIR-I; 650–950 nm), thereby maximizing light penetration depth. We illustrate the multimodal nature of this nanoparticle system through correlative imaging based on the magnetic, plasmonic, and fluorescent properties of IOAuNS in various biological models (2D cell cultures, 3D spheroid models, and *ex situ* brain tissue), thereby highlighting the challenges involved in the characterization of biological models with varying complexity.

METHODS

Materials. Ferric chloride hexahydrate ($\text{FeCl}_3 \cdot 6\text{H}_2\text{O}$, $\geq 98\%$, Sigma-Aldrich), poly(vinylpyrrolidone) (PVP360; Sigma-Aldrich), sodium acetate anhydrous (ReagentPlus, $\geq 99.0\%$, Sigma-Aldrich), ethylene glycol (ReagentPlus, $\geq 99\%$, Sigma-Aldrich), absolute ethanol ($\text{CH}_3\text{CH}_2\text{OH}$, Sigma-Aldrich), hydrogen tetrachloroaurate trihydrate ($\text{HAuCl}_4 \cdot 3\text{H}_2\text{O}$, $\geq 99.9\%$, Sigma-Aldrich), sodium citrate tribasic dihydrate ($\geq 98\%$, Sigma-Aldrich), sodium borohydride (NaBH_4 , ReagentPlus, 99%, Sigma-Aldrich), silver nitrate

(AgNO_3 , $\geq 99\%$, Sigma-Aldrich), L-ascorbic acid (AA, $\geq 99\%$, Sigma-Aldrich), hydrochloric acid solution (HCl, 37 wt%, Panreac), 2-naphthalenethiol (2-NAT, 99%, Sigma-Aldrich), 4-biphenylthiol (4-BPT, 97%, Sigma-Aldrich), chloroform (CHCl_3 , $\geq 99.8\%$, Sigma-Aldrich), HS-PEG-COOH (MW 3000 Da, Iris Biotech), DY633 ($\lambda_{\text{ex}} = 637$ nm, $\lambda_{\text{em}} = 657$ nm, Dyomics), and TAMRA (Molecular Probes, Life Technologies, #A1318, $\lambda_{\text{ex}} = 544$ nm, $\lambda_{\text{em}} = 571$ nm, Fisher Scientific) were prepared and used without further treatment. Milli-Q water was used for all the experiments.

NP Synthesis Methods. Multicore IONP Synthesis. For the preparation of multicore IONPs, a previously reported synthetic procedure was followed.²⁶ Briefly, 0.21 mmol of iron chloride hexahydrate was dissolved in 36.3 mL of ethylene glycol under stirring. Then, 516.6 μmol of PVP360 was slowly added to the solution under vigorous stirring, and the solution was heated (<100 °C). When the reactants were completely dissolved, 5.2 mmol of sodium acetate was added to the solution. The mixture was placed in a Teflon autoclave and heated in a drying oven for 4 h at 200 °C. Finally, the solution was cooled, and the particles were washed twice by centrifugation (9000 rpm, 20 min) with ethanol and one additional wash with Milli-Q water.

AuNP Synthesis (4 nm). For the synthesis of 4 nm Au seeds, a previously reported method was used.²⁷ In brief, 0.6 mL of freshly prepared 0.1 M NaBH_4 solution was quickly added under vigorous stirring to a 20 mL of solution containing 2.5×10^{-4} M HAuCl_4 and 2.5×10^{-4} M sodium citrate. The formation of Au NPs was immediately observed by a color change. The colloidal dispersion was stored at 4 °C and used as seeds within 2–5 h.

AuNP Synthesis (15 nm). For the synthesis of 15 nm Au seeds, 95 mL of 0.5 mM HAuCl_4 was heated under vigorous stirring until boiling and then 5 mL of 34 mM citrate solution was added. After 15 min of boiling, the solution was cooled down and stored at 4 °C.

IOAuNP Synthesis. For the decoration of IONPs with 4 nm AuNPs,²⁸ 5 mL of iron oxide nanoparticles [Fe] = 14 mM (Z-potential: -2 mV) was placed in a 40 mL glass vial and separated using a magnet, followed by removal of the solution and addition of 25 mL of gold nanospheres at the desired concentration (Table S1). The mixture was left under sonication for 30 min and stirred in a vortex mixer for 1.5 h. The product was washed several times with the help of a magnet to ensure complete removal of the gold nanospheres that were not attached to IONPs. The final gold concentration of IOAuNP was analyzed by ICP-MS.

IOAuNS Synthesis. Typically, 10 mL of HAuCl_4 at different concentrations was placed in a 20 mL glass vial. Then HCl was added, and immediately after, a solution containing the IOAuNSs was incorporated as seeds, the concentration of gold being varied as shown in Table S2. Then, AgNO_3 and ascorbic acid were simultaneously and quickly added to the solution. A fast change from brown to blue indicates gold nanostar formation. Subsequently, HS-PEG-COOH was added to stabilize the final particles. The different amounts and concentrations of the reactants used for the fabrication of IOAuNSs are summarized in Table S2. The solution was stored at 4 °C until further use. Because of the magnetic nature of the IOAuNSs, for all the reactions a specially designed stirrer made of poly(lactic acid) (PLA) was 3D-printed and connected to a mechanical stirrer to ensure effective mixing of the reactants (Figure S1).

SERS Encoding of IOAuNSs. The probes were encoded using different Raman-active molecules, following an established protocol based on successive phase transfer.¹⁰ Briefly, 5 mL of IOAuNPs (total concentration of metals [Au + Fe] = 1.5 mM) was placed in a test tube. 2 mL of 4-BPT (10 mM) in chloroform and 16 μ L of HCl were added, and the mixture was stirred for 2 h to enable phase transfer. Finally, the particles located in the organic phase (bottom phase) were recovered and washed twice with chloroform by centrifugation (9000 rpm, 5 min).

PMA Functionalization of IOAuNSs. The dispersion of IOAuNS@4-BPT or IOAuNS@2-NAT was placed in a round-bottom flask, and 100 μ L of 0.05 M dodecylamine-modified polyisobutylene-*alt*-maleic anhydride amphiphilic polymer (PMA) was added and stirred. The solvent was evaporated in a rotary evaporator, and the particles were redispersed in 5 mL of water and 1 mL of NaOH (pH = 12). The particles were washed 3-fold by centrifugation (9000 rpm, 5 min) or until neutralization. The PMA used to wrap the Raman-encoded IOAuNS was prepared following previous reports.^{10,29} PMA comprises polyisobutylene-*alt*-maleic anhydride (hydrophilic backbone) on which 75% of the anhydride rings have been reacted with dodecylamine (hydrophobic chain). The polymer structure is represented in Figure S2.

PMA Functionalization with Fluorescent Dyes. Labeling of NPs with fluorophores was performed on PMA functionalized with TAMRA dye and DY633 dye (see Figure S3). The procedure was conducted as previously reported.³⁰ The excitation and emission spectra of the particles coated with the dye-modified polymer are shown in Figure S4.

NP Characterization. Standard Characterization. All NPs were characterized using TEM, ICP-MS, and UV–vis–NIR. UV–vis–NIR extinction spectra were recorded using an Agilent 8453 UV–vis diode array spectrophotometer, normalizing spectra at 400 nm. ICP-MS analysis was conducted using an ICP-MS Agilent 7500ce to determine the concentration of Au and Fe. Samples containing biological material (cells or spheroids) were digested in aqua regia for 48 h, followed by addition of H₂O₂ and continued heating until a clear and transparent solution was observed. The samples were cooled to RT and subsequently measured. TEM images were collected with a JEOL JEM-1400PLUS transmission electron microscope operating at 120 kV using carbon-coated 400 square mesh Cu grids.

Z-Sizer Measurements. A Malvern Zetasizer 3000 HS particle size analyzer (Malvern Instruments, UK) was used to measure zeta-potential and dynamic light scattering (DLS), from which hydrodynamic diameter distributions were obtained. Samples were placed in disposable cuvettes of 1 cm optical path length using a diluted (1:100) NP solution, using distilled water as solvent. The width of the DLS hydrodynamic diameter distribution is characterized by the polydispersity index (PDI). In the case of a monomodal distribution (Gaussian) calculated by means of cumulant analysis, $PDI = (\sigma/Z_{avg})^2$, where σ is the width of the distribution and Z_{avg} the average diameter of the particle's population.

Electron Tomography. IOAuNSs were diluted in water to a final concentration of 0.05 mM and drop-cast on a carbon-coated 400 square mesh Cu grid. The samples were then left to dry at ambient temperature. TEM images were acquired using an aberration-corrected “cubed” Thermo Fisher Scientific-Titan electron microscope operated at an acceleration voltage

of 300 kV, with a camera length of 58–105 mm. Atomic resolution scanning TEM (STEM) and high angular annular dark field (HAADF) images were acquired using a convergence angle of 20 mrad. Tomography tilt series were acquired using a Fischione 2020 tomography holder over $\pm 76^\circ$ with tilt increments of 2° . Typically, each angle consisted of a $1k \times 1k$ STEM HAADF image using 12 ms dwell time. The images acquired manually at each angle were aligned with respect to each other, and the tomogram's rotation axis was determined with mathematical precision through phase correlation. Finally, the 3D reconstruction was achieved using 25 SIRT cycles. A bandwidth limit was also applied to the SIRT reconstruction in real and Fourier space to achieve a high-quality reconstruction with minimized missing wedge artifacts.

STEM EELS Imaging. The Fe oxidation state was determined by electron energy loss spectroscopy (EELS) using an aberration-corrected “cubed” FEI-Titan electron microscope operated at an acceleration voltage of 200 kV. Lower acceleration voltages were tried; however, this led to significant cupping artifacts. The energy resolution provided by the electron monochromator as measured from the full width at half-maximum of acquired zero-loss peaks was 0.2 eV, the dispersion of the spectrometer was set to 0.01 eV/channel, and 2000 channels are used to cover an energy range from 704 to 724 eV, being the entire Fe L_{2,3} edge. The pixel size equals 1.8 nm (65 \times 65 pixels) for higher magnification single-particle EELS mapping, which is sufficient to distinguish any variation in oxidation state throughout the nanoflower's substructure. Lower magnification EELS maps with a pixel size of 20 nm² was used to determine oxidation state variation within different nanoflowers from both samples.

Surface Area Measurement. To extract the accessible and external Au surface area relevant for further functionalization, Fe and Au phases were identified by a manual segmentation process using Amira software. As the Au surface contained voids and areas of exposed Fe₂O₃ core, the total Fe surface could not be directly subtracted from the total surface (internal and external Au surface) of Au. Rather, the Fe surface in contact with Au must be calculated first, so that accurate accessible Au surface areas could be derived. Using a surface generation module, boundary surfaces can be extracted and later removed for a final Au surface area.

SERS. Characterization of the SERS signal of IOAuNS@4-BPT and IOAuNS@2-NAT was performed with a Raman microscope (inVia Reflex, Renishaw, Wotton-under-Edge, U.K.) equipped with a -60° C Peltier-cooled front-illuminated CCD detector (1024 \times 512 pixel² chip), using a 785 nm laser excitation source (maximum output 270 mW) and a 1200 lines/mm diffraction grating. For the experiments 300 μ L of each aqueous solutions was placed in a glass vial. SERS spectra were collected using a 10 \times objective (NA = 0.25; Leica Microsystems, Wetzlar, Germany) in expanded scan mode, with an integration time of 10 s and at a laser power of 52.5 mW. All the spectra were analyzed using the WiRE4.4 software (Renishaw, Wotton-under Edge, U.K.) to eliminate cosmic rays, and the correction of the baseline in the spectra was performed on Matlab, using the Beads function.

Magnetism. ZFC/FC measurements were performed at 100 Oe and within a temperature range of 5–300 K, using a Quantum Design MPMS3 VSM-SQUID magnetometer with a sensitivity of 10^{-8} emu up to a maximum field of 7 T. The hysteresis loops were measured in a vibrating sample

magnetometer (VSM) with a sensitivity of 5×10^{-6} emu, up to a maximum field of 18 kOe working at room temperature.

Cell Culture. MCF7 cells were purchased from the ATCC. Human dermal fibroblasts (HDF), fetal bovine serum (FBS), penicillin–streptomycin (PS), DMEM, lactate dehydrogenase (LDH) assay, and NucBlue were purchased from Invitrogen. Propidium iodide (PI) was purchased from Sigma. MCF7 and HDF cells were grown in DMEM supplemented with 10% FBS and 1% PS (herein termed complete DMEM, cDMEM).

IOAuNS Cytotoxicity Tests. The cytotoxicity of IOAuNSs in MCF7 cells was evaluated using the LDH assay and PI staining. Cells were seeded at 1.6×10^5 cells/cm² in 96-well plates to analyze the cytotoxicity by LDH assay and at 9×10^4 cells/cm² in 96-well imaging plates (Ibidi) for characterization by microscopy. The following day, IOAuNS were added at concentrations ranging from 0.25 to 0.031 mM (total metal ion concentration). After 24 h, the NP solution was removed and rinsed with media. The media was renewed again 6 h later to remove IOAuNSs in suspension and on the bottom of the plate. The presence of aggregated NPs was monitored daily by optical microscopy. The LDH test was performed using the standard protocol 48 h post addition of IOAuNSs. For analysis via imaging, PI was added to a final concentration of 500 nM, and nuclei were stained using NucBlue. Images of 1×1.3 mm² were acquired with a Cell Observer microscope (Axio Observer, Zeiss) 48 h after the addition of IOAuNSs. Postprocessing and quantification of cells were conducted with ImageJ, and data were represented as a percentage of dead cells.

Spheroids Formation. Spheroids were formed from cells, with and without preincubation steps with IOAuNSs. In the case of spheroids that were exposed to IOAuNS post formation, MCF7 and HDF cells were mixed in a 1:1 ratio using a final cell number of 1.7×10^4 cells/spheroid (μ -shaped plate growth method) and left for 3 days to form the spheroid. A 25 μ L dispersion of IOAuNSs (1:1 mixture of IOAuNS@4-BPT@TAMRA and IOAuNS@2-NAT@DY633, final ion concentration 0.05 mM) in cDMEM was made in a 500 μ L Eppendorf and ca. 5 spheroids added. Using a rotisserie rotator placed in an incubator at 37 °C, 5% CO₂, spheroids were rotated during 24 h to help achieve an even distribution of IOAuNSs around spheroids. Spheroids were subsequently retrieved and used for imaging studies or fixed using 4% formaldehyde for later imaging and embedding in OCT freezing media.

For spheroids exposed to IOAuNSs pre-formation, MCF7 and HDF cells were seeded in 12-well plates (8×10^4 MCF and 6×10^4 HDF cells/mL) and once adhered, IOAuNS@4-BPT@TAMRA and IOAuNS@2-NAT@DY633 were added to MCF7 and HDF cells, respectively, at a final concentration of 0.05 mM. After 24 h, non-endocytosed IOAuNSs were removed via washing, and cells detached using trypsin-EDTA. Cells were readjusted to 8.6×10^4 cells/mL and mixed in a 1:1 ratio. Cells (1.7×10^4 cells, 200 μ L) were added to μ -shaped 96-well plates and incubated at 37 °C, 5% CO₂ for 3 days for spheroid formation to occur. Spheroids were subsequently retrieved and used for imaging studies or fixed using 4% formaldehyde for later imaging and embedding in OCT freezing media.

Multimodal Imaging. Cell Preparation. 2D SERS mapping was conducted using MCF7 cells preincubated with IOAuNSs from series a, b, and c. In brief, MCF7 cells were seeded at 2.8×10^4 cells/cm² in 12-well plates and allowed to

adhere. The following day, IOAuNSs diluted in cDMEM were added (0.05 mM final total ion concentration), and after 24 h, non-endocytosed IOAuNSs were removed and cells detached using trypsin–EDTA. For SERS imaging, cells were seeded in 35 mm glass-bottomed dishes (5×10^4 cells/dish), and after 2–3 h of incubation, SERS mapping was undertaken using the settings described below. For MRI, a volume containing 2×10^5 cells was centrifuged and resuspended to 400 μ L of PBS. Subsequently, 100 μ L (containing 5×10^4 cells) was dispersed into each well of the phantom for MRI imaging. For ICP measurements, a volume of cell solution containing 5×10^4 cells was centrifuged, concentrated in 50 μ L of PBS, and frozen at –20 °C. To promote cell lysis, three freeze–thaw cycles were performed. The samples were subsequently digested using aqua regia, aided by microwave digestion (Table S3). For fluorescence confocal imaging, 1.3×10^4 cells (1:1 mixture of HDF and MCF7 cells previously exposed to IOAuNS@4-BPT@TAMRA and IOAuNS@2-NAT@DY633, respectively) were seeded in 35 mm glass-bottomed dishes with a 500 μ m etched grid (Ibidi) and allowed to adhere. The following day media was removed, and samples were fixed and permeabilized using 4% formaldehyde and Triton X-100. Immunostaining to identify MCF7 and HDF cells was performed using antibodies against E-cadherin and TE7 (both Novusbio), respectively. Appropriate matching secondary antibodies with AlexaFluor 405 and 633 fluorescent labels were used at a 1/400 dilution. Samples were stored in PBS at 4 °C until imaged.

SERS Imaging of Cells. SERS measurements were performed with a Raman microscope (inVia Reflex, Renishaw, Wotton-under-Edge, U.K.) equipped with a –60 °C Peltier-cooled front-illuminated CCD detector (1024×512 pixel²), using a 785 nm laser excitation source (maximum output 270 mW) and a 1200 lines/mm diffraction grating. SERS maps were recorded in static mode (centered of scattered wavenumber 1450 cm⁻¹) using a 40 \times dip-in water immersion objective (numerical aperture, NA = 0.8; Nikon Corporation, Tokyo, Japan). For single cell measurements, areas of ca. 30 \times 30 μ m² containing one single cell, were imaged with 0.5 s integration time, at 12.08 mW laser power at the surface and a step size of 2 μ m. All spectra were first analyzed using the WiRE 4.4 software (Renishaw, Wotton-under Edge, U.K.) to correct the baseline in the spectra (intelligent 11th polynomial order) and eliminate cosmic rays. Then, the maps were analyzed with a MLRA-based supervised algorithm developed in a previous work,³² to represent in the cellular images only the spectra similar to the SERS signal of the corresponding nanoparticles.

SERS Imaging of Spheroids. SERS mapping of spheroids involved placing individual spheroids inside a homemade holder³¹ on top of a small drop of dental glue to fix the spheroid position.

SERS mapping along xz was performed in a Renishaw Raman microscope (inVia Reflex, Renishaw, Wotton-under-Edge, U.K.). An area of 800×430 μ m² was imaged with 0.7 s integration time, 12.08 mW laser power at the surface, and a step size of 6 and 10 μ m in x and z directions, respectively.

Additional SERS measurements of the spheroids were performed with a WITec confocal Raman microscope (Alpha300R, WITec GmbH, Ulm, Germany) equipped with a –60 °C Peltier-cooled CCD detector (1024×128 pixel² chip), using a 785 nm laser excitation source (maximum output 83 mW) and a 300 lines/mm diffraction grating. The center of scattered wavenumber was set to 1450 cm⁻¹, and the

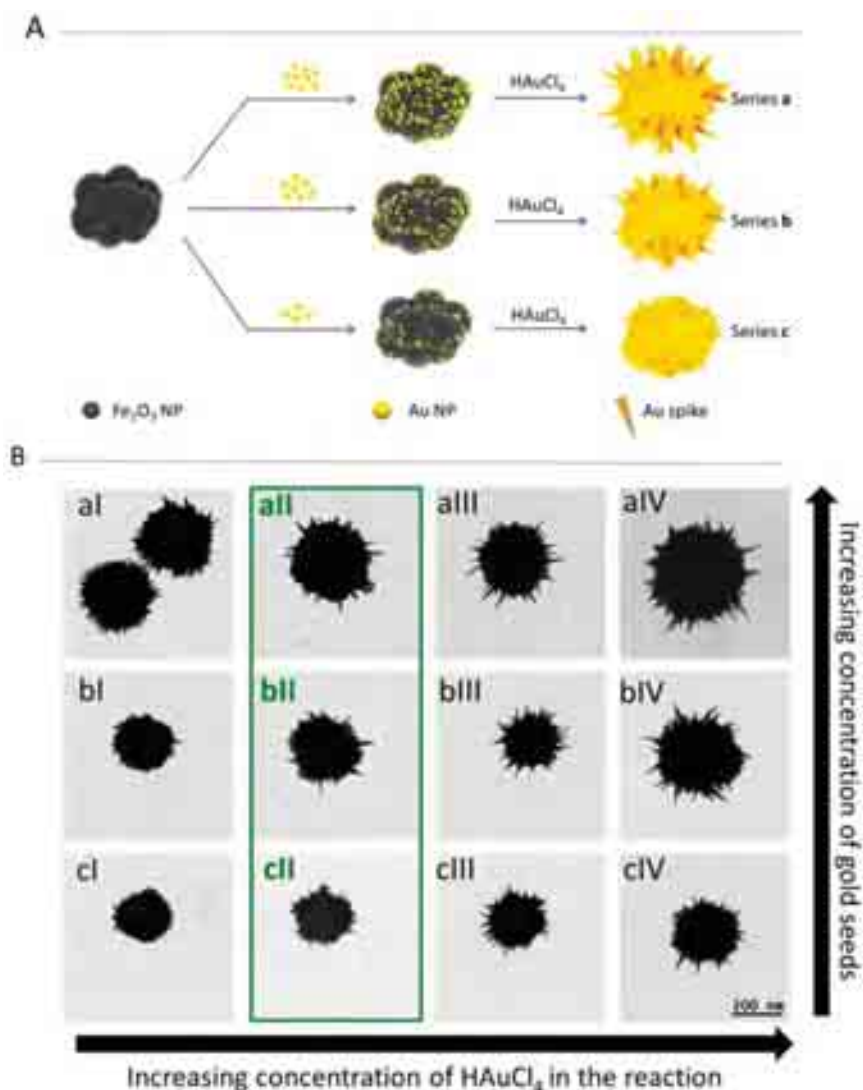


Figure 1. (A) Scheme of the various steps involved in the synthesis of IOAuNS, comprising the addition of varying amounts of AuNPs onto IONPs and subsequent reduction of HAuCl_4 to obtain different spiky shell structures. (B) TEM images of IOAuNS obtained from series a–c (increasing AuNP coverage) and I–IV (increasing added HAuCl_4). Series II (highlighted in a green box) was selected for further experiments. All the images are at the same magnification. Additional low-magnification TEM images are provided in Figure S9. The $[\text{Au}]/[\text{Fe}]$ molar ratios, measured by ICP-MS, are aI = 3.6, aII = 2.7, aIII = 2.6, aIV = 0.97, bI = 1.7, bII = 1.2, bIII = 1.0, bIV = 0.2, cI = 0.58, cII = 0.35, cIII = 0.25, and cIV = 0.13.

signal was recorded using a N-achroplan 20 \times dip-in water immersion objective (NA = 0.5; Zeiss, Jena, Germany). For the measurement of the outer edge of a live spheroid, a volume of $84 \times 84 \times 70 \mu\text{m}^3$ was imaged with a 5 mW laser power, 0.01 s integration time, and step sizes of $2 \mu\text{m}$ in xy and $5 \mu\text{m}$ in z directions. For the transversal cut, an area of $360 \times 560 \mu\text{m}^2$ was imaged with a 10 mW laser power, 0.1 s integration time, and a step size of $5 \mu\text{m}$. For postincubated spheroids a volume of $400 \times 380 \times 150 \mu\text{m}^3$ containing a quarter of the spheroid was imaged with a 10 mW laser power, 0.1 s integration time, and step sizes of $5 \mu\text{m}$ in xy and $10 \mu\text{m}$ in z . For the measurement of the spheroid slice, an area of $635 \times 875 \mu\text{m}^2$ was imaged with a 10 mW laser power, 0.1 s integration time, and a step size of $5 \mu\text{m}$. Prior to data analysis, SERS spectra were pretreated by cosmic ray removal and background subtraction (Shape 100), both implemented in the Project FIVE plus software (WITec, Um, Germany). To identify the known Raman reporter spectrum, the TrueCom-

ponent tool, also embedded in the same software package, was applied.

Ex Vivo Sample Preparation. A mouse brain was extracted from a cadaveric specimen provided by our animal facility (no animals were expressly used for this study) and casted in a Falcon tube with 15 mL of agarose solution (1.6% w/v). Then, $5 \mu\text{L}$ of IOAuNS@2-NAT@DY633, cells incubated with IOAuNS@2-NAT@DY633, and PBS were injected in the tissue with the help of a stereotaxic frame and a Hamilton syringe. After MRI imaging studies, the brain was extracted from the agarose, and then it was immersed in 10% formalin overnight and subsequently in sucrose (30% in PBS solution) for 2 days for fixation and cryopreservation of the tissue. Finally, the brain was frozen and kept at -80°C until posterior use.

SERS Imaging of Brain Slices. SERS imaging of brain histology slices was performed on top of a quartz slide. SERS measurements were performed with a confocal Raman

microscope (Alpha300R, WITec GmbH, Ulm, Germany) equipped with a -60 °C Peltier-cooled CCD detector (1024×128 pixel² chip), using a 785 nm laser excitation source (maximum output 83 mW) and a 300 lines/mm diffraction grating. The center of scattered wavenumber was set to 1450 cm⁻¹, and the signal was recorded using a 20 \times objective (NA = 0.4; Nikon Corporation, Tokyo, Japan). For SERS measurements of brain samples, two areas of 680×250 and 350×350 μm^2 were imaged with a 5 mW laser power, 0.05 s integration time, and step size of 3 μm . Prior to data analysis, SERS spectra were pretreated by cosmic ray removal and background subtraction (Shape 100), both implemented in the Project FIVE plus software (WITec, Um, Germany). To identify the known Raman reporter spectrum, the TrueComponent tool, also embedded in the same software package, was applied.

Confocal Fluorescence Microscopy. Fluorescence images of biological samples were obtained with a Zeiss 880 confocal microscope. To image whole spheroids, the sample was immobilized in a 0.5 cm silicon well printed on a coverslip (total volume ca. 50 μL), with a 1 cm circular glass coverslip placed on top to avoid evaporation. TAMRA- and Dy633-containing IOAuNSs were imaged using 561 and 633 nm laser sources, with detectors set to ca. 595 ± 25 and 680 ± 25 nm, respectively. A Plan-apochromat $\times 10$ objective (NA = 0.45, Zeiss) was used to obtain z-stacks of ca. 200 μm . A 3-pixel mean filter was applied prior to obtaining maximum intensity projections (MIP). 2D images of cocultured HDF and MCF7 cells, preincubated with IOAuNS@4-BPT@TAMRA and IOAuNS@2-NAT@DY633, respectively, were also obtained using a Plan-apochromat $\times 20$ objective (NA = 0.8, Zeiss) and 405, 488, 561, and 633 nm laser excitation sources. For brain imaging, slices were cut using a cryotome and collected on quartz slides. A Plan-apochromat $\times 10$ objective (NA = 0.45, Zeiss) was used with 633 nm excitation. The tile feature of the ZEN software was used to produce an overview of the whole brain slice.

MRI Phantom Imaging. Agar was dissolved in hot water (15 mL, 1.6% w/v), placed in a plastic mold, and left to solidify at room temperature. Once hardened, 32 wells of 2 mm diameter were drilled in the gel. To have a perfectly flat bottom in each well, 20 μL of 0.4% agar solution was pipetted into the base of each well and left to solidify. Then, 50 μL of the desired sample was deposited in each well and completely covered with 0.9% agar solution. A scheme of the phantoms containing the distribution of the holes and the concentrations of the samples is shown for cells in Figure S5A and for spheroids in Figure S5B.

MRI Imaging of Brain Slices. The brain images were performed in a 11.7 T horizontal bore Bruker Biospec 117/16 USR scanner (Bruker Biospin, Ettlingen, Germany).

Biological TEM. Cells and spheroids were prepared for TEM imaging by first fixing the sample with 2% formaldehyde/2.5% glutaraldehyde in Sorensen's buffer, followed by OsO₄ fixation/staining and dehydration in an ethanol series. Finally, samples were embedded in Spurr's resin, followed by cutting 100 nm thick slices using an ultramicrotome.

RESULTS AND DISCUSSION

Synthesis of Magnetic–Plasmonic Nanoparticles.

Multicore iron oxide nanoparticles (IONPs) were prepared by means of a polyol-mediated solvothermal synthesis approach,²⁶ with slight modifications. Briefly, iron(III) chloride was dissolved in ethylene glycol, a short-chain polyol, followed

by addition of poly(vinylpyrrolidone) (PVP; MW 360 kDa) as a capping agent. Next, sodium acetate (NaAc) was incorporated to the reaction mixture to promote the hydrolysis of Fe³⁺ ions, thereby controlling both nucleation and the final particle morphology. As can be observed in Figure S6A, this process results in the formation of maghemite ($\gamma\text{-Fe}_2\text{O}_3$) IONPs, composed of multiple 5 nm crystallites adding up to a final average diameter of 119 ± 25 nm, as measured by transmission electron microscopy (TEM). From prior literature, we expect the synthesized IONPs to provide our system with the appropriate magnetic properties for use as T2 contrast agents.³²

The coating of IONPs with a spiky Au shell comprised two synthetic steps. IONPs were first decorated by addition of premade AuNP seeds, which spontaneously adsorb on the IONP surface and subsequently act as nucleation points for growth and branching into the final Au shell. A scheme of the synthetic process of each step is shown in Figure 1A. We investigated the use of AuNPs with diameters of 4 and 15 nm as seeds (Figure S6B), synthesized using previously described methods.^{27,33} Whereas uniform surface adsorption was observed for both NP types (Figure S6C), a higher density of adsorbed NPs was achieved using 4 nm AuNPs, leading to a better control over shell growth. We thus proceeded with this sample to optimize the density of AuNPs on the IONP surface for subsequent spike growth. By increasing the relative concentration of AuNPs with respect to that of IONPs, surface coverage was gradually increased (Figure S7). However, conventional 2D TEM imaging is insufficient to accurately determine the density of AuNPs at the IONPs surface, and therefore electron tomography was applied (Figure S8A,B). In the final step, the growth of sharp tips was promoted by seeded growth on the iron oxide-supported Au seeds by adapting a reported procedure for surfactant-free AuNS.³⁰ Electron tomography was used to reveal the 3D configuration of the shell and the sharp tips therein (Figure S8C). The branching degree of the resulting IOAuNSs could be finely tuned by gradually varying the amount of HAuCl₄ added in the final growth step (Figures 1 and S9). To summarize, IOAuNSs with smaller overall diameters were obtained from iron oxide cores with a lower density of AuNPs (series a–c in Figure 1B). Additionally, longer spikes and hence overall larger IOAuNSs were grown when increasing the amount of HAuCl₄ added in the growth step (sequence I–IV in Figure 1B). The inorganic core–shell size of IOAuNS was carefully evaluated from TEM images (Table S4 and Figure S10).

Electron Microscopy Analysis. To obtain quantitative information about the thickness and structure of gold shells (e.g., number of spikes) covering the iron oxide cores, a detailed characterization by electron microscopy and electron tomography was carried out. Such an analysis is important to evaluate the surface area for each IOAuNS sample, which is in turn needed toward optimization of further coating and functionalization steps. For all experiments, IOAuNS series II was chosen because it yields smaller IOAuNS, while maintaining the presence of well-defined spikes (Table S4). Additionally, electron tomography experiments are facilitated by minimizing artifacts that may appear at relatively large thickness. As shown in Figure 1B, for a fixed amount of added HAuCl₄, thicker gold shells are obtained when increasing the initial coverage of IONP cores with AuNPs. Representative 3D visualizations of the structures retrieved by high-angle annular

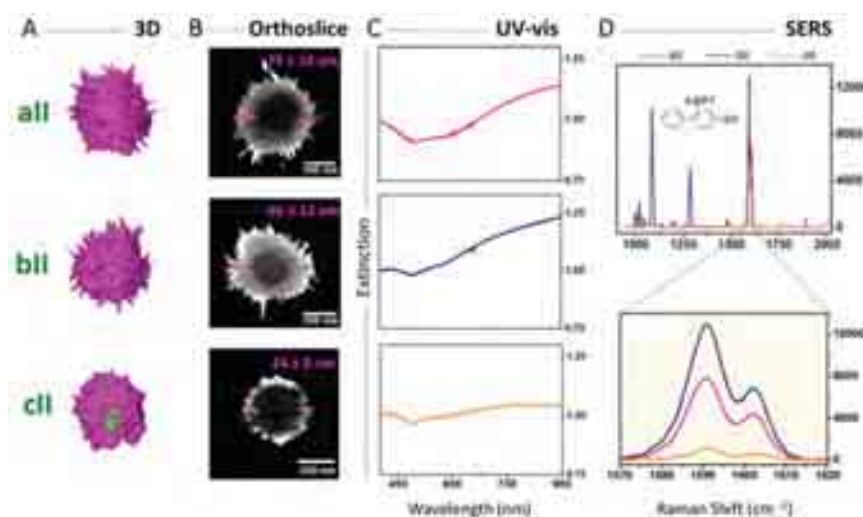


Figure 2. (A) Representative 3D visualizations of electron tomography reconstructions corresponding to particles aII, bII, and cII. (B) Orthoslices through the 3D electron tomography reconstructions shown in (A). The double-head arrows indicate the thickness of the gold shells. (C) Normalized (at 400 nm) UV–vis–NIR spectra for the different samples in IOAuNS@4-BPT series II. (D) SERS spectra from IOAuNS@4-BPT series II. Spectra were measured in aqueous dispersion at the same iron concentration, $[\text{Fe}] = 0.1 \text{ mM}$.

dark field (HAADF) electron tomography are shown in Figure 2. Our results showed complete gold shell formation for samples aII and bII, but defects were observed for cII (Figure 2A). Careful inspection of orthoslices through 3D reconstructed data sets yielded the average gold shell thickness for samples aII ($75 \pm 15 \text{ nm}$), bII ($66 \pm 12 \text{ nm}$), and cII ($24 \pm 5 \text{ nm}$), as illustrated in Figure 2B.

Electron tomography results additionally provide reliable values of the IOAuNS surface area, which are required for further surface functionalization. Using a manual segmentation process and a surface generation module, boundary surfaces were extracted for Au surface area determination (see details in the Methods section and surface area values in Figure S11). Interestingly, the experimental values were in agreement with a geometrical model, based on a hexagonal arrangement of spikes with randomly assigned lengths (see more details on the model in the Supporting Information).

Magnetic Properties. We recorded zero-field cooled (ZFC) and field cooled (FC) magnetization curves, as well as magnetic hysteresis loops, to characterize the magnetic response from the iron oxide cores.³⁴ The Fe_2O_3 composition of the cores was first confirmed by electron energy loss spectroscopy (EELS), using IOAuNS bII as a representative sample (Figure S12A,B). To test for potential further oxidation over time, which would affect the magnetic properties, hysteresis loops were recorded for both freshly prepared and aged (6 months postsynthesis) IONPs. A saturation magnetization of $50 \text{ A}\cdot\text{m}^2/\text{kg}$ was measured in both cases (Figure S12C), which is slightly lower than the saturation magnetization of bulk maghemite ($74 \text{ A}\cdot\text{m}^2/\text{kg}$),³⁵ likely due to surface disorder effects on Fe_2O_3 nanoflowers.³⁶ Additionally, comparison of ZFC/FC curves for IONP and IOAuNSs indicated no significant changes in the magnetic properties at constant magnetic field (Figure S12D), suggesting that the presence of the Au shell has not effect on the magnetic properties of the iron oxide cores, in agreement with previous reports.¹² Taken together, these results confirm a maghemite phase of IONPs with only negligible traces of the Verwey transition³⁷ and a near-superparamagnetic behavior characterized by low remanence and coercivity.

SERS Encoding. It is well-known that AuNPs can be readily functionalized with thiolated molecules due to the stability of thiol–metal bonding. We therefore selected two standard thiolated Raman-active reporter molecules, namely 4-biphenylthiol (4-BPT) and 2-naphthalenethiol (2-NAT), for surface functionalization and encoding of IOAuNS, required for subsequent SERS imaging. RaR adsorption onto IOAuNSs was promoted by using a previously reported phase-transfer method,³⁸ in which the nanoparticles are transferred into an organic solvent containing the Raman reporter and subsequently coated with PMA, thereby resulting in the SERS-encoded IOAuNS versions: IOAuNS@4-BPT and IOAuNS@2-NAT. The addition of an external PMA layer renders IOAuNSs hydrophilic, thus allowing their redispersion in water for further use in biological environments. Raman shifts for the most prominent vibrations in 4-BPT and 2-NAT are listed in Table S5. A complete analysis of the average hydrodynamic diameter of the encoded IOAuNSs is shown in Table S4 and Figure S10.

All IOAuNS samples were successfully encoded with Raman reporter molecules; UV–vis–NIR and SERS spectra for the complete series (a–c and I–IV) are shown in Figure S13. Taking into account morphology considerations (see above), IOAuNS@4-BPT series II were studied in detail. SERS measurements were performed by fixing the NP concentrations, based on iron content ($[\text{Fe}] = 0.1 \text{ mM}$), as opposed to gold, so that we could study the role of the gold shell thickness and morphology on SERS intensity. Considering that biological tissues are particularly transparent at wavelengths between 650 and 950 nm (first biological window, BW-I) and that IOAuNS were selected to display LSPR within the NIR range, a 785 nm laser was used for all SERS measurements. All of the studied IOAuNSs display a significant absorbance within the BW-I, as shown in Figure 2C. At the excitation laser wavelength of 785 nm, a higher SERS intensity was recorded for 4-BPT in IOAuNS bII (Figure 2D). It has been widely reported that the presence of well-defined spikes within the structure of Au NPs can strongly contribute to the enhancement of the Raman signal of adsorbed molecules, acting as intrinsic hot spots. In this regard, the significantly lower SERS

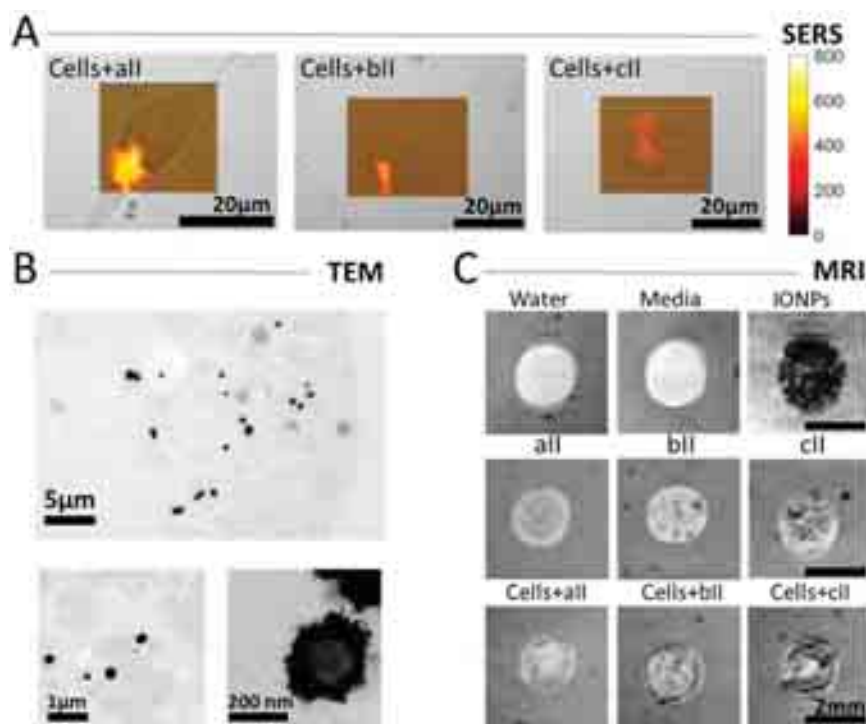


Figure 3. (A) Bright-field images, with overlaid SERS maps, of MCF7 cells preloaded with IOAuNS@4-BPT from series II. (B) Representative TEM images of IOAuNS@4-BPT bII internalized inside cells. Additional images are provided in Figures S12 and S13. (C) MRI images of agarose phantoms containing series II IOAuNS, both alone and incubated with cells, as labeled.

intensity recorded for particles cII is likely due to the less defined and more polydisperse spikes, as reflected by a broader LSPR band.³⁹

Multimodal Cell Imaging. The use of nanoparticles as contrast agents in any biological application requires biocompatibility, stability, and, in most cases, efficient cellular uptake. We verified the uptake of IOAuNS by conducting SERS mapping of MCF7 cells after incubation with IOAuNS@4-BPT. The results are summarized in Figures 3A and S14, confirming the colocalization of IOAuNS with MCF7 cells. Additional high-resolution 3D SERS maps of MCF7 cells incubated with IOAuNS@4-BPT-bII were also conducted to better determine their spatial distribution within a single cell (Figure S15). As the 2D image and the 3D reconstruction from confocal Raman microscopy indicate, IOAuNS@4-BPT seems to be organized inside vesicles, suggestive of endosomes, throughout the volume of the cell. Similar conclusions could be made from TEM imaging of resin-embedded MCF7 cells (Figures 3B and S16). Importantly, no sign of cytotoxicity was observed, which was confirmed by exposing MCF7 cells to different concentrations of IOAuNS@4-BPT-bII for 24 h, followed by cytotoxicity analysis using the commercial lactate dehydrogenase (LDH) assay and membrane permeability staining (Figure S17). These results suggest successful cellular uptake and confirm the biocompatible nature of IOAuNS, which are thus suitable contrast agents for SERS imaging. Additionally, NPs coated with PMA have been proven to be compatible with a wide variety of cell lines.¹⁰

We proceeded next to analyze the use of the same hybrid NPs as T2 contrast agents for MRI. As the iron oxide core size plays a major role in these experiments, IOAuNS concentrations were adjusted based on the total (Fe + Au) metal concentration. Compared to SERS imaging, a lower IOAuNS

concentration was chosen (0.05 mM) because of the increased sensitivity of the technique at these settings. Phantoms were prepared by using an agarose block (40 mm diameter), in which holes (2 mm diameter) were carefully drilled, wherein cells preincubated with IOAuNSs were subsequently placed. Each agarose phantom contained a sufficient number of holes to accommodate also appropriate controls, including cell media, water, IONP, and IOAuNS. As can be observed in Figure 3C, dark contrast (typical for T2 contrast agents) appeared only in those samples containing IONP and IOAuNS, with or without cells. As expected, higher concentrations of Fe in IOAuNS ($c > b > a$) resulted in higher contrast (see also Figure S18). It should however be considered that differences in contrast may also be related to thinner or incomplete gold shells, as observed along the various series (see Figure 2B), which may allow water to come into closer contact with the iron oxide core.⁴⁰ More concentrated and darker contrast was observed in the MRI images of MCF7 cells with internalized IOAuNSs, most likely due to NP aggregation within endosomes.^{41,42} MRI images of the respective samples from the IOAuNS series I–IV are shown in Figure S18.

Multimodal Imaging in Cell Spheroids. We next tested the activity of IOAuNS as contrast agents for multimodal imaging in a 3D spheroid cell model. Spheroids constitute an excellent and accessible alternative model to more traditional 2D cell culture studies, as they better represent the complex 3D environment occurring *in vivo*, often incorporating mixed cell types and gradients in nutrients and waste products.⁴³ Furthermore, the complications involved in NP delivery due to the presence of an extracellular matrix (ECM) or poor NP penetration are better mimicked in spheroids compared to 2D cell experiments.⁴⁴ We thus explored the use of spheroids

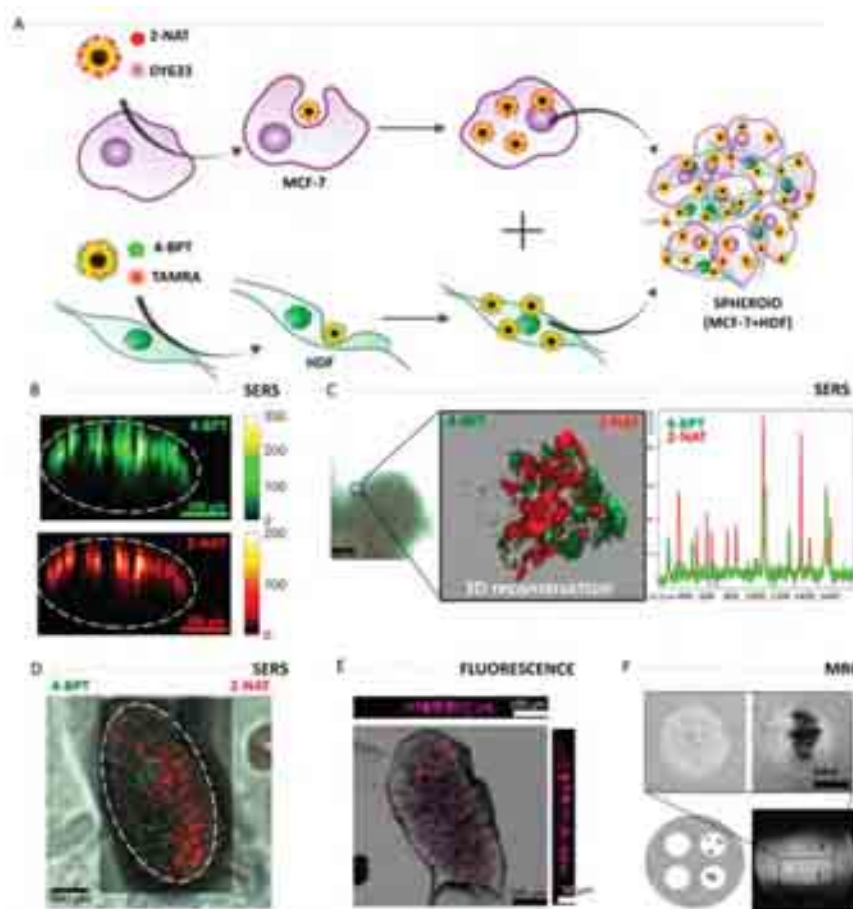


Figure 4. (A) Schematic illustration of spheroid preparation. MCF-7 and HDF cells were preincubated with IOAuNS@4-BPT@TAMRA and IOAuNS@2-NAT@DY633, respectively, prior to coculture into the spheroid. (B) SERS mapping along the xz plane of live spheroids showing pixels corresponding to 4-BPT (green) and 2-NAT (red). A total area of $800 \times 430 \mu\text{m}^2$ was imaged, with a resolution of $5 \times 10 \mu\text{m}^2$. Data were analyzed by multiple linear regression analysis (MLRA). The white dotted line highlights the edge of the spheroid. (C) SERS mapping and 3D reconstruction of a selected volume at the outer edge of a live spheroid (bright-field image also shown). A total volume of $84 \times 84 \times 70 \mu\text{m}^3$ (xyz) was probed, with a resolution of $2 \times 2 \times 5 \mu\text{m}^3$ (xyz). Data were analyzed by TCA. (D) SERS map of a transversal cut (area $360 \times 560 \mu\text{m}^2$, $50 \mu\text{m}$ in thickness) of a fixed and embedded spheroid, showing the presence of 4-BPT and 2-NAT positive pixels throughout the xy plane. Data were analyzed by MLRA. (E) Orthogonal projection collected by confocal fluorescence imaging of a transversal cut ($50 \mu\text{m}$ in thickness) through a fixed and embedded spheroid. (F) MRI images from spheroids, with (right-hand-side circles) and without (left-hand-side circles) IOAuNS, planted in a phantom.

comprising MCF7 cancer cells and fibroblasts (HDF) as a 3D model for multimodal imaging with IOAuNS. We initially pre-labeled the separate cell populations with two different RaR-labeled IOAuNS (from here on, we used IOAuNS-bII for further characterization), which were also fluorescently labeled to allow correlative confocal fluorescence microscopy. To do so, the PMA used to encapsulate IOAuNSs was chemically modified with TAMRA and DY633 fluorescent dyes (see structures in Figure S3 and optical characterization in Figure S4). 4-BPT and 2-NAT were used as Raman reporters, no significant changes in the intensity and the fingerprint of their SERS spectra were detected in the presence of the fluorescent dyes (Figure S19).

We selected 4-BPT and 2-NAT because they offer clearly distinguishable fingerprints and can be analyzed using multivariate methods (see Table S5 and Methods section for details) to differentiate more precisely cell populations in a coculture system. Thus, MCF7 cells were labeled with IOAuNS@4-BPT@TAMRA, and HDF cells with IOAuNS@2-NAT@DY633 (Figure S20). Spheroids were formed using

round-bottomed wells, using an initial seeding concentration of 1.7×10^4 cells/spheroid (total combined cells, mixed at a 1:1 ratio; see scheme in Figure 4A). Live SERS imaging of the whole spheroid was first performed to probe the overall location of the multimodal NPs. As shown in Figure 4B,C, whereas both RaRs can be clearly identified in the SERS maps, and 3D reconstructions can be obtained, IOAuNSs appear to be located only at the outer layer of the spheroid. Considering that spheroid-containing cells were pre-labeled with IOAuNSs, this result was unexpected—IOAuNSs should have been distributed throughout the entire spheroid volume. We thus examined a slice of the spheroid after fixation and microtome cutting by conducting SERS mapping and fluorescence confocal imaging on the central part of the spheroid. As can be observed in Figure 4D,E, this measurement confirmed the presence of both types of SERS-encoded NPs throughout the xy plane, suggesting that the lack of SERS signal in the center of the spheroid in live samples stemmed from limitations in the penetration depth of the incident laser, loss of laser focus, and backscattered signal to the spectrometer, principally due to the

large amount of IOAuNS in the sample, which cause absorption and diffuse multiple scattering of light. We subsequently examined the spheroids using MRI, by placing five spheroids per hole in the agarose phantoms. Contrast was clearly observed for the spheroids containing IOAuNS, with intense dark areas corresponding to the spheroids (Figure 4F).

To mimic a more realistic situation, a second model of IOAuNS–spheroid interaction was developed. When NPs are administered *in vivo* for imaging purposes, NP penetration into the site of interest is determined by various factors, including the enhanced permeation and retention (EPR) effect, the tumor microvasculature, and potential spatial inhomogeneities in the NP delivery. We thus formed the spheroids first (again comprising MCF7 and HDF cells) and subsequently exposed them to a mixture of IOAuNS@BPT@TAMRA and IOAuNS@2NAT@DY633 (Figure S21A). Because of the size of IOAuNS, some sedimentation was observed during the studied period. To avoid this issue, we incubated IOAuNS with spheroids inside Eppendorf tubes in a rotisserie rotator stored in an incubator at 37 °C overnight. We first conducted confocal and SERS imaging of the whole live spheroid, again to determine IOAuNS distribution (Figure S21B,C). Similar results were observed as in the previous experiment, with limited capacity to determine the distribution of the NPs in deeper buried layers. Although it appeared that NPs were only located at the outer edge of the spheroids, this could only be confirmed by fixing and making a transversal cut along the *xy* plane. Indeed, SERS imaging clearly showed the presence of IOAuNS at the outer 100 μm layer of the spheroid, with no signal recorded from the inner core (Figure S21D). Thus, we proved that IOAuNSs are suitable contrast agents for spheroid imaging, and although they do penetrate the complex 3D model, a certain limitation was found in the light penetration depth that can be achieved.

Correlative Imaging in an *Ex Vivo* Model. In our pursuit of increasing complexity of the biological model, the next step comprised implementing the NP contrast agents for multimodal imaging in *ex vivo* models. For this purpose, we chose to conduct intracerebral injections into an excised mouse brain. The brain is an organ that provides a tissue with homogeneous low-level background contrast in MRI and which is sufficiently large to apply multiple injections of different materials for comparison. Considering that we aimed at conducting SERS and fluorescence imaging on sliced tissue measuring a few tens of micrometers in thickness, MCF7 cells were chosen as the carriers of IOAuNS (using IOAuNS functionalized with 2-NAT and DY633 for SERS and fluorescence microscopy, respectively) because the injection of free IOAuNSs posed the problem of NPs diffusing into the tissue, inducing a significant reduction in SERS and fluorescence signals. First, MCF-7 cells were incubated overnight with IOAuNS@2-NAT@DY633, at a final total (Fe + Au) metal concentration of 0.05 mM, previously shown to be suitable for MRI imaging. Cells were trypsinized and concentrated to 2×10^6 cells/mL before injecting 5 μL into the right brain hemisphere. A second injection of IOAuNS@2-NAT@DY633, at the same estimated concentration in the cell-containing sample, was injected into the left hemisphere as a NP control. PBS buffer was also injected in the upper part of the brain as a media control. A schematic view of the layout is shown in Figure 5A. For MRI measurements, the entire brain was placed in the MRI scanner for imaging, whereas SERS and fluorescence images were obtained a posteriori, using the same brain tissue cut with a

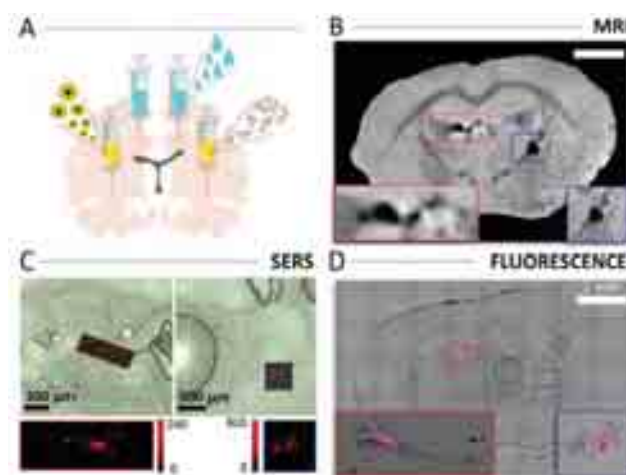


Figure 5. (A) Schematic illustration of different injections into a mouse brain, both with (right hemisphere; blue boxes in panels B–D) and without cells (left hemisphere; red boxes in panels B–D), as well as a PBS buffer control (top part of both left and right hemispheres). (B–D) Summary of results from MRI (B), SERS (C), and fluorescence (D) imaging.

microtome. As can be clearly observed in Figure 5B, MRI imaging shows dark contrast where the injections were performed. Both free IOAuNS and IOAuNS-endocytosed MCF7 cells were visible in multiple slices (see Figure S22). Subsequently, SERS and fluorescence imaging of brain tissue cuts demonstrated the suitability of these techniques for IOAuNS detection and mapping (Figure 5C,D). Whereas sample processing was arguably more complicated and laborious due to the numerous cuts to be made and sequential verification of positive signal, both techniques proved suitable for imaging of multimodal NPs at different spatial resolutions and concentrations.

CONCLUSIONS

We have developed a colloidal system comprising hybrid NPs with magnetic and plasmonic components, which can act as contrast agents for multimodal imaging, combining SERS, MRI, and fluorescence imaging. The NPs showed high versatility for imaging biological samples, ranging from 2D cell cultures to *ex vivo* models. We demonstrated that the overall particle size can be tuned by varying two key synthesis parameters, namely, the concentration of gold spheres used as the nucleation points upon adsorption on iron oxide cores and the added gold precursor for spike seeded growth. Through variation of these parameters, we achieved the fabrication of particles with different morphologies and sizes, which therefore display different optical properties. Whereas a low density of gold spheres on the surface of IONP cores leads to smaller final particles with incomplete gold shells and short tips, a higher Au NP density and higher concentration of HAuCl₄ in the seeded-growth reaction resulted in complete shell formation with well-defined spikes. The morphology of IOAuNS can thus be tuned accordingly and was optimized to obtain NPs with suitable properties for application in bioimaging. Whereas most published studies calculate the surface area of complex NPs for subsequent functionalization by assuming the volume of a sphere while using stars, we showed here a simple geometry model for realistic estimation of the surface area, which is more accurate toward efficient NP

functionalization, while a better description of the surface morphology can be reached when complemented with 3D tomography data. We applied the results of this model to the surface functionalization of IOAuNS with Raman-active molecules and fluorescent dyes and then demonstrated their noncytotoxic nature in MCF7 breast cancer and fibroblast cells. With regards to the multimodal imaging properties of the IOAuNSs, SERS signal enhancement was found to be largely dependent on their absorbance and the density of hot spots (tips), so that the best candidates for SERS were smaller NPs with complete gold shells and well-defined spikes (IOAuNS bII). MRI experiments demonstrated that all particles provided T2 contrast due to the γ -Fe₂O₃ magnetic cores, regardless of the presence of any further SERS or fluorescence functionalization. Furthermore, magnetic characterization of the NPs showed that the gold shell thickness did not affect the magnetic properties of the iron oxide cores. Both these aspects are particularly important for multimodal contrast agents, where the addition of one extra imaging component may hinder the efficacy of another. In summary, iron oxide–gold hybrid nanoparticles with controlled sizes were employed for SERS, MRI, and fluorescence imaging within complex biological models. The synthesized IOAuNSs can thus be used as an interesting alternative to conventional contrast agents, achieving valuable information from each imaging technique that could improve the accuracy of the actual diagnostic methods. These findings open up the possibility of expanding the use of multimodal NPs for combination of imaging with photothermal therapy and magnetic targeting of cells and tissues, thus achieving theranostic and imaging with the same NPs.

■ ASSOCIATED CONTENT

Supporting Information

The Supporting Information is available free of charge at <https://pubs.acs.org/doi/10.1021/acs.jpcc.2c06299>.

Additional characterization of IOAuNS, calculation of IOAuNS surface area, magnetic properties, polymer coating, SERS measurements, cellular uptake, cell viability, MRI experiments in 2D cell models, characterization of 3D cell models, and phantoms preparation (PDF)

■ AUTHOR INFORMATION

Corresponding Authors

Dorleta Jimenez de Aberasturi – CIC biomaGUNE, Basque Research and Technology Alliance (BRTA), 20014 Donostia-San Sebastián, Spain; Centro de Investigación Biomédica en Red, Bioingeniería, Biomateriales y Nanomedicina (CIBER-BBN), 20014 Donostia-San Sebastián, Spain; Ikerbasque - Basque Foundation for Science, 48009 Bilbao, Spain;

orcid.org/0000-0001-5009-3557;

Email: djimenezdeaberasturi@cicbiomagune.es

Luis M. Liz-Marzán – CIC biomaGUNE, Basque Research and Technology Alliance (BRTA), 20014 Donostia-San Sebastián, Spain; Centro de Investigación Biomédica en Red, Bioingeniería, Biomateriales y Nanomedicina (CIBER-BBN), 20014 Donostia-San Sebastián, Spain; Ikerbasque - Basque Foundation for Science, 48009 Bilbao, Spain; orcid.org/0000-0002-6647-1353; Email: llizmarzan@cicbiomagune.es

Authors

Cristina de la Encarnación – CIC biomaGUNE, Basque Research and Technology Alliance (BRTA), 20014 Donostia-San Sebastián, Spain; Department of Applied Chemistry, University of the Basque Country, 20018 Donostia-San Sebastián, Spain

Elisa Lenzi – CIC biomaGUNE, Basque Research and Technology Alliance (BRTA), 20014 Donostia-San Sebastián, Spain; Centro de Investigación Biomédica en Red, Bioingeniería, Biomateriales y Nanomedicina (CIBER-BBN), 20014 Donostia-San Sebastián, Spain

Malou Henriksen-Lacey – CIC biomaGUNE, Basque Research and Technology Alliance (BRTA), 20014 Donostia-San Sebastián, Spain; Centro de Investigación Biomédica en Red, Bioingeniería, Biomateriales y Nanomedicina (CIBER-BBN), 20014 Donostia-San Sebastián, Spain

Beatriz Molina – CIC biomaGUNE, Basque Research and Technology Alliance (BRTA), 20014 Donostia-San Sebastián, Spain; Present Address: Biobide Spain, Paseo Mikeletegi 56 Bajo, 20009 Donostia-San Sebastián, Spain

Kellie Jenkinson – EMAT and NANOLab Center of Excellence, University of Antwerp, 2020 Antwerp, Belgium

Ada Herrero – CIC biomaGUNE, Basque Research and Technology Alliance (BRTA), 20014 Donostia-San Sebastián, Spain; Centro de Investigación Biomédica en Red, Bioingeniería, Biomateriales y Nanomedicina (CIBER-BBN), 20014 Donostia-San Sebastián, Spain

Lorena Colás – CIC biomaGUNE, Basque Research and Technology Alliance (BRTA), 20014 Donostia-San Sebastián, Spain

Pedro Ramos-Cabrer – CIC biomaGUNE, Basque Research and Technology Alliance (BRTA), 20014 Donostia-San Sebastián, Spain; Ikerbasque - Basque Foundation for Science, 48009 Bilbao, Spain; orcid.org/0000-0003-0368-7031

Jhoan Toro-Mendoza – CIC biomaGUNE, Basque Research and Technology Alliance (BRTA), 20014 Donostia-San Sebastián, Spain; orcid.org/0000-0003-4916-7445

Iñaki Orue – SGIKER, Servicios Generales de Investigación, University of the Basque Country, 48940 Leioa, Spain

Judith Langer – CIC biomaGUNE, Basque Research and Technology Alliance (BRTA), 20014 Donostia-San Sebastián, Spain; Centro de Investigación Biomédica en Red, Bioingeniería, Biomateriales y Nanomedicina (CIBER-BBN), 20014 Donostia-San Sebastián, Spain; orcid.org/0000-0003-3527-5728

Sara Bals – EMAT and NANOLab Center of Excellence, University of Antwerp, 2020 Antwerp, Belgium; orcid.org/0000-0002-4249-8017

Complete contact information is available at: <https://pubs.acs.org/10.1021/acs.jpcc.2c06299>

Notes

The authors declare no competing financial interest.

■ ACKNOWLEDGMENTS

The authors acknowledge financial support from the European Research Council (ERC-AdG-2017, 787510) and MCIN/AEI/10.13039/501100011033 through grants PID2019-108854RA-I00 and Maria de Maeztu Unit of Excellence No. MDM-2017-0720. S.B. and K.J. acknowledge financial support from the European Commission under the Horizon 2020

Programme by Grant No. 823717 (ESTEEM3) and ERC Consolidator Grant No. 815128 (REALNANO).

REFERENCES

- (1) Ashammakhi, N.; Ahadian, S.; Darabi, M. A.; El Tahchi, M.; Lee, J.; Suthiwanich, K.; Sheikhi, A.; Dokmeci, M. R.; Oklu, R.; Khademhosseini, A. Minimally Invasive and Regenerative Therapeutics. *Adv. Mater.* **2019**, *31*, 1804041.
- (2) Louie, A. Multimodality Imaging Probes: Design and Challenges. *Chem. Rev.* **2010**, *110*, 3146–3195.
- (3) Lee, D. E.; Koo, H.; Sun, I. C.; Ryu, J. H.; Kim, K.; Kwon, I. C. Multifunctional Nanoparticles for Multimodal Imaging and Theragnosis. *Chem. Soc. Rev.* **2012**, *41*, 2656–2672.
- (4) Alvares, R. D. A.; Szulc, D. A.; Cheng, H. L. M. A Scale to Measure MRI Contrast Agent Sensitivity. *Sci. Rep.* **2017**, *7*, 15493.
- (5) Pierce, M. C.; Javier, D. J.; Richards-Kortum, R. Optical Contrast Agents and Imaging Systems for Detection and Diagnosis of Cancer. *Int. J. Cancer* **2008**, *123*, 1979–1990.
- (6) Hou, W.; Xia, F.; Alfranca, G.; Yan, H.; Zhi, X.; Liu, Y.; Peng, C.; Zhang, C.; de la Fuente, J. M.; Cui, D. Nanoparticles for Multimodality Cancer Diagnosis: Simple Protocol for Self-Assembly of Gold Nanoclusters Mediated by Gadolinium Ions. *Biomaterials* **2017**, *120*, 103–114.
- (7) Betzer, O.; Perets, N.; Angel, A.; Motiei, M.; Sadan, T.; Yadid, G.; Offen, D.; Popovtzer, R. In Vivo Neuroimaging of Exosomes Using Gold Nanoparticles. *ACS Nano* **2017**, *11*, 10883–10893.
- (8) Rastinehad, A. R.; Anastos, H.; Wajswol, E.; Winoker, J. S.; Sfakianos, J. P.; Doppalapudi, S. K.; Carrick, M. R.; Knauer, C. J.; Taouli, B.; Lewis, S. C.; Tewari, A. K.; Schwartz, J. A.; Canfield, S. E.; George, A. K.; West, J. L.; Halas, N. J. Gold Nanoshell-Localized Photothermal Ablation of Prostate Tumors in a Clinical Pilot Device Study. *Proc. Natl. Acad. Sci. U. S. A.* **2019**, *116*, 18590–18596.
- (9) Lenzi, E.; Jimenez de Aberasturi, D.; Liz-Marzán, L. M. Surface-Enhanced Raman Scattering Tags for Three-Dimensional Bioimaging and Biomarker Detection. *ACS Sens.* **2019**, *4*, 1126–1137.
- (10) Jimenez de Aberasturi, D.; Serrano-Montes, A. B.; Langer, J.; Henriksen-Lacey, M.; Parak, W. J.; Liz-Marzán, L. M. Surface Enhanced Raman Scattering Encoded Gold Nanostars for Multiplexed Cell Discrimination. *Chem. Mater.* **2016**, *28*, 6779–6790.
- (11) García-Astrain, C.; Lenzi, E.; Jimenez de Aberasturi, D.; Henriksen-Lacey, M.; Binelli, M. R.; Liz-Marzán, L. M. 3D-Printed Biocompatible Scaffolds with Built-In Nanoplasmonic Sensors. *Adv. Funct. Mater.* **2020**, *30*, 2005407.
- (12) Reguera, J.; Jiménez De Aberasturi, D.; Henriksen-Lacey, M.; Langer, J.; Espinosa, A.; Szczupak, B.; Wilhelm, C.; Liz-Marzán, L. M. Janus Plasmonic-Magnetic Gold-Iron Oxide Nanoparticles as Contrast Agents for Multimodal Imaging. *Nanoscale* **2017**, *9*, 9467–9480.
- (13) Zhou, Z.; Yang, L.; Gao, J.; Chen, X. Structure-Relaxivity Relationships of Magnetic Nanoparticles for Magnetic Resonance Imaging. *Adv. Mater.* **2019**, *31*, 1804567.
- (14) Wang, G.; Gao, W.; Zhang, X.; Mei, X. Au Nanocage Functionalized with Ultra-Small Fe₃O₄ Nanoparticles for Targeting T1-T2 Dual MRI and CT Imaging of Tumor. *Sci. Rep.* **2016**, *6*, 28258.
- (15) Zeng, J.; Gong, M.; Wang, D.; Li, M.; Xu, W.; Li, Z.; Li, S.; Zhang, D.; Yan, Z.; Yin, Y. Direct Synthesis of Water-Dispersible Magnetic/Plasmonic Heteronanostructures for Multimodality Biomedical Imaging. *Nano Lett.* **2019**, *19*, 3011–3018.
- (16) Wang, W.; Hao, C.; Sun, M.; Xu, L.; Xu, C.; Kuang, H. Spiky Fe₃O₄@Au Supraparticles for Multimodal in Vivo Imaging. *Adv. Funct. Mater.* **2018**, *28*, 1800310.
- (17) Jeon, M.; Halbert, M. V.; Stephen, Z. R.; Zhang, M. Iron Oxide Nanoparticles as T1 Contrast Agents for Magnetic Resonance Imaging: Fundamentals, Challenges, Applications, and Prospectives. *Adv. Mater.* **2021**, *33*, 1906539.
- (18) Quintanilla, M.; Henriksen-lacey, M.; Renero-Lecuna, C.; Liz-Marzán, L. M. Challenges for Optical Nanothermometry in Biological Environments. *Chem. Soc. Rev.* **2022**, *51*, 4223–4242.
- (19) Kouhpanji, M. R. Z.; Stadler, B. J. H. A Guideline for Effectively Synthesizing and Characterizing Magnetic Nanoparticles for Advancing Nanobiotechnology: A Review. *Sensors* **2020**, *20*, 2554.
- (20) Li, J.; Hu, Y.; Yang, J.; Wei, P.; Sun, W.; Shen, M.; Zhang, G.; Shi, X. Hyaluronic Acid-Modified Fe₃O₄ at Au Core/Shell Nanostars for Multimodal Imaging and Photothermal Therapy of Tumors. *Biomaterials* **2015**, *38*, 10–21.
- (21) Hou, X.; Wang, X.; Liu, R.; Zhang, H.; Liu, X.; Zhang, Y. Facile Synthesis of Multifunctional Fe₃O₄@SiO₂@Au Magneto-Plasmonic Nanoparticles for MR/CT Dual Imaging and Photothermal Therapy. *RSC Adv.* **2017**, *7*, 18844–18850.
- (22) Tomitaka, A.; Arami, H.; Ahmadivand, A.; Pala, N.; McGoron, A. J.; Takemura, Y.; Febo, M.; Nair, M. Magneto-Plasmonic Nanostars for Image-Guided and NIR-Triggered Drug Delivery. *Sci. Rep.* **2020**, *10*, 10115.
- (23) Hemery, G.; Keyes, A. C.; Garaio, E.; Rodrigo, I.; Garcia, J. A.; Plazaola, F.; Garanger, E.; Sandre, O. Tuning Sizes, Morphologies, and Magnetic Properties of Monocore versus Multicore Iron Oxide Nanoparticles through the Controlled Addition of Water in the Polyol Synthesis. *Inorg. Chem.* **2017**, *56*, 8232–8243.
- (24) Mehdipour, M.; Gloag, L.; Lian, J.; Tilley, R. D.; Gooding, J. J. Zero-Valent Iron Core-Iron Oxide Shell Nanoparticles Coated with Silica and Gold with High Saturation Magnetization. *Chem. Commun.* **2021**, *57*, 13142–13145.
- (25) Kolosnjaj-Tabi, J.; Javed, Y.; Lartigue, L.; Volatron, J.; Elgrabli, D.; Marangon, I.; Pugliese, G.; Caron, B.; Figuerola, A.; Luciani, N.; Pellegrino, T.; Alloyeau, D.; Gazeau, F. The One Year Fate of Iron Oxide Coated Gold Nanoparticles in Mice. *ACS Nano* **2015**, *9*, 7925–7939.
- (26) Gavilán, H.; Sánchez, E. H.; Brollo, M. E. F.; Asín, L.; Moerner, K. K.; Frandsen, C.; Lázaro, F. J.; Serna, C. J.; Veintemillas-Verdaguer, S.; Morales, M. P.; Gutiérrez, L. Formation Mechanism of Maghemite Nanoflowers Synthesized by a Polyol-Mediated Process. *ACS Omega* **2017**, *2*, 7172–7184.
- (27) Jana, N. R.; Gearheart, L.; Murphy, C. J. Seeding Growth for Size Control of 5–40 nm Diameter Gold Nanoparticles. *Langmuir* **2001**, *17*, 6782–6786.
- (28) Zou, F.; Ding, Q.; Tran, V. T.; Wang, G.; Zhang, Y.; Kang, S.; Lee, J.; Zhou, H. Magnetically Recyclable Catalytic Activity of Spiky Magneto-Plasmonic Nanoparticles. *RSC Adv.* **2015**, *5*, 56653–56657.
- (29) Pellegrino, T.; Manna, L.; Kudera, S.; Liedl, T.; Koktysh, D.; Rogach, A. L.; Keller, S.; Radler, J.; Natile, G.; Parak, W. J. Hydrophobic Nanocrystals Coated with an Amphiphilic Polymer Shell: A General Route to Water Soluble Nanocrystals. *Nano Lett.* **2004**, *4*, 703–707.
- (30) Jimenez de Aberasturi, D.; Henriksen-Lacey, M.; Litti, L.; Langer, J.; Liz-Marzán, L. M. Using SERS Tags to Image the Three-Dimensional Structure of Complex Cell Models. *Adv. Funct. Mater.* **2020**, *30*, 1909655.
- (31) Lenzi, E.; Henriksen-lacey, M.; Molina, B.; Langer, J.; de Albuquerque, C. D. L.; Jimenez de Aberasturi, D.; Liz-Marzán, L. M. Combination of Live Cell Surface-Enhanced Raman Scattering Imaging with Chemometrics to Study Intracellular Nanoparticle Dynamics. *ACS Sens.* **2022**, *7*, 1747–1756.
- (32) Lartigue, L.; Hugounenq, P.; Alloyeau, D.; Clarke, S. P.; Lévy, M.; Bacri, J. C.; Bazzi, R.; Brougham, D. F.; Wilhelm, C.; Gazeau, F. Cooperative Organization in Iron Oxide Multi-Core Nanoparticles Potentiates Their Efficiency as Heating Mediators and MRI Contrast Agents. *ACS Nano* **2012**, *6*, 10935–10949.
- (33) Turkevich, J. Colloidal Gold. Part I - Historical and Preparative Aspects, Morphology and Structure. *Gold Bull.* **1985**, *18*, 86–91.
- (34) Bertuit, E.; Benassai, E.; Meriguet, G.; Greneche, J. M.; Baptiste, B.; Neveu, S.; Wilhelm, C.; Abou-Hassan, A. Structure-Property-Function Relationships of Iron Oxide Multicore Nanoflowers in Magnetic Hyperthermia and Photothermia. *ACS Nano* **2022**, *16*, 271–284.
- (35) Shafi, K. V. P. M.; Ulman, A.; Dyal, A.; Yan, X.; Yang, N. L.; Estournès, C.; Fournès, L.; Wattiaux, A.; White, H.; Rafailovich, M.

Magnetic Enhancement of γ -Fe₂O₃ Nanoparticles by Sonochemical Coating. *Chem. Mater.* **2002**, *14*, 1778–1787.

(36) Kucheryavy, P.; He, J.; John, V. T.; Maharjan, P.; Spinu, L.; Goloverda, G. Z.; Kolesnichenko, V. L. Superparamagnetic Iron Oxide Nanoparticles with Variable Size and an Iron Oxidation State as Prospective Imaging Agents. *Langmuir* **2013**, *29*, 710–716.

(37) Yadav, B. S.; Singh, R.; Vishwakarma, A. K.; Kumar, N. Facile Synthesis of Substantially Magnetic Hollow Nanospheres of Maghemite (γ -Fe₂O₃) Originated from Magnetite (Fe₃O₄) via Solvothermal Method. *J. Supercond. Nov. Magn.* **2020**, *33*, 2199–2208.

(38) Serrano-Montes, A. B.; Jimenez de Aberasturi, D.; Langer, J.; Giner-Casares, J. J.; Scarabelli, L.; Herrero, A.; Liz-Marzán, L. M. A General Method for Solvent Exchange of Plasmonic Nanoparticles and Self-Assembly into SERS-Active Monolayers. *Langmuir* **2015**, *31*, 9205–9213.

(39) Rodríguez-Lorenzo, L.; Alvarez-Puebla, R. A.; Pastoriza-Santos, I.; Mazzucco, S.; Stéphan, O.; Kociak, M.; Liz-Marzán, L. M.; García de Abajo, F. J. Zeptomol Detection through Controlled Ultrasensitive Surface-Enhanced Raman Scattering. *J. Am. Chem. Soc.* **2009**, *131*, 4616–4618.

(40) LaConte, L. E. W.; Nitin, N.; Zurkiya, O.; Caruntu, D.; O'Connor, C. J.; Hu, X.; Bao, G. Coating Thickness of Magnetic Iron Oxide Nanoparticles Affects R2 Relaxivity. *J. Magn. Reson. Imaging* **2007**, *26*, 1634–1641.

(41) Zhou, H.; Tang, J.; Li, J.; Li, W.; Liu, Y.; Chen, C. In Vivo Aggregation-Induced Transition between T1 and T2 Relaxations of Magnetic Ultra-Small Iron Oxide Nanoparticles in Tumor Microenvironment. *Nanoscale* **2017**, *9*, 3040–3050.

(42) Wang, Y.; Li, X.; Chen, P.; Dong, Y.; Liang, G.; Yu, Y. Enzyme-Instructed Self-Aggregation of Fe₃O₄ Nanoparticles for Enhanced MRI T2 Imaging and Photothermal Therapy of Tumors. *Nanoscale* **2020**, *12*, 1886–1893.

(43) Costa, E. C.; Moreira, A. F.; de Melo-Diogo, D.; Gaspar, V. M.; Carvalho, M. P.; Correia, I. J. 3D Tumor Spheroids: An Overview on the Tools and Techniques Used for Their Analysis. *Biotechnol. Adv.* **2016**, *34*, 1427–1441.

(44) Pulagam, K. R.; Henriksen-Lacey, M.; Uribe, K. B.; Renero-Lecuna, C.; Kumar, J.; Charalampopoulou, A.; Facoetti, A.; Protti, N.; Gómez-Vallejo, V.; Baz, Z.; Kumar, V.; Sánchez-Iglesias, A.; Altieri, S.; Cossio, U.; Di Silvio, D.; Martínez-Villacorta, A. M.; Ruiz de Angulo, A.; Rejc, L.; Liz-Marzán, L. M.; Llop, J. In Vivo Evaluation of Multifunctional Gold Nanorods for Boron Neutron Capture and Photothermal Therapies. *ACS Appl. Mater. Interfaces* **2021**, *13*, 49589–49601.

Recommended by ACS

Efficient Magneto-Luminescent Nanosystems based on Rhodamine-Loaded Magnetite Nanoparticles with Optimized Heating Power and Ideal Thermosensitive Fluorescence

Idoia Castellanos-Rubio, Maite Insausti, *et al.*

OCTOBER 27, 2022

ACS APPLIED MATERIALS & INTERFACES

READ 

Insights into the Effect of Magnetic Confinement on the Performance of Magnetic Nanocomposites in Magnetic Hyperthermia and Magnetic Resonance Imaging

Stefania Scialla, Juan Gallo, *et al.*

NOVEMBER 07, 2022

ACS APPLIED NANO MATERIALS

READ 

Coordination-Driven Self-Assembly of Iron Oxide Nanoparticles for Tumor Microenvironment-Responsive Magnetic Resonance Imaging

Jinhong Hou, Leyu Wang, *et al.*

NOVEMBER 03, 2022

ANALYTICAL CHEMISTRY

READ 

Magnetic Mesoporous Silica Nanorods Loaded with Ceria and Functionalized with Fluorophores for Multimodal Imaging

Jan Grzelak, Martí Gich, *et al.*

FEBRUARY 10, 2022

ACS APPLIED NANO MATERIALS

READ 

Get More Suggestions >

